THE CONSOLIDATION BEHAVIOUR OF GASSY SOIL

A thesis submitted to

The University of Oxford

by

Stephen David Thomas M.Sc.

Jesus College

for

The Degree of Doctor of Philosophy

Trinity 1987

To my wife Jane

Theory not founded on practice is empty; practice uninformed by theory is blind.

(Sam Watson, Jr.)

The Consolidation Behaviour of Gassy Soil

by

Stephen D. Thomas

Jesus College

A thesis submitted to the University of Oxford
for the degree of Doctor of Philosophy

Trinity 1987

ABSTRACT

The consolidation behaviour of gassy soil has been studied in a programme of experimental and theoretical research.

This research is of particular importance to the offshore geotechnical industry as the presence of gas in the seabed can have a dramatic effect on the material properties of a marine sediment. Initial numerical modelling based on existing unsaturated soil theory combining the gas and the water phase into a compressible fluid in the pores of a compressible soil skeleton failed to simulate the soil behaviour previously observed experimentally at Oxford. Therefore, there was scope for further study in this field.

Chapters 2 to 4 describe the experimental preparation, consolidation technique and experimental results of the two series of tests on artificially prepared gassy soil samples. The results of these tests indicated that the gas appeared to be affected by the total stress rather than the pore water pressure, with the saturated soil matrix outside the gas voids being controlled by the consolidation stress.

Chapter 5 presents the one-dimensional numerical modelling of the experimental results. Poor simulations were again made using compressible fluid theory. Treating the gas as compressible solid inclusions embedded in a saturated soil matrix, however, resulted in excellent simulations of the observed pore water pressures and settlements. Chapter 6 attempts to explain the results of the experimental and numerical modelling in terms of elastic and plastic soil behaviour. This includes the introduction to the double compressibility model in which the deformation behaviour of the saturated matrix is governed by changes in consolidation stress, whereas that of the gas is governed by changes in total stress.

Chapter 7 presents the development of the governing gassy soil consolidation equations under both plane strain and axisymmetric conditions. Chapter 8 describes the approximation of the governing consolidation equations using the Galerkin finite element method in terms of nodal displacements and pore water pressures. The resulting finite element approximation is subsequently formulated for rectangular elements under plane strain and axisymmetric conditions in Chapter 9.

The remainder of the thesis describes the structure of the finite element model DCFEM2 and the constitutive relationships that are required for such a model. The code is verified with existing analytical solutions and then is used to simulate the observed gassy soil behaviour under laboratory and field conditions.

ACKNOWLEDGEMENTS

In finally reaching the stage where this thesis can be placed between two covers, my thanks are due to a number of people who have played a significant role in helping it to take shape.

Firstly, I am indebted to my supervisor, Dr. Gilliane C. Sills, who not only helped me to focus my ideas and find direction in the initial stages of the research, but also provided continuing advice and support throughout. I am sincerely grateful for the time she devoted to technical discussions of my work, and for her ability to know when it was best to stand back and when best to intervene. As well as her commitment to her students on both a personal and professional level, Dr. Sills has created an environment conducive to research. The team she has built up, comprising students and research and technical staff, proved to be a motivating force and I have benefitted enormously from being one of its members.

Indeed, I would like to thank all the other members of the soil mechanics group for the help they have extended to me. Although I cannot mention them all by name, I trust they know who they are and how grateful I am.

For helping me to put my work into a presentable form, my thanks are due to Miss Sukie Clarke for her patience and skill in typing the manuscript--which was not an easy task by any means. The help of Miss Karen Smart, particularly in typing the figure legends, was also invaluable. Moreover, a special mention must go to the staff in the Photographic and Reprographic Departments for their professionalism and care in reproducing this thesis.

I would also like to acknowledge the financial support of the Science and Engineering Research Council and the CASE Award provided by Fugro Ltd. which made my research possible in the first place. Apart from the financial aid, the latter gave me the opportunity to gain some valuable experience within industry.

In addition, I am grateful to Jesus College for the support given during my studies and the additional funding provided at the end to assist me whilst writing up. I would especially like to express my thanks to Mr John Ward for his moral support and encouragement throughout.

Finally, I would like to thank my family and friends for being there and helping me through. In particular, it was my wife Jane who believed in me and helped me to have faith in myself and my own ideas.

Without the help of all the above, I would not now be in a position to present to the reader the results of my thinking and my research. I am indeed, truly grateful.

TABLE OF CONTENTS

LIST OF FIGURES

LIST OF FIGURES (CONTINUED)

LIST OF FIGURES (CONTINUED)

LIST OF FIGURES (CONTINUED)

LIST OF TABLES

LIST OF PLATES

LIST OF NOTES

NOTATION

a	Internal radius of hollow sphere
a	Half width of ellipsoidal gas void
A	Cross-sectional area of sample
A_r	Aspect ratio of gas void [width/height]
c	Half height of ellipsoidal gas void
c_k	Compressibility of fluid phase k
c_h	Coefficient of consolidation in horizontal direction
c_v	Coefficient of consolidation in vertical direction
C_c	Compression index
d	Total derivative
e_j	Unit gravitational vector
e_c	Compressible solid void ratio, $[v_c/v_s]$
e_g	Gas void ratio, $[v_g/v_s]$
e^*_g	Normalized gas void ratio
e_t	Total void ratio, $[(v_g + v_w)/v_s]$
e_w, e_m	Water or matrix void ratio, $[v_w/v_s]$
e^{100}	Void ratio at an average vertical effective stress of 100 kPa
E	Young's modulus
f_o	Initial volume fraction of gas voids
F_i	Body force vector
g	Acceleration due to gravity
G_u, G_d	Undrained/Drained shear modulus of saturated soil
G^o_u, G^o_d	Undrained/Drained shear modulus associated with the gas phase
G'_u, G'_d	Undrained/Drained shear modulus associated with the soil matrix
h	Thickness of soil sample
h_o	Initial thickness of soil sample
h_{50}	Height of sample at time, t_{50}
H	Henry's coefficient of solubility
I_r	Rigidity index, $[G_u/s_u]$
k	Soil permeability

k^i	Intrinsic permeability
k_{ij}	Permeability tensor
k_h	Horizontal permeability
k_{rw}	Relative permeability, $[k/k_{sat}]$
k_{sat}	Saturated soil permeability
k_v	Vertical permeability
K_u, K_d	Undrained/Drained bulk modulus of saturated soil
K_u^o, K_d^o	Undrained/Drained bulk modulus associated with the gas phase
K_u', K_d'	Undrained/Drained bulk modulus associated with the soil matrix
K_o	Coefficient of earth pressure at rest
L	Width of rectangular finite element
M	Height of rectangular finite element
m_m	Mean coefficient of volume change
m_v	Vertical coefficient of volume change
M_g	Gas Mobility
M_w	Water Mobility
M_r	Mobility ratio $[M_g/M_w]$
n	Constant in non-linear elastic stress-strain relationship
n_g	Porosity of gas phase $[v_g/(v_s + v_w + v_g)]$
n_w	Porosity of water phase $[v_w/(v_s + v_w + v_g)]$
N_i	Finite element shape function
p	Mean normal stress
p′	Mean normal effective stress
p_c	Capillary pressure, $[u_g - u_w]$
P_i	Internal isotropic stress
P_o	External isotropic stress
q	Deviator stress
q_{max}	Maximum value of deviator stress
r	Radial axis
R	External radius of hollow sphere
R_c	Radius of curvature of gas-water meniscus
R_p	Particle radius

S, S_w	Water saturation, $[v_w/(v_w + v_g)]$
S_g	Gas saturation, $[v_g/(v_w + v_g)]$
s_u	Undrained shear strength
t	Time
t_{50}	Time at which 50% of consolidation has occurred
T	Surface tension between methane and water
u_a	Atmospheric pressure
u_g	Gas pressure
u_g^*	Absolute gas pressure, $[u_g + u_a]$
u_w	Pore water pressure
u_w'	Excess pore water pressure
$\bar{u}_w$	Average pore water pressure
U	Dimensionless pore water pressure, $[2c_v \Delta u/Ah^2]$
v_g	Volume of gas
v_s	Volume of solid soil particles
v_w	Volume of pore water
V_{gi}	Gas velocity vector
V_{si}	Solid velocity vector
V_{wi}	Water velocity vector
w_i	Total displacement vector
W_i	Darcy velocity vector, $[n_w(V_w - V_s)]$
x_i	Cartesian axes
z	vertical axis
α	Stress transfer coefficient
γ_f	Specific weight of fluid, f
γ_w	Specific weight of water
δ_{ij}	Kronecker delta, [1 for i=j; 0 for i≠j]
∂	Partial derivative
ε	Deviator strain, $2(\varepsilon_1 - \varepsilon_3)/3$
ε_1	Axial strain
ε_3	Radial strain
ε_{ij}	Total strain tensor

ε^{o}_{ij}	Strain associated with gas deformation
ε'_{ij}	Strain associated with soil matrix deformation
χ	Bishop's coefficient for partly saturated soils
λ	Lame's elastic constant
μ_g	Dynamic viscosity of gas
μ_w	Dynamic viscosity of water
ν	Poisson's Ratio
ρ_g	Gas density
ρ_w	Water density
σ_h	Horizontal total stress
σ'_h	Horizontal consolidation stress, $[\sigma_h - u_w]$
σ_m	Mean total stress
σ'_m	Mean consolidation stress, $[\sigma_m - u_w]$
σ_v	Vertical total stress
σ'_v	Vertical consolidation stress, $[\sigma_v - u_w]$
σ_{ij}	Total stress tensor
σ'_{ij}	Consolidation stress tensor, $[\sigma_{ij} - u_w\delta_{ij}]$
τ	Dimensionless time, $[c_v t/h^2]$ or $[4Ktk/\gamma_w r^2]$
τ_{oct}	Octahedral shear stress
ξ	Horizontal local coordinate
η	Vertical local coordinate
ζ	Dimensionless distance into sample, [z/h]

CHAPTER 1

INTRODUCTION

1.1 Introduction to Gassy Soil

1.2 The Behaviour of Unsaturated Marine Soils

1.3 The Volume Change Behaviour of Unsaturated Soils

1.4 The Consolidation Behaviour of Unsaturated Soils

1.5 Research Performed at Oxford

- 1.5.1 Early work
- 1.5.2 The work of Nageswaran (1983)
- 1.5.3 The work of Wheeler (1986)

1.6 Engineering Definitions Associated with Gassy Soils

1.7 Aims and Objectives of Research

1.8 Initial Numerical Modelling

- 1.8.1 Model 1
- 1.8.2 Model 2
- 1.8.3 Model 3

1.9 Summary

CHAPTER 1

INTRODUCTION

1.1 Introduction to Gassy Soil

The dramatic increase in offshore activity in recent years has led to the demand for further understanding of marine soils and the specific engineering problems related to such soils. These problems include high rates of sediment deposition or scour producing possible different soil profiles before and after construction, dynamic loading effects due to tidal or storm loading and recently, the discovery of undissolved gas in the seabed. The presence of free gas in the seabed poses a difficult problem to the soils engineer, for although a particular design criterion may be based on undrained soil conditions, due to the compressibility of the gas, this undrained process cannot be assumed to be a no volume change condition as is the case for a fully saturated soil.

Although unsaturated soils are present onshore, the pore gas is almost always air with the pores generally connected to each other and continuing in this state to the surface of the soil, therefore producing a uniform atmospheric pore gas pressure throughout. In unsaturated marine soils, however, the gas is most commonly methane and originates from within the soil rather than from a source outside the soil domain. In addition, the degrees of saturation of an unsaturated marine soil normally lie in the range of 0.85 to 1.0. Under these conditions the gas exists in discrete occluded bubbles with no connection between them. Nageswaran (1983) describes this type of soil as a "gassy soil", a definition limited at present to marine sediments.

The structure of this type of soil can vary significantly depending on the relative sizes of the gas bubbles and the soil grains. Wheeler (1986) presents two extreme cases of the possible structure of a gassy soil. Figure 1.1a depicts the case in which the pore gas exists in numerous small bubbles within the pores of the soil matrix, whereas Figure 1.1b presents an alternative soil structure in which the fewer gas bubbles are much larger than the soil grains. Terzaghi (1944) terms the gas in the second of these options "gas voids"--as opposed to "gas bubbles" for the first case. The structure of the soil in this

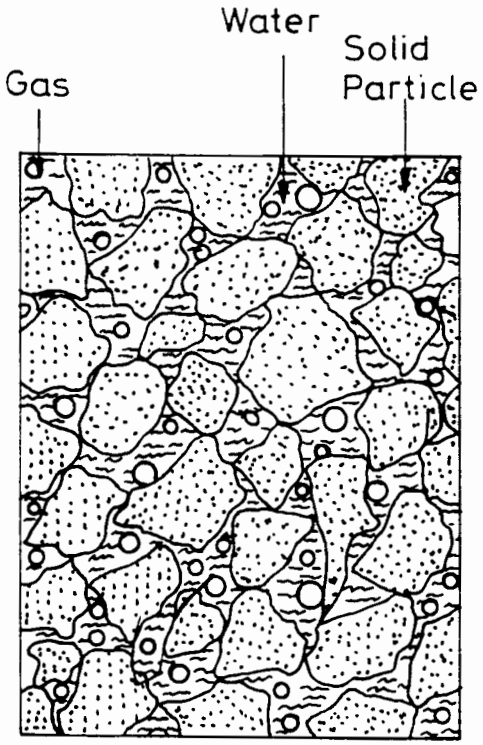

Gas bubbles much smaller than soil particles

Figure 1.1a

Unsaturated soil idealized as a compressible fluid in a soil matrix (Wheeler, 1986)

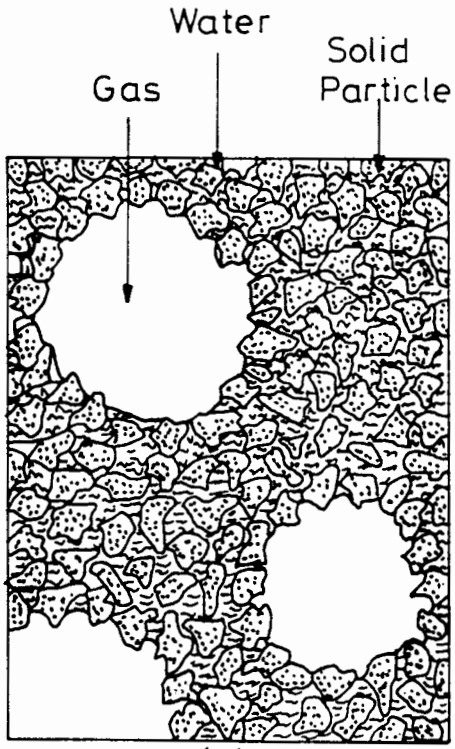

Gas bubbles much larger than soil particles

Figure 1.1b

Unsaturated soil idealized as large gas voids in a saturated soil matrix (Wheeler, 1986)

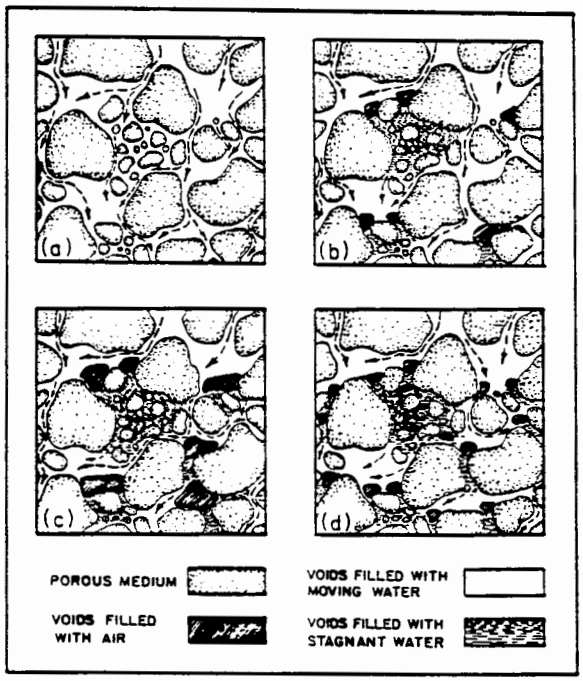

Distribution of air and water in a porous medium; (a) voids saturated with water; (b) five per cent air in voids; (c) ten per cent air in voids (large voids only); (d) ten per cent air in voids (all void sizes affected)

Figure 1.2 Conceptual model of an unsaturated soil for varying degrees of saturation (Orlob and Radhakrishna, 1958)

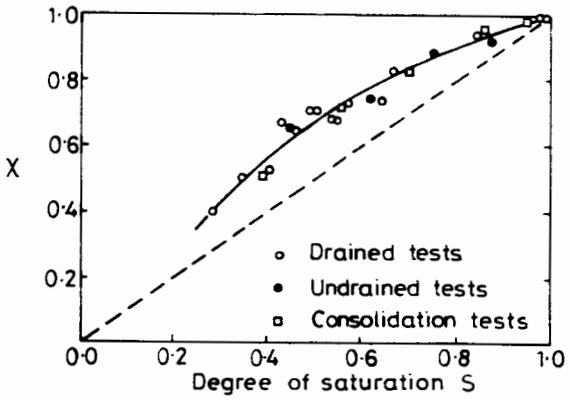

Figure 1.3

Experimental values of χ for Braehead silt (Bishop and Donald, 1961)

second instance (termed "the large bubble model" by Wheeler), somewhat resembles that of a Swiss cheese with the discrete gas voids surrounded by a saturated soil matrix. From photographic and experimental evidence produced at Oxford, it appears that a gassy soil takes the form of the second type of unsaturated soil.

1.2 The Behaviour of Unsaturated Marine Soils

The gas found in the seabed may come from three sources. The first is vulcanogenic gas which is produced by submarine volcanic or geothermal processes. The second is thermogenic gas which is produced by the diffusion of gas upward from a depth where it was originally produced by thermal cracking of the complex organic compounds. The vast majority of the gas in the seabed, however, is methane, which is produced by biogenic bacterical activity on organic matter under anaerobic conditions. The gas produced by this process is known as biogenic gas. In general, there is a depth below the surface of the seabed where methane does not appear as the sediment in this region contains dissolved oxygen in the pore water, thereby allowing only aerobic reduction to occur with no production of methane. Claypool and Kaplan (1974) observed that this depth can be up to two metres below the mudline. However, Kanwisher (1962) stated that although there can be up to a one metre depth where aerobic reduction takes place, the dissolved oxygen is ultimately used up allowing anaerobic reduction to take over. This would leave only an aerobic layer in the order of 1 cm below which anaerobic reduction could occur allowing methane production in sufficiently large quantities for an unsaturated marine soil to be formed. As the depth increases, however, the amount of methane is limited by the availability of organic matter. This process is described in more detail by Nageswaran (1983) and by Claypool and Kaplan (1974).

Therefore, from the above description of the origin of marine gas, it is not surprising to find that unsaturated marine sediments occur in regions of high organic deposition such as the mouths of rivers, river estuaries or river deltas. A good example of a region of an unsaturated marine soil caused by high organic deposition is the Mississippi Delta where much work has been carried out on the behaviour of the unsaturated sediment in that area (Whelan et al., 1976).

However, there have been reports of other areas of gassy sediment not immediately associated with high organic deposits such as the North Sea (Fannin, 1979). Other regions of gassy marine sediments include offshore areas of British Columbia, New Zealand, the Thames Estuary and the British Channel.

Apart from direct sampling, the presence of gas in marine soil can be detected using acoustic measurements (Anderson and Hampton, 1980). Bubbles of gas in a soil produce a dramatic attenuation of acoustic signals so that regions of gassy sediment appear as dark patches in the seismic records. The phenomenon is known as acoustic blanking or acoustic turbidity and is caused by the absorption of most of the energy by the gas bubbles.

The measurement of the quantity of the gas on the seabed, however, is more difficult than the detection of it. The technique used at present to quantify the amount of gas in the seabed is direct sampling or coring. Unfortunately, as the core is brought to the surface from the seabed, there is a large increase in the volume of the sample. This is due to the large reduction in total stress, pore water pressure and pore gas pressure which causes not only expansion of the gas, but also the exsolution of dissolved gas from the pore water. This increase in volume can be seen as the samples appear to "grow" out of the core liners, followed by the escape of large volumes of pore gas to the atmosphere (Esrig and Kirby, 1977). In order to evaluate the in situ saturation of the soil, it is necessary to minimize the loss of gas during sampling as the measurement of the saturation of the recovered sample is critical to the calculation. To calculate the in situ gas content from a combination of Boyle's gas law and Henry's law of solubility, an estimate of the in situ gas pressure must be made. The normal estimate made is that the pore gas pressure is equal to the pore water pressure. This technique was used by Esrig and Kirby (1977) on standard cores in the evaluation of the in situ saturation in the Mississippi Delta. They found that the sediments ranged in saturation from 0.9 to 1.0.

This method of evaluating the in situ gas content is not very accurate due to both sample disturbance resulting in the loss of gas and the assumptions of in situ gas pressures. However, acoustic work is presently being undertaken at Oxford University by Gardner (1987) who has developed a method of evaluating the

saturation of a gassy soil from the measurement of sound speed and attenuation in the laboratory. The ultimate aim of this research is to produce an acoustic probe for the evaluation of in situ gas content.

1.3 The Volume Change Behaviour of Unsaturated Soils

Terzaghi (1923) showed experimentally that for a saturated soil, the stress controlling the volume change and strength behaviour can be defined by the difference between the total stress, σ, and the pressure of the pore fluid, u. This controlling stress became known as the effective stress, σ', defined as

$$\sigma' = \sigma - u \tag{1.1}$$

where u is the pore water pressure when completely saturated with water and the air pressure when completely dry.

Early research on land based unsaturated soils assumed that the gas exists in the soil within the pores of the soil matrix. A typical assumption of the structure of an unsaturated soil was presented by Orlob and Radhakrishna (1958) as illustrated in Figure 1.2, where it can be seen that the position of the soil grains do not significantly change with the amount of gas that is present. On the basis of this assumption, it is clear why Bishop (1959) extended the Terzaghi equation to produce an effective stress equation for unsaturated soils

$$\sigma' = \sigma - \chi u_w - (1-\chi)u_g \tag{1.2}$$

where u_w and u_g are the pore water and pore gas pressures respectively, σ is the total stress and σ' is the effective stress. The parameter χ is known as Bishop's coefficient which is assumed to vary with the degree of saturation. The above equation is based on the fact that the water and gas pressures, differing due to surface tension effects, act over different areas of soil grains when the soil is partly saturated.

This equation appeared to be confirmed when Bishop and Donald (1961) evaluated values of χ from measured strength values of a Braehead silt at known soil saturations under drained triaxial conditions. The parameter χ was also evaluated from undrained triaxial tests and one-dimensional consolidation tests. The values of χ from the three different series of tests were plotted against the water saturation, S_w, as illustrated in Figure 1.3. Bishop and

Donald took this series of tests as confirmation of the unique behaviour of χ with S_w for this particular soil.

Jennings and Burland (1962), however, illustrated that the volume change of an unsaturated soil may not always be linked to the single effective stress as defined by Bishop (1959). Nevertheless, it was found that this equation may be applied to soils with degrees of water saturation above a critical saturation. This critical degree of saturation may be as low as 0.2 for coarse granular materials, 0.4 to 0.5 for silts, while for clayey soils the critical saturation is upwards of 0.85. Bishop and Blight (1963) confirmed this behaviour and found that the parameter χ was path dependent. They also suggested that the void ratio was dependent on the parameters $(\sigma-u_g)$ and (u_g-u_w), which were more appropriate to describe the volume change behaviour of partly saturated soils. However, these authors show that the relationship between shear strength and Bishop's single effective stress is less sensitive to the stress path.

Matyas and Radhakrishna (1968) abandoned the effective stress concept and suggested that the volume change behaviour can be expressed as a function of two independent stress components or state variables given as $(\sigma-u_g)$ and (u_g-u_w). Experimental tests by the above authors found that both the porosity, n, and the degree of saturation, S, were related to the above two state variables. When values of n and S were plotted against the state variables, a unique three-dimensional "state surface" was obtained for each case as illustrated in Figures 1.4a and 1.4b. The uniqueness of the void ratio and saturation versus the two state variables was verified experimentally by Fredlund and Morgenstern (1976) with a series of tests under isotropic and one-dimensional conditions.

In a following paper, Fredlund and Morgenstern (1977) considered a three-dimensional representative element of an unsaturated soil containing a large number of particles such that it qualifies as a continuum. A typical element is illustrated in Figure 1.5a. The authors treat this unsaturated soil as a four phase system, the phases being (i) soil particles (ii) water (iii) gas and (iv) contractile skin. The contractile skin is the thin layer that separates the water and gas phases. A free body diagram of the forces on the element of unsaturated soil is given in Figure 1.5b. The equilibrium equation for this

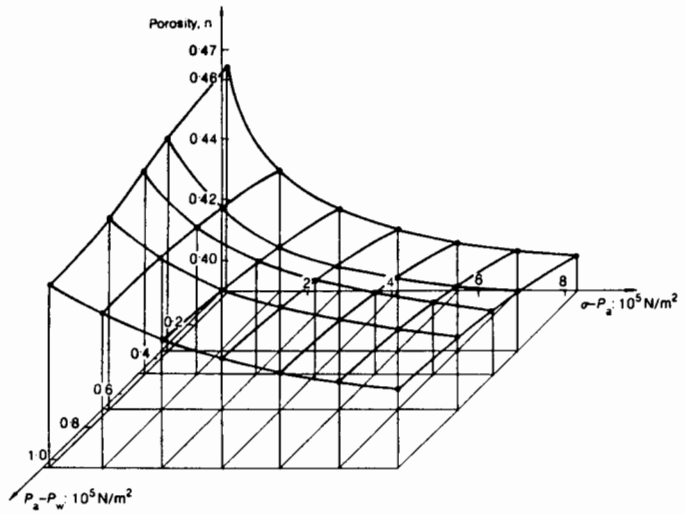

Figure 1.4a State surface for porosity (Matyas & Radhakrishna)

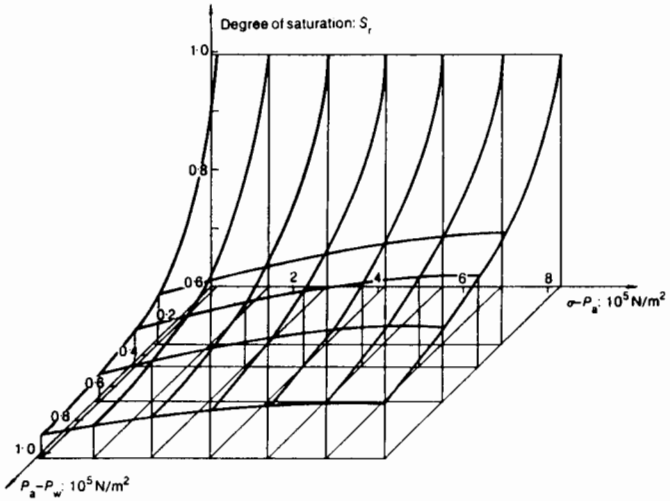

Figure 1.4b State surface for degree of saturation (Matyas & Radhakrishna, 1968)

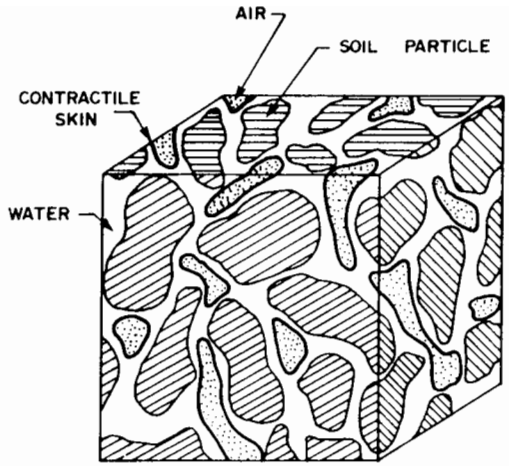

Figure 1.5a Unsaturated soil idealized as a four phase material (Fredlund and Morgenstern 1977)

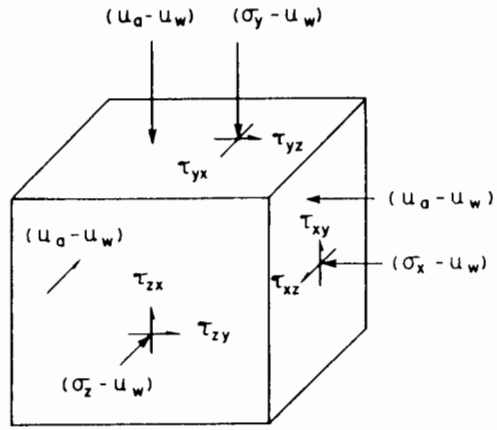

Figure 1.5b Stresses on an element of unsaturated soil (Fredlund and Morgenstern, 1977)

element of soil can be written as

$$\frac{\partial \sigma_{ij}}{\partial x_i} - \frac{\partial u_w}{\partial x_i} \delta_{ij} = F_{cwj} + F_{cgj} + F_{pwj} + n_g \frac{\partial p_c}{\partial x_i} \delta_{ij} \quad (1.3)$$

where F_{cwj} and F_{cgj} are the components of the drag of water and gas on the contractile skin, F_{pwj} is the component of the drag force of the water on the soil particles and p_c is the capillary pressure $(u_g - u_w)$.

Although it is possible to define the equilibrium conditions by the one tensorial equation 1.3, the authors state that the strain is governed by the two independent state variables $(\sigma_{ij} - u_w\delta_{ij})$ and $(u_g - u_w)\delta_{ij}$. Therefore, it is not possible to write a single constitutive equation governing the behaviour of this material as the strains are not controlled by a single stress variable. The total strain can be evaluated by summing the individual strain components as

$$\varepsilon_{ij} = \varepsilon^1_{ij} + \varepsilon^2_{ij} = f_1[(\sigma_{ij} - u_w\delta_{ij})] + f_2[(u_w - u_a)\delta_{ij}] \quad (1.4)$$

where ε^1_{ij} and ε^2_{ij} are the strains caused by the two independent state variables.

1.4 The Consolidation Behaviour of Unsaturated Soils

The governing equation for the consolidation of a saturated soil was first derived by Terzaghi (1944) as described at the end of Chapter 5. He combined the conservation of volume of an element of saturated soil with Darcy's law of flow through a porous medium in one-dimension to produce the equation.

$$c_v \frac{\partial^2 u'_w}{\partial z^2} = \frac{\partial u'_w}{\partial t} \quad (1.5)$$

where u'_w is the excess pore pressure and c_v is the coefficient of consolidation,

$$c_v = \frac{k}{\gamma_w m_v} \quad (1.6)$$

k is the soil permeability, γ_w is the specific weight of water and m_v is the coefficient of volume change in the vertical direction. This equation was subsequently solved analytically by Taylor (1948) who used a Fourier series to produce a series solution for the case of one-dimensional consolidation of a homogeneous soil due to the application of a single increment of total stress with drainage allowed from both faces or a single face of a soil sample.

When an analytical solution is not available for the modelling of a particular engineering process, other more flexible, although more approximate methods of solution may be used. These are known as numerical methods. Two

popular methods that are extensively used are the finite difference method and the finite element method. Both methods involve splitting up or "discretizing" the solution domain into smaller subdomains which may be analyzed separately.

In the following section there follows a survey of the numerical modelling developed to solve the equations governing the consolidation process of saturated and partly saturated soils.

Abbot (1960) developed a one-dimensional non-linear finite difference model to solve the Terzaghi consolidation equation for a multi-layered saturated soil system using small strain theory. This approach was extended by Schiffman and Gibson (1964) to include the non-linear effects of the variation of permeability and compressibility.

Gibson, England and Hussey (1967) extended the consolidation theory of a saturated soil to include large strain behaviour in which an elementary unit of mass and not volume is considered. This theory correctly evaluates the Darcy velocity with respect to the soil skeleton rather than to the volumetric coordinates as inherent in the Terzaghi derivation.

Barden (1965) presented the equations governing the one-dimensional consolidation behaviour of a partly saturated soil. The equations presented govern the flow of water and a compressible gas through the pores of a compressible soil. To simplify the overall behaviour, Barden subdivided the general consolidation process into five subprocesses. Each subprocess is dependent on the degree of saturation of the soil. For soils of saturation in the range of 0.9 to 1.0 Barden assumed that as the bubbles were in occluded form, the two fluid phases could be combined to produce a single compressible fluid. The gas and water pore pressures were assumed equal, from which the effective stress principle could be used. Based on this assumption, the Terzaghi consolidation equation was produced in modified form which included the compressibility and solubility of the gas. This modified equation was then solved using the finite difference method and utilizing the same approach as Schiffman and Gibson (1964).

A major step in the development of consolidation theory was made by Biot (1941) who coupled the equation governing the deformation of an elastic solid

with the equation governing the flow of a compressible fluid through a compressible porous medium. Also incorporated in the equations was that the Darcy velocity could be correctly described by the average fluid velocity relative to the solid velocity. The equations were developed under three dimensional cartesian conditions and can be written in tensorial notation as

$$G \frac{\partial^2 w_i}{\partial x_j \partial x_j} + G \frac{\partial^2 w_j}{\partial x_j \partial x_i} + \lambda \frac{\partial^2 w_j}{\partial x_i \partial x_j} - \frac{\partial u_f}{\partial x_i} = \frac{\partial \tilde{\sigma}'_{ij}}{\partial x_j} - F_i \qquad (1.7)$$

and

$$\frac{\partial}{\partial x_i}\left[\frac{k_{ij}}{\gamma_f}\left(\frac{\partial u_f}{\partial x_j} - \gamma_f e_j\right)\right] = c_f n_f \frac{\partial u_f}{\partial t} + \frac{\partial}{\partial t}\left[\frac{\partial w_i}{\partial x_i}\right] \qquad i,j = 1,2,3 \qquad (1.8)$$

where λ and G are the Lamé elastic constants, w_i is the displacement vector, u_f is the pore fluid pressure, n_f is the soil porosity, c_f and γ_f are the compressibility and specific weight of the pore fluid, e_j is the unit gravitational direction vector, k_{ij} is the soil permeability tensor, F_i is the body force vector and $\tilde{\sigma}'_{ij}$ is the initial effective stress tensor on the soil.

Booker (1972) developed a numerical method for the solution of Biot's equations under plane strain conditions. The basic equations are made independent of time by the application of a Laplace transform. The finite element analysis is then performed in the Laplace transform space, and the approximate transforms inverted to obtain the solution. Ghaboussi and Wilson (1973) used the finite element method in space and the finite difference method in time to solve the Biot equations under two-dimensional plane strain and axisymmetric conditions.

Carter, Small and Booker (1977) extended small strain Biot consolidation theory to include the effect of finite deformation. The three-dimensional formulation allows for the occurrence of finite geometry changes and finite elastic strains during the consolidation process. The governing equations are subsequently solved using the finite element method for plane strain conditions.

The formulation and numerical solution for problems involving finite deformations of an elasto-plastic material was developed by Carter, Booker and Davis (1977). This work was extended by Carter, Booker and Small (1979) to the development of a theoretical formulation and numerical solution method for the problem of time dependent consolidation of an elasto-plastic soil subject to

finite deformations. The soil is assumed to be a two-phase material with a skeleton which may yield according to a general yield criterion with plastic flow governed by a general flow law, and whose pore fluid flows according to Darcy's Law.

A comprehensive review of many available numerical models for the analysis of soil consolidation can be found in Britto and Gunn (1987).

There has been much work over recent years in the development and simulation of the flow of multiphase fluids in a porous medium. The flow equations for two immiscible incompressible fluids with equal pore pressures in an incompressible porous medium become the highly non-linear equations given by Buckley and Leverett (1942). Settari and Aziz (1975) modelled these equations using a one-dimensional finite difference model. The continuity equations governing the flow of two fluid phases in a porous medium have been formulated into finite element approximations by a variety of authors, including Settari, Price and Dupont (1977) and Lewis, Verner and Zienkiewicz (1975).

A comprehensive description of the flow equations describing the movement of compressed air and water in an incompressible porous medium is presented by Meiri and Karadi (1982). The equations consider the individual fluid flow of each phase under their respective pressure gradients, the compressibility of the air phase, the solubility of the air in the pore water as a function of the air pressure, and the transport of water vapour in the air phase. A finite element formulation of the governing equations is presented in which--due to the sharp fluid fronts that are present in such a process--an upstream weighting technique is used rather than the normal Galerkin weighted residual method.

A three-dimensional integrated finite difference model (IFDM) was developed by Narasimhan and Witherspoon (1978) to simulate the fluid flow in a partly saturated porous medium which can deform only in the vertical direction. The difference between the gas and water pore pressures, known as the capillary pressure, is a function of saturation from which Bishop's equation is used to evaluate the effective stress. The resulting model is appropriate when solving problems due to desaturation, pumping and fluid injection, but not for problems due to surface structural loading or soil excavation.

Lloriet and Alonso (1980) applied a one-dimensional finite element formulation to the equations governing the consolidation of a soil containing two immiscible fluids. The authors appear to be the first to abandon the effective stress concept when developing a numerical model and chose to define void ratio in terms of two independent state variables as described by Matyas and Radhakrishna (1968). The state variables chosen were $(\sigma-u_g)$ and (u_g-u_w).

Chang and Duncan (1983) treated the consolidation process using a coupled flow and stress analysis. A Modified Cam-Clay model is used to simulate the behaviour of compacted soils. The water and air phases are treated as one homogeneous pore fluid with the compressibility evaluated from a combination of Boyle's law, Henry's Law of solubility and surface tension effects. In addition, it is assumed that the two fluids remain as a mixture and do not flow independently. The equations are formulated using the finite element weighted residual method for two-dimensional plane strain and axisymmetric conditions.

1.5 Research Performed at Oxford

1.5.1 Early work

Research into the behaviour of unsaturated marine soils was begun at Oxford in 1978 by Dr. G.C. Sills and her research group. The work commenced with a series of field tests designed to measure the pore water pressure response in the seabed in areas where gas was known to exist in the marine sediment. A differential piezometer was used for this purpose which measures the difference between the pore water pressure at a point below the mudline and the hydrostatic pressure at the same point. For a saturated marine soil, the pore water pressure and the hydrostatic pressure are identical throughout a complete tidal cycle. In areas of unsaturated marine soils, however, it was found that any increment of total stress on the seabed due to the change in water depth, did not produce the same increment of pore water pressure response. This was interpreted as being due to the partial transference of the total stress increment to the soil skeleton in the form of effective stress caused by the compressibility of the pore gas.

These early results indicated that gas in the seabed could have a significant effect on the geotechnical behaviour of the soil. As a consequence, this has so far resulted in a further nine years of research on gas bearing marine soils which is still in progress at Oxford University.

1.5.2 The work of Nageswaran (1983)

Nageswaran (1983) spent three years studying the effect of gas bubbles on the behaviour of the seabed and performed some field tests in areas in which gas was known to exist. Due to the extreme difficulty in obtaining undisturbed samples of gassy soil for laboratory testing, however, an alternative approach to experimental testing was required. Consequently, Nageswaran developed a successful technique for producing a soil sample containing a uniform repeatable distribution of gas bubbles in soft estuarine silt. This was performed by introducing methane slowly into a soil slurry via the chemical zeolite. This process became known as the "zeolite molecular sieve technique" and is described at a later stage in Section 2.2. A typical unsaturated soil sample prepared using this technique is presented later in Plate 2.1. It can be seen that rather than existing in the original pore structure of the soil, the gas appears to form discrete occluded bubbles surrounded by an otherwise saturated soil matrix. Nageswaran then termed this type of soil "gassy soil", which he defined as "A partially saturated soil with sufficiently high degrees of saturation for the gas to exist in discrete bubble form."

Nageswaran also developed an oedometer which was capable of consolidating a gassy soil from a slurry, measuring the stresses and pore pressures in the sample and separating the drained gas and water phases.

In order to understand the behaviour of gassy soils, Nageswaran performed four series of one-dimensional consolidation tests in this specially designed oedometer. The first series of tests (test series A) involved consolidating gassy soil samples with water saturations ranging from 0.8 to 1.0. The samples were drained from the bottom face through the piston with pore water pressure measured on the undrained top face. Figure 1.6 presents a typical settlement time plot for one-dimensional consolidation. It can be seen that for the gassy samples there is an initial instantaneous settlement due to the compression of

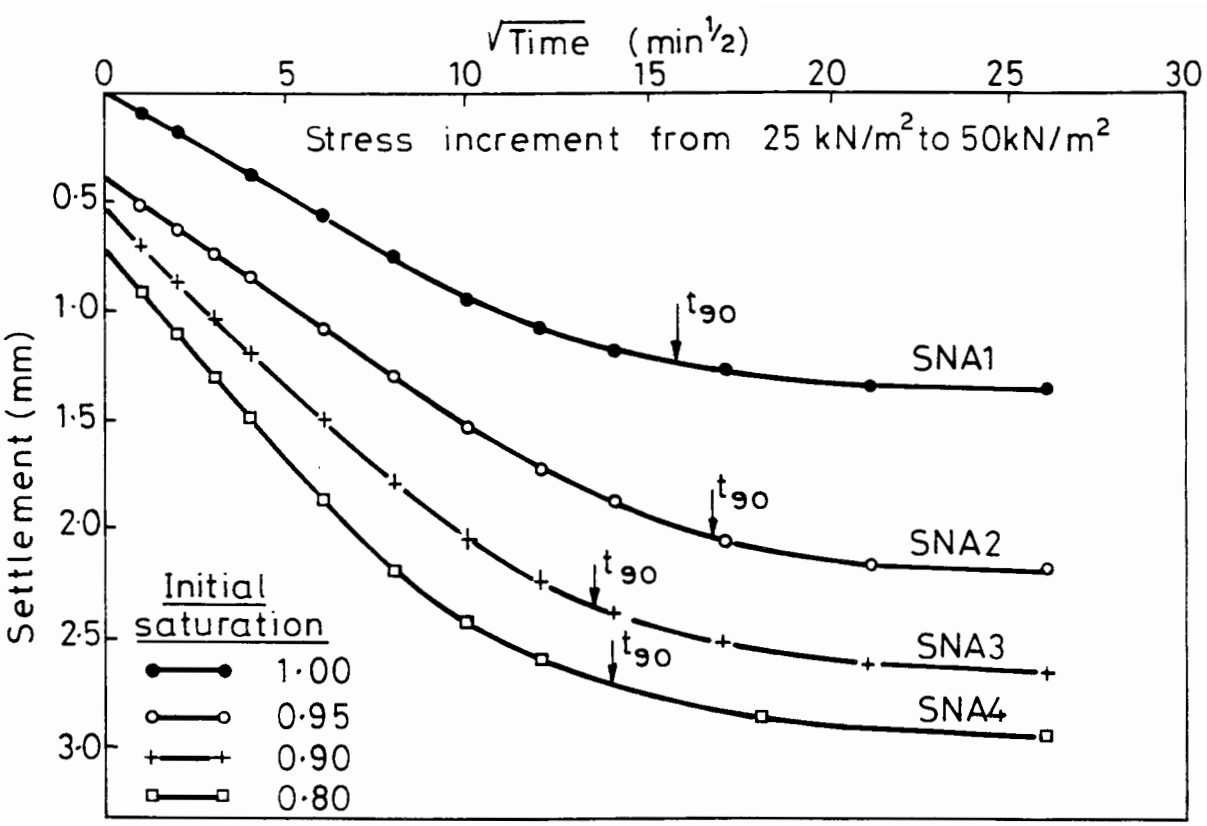

Figure 1.6 Typical settlement-time plots for one-dimensional consolidation (Nageswaran, 1983)

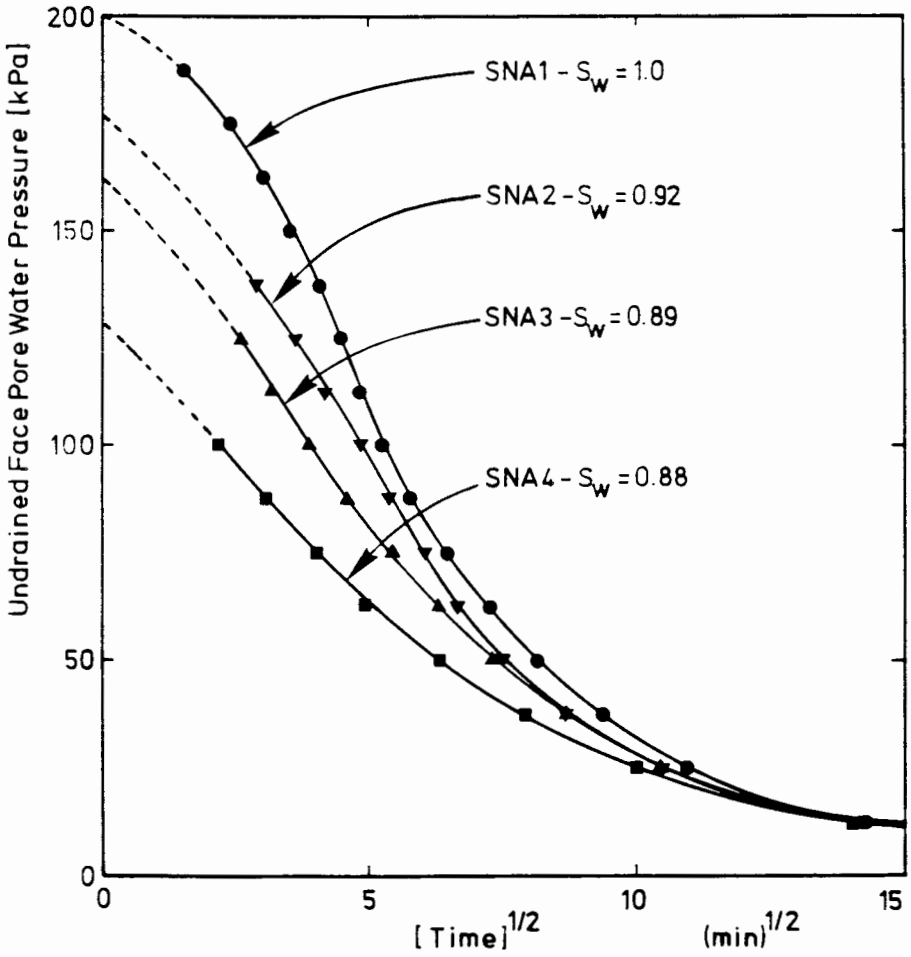

Figure 1.7 Typical undrained face pore water pressure-time plots for one-dimensional consolidation (Nageswaran, 1983)

the gas. It can also be seen that the higher the initial gas content, the higher the initial settlement. The behaviour of the pore water pressure measurement with time on the top undrained face is illustrated in Figure 1.7. It can be seen that for the saturated soil the undrained face pore pressure almost reaches the increment of vertical stress. This figure also illustrates that as the gas content becomes higher, the increment of pore water pressure becomes lower. Nageswaran interpreted this behaviour as due to the compression of the pore fluid causing the applied increment to be shared between the pore pressure and the effective stress. At this stage this would appear to be a reasonable assumption. It should be noted, however, that although any collection of gas in the top cap may be removed, there is no provision for the removal of gas that may have drained from the bottom face of the soil sample. Therefore it may be possible that if any gas were trapped in the drainage lines or the porous disk, this would also cause a slight drained response producing a lower measured pore water pressure increase.

Test series B involved the one-dimensional consolidation of gassy soil samples with drainage occurring from the top face. Due to the problems caused by the gas entering the porous stone on the piston face, no pore water pressure measurements were made on the undrained face during this test series. Instead, this series of tests concentrated on the measurement of the volumes of the gas and water that drained from the sample. It was assumed that the pore gas pressure was equal to the pore water pressure at all times, which in turn led to the assumption that the volume of gas lost from the soil sample was equal to the volume of the gas that was collected in the top cap at the end of each step of loading. From this assumption it was possible to evaluate the saturation of the gassy soil after each stage of the test. Figure 1.8 presents the total void ratio for all tests plotted against the vertical consolidation stress at the end of each stage. It can be seen that there is no unique relationship between these parameters. Wheeler (1986) pointed out the inapplicability of the Bishop type effective stress approach for soil containing gas bubbles. He illustrated this point by considering the results of the fully saturated test SNB1 and the 88% saturated test SNB3 as illustrated in Figure 1.9. From this figure, for the

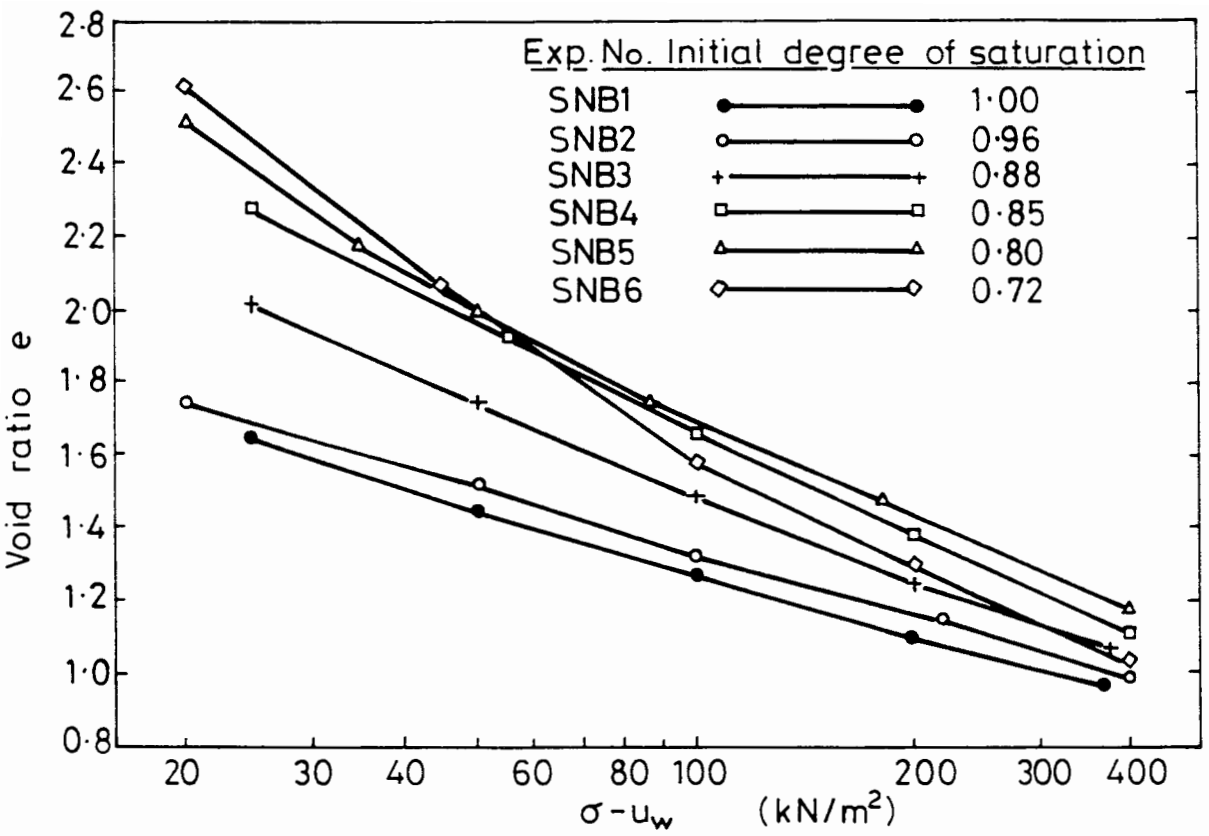

Figure 1.8 Variation of void ratio during one-dimensional consolidation (Nageswaran, 1983)

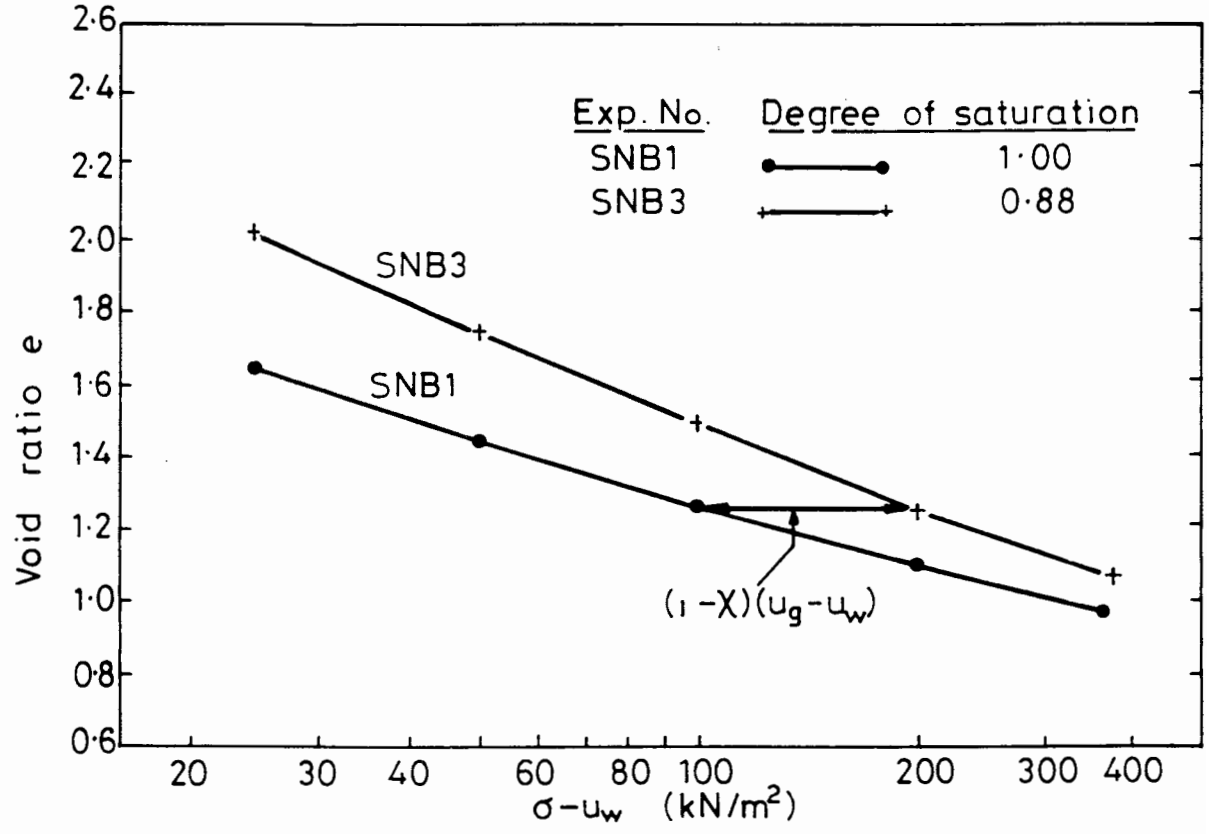

Figure 1.9 Application of Bishop's effective stress law to one-dimensional consolidation results (Wheeler, 1986)

same void ratio of 1.25 the value of $(\sigma_v - u_w)$ for SNB3 is 200 kPa whereas the effective stress from SNB1 is actually 100 kPa. Wheeler rearranged Bishop's effective stress equation to give

$$\sigma' = \sigma - u_w - (1-\chi)(u_g - u_w) \qquad (1.9)$$

which, with a value of χ of about 0.9 (obtained for a saturation of 88% from Figure 1.3) substituted in the above equation, suggested a pressure difference $(u_g - u_w)$ of about 1000 kPa. This is most unlikely and was shown to be impossible by Wheeler who considered the minimum possible radius of curvature of the meniscus forming the interface between gas and water. After some theoretical work, Wheeler suggested to Nageswaran that the results of the consolidation tests may show better correlation if the product of the water saturation and void ratio ($S_w e$) are plotted against $(\sigma_v - u_w)$. Figure 1.10 presents the results of Nageswaran for the soils containing discrete bubbles ($S_w > 0.85$). It can be seen that plotting the results in this way brings the results closer to a unique line. Nageswaran also plotted $(1+e)S_w$ versus $(\sigma_v - u_w)$ as shown in Figure 1.11. This also produces a unique, although purely empirical relationship.

Test series C concentrated on consolidation testing of gassy soils under low consolidation stresses (<100kPa). The same type of void ratio versus consolidation stress behaviour was observed as test series A. Nageswaran also reported that for soils with a water saturation above 85% there was little change in the degree of saturation. For soils below this critical degree of saturation, however, the water saturation increased as a higher proportion of gas than water was lost. The findings of this test series were consistent with the saturation behaviour of tests series B, as illustrated in Figure 1.12.

Nageswaran interpreted these results in terms of the relative permeabilities of the water and gas. He suggested that for soil of 85% saturation or higher, the water and gas flow from the sample in the same proportions, a possible explanation being that the gas is carried in the form of small bubbles from the sample. For soils below 85% saturation, Nageswaran suggested that the gas voids become interconnected and the gas permeability becomes higher than the water permeability.

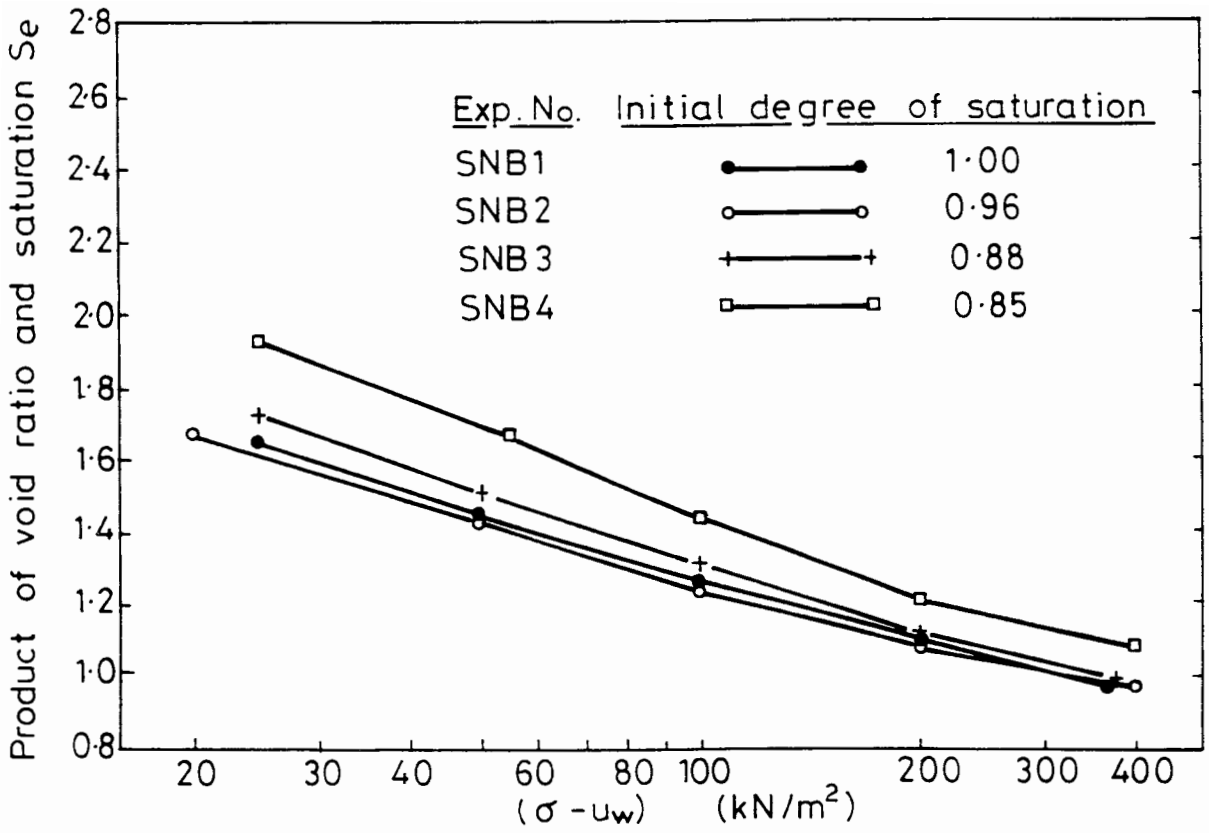

Figure 1.10 Product of void ratio and saturation during one-dimensional consolidation (Nageswaran, 1983)

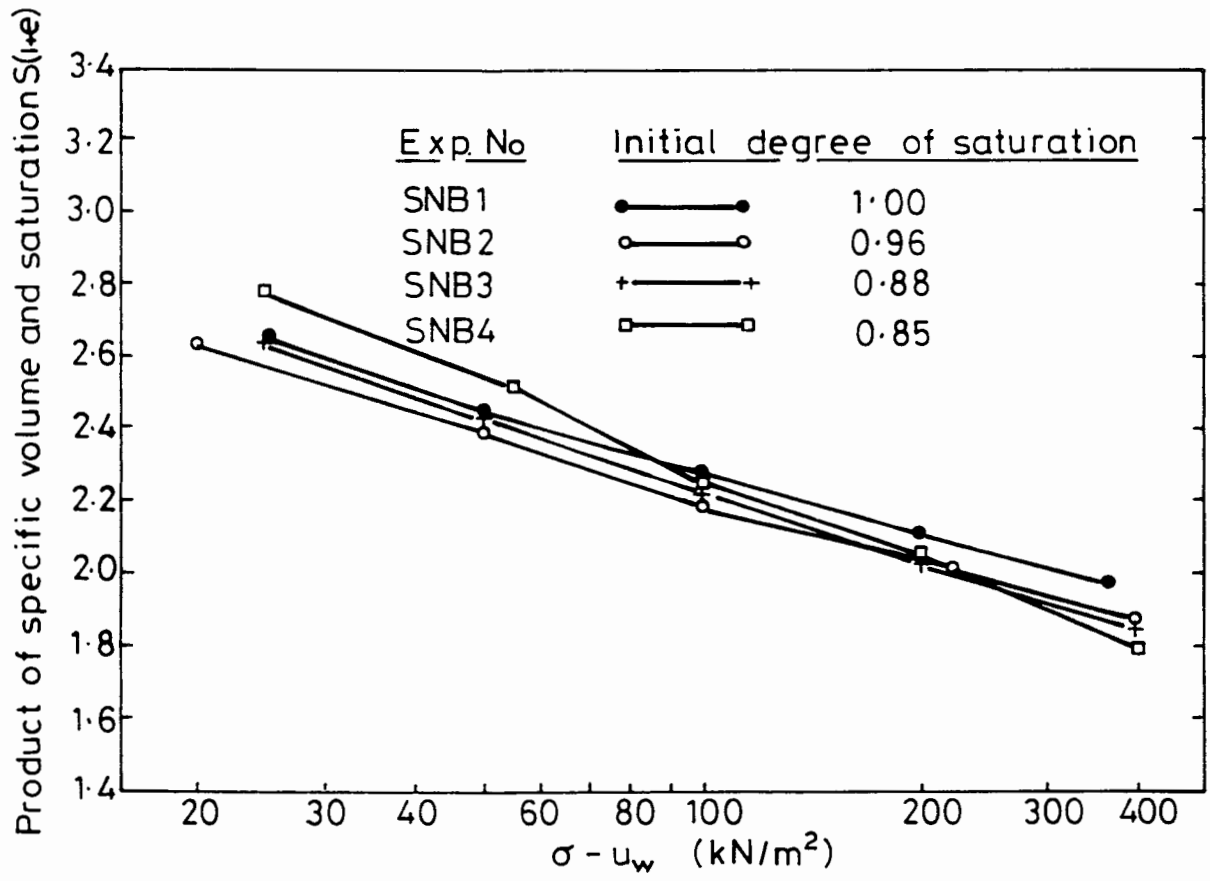

Figure 1.11 Product of specific volume and saturation during one-dimensional consolidation (Nageswaran, 1983)

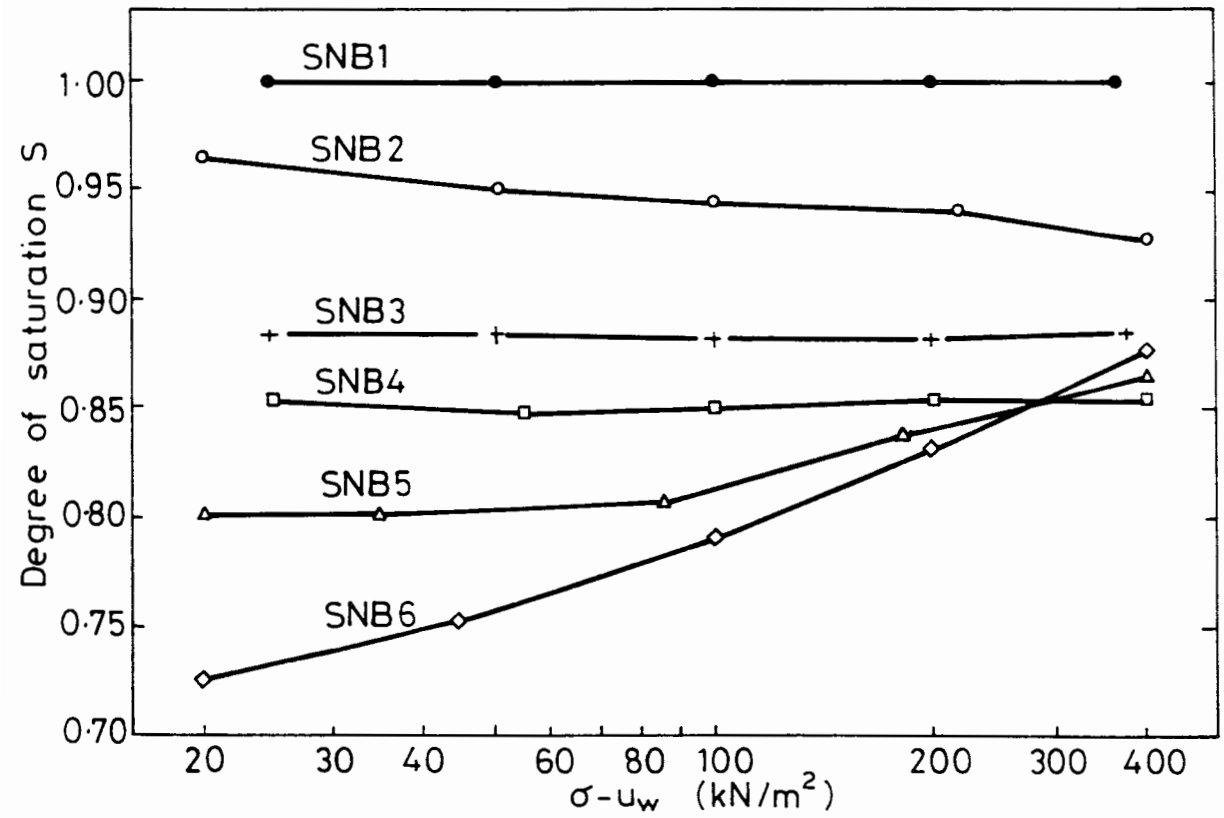

Figure 1.12 Variation of degree of saturation during one-dimensional consolidation (Nageswaran, 1983)

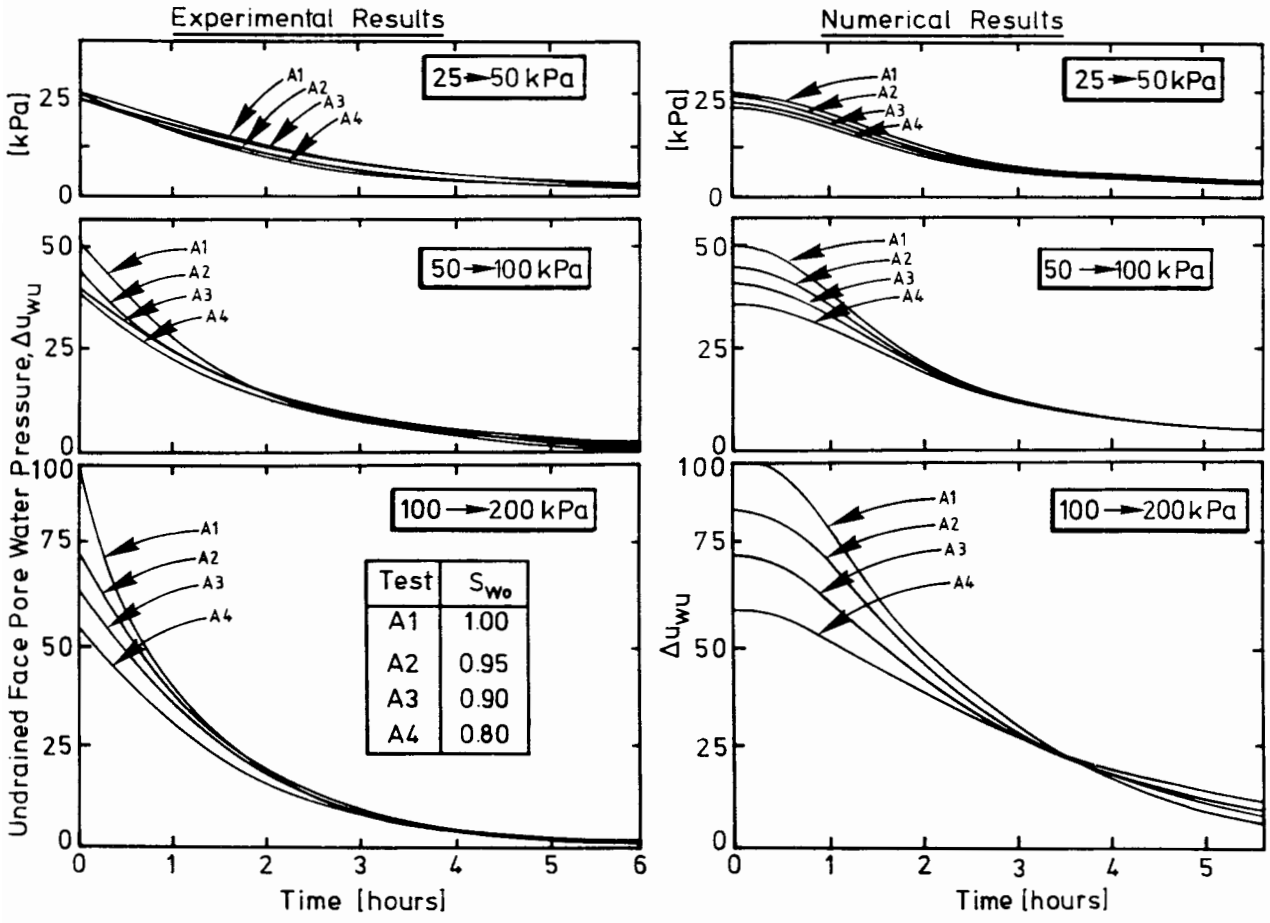

Figure 1.13 Comparison between experimental and numerical undrained face pore water pressure during consolidation (Nageswaran, 1983)

Finally, test series D consolidated gassy soil samples using top and bottom face drainage both under atmospheric back pressure and under a back pressure of 50 kPa. These experiments illustrated that an increase in back pressure reduces the amount of free gas in a gassy soil.

In order to simulate the consolidation behaviour of gassy soil in the laboratory, Nageswaran developed a theoretical model based on the large strain continuity expression given by Gibson, England and Hussey (1967). Nageswaran assumed that the water and gas could be combined to give a single homogeneous compressible pore fluid. He also assumed that the pore gas would flow in the same proportion as the pore water with the gas being transported as small bubbles in the pore water. To model the deformation behaviour, Nageswaran assumed a linear relationship between ($S_w e$) and $\log_{10}(\sigma_v - u_w)$.

Based on these assumptions, a one-dimensional finite difference program was written to model this large strain theory. Simulations were made of the consolidation tests producing time dependent values of settlement and undrained face pore pressure. Figure 1.13 compares the experimental with the simulated pore water pressure on the undrained face for test series SNA. The initial pore water pressure response is fairly well simulated. This is followed by both experimental and numerical values of pore water pressure dissipating to atmospheric pressure, although the shape of the dissipation curve is not well modelled. It must be noted here that this experimental result would also occur if there were slight drainage due to gas trapped in the porous disk on the top undrained face or in the drainage lines in the piston. Figure 1.14 compares the observed and simulated time dependent settlement of a series of gassy soil samples. Again the initial behaviour is well modelled. However, as any displacement is divided by the final displacement, Nageswaran is forcing the final experimental value to unity, so it is not surprising that the remainder of the simulation also appears to be well modelled. A more suitable comparison would be to compare the total settlement normalized with the initial thickness of the sample, as this would compare the total amount of drained displacement.

This model was also used in the simulation of gassy sediment subjected to a sinusoidal stress variation. A gassy soil slurry is consolidated under self

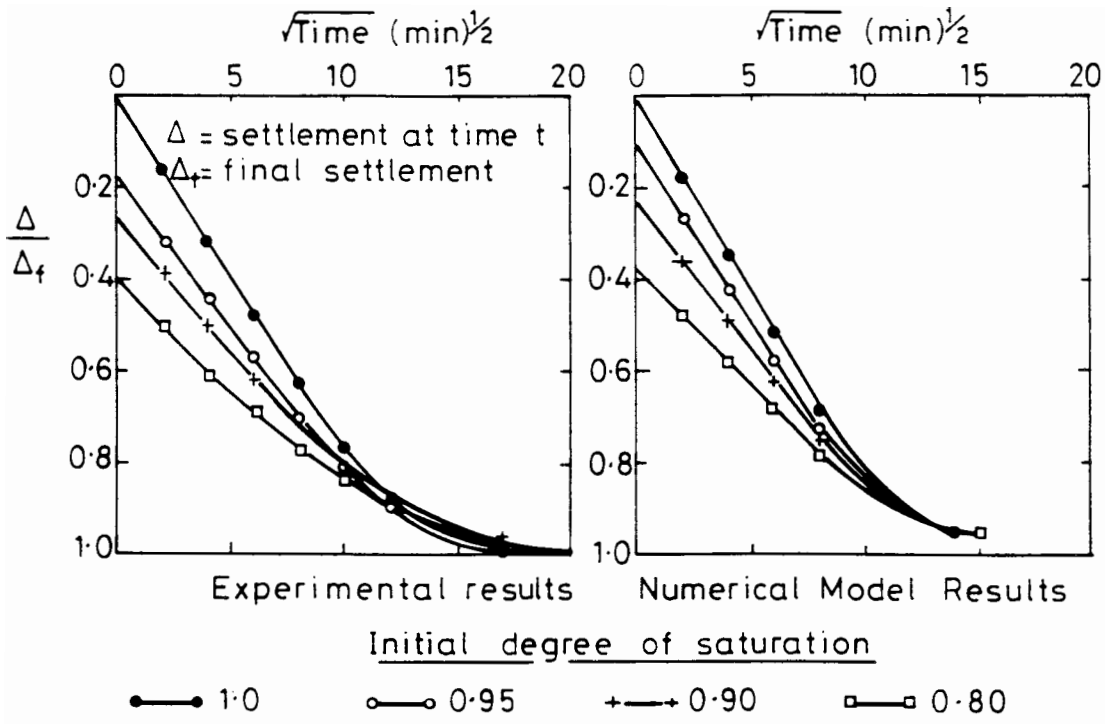

Figure 1.14 Comparison between experimental and numerical results of settlement during consolidation (Nageswaran, 1983)

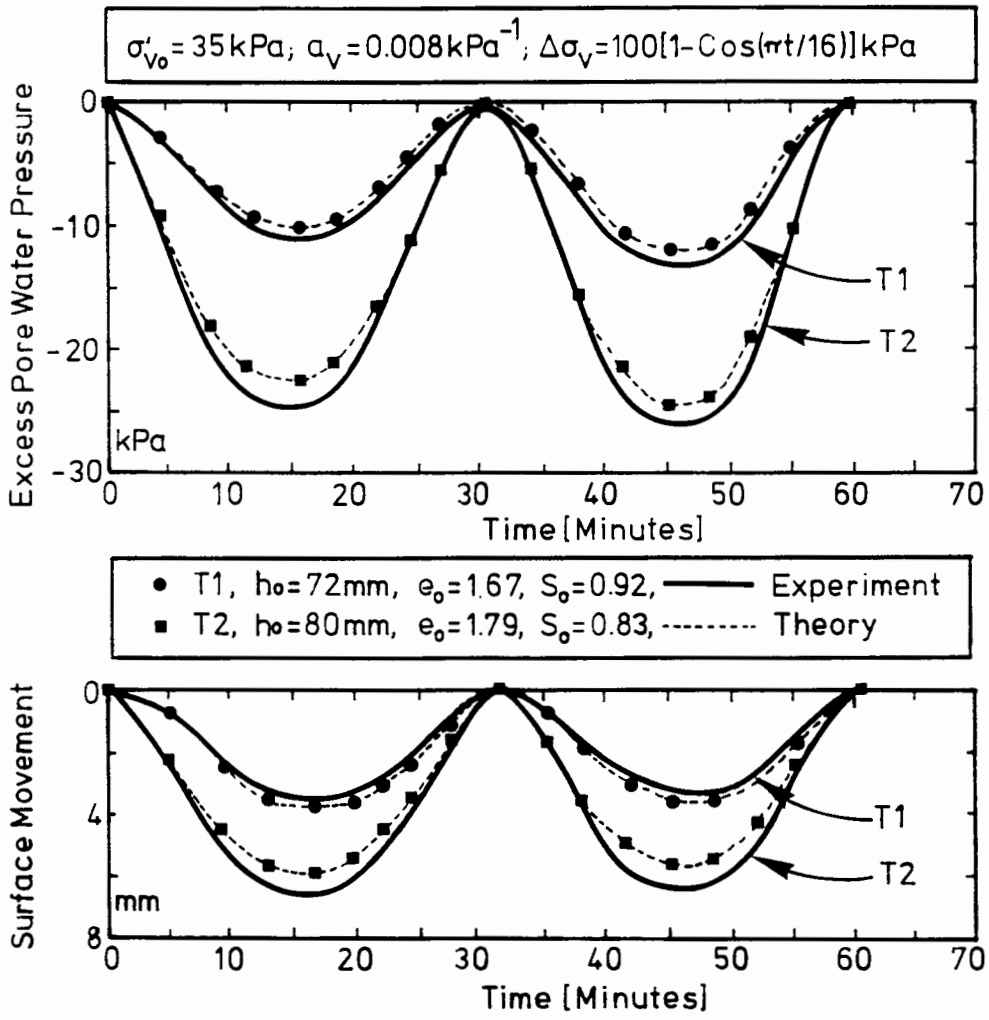

Figure 1.15 Comparison between experimental and numerical results of gassy soil response due to sinusoidal loading (Nageswaran, 1983)

weight in a perspex tube. A sinusoidally varying head is applied to the sample and the difference in pore water pressure between the top and bottom of the sample is measured. This behaviour was modelled successfully by the theoretical model of Nageswaran. A comparison between the experimental and theoretical results is presented in Figure 1.15.

1.5.3 The work of Wheeler (1986)

Wheeler performed a rigorous programme of experimental and theoretical research into the behaviour of gassy soil under triaxial conditions. The experimental work was performed on samples of gassy soil which were prepared in the laboratory using the zeolite molecular sieve technique. The majority of the experimental work was concentrated on obtaining values of undrained shear strengths for gassy soils with a range of gas contents and consolidated to a variety of initial consolidation pressures. Although the main aim of the research was to obtain values of shear strength, values of undrained shear modulus and undrained bulk modulus were also obtained. In addition, as the samples were initially consolidated isotropically to a required cell pressure, a value of void ratio was obtained for each test which corresponded to a known value of mean consolidation pressure.

The experimental procedure used by Wheeler involved first preparing the gassy soil slurry using the molecular sieve technique, then pouring the soil slurry into 38 mm diameter perspex moulds for initial one-dimensional consolidation. The load was applied in two stages, the first load being applied as soon as the slurry was poured into the cell. The samples were consolidated for three days under an applied load of 50 kPa, which was the lowest stress level at which the gassy soil samples could be extruded successfully from the perspex moulds. The samples were then trimmed to the correct length, surrounded with a rubber membrane and then set up in the triaxial cell. The inner and outer cells were then assembled and the sample was isotropically consolidated to the required cell pressure which removed the effects of any one-dimensional stress history. In the series of tests performed by Wheeler, the samples were consolidated isotropically to stress levels ranging from 100 kPa to 400 kPa.

After completion of the isotropic consolidation, which was effectively accomplished within three to four days, the sample was then sheared by applying a further uniaxial displacement of 0.02 mm/min under undrained conditions. During this shearing stage, values of axial load, piston displacement, pore water pressure and sample volume change were monitored with time. The cell pressure remained constant during this stage. Unlike a saturated soil sample, there is a volume change of the gassy soil sample under undrained conditions due to the compression and dissolution of the gas. This volume change is measured in the triaxial cell by the volume of water that enters the inner cell from the outer cell in order to maintain the prescribed value of cell pressure. Wheeler's sample was sheared to failure with the test terminated at a strain of 15% or at 2% higher than failure strain, whichever was the greater. In order to evaluate the saturation at the end of the test, the sample, if not already saturated, was subjected to an increase in cell pressure by an amount of 200 to 300 kPa. Thus all the free gas would be forced into solution producing a fully saturated sample. As the total volume change was recorded throughout the test, it was then possible from the knowledge of the volume of the saturated sample at the end of the test to evaluate the free volume gas at all times.

Although the main purpose of Wheeler's work was to look at the shear strength properties of gassy soil, he also attempted to produce a theoretical explanation for most of his experimental findings. The theoretical modelling was found to have a variable degree of success.

As the gassy soil samples were consolidated isotropically to a known consolidation pressure from which the volumes of the solids, water and gas phases could be calculated for each test, it was possible to evaluate the void ratio at this point. Implementing his own suggestion that Nageswaran had followed, he plotted the matrix void ratio against the mean consolidation pressure on a log scale. This is illustrated in Figure 1.16 which shows that the relationships between the mean consolidation pressure and the matrix void ratio ($e_m = S_w e$) are brought closer towards the saturated soil relationship.

The theoretical approach in the modelling of this behaviour involved treating the saturated soil matrix that surrounds the gas voids as either an

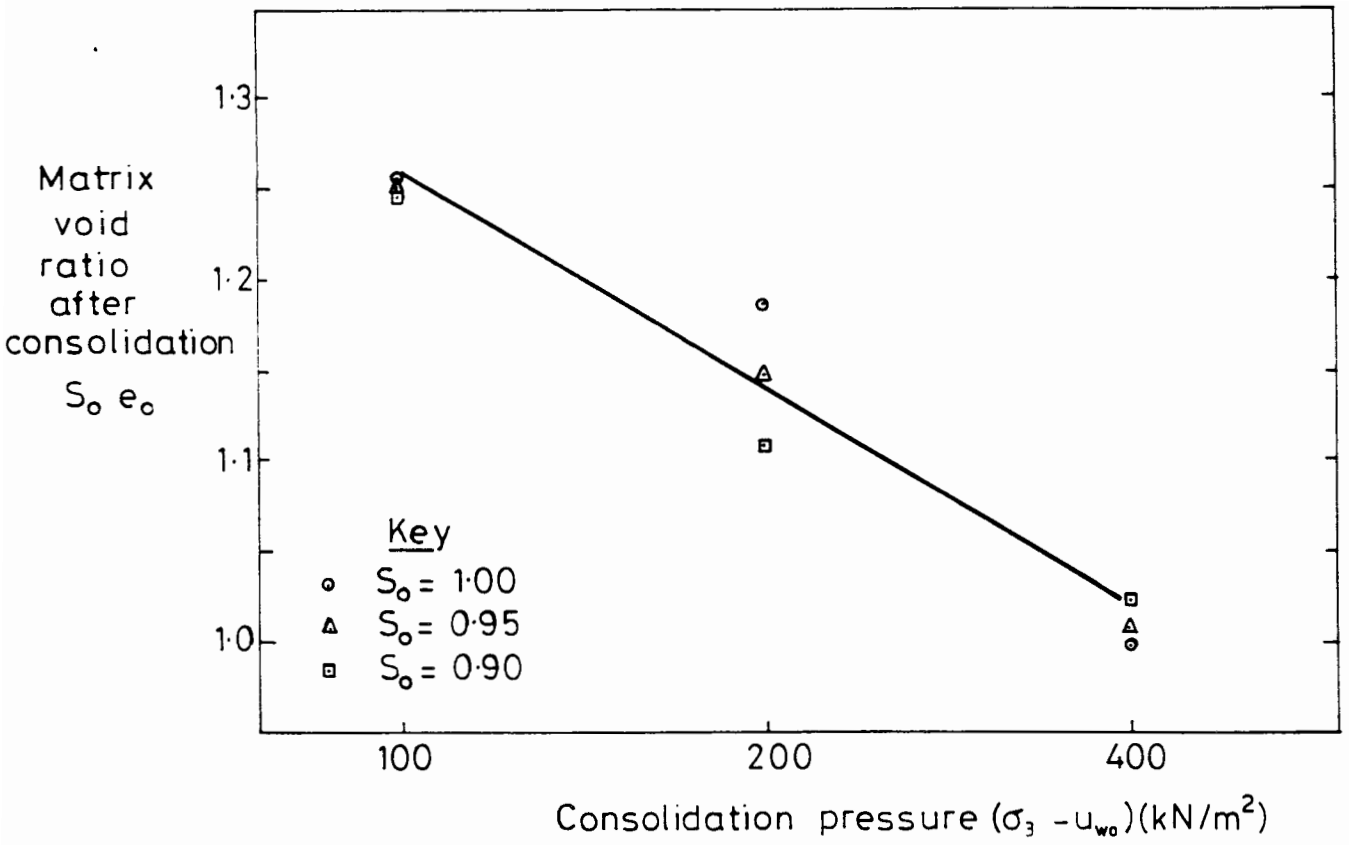

Figure 1.16 Product of void ratio and saturation versus isotropic consolidation pressure (Wheeler, 1986)

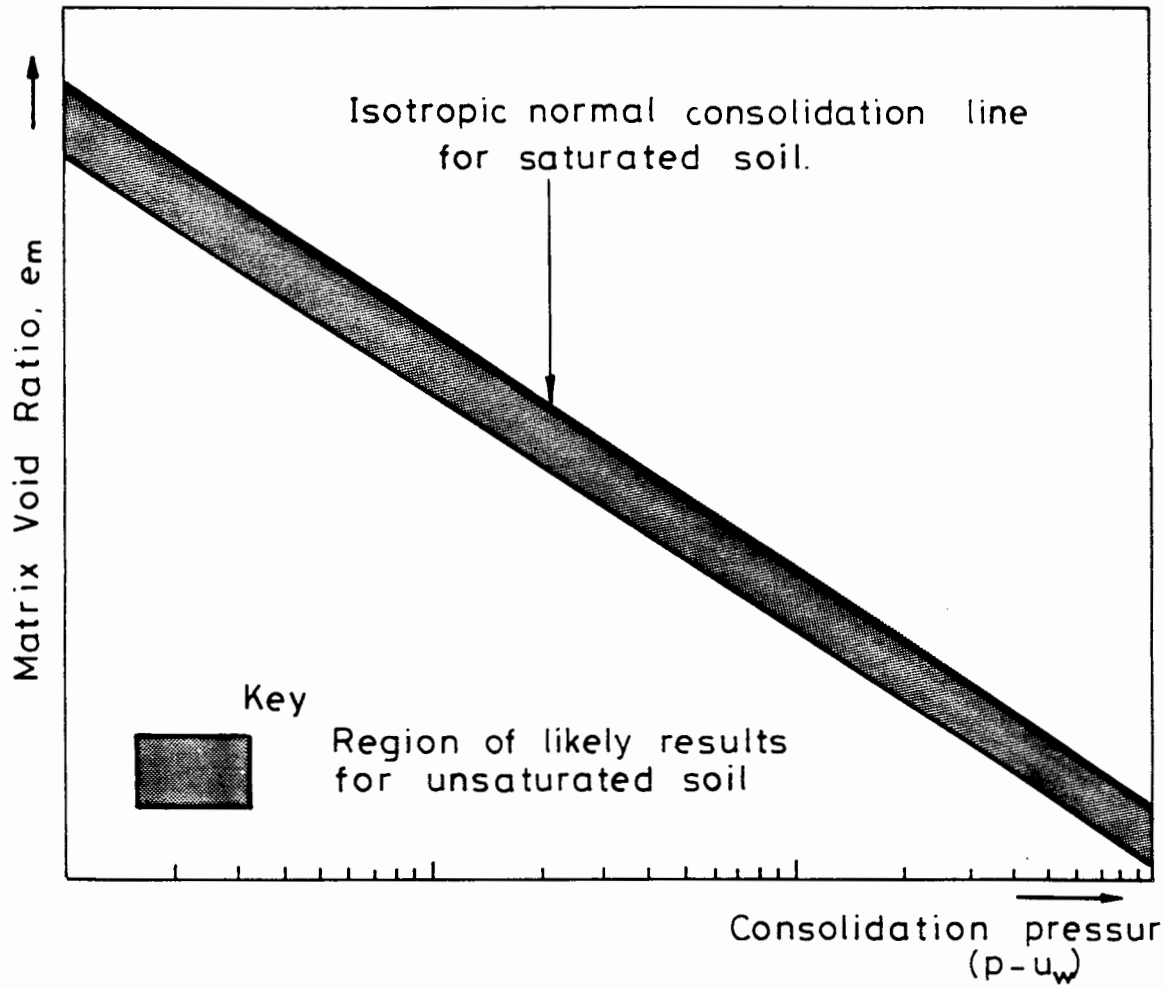

Figure 1.17 Isotropic consolidation of large bubble mode (Wheeler, 1986)

elastic solid or as a perfectly plastic medium. Both these analyses of this material produce a theoretical matrix void ratio slightly lower than the void ratio of a fully saturated soil under the same consolidation pressure. Combining both these theories, Wheeler suggested that the matrix void ratio for a gassy soil for isotropic conditions would most likely fall in the region just below the saturated soil line as illustrated in Figure 1.17. It must be noted that in this analysis, however, the gas pressure is assumed to be equal to the atmospheric back pressure. From the equation of local stress produced by Wheeler, the gassy soil matrix void ratio would become closer to the saturated soil void ratio at the same consolidation pressure if the gas pressure were higher than the pore water pressure.

During the early stages of the shearing process it is possible to obtain a value of undrained shear modulus and undrained bulk modulus. These moduli are found from the slopes of the curves of deviator stress versus deviator strain and deviator stress versus volumetric strain respectively. These moduli are defined by Atkinson and Bransby (1978) as

$$G_u = \Delta\sigma_1/(3\Delta\varepsilon_1 - \Delta\varepsilon_v) = \Delta\sigma_1/3\varepsilon \qquad (1.10)$$

and

$$K_u = \Delta\sigma_1/3\Delta\varepsilon_v \qquad (1.11)$$

For both cases, Wheeler computed the secant modulus at a deviator stress of half the failure value. The moduli were computed for each of the triaxial tests. In the theoretical analysis of elastic moduli, Wheeler treated the gassy soil as an elastic medium containing a number of spherical inclusions. Wheeler used the mathematical expression derived by Hill (1965) for the elastic behaviour of a composite material consisting of a volume fraction, f_o, of spherical inclusions (shear modulus G′, bulk modulus K′) embedded in a continuous matrix (shear modulus G°, bulk modulus K°).

Wheeler evaluated the combined elastic moduli under a variety of conditions, including instantaneous undrained moduli, long term undrained moduli and drained moduli. Figure 1.18 presents the experimental measurement of the shear modulus of a gassy soil normalized with respect to the shear modulus of a saturated soil at the same stress level. The moduli are all plotted against the

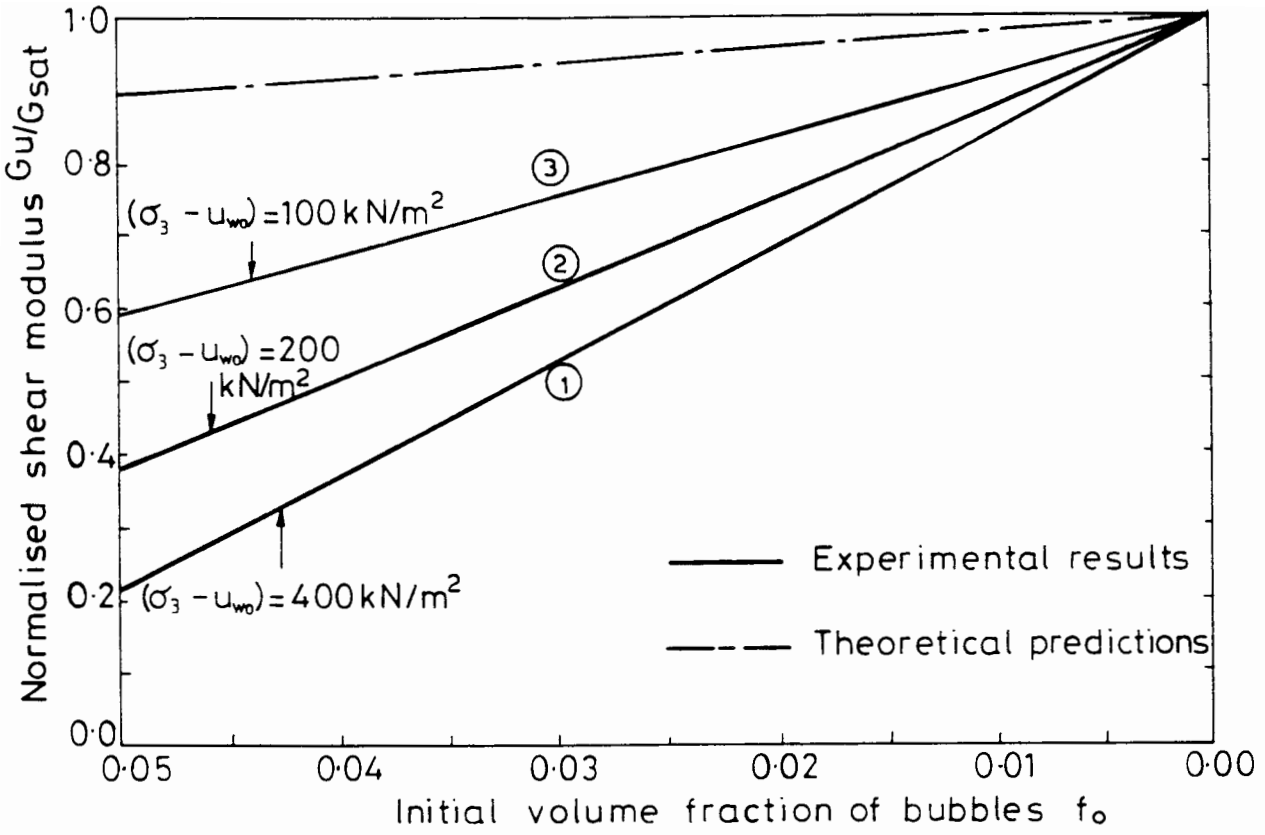

Figure 1.18 Comparison between experimental and theoretical values of undrained shear modulus (Wheeler, 1986)

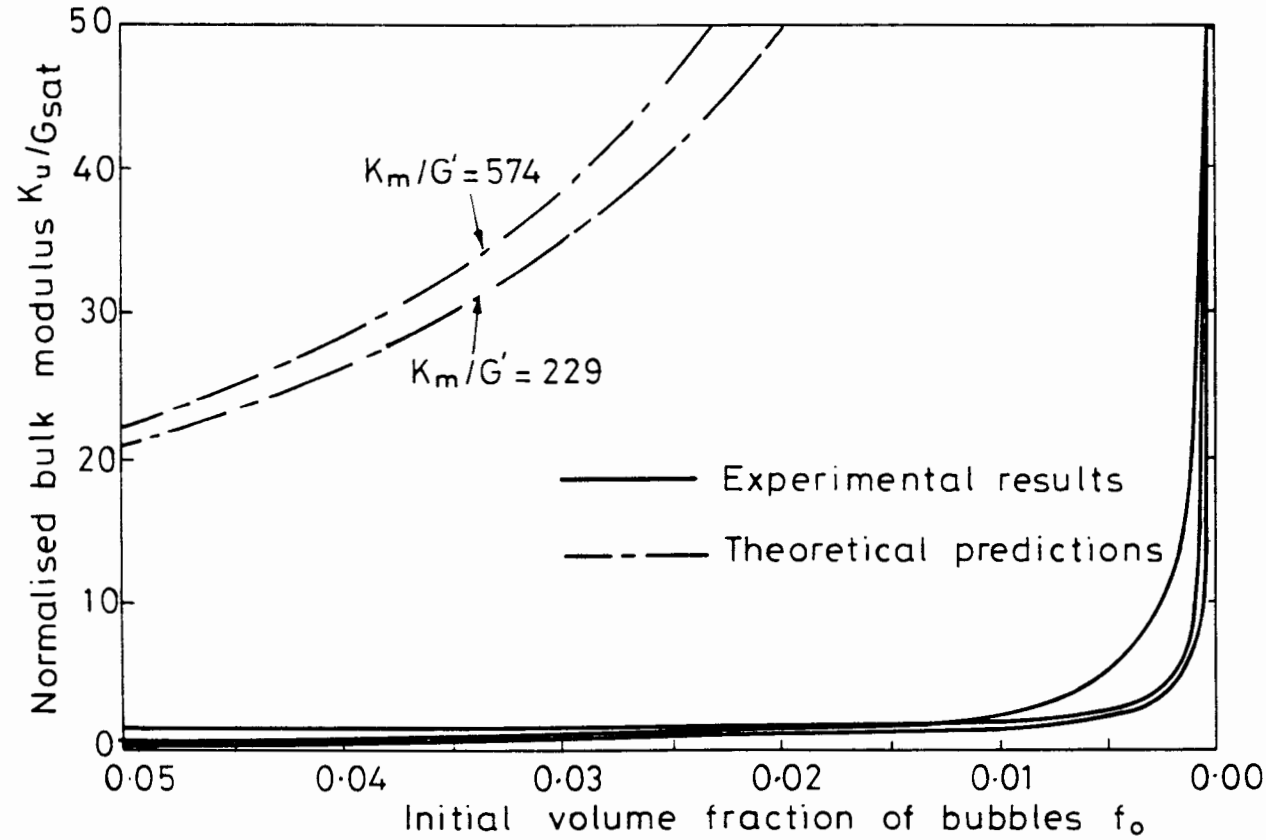

Figure 1.19 Comparison between experimental and theoretical values of bulk modulus (Wheeler, 1986)

initial gas volume fraction. Also plotted on the same axis are Wheeler's theoretical predictions. Similarly, the experimental results of bulk moduli are plotted against the initial gas volume fraction and compared with the theoretical prediction in Figure 1.19.

The main aim of Wheeler's work concentrated on the shear strength behaviour of a gassy soil. Figure 1.20 illustrates this behaviour at various stress levels from his triaxial tests. The shear strengths in this figure have been normalized with the shear strength of a fully saturated soil at the same stress level. It is interesting to note that the presence of gas bubbles reduces the strength of the soil in some circumstances, but increases it in others.

Wheeler presents a lower and upper bound theoretical solution for the shear strength of a gassy soil. The lower bound solution is based on the work by Green (1972) who developed a detailed analysis of the yield behaviour of a rigid perfectly plastic von Mises type material containing empty spherical cavities. This lower bound solution produced a reduction of shear strength due to the presence of gas bubbles. The upper bound solution is based on the fact that during the shearing process it is possible that a certain volume of the pore water could drain into the gas void. This would result in an overall slight drained condition in the soil matrix producing compression of the soil, which in turn produces an increase in shear strength. This process was termed by Wheeler "bubble flooding". Figure 1.21 compares the experimental results with the upper and lower bound solutions. It can be seen that the various experimental curves all fit neatly within the theoretical upper and lower theoretical bounds.

1.6 Engineering Definitions Associated with Gassy Soils

At this stage it is necessary to introduce various definitions pertaining to a gassy soil that are used throughout this thesis. The work of Wheeler and Nageswaran illustrated that the gas exists as discrete gas voids surrounded by a saturated soil matrix. Consequently, the void ratio of this saturated soil matrix can then be found from

$$e_w = v_w/v_s \tag{1.12}$$

where v_w and v_s are the water and solid volumes in a given element of soil. In

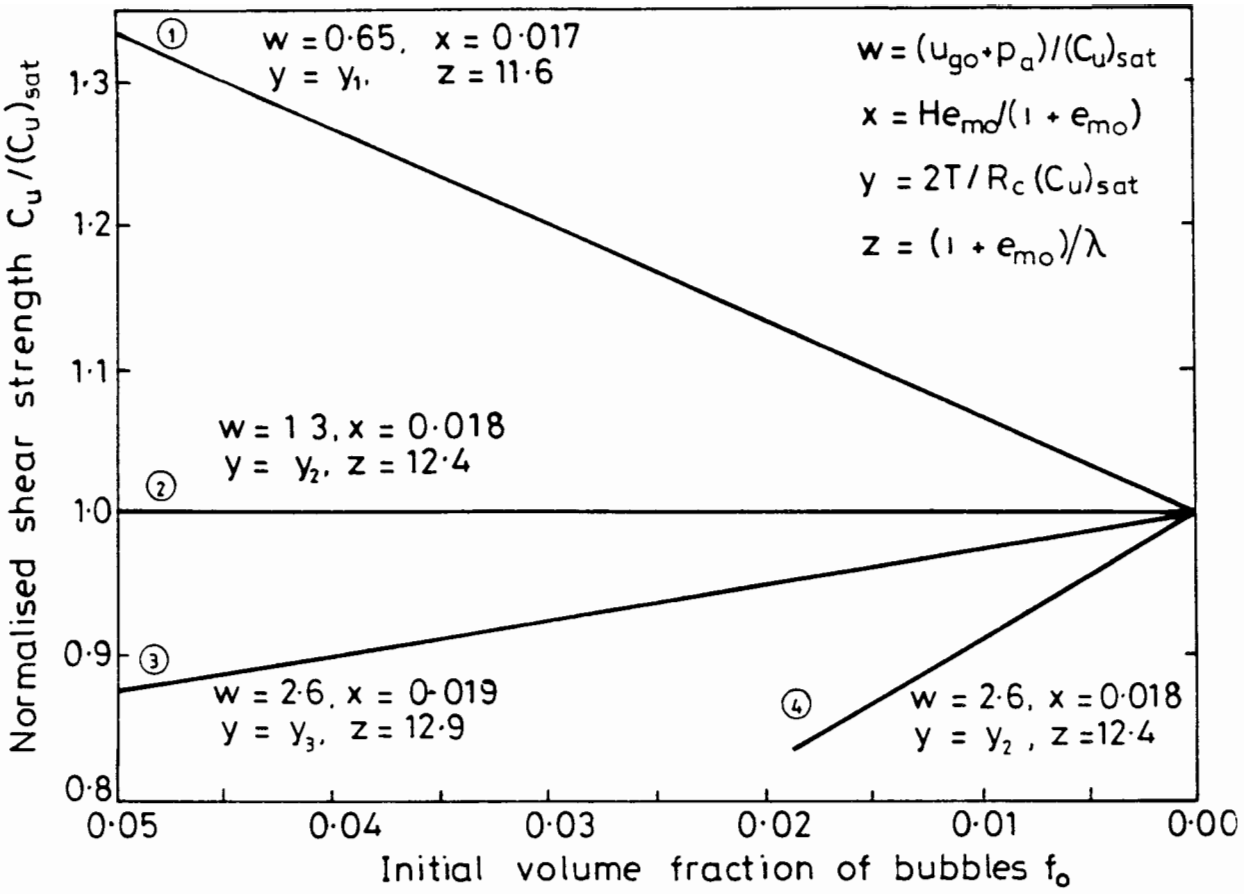

Figure 1.20 Experimental results of undrained shear strength (Wheeler, 1986)

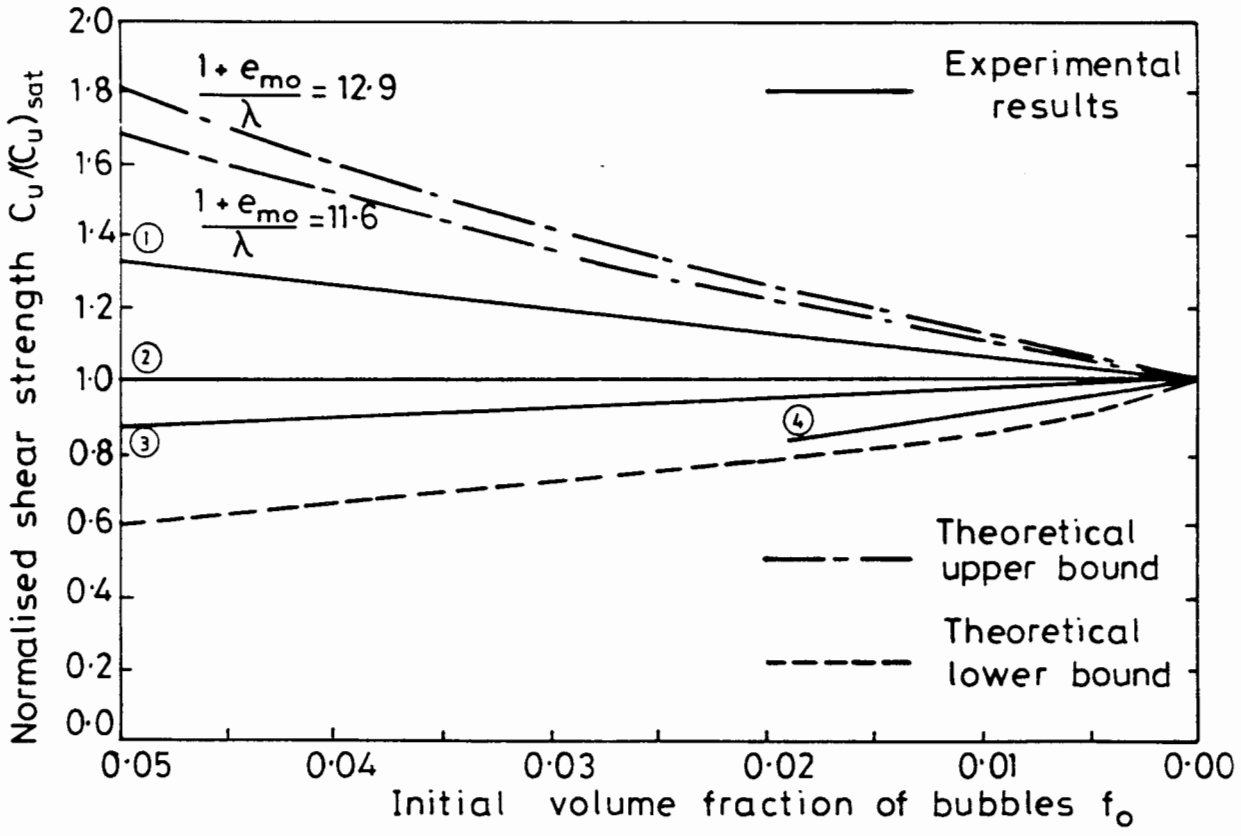

Figure 1.21 Theoretical and experimental values of undrained shear strength (Wheeler, 1986)

[See Wheeler (1986) for explanation of figure notation]

addition, the volume of the gas voids may also be normalized with respect to the solid volume to give the gas void ratio as

$$e_g = v_g/v_s \tag{1.13}$$

where v_g is the gas volume in a given element of soil. The addition of these two equations yields the total void ratio given by

$$e_t = (v_w + v_g)/v_s = v_w/v_s + v_g/v_s = e_w + e_g = e_t \tag{1.14}$$

Furthermore, for a saturated soil, properties such as void ratio and shear strength are dependent on the effective stress $(\sigma - u_w)$. From the experimental work of Nageswaran and Wheeler, the matrix void ratio also appears to be related to the parameter $(\sigma - u_w)$. This should not be called effective stress, however, as this is not necessarily the stress that controls the soil behaviour as it does a saturated soil. Nevertheless, this parameter does appear to govern the consolidation behaviour. Consequently, $(\sigma - u_w)$ is termed the "consolidation stress" such that

$$\sigma'_v = \sigma_v - u_w \tag{1.15}$$

defines the vertical consolidation stress, and

$$\sigma'_m = \sigma_m - u_w \tag{1.16}$$

defines the mean consolidation stress. It must be noted that this parameter becomes the effective stress for a fully saturated soil.

1.7 Aims and Objectives of Research

The original aim of this research was to develop a theoretical model, based on previous experimental findings, to simulate the consolidation behaviour of gassy soil under laboratory and field conditions. The theory could then be formulated into a numerical model which could simulate more complex problems associated with changing material behaviour and irregular geometric conditions.

The first objective was to simulate a typical settlement-time response from the experimental work of Nageswaran (1983). Figure 1.6 presents the family of settlement-time curves produced by the application of a 100 kPa vertical stress increment on 20 mm thick samples of gassy soil of varying degrees of saturation, all under an existing consolidation stress of 100 kPa. The following section describes the theoretical approach and the subsequent numerical formulation used to simulate such soil behaviour.

1.8 Initial Numerical Modelling

Barden (1965) presented the general equations of gas and water flow in an unsaturated soil in one-dimension as

$$\frac{\partial}{\partial z}\left[\rho_w M_w \frac{\partial u}{\partial z}w\right] = \frac{\partial}{\partial t}\left[n_w \rho_w S_w\right] \tag{1.17}$$

for the water phase, and

$$\frac{\partial}{\partial z}\left[\rho_g M_g \frac{\partial u}{\partial z}g + H \rho_w M_w \frac{\partial u}{\partial z}w\right] = \frac{\partial}{\partial t}\left[n_g \rho_g (S_g + HS_w)\right] \tag{1.18}$$

for the gas phase, where M_w and M_g are the mobilities of the water and the gas phases respectively as defined by

$$M_w = \frac{k^i}{\mu_w} = \frac{k}{\gamma}w \quad ; \quad M_g = \frac{k^i}{\mu_g} = \frac{k}{\gamma}g \tag{1.19}$$

where k^i is the intrinsic permeability, μ is the phase viscosity, k is the soil permeability and γ is the specific weight which apply to both phases.

This research is concerned with gassy soils which have a degree of saturation in excess of 0.85. Under this condition, the value of the combined fluid compressibility is not high and can be treated as slightly compressible, from which the spatial derivative of density is neglected with the time dependent derivative remaining. In addition, Figure 1.12 illustrates that for soils greater than 0.85 saturation, there is very little change in the saturation of a gassy soil during the consolidation process. As it is well documented that for a given soil the difference between the gas and water pressure, known as the capillary pressure, is dependent on the degree of saturation (Collins, 1961), it would then follow that the capillary pressure $(u_g - u_w)$ would also change little during the consolidation process. Based on these assumptions, the equations given by Barden can be modified to give

$$\frac{\partial}{\partial z}\left[M_w \frac{\partial u}{\partial z}w\right] = (m_v + n_w c_w)\frac{\partial u}{\partial t}w + n_w \frac{\partial S}{\partial t}w \tag{1.20}$$

for the water phase, and

$$\frac{\partial}{\partial z}\left[(M_g + H M_w)\frac{\partial u}{\partial z}g\right] = (m_v + n_g c_g)(S_g + HS_w)\frac{\partial u}{\partial t}w - n_g \frac{\partial S}{\partial t}w \tag{1.21}$$

for the gas phase.

These two equations were approximated using a one-dimensional Galerkin finite element formulation. The two dependent variables in this formulation are the pore water pressure, u_w, and the water saturation, S_w. Linear finite

elements were used for the approximation in the spatial domain, with the finite difference method used in the time domain.

The FORTRAN code developed from this formulation, named PHASE2, was first verified by solving the Terzaghi consolidation equation in one-dimension for a soil containing either an incompressible or compressible fluid. By modifying the saturations and the phase compressibilities, it was possible to verify both equations 1.19 and 1.20. To test the coupled effect of the model, PHASE2 was used to solve the non-linear Buckley-Leverett equations for which an analytical solution--for a simple permeability-saturation relationship--was given by Collins (1961). Excellent comparisons between PHASE2 and all analytical solutions were obtained.

To simulate the gassy soil consolidation behaviour as observed under laboratory conditions, three different modelling approaches were used which all employed the code PHASE2. These are presented in the following sections.

1.8.1 Model 1

The first attempt at simulating the consolidation behaviour of gassy soil assumed that the gas exists in small discrete bubbles within the pores of the soil matrix. This is the modelling approach used by Barden (1965) for soils of low gas content. He assumed that the gas and water can be combined to produce a single compressible fluid. He also assumed that due to the small proportion of gas present, the Terzaghi effective stress equation would still hold. Based on these assumptions, Barden presented the consolidation equation for a soil containing small bubbles of gas in the pore water as

$$\frac{\partial}{\partial z}\left[\frac{k_w}{\gamma_w}\frac{\partial u_w}{\partial z}\right] = (m_v + n_g c_g)\frac{\partial u_w}{\partial t} \qquad (1.22)$$

It was then possible to solve this equation using PHASE2 by assuming that the soil is fully saturated with water of compressibility $n_g c_g / n_w$. More specifically, if the gas pressure is equal to the pore water pressure, then from Boyle's gas law the compressibility can be related to the pore pressure from

$$c_w n_w = c_g n_g = n_w(1 - S_w)/(u_w + u_a) \qquad (1.23)$$

for a zero value of Henry's coefficient of solubility. PHASE2 was run for five different soil saturations ranging from 0.8 to 1.0. Figure 1.22 illustrates the

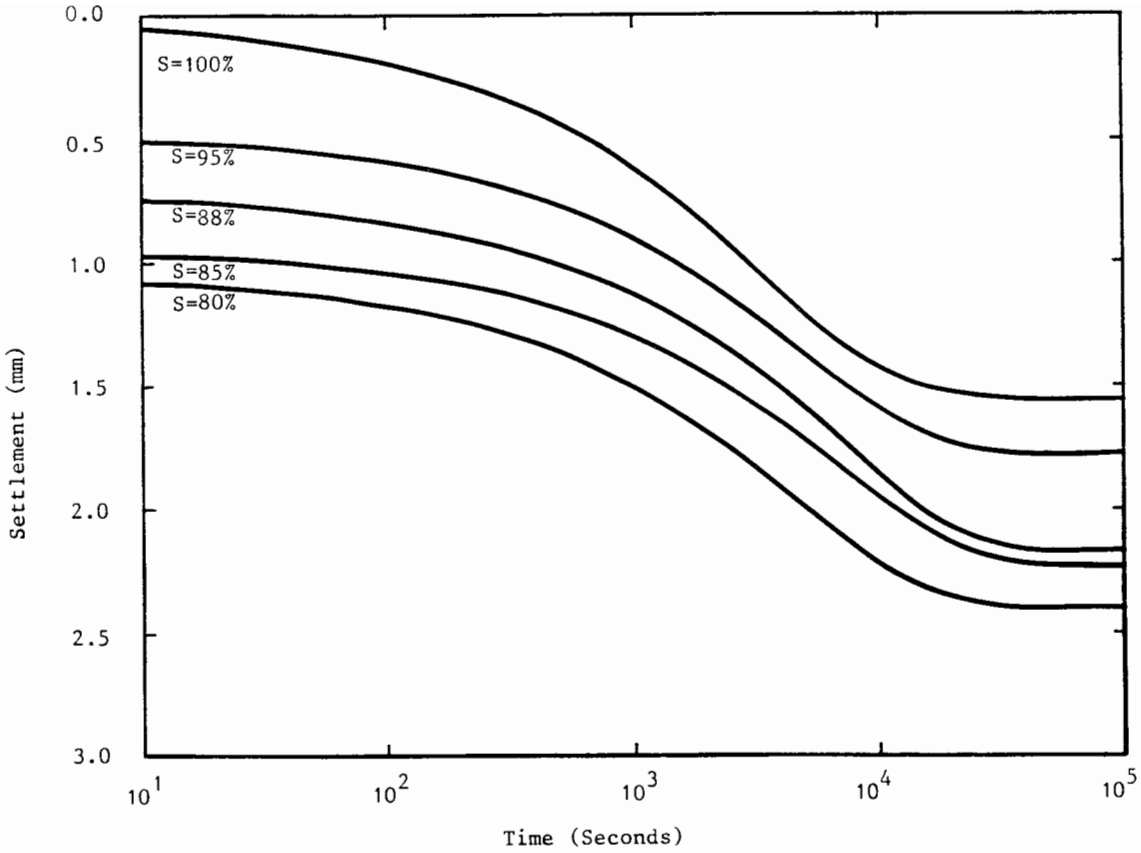

Figure 1.22 Experimental settlement-time response during gassy soil consolidation (Nageswaran, 1983)

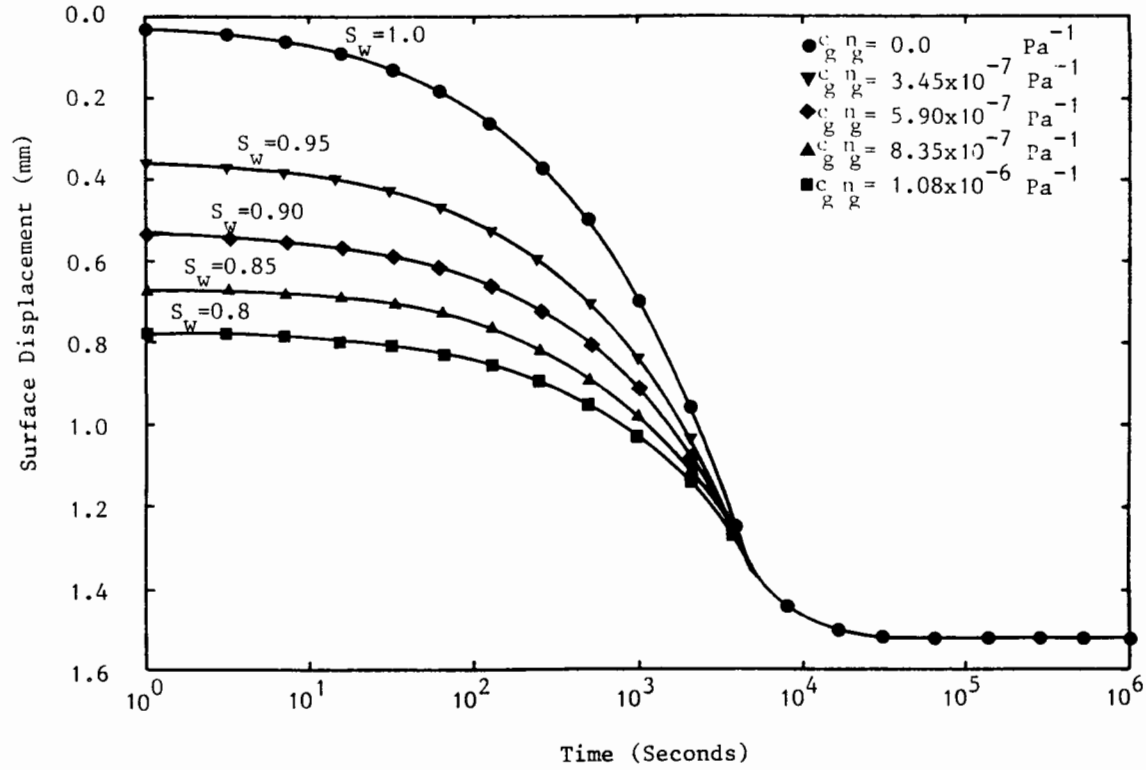

Figure 1.23 Numerical prediction of consolidation behaviour using Model 1

settlement versus log time adapted from the results of Nageswaran for a series of gassy soils. All samples have an initial height of 20 mm, a permeability of 3×10^{-8} m/min and a coefficient of volume change m_v, of 0.6 MPa^{-1}.

The resulting settlement versus the log of time for the series of saturations is presented in Figure 1.23. It can be seen that the initial displacement behaviour is modelled quite well. Whereas the experimental results all produce different final settlements for each degree of saturation, however, the numerical results all produce an identical final settlement after all pore pressures have dissipated. Figure 1.26a presents the type of void ratio behaviour of a gassy soil for saturations of 90%, 95% and 100% that have been observed experimentally. In Model 1, it is assumed that the gas and water combine to form a single compressible fluid which saturates the soil. Consequently, irrespective of the degree of saturation, a soil begins with a void ratio at Point A. On application of a load of 100kPa, the gas will compress producing an undrained void ratio and effective stress change leading to Point B. This point will depend on a combination between the saturation and compressibility of the gas, the soil compressibility and magnitude of the applied load. On drainage, the pore water pressure will dissipate resulting in the final value of the consolidation stress reaching a value of 200 kPa.

1.8.2 Model 2

This model onces again assumed that the pore water and the pore gas combine to form a single compressible fluid. It was also assumed that the soil will deform due to changes in vertical consolidation stress. However, from the experimental results of Nageswaran (1983), it appears that the soil has a different void ratio-consolidation stress relationship depending on the initial saturation of the sample. Therefore, for this model the assumption was made that there is a separate e:log σ'_v relationship for each of the tests with a different initial degree of saturation. The resulting settlement versus log time result is presented in Figure 1.24. Figure 1.26b illustrates the undrained-drained void ratio change for a 90% saturated sample. For undrained conditions the void ratio moves from Point A to Point B. For drained conditions the void ratio continues to move down this same 90% consolidation line to the

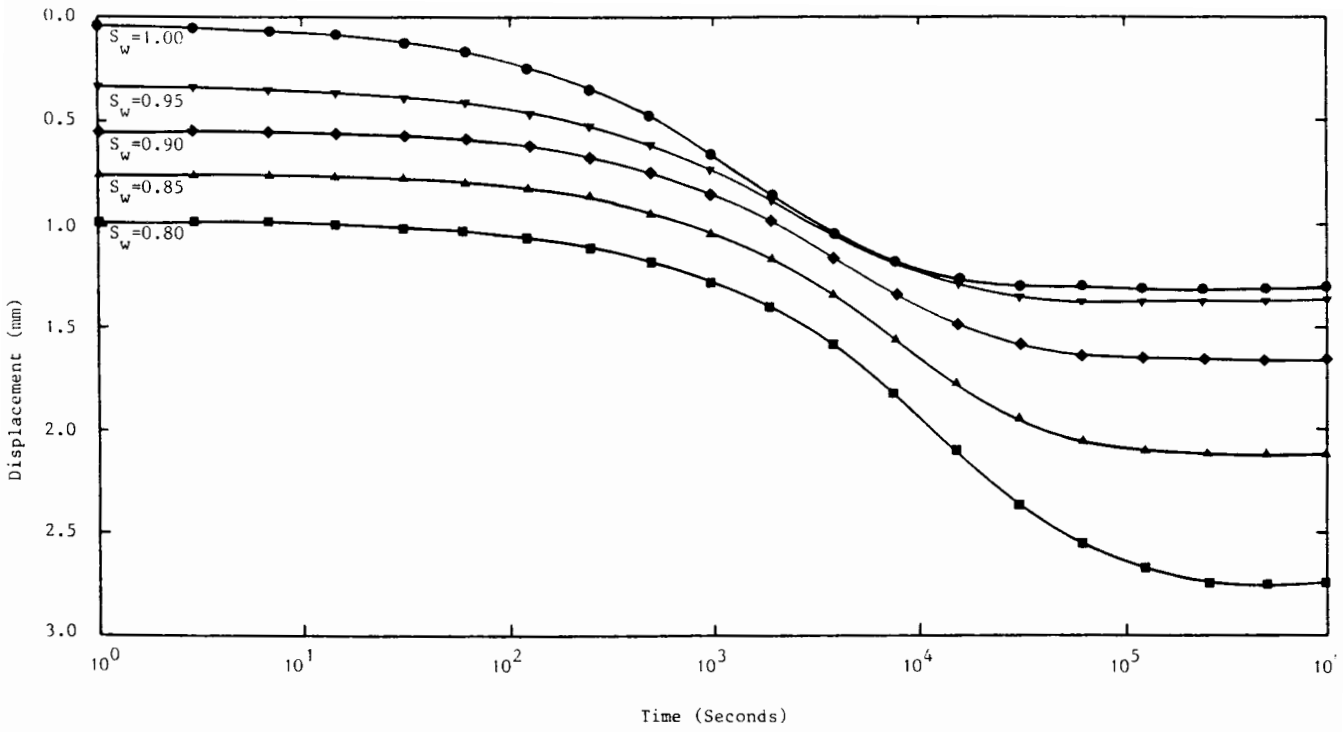

Figure 1.24 Numerical prediction of consolidation behaviour using model 2

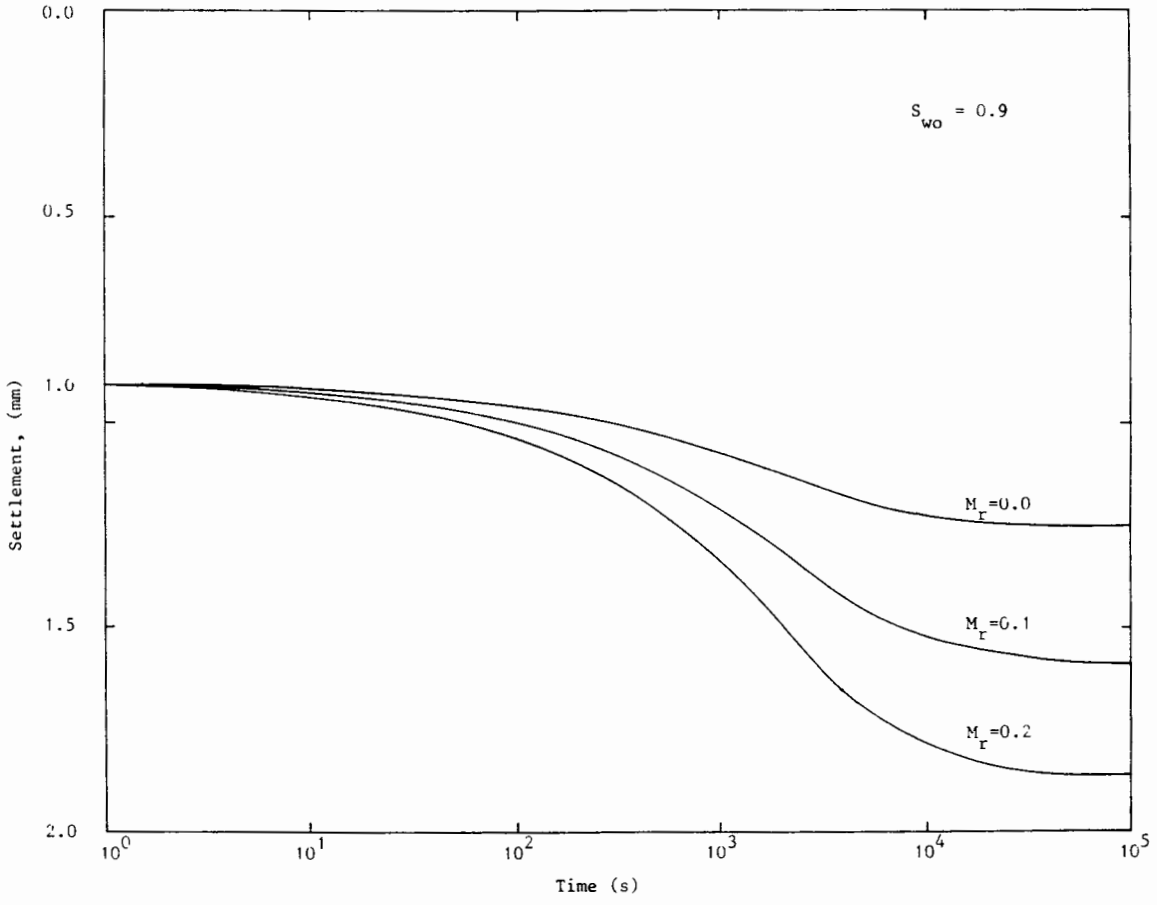

Figure 1.25 Effect of mobility ratio on the prediction of consolidation behaviour using model 3

final Point C, when all pore water pressures have dissipated. Although it appears from Figure 1.24 that the settlement behaviour has been modelled successfully, it must be realized that the void ratio versus consolidation stress relationships are those obtained from the experimental results. It is therefore not surprising that the simulation appears to be successful.

1.8.3 Model 3

The third model treated the gas and water as having two separate phases. Under these conditions the degree of saturation may change depending on the changes in both the water and the free gas. Therefore, although the same empirical e:log σ'_v relationships are used to describe the gassy soil compressive behaviour as Model 2, this model chooses a relationship based on the current value of saturation and not the saturation at the start of the test. In addition, Model 3 does not assume that the gas and water flow in the same proportions as was the case for the previous two models. Instead, PHASE2 is able to allocate a permeability, or mobility, to each phase. Mobility is simply the soil permeability divided by the specific weight of each phase. The gas mobility is normally related to the water mobility by the term "mobility ratio"

$$M_r = M_g/M_w \tag{1.24}$$

Figure 1.25 presents the settlement-log time curve for a gassy soil of initial saturation 0.9 for mobility ratios of 0.0, 0.1, and 0.2. It can be seen that the final settlement is highly sensitive to this parameter. To illustrate the change in saturation during consolidation, Figure 1.26c presents the void ratio path during the consolidation process for a gassy soil of 90% initial saturation. Under undrained conditions the void ratio moves from Point A to Point B, with no flow of either of the fluid phases. Due to the compression of the gas phase, however, the saturation will increase and the void ratio will move from the 90% line to the 95% line. On drainage, both water and gas will leave the sample, and for this particular case the void ratio will rejoin the 90% line at Point C.

To illustrate further the effect of the mobility ratios, Figure 1.27 illustrates the paths taken in e:log σ'_v space for the three different mobility

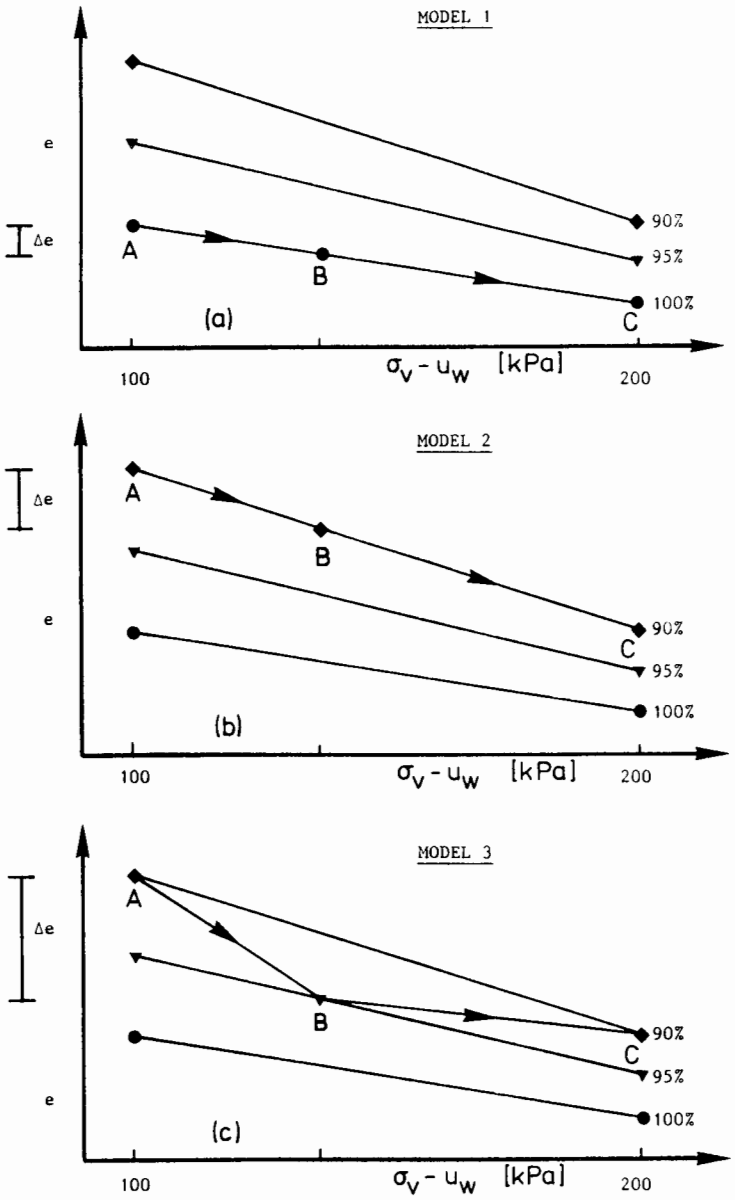

Figure 1.26 Illustration of undrained-drained behaviour using three separate models incorporated into PHASE2

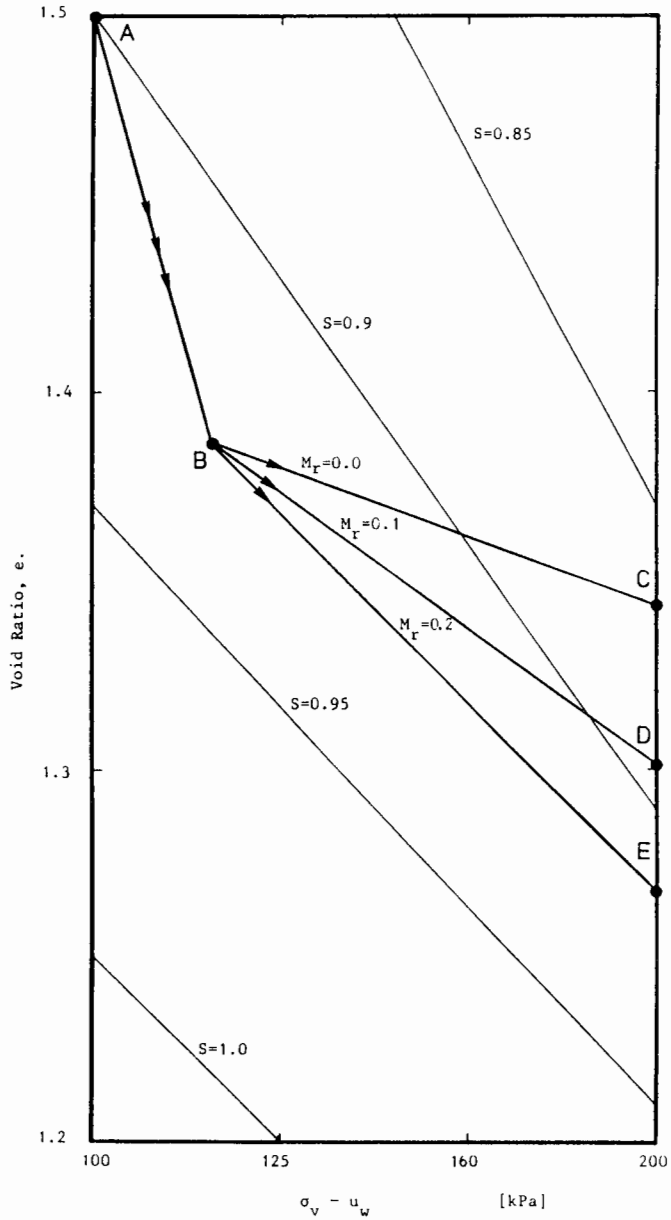

Figure 1.27 The effect of mobility ratio on the void ratio of a gassy soil during consolidation

ratios, 0.0, 0.1 and 0.2, used to evaluate the results of Figure 1.25. Again under undrained conditions, there is no flow of either fluid, only a compression of the gas phase causing both an increase in saturation and consolidation stress resulting in the path A to B for all mobility ratios. For the drained stage, however, a low mobility ratio (M_r= 0.0) produces a high final gas content (low saturation) and will end up at point C. As the mobility ratio increases allowing more gas to leave the sample, higher saturations will be produced resulting in a final Point D for M_r = 0.1 and a Point E for M_r = 0.2.

1.9 Summary

This introductory chapter describes the presence and origin of a gassy marine soil and also looks at some of the problems associated with the presence of such soil to a marine geotechnical engineer. The low gas content of these naturally occurring gassy soils produces a situation in which the gas is in occluded form within the soil. It is possible, however, that the gas could exist as small bubbles within the original structure of the soil skeleton, or as large bubbles surrounded by a saturated soil matrix.

A review of the theoretical and numerical modelling of the consolidation behaviour of unsaturated soils is then presented, where at one extreme the water and gas were treated as a single compressible fluid, while at the other extreme the unsaturated soil was described as a four phase material. This is followed by a description of the gassy soil research that has taken place at Oxford University over the last nine years, with the main emphasis on the work of Nageswaran (1983) and Wheeler (1986).

Finally, based on the theory obtained in the literature, an attempt is made to simulate numerically the experimental consolidation results of Nageswaran. Three types of theory are utilized ranging from a single compressible pore fluid to a fully three phase theory, with all three models formulated using the finite element method. Unfortunately there was only limited success using these theories, and in general the simulation could only be described as poor. Consequently, it was decided that there was insufficient information available to model gassy soil consolidation adequately and that further experimental consolidation tests on this material should be performed.

CHAPTER 2

SAMPLE PREPARATION AND EXPERIMENTAL APPARATUS

CHAPTER 2

SAMPLE PREPARATION AND EXPERIMENTAL APPARATUS

2.1 Introduction

The previous chapter illustrated clearly that the approach normally taken in the numerical or theoretical modelling of unsaturated soils fails to simulate the consolidation behaviour of gassy soils as observed by the experiments of Nageswaran (1983). Therefore, in order to produce any successful simulation of gassy soil consolidation behaviour, it is first necessary to comprehend the physics of the problem and to obtain an understanding of the processes that occur during such consolidation. The work of Nageswaran (1983) gave an insight into the consolidation behaviour of gassy soil and illustrated the problems associated with the testing of such a material. It is felt, however, that there is scope for improvement in both the experimental techniques and the interpretation of the results to warrant further experimentation.

The primary purpose of this experimental work is to understand the consolidation process and the behaviour of each of the three phases in a gassy soil. A further aim would be to obtain constitutive relationships between the soil properties and soil parameters, such as stress and pore water pressure. The secondary purpose of this experimental work is to produce physical responses which can be simulated using any subsequent theory that may be developed.

This chapter describes the laboratory preparation of a gassy soil sample, followed by a description of the apparatus used for the formation of a soil sample from a slurry and the subsequent consolidation testing on this sample.

2.2 Sample Preparation

Both Nageswaran (1983) and Wheeler (1986) performed their respective experimental tests using Combwich mud, a clayey silt from the estuary of the River Parrett at Combwich in Somerset. As this experimental work is intended not only to extend the understanding of gassy soil behaviour but also to enhance the results from previous experiments, Combwich mud was also chosen as the soil in this research.

The Combwich mud was collected from below the high water line from the River Parrett. The mud was then sieved using tap water through a standard 63 μm mesh. After allowing settlement to take place, the soil slurry was then transferred to a five gallon container. All the experimental tests were subsequently performed on samples of soil taken from this same container. Density tests were then performed on this soil producing a solid density of 2.637 g/cc. The particle size distribution of Combwich mud, as obtained by Nageswaran (1983), is presented in Figure 2.1.

In order to produce samples of gassy soil in the laboratory, a technique is used termed the "zeolite molecular sieve technique" which was developed by Nageswaran at Oxford University. This technique enables a controlled distribution of methane gas bubbles to be introduced into a sample of otherwise saturated soil. Methane gas is chosen as it is the gas most commonly found in marine sediments. The above technique is described in detail by Nageswaran (1983), Sills and Nageswaran (1984) and recently by Wheeler (1986).

The zeolite molecular sieve technique involves first removing the water of hydration from a zeolite powder (Type 5A, solid density 2.41 g/cc), followed by the impregnation of the crystal structure of the zeolite with methane. When this "methane charged" zeolite powder is then mixed with a soil slurry, the zeolite--which has a natural affinity or preference for water--will take up the water from the slurry into its crystal structure, thus releasing the methane gas. This released gas in turn forms bubbles in the soil slurry.

In order to impregnate the zeolite with methane, the zeolite is first oven dried at 105°C for 24 hours. This removes the water of hydration. The required weight of zeolite is then placed in an evacuation chamber and subjected to a vacuum to remove the air from the zeolite crystals. Two lines are attached to the evacuation chamber, a vacuum line and a line to a methane bottle. After the zeolite has been under vacuum conditions for 24 hours, the vacuum line is closed followed by the opening of the methane line. In this way, no air can then re-enter the pressure chamber. The zeolite is then subjected to a methane gas pressure at 200 kPa for a further 24 hours.

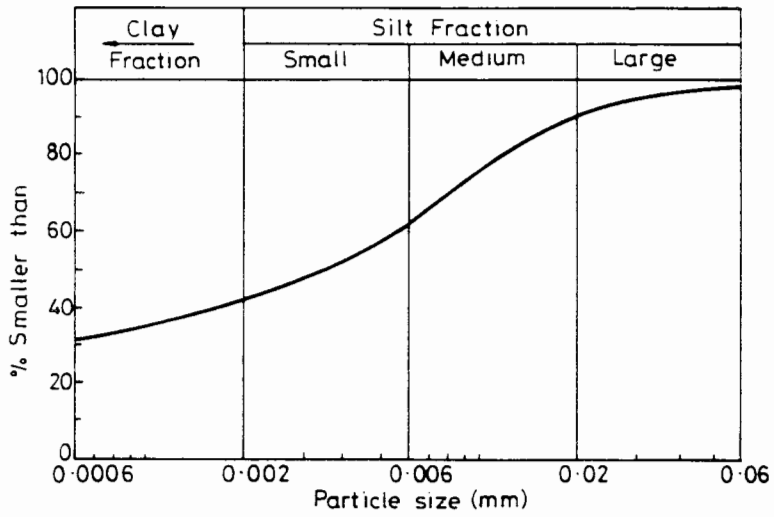

Figure 2.1 Particle size distribution of Combwich mud (Nageswaran, 1983)

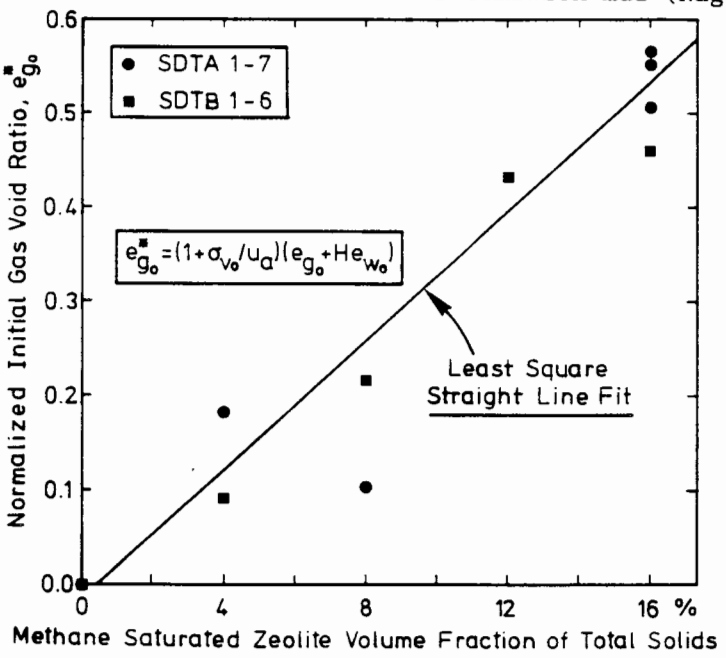

Figure 2.2 Normalized initial gas void ratio versus initial methane saturated zeolite volume fraction

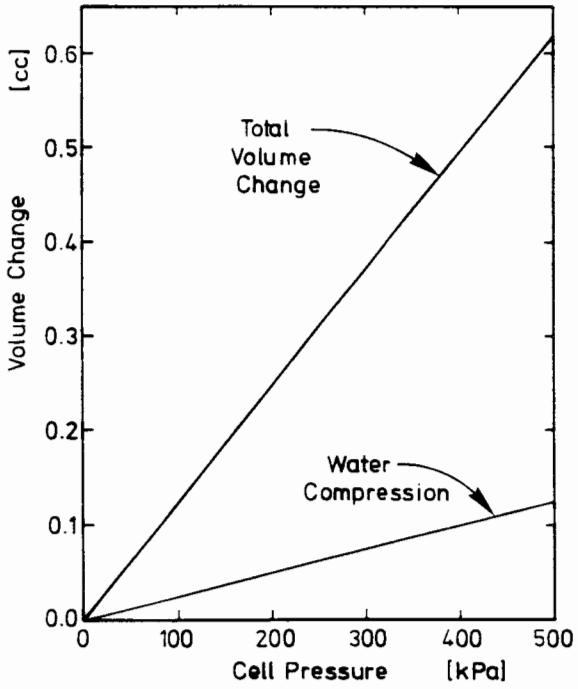

Figure 2.3 Calibration of oedometer cell

As the experimental testing programme involves examining the consolidation behaviour of soils of different gas contents, it is necessary to vary the initial volume of methane that is introduced into the soil slurry. This may be achieved by changing the volume of methane charged zeolite. Due to the fact that the physical properties of the soil and the zeolite are not identical (Nageswaran, 1983), however, it is important that the proportion of total zeolite volume to total solid volume remains constant for all tests despite the difference in gas content. In all the tests performed in this research, 16% of the total solid volume is made up by zeolite. If for example 12% of this zeolite is to be methane charged, then 4% by volume must be made up of water saturated zeolite. Water saturated zeolite is prepared by stirring a zeolite slurry for 24 hours in an orbital shaker whilst subjected to vacuum conditions.

At the same time as the zeolite is prepared, the Combwich mud is prepared to a bulk density of approximately 1.3 g/cc. This is performed by adding water to the slurry while mixing using a mechanical mixer. The required mass of the soil slurry is then poured into a mixing bowl and hand mixed with any water saturated zeolite. It must be noted that it is the volume of solids that is important, and therefore a water bottle may be used to ensure that all the zeolite slurry is mixed with the soil. Gentle hand mixing ensures that the minimum of air enters the soil slurry.

The methane charged zeolite is then emptied from the opened pressure chamber into the soil slurry, and again it is important that all the zeolite is incorporated. This mixture is then stirred by hand until no white traces of zeolite powder can be seen. The slurry, bowl and mixer are then weighed and the slurry is poured into the awaiting consolidation cell. The remaining slurry, bowl and mixer are then reweighed so as to evaluate the exact weight of slurry that entered the cell. A sample of the remaining slurry is then taken to evaluate the moisture content, from which the weight of solid entering the cell can be calculated.

The test is designed so that the slurry is poured into the consolidation cell leaving approximately 50 mm clearance between the top of the slurry and the top of the cell wall. This space is then carefully filled with de-aired water.

When the water is just level with the top of the cell wall, the filtering system --consisting of a millipore filter, a stainless steel mesh and a perforated steel plate--is then placed in position over the top end of the cell, followed by the perspex top cap, aluminium ring and the holding down bolts.

The sample is then subjected to a stress via the piston of approximately 3 kPa. This is enough pressure to start moving the slurry slowly towards the top face. Thus the water placed on top of the slurry emerges from the steel plate and gradually fills the top cap. In this way no air becomes trapped in the filtering system, as is the case when the top cap is flooded from above. When the top cap and drainage lines are completely saturated, the loading stress on the piston is increased to 35 kPa, with the water permitted to drain from the summit of the top cap. This immediate application of stress follows the procedure of Wheeler (1986), but contrasts with the procedure used by Nageswaran (1983) who waited 24 hours for all the gas to be released before applying any load to the soil. Wheeler found, however, that a more uniform distribution of gas bubbles is produced if the load is applied immediately so that the soil is consolidating as the gas is being released. For soil tests requiring an initial sample thickness of around 20 mm, settlement and dissipation of pore water pressures were found to be completed in under 24 hours.

To illustrate the relationship between the initial generated gas volume and the proportion of methane saturated zeolite used, it is first necessary to define the normalized gas void ratio as

$$e_g^* = (e_g + H\, e_w)(1 + \sigma_v/u_a) \qquad (2.1)$$

where e_g^* is the normalized gas volume, e_g is the free gas void ratio, H is Henry's coefficient of solubility (H=0.0333 for methane in water, Yamamoto, et al., 1976), e_w is the water void ratio, σ_v is the initial total vertical stress and u_a is the atmospheric pressure. This normalized gas volume takes into account both the free and dissolved gas that is present in the soil and the different initial consolidation pressures. Figure 2.2 presents the initial normalized gas void ratio for two series of tests performed in this research versus the solid fraction of methane saturated zeolite. This figure illustrates

that a general trend exists between the volume fraction of methane saturated zeolite and the initial normalized gas void ratio, although it can also be seen that the relationship between these two parameters is very unpredictable.

The gas bubbles that are produced by the zeolite molecular sieve technique have been found to be in the range of 0.02 to 2 mm in diameter (Gardner, 1987). As stated by both Wheeler and Nageswaran, comparison with the particle size distribution--as presented in Figure 2.1--illustrates that the gas bubbles are considerably larger than a typical soil particle. This can be quite clearly seen from the photograph of a gassy soil produced by Nageswaran as presented in Plate 2.1. The sample in this photograph has a saturation of approximately 80% and has been consolidated to a one-dimensional stress of 35 kPa. This gassy soil structure is in marked contrast to a saturated soil consolidated to the same stress level as shown in Plate 2.2. It is clear from these two photographs that the gas voids are much larger than the individual soil particles.

2.3 Description of Apparatus

The apparatus used to form and consolidate the gassy soil samples consisted of a specially designed oedometer cell. This cell required not only specifications normally encountered when consolidating a saturated soil, but also a number of increased specifications due to the presence of undissolved gas. The specifications required for such a consolidation cell include:

- The measurement of total vertical stress on the soil sample.
- The measurement of pore water pressure on the undrained face.
- The capability to consolidate a soil from a slurry.
- The capability to separate the free gas from the pore fluid that drains from the sample on consolidation.
- The independent evaluation of the volumes of each of the three phases (solid, water and free gas) throughout the consolidation test.
- The option of evaluating horizontal total stresses.

The cell used during this research was initially developed by Nageswaran (1983). Although there have been several modifications to this cell for the purpose of this research, the main structure of the cell has not been altered.

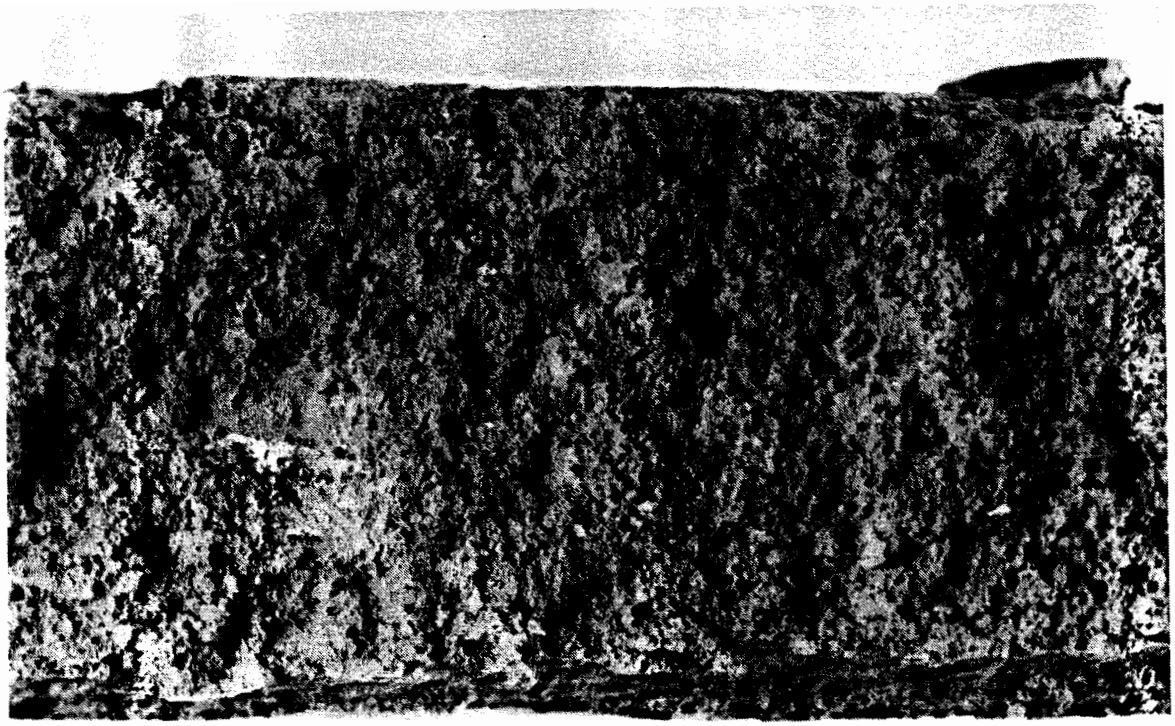

Plate 2.1 Appearance of Gassy Soil. Magnified x 6
Degree of Saturation = 0.8, 1-D Consolidation to 35 kPa
(Nageswaran, 1983)

Plate 2.2 Appearance of Saturated Soil. Magnified x 6
Degree of Saturation = 1.0, 1-D Consolidation to 35 kPa
(Nageswaran, 1983)

A schematic description of the oedometer cell is presented in Figure 2.4, illustrating the cell, the piston, the base and the top cap. At the start of a consolidation test, the gassy soil slurry is poured into the cell above the piston. The top cap and drainage filters are bolted down into the top of the cell by an aluminium ring and three holding down bolts. The soil slurry is then loaded from the bottom undrained face. Drainage of pore fluids occurs from the top face, which for drained conditions is maintained at atmospheric pressure.

The piston, which is machined from a solid block of brass, contains a total stress transducer such that the face of the transducer is in contact with the undrained face of the soil sample. The transducer's power supply and received signal leads continue through the piston and guiding ram to emerge from a hole at the end of the hollow guiding ram. These leads are then connected to the power supply block, which also receives the return signal from the transducers.

Also embedded in the piston is a porous stone for the measurement of the pore water pressure on the undrained face of the soil sample. A coiled water filled nylon tube is connected at one end of the passage directly beneath the porous stone. The tube then passes through the water filled cavity beneath the piston to be fixed at the other end to a passage that leads through the base of the oedometer. A second water filled nylon tube connects the outside of this passage to a water filled perspex block containing a pressure transducer. This arrangement produces a direct water link between the pore water and the transducer face, so that any change in pore water pressure can be measured by the stress transducer.

The cell is made from a stainless steel tube of 4.25 inches (107.95 mm) inside diameter and 10mm wall thickness. The cell is bolted to the stainless steel base with the aid of three brackets which are welded to the outside of the cell wall at 120° to each other. The piston is then able to slide unobstructed throughout the entire height of the cell, thereby permitting large strain consolidation of a soil slurry. The cell is easily separated from the base and piston by removing the three outside bracket bolts and lifting the cell so it slides off the piston.

The piston has a radial clearance of 0.5 mm with the cell wall and is sealed with the use of an O-ring. The piston is held in position with the use of a

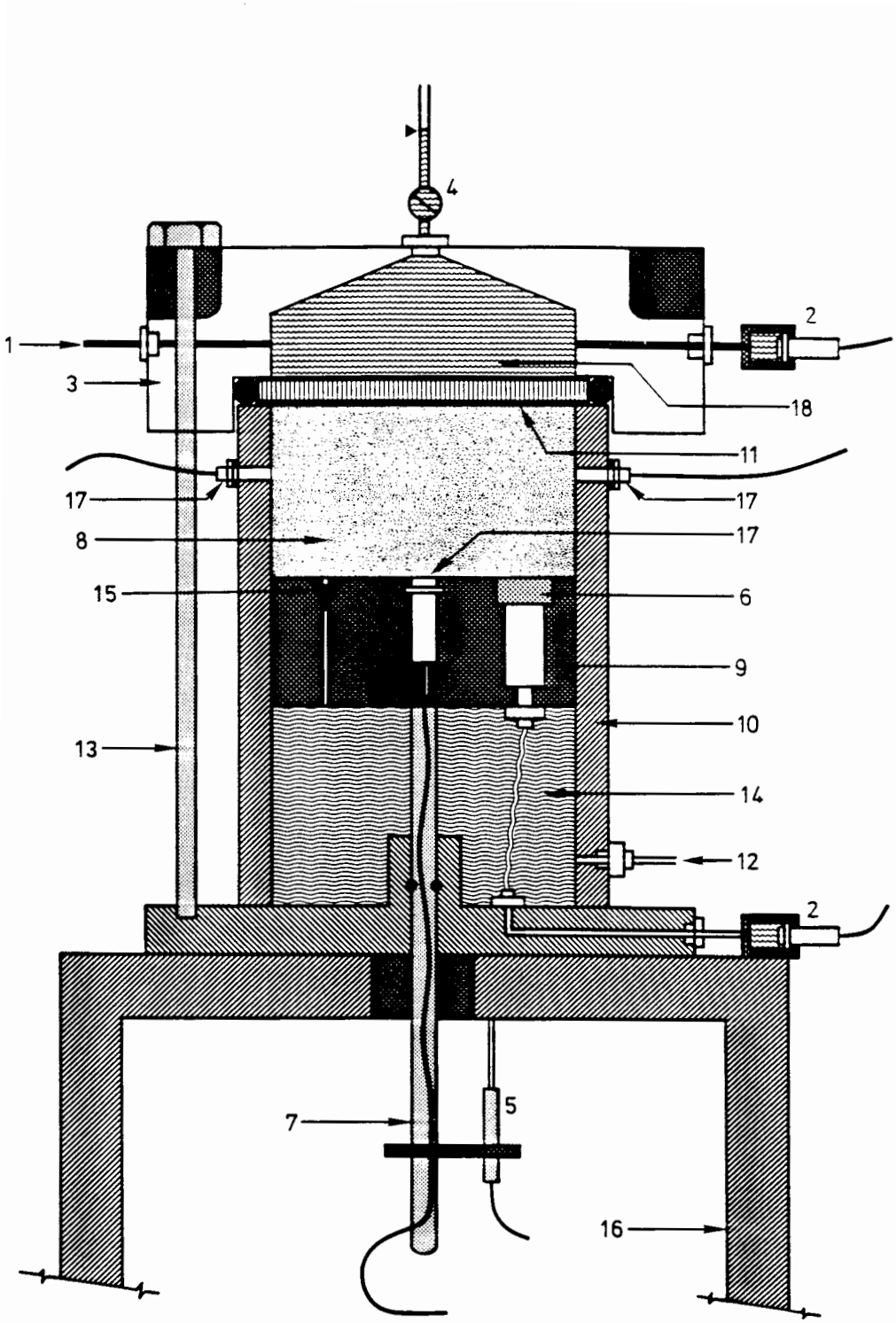

1	Drainage Port	10	Cylinder Wall
2	Pressure Transducer	11	Filtering System
3	Top Cap	12	Water Reservoir Inlet
4	Tap Valve	13	Holding Down Bolt
5	Displacement Transducer	14	Water Reservoir
6	Porous Stone	15	Bleed Screw
7	Guide Rod	16	Support Frame
8	Soil Sample	17	Total Stress Transducer
9	Piston	18	Drainage Water

Figure 2.4 Schematic description of oedometer cell

guiding ram which consists of a 200 mm steel tube of 19 mm outside diameter and 3 mm wall thickness which screws into the underside of the piston onto an H-ring to seal this joint. The use of PTFE tape around the ram ensures a good seal. The ram is guided by a plain bush which is machined from a solid block of brass and embedded in turn into the stainless steel oedometer base.

For the test series B, described later, two miniature horizontal stress transducers are threaded into the side of the cell wall at a distance of 10 mm from the top. These transducers are sealed using a silicon sealant which is also used to produce a smooth surface which is in contact with the side of the soil sample.

The cell and base are bolted down to a rigid frame which is fixed to the floor. Clamped to the guiding ram beneath the base and frame is a displacement transducer which measures the displacement of the ram relative to the rigid frame, thus measuring the displacement of the piston relative to the cell.

The top cap is machined out of a solid 35 mm thick perspex slab. The underside or inside of the cap is hollowed out to give a coned cavity pitched 15° to the horizontal in order to collect any gas that may enter the top cap from the soil. There are three outlets from the top cap. One is at the top centre of the cap where a tap valve is connected. Another leads to a water filled perspex block connected to a pressure transducer so that the water pressure in the cap can be measured. A third outlet connects the top cap to a volume change burette which measures the water volume that leaves the top cap.

The top cap is held in position by an aluminium ring which is bolted down to the base with the use of three holding down bolts spaced at 120°. To prevent the soil from entering the top cap, a sintered bronze disk and a millipore filter are initially used to drain the pore fluids from the soil. This filtering layer is held in position between the top cap and the cell wall. The assembled cell, top cap, base and frame are presented in a side view in Plate 2.3 and from above in Plate 2.4. A view of the inside of the cell with the top cap and filtering system removed is presented in Plate 2.5. Illustrated in this photograph are the total stress transducer and pore water pressure port on the piston face and the horizontal stress transducers in the side wall of the cell.

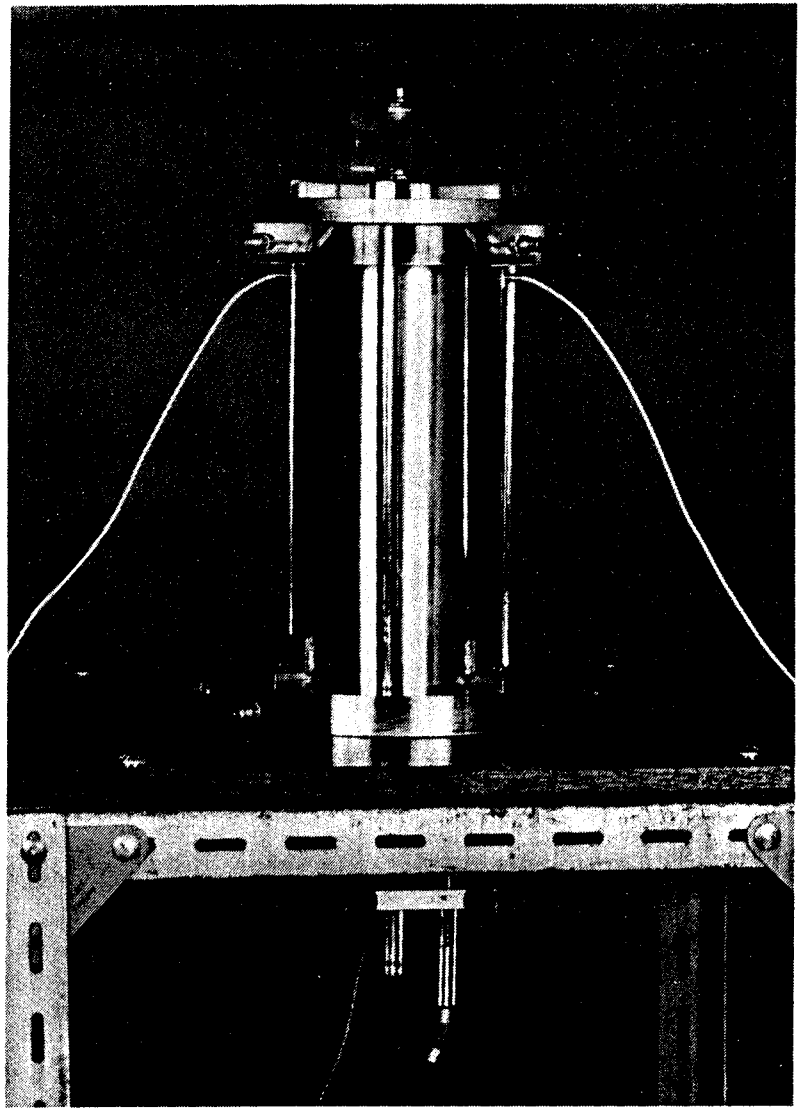

Plate 2.3 The Oedometer Cell

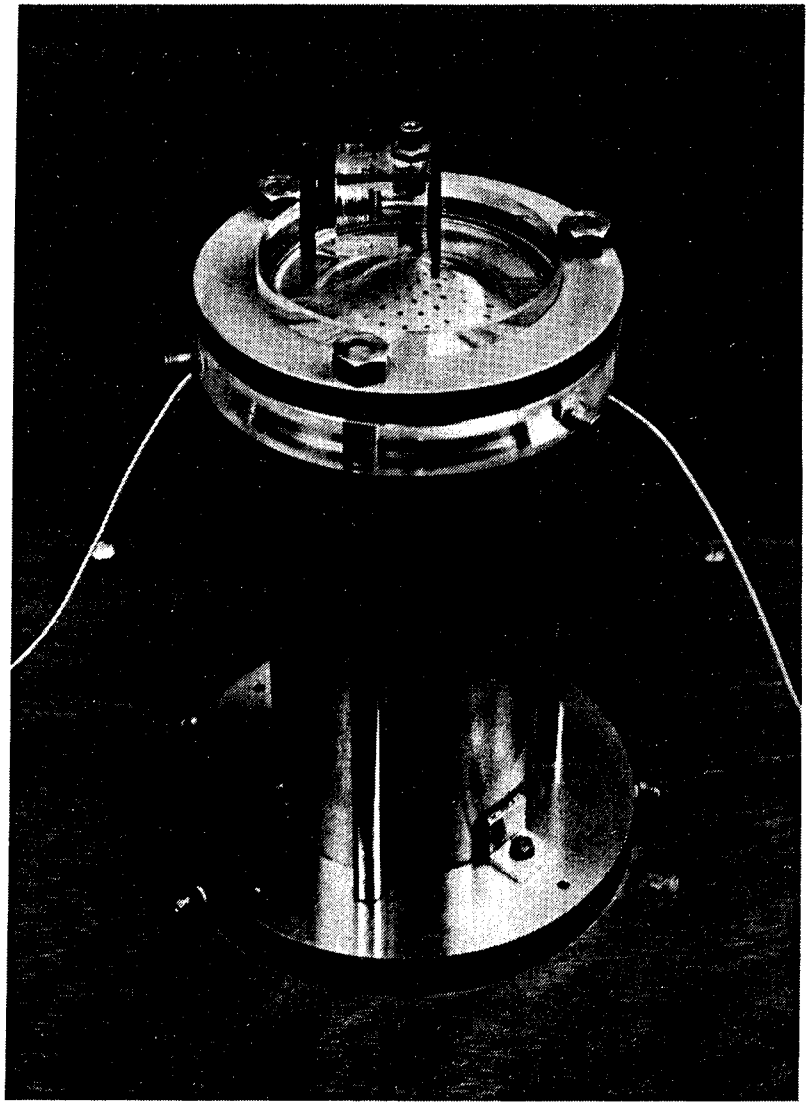

Plate 2.4 Oblique View of the Oedometer Cell

2.4 Calibration and Modification of Oedometer

The calibration of the oedometer was performed by first saturating the cell, top cap and sintered bronze disk with de-aired water. The cell was pressurized in steps up to 500 kPa by applying an increase in the water pressure beneath the piston. The object of this calibration was to evaluate the compliance of the apparatus due to an increase in the cell pressures. Early calibration illustrated an initial bedding in of the top cap on the O-ring seals. Rigorous tightening of the holding down bolts, however, meant that this bedding in stage could be virtually eliminated.

The resulting calibration between the total volume calculated from the piston displacement and the pore pressure inside the cell is presented in Figure 2.3. Also presented in Figure 2.3 is the volume change that would be caused by the compression of the water in the cell ($c_w = 4.58 \times 10^{-7} kPa^{-1}$). The net volume change due to the expansion of the apparatus (which is almost exclusively caused by the stretching of the holding down bolts) is then the difference between the two lines of Figure 2.3, which can be approximated by

$$\frac{\Delta v}{\Delta u_w}_e \simeq 0.001 \quad cc/kPa \tag{2.2}$$

Thus for any measurement of total volume, the actual volume of the sample is Δv_e higher than measured. Thus Δv_e must be added to any measured volume to give the actual volume of the sample.

During the initial consolidation tests on gassy soil samples, it was discovered that the sintered bronze disk--which forms the drained boundary to the soil--became desaturated over the period of testing. Consequently, as the technique used for the measurement of free gas volume would combine the gas in the filter and the gas in the soil, it is impossible to separate these gas volumes--with the result that an accurate measurement of the soil saturation is difficult to make.

To overcome this problem, a filtering system was designed which not only supported the soil allowing free drainage at the soil boundary, but also did not retain any free gas. The design consists of a three layer system. The layer is given strength by using a 3 mm thick stainless steel plate which is perforated with 3 mm holes. A millipore filter is positioned so that it is in contact with

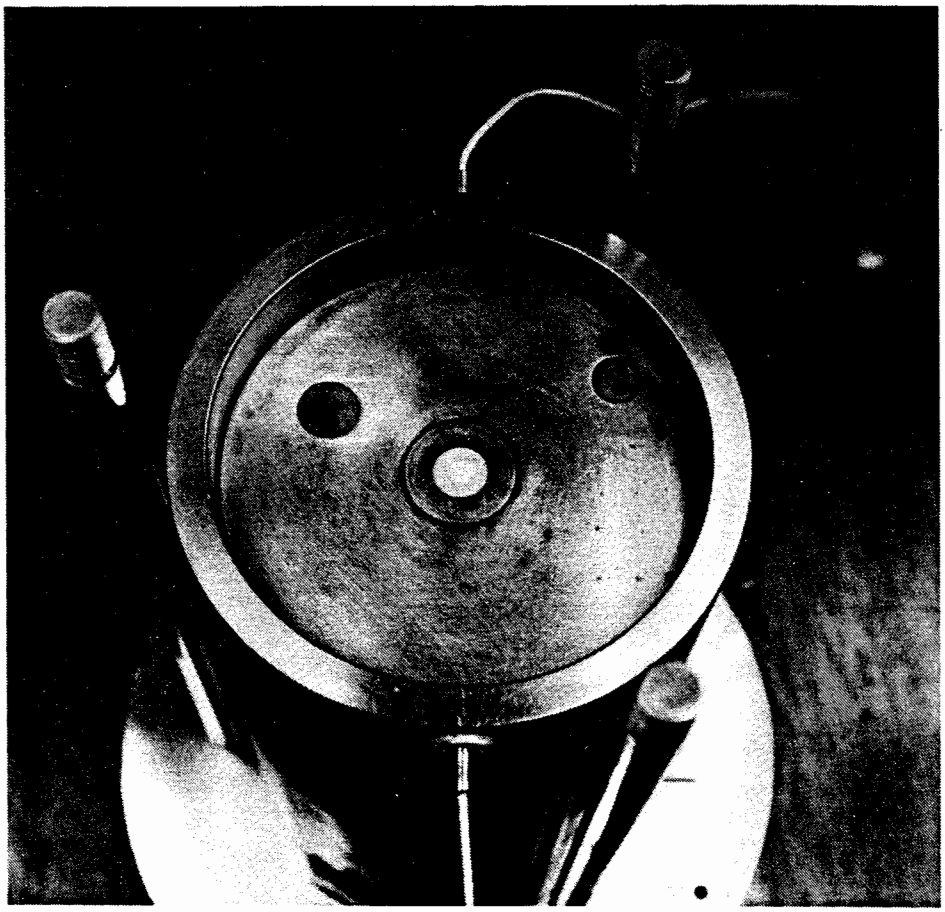

Plate 2.5 Inside View of the Oedometer Cell

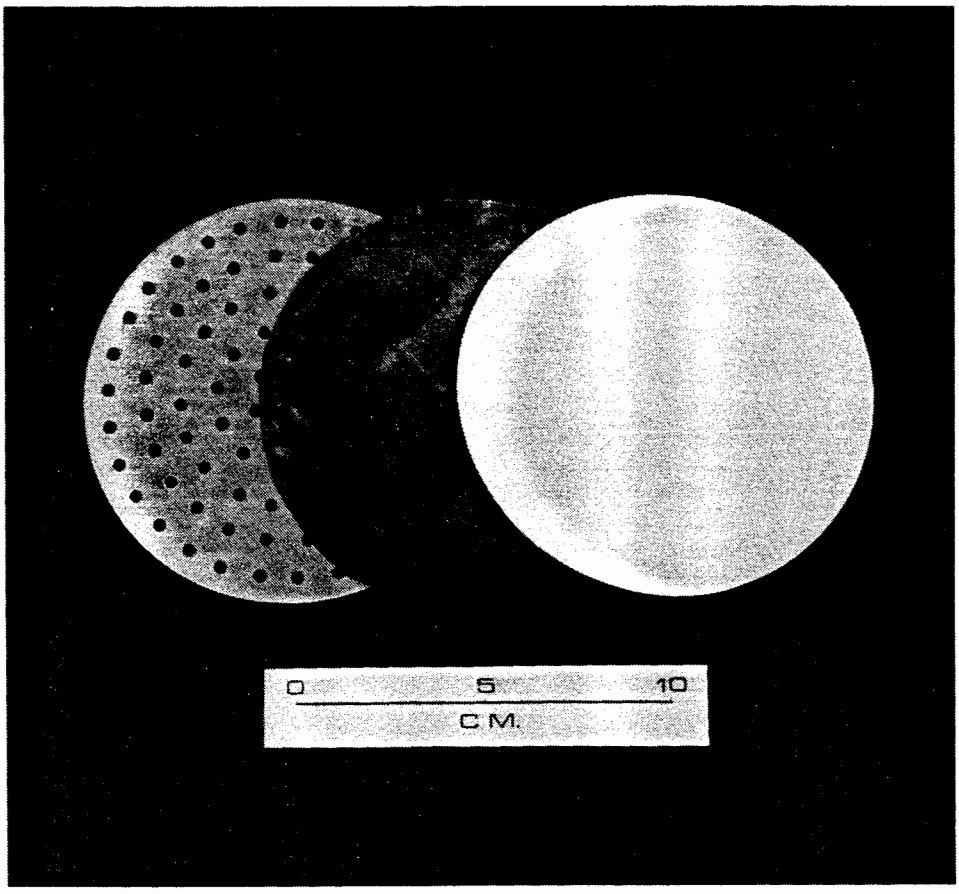

Plate 2.6 Three Layer Soil Filtering System

the soil surface, which is the layer that filters the pore fluid. The final layer, which is sandwiched between the filter and the plate, consists of a fine stainless steel mesh fabric of 0.2 mm in thickness (courtesy of G. Bopp & Co., London). This layer supports the millipore filter and prevents it punching through the holes in the steel plate. This three layer filtering system is illustrated in Plate 2.6. The perforated stainless steel plate can also be seen through the perspex top cap in Plate 2.4.

2.5 Measurement of Sample Thickness

The displacement of the piston relative to the cell is measured using a linear voltage displacement transducer (LVDT) which is clamped to the guiding ram as illustrated in Plate 2.3. and Figure 2.4. The linear calibration of the LVDT, made using a precision micrometer, was performed several times during the testing programme. In order to evaluate the actual thickness of the soil sample from the change in piston displacement, however, the transducer signal must be known at a prescribed sample thickness. As the LVDT must be removed from the guiding ram after each test in order to extrude the sample, the signal at a prescribed thickness must be obtained before each consolidation test. This initializing procedure of the LVDT involves placing a machined metal slab of known thickness in the cell. The piston is slowly raised until the top of the slab just comes into contact with a metal strip that is placed across the top of the open cell. This procedure is repeated until three identical readings are made by the LVDT. From the knowledge of the LVDT signal at a prescribed thickness, the thickness of a sample can be evaluated at all times throughout a consolidation test. The total volume of the sample can then be found by simply multiplying the sample thickness by the cross-sectional area of the cell.

2.6 Measurement of Pore Water Volume

Unlike the measurement of the total volume of the sample which can be made as the test proceeds, the measurement of the pore water volume can only be made after the sample is oven dried so that the amount of water in the sample at the end of the test can be evaluated.

During the initial consolidation of the sample from a slurry to the required consolidation stress, the volume of water that drains from the sample is not measured. During this period, both the drainage water and any gas that leave the sample are removed from the apparatus via a drainage line connected to the summit of the coned cap. This drainage line is closed with the aid of a tap valve at the end of initial consolidation. A water filled nylon tube is then connected from a volume change burette to an outlet at the side of the top cap. The top cap is then gently flushed through with water to remove any gas bubbles that may have collected in the drainage lines. At this point, with the top cap saturated and before any loading is applied, the first burette reading is made which signals the start of the consolidation test.

During consolidation of a gassy soil sample, both pore water and gas are expelled. The gas is seen to collect in the top of the coned perspex cap with the water displaced into the volume change apparatus. As the burette reading is affected by both water and gas volume changes, however, any gas present in the top cap must be removed to measure the change in water volume. To remove any build up of gas without the loss of any water, the tap at the summit is opened and a small volume of air is gently forced into the top cap to remove any water that is held above the accumulated gas. It is then possible to allow the gas to flow from the sample until the water replaces the gas up to a predetermined point just above the tap. A schematic description of this procedure is illustrated in Figures 2.5a to 2.5c.

A shortcoming of this method, however, is that the burette reading only gives a true measure of water volume change after each correction has been made. Figure 2.6 illustrates a typical sequence of burette readings. At the start of the test the volume change is zero, but as the consolidation procedes the measured burette water displacement will be higher than the pore water volume that drains from the soil. After each "release of gas", however, a true water reading is obtained. As this process is repeated a number of times during a test, it is then possible to produce a reasonable curve through these "true" points to give a corrected volume of drained water throughout the test as shown in Figure 2.6.

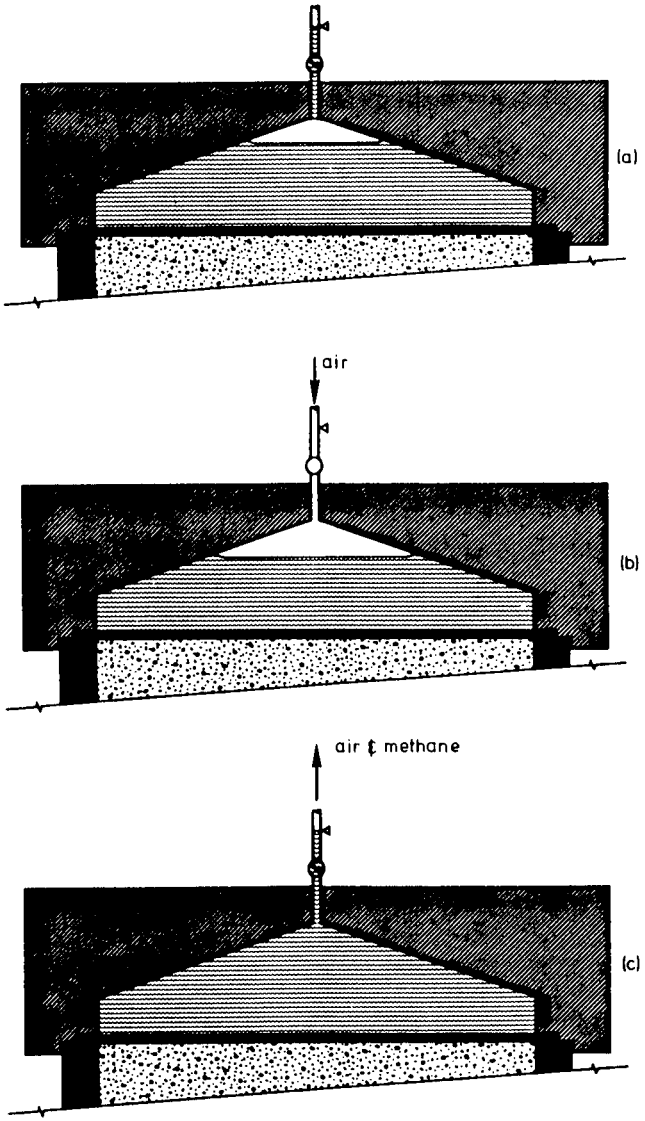

Figure 2.5 Illustration of gas removal from top cap

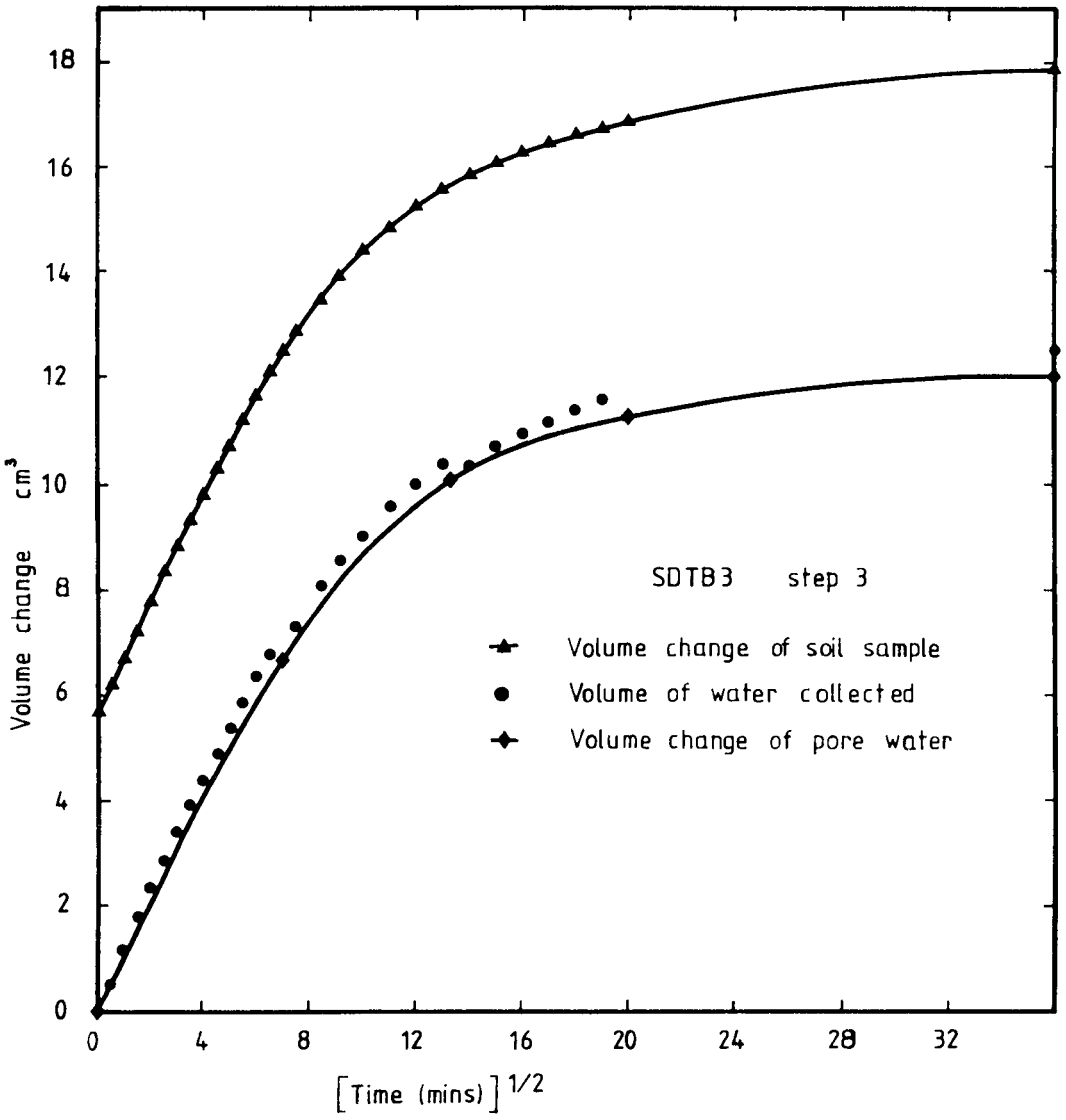

Figure 2.6 Evaluation of the volume change of pore water

This water measurement is made throughout the loading and unloading of a soil sample. When the test is completed and a final burette reading is made, the soil sample is removed from the cell and weighed immediately. The sample is then oven dried at 105° for 24 hours and then reweighed. The difference in weights is the weight of pore water present in the sample at the end of the test. Therefore from this final weight of water, it is then possible to back calculate the volume of water that was present in the sample at all times throughout the consolidation test.

2.7 Measurement of Free Gas Volume

Again, the gas volume can only be evaluated after the test has been completed. Although the total volume of the sample can be measured directly throughout the test, the solid and water volumes can only be found at the end of the test from the measurement of the wet and dry weights of the soil sample. The volume of free gas can then simply be found from

$$v_g = v_t - v_s - v_w \qquad (2.3)$$

The advantage of using this method is that no assumptions about the pressure of the gas have to be made as for the method used by Nageswaran (1983).

2.8 Measurement of Total Vertical Stress

Due to the friction of the O-rings on the piston and on the guiding ram, the pressure that is applied below the piston is not fully transferred to the soil sample. It is therefore necessary to measure directly the stress on the surface of the soil. This stress is measured using an integrated silicon chip pressure transducer, manufactured by Druck Ltd., which has a range of 0-500 kPa. This transducer is mounted inside the piston with only the face visible from inside the cell. In order to produce a level surface with the soil sample, the slight recess in the transducer is filled with a self levelling silicon sealant (Dow Corning 734 RTV). This is the same material that forms the main body of the miniature stress transducers produced by Gaeltec Ltd.

The Druck transducer is then calibrated both inside and outside of the cell. The calibration coefficient was the same in both cases illustrating that all pressure was transferred through the silicon sealant, although there was a

different zero offset caused by the different types of mounting between the piston and the calibration block.

2.9 Measurement of Total Horizontal Stress

In order to measure the horizontal stresses on the side of the cell, two miniature stress transducers are embedded in the cell wall directly opposite each other. The miniature transducers used in the tests were both 3Ea "specials" manufactured by Gaeltec Ltd., and were designed to screw into the side of the cell from the outside to give a 0.5mm clearance between the transducer face (4 mm diameter) and the inside face of the cell.

The transducer face is then sprayed with a fine layer of silicon grease and the recess filled with self levelling sealant (Dow Corning 734 RTV). This sealant is the same material that forms the main body of the Gaeltec transducers. This technique simply extends the existing transducers to the required location. Whilst the sealant is still fluid, the excess is wiped off using a straight edge to produce a smooth curved face which matches the curved surface of the cell wall. A horizontal and vertical section of the assembled transducer is presented in Figure 2.7. These transducers are calibrated before and after each test as the mounting procedure must be repeated before each consolidation test.

2.10 Measurement of Pore Water Pressure

The pore water pressures on the undrained and drained faces of the soil sample are measured using 350 kPa range Druck transducers. These transducers are housed in perspex blocks and are connected to the pore water pressure ports in the oedometer by de-aired water filled nylon tubing.

During the initial consolidation of a gassy soil from a slurry--despite an early fall of the observed pore water pressure measurement on the undrained face towards atmospheric--the measured pressure value would suddenly leap up, after about 12 hours, to an inflated value with no further fall with time. This phenomenon is certainly caused by the presence of the gas entering the porous stone and causing a break in the connection between the water in the measuring system and the pore water in the soil. Trials were made using a larger diameter

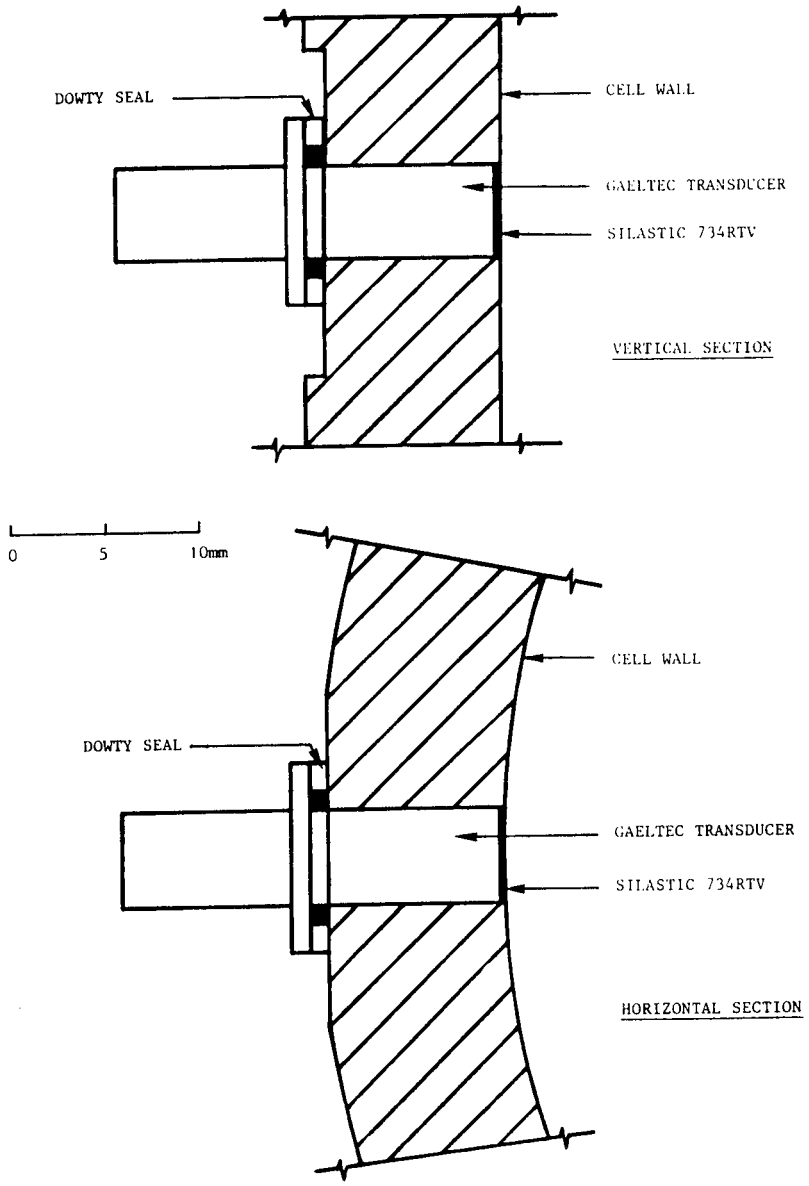

Figure 2.7 Schematic description of horizontal stress transducer

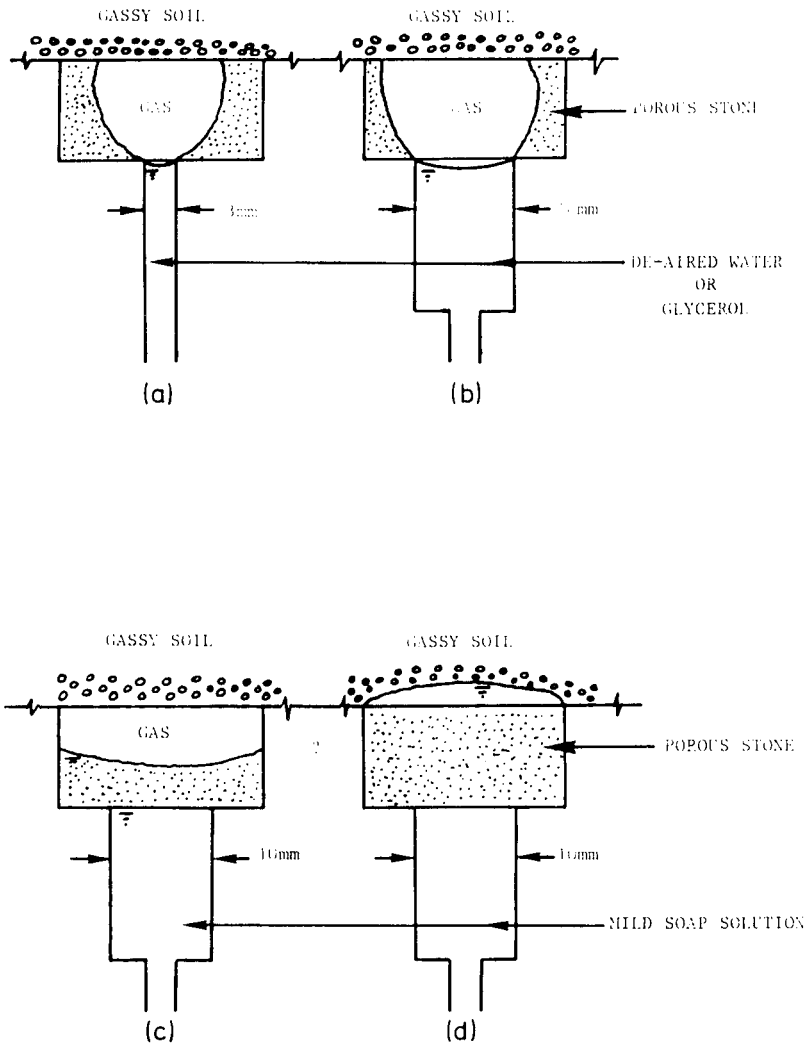

Figure 2.8 Schematic description of pore water pressure measurement

hole cut into the piston and saturating the porous stone with glycerine instead of water. All cases produced an inflated value of pore pressure measurement. It is not clear as to the exact mechanism that causes this gas intrusion. Figures 2.8a and 2.8b, however, illustrate two possible scenarios that could produce an increased pressure caused by the formation of a gas-water meniscus over the neck of the hole cut into the piston.

In a last attempt to produce a true reading of pore water pressure, the high air entry porous stone was saturated using a mild soap solution in the hope that the effect of the surface tension, and thus the pressure difference between the phases, would be reduced. It was found that this technique did allow a dissipation of pore water pressure to atmospheric pressure. This pore water pressure reading, however, could only be maintained for about three days before there was a sudden leap in the pore pressure reading. This was assumed to be due to the entry of gas into the porous stone suggesting that prior to this event it was the pore water pressure that had been recorded.

The accuracy of the transducer measurements are specified by the manufacturers to be in the order of 0.01%. However, on calibration of the transducers when mounted in the cell, the cell pressure differed by up to 0.3% when measured by the total stress and pore water pressure transducers although typically the discrepancies were in the order of 0.1%.

Therefore before each test, the porous stone and the nylon tubing between the stone and the pressure transducer were saturated with a mild soap solution. Figures 2.8c and 2.8d illustrate two possible scenarios of using a mild soap solution. It is possible that gas enters the stone but on contact with the soap solution, the surface tension breaks down causing no pressure difference between the water and gas phases. It is also possible that the soap solution enters the gassy soil breaking down the bubbles in the sample and producing a localized area of saturated soil for which it is possible to measure the pore water pressure. Therefore, using the above technique there is a choice between completing a test in three days in which pore water pressure can be measured on the undrained face, and performing a consolidation test over a longer time period in which pore water pressures cannot be measured on the undrained face.

2.11 Arrangement of Apparatus and Processing of Data

A schematic description of the consolidation apparatus and the data logging system is illustrated in Figure 2.9. Each transducer is powered from a power block which also receives the return signal. The received signals are transferred to the OUEL VAX 11/780 via a data logger and a Commodore 64 micro computer. The file containing the raw data is then used as input to the data processing program SOLTRAN which was written to convert this raw data to engineering units. An option is also available to produce a graphical output of these results either on the video screen or as a hardcopy.

2.12 Summary

This chapter first describes the method of producing a gassy soil in the laboratory using the "zeolite molecular sieve technique". This is followed by the description of the apparatus used to form a gassy soil sample from a slurry and to perform a consolidation test on such a sample. This apparatus consists of a specially designed oedometer in which both horizontal and vertical total stresses can be measured. Pore water pressures can be measured on both the drained and undrained faces, although the measurement on the undrained face can only be maintained for about three days. In order to measure the volume of pore water that leaves the soil sample, the gas and water that drain from the soil are separated using a coned top cap. The gas is carefully released from the top of the cap while the water flows from the cap to the volume change burette. The thickness and hence the total volume of the sample is evaluated with the use of a displacement transducer which is clamped to the guiding ram beneath the cell. From the knowledge of the total volume of the sample, the final volume of the solid grains and the pore water and the changes in pore water volume throughout the test, it is possible to evaluate directly the volumes of all the three phases at all times during a consolidation test. Finally, the electrical signals from the pressure transducers are read during the test by a data logger. These results are then transferred to the OUEL VAX 11/780 computer via a Commodore micro computer. These results can then be processed and a graphical output obtained.

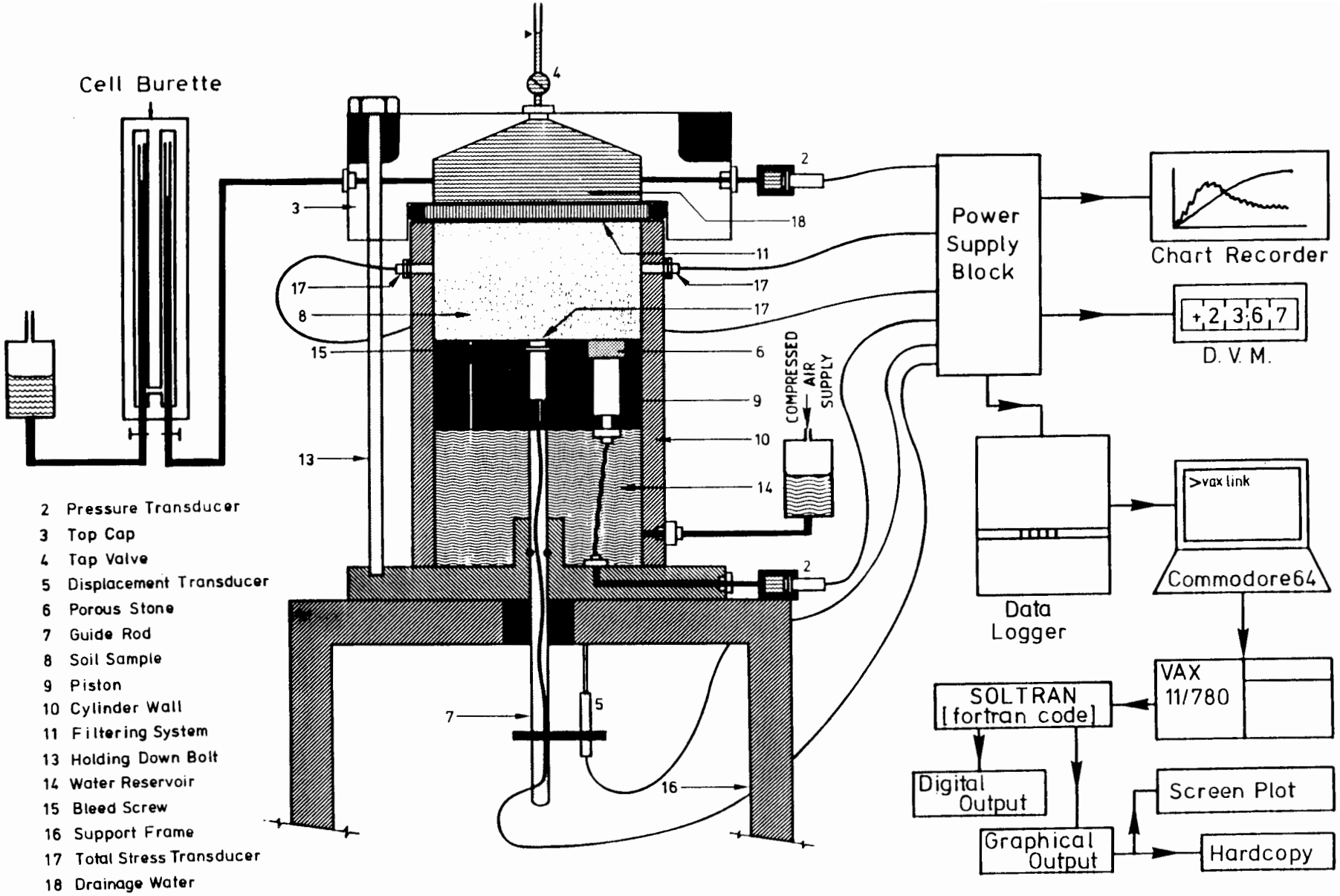

Figure 2.9 Schematic description of consolidation apparatus and data logging equipment

CHAPTER 3

LABORATORY TESTING PROCEDURE

CHAPTER 3

LABORATORY TESTING PROCEDURE

3.1 Introduction

This chapter presents the laboratory testing procedure that has been used to give an understanding of the consolidation behaviour of a gassy soil.

3.2 Early Consolidation Testing

The first series of experimental tests was performed on samples of saturated and gassy soil using the apparatus that was originally used by Nageswaran (1983). The samples were prepared in the oedometer as described in Section 2.3 and initially consolidated to the required consolidation pressure of 35 kPa. When dissipation of pore water pressures and settlements were complete, the sample was loaded with an increment of vertical stress. This stress caused an immediate increase in pore water pressure, and for a gassy soil, an immediate displacement due to the volume change of the gas. This immediate compression was then followed by a further volume change caused by the subsequent loss of fluids from the soil and the dissipation of pore water pressure. At the end of each stress increment, it was then possible to evaluate the total void ratio and the total stress on the sample. Nageswaran (1983) used the technique of measuring the volume of gas that collected in the top cap and assumed that this volume had been lost from the voids of the soil. This would only be true, however, if the gas pressure were equal to the pore water pressure. As it is impossible to measure the gas pressure directly, this is not a wise assumption to make.

In addition, on application of the vertical stress increment to a gassy soil, there is an immediate settlement of the soil due to the compression of the free gas. Any time dependent volume changes that may occur, however, such as local consolidation around the gas voids and the dissolution of gas into the pore water, are difficult to separate from the volume changes caused by the dissipation of pore water pressures under drained conditions. Therefore, this type of consolidation test produced neither a good indication of undrained or

drained conditions. On the basis of these early tests, it was then decided to design different consolidation tests to highlight the behaviour of a gassy soil under drained and undrained conditions.

3.3 One-Dimensional Consolidation of a Gassy Soil - Short Term Method

Due to the diffusion of gas into the porous element of the pore water pressure measuring system, it was only possible to measure the pore water pressure over a period of about three days. Therefore, to make use of this pore water pressure measurement, the consolidation test must be completed--from pouring the slurry into the cell to removing the consolidation sample--within this time limit.

3.3.1 Consolidation using a gradual increase in total stress

In order to complete a consolidation test within the time limit allowed for a measurement of pore water pressure on the undrained face, it was decided to apply the total stress gradually to the sample while allowing free drainage to occur at the top face boundary, which is maintained at atmospheric pressure. In this way it is possible to increase the effective stress gradually throughout the sample, producing at the same time only low pore water pressures. In addition, with the drainage boundary at atmospheric pressure, the gas that leaves the sample can be taken into account throughout the test.

To compare the behaviour of the pore water pressure profiles between a conventional stepwise consolidation test and a gradual increase in total stress, Figures 3.1a and 3.1b illustrate the response of the total stress, effective stress and pore water pressure for both these loading conditions. It can be seen that for a single incremental increase in total stress, there is an equal increase in pore water pressure followed by the dissipation of pore water pressures to atmospheric, whereas for a gradual increase in total stress, the pore water pressure remains low with the effective stress increasing almost uniformly thoroughout the soil domain.

If the total stress on a soil sample is not constant, however, then the variation in the total stress with time must be included in the governing

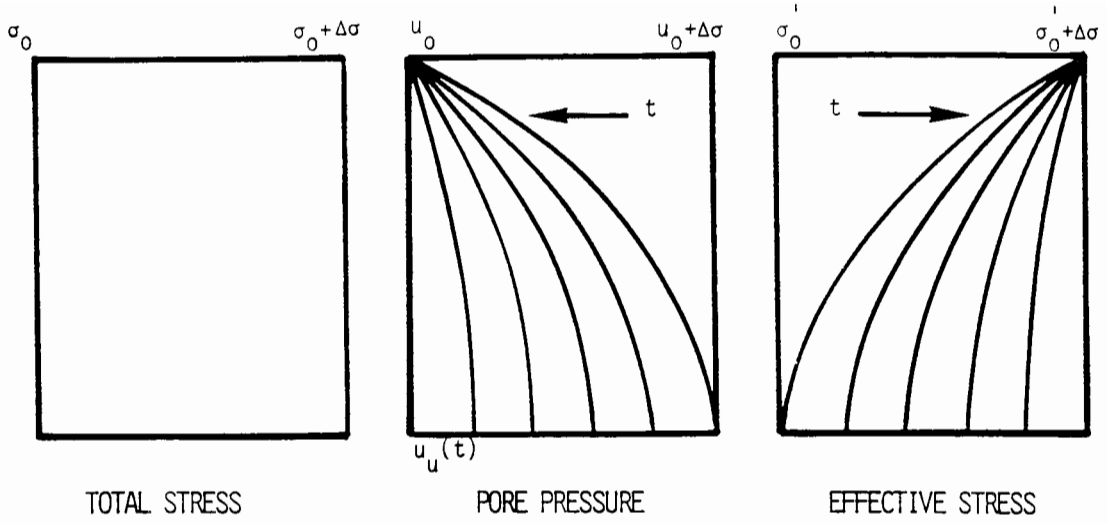

Figure 3.1a Isochrones due to a single increment of total stress

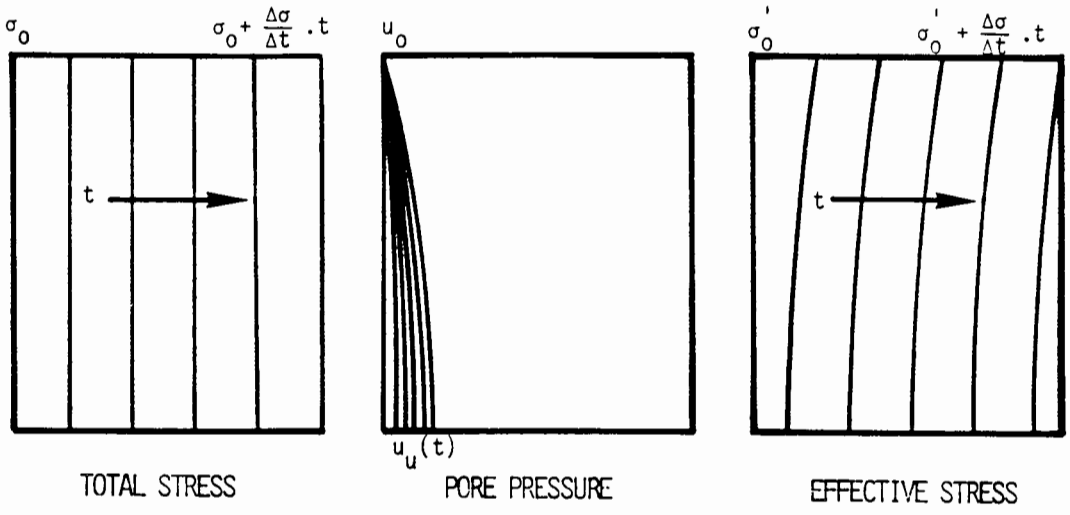

Figure 3.1b Isochrones due to a gradual increase in total stress

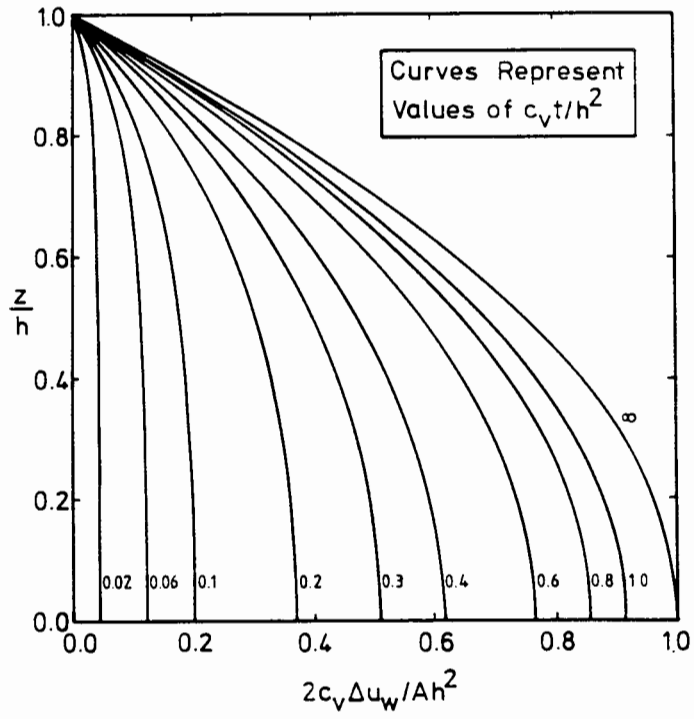

Figure 3.2 Isochrones due to a linear increase in total stress

consolidation equation. Consequently, Terzaghi's consolidation equation in one-dimension, neglecting the effect of gravity, can be written as

$$\frac{\partial}{\partial z}\left(\frac{k_w}{\gamma_w}\frac{\partial u_w}{\partial z}\right) = m_v\frac{\partial u_w}{\partial t} - m_v\frac{\partial \sigma_v}{\partial t} \tag{3.1}$$

where k_w is the soil permeability, γ_w is the specific weight of the water, m_v is the coefficient of volume change, σ_v is the total vertical stress and u_w is the pore water pressure.

3.3.2 Consolidation using a linear increase in total stress

From the consolidation equation 3.1, it can be seen that if the total stress varies linearly with time, with the assumption that the spatial variation of permeability is small, the equation may be simplified to give

$$c_v\frac{\partial^2 u_w}{\partial z^2} = \frac{\partial u_w}{\partial t} - A \tag{3.2}$$

where the coefficient of consolidation, c_v, is defined as

$$c_v = k_w/m_v\gamma_w \tag{3.3}$$

with the rate of change of total stress defined as

$$A = \partial\sigma_v/\partial t \tag{3.4}$$

The governing equation 3.2 is similar to the equation governing heat flow in a slab of conductive material with heat produced in it at a constant rate. The resulting pore water pressure distribution, assuming small strains, may be adapted from Carslaw and Jaeger (1959, pp. 130-131), to give

$$U = 1 - \zeta^2 - \frac{32}{\pi^3}\sum_{n=0}^{n=\infty}\left\{\frac{(-1)^n}{(2n+1)^3}\,\mathrm{Cos}\left[\frac{(2n+1)\pi\zeta}{2}\right]\exp\left[-\frac{(2n+1)^2\pi^2\tau}{4}\right]\right\} \tag{3.5}$$

where

$$U = 2c_v\Delta u/Ah^2 \tag{3.6}$$

$$\zeta = z/h \tag{3.7}$$

and

$$\tau = c_v t/h^2 \tag{3.8}$$

in which h is the height of the soil sample and Δu is the increase in pore water pressure within the soil. The value of the pore water pressure at the undrained boundary can be obtained by setting z = 0 to give

$$U_u = 1 - \frac{32}{\pi^3}\sum_{n=0}^{n=\infty}\left\{\frac{(-1)^n}{(2n+1)^3}\exp\left[-\frac{(2n+1)^2\pi^2\tau}{4}\right]\right\} \tag{3.9}$$

The pore water pressure distribution reaches steady state when $t \rightarrow \infty$ to give

$$U_{\infty} = 1 - \zeta^2 \tag{3.10}$$

which is a parabolic distribution of pore water pressure. Figure 3.2 illustrates the distribution of the pore water pressure along the height of the soil sample at various values of dimensionless time, τ.

3.3.3 Approximation of linear increase in total stress

The problem which then arose was how to apply a linear increase of total stress to the soil sample. Various types of flow restrictors were applied over the lines between the water reservoir beneath the piston and the air-water interface. All the restrictors produced a smooth increase in total stress with time, but none gave a linear increase with time. Eventually, it was decided that it was more important to obtain a linear increase in total stress than a smooth increase. Therefore, it was decided to increase the total stress in small constant increments every eight minutes. In this way, an overall linear stress increase was obtained.

3.3.4 Comparison between solutions of linear and stepwise total stress increase

If a stepwise increase of total stress is represented by several consolidation tests starting at different times, then if one increment of stress on the soil is considered, there will be an immediate increase in pore water pressure followed by dissipation over the following increment Δt. The change in pore water pressure on the undrained face for this increment of loading has been solved by Taylor (1948) and is given by

$$\Delta u/\Delta\sigma = 1 - \frac{32}{\pi^3} \sum_{n=0}^{n=\infty} \left\{ \frac{(-1)^n}{(2n+1)^3} \exp\left[-(2n+1)^2 \tau \right] \right\} \tag{3.11}$$

which may be expressed as

$$\Delta u/\Delta\sigma = f(\Delta t) \tag{3.12}$$

Thus if the stress is applied in increments of $\Delta\sigma$ after each time increment Δt, then after one step the increase in pore water pressure on the undrained face is

$$\Delta u = \Delta\sigma - \Delta\sigma\, f(\Delta t) = \Delta\sigma\, [1-f(\Delta t)] \tag{3.13}$$

and after two steps is

$$\Delta u = \Delta\sigma[1-f(\Delta t)] + \Delta\sigma\, [1-f(2\Delta t)] \tag{3.14}$$

and after N steps is

$$\Delta u = \Delta\sigma \sum_{n=1}^{n=N} [1-f(n\Delta t)] \qquad (3.15)$$

The resulting tooth-like pore water response is then plotted against the results of equation 3.9 in Figure 3.3. It can be seen that even though the increments of time are fairly large, if the continuous solution is started $\Delta t/2$ before the first loading increment, the corresponding pore water pressure at the mid-point of the following time increments is almost identical.

In addition, if it is assumed that the pore water pressure has a parabolic distribution over the thickness of the sample, then the average pore water pressure $\bar{u}$ over the sample may be given as

$$\bar{u}_w = \frac{1}{3} u_{wd} + \frac{2}{3} u_{wu} \qquad (3.16)$$

where u_{wu} is the measured pore water pressure on the undrained face and u_{wd} is the back pressure on the drained face. The resulting average vertical consolidation stress can then be found by subtracting the mean pore water pressure from the total vertical stress as depicted in Figure 3.4. It is then possible to plot various soil properties such as void ratio, permeability and compressibility against the vertical consolidation stress throughout the test.

3.3.5 Validity of the average consolidation stress and void ratio

One of the main purposes of the consolidation test is to evaluate the relationship between the consolidation stress and the void ratio of the soil. The advantage of a conventional consolidation test is that at the end of each 24 hours, all pore water pressures have dissipated and therefore, the consolidation stress is constant throughout the soil. Hence there is no need for averaging the consolidation stresses and void ratios. Using the linear increase in total stress, however, the question arises as to how accurate the final relationship is between the average consolidation stress and the average void ratio as compared with the true consolidation stress versus void ratio relationship.

In order to simulate this effect, a one-dimensional finite element program was written in which the Terzaghi equation for the consolidation of a saturated soil, given by

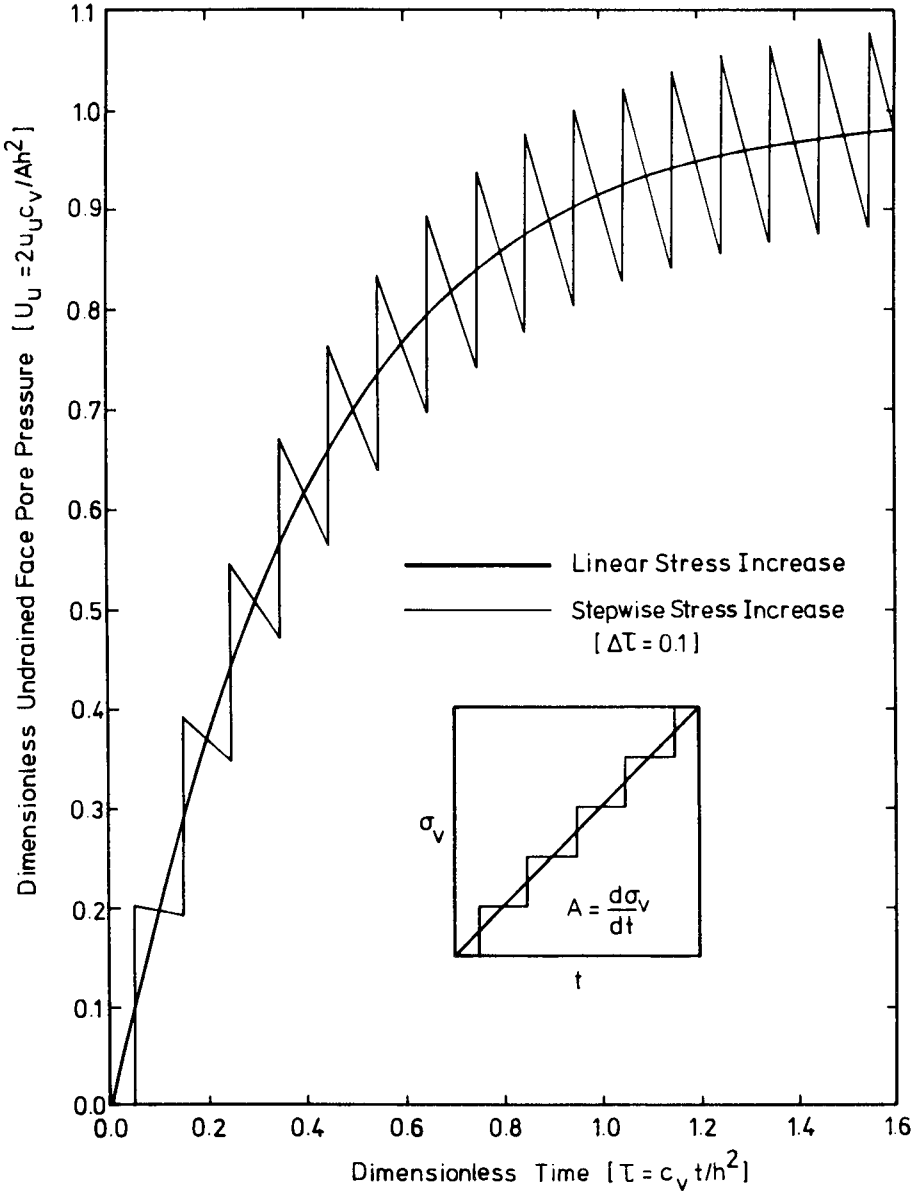

Figure 3.3 Comparison between a linear and stepwise linear increase in total stress

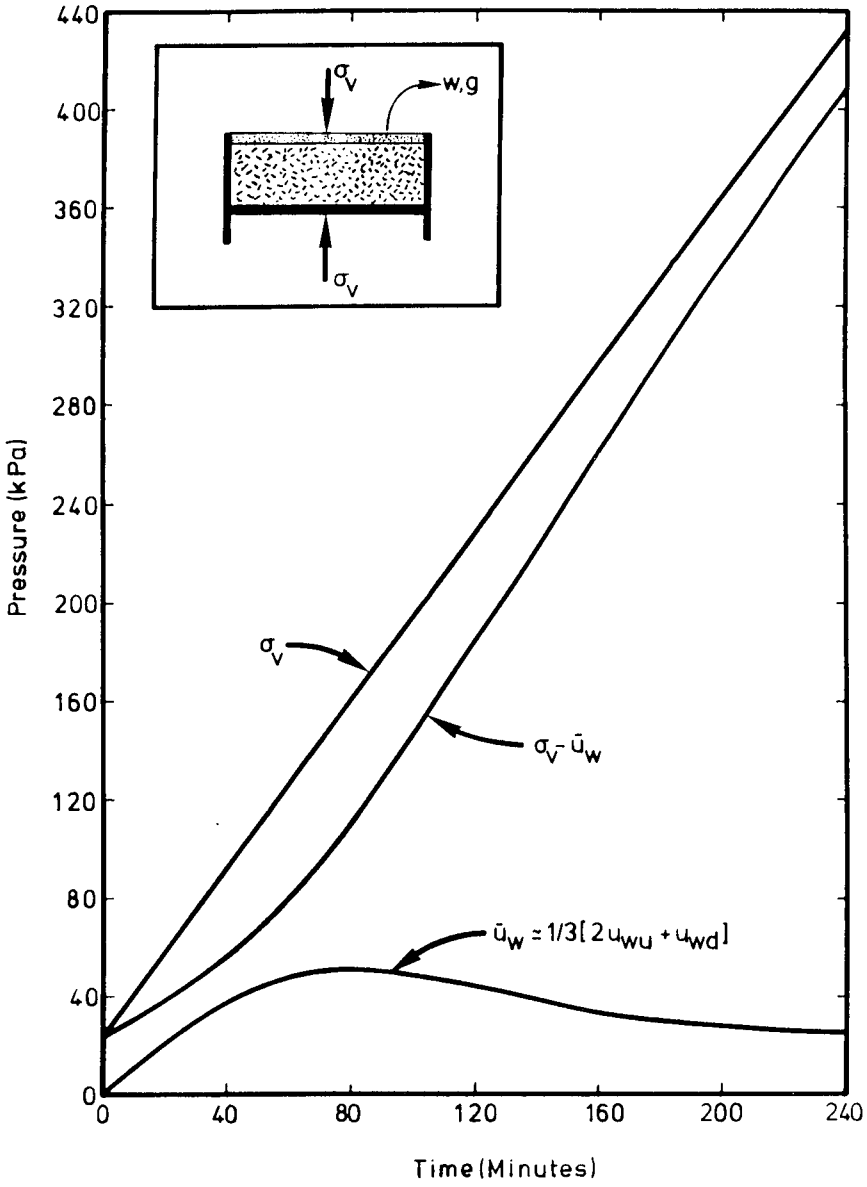

Figure 3.4 Approximation of average effective stress and pore water pressure

$$\frac{\partial}{\partial z}\left(\frac{k}{\gamma}\frac{\partial u_w}{\partial z}\right) = m_v \frac{\partial u_w}{\partial t} - m_v \frac{\partial \sigma_v}{\partial t} \qquad (3.17)$$

was approximated using the Galerkin weighted residual method. Linear two noded finite elements were used to discretize the domain. The elements also reduced in length as the consolidation proceeded. The physical properties of the soil included a non-linear relationship between the permeability and consolidation stress and between void ratio and consolidation stress.

Using this program, it was then possible to simulate the consolidation of a 20 mm thick soil sample with an initial consolidation stress of 35 kPa subject to an increase in total stress of 90 kPa/hr. At this rate of loading, a total stress of 400 kPa could be reached in about four hours. Figure 3.5 illustrates the simulated pore water pressure on the undrained face during the test. In addition, the average pore water pressure found by the integration of the pore pressure distribution after each time increment and also the average pore pressure based on a parabolic distribution of pore pressure, are presented in Figure 3.5. It can be seen that there is a discrepancy between the two averaged pore pressures at early time, but that in general the agreement is very close.

Figure 3.6 compares the consolidation stress versus void ratio relationships. The continuous line represents the relationship that was fed into the numerical model as the actual soil behaviour. The solid circles represent the relationship between the average void ratio and the average consolidation stress based on a parabolic distribution of pore water pressure. It can be seen that at this rate of loading, the average consolidation stress versus the average void ratio is a very good approximation of the actual soil behaviour, even though there can be up to 75 kPa difference between the drained and undrained pore water pressures.

3.4 Test Series A - Linear Increase in Total Stress

This test series consisted of consolidating seven samples of soils of varying gas contents. The initial saturation, void ratios and consolidation pressure for each of these tests are presented in Table 3.1.

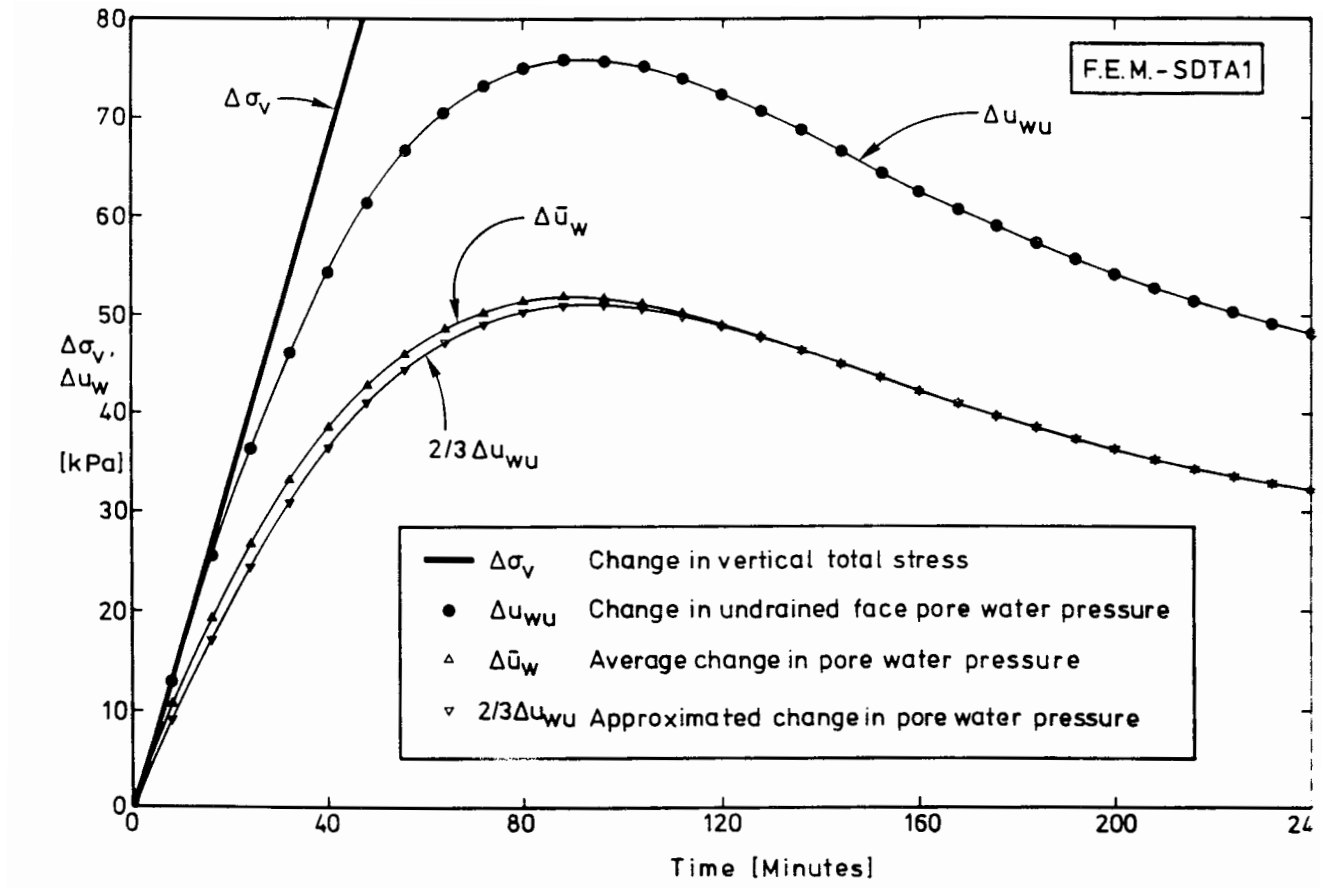

Figure 3.5 Accuracy of average pore water pressure during consolidation

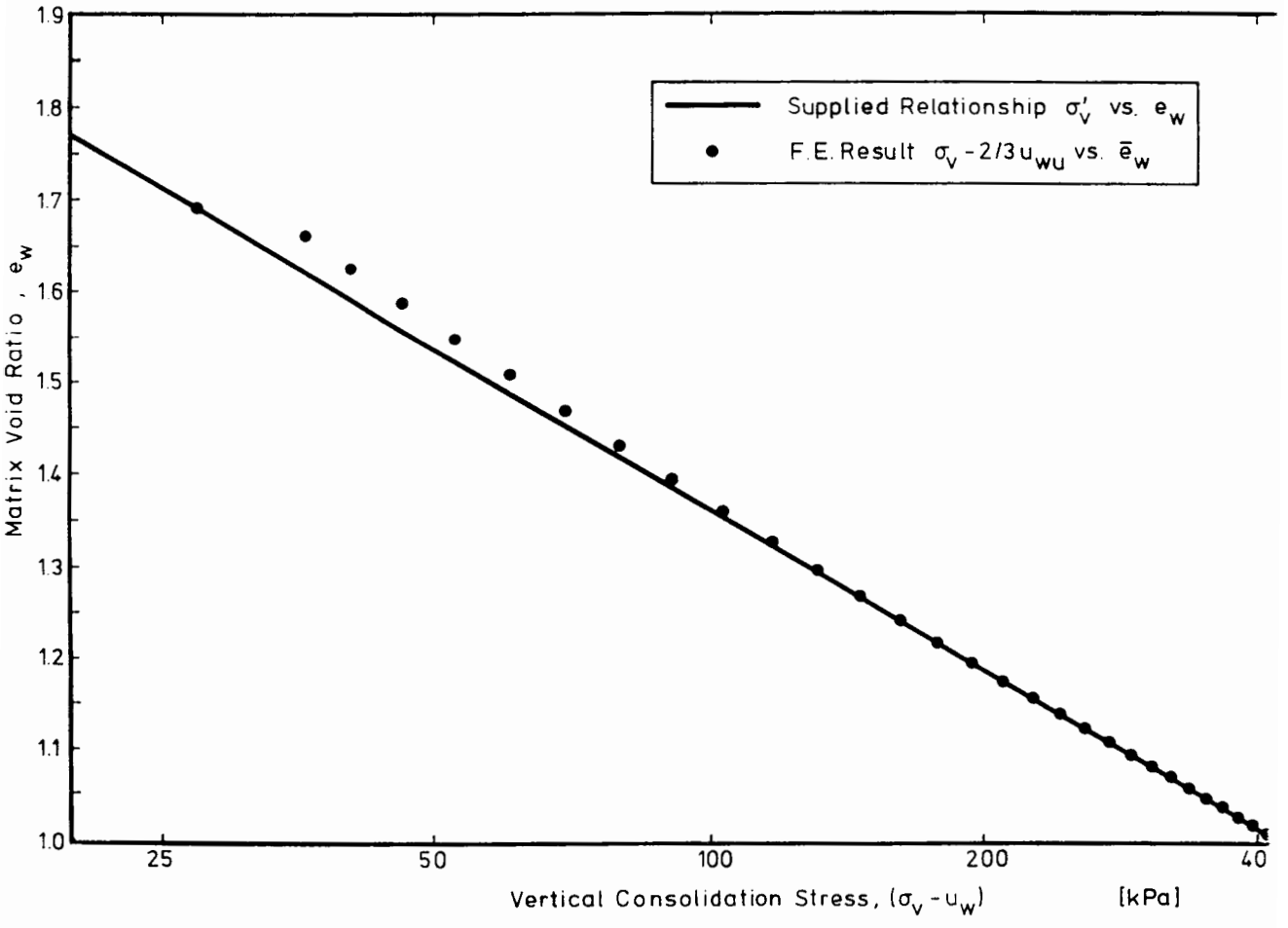

Figure 3.6 Comparison between the actual and calculated void ratio versus effective stress during consolidation

Table 3.1 Specifications of Test Series A

TEST	σ_v° [kPa]	$\Delta\sigma_v/\Delta t$ [kPa/min]	h° [mm]	e_w°	e_w^{100}	e_g°	e_g^{100}	e_t°	e_t^{100}	S_w°	S_w^{100}
SDTA1	34.88	1.695	16.62	1.627	1.374	0.000	0.000	1.627	1.374	1.000	1.000
SDTA2	17.20	1.707	16.56	1.802	1.378	0.407	0.210	2.209	1.589	0.816	0.867
SDTA3	18.88	1.685	16.25	1.773	1.378	0.023	0.006	1.796	1.384	0.987	0.996
SDTA4	22.67	1.695	17.28	1.758	1.385	0.348	0.193	2.106	1.578	0.835	0.879
SDTA5	21.58	1.696	17.34	1.765	1.386	0.091	0.059	1.857	1.445	0.950	0.959
SDTA6	24.49	1.695	17.28	1.720	1.377	0.385	0.200	2.105	1.577	0.817	0.873
SDTA7	47.75	1.696	17.97	1.530	1.390	0.000	0.000	1.530	1.390	1.000	1.000

Table 3.2 Specifications of Test Series B

TEST SDTB1

σ_v [kPa]	σ_h [kPa]	u_w^b [kPa]	u_w^t [kPa]	σ'_v [kPa]	σ'_h [kPa]	σ_m [kPa]	σ'_m [kPa]	e_w	e_t	S_w
51.7	37.0	0.0	0.0	51.7	37.0	41.9	41.9	1.445	1.445	1.000
106.8	91.8	49.7	48.9	57.5	42.5	96.8	47.5	1.445	1.445	1.000
100.6	79.7	9.9	0.0	94.0	76.4	86.7	82.3	1.318	1.318	1.000
201.3	181.9	105.0	101.3	98.2	78.8	188.4	85.2	1.318	1.318	1.000
191.1	141.6	2.8	0.0	189.2	140.6	158.1	156.8	1.156	1.156	1.000
408.7	355.2	197.9	196.6	211.5	158.0	373.0	175.8	1.156	1.156	1.000
399.8	314.9	3.3	0.0	397.6	313.8	343.2	341.7	1.002	1.002	1.000

TEST SDTB2

σ_v [kPa]	σ_h [kPa]	σ_m [kPa]	u_w^t [kPa]	σ'_v [kPa]	σ'_h [kPa]	σ'_m [kPa]	e_w	e_g	e_t	S_w
67.1	55.2	59.2	0.0	67.1	55.2	59.2	1.415	0.228	1.643	0.861
102.5	83.7	90.0	40.3	62.2	43.4	49.7	1.415	0.172	1.587	0.892
112.7	89.1	97.0	0.0	112.7	89.1	97.0	1.296	0.172	1.486	0.833
202.5	185.4	191.1	111.3	91.4	74.3	80.0	1.296	0.091	1.387	0.934
197.0	170.3	179.2	0.0	197.0	170.3	179.2	1.143	0.099	1.242	0.920
420.8	380.1	393.7	227.7	192.3	152.4	165.7	1.143	0.016	1.159	0.986
375.9	315.66	335.7	0.0	375.9	315.6	335.7	0.987	0.033	1.020	0.968

TEST SDTB3

σ_v [kPa]	σ_h [kPa]	σ_m [kPa]	u_w^t [kPa]	σ'_v [kPa]	σ'_h [kPa]	σ'_m [kPa]	e_w	e_g	e_t	S_w
29.1	30.5	30.0	0.0	29.1	30.5	30.0	1.590	0.275	1.865	0.853
50.1	46.8	47.9	25.3	24.9	21.5	22.6	1.590	0.238	1.828	0.870
51.1	37.6	42.1	0.0	51.1	37.6	42.1	1.468	0.232	1.700	0.864
99.0	81.2	87.1	50.1	48.9	31.1	37.0	1.468	0.164	1.632	0.900
98.8	73.1	81.7	0.0	98.8	73.1	31.7	1.309	0.165	1.474	0.888
207.6	176.2	186.7	110.2	97.4	66.0	76.5	1.309	0.082	1.391	0.941
192.7	132.8	152.8	0.0	192.7	192.7	152.8	1.152	0.088	1.240	0.929

TEST SDTB4

σ_v [kPa]	σ_h [kPa]	σ_m [kPa]	u_w^t [kPa]	σ'_v [kPa]	σ'_h [kPa]	σ'_m [kPa]	e_w	e_g	e_t	S_w
26.2	22.1	23.5	0.0	26.2	22.1	23.5	1.630	0.116	1.746	0.943
51.1	43.1	45.8	28.2	22.9	14.9	17.6	1.630	0.094	1.724	0.945
50.3	42.3	45.0	0.0	50.3	42.3	45.0	1.486	0.091	1.577	0.942
99.3	86.7	90.9	53.7	45.7	33.1	37.3	1.486	0.057	1.543	0.963
97.2	81.5	86.7	0.0	97.2	81.5	86.7	1.310	0.061	1.371	0.956
198.4	190.4	193.1	107.2	91.2	83.2	85.9	1.310	0.020	1.330	0.985
183.3	165.1	171.2	0.0	183.3	165.1	171.2	1.144	0.030	1.174	0.974

TEST SDTB5

σ_v [kPa]	σ_h [kPa]	σ_m [kPa]	u_w^t [kPa]	σ'_v [kPa]	σ'_h [kPa]	σ'_m [kPa]	e_w	e_g	e_t	S_w
32.7	24.9	27.5	0.0	32.7	29.1	27.5	1.641	0.013	1.654	0.992
61.0	48.3	52.5	23.5	37.5	24.8	29.0	1.641	0.010	1.651	0.994
58.5	39.3	45.7	0.0	58.5	39.3	45.7	1.501	0.010	1.511	0.993
100.3	75.1	43.5	34.7	65.7	40.4	48.8	1.501	0.008	1.509	0.995
104.1	65.73	78.5	0.0	104.1	65.7	78.5	1.360	0.006	1.366	0.996
201.8	159.1	173.3	82.3	119.5	76.8	91.0	1.360	0.000	1.360	1.000
195.0	116.8	142.9	0.0	195.0	116.8	142.9	1.203	0.000	1.203	1.000

TEST SDTB6

σ_v [kPa]	σ_h [kPa]	u_w^b [kPa]	u_w^t [kPa]	σ'_v [kPa]	σ'_h [kPa]	σ_m [kPa]	σ'_m [kPa]	e_w	e_t	S_w
32.1	21.9	0.3	0.0	31.9	21.7	25.3	25.1	1.611	1.611	1.000
52.8	41.0	18.3	16.2	33.2	23.4	44.9	27.3	1.611	1.611	1.000
51.0	36.7	2.6	0.0	49.3	35.0	41.5	39.7	1.517	1.517	1.000
100.1	85.1	49.5	48.7	50.9	35.9	90.1	40.8	1.517	1.517	1.000
105.7	81.4	3.0	0.0	103.7	83.1	89.5	87.3	1.318	1.318	1.000
206.6	183.0	98.2	97.4	108.7	85.1	190.9	92.9	1.318	1.318	1.000
194.4	149.8	3.5	0.0	191.9	147.5	164.7	162.2	1.170	1.170	1.000

For each test, the sample was first prepared as described in Section 2.2. The first day of the three day test involved the simultaneous consolidation of the soil and formation of the gas bubbles. At the beginning of the second day the consolidation test was ready to start. The gas that had collected in the top cap was removed and the volume change apparatus was connected to the cell. The data logging system was then started so that displacement, total stress, drained and undrained pore water pressures were read every eight minutes. After four minutes, the first increment of 14 kPa was applied to the sample by increasing the air pressure supply to the air-water interface. This was followed by a reading at eight minutes.

This process was then repeated such that the readings taken by the data logger were at times 0, 8, 16, 24, 32 ... minutes, whilst the total stress was increased at times 4, 12, 20, 28, 36 ... minutes. This was continued until the average consolidation stress had reached 400 kPa. At this point no further increase in total stress was applied. The total stress was kept constant for about 1 hour, thus allowing further settlement and dissipation of pore water pressures. This was followed by the unloading of the sample.

Due to the large negative pore water pressures that are set up in the soil sample when the load is suddenly removed, it was decided to unload the soil sample slowly so that the pore water pressure on the undrained face remained at -10kPa. It was interesting to note that during the initial unloading, the load could be removed quite rapidly, but after the consolidation stress had fallen below about 50 kPa, the total stress had to be removed far more slowly in order to maintain a -10 kPa undrained face pore pressure. After all load was removed, the remaining pore water pressures were then allowed to dissipate overnight.

The sample was then carefully removed from the cell on the third day ensuring that no soil was left in the cell. The sample was then immediately weighed and placed in an oven at 105° for 24 hours.

3.5 One-Dimensional Consolidation of a Gassy Soil - Long Term Method

It was next decided to perform a conventional series of consolidation tests on samples of soils of varying gas contents. The technique used was similar to

that used by Nageswaran (1983), but had some important differences in order to evaluate the volumes of water and gas throughout the tests. For this series of tests, two additional stress transducers were incorporated into the cell wall in order to measure the horizontal stresses during the consolidation process as described in Chapter 2. As this test took seven days to complete, however, it was not possible to make any accurate pore water pressure measurements on the undrained face for reasons which are also explained in Chapter 2.

3.6 Test Series B - Three Stage Loading of Total Stress

This test series involved the consolidation of six samples of soil containing varying gas contents. The preparation of the gassy and saturated soil samples was similar to that for test series A. Due to the presence of the horizontal stress transducers, however, it was necessary to produce thicker samples so that the transducers were in contact with the soil at all times. The initial saturations, void ratios, gas contents and consolidation pressures are presented for each test in Table 3.2. Due to this increase in thickness, 60 hours were allowed for consolidation from a slurry to the required consolidation pressure of approximately 30 kPa.

3.6.1 Undrained conditions

The consolidation test started with the application of an increment of total stress. This was performed with the drainage lines closed. An immediate volume change of the sample was observed due to the compression of the gas. Settlement continued to occur after this initial load, however, even though there was no loss in pore water. This time dependent settlement could be due to a number of reasons, including local consolidation around the gas voids, dissolution of the gas into the pore water and the friction between the cell wall and the sample. The last of these reasons would explain how the pore pressure measured on the top face of the sample increased slowly to its eventual final measured value. This undrained settlement was completed after about two hours. Figure 3.7 illustrates a typical undrained settlement with time.

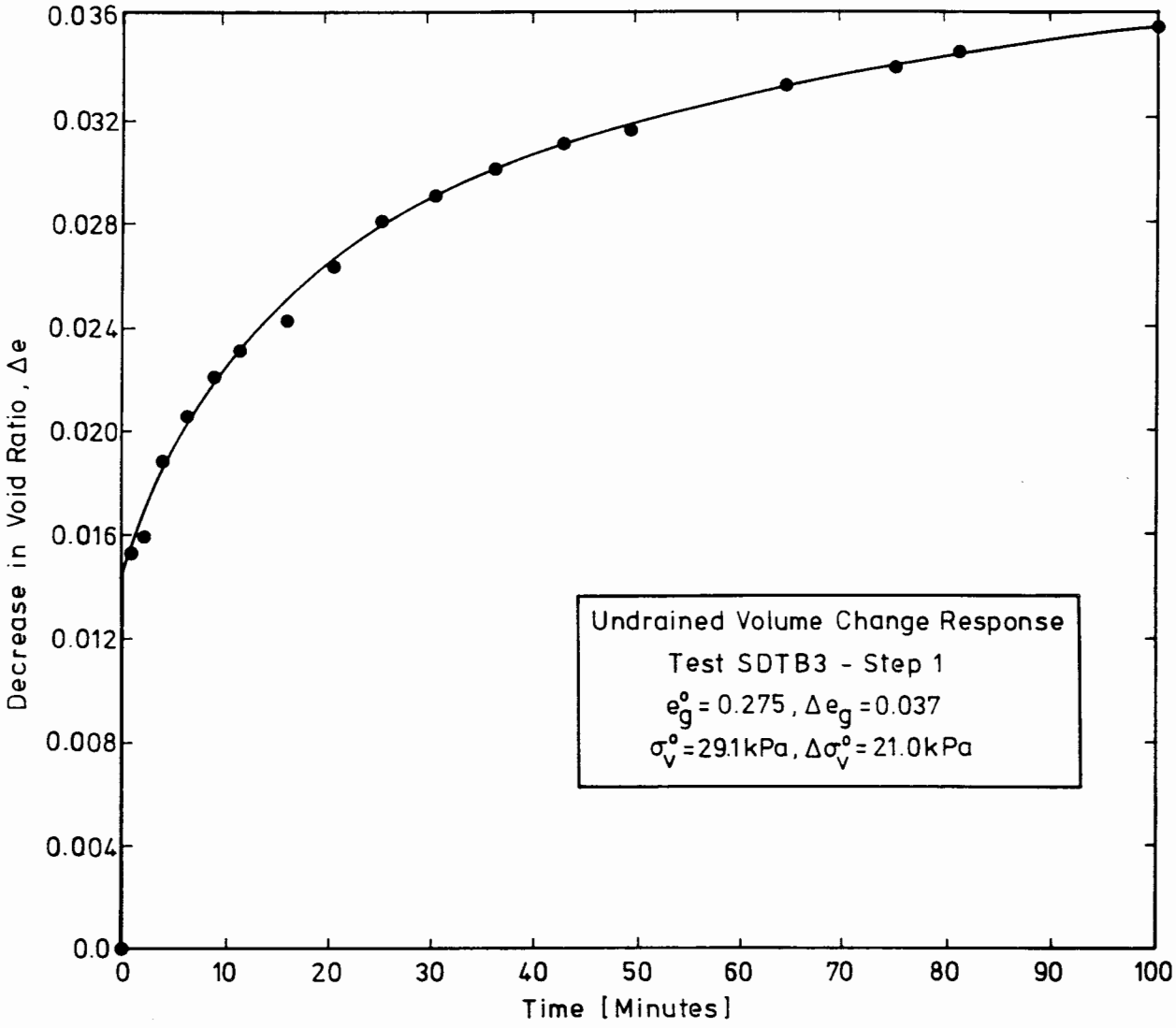

Figure 3.7 Typical time-dependent undrained settlement response

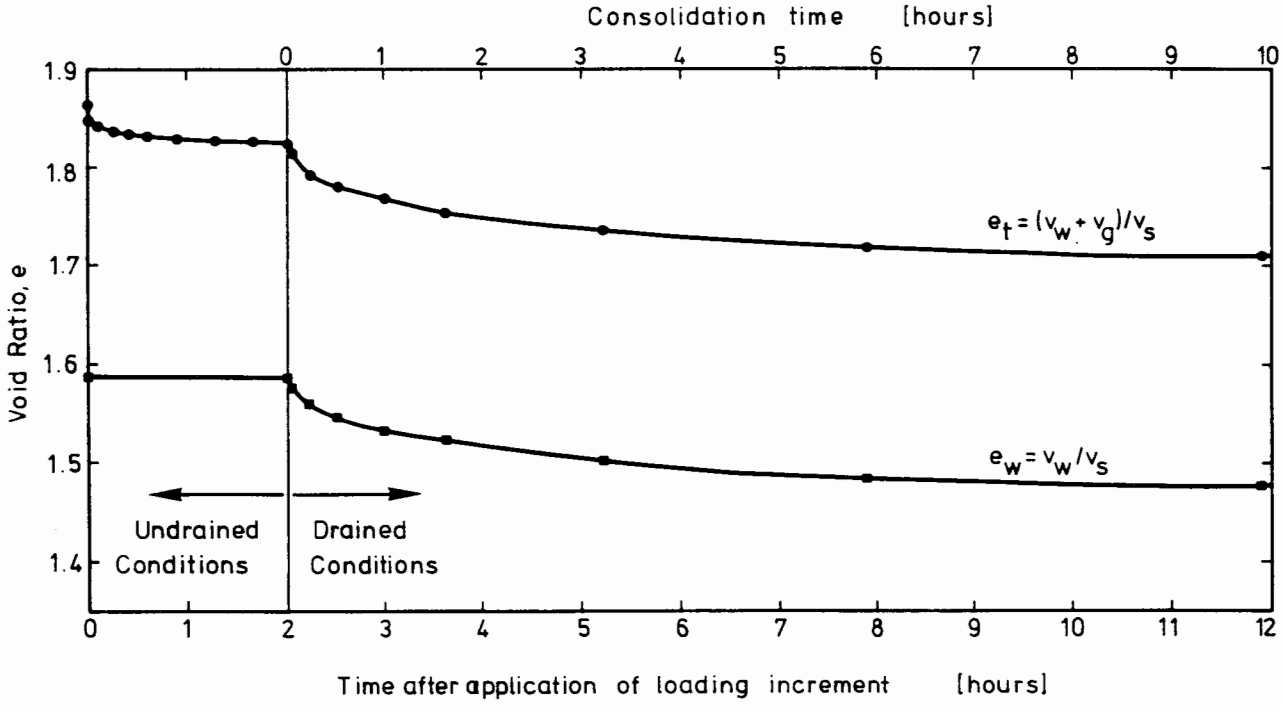

Figure 3.8 Typical time-dependent undrained-drained settlement response

3.6.2 Drained conditions

When there was no further increase in settlement, the data logging system was reset and the drainage taps were opened. For drained conditions, this is considered to be the start of the consolidation test. Readings of settlement, total stress (vertical and horizontal) and the volume change of pore water were made as the test progressed. Readings were taken at equal increments of the square root of time (0.25 min, 1 min, 2.25 min, 4 min, 6.25 min ...). The readings were taken until there was no further change in settlement. Figure 3.8 presents the combined result of a typical time dependent undrained displacement followed by a time dependent drained settlement. This process of undrained and drained conditions was then repeated twice more so that three increments of load had been applied to the sample. After no further loading was required, the sample was then unloaded gradually to avoid large suction pressures. The samples were then measured, weighed, dried and reweighed to obtain the volume of the individual phases.

3.7 Summary

Due to the failure of conventional consolidation testing to produce the required understanding of the consolidation behaviour of gassy soil, this chapter presents the procedure for two consolidation techniques for the testing of gassy soil. The first test can be completed in three days, during which it is possible to measure the pore water pressure on the undrained face. This enables the value of the average consolidation stress and the average void ratio to be evaluated at many points throughout the test. Numerical modelling of this procedure has shown that this resulting relationship is very close to the actual void ratio-consolidation pressure relationship.

The second test separates the undrained from the drained conditions by applying the increment of vertical stress whilst allowing no drainage from the soil sample. After the completion of all undrained settlements, the drainage taps are opened and consolidation is allowed to proceed.

CHAPTER 4

EXPERIMENTAL RESULTS

CHAPTER 4

EXPERIMENTAL RESULTS

4.1 Introduction

This chapter presents the experimental results from the two series of consolidation tests performed on samples of gassy soil. Pore water pressure response and settlement behaviour are presented for each test. These results illustrate the consolidation behaviour of gassy soil and various soil parameters are evaluated. These include the coefficient of volume change, m_v, the coefficient of consolidation, c_v, the soil permeability, k_v, the coefficient of earth pressure at rest, K_o, and the compressibility of the gas, c_g.

4.2 Test Series A

4.2.1 Compressibility behaviour of gassy soil

The previous chapter described the evaluation of the average vertical consolidation stress and the average void ratio during a consolidation test in which there is a linear increase in total stress. The average vertical consolidation stress is defined as

$$\bar{\sigma}'_v = \sigma_v - \bar{u}_w = \sigma_v - (2u_{wu} + u_{wd})/3 \qquad (4.1)$$

where $\bar{u}_w$ is the average pore water pressure, and u_{wu} and u_{wd} are the pore water pressures measured on the undrained and drained faces respectively. The average void ratio is defined as the total volume of the voids divided by the volume of the solids, which may be written as

$$e_t = (v_w + v_g)/v_s \qquad (4.2)$$

where e_t is the total void ratio, v_w is the total water volume, v_g is the total gas volume and v_s is the total volume of the solids. Figure 4.1 illustrates the relationship between the total void ratio of the gassy soil and the vertical consolidation stress. It must be noted that S_{100} indicates the degree of saturation of the soil at an average vertical consolidation pressure of 100 kPa. It can be seen from this figure that there is no unique relationship between the total void ratio and the consolidation stress. This result agrees with the work

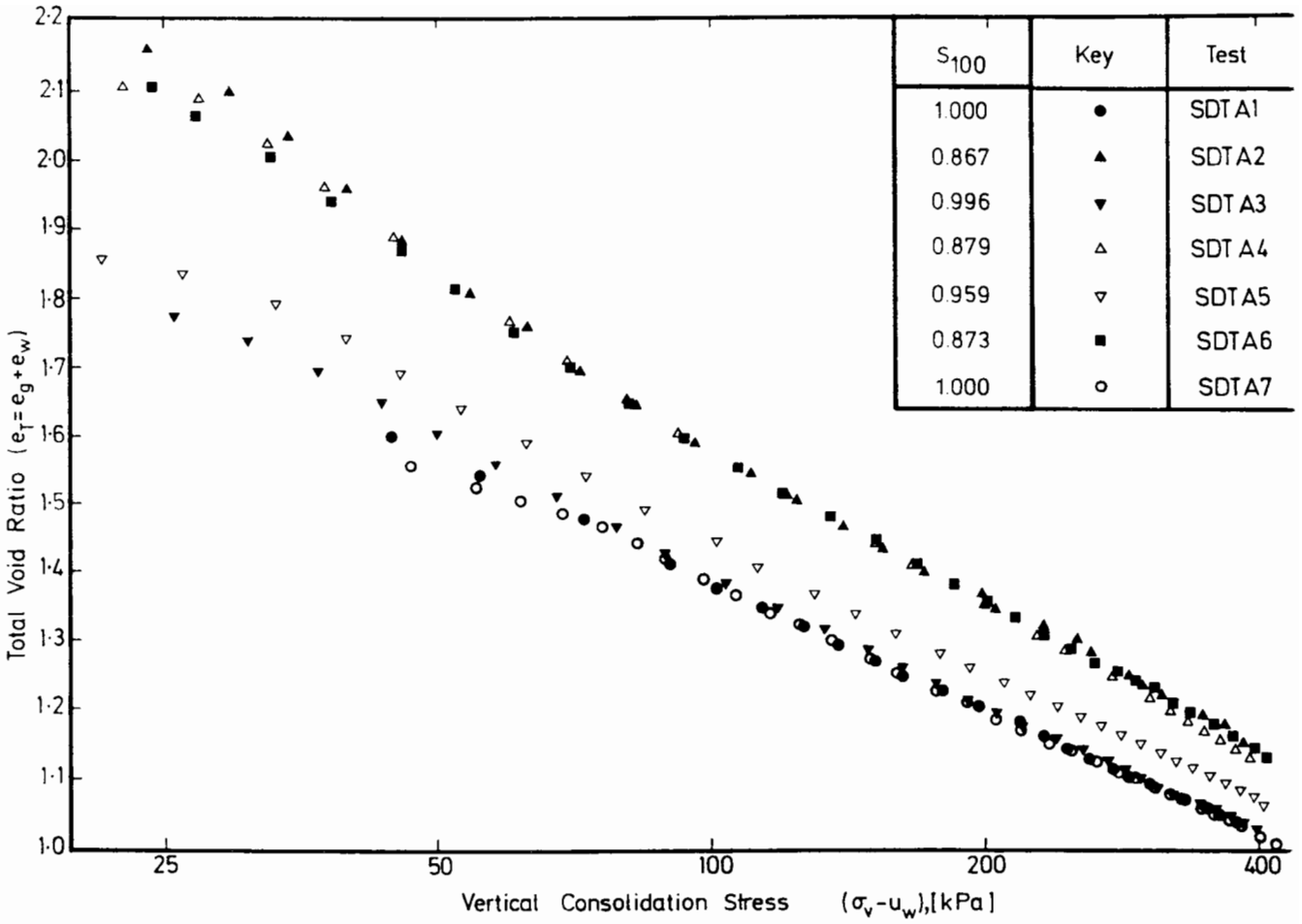

Figure 4.1 Total void ratio versus vertical consolidation stress for test series A

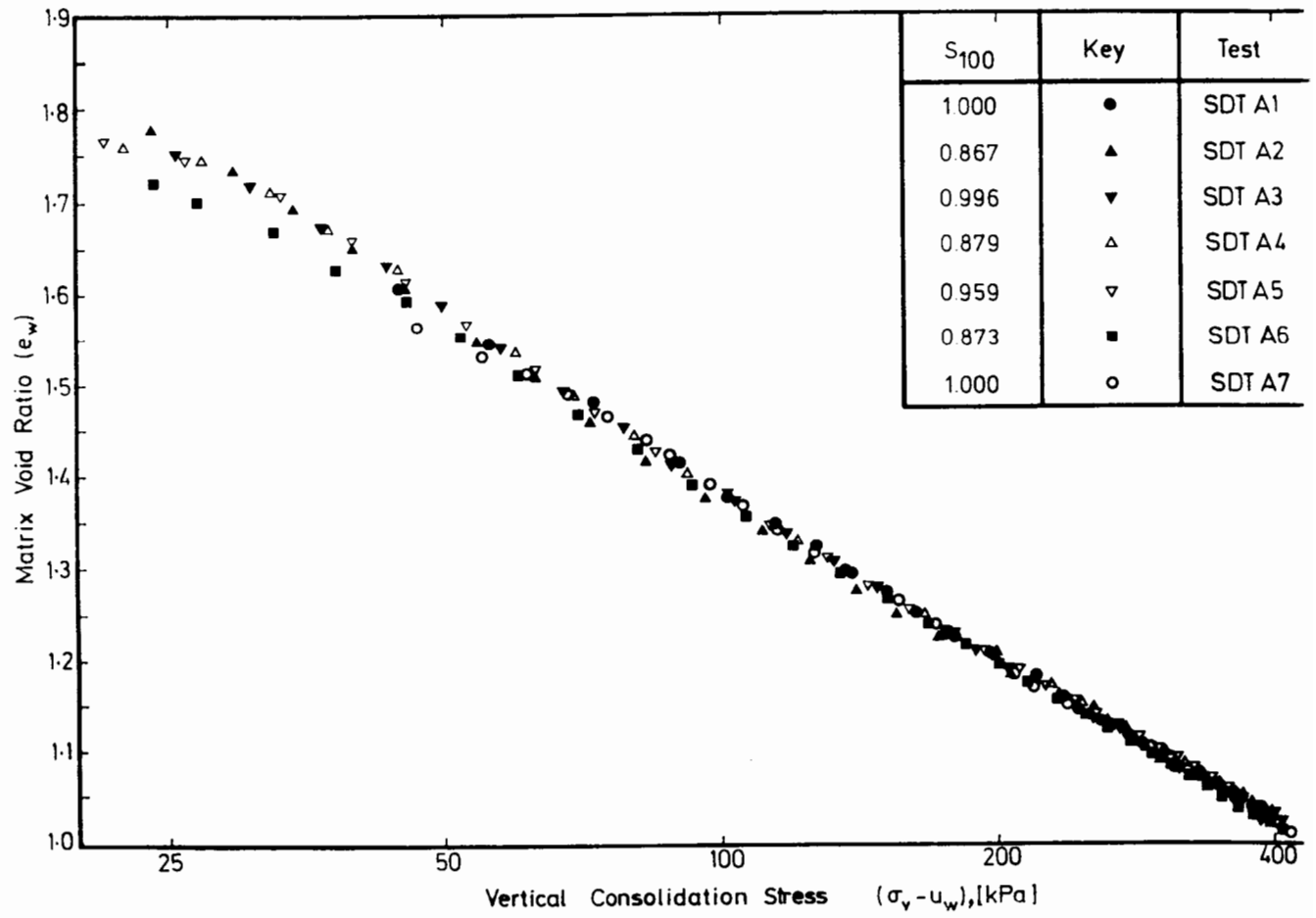

Figure 4.2 Matrix void ratio versus vertical consolidation stress for test series A

of Nageswaran (1983) and Wheeler (1986) which also found no unique relationship between the total void ratio and the consolidation stress. On close examination of gassy soil, however, it can be seen that the gas exists in relatively large voids surrounded by a saturated soil matrix. The void ratio of the saturated soil matrix is then equal to the volume of water divided by the volume of the solid. This parameter was termed by Wheeler (1986) the "matrix void ratio" and may be written as

$$e_w = \frac{v_w}{v_s} = \left(\frac{v_w}{v_w + v_g} \right) \left(\frac{v_w + v_g}{v_s} \right) = S_w \, e_t \qquad (4.3)$$

where S_w is the water saturation. Wheeler used the parameter e_m to describe the matrix void ratio. As this parameter is obtained by dividing the volume of water by the volume of solids, however, it is felt here that e_w is a more appropriate term of definition.

For the consolidation test series A, it was possible to evaluate the gas and water volumes at all times throughout the test. Therefore, at each point of measurement of total stress and pore water pressure, it was also possible to obtain the water volume and hence the matrix void ratio of the sample. Figure 4.2 presents the calculated matrix void ratio plotted against the logarithm of the average vertical consolidation stress for tests SDTA1 to SDTA7. This figure illustrates clearly a unique relationship between the vertical consolidation stress and the matrix void ratio. This unique line of Figure 4.2 can be described by

$$e_w = 2.557 - 0.589 \log_{10} (\sigma_v - u_w) \qquad (4.4)$$

The above result compares very well with the void ratio versus vertical consolidation stress for a saturated soil as produced by Nageswaran. However, the slope of the above relationship is about fifty percent higher than that obtained by Wheeler for isotropic consolidation.

4.2.2 Pore water pressure response

At this stage of the research it was believed that the gas and the pore water could be treated as a single homogeneous compressible fluid. The equation

governing the consolidation of this material for changes in total stress can be extended from equation 1.22 to give

$$\frac{\partial}{\partial z}\left[\frac{k_w}{\gamma_w}\frac{\partial u_w}{\partial z}\right] = (m_v + n_g c_g)\frac{\partial u_w}{\partial t} - m_v\frac{\partial \sigma_v}{\partial t} \tag{4.5}$$

Therefore under undrained conditions, as there is no fluid flow in the soil, the left-hand side of this equation can be set to zero, producing

$$(m_v + n_g c_g)\frac{du_w}{dt} = m_v\frac{d\sigma_w}{dt} \tag{4.6}$$

thus

$$\frac{du_w/dt}{d\sigma_v/dt} = \frac{du_w}{d\sigma_v} = \frac{m_v}{m_v + n_g c_g} \tag{4.7}$$

Consequently, any increase in total stress would cause an increase in gas pressure, which in turn would produce gas compression. Simultaneously, the reduction in the pore water pressure--caused by the gas compression--would produce an increase in effective stress, causing an undrained settlement of the soil equal to the volume change of the gas. If this were true, it could be confirmed by observing the changes in pore water pressure at early time on the undrained face of the soil samples. From equations 4.5 to 4.7, it can be shown that for a saturated soil at early time the slope of the total stress and undrained face pore water pressure curves versus time would be the same.

For a gassy soil, however, the pore water pressure slope would be significantly lower. This can be illustrated by considering a gassy soil of initial gas content, n_g, of 0.1 with the initial gas pressure at atmospheric and with a soil coefficient of volume change of $2MPa^{-1}$. Equation 4.7 shows that the initial slope of the pore water pressure curve with time would be about two thirds of the slope of the total vertical stress with time. Figure 4.3 presents the pore water pressure response on the undrained face of the gassy soil sample SDTA6 (initial saturation 82%) with time. Superimposed on this figure is the increase in total stress with time. It can be seen that the initial slope of the pore water pressure curve is almost identical to that of the total stress. This was seen for all the tests, gassy and saturated soils alike. For all samples, the pore water pressure response appeared to be that of a saturated soil even though the gassy soils produced a settlement due to gas compression and dissolution.

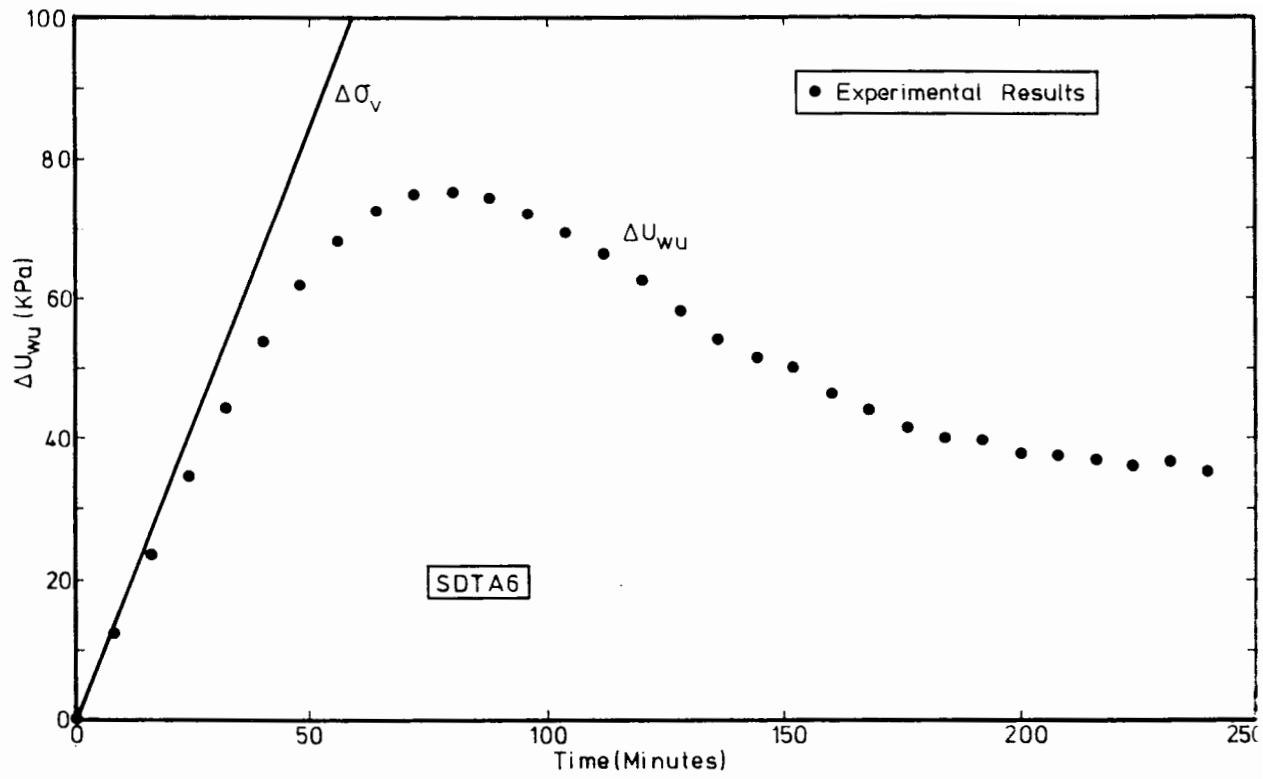

Figure 4.3 Undrained face pore water pressure response for test SDTA6

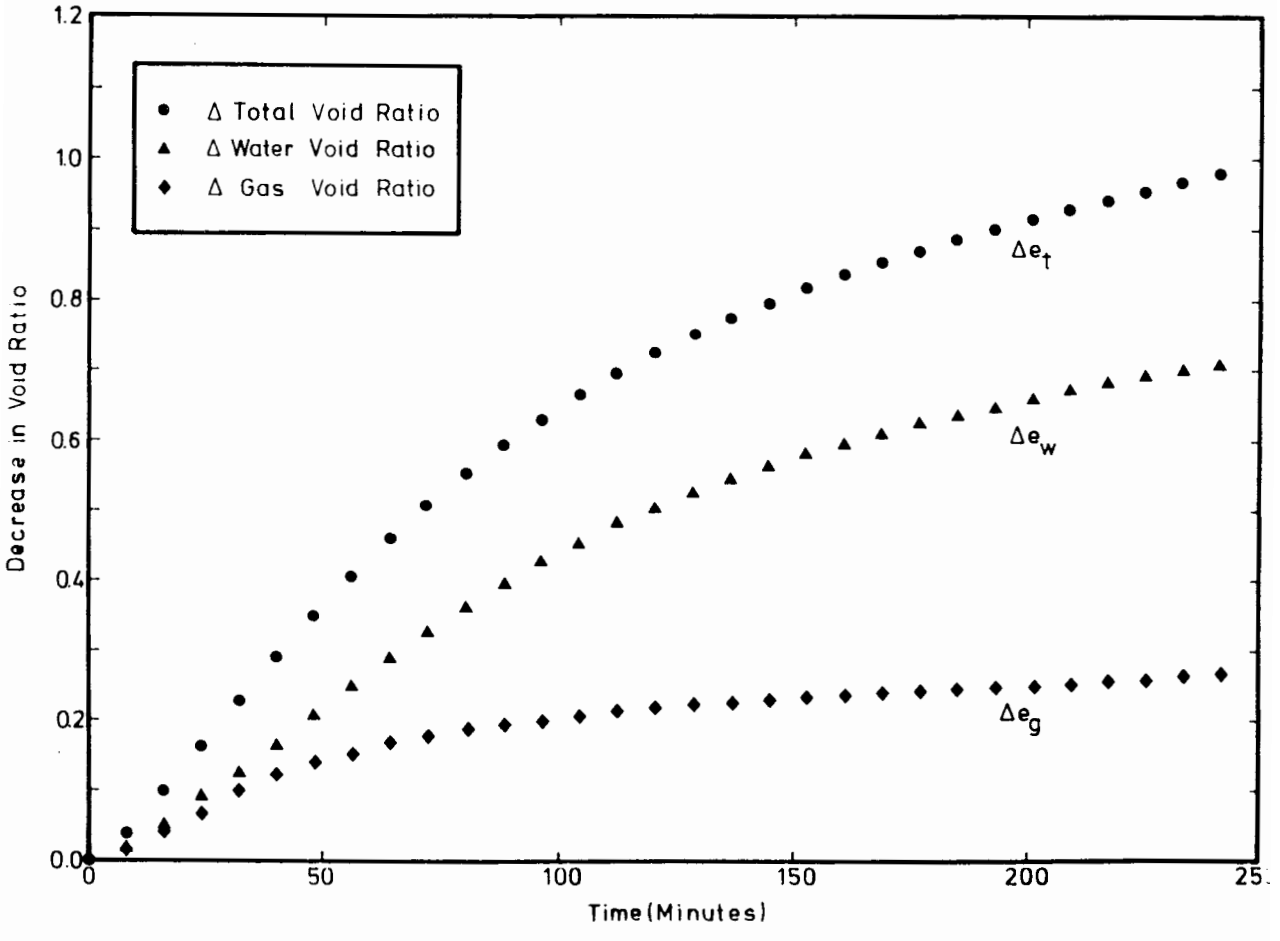

Figure 4.4 Change in void ratio versus time for test SDTA6

In addition, it can be observed from Figure 4.3 that instead of flattening out at late time to a constant value of pore water pressure--as suggested by the small strain analytical solution depicted in Figure 3.3--the pore pressure curve drops gradually towards the end of the test, even though there is still a linear application of total stress. It is possible that this is the result of an increase in the value of the coefficient of consolidation during the test due to the increase in consolidation pressure. Later large strain numerical analysis, however, illustrates that due to the settlement of the sample, the path length of the drainage fluids is reduced over the period of the consolidation test. The reduction of this drainage path length would speed up the consolidation process, thereby causing a reduction in the pore water pressure on the undrained face of the soil sample.

4.2.3 Gas volume response

If the gas and water were assumed to behave as a single compressible fluid, it would be expected that the gas volume would initially decrease as the pore water pressure--and hence gas pressure--increased. The gas volume would continue to decrease until the pore water pressure reached its maximum value and then began to fall. It would also be expected that the gas would start to expand and that by the end of the loading period--when the pore water pressures revert back to the atmospheric pressure--the final gas volume would be close to its initial volume.

This scenario was far from the response obtained when the gas volume was calculated, however. Figure 4.4 illustrates the decrease in total, matrix and gas void ratios during the linear increase in total stress consolidation test performed on sample SDTA6. It can be seen from this figure that the gas volume does indeed decrease as expected at the start of the test. However, the gas volume continually decreases--thereby illustrating a continuous increase in the gas pressure--throughout the loading period of the test, even when the pore water pressure begins to decrease. This behaviour occurred for all the gassy soil tests and at this stage, it became clear that the initial assumption that the pore water pressure and gas pressure were directly related was invalid.

4.2.4 Gas pressure response

During the laboratory consolidation test it was possible to evaluate the gas volume at all times. In order to obtain the gas pressure throughout the test, however, it is necessary to have knowledge of the gas pressure at a particular gas volume. This would effectively prescribe the mass of gas present in the sample. From the knowledge of the gas volume change and the use of Boyle's gas law and Henry's law of solubility, it would then be possible to evaluate the gas pressure at all times throughout the test.

For the initial calculation of gas pressure throughout a consolidation test, it was assumed that at the end of the test--when all pore water pressures had dissipated to atmospheric and all total stress had been removed--the gas pressure would also be at atmospheric pressure. This value was used to back calculate the gas pressure throughout the test from the measurements of free gas volume change assuming that Henry's solubility coefficient was zero.

From this initial calculation of gas pressure response, it immediately became apparent that the gas pressure has no relationship with the pore water pressure. The most surprising result was that the gas pressure appeared to be dominated by the total vertical stress. Therefore, these results suggested that a much better estimate of gas pressure would be to assume that it was equal to the total vertical stress at the start of the consolidation test.

Based on the above findings, the calculation of gas pressure was repeated assuming that the gas pressure was equal to the total vertical stress at the start of the test. In addition, the first series of calculations assumed that either the gas is insoluble in the pore water, or that there is insufficient time for the gas to move into solution. For both these cases, Henry's coefficient of solubility, H, has a value of zero. Consequently, it is assumed that all the gas in the soil sample exists as free gas with no discharge of the gas from the sample either due to free drainage or in the form of dissolved gas within the drained pore water.

The gas pressure calculation advances with time over each increment of load such that the gas volume and gas pressure are known at the start of the loading

increment. To illustrate this calculation a volume of gas, v_{gA}, at a gas pressure, u_{gA}, is considered at a point A, as illustrated in Figure 4.5a. After a certain time and increase in total stress and gas pressure, the gas volume becomes v_{gB} at point B. Therefore, from Boyle's Law the pore pressure at point B can be found by

$$u^*_{gB} = u^*_{gA} \, v_{gA}/v_{gB} \tag{4.8}$$

where u^*_g is the absolute gas pressure

$$u^*_g = u_g + u_a \tag{4.9}$$

and u_a is atmospheric pressure. The calculated gas pressure is then used as the starting pressure for the next calculation increment. In this way, the calculation marches in time from the beginning to the end of the test.

To illustrate the results of this calculation, Figure 4.6 presents the calculated gas pressures for the gassy soil tests SDTA2, A4, A5 and A6 based on the assumption that H = 0. (SDTA3 is not included as it becomes saturated early in the test.) The striking relationship of the gas pressure with the total stress can be seen immediately, as can its apparent independence of the pore water pressure.

The second method of estimation of the gas pressure assumes that the gas is soluble in the pore water with a Henry's solubility coefficient of 0.0333. It is also assumed that the gas is instantly soluble in the pore water immediately a change in the gas pressure occurs. This assumption, coupled with the assumption for the first method of gas pressure estimation, should then produce a lower and upper limit of gas pressure. Assuming that the gas dissolves in the pore water, there are now three ways in which a loss in gas volume occurs during the consolidation process. The first is the loss of free gas due to gas compression. The second is due to the extra mass of gas that becomes dissolved in the pore water, and the third is the loss of gas in dissolved form that is transported from the sample by the drained pore water.

At this point it is helpful to explain the concept of Henry's solubility law and its effect on a gassy soil. According to Henry's law, the concentration of dissolved gas is dependent on the free gas pressure. The higher the gas

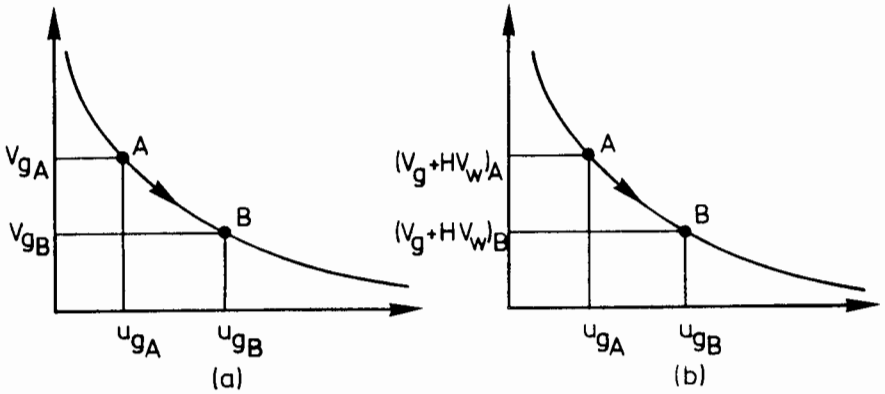

Figure 4.5 Illustration of gas volume change due to an increase in gas pressure

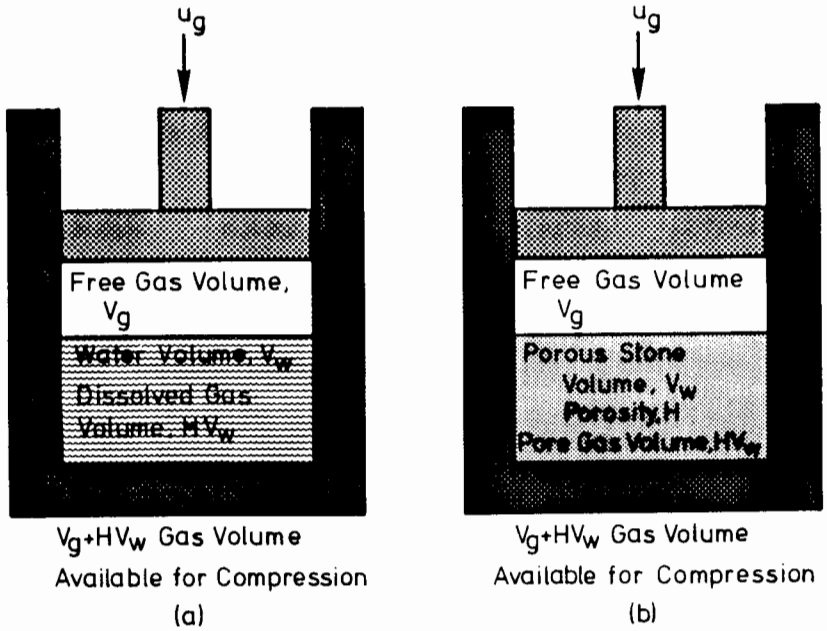

Figure 4.7 Porous stone analogy in the treatment of the dissolved gas compressibility

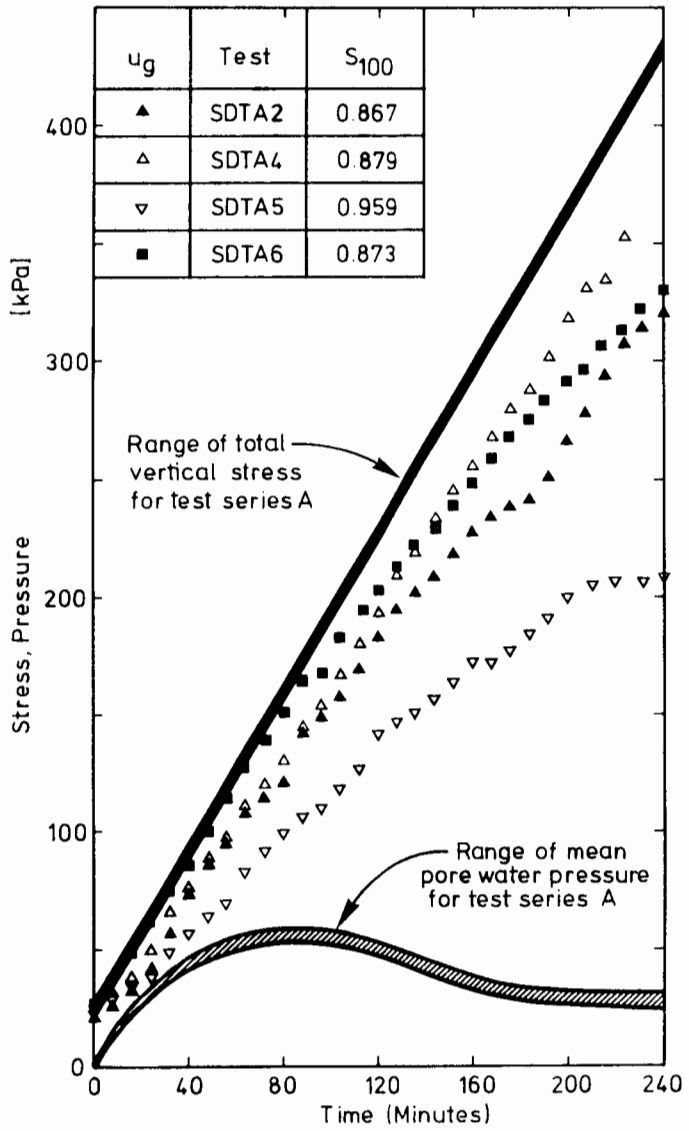

Figure 4.6 Evaluation of gas pressures for test series A for H = 0

pressure, u_g, the greater the amount of gas that will be forced into solution. This dissolved gas concentration, H, is termed "Henry's coefficient of solubility" and has a value of 0.0333 for methane in water at 20°C (Yamamoto, et al., 1976).

Fredlund (1976) presents a simple approach to Henry's law by introducing the porous stone analogy. This analogy stems from the fact that if the mass concentration of the gas dissolved in the pore water is directly proportional to the free gas pressure, then from Boyle's law, it follows that the equivalent volume concentration is constant and independent of the gas pressure. This constant is Henry's coefficient of solubility, H. Fredlund replaces the physical problem of water, free gas and dissolved gas under pressure as depicted in Figure 4.7a by free gas and a porous stone of porosity H as illustrated in Figure 4.7b. Subsequently, instead of calculating the mass of gas that enters the water due to the increase in gas pressure, the porous stone analogy simply states that there is an additional free gas volume Hv_w available for compression. Therefore, Boyle's and Henry's laws can be combined to give

$$(v_g + Hv_w)(u_g + u_a) = \text{constant} \tag{4.10}$$

Returning to the calculation of the gas pressures for test series A, an example problem is illustrated in Figure 4.5b where the water and gas volumes and the gas pressure are known at point A. After an increment of time and stress there is a volume change of gas and a volume Δv_w of pore water that drains from the sample. Thus from Boyle's law and Henry's law

$$u^*_{gA}(v_{gA} + Hv_{wA}) = u^*_{gB}(v_{gB} + Hv_{wB}) + Hu^*_g \Delta v_w \tag{4.11}$$

It is then assumed that the pressure at which the gas leaves the sample, u^*_g, may be approximated by the average gas pressure $(u^*_{gA} + u^*_{gB})/2$. Consequently, the above equation may be written as

$$u^*_{gA}(v_{gA} + Hv_{wA} - H\Delta v_w/2) = u^*_{gB}(v_{gB} + Hv_{wB} + H\Delta v_w/2) \tag{4.12}$$

from which the gas pressure at point B can be given by

$$u^*_{gB} = u^*_{gA}\,(v_{gA} + H\bar{v}_w)/(v_{gB} + H\bar{v}_w) \tag{4.13}$$

where

$$\bar{v}_w = (v_{wA} + v_{wB})/2 \qquad (4.14)$$

Equation 4.10 is assumed to hold during the test when there is water flowing from the sample. When there is unloading of the sample and water enters the soil, it is assumed that this water contains no dissolved gas. Thus the estimation of gas pressure during unloading conditions becomes

$$u_{gB} = u_{gA} (v_{gA} + Hv_{wA})/(v_{gB} + Hv_{wB}) \qquad (4.15)$$

4.2.5 Estimation of gas pressure for test SDTA6

Figure 4.8 illustrates the behaviour of sample SDTA6 under a linear increase in total stress, followed by a transient stage where there is no change in total stress, then followed by a decrease in total stress such that the pore water pressure on the undrained face is held at -10 kPa.

Also plotted in this figure are the free gas volume, average pore water pressure and the estimate of mean total stress throughout the test. Superimposed on this plot are the results of the gas evaluation based on the assumptions presented in the previous section.

It can be seen from this figure that the gas pressure, using either of the estimates for the value of H, does not follow in any way the behaviour of the average pore water pressure. It appears instead that the gas pressure is highly dependent on the total stress applied to the sample. Apart from the gradual rise of gas pressure with total stress, the most convincing fact is that as soon as the total stress ceases increasing, the gas pressure does likewise. On unloading of the soil sample, however, it can be seen that the pore pressure does not fall immediately the total stress is reduced. The pore pressure is not seen to fall until some time after the start of unloading and where the total stress is well below that of the estimated gas pressure. Thus it would appear from Figure 4.8 that the gas pressure "lags behind" the total stress. An interpretation of this behaviour is presented at a later stage in Chapter 6.

4.2.6 Empirical expression for gas pressure

Figure 4.8 illustrates that the gas pressure appears to lag behind the total stress on the sample. This would indicate that there is a difference in

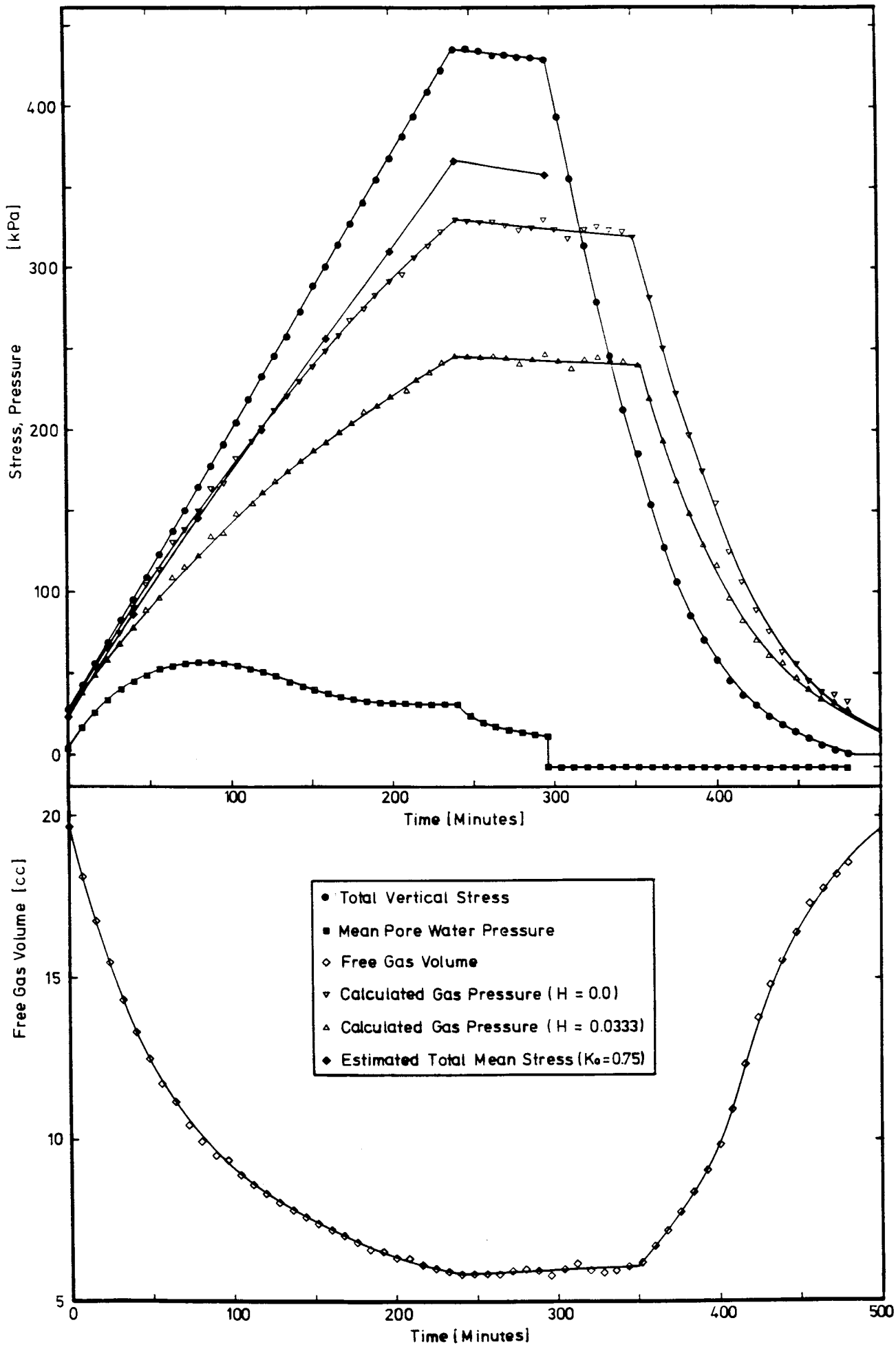

Figure 4.8 Illustration of phase volumes and pressures for test SDTA6

these values by a certain amount, which could be either positive or negative depending on whether loading or unloading conditions prevail. In addition, the difference in the total stress and the gas pressure may not be constant and may vary with properties such as shear strength or gas volume fraction. This difference may be expressed as

$$| \sigma - u_g | \leq F(s_u, n_g) \tag{4.16}$$

where σ may be the vertical or mean total stress, s_u is the soil matrix shear strength and n_g is the gas volume fraction. On observation of Figure 4.8, however, it appears that the gas pressure is almost linearly dependent on the total stress under normal consolidation conditions. Although this is a purely empirical relationship, the gas pressure can be approximated quite well by the expression

$$u_g = \alpha\sigma \tag{4.17}$$

where σ may be the vertical or the mean total stress. The parameter α is the proportion of the total stress that is transferred through the soil matrix to the gas voids. This parameter has consequently been termed the "stress transfer coefficient". It is this empirical expression that is used in the later numerical modelling of the consolidation tests.

4.2.7 Evaluation of soil permeability

One of the advantages of the consolidation of a soil sample by applying a linear increase in total stress is that for the majority of the test, the pore water pressure distribution is close to parabolic. Based on this assumption of a parabolic distribution, it is then possible to determine the pore water pressure gradient at the drained face of the soil sample. This pore water pressure gradient at the drained face, neglecting any gravity effects, can be written as

$$\left.\frac{du_w}{dz}\right|_{z=h} = - 2\, u_{wu}/h \tag{4.18}$$

where u_{wu} is the measured pore water pressure on the undrained face and h is the

height of the sample. Therefore, as both these parameters are measured throughout the consolidation test, then the pore water pressure gradient can also be evaluated. In addition, Darcy's law can be introduced as

$$W_z = \frac{Q}{A} = - \frac{k_z}{\gamma_w} \frac{du_w}{dz} \tag{4.19}$$

where W_z is the Darcy velocity--defined as the approach velocity of the pore water relative to the soil grains--Q is the total flow rate leaving the soil sample, A is the cross-sectional area of the sample, γ_w is the specific weight of the water, du_w/dz is the pore water pressure gradient and k_z is the soil permeability. It must be noted that the soil permeability, k, depends upon the intrinsic permeability, k^i--which is the property of the porous material only --the dynamic viscosity of water, μ_w, and the specific weight of the water, γ_w. This permeability relationship can be written as

$$\frac{k}{\gamma_w} = \frac{k^i}{\mu_w} \tag{4.20}$$

Therefore in order to evaluate the range of permeability for this soil, it is necessary to evaluate the Darcy velocity throughout the test.

This evaluation of Darcy velocity can be performed by separating the drained water and gas. It is then possible to evaluate the volume of pore water that drains from the sample with time. The velocity is evaluated from the derivative of the volume of pore water discharge with time, divided by the cross-sectional area of the sample. This is given by

$$W_z = \frac{1}{A} \frac{dv_w}{dt} \tag{4.21}$$

where v_w is the volume of water that drains from the soil and A is the cross-sectional area of the sample. The best method of evaluating the slope of the water volume discharge with time was found to be to use a best fit cubic spline curve through the data points. This technique was provided by a NAG routine on the OUEL VAX 11/780. This routine was also able to output the derivatives of the slope at the data points. These gradients were divided by the cross-sectional area to give the net water velocity at the drained face. Furthermore, as the drained face is a fixed boundary in space so that there can be no solid

movement across this boundary, all flow measured is that relative to the solid grains. Therefore this calculated velocity on the undrained face is also the Darcy velocity. The soil permeability may then be evaluated from

$$k_z = \gamma_w W_z h/2u_{wu} \qquad (4.22)$$

This procedure was applied to the seven tests SDTA1 to SDTA7. The resulting values of permeability are plotted against vertical consolidation stress in Figure 4.9. It must be noted that the abscissa on this plot is the consolidation stress at the drained face and not the average consolidation stress. For this series of tests the back pressure is atmospheric. Therefore the consolidation stress on the drained face is simply the total vertical stress. It can be seen from Figure 4.9 that as consolidation proceeds and the consolidation stress increases, the soil permeability decreases. It might also be expected that the permeability of gassy soils would be lower than that of saturated soils. However, there appears to be no consistent variation of the permeability due to the presence of gas.

Finally, to test the validity of this method of permeability calculation, a large strain numerical model based on Terzaghi theory was used to simulate the consolidation of a saturated sample. The model used the soil stress-strain relationship presented in Figure 4.2, and a permeability versus consolidation stress relationship similar to that in Figure 4.9. The resulting output from the finite element program included the pore water pressure on the undrained face and flow of water from the sample with time. These two parameters were then used to evaluate soil permeability as for an experimental result.

Figure 4.10 compares the actual value of the permeability curve, used as input, with the calculated value of permeability based on a parabolic distribution of pore water pressure. It can be seen that the comparison is only fair for the majority of the range of consolidation stress. The calculated values of permeability are generally higher than the actual values. Therefore, based on these findings, Figure 4.9 should only be used as a guide to the permeability behaviour, as the actual permeability will lie somewhat lower than calculated.

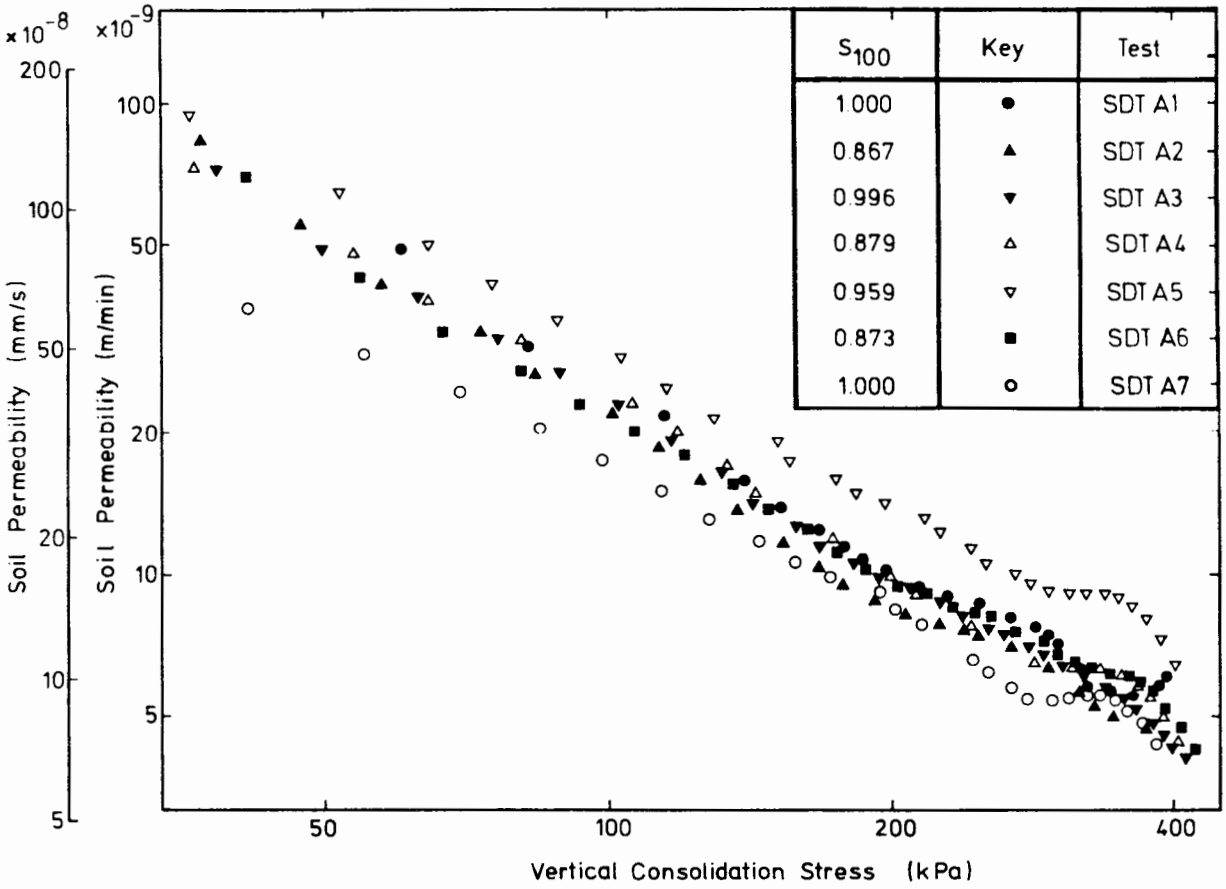

Figure 4.9 Soil permeability versus vertical consolidation stress for test series A

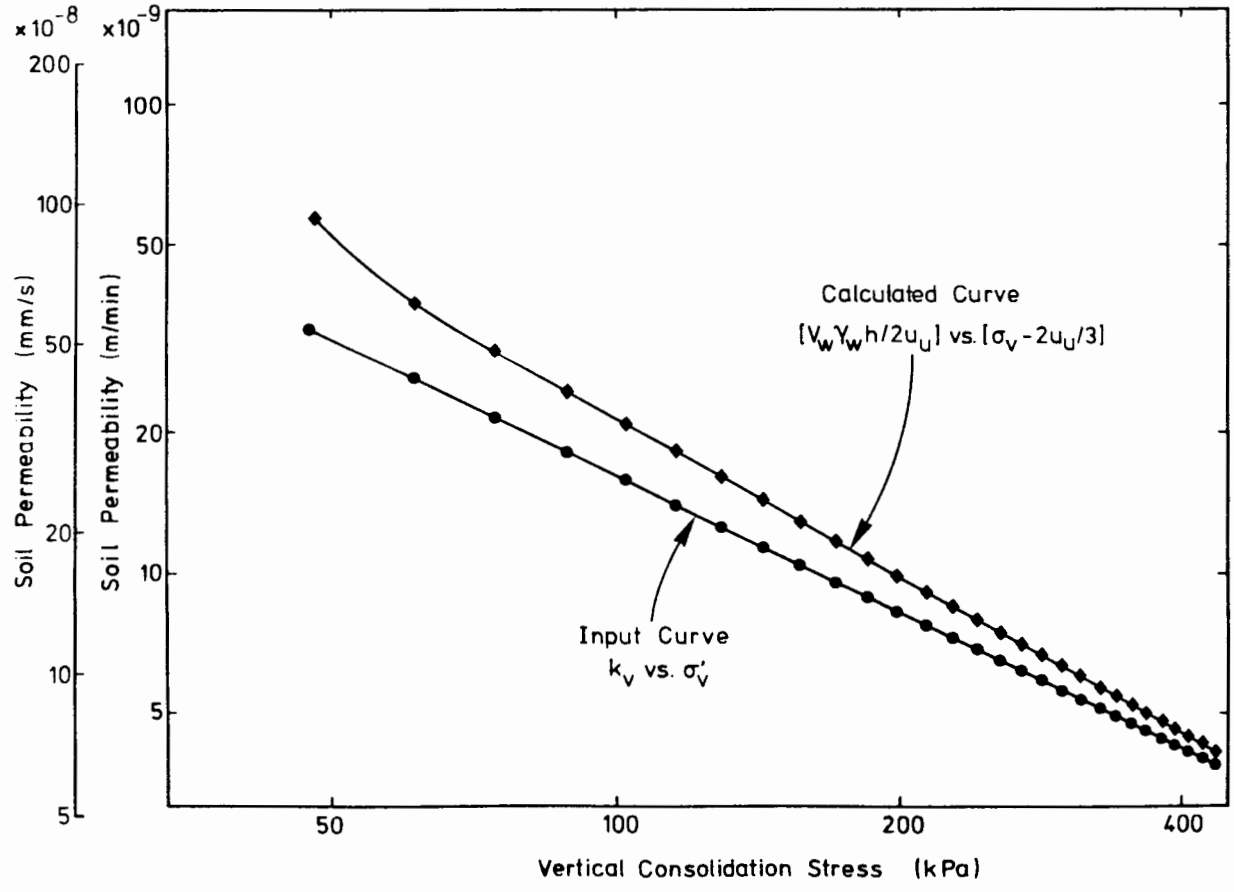

Figure 4.10 Comparison between a supplied and calculated permeability versu consolidation stress

4.3 Test Series B

Each consolidation test in this test series lasted a period of approximately seven days. As explained in Chapter 2, it was not possible to obtain any reliable long term undrained face pore water pressure measurements. To obtain more information from this series of tests, however, two miniature stress transducers were mounted on opposite sides of the oedometer cell in order to measure horizontal total stresses. The specification of these transducers is presented in Section 2.9. The testing procedure used in test series B is presented in detail in Chapter 3.

4.3.1 Relationship between void ratio and consolidation stress

In the same way as for the tests of series A, it was possible to evaluate the average void ratio at all times for the tests of series B. Unlike series A, however, it was only possible to obtain the consolidation stress when the pore water pressure became constant throughout the sample. This occurred only at the end of a loading test when all pore water pressures dissipated back to atmospheric pressure, and at the end of an undrained loading stage when there was no further settlement and the pore water pressure was assumed to be at a constant value throughout the sample. This pore water pressure could then be found using the pressure transducer which measures the pore water pressure on the top face. Thus under these conditions, the vertical consolidation stress can be found from

$$\sigma'_v = \sigma_v - u_w \tag{4.23}$$

and the mean consolidation stress from

$$\sigma'_m = (\sigma_v + 2\bar{\sigma}_h)/3 - u_w \tag{4.24}$$

where $\bar{\sigma}_h$ is the average value of the measured horizontal total stress.

Figure 4.11 presents the total void ratio versus the vertical consolidation stress for the six soil samples SDTB1 to SDTB6. Again it can be seen that there is no unique relationship between these curves. As for test series A, however, when the matrix void ratio is plotted against the vertical consolidation stress in Figure 4.12, it can be seen that the curves are certainly brought together to

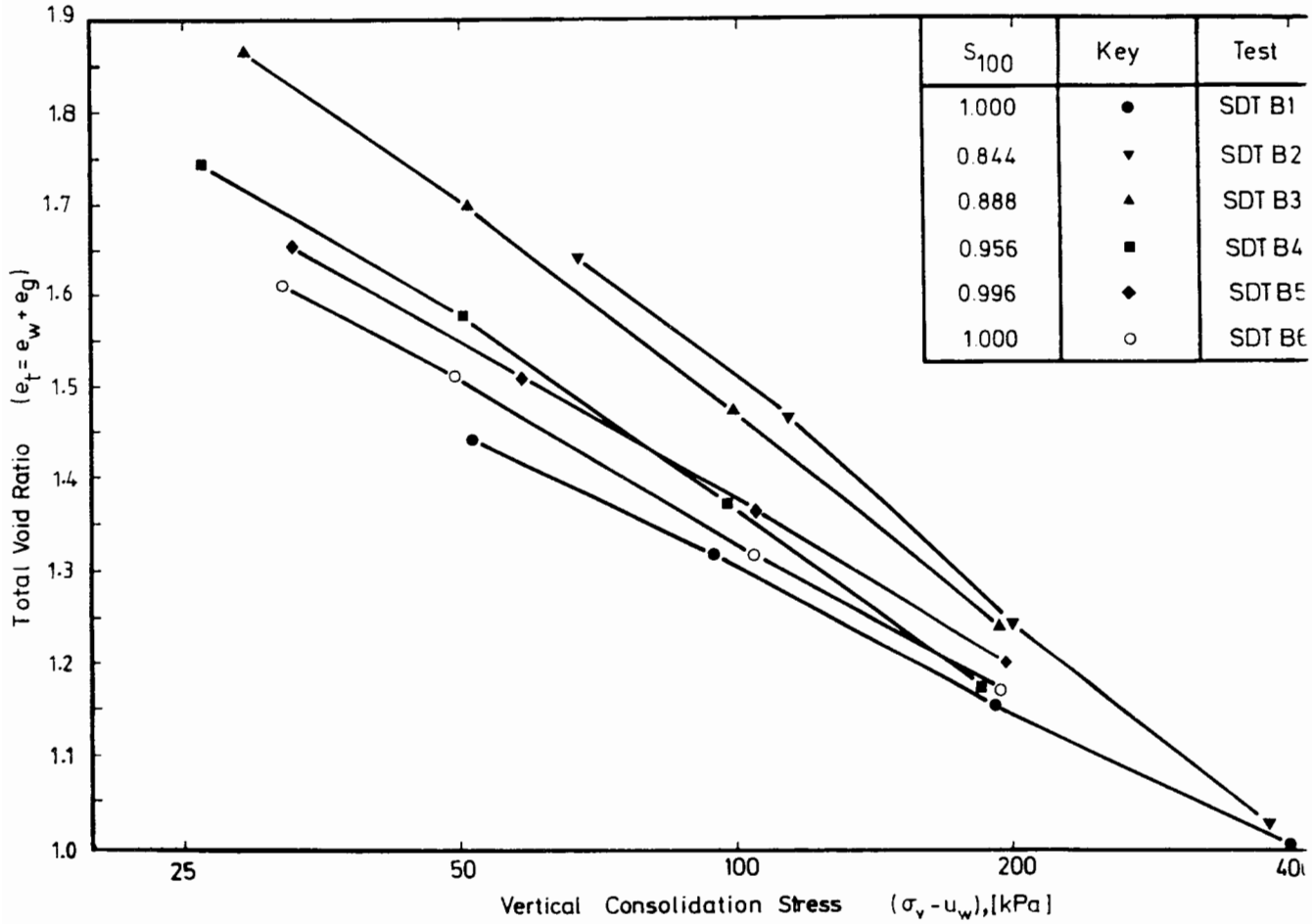

Figure 4.11 Total void ratio versus vertical consolidation stress for test series B

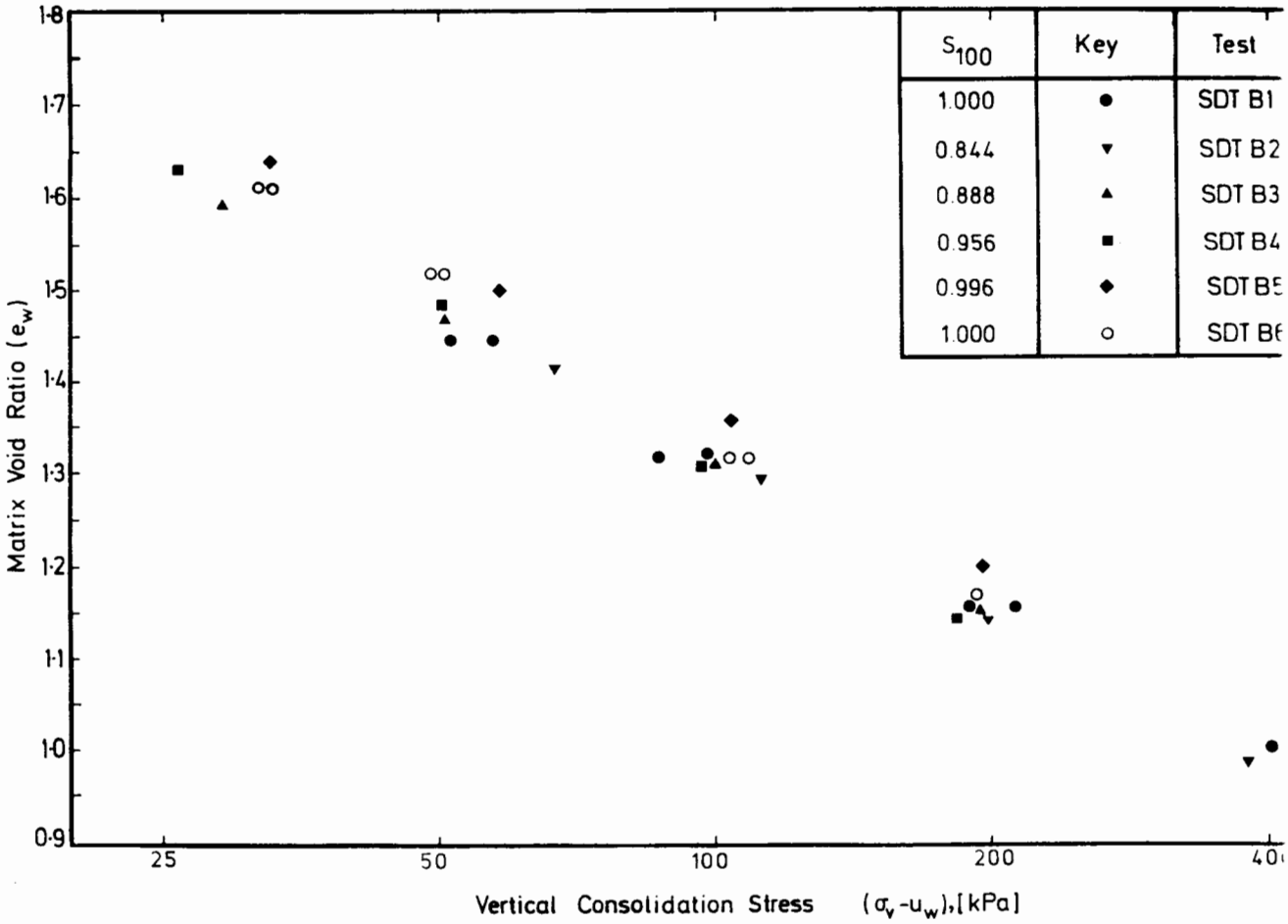

Figure 4.12 Matrix void ratio versus vertical consolidation stress for test series

a unique band, if not a unique line. A least square straight line fit through these points produces the equation

$$e_w = 2.425 - 0.552 \log_{10} (\sigma_v - u_w) \quad (4.25)$$

To compare the results of test series A and B, Figure 4.13 presents the least square best fit lines for these two test series. It can be seen that the compressibility index is fairly close, indicated by the lines being almost parallel. Series B, however, produces a lower line than Series A. There are two possible reasons for this. The first is that test Series B--as it is consolidated over a longer period--may have a lower void ratio due to the occurrence of secondary compression or creep. The second is that due to the effect of friction between the piston and the cell wall, in some tests the total stress on the sample was observed to decrease towards the end of the test. This would cause part of the sample to be slightly over consolidated. Both of these cases would cause the line to lie below that obtained from Series A.

Furthermore, as the horizontal stresses are measured in this series of tests, it is also possible to evaluate the mean consolidation stress on the soil sample. Figure 4.14 presents the matrix void ratio now plotted against the mean consolidation stress. The resulting plot is even closer to a unique line than Figure 4.12. A least square straight line fit through these points produces the equation

$$e_w = 2.412 - 0.565 \log_{10}(\sigma_m - u_w) \quad (4.26)$$

4.3.2 Behaviour of the fluid phases during undrained conditions

After the soil had been consolidated from a slurry to the required consolidation pressure of approximately 35 kPa, it was then possible to obtain the vertical and mean consolidation stresses from the fact that all pore water pressures would have dissipated back to the value of the atmospheric pressure. The sample was then subjected to an increment of total stress via the piston on the undrained face. As described in Chapter 3, an immediate displacement of the sample followed due to the compression of the gas, succeeded by a time dependent undrained settlement. After a period of about one hour, the majority of this settlement was complete. The drainage taps were kept closed for a further one

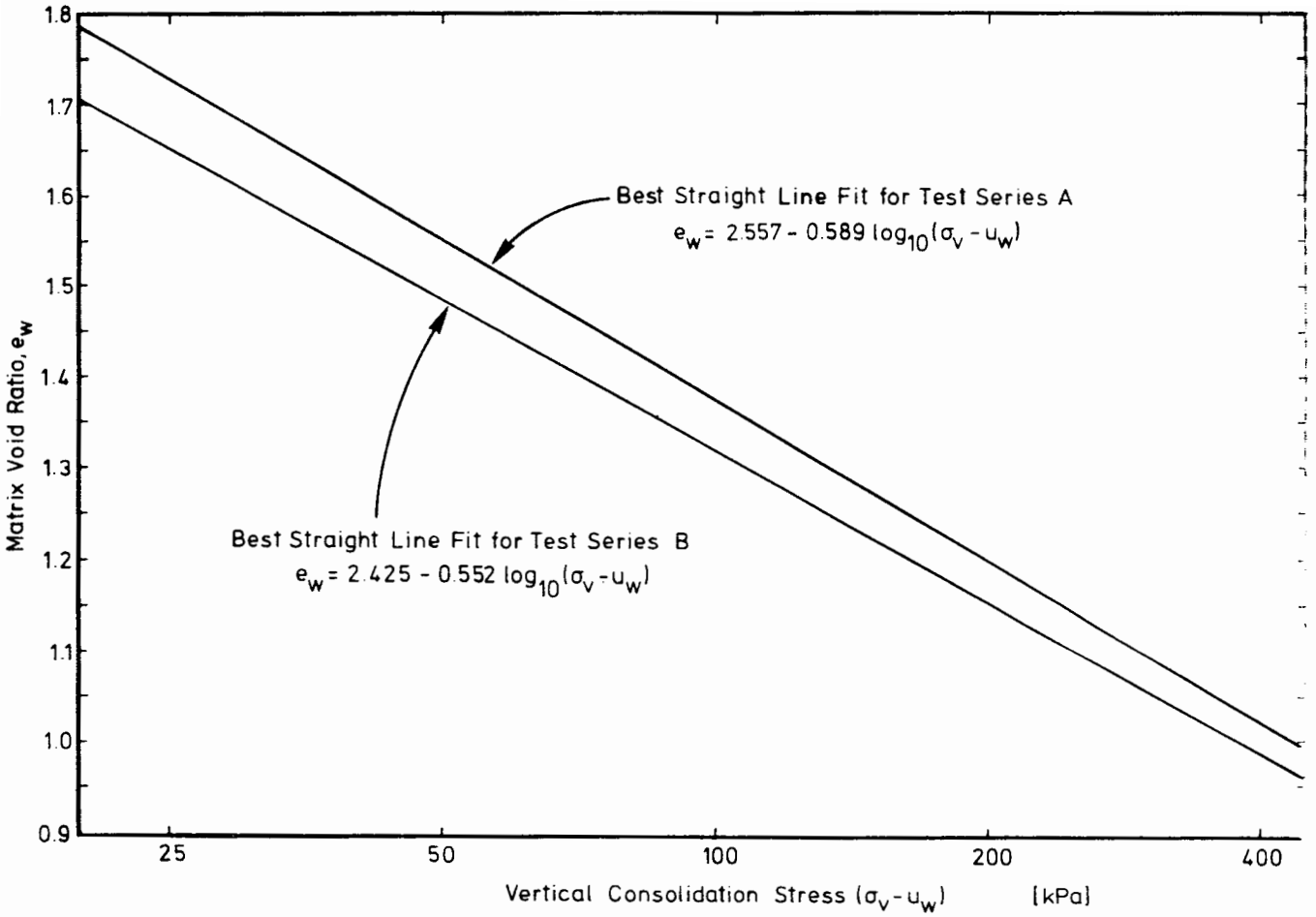

Figure 4.13 Matrix void ratio behaviour for test series A and B

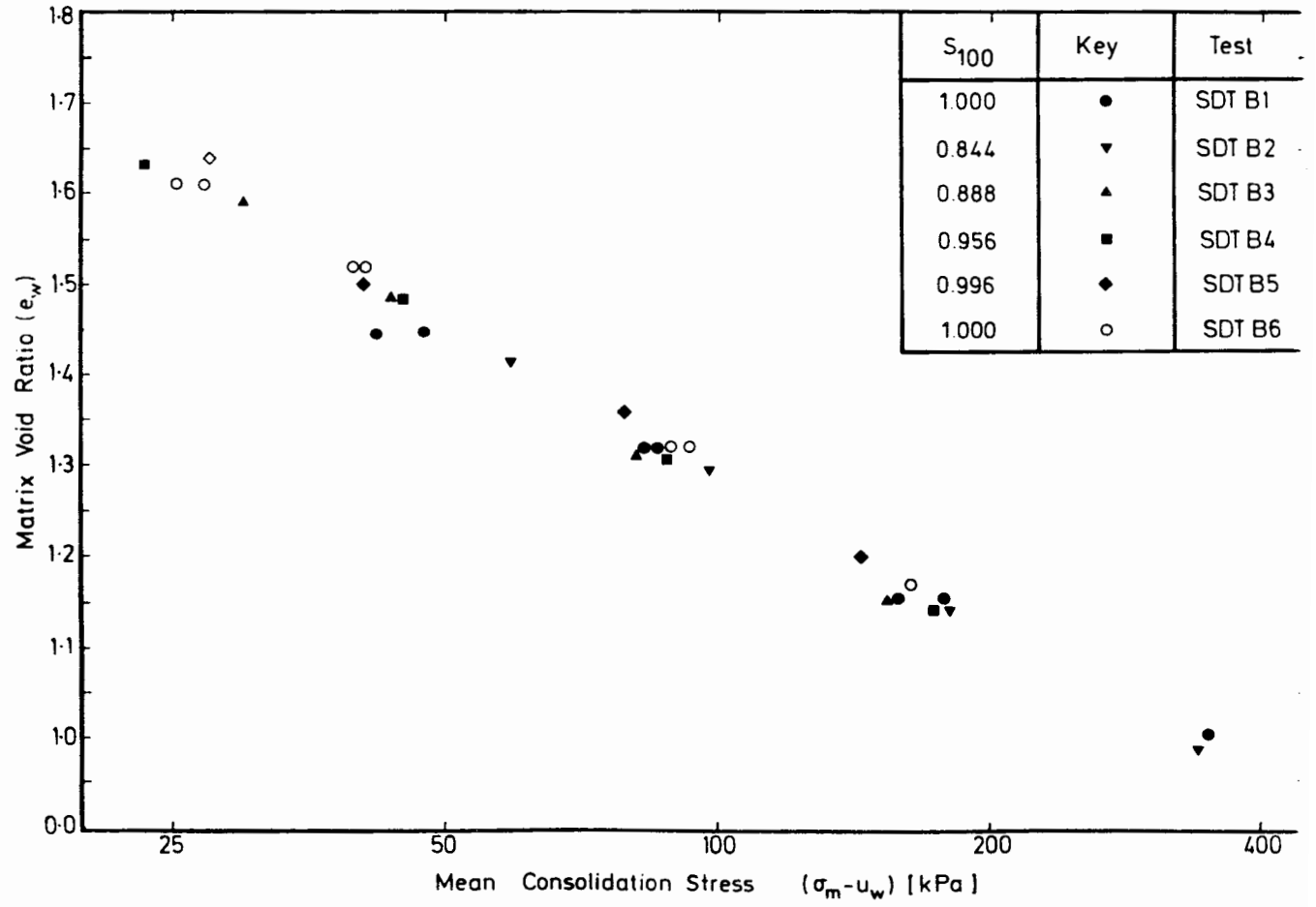

Figure 4.14 Matrix void ratio versus mean consolidation stress for test series B

hour, however, to ensure that all pore water pressures were constant throughout the sample. At this point the pore water pressure on the top face, the total vertical and horizontal stresses and the thickness of the sample were all measured. From these measurements it was then possible to evaluate the void ratio and the consolidation stress. The drainage taps were then opened which indicated the start of the drainage stage. Again, total stresses and soil thickness were measured throughout the drainage period in addition to measuring the volume of pore water that left the sample in the form of drainage fluid.

After each test was performed, it was possible to evaluate the volumes of each phase during the entire test. For the saturated tests SDTB1 and SDTB6 there were no initial displacements and all volume changes were due to the loss in pore water. Figures 4.15 to 4.18 present the void ratios of each of the fluid phases for the gassy soil tests SDTB2 to SDTB5. It must be noted that in these four figures, the time at which the test starts is actually the time at which the drainage taps are opened. What appears to be an instantaneous change in gas volume is actually that volume change which took place over the undrained period of approximately two hours prior to the opening of the drainage taps.

It can be seen immediately from these figures that there is a consistent behaviour for all tests. Considering Figure 4.15 which illustrates the consolidation behaviour of gassy soil sample SDTB2, it can be seen that as expected, the initial volume change is solely due to the volume change of the gas with no change in the water volume. On opening of the drainage taps, it can be seen that the total volume of the sample immediately begins to change due to the loss of pore water. This volume change is evaluated from the changes in the thickness of the sample. In addition, from the measurement of the volume of pore water that leaves the sample, it is possible to evaluate the volume change of the pore water that is present within it. The difference between the change in volume of the soil sample and the change in volume of the pore water equals the volume change of the gas phase. It can be seen from Figure 4.15 that the change in volume during drainage conditions is almost exclusively due to the loss in volume of pore water. The volume change of gas is extremely small during the drained stage, even though there is a large change in pore water

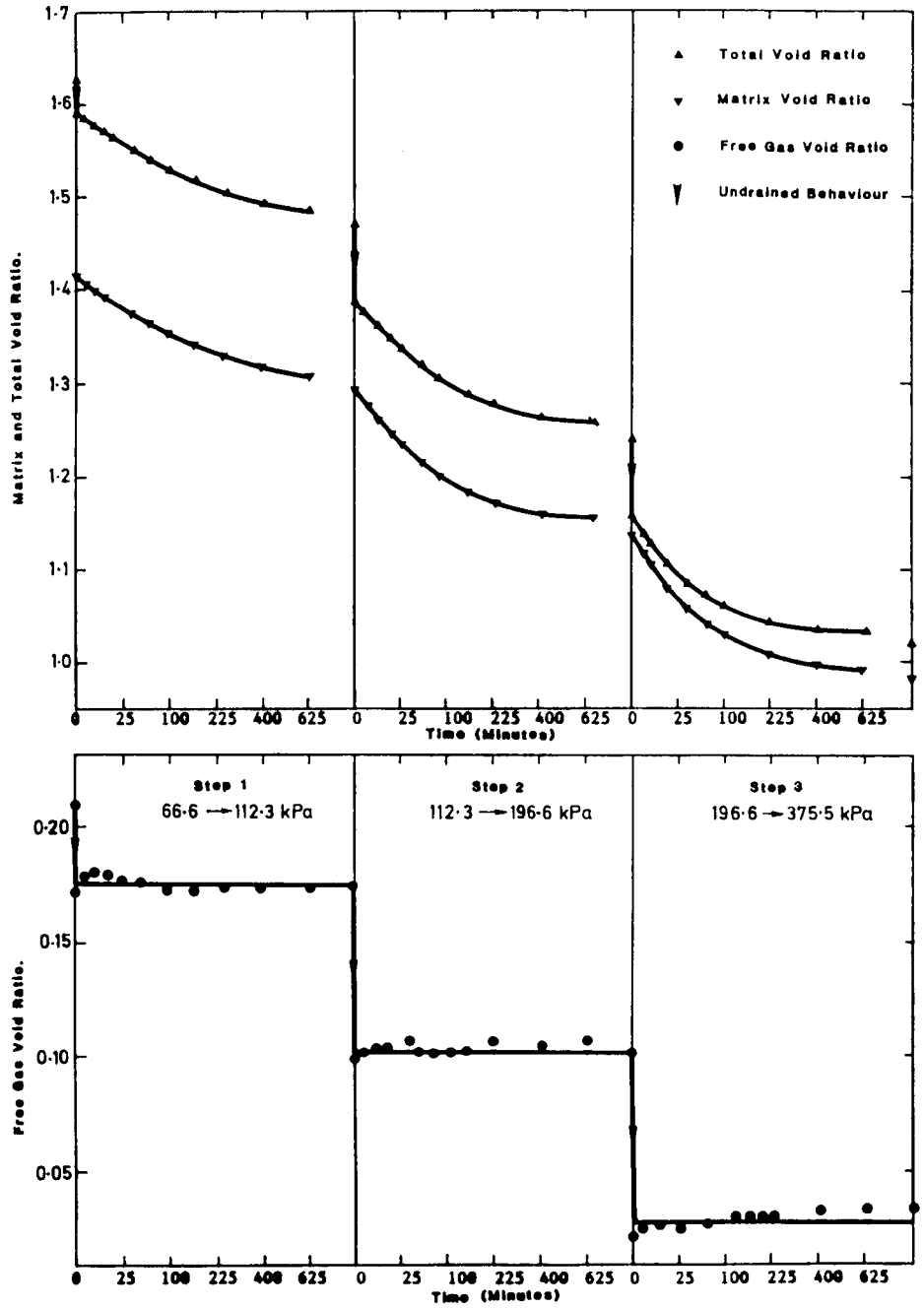

Figure 4.15 Components of Void Ratio versus Time for Test SDTB2

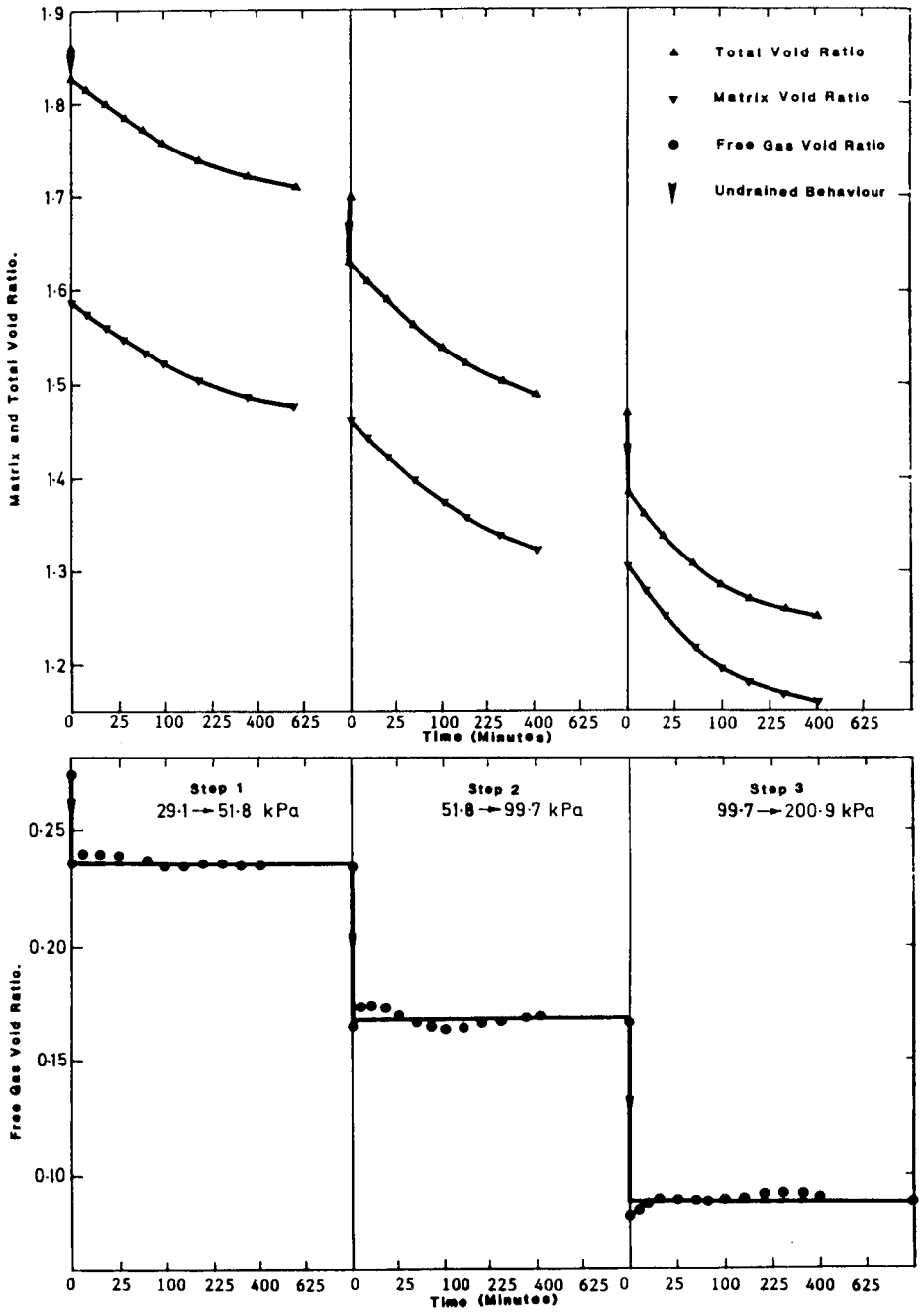

Figure 4.16 Components of Void Ratio versus Time for Test SDTB3

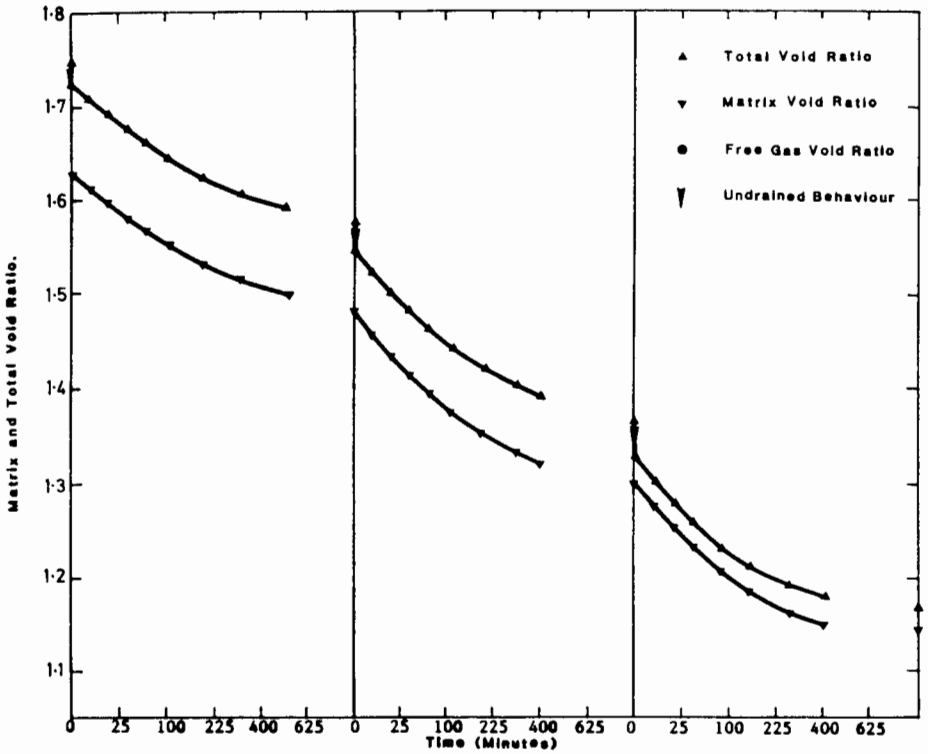
Matrix and Total Void Ratio.
Total Void Ratio
Matrix Void Ratio
Free Gas Void Ratio
Undrained Behaviour
Time (Minutes)

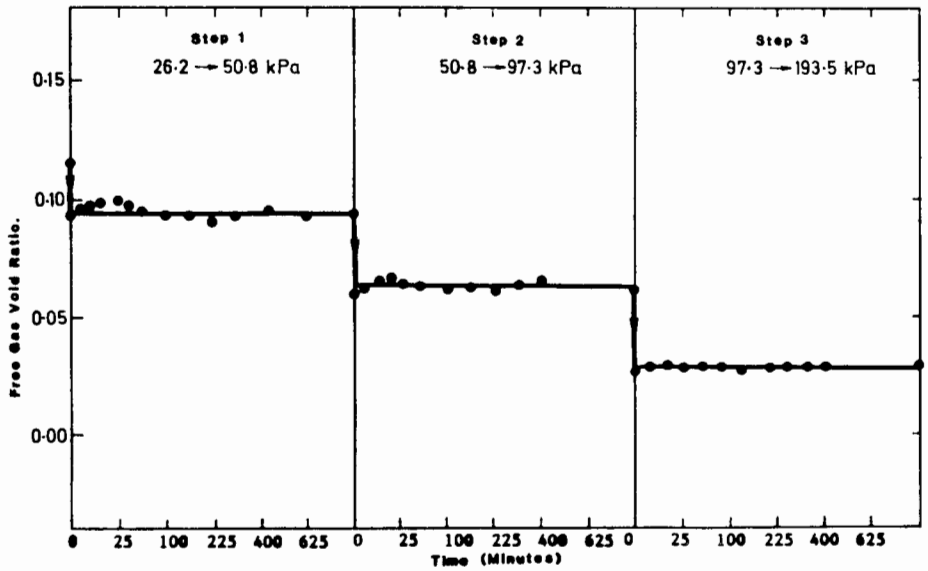
Free Gas Void Ratio.
Step 1
26·2 → 50·8 kPa
Step 2
50·8 → 97·3 kPa
Step 3
97·3 → 193·5 kPa
Time (Minutes)

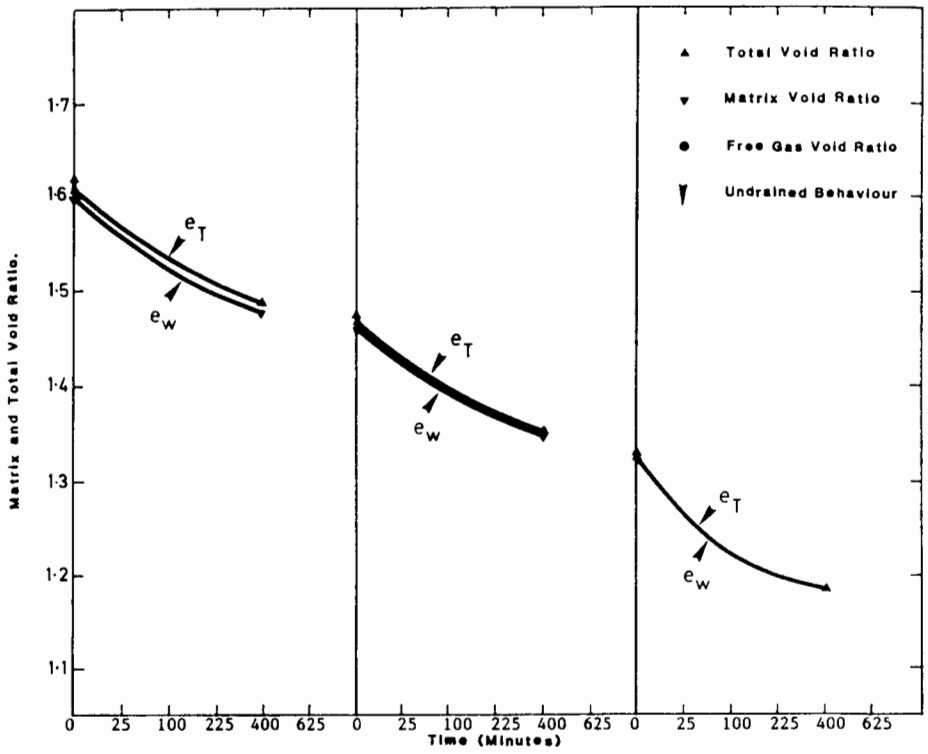
Matrix and Total Void Ratio.
Total Void Ratio
Matrix Void Ratio
Free Gas Void Ratio
Undrained Behaviour
Time (Minutes)

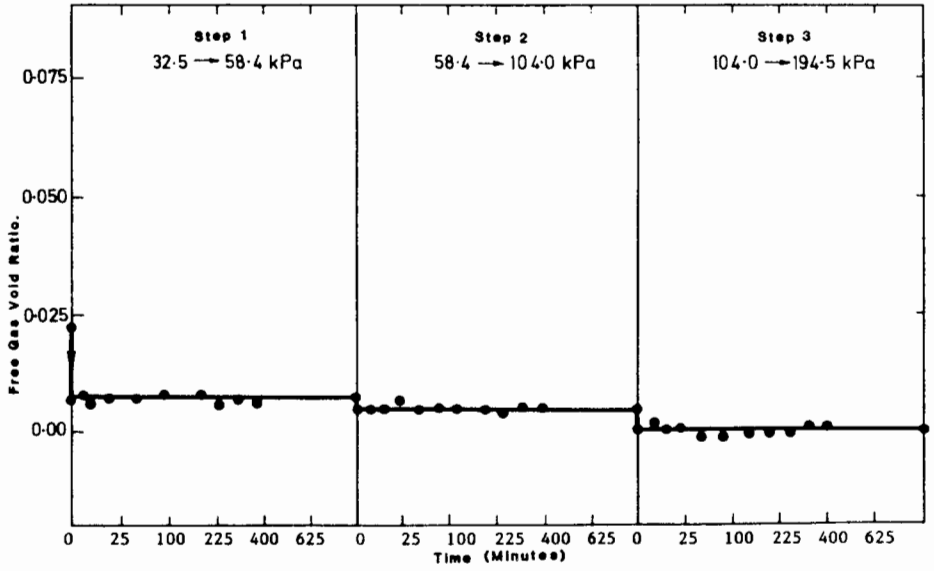
Free Gas Void Ratio.
Step 1
32·5 → 58·4 kPa
Step 2
58·4 → 104·0 kPa
Step 3
104·0 → 194·5 kPa
Time (Minutes)

pressure. (Note that the gas void ratio axis in Figures 4.15 to 4.18 is expanded to highlight any fluctuation in gas void ratio.)

Finally, it can be seen from Figures 4.15 to 4.18 that the gas volume appears to be controlled once again by changes in the total stress. This agrees with the conclusion made from test series A.

4.3.3 Measurement of K_o for a gassy soil

For test series B, it is possible to evaluate the horizontal and vertical consolidation stresses at the end of both the undrained and drained stages. The measured values of the top face pore water pressure, vertical and horizontal stresses and the water and gas void ratios are presented in Table 3.2.

In order to compare the relationship between the horizontal and vertical consolidation stresses, these two parameters are plotted on logarithmic scales in Figure 4.19. The first immediate observation from this is that there appears to be no significant difference between the results of the saturated and gassy soils, although producing a least square best fit separately through the saturated and gassy results does produce a slightly different behaviour as illustrated in Figure 4.19. In order to evaluate the average value of K_o for all the samples a least square best straight line fit is made through all the data points to give

$$\log_{10}(\sigma'_h/u_a) = 0.988 \log_{10}(\sigma'_v/u_a) - 0.1228 \qquad (4.27)$$

from which

$$K_o = \sigma'_h/\sigma'_v = 0.754 (\sigma'_v/u_a)^{-0.012} \qquad (4.28)$$

This yields a range of K_o between 0.76 and 0.74 for σ'_v=25 kPa and σ'_v=400 kPa respectively. Therefore, under this stress range, K_o is approximated as 0.75.

4.3.4 Undrained horizontal stress behaviour

In addition to the measurement of the absolute value of the horizontal stress at the end of each test, information may also be obtained from the increment of horizontal stress under undrained conditions. The increments of vertical and horizontal total stress are presented in Table 4.1. Compressible fluid theory would predict a horizontal stress increment lower than the vertical stress increment due to the compressibility of the gas. The relationship

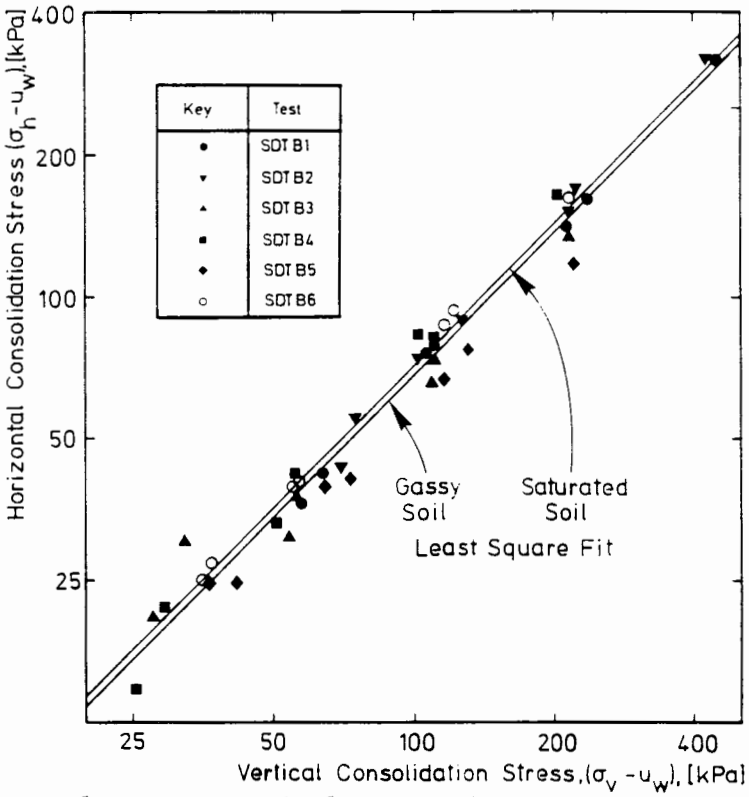

Figure 4.19 Horizontal versus vertical consolidation stress for test series B

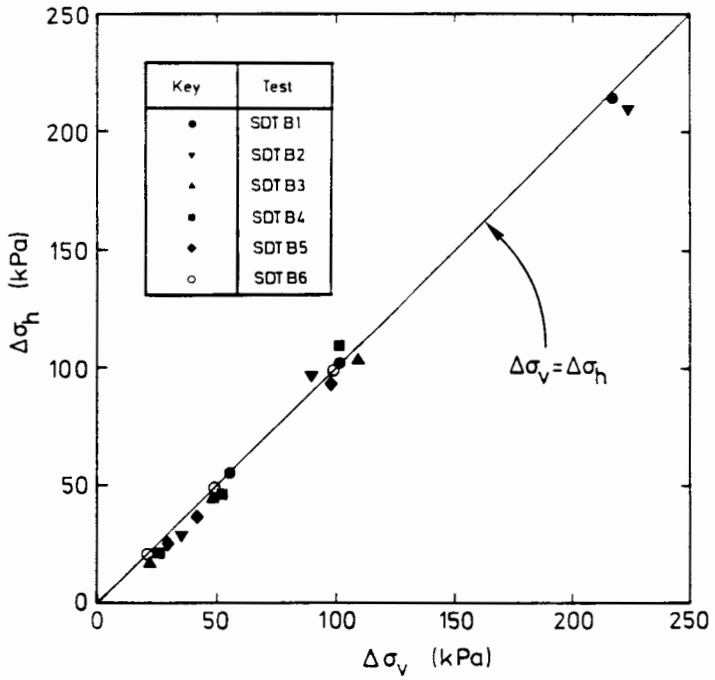

Figure 4.20 Horizontal versus vertical stress increment for test series B

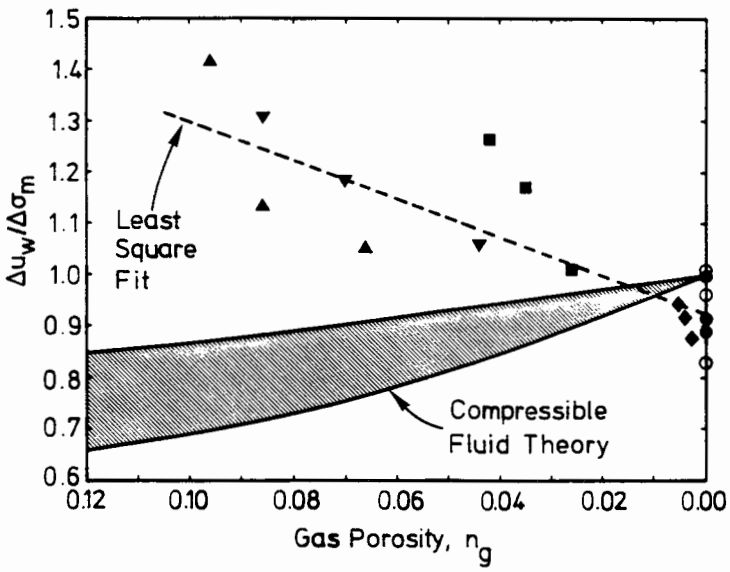

Figure 4.21 Normalized undrained pore water pressure change versus gas porosity

Table 4.1 Evaluation of Consolidation Parameters for Test Series B.

TEST-STAGE	n_g	$\Delta\sigma_v$ [kPa]	$\Delta\sigma'_v$ [kPa]	$\Delta\sigma_h$ [kPa]	$\Delta\sigma'_h$ [kPa]	$\Delta\sigma_m$ [kPa]	$\Delta\sigma'_m$ [kPa]	Δu_w [kPa]	$\frac{\Delta u_w}{\Delta\sigma_m}$	σ'_{v50} [kPa]	σ'_{m50} [kPa]	Δe_w	e_{t50}	m_v MPa^{-1}	m_m MPa^{-1}	t_{50} [min]	h_{50} [mm]	c_v mm^2/min	$c_v m_v \gamma_w$ [m/min]	$c_v \bar{m}_v \gamma_w$ [m/min]
SDTB1-1	0.000	55.1	42.3	54.8	39.4	54.9	40.4	48.9	0.890	72.9	62.1	0.127	1.382	1.261	1.320	121.0	27.33	1.210	1.28(-8)	1.12(-8)
SDTB1-2	0.000	100.7	95.2	102.2	64.2	101.7	74.5	101.3	0.996	141.6	119.5	0.162	1.237	0.761	1.170	74.0	25.62	1.739	1.23(-8)	1.69(-8)
SDTB1-3	0.000	217.6	204.8	213.6	173.2	214.9	183.7	196.6	0.915	293.4	249.3	0.154	1.080	0.355	4.270	56.3	23.65	1.949	6.92(-9)	6.94(-9)
SDTB2-1	0.086	35.4	45.6	28.5	33.9	30.8	37.8	40.3	1.306	89.9	78.1	0.119	1.528	1.389	1.250	97.0	20.71	0.867	1.20(-8)	9.00(-9)
SDTB2-2	0.070	89.8	84.3	96.3	81.2	94.2	82.2	111.1	1.180	154.9	138.1	0.153	1.315	0.784	0.804	53.3	18.98	1.324	1.04(-8)	8.83(-9)
SDTB2-3	0.044	223.8	178.9	209.8	145.3	214.5	156.5	226.3	1.055	286.5	257.5	0.156	1.090	0.417	0.477	30.3	17.14	1.903	7.94(-9)	7.57(-9)
SDTB3-1	0.096	21.0	22.0	16.6	7.1	18.1	12.1	24.9	1.374	40.1	36.1	0.112	1.764	2.007	3.360	81.1	23.15	1.296	2.60(-8)	3.63(-8)
SDTB3-2	0.086	47.9	47.7	43.6	35.5	45.0	39.6	50.1	1.113	75.0	61.9	0.159	1.585	1.308	1.550	67.3	21.38	1.332	1.73(-8)	1.73(-8)
SDTB3-3	0.067	108.8	93.9	96.6	59.7	100.6	71.1	110.2	1.095	145.8	117.2	0.157	1.315	0.722	0.954	41.0	19.60	1.836	1.33(-8)	1.46(-8)
SDTB4-1	0.042	24.9	24.1	21.0	20.2	22.3	21.5	28.0	1.258	38.3	34.2	0.144	1.651	2.254	2.520	81.0	22.31	1.204	2.71(-8)	2.53(-8)
SDTB4-2	0.035	49.0	46.9	52.5	39.1	51.3	41.7	52.8	1.028	73.8	65.8	0.176	1.458	1.527	1.720	74.8	20.78	1.131	1.73(-8)	1.62(-8)
SDTB4-3	0.026	101.2	86.1	108.3	83.7	105.9	84.5	105.2	0.993	140.3	129.0	0.166	1.252	0.856	0.872	50.4	19.06	1.412	1.21(-8)	1.03(-8)
SDTB5-1	0.005	28.3	25.9	23.7	14.3	25.1	18.2	23.5	0.935	45.6	36.6	0.140	1.581	2.123	2.980	75.7	21.18	1.160	2.46(-8)	2.88(-8)
SDTB5-2	0.004	41.8	45.6	35.5	26.5	37.4	32.8	34.8	0.930	81.3	62.1	0.141	1.434	1.271	1.760	75.7	20.00	1.036	1.32(-8)	1.53(-8)
SDTB5-3	.0025	97.7	90.9	87.3	51.0	90.8	64.3	82.4	0.907	149.5	110.7	0.157	1.282	0.757	1.070	42.9	18.71	1.600	1.21(-8)	1.43(-8)
SDTB6-1	0.000	20.7	17.4	18.9	14.6	19.5	15.5	16.2	0.831	40.6	33.4	0.096	1.564	2.241	2.320	82.0	20.65	1.019	2.28(-8)	1.98(-8)
SDTB6-2	0.000	49.1	54.5	48.4	47.6	48.6	49.9	48.7	1.002	76.5	65.4	0.199	1.418	1.511	1.720	81.0	19.47	0.917	1.39(-8)	1.32(-8)
SDTB6-3	0.000	100.9	88.2	101.5	74.9	101.3	79.3	97.4	0.962	147.8	127.0	0.148	1.244	0.748	0.873	39.7	17.60	1.529	1.14(-8)	1.12(-8)

between the vertical and horizontal stress increment can then be derived from equation 4.5 to give

$$\Delta\sigma_h = \Delta\sigma_v (m_v + K_o n_g c_g)/(m_v + n_g c_g) \quad (4.29)$$

where n_g is the gas porosity, c_g is the gas compressibility and m_v is the soil vertical coefficient of volume change. From the above equation, the change in horizontal and vertical stress would only be identical if either the gas volume fraction was zero or K_o was equal to unity.

Figure 4.20 presents the increment of total horizontal stress versus the increment of total vertical stress. Also plotted is the relationship expected for a saturated soil under undrained conditions. This corresponds to an undrained Poisson's ratio equal to 0.5. Figure 4.20 illustrates that for undrained conditions, an increment of horizontal total stress can be assumed equal to the increment of vertical stress for both gassy and saturated soils.

4.3.5 Pore water pressure response under undrained conditions

Although for this series of tests it was not possible to obtain reliable readings of pore water pressure on the piston, it was possible to obtain a genuine reading of pore water pressure on the top face of the sample under undrained conditions. It was assumed that at the end of undrained conditions, the pore water pressure would be constant throughout the sample. Again, if it is assumed that the gas existed as small occluded bubbles in the pore structure of the soil and acted as a compressible fluid, the pore water pressure response due to an increment of total vertical stress, $\Delta\sigma_v$, under undrained conditions can be adapted from equation 4.7 to give

$$\Delta u_w = \Delta\sigma_v m_v/[m_v + (n_g + H n_w)c_g] \quad (4.30)$$

where n_w is the water porosity and H is Henry's coefficient of solubility. Figure 4.21 presents the measured values of $\Delta u_w/\Delta\sigma_m$ versus initial gas volume fraction for each undrained loading increment for tests SDTB1 to SDTB6. Also plotted in this figure is the range of values expected using the compressible fluid theory from equation 4.24. Despite the considerable scatter of the data, it can be seen that for a gassy soil there is a definite trend which shows that

as the gas volume fraction increases, there is an increased pore water pressure generation above the value of the mean total stress increment. For Figure 4.21, the relationship between the total stress increment and the pore water pressure increment can be written in the form

$$\Delta u_w = B\Delta\sigma_m(1 + An_g) \tag{4.31}$$

Ideally the value of B should be unity. However, it is virtually impossible to saturate fully a piece of apparatus that is designed to contain a sample of gassy soil. Thus on compression of the soil, there may be some compression of gas outside the soil sample which in effect would lead to a slight drained condition that would produce some increase of the consolidation stress on the soil skeleton, resulting in a reduced value of pore water pressure. Therefore, even a sample that is almost saturated may have a B value less than unity. A least square straight line fit through Figure 4.21 produces the equation

$$\Delta u_w = 0.926\ \Delta\sigma_m(1 + 4.04\ n_g) \tag{4.32}$$

4.3.6 Relationship between gas pressure and total stress

Test series A illustrated clearly that the gas pressure was not related to the pore water pressure, but appeared to be dependent on the total stress. Under loading conditions for a normally consolidated gassy soil, the following was suggested for gas pressure

$$u_g = \alpha\,\sigma \tag{4.33}$$

where u_g is the gas pressure, α is the stress transfer coefficient and where σ could be the vertical or mean total stress. In addition, Figures 4.15 to 4.18 illustrate that for test series B, the gas volume and hence the gas pressure appear to be dependent on the total stress. Therefore in the same way as the matrix void ratio is plotted against the logarithm of consolidation stress, Figure 4.22 presents the total gas void ratio ($e_g + He_w$) versus the logarithm of total vertical stress for the gassy soil tests SDTB2 to SDTB5. It can be seen that for each test there is a definite relationship between the gas void ratio and the total vertical stress. Due to the different initial gas content of each test, however, these curves are not unique. Figure 4.23 presents the same gas

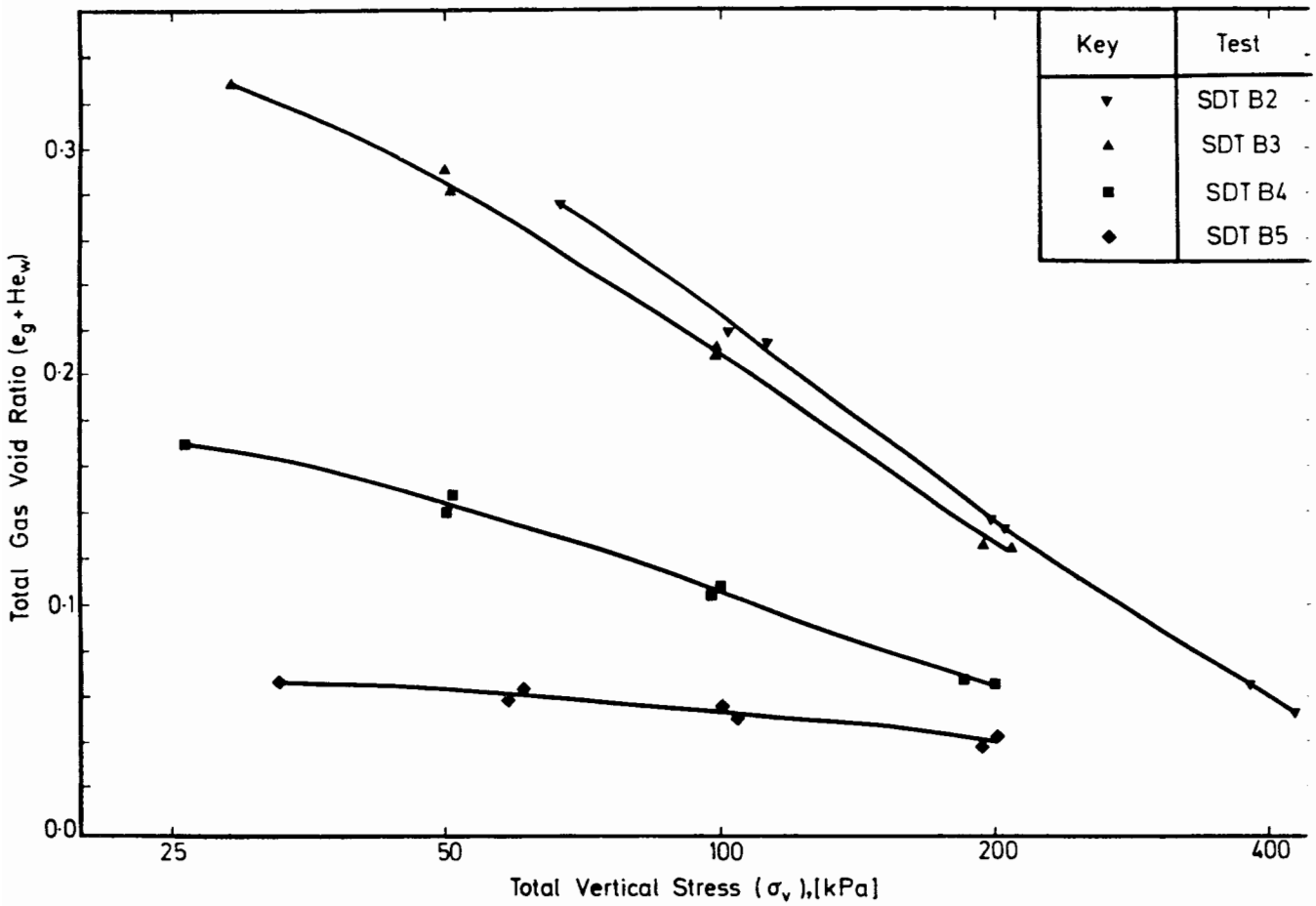

Figure 4.22 Total gas void ratio versus total vertical stress for test series B

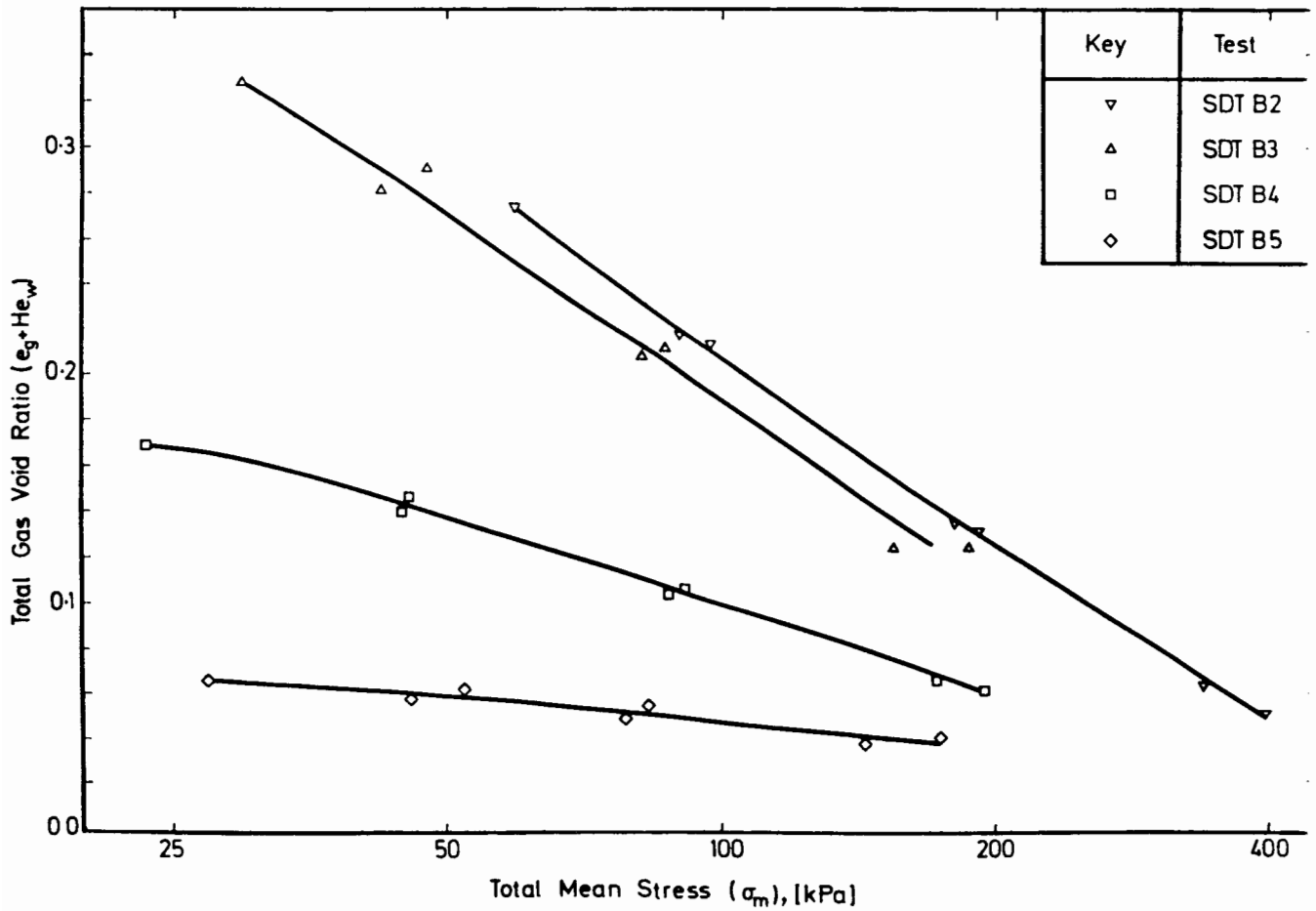

Figure 4.23 Total gas void ratio versus total mean stress for test series B

void ratios, but plotted this time against the total mean stress. Again, the same type of behaviour is observed as in Figure 4.22.

In order to compare the behaviour of these four tests, the assumption was made that at the start of the first application of undrained loading (after initial consolidation) the gas pressure is equal to the total stress. This assumption is based on the fact that the initial load is applied to the soil when the shear strength is very low, thus allowing all of the applied stress to be transferred to the gas void. On the basis of this assumption it is then possible to evaluate the equivalent gas void ratio at zero total stress as

$$e_g^o + H\, e_w^o = (e_g^i + He_w^i)(1 + \sigma^i/u_a) \tag{4.34}$$

where u_a is the atmospheric back pressure, the superscript "o" denotes the void ratios at atmospheric pressure, and the superscript "i" denotes the initial void ratios and stresses at the start of the first increment of stress. It is then possible to obtain a normalized value of void ratio which may be written as

$$(e_g + He_w)/(e_g^o + H\, e_w^o) = (e_g + He_w)/[(e_g^i + He_w^i)(1 + \sigma^i/u_a)] \tag{4.35}$$

Figure 4.24 presents these normalized values of void ratio plotted against both the total vertical and mean stress. It can be seen that by normalizing these curves, they are brought together to almost a unique line.

Based on this result, the same principle was then applied to the tests of series A. The resulting relationship between the total vertical stress and the normalized gas volume is presented in Figure 4.25. It can be seen that although the curves have been brought together, they do not produce such a unique relationship as for test series B. It is interesting to note, however, that for those soils with an initial free gas porosity close to zero (Tests SDTB5, SDTA3, SDTA5), the resulting curves are at a higher value than the remainder of them.

To compare these experimental results with the simple empirical expression given by equation 4.33, the gas pressure must first be evaluated throughout the test. Therefore starting from the point σ = 25 kPa, the theoretical total normalized gas volume may be found from

$$(e_g + H\, e_w)/(e_g^o + H\, e_w^o) = u_a/(u_a + \alpha\sigma) \tag{4.36}$$

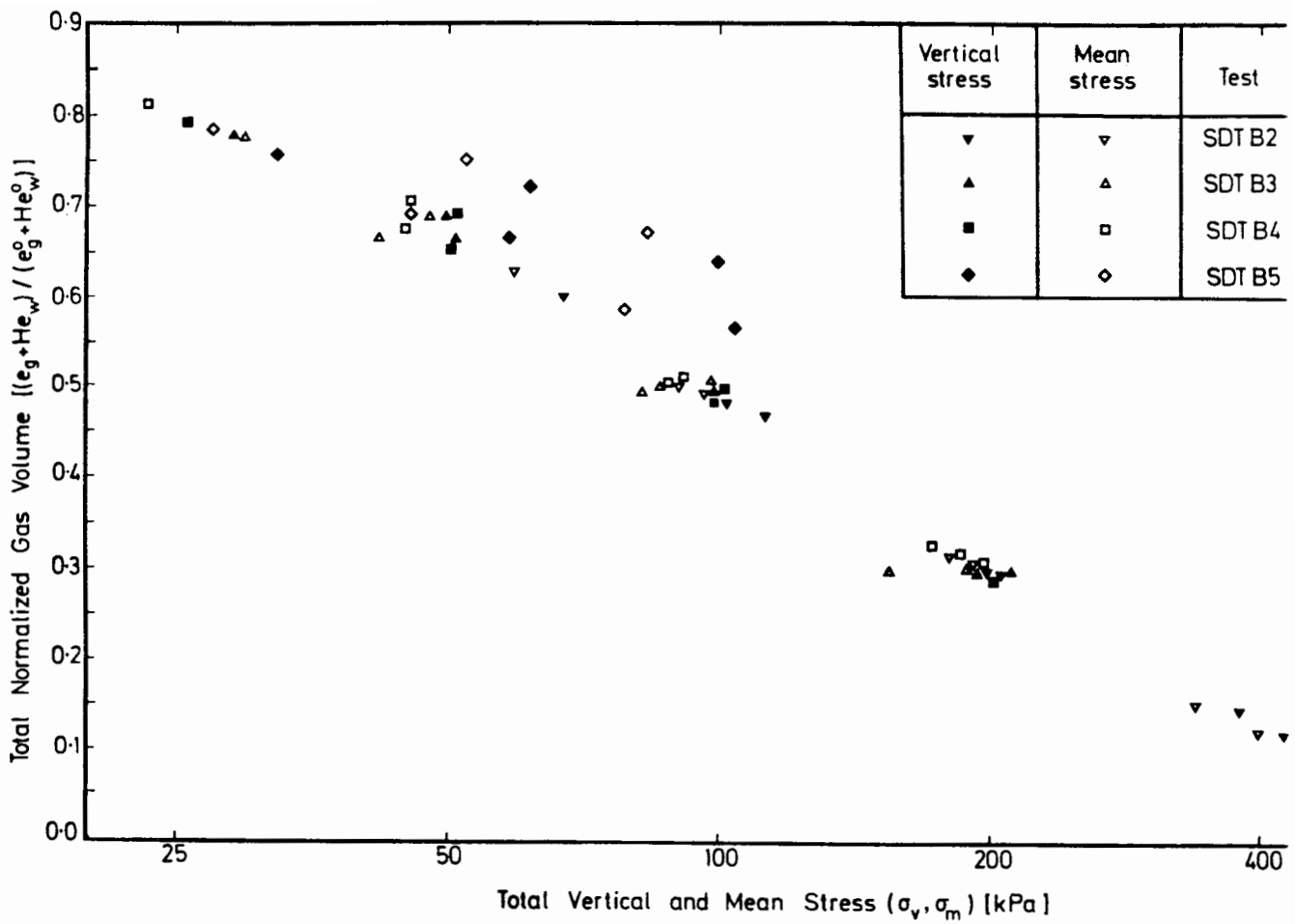

Figure 4.24 Total normalized gas volume versus total stress for test series B

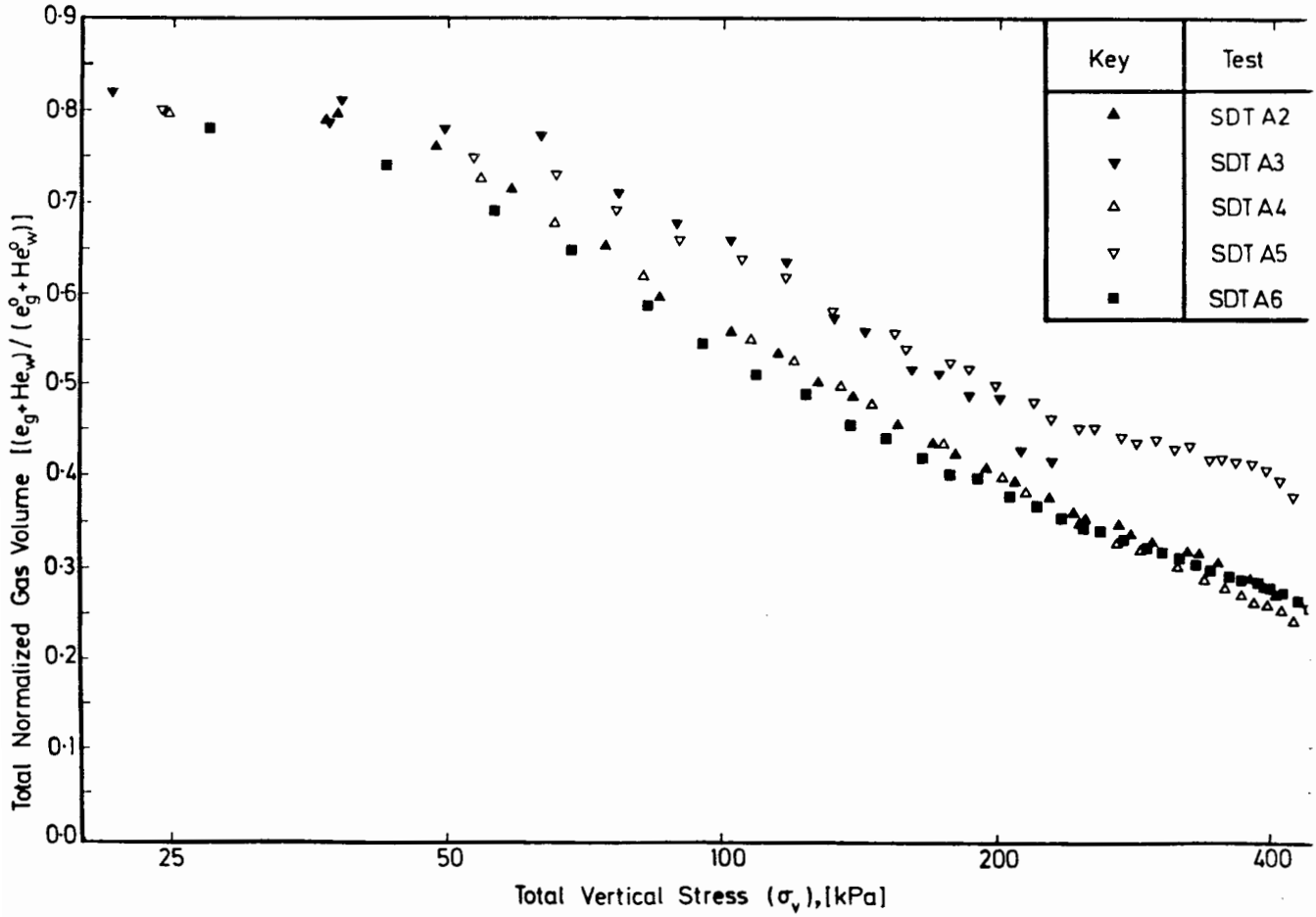

Figure 4.25 Total normalized gas volume versus total stress for test series A

where σ can be the mean or vertical total stress, u_a is the atmospheric back pressure and α is the stress transfer coefficient. The resulting theoretical behaviour is superimposed onto the results of test series B in Figure 4.26, and onto the results of test Series A in Figure 4.27. It can be seen that for test series B (sudden application of total stress), a value of $\alpha = 1.0$ gives a good representation of the resulting change in gas volume. For test series A (stress increased linearly with time), α has to range from 0.4 to 0.7 to cover the volume change behaviour. For soils of higher gas content, however, $\alpha = 0.7$ gives the best representation of the data.

4.2.7 Evaluation of soil permeability

For the gassy soil samples in this series of tests, it was found that it is not possible to obtain any reliable measurements of pore water pressure on the undrained face. For this reason, it is impossible to produce a direct measurement of the soil permeability as was the case for test series A. Therefore for this series of tests, the soil permeability can only be found indirectly from the coefficient of consolidation and the coefficient of volume change.

The coefficient of consolidation is evaluated by considering the time at which 50% of the total drained settlement has taken place. As there is an initial undrained settlement, this time value, t_{50}, has been defined as the time when 50% of the total water loss has taken place. The value of the coefficient of consolidation can then be evaluated from (Scott, 1974)

$$c_v = 0.196\ h_{50}^2/t_{50} \qquad (4.37)$$

where h_{50} is the height of the sample at time t_{50}. The evaluated values of c_v for all stages of tests SDTB1 to SDTB6 are presented earlier in Table 4.1 and are plotted against the average vertical consolidation pressure in Figure 4.28. This figure illustrates that there is no apparent consistent variation of the coefficient of consolidation with gas content.

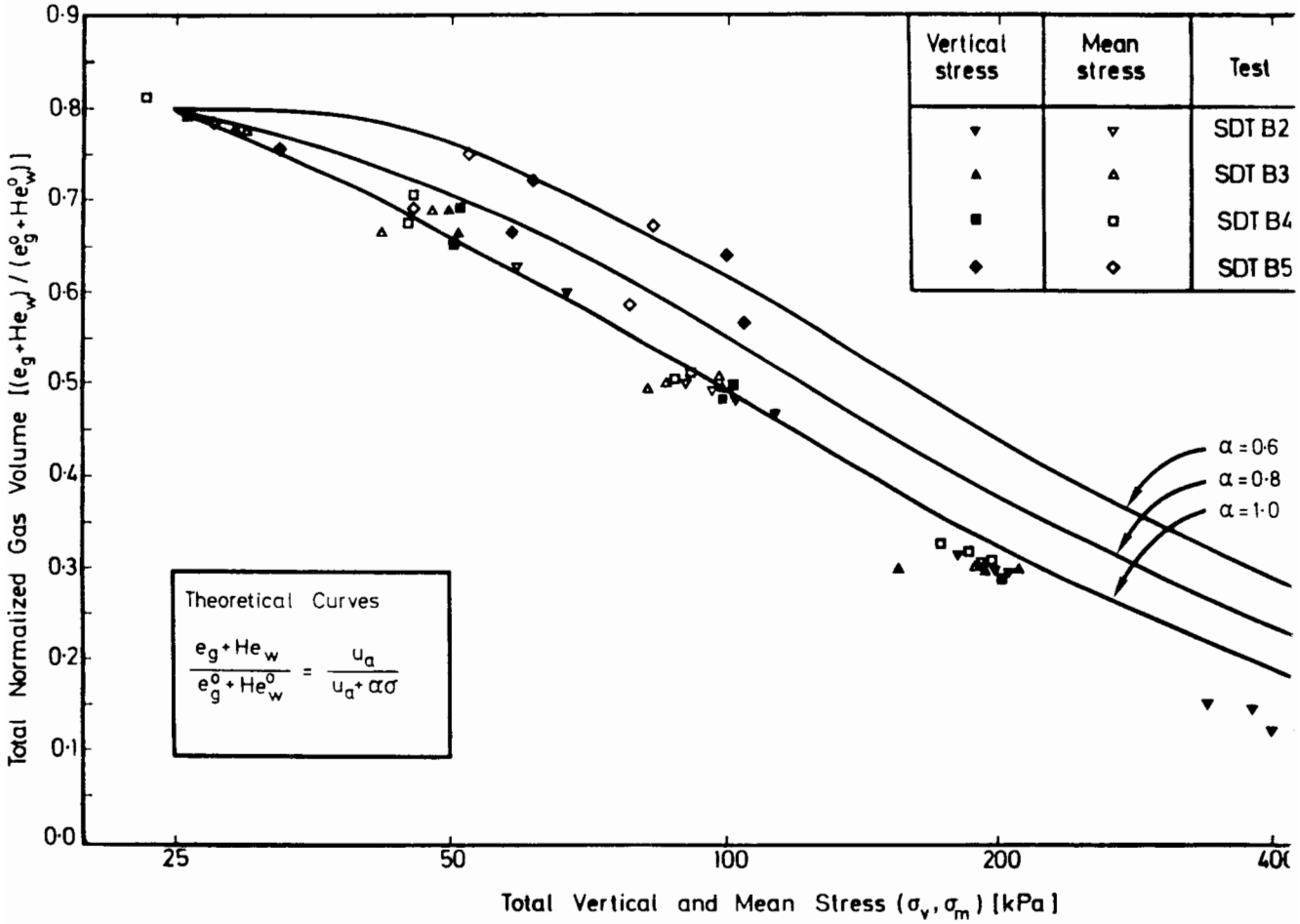

Figure 4.26 Theoretical versus experimental normalized gas volume for test series B

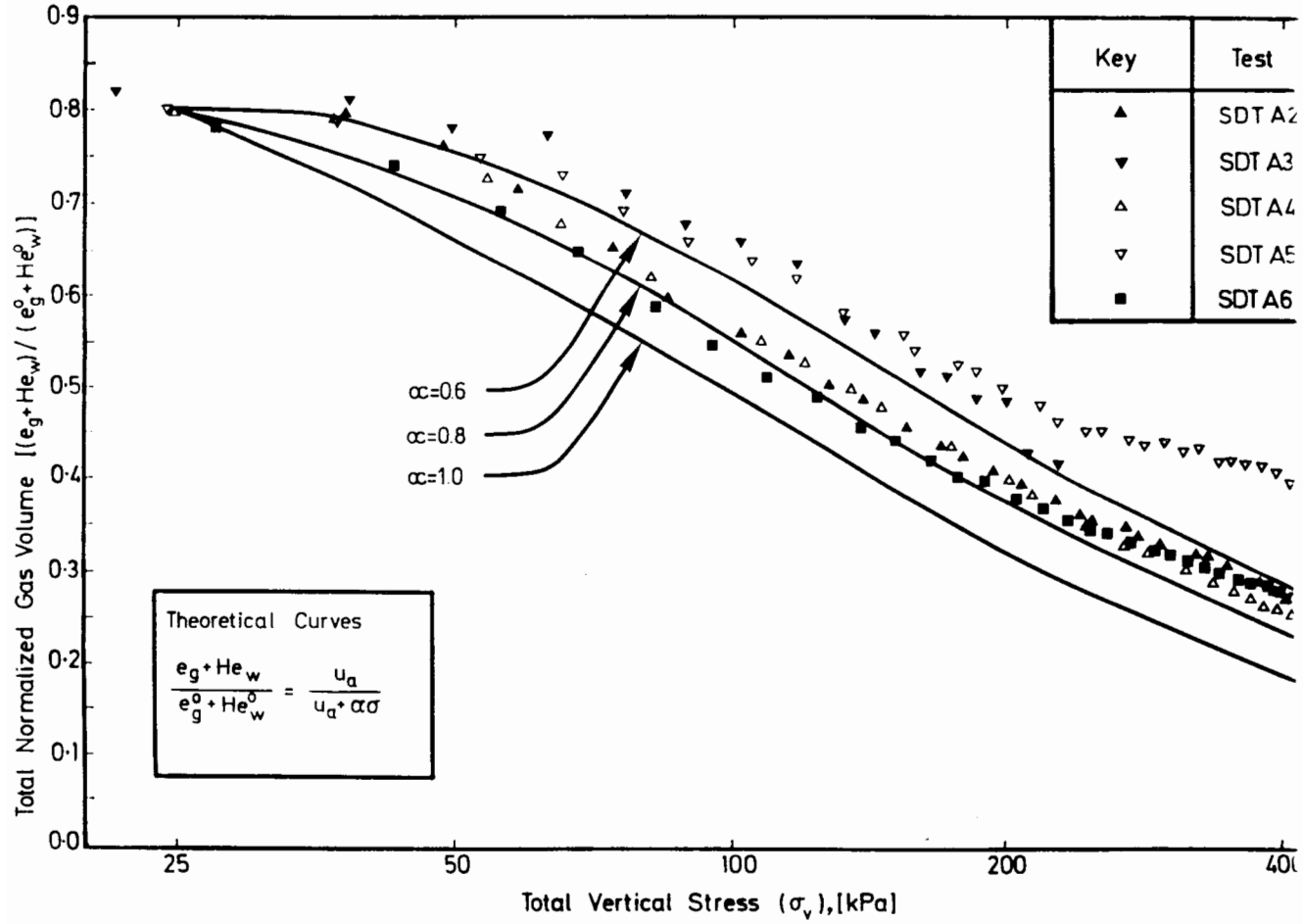

Figure 4.27 Theoretical versus experimental normalized gas volume for test series

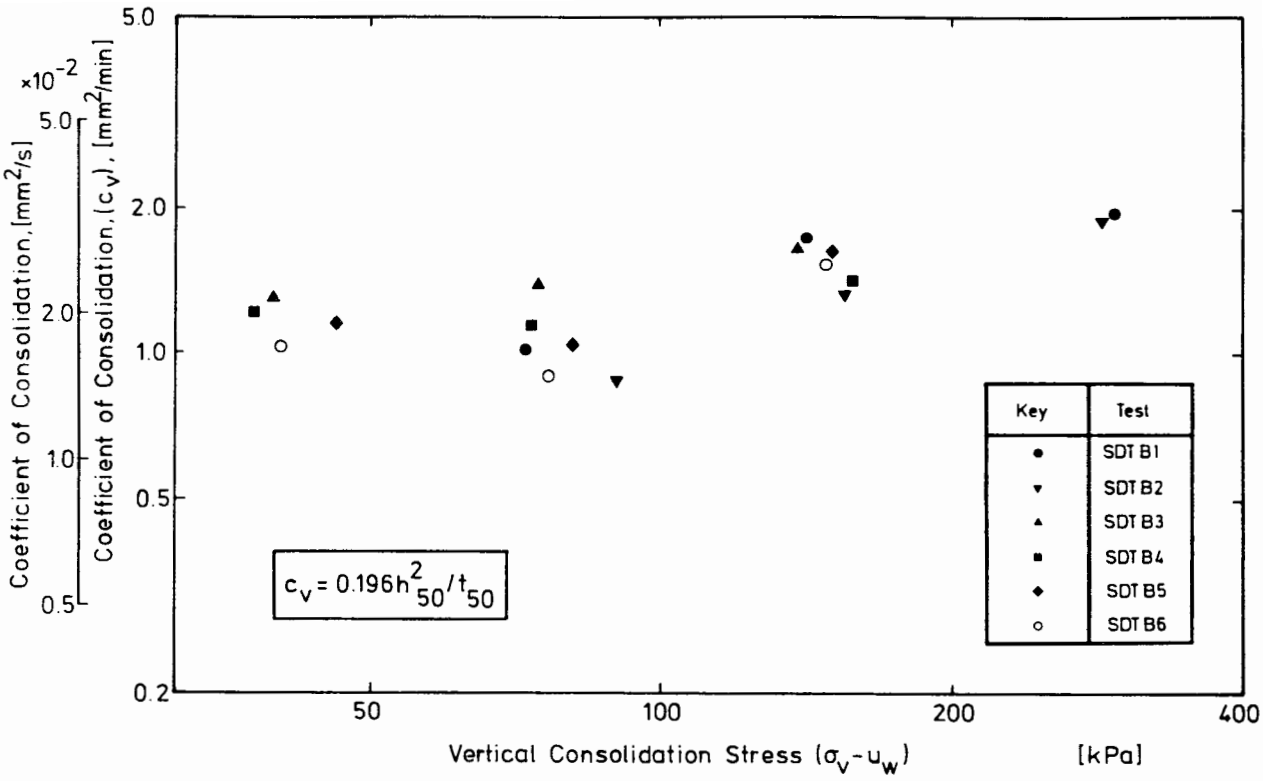

Figure 4.28 Coefficient of consolidation versus consolidation stress for test series

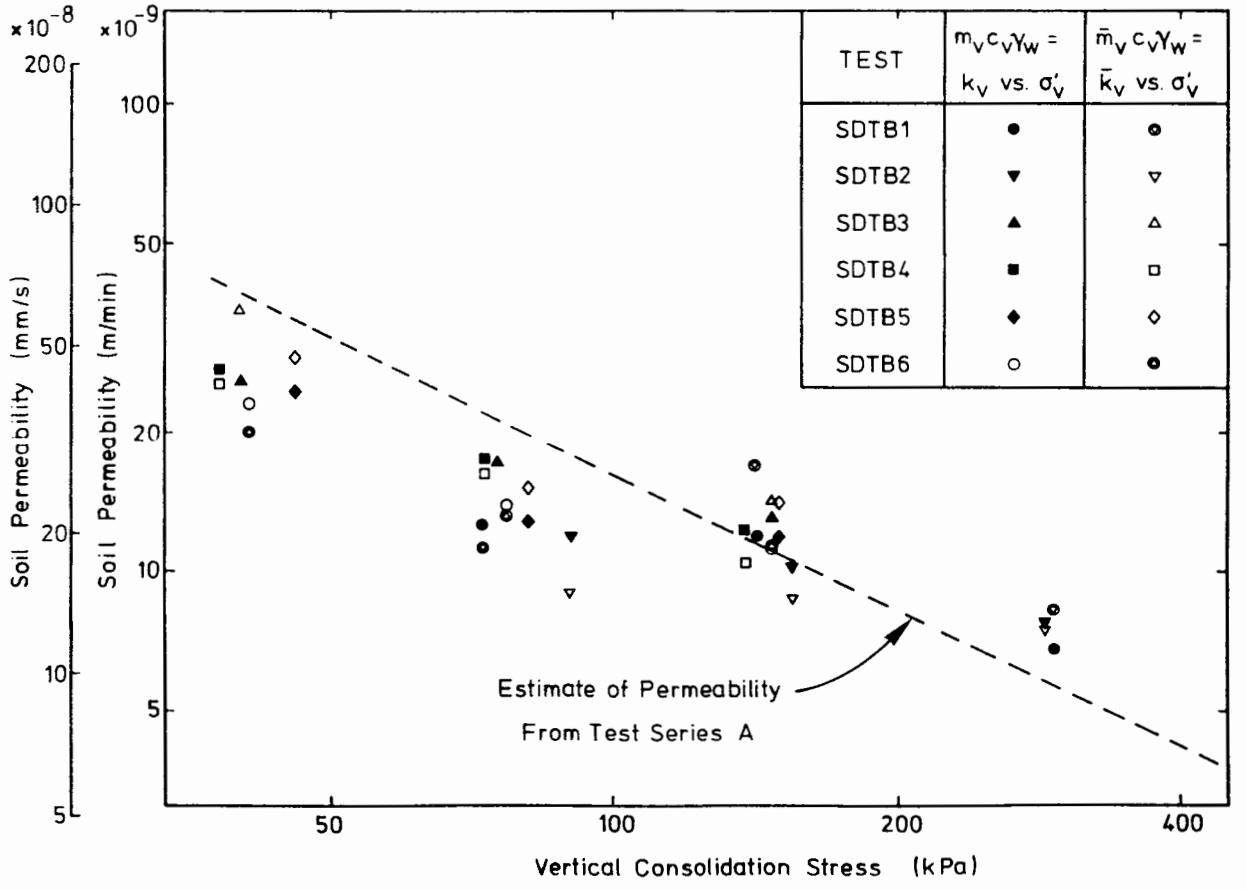

Figure 4.29 Soil permeability versus consolidation stress for test series B

The next stage is to evaluate the coefficient of volume change. For a one-dimensional consolidation test, this coefficient can be evaluated in the vertical direction from

$$m_v = \frac{1}{1 + e_t} \frac{\Delta e_w}{\Delta \sigma'_v} \tag{4.38}$$

where m_v is the vertical coefficient of volume change, e_t is the total void ratio, $\Delta\sigma'_v$ is the change in vertical consolidation stress and Δe_w is the change in water void ratio over the increment of consolidation. The soil permeability can then be found from

$$k_v = c_v \, m_v \, \gamma_w \tag{4.39}$$

Values of k_v and m_v for each increment of consolidation are presented in Table 4.1. Comparisons using the non-linear large strain numerical model indicated that the evaluated soil permeability should be plotted against the average value of the initial and final vertical consolidation stresses to produce a point on the actual soil permeability versus consolidation stress line. Accordingly, Figure 4.29 presents the calculated soil permeability plotted against the average vertical consolidation stress.

In addition, due to the presence of two horizontal stress transducers, it is possible to evaluate the changes in mean stress over an increment of consolidation. Therefore, it is then possible to evaluate the mean coefficient of volume change, m_m, as

$$m_m = \frac{1}{1 + e_t} \frac{\Delta e_w}{\Delta \sigma'_m} \tag{4.40}$$

where $\Delta\sigma'_m$ is the change in mean consolidation stress. From this equation, it is possible to obtain an alternative value of the vertical soil permeability from

$$\bar{k}_v = c_v \, \bar{m}_v \, \gamma_w = \frac{c_v \, \gamma_w}{1+e_t} \frac{\Delta e_w}{\Delta \sigma'_v} = \frac{c_v \, \gamma_w}{1+e_t} \frac{\Delta e_w}{\Delta \sigma'_m} \left(\frac{1+2K_o}{3}\right) = c_v \, m_m \, \gamma_w \left(\frac{1+2K_o}{3}\right) \tag{4.41}$$

The values of soil permeability calculated using a value of K_o of 0.75, are presented in Table 4.1 and are plotted against the average vertical consolidation stress in Figure 4.29. Once again, this figure illustrates that there is no apparent variation of permeability with gas content, although the great deal of scatter of these results may obscure any trend that does exist.

When the above results are compared with those of test series A (as presented in Figure 4.9), the permeability values of test series B are lower than for test series A. Figure 4.10 illustrates, however, that for test series A the actual permeabilities would have been lower if the test had been carried out at a slower rate, thereby reducing the inaccuracies in the calculation of permeability. An estimate of the permeability behaviour of test series A is then made with the help of a large strain numerical consolidation model. The estimate of the permeability relationship for test series A is then superimposed onto Figure 4.29 to give a fair comparison with the results of test series B.

4.4 Summary

The main body of this chapter describes the results of two series of consolidation tests. The first, test series A, applies the total stress in small equal increments so that drainage and consolidation can occur as the load is applied. The second, test series B, applies the load in three daily increments, each followed by dissipation of pore water pressures to atmospheric back pressure. The results of test series A clearly show that there is no unique relationship between the vertical consolidation stress and the total void ratio for soils of varying gas content. When the vertical consolidation stress is plotted against the matrix void ratio, however, a unique line is perceived.

To observe the behaviour of the gas, the gas pressure was calculated using Boyle's and Henry's laws from the volume change behaviour of the gas during loading and unloading. Under loading conditions, the gas pressure appears to be dependent--almost linearly dependent--on the total vertical stress. The same appears true for the transient period when there is no change in total stress. When the soil is unloaded, however, there is no change in gas volume or pressure until the total stress has fallen well below that of the estimated gas pressure. Results of soil permeability were produced which illustrated a variation with vertical consolidation pressure, but no apparent variation with gas content.

Test series B illustrates once again that the matrix void ratio is dependent on the value of consolidation stress, although for this series of tests, matrix void ratio when plotted against mean consolidation stress produced

a narrower band of data than when plotted against the vertical consolidation stress. Observation of the behaviour of the gas and water phases during the undrained-drained consolidation tests illustrated that under undrained conditions, the only volume change was that due to the compression and dissolution of the gas. This was expected, but the fact that the pore water pressure increment was larger than the total stress increment was not.

During drained conditions it was found that there was no significant change in gas volume, the drained settlement being produced almost exclusively by the loss of pore water from the sample. A method was then used to normalize the gas volume changes during the consolidation tests by dividing by the equivalent initial gas volume at atmospheric pressure. It was found that there was a definite relationship between the total stress and the normalized gas volume, yet it was not clear whether this should be the mean or vertical total stress. This method was also applied to the results of test series A to produce again a normalized gas volume versus total vertical stress plot. These results did not produce such a unique behaviour as series B.

To compare the experimental results with the empirical expression for gas pressure, values of $u_g = \alpha\sigma$ were superimposed on these plots for various values of the stress transfer coefficient, α, with the additional assumption that the gas pressure was equal to the total stress at 25 kPa. (This being the average initial stress for all tests.) It can be seen that even though the empirical expression for gas pressure is very simple, the resulting comparison is very good. In general, the results of test series B could be represented by $\alpha = 1.0$ and test series A by $\alpha = 0.7$.

Finally, the soil permeability results were evaluated for test series B by first evaluating the coefficient of consolidation and then the coefficient of volume change. The results produced a great deal of scatter, but compared very well with the adjusted values of test series A. Again there appeared to be no variation of soil permeability with gas content.

CHAPTER 5

ONE-DIMENSIONAL NUMERICAL MODELLING

CHAPTER 5

ONE-DIMENSIONAL NUMERICAL MODELLING

5.1 Introduction

The next stage in the analysis of the consolidation behaviour of gassy soil is to simulate the results of the test series A and B. The approach used at this stage was to begin with the simplest analysis, bringing in extra complexities only when necessary. Following this approach, the first step was to simulate the consolidation behaviour of a fully saturated soil.

5.2 Numerical Modelling of Test Series A

5.2.1 Modelling of test SDTA1

In order to model the consolidation behaviour of a saturated soil, the one-dimensional consolidation equation was used--as developed by Terzaghi (1944) and presented in equation 1.5. The derivation of this equation is based on the conservation of the mass of water flowing through an element of saturated soil. This derivation is described in Note 5.1 at the end of this chapter. This consolidation equation was approximated utilizing the Galerkin finite element formulation with simple two-noded linear finite elements. The formulation was then converted to FORTRAN code and written on a VAX 11/780 computer. The code was named UNIFLOW as there is only one degree of freedom, u_w, in this model.

UNIFLOW is a non-linear model as both soil permeability and water void ratio are input as non-linear functions of the vertical consolidation stress. The constitutive relationships chosen for these two soil parameters are presented in Figures 5.1 and 5.2 for the logarithm of the permeability and the matrix void ratio respectively, versus the logarithm of the vertical consolidation stress. In addition to these non-linearities, it soon became clear that due to the large vertical deformations that take place over such a large stress range (50 to 400 kPa), it is necessary for this test to update the size of the finite element mesh at the end of each time step such that each finite element always contains the same mass of solid particles.

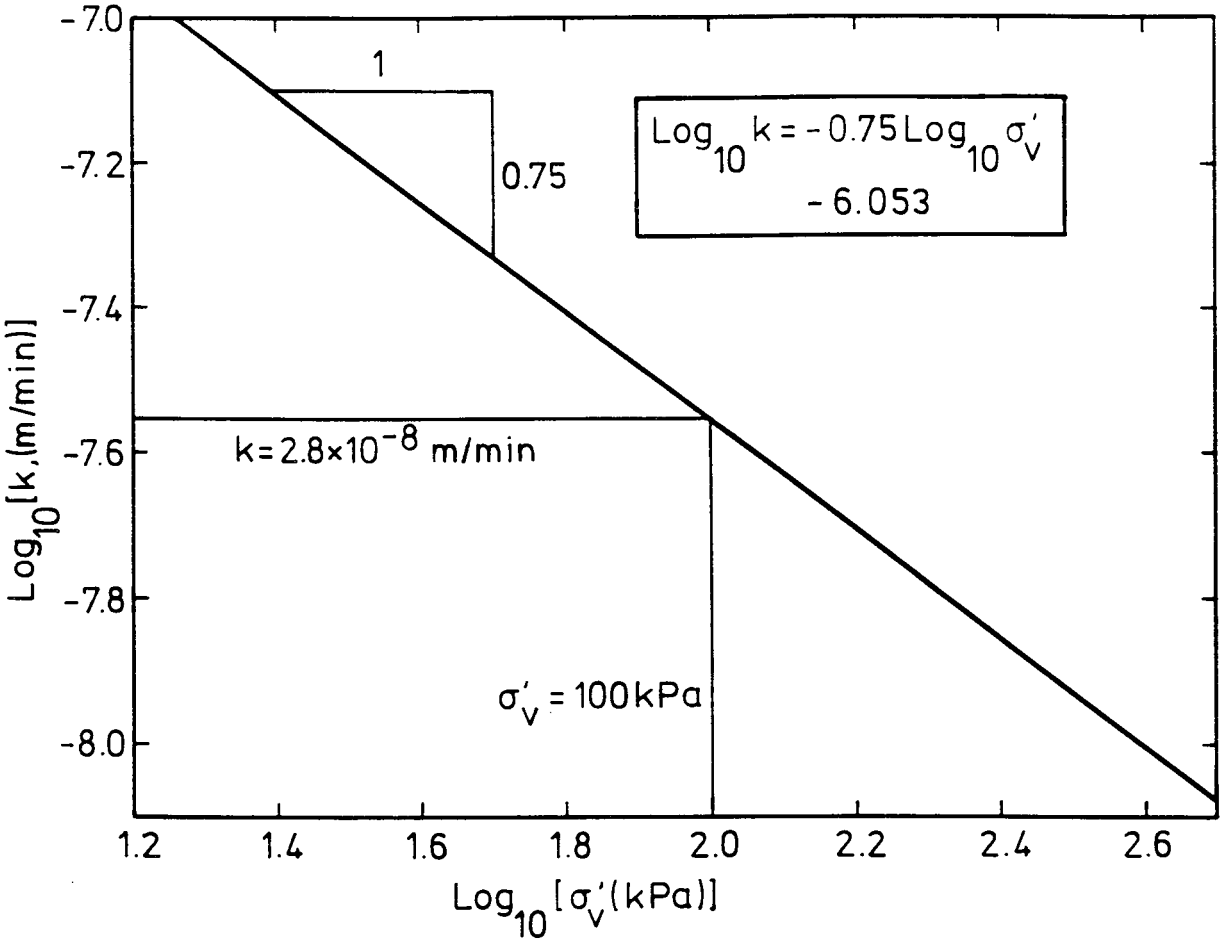

Figure 5.1 Typical permeability/consolidation stress relationship used by UNIFLOW

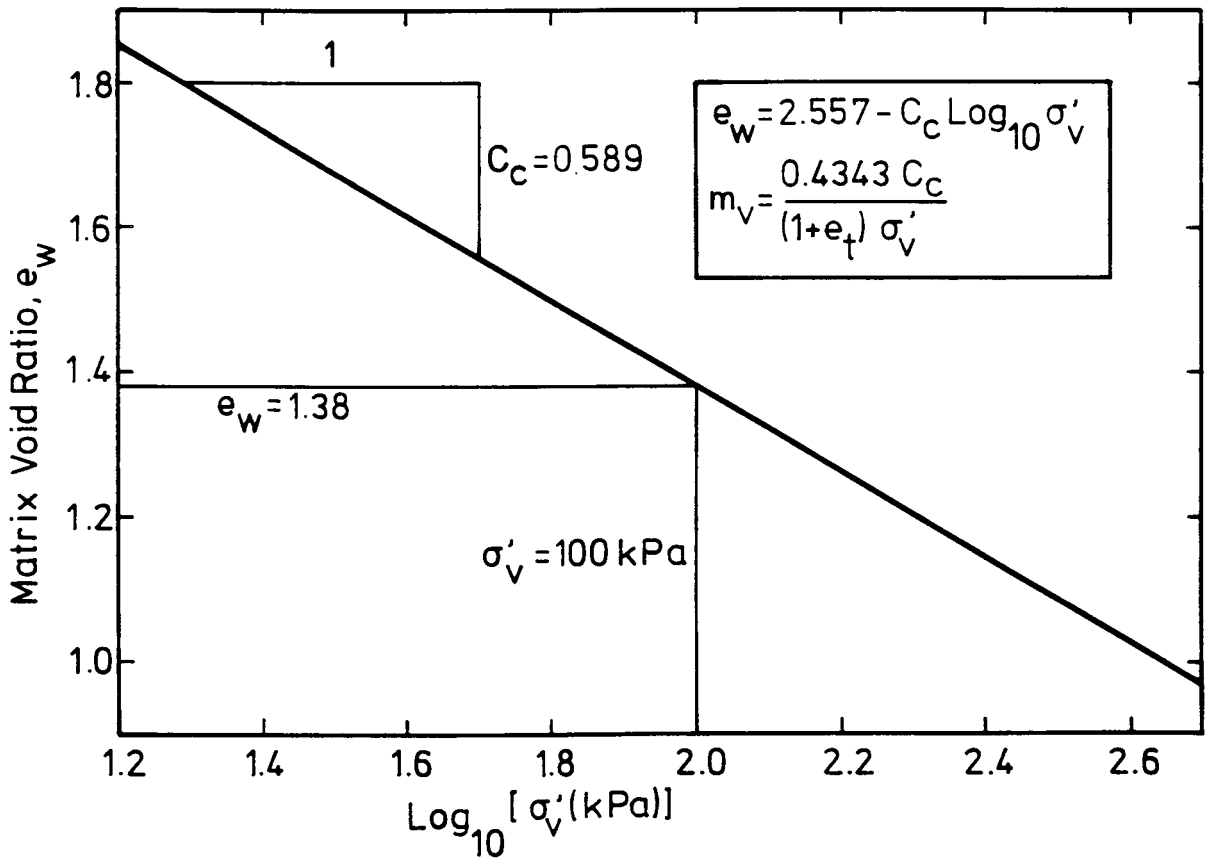

Figure 5.2 Typical matrix void ratio/consolidation stress relationship used by UNIFLOW

Using both a deforming element mesh (which takes into account the large strain behaviour of the soil sample) and a non-deforming mesh (which is appropriate only for small strain conditions) with all other soil parameters constant, UNIFLOW was used to simulate the one-dimensional consolidation behaviour of a saturated soil subjected to a linear increase of total stress. The resulting undrained face pore water pressure response and soil settlement behaviour for both large strain and small strain assumptions are presented in Figure 5.3. It can be seen from this figure that for these soil properties, there is a significant difference between the pore water pressure and settlement response with time. The pore water pressure on the undrained face is lower for the deforming mesh as--due to the reduction in thickness of the sample--the drainage path will be reduced causing a more rapid drainage of the soil. In addition, the deformable mesh will always produce a lower settlement response because of the reduction in the thickness of the sample. For each increment of time, the increment of settlement is found by multiplying the calculated strain by the sample thickness. Therefore, as the non-deforming mesh always assumes that the thickness is the same as the initial thickness, the overall settlement will be larger than for the deforming mesh. As a result of the above numerical experiment, it was made clear that it was necessary to use a deformable mesh to simulate the consolidation over the stress range encountered in test SDTA1.

In order to simulate the saturated soil behaviour of test SDTA1, it was necessary to adjust the soil permeability-effective stress relationship so as to produce a good match of the pore water pressure response on the undrained face. Accordingly, it must be noted that Figure 5.1 presents an adjusted permeability effective stress relationship to produce an adequate simulation of the pore water pressure behaviour, whereas Figure 5.2 presents the relationship that was obtained from the experimental series of tests. Figure 5.4 compares the permeability-effective stress relationship that was used in the simulation of test SDTA1 with the permeability relationships that were obtained from direct measurement. Unfortunately, these do not compare as well as one would like. The required permeability is higher than the direct measurement of permeability. The reason for this behaviour is not entirely clear. One possible explanation

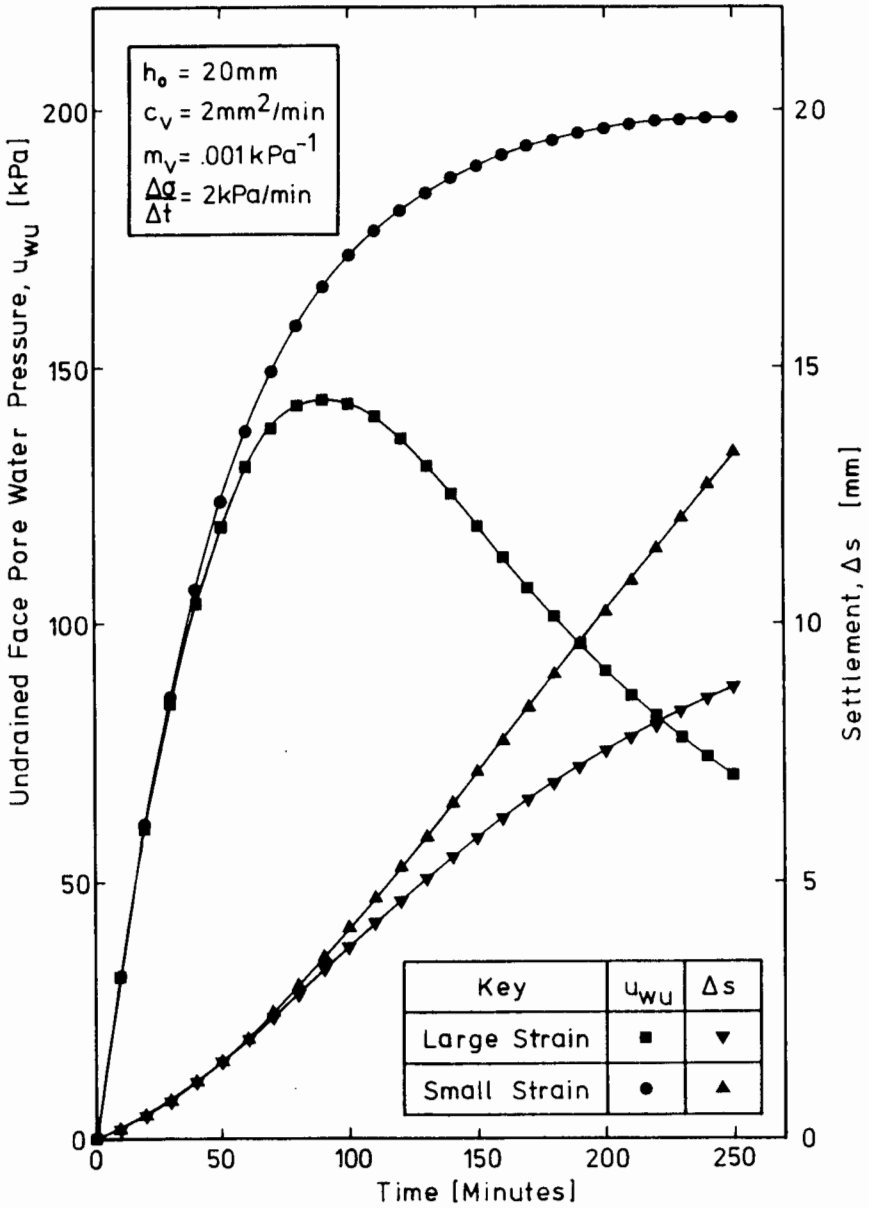

Figure 5.3 The effect of large and small strain assumptions on the consolidation behaviour of a saturated soil

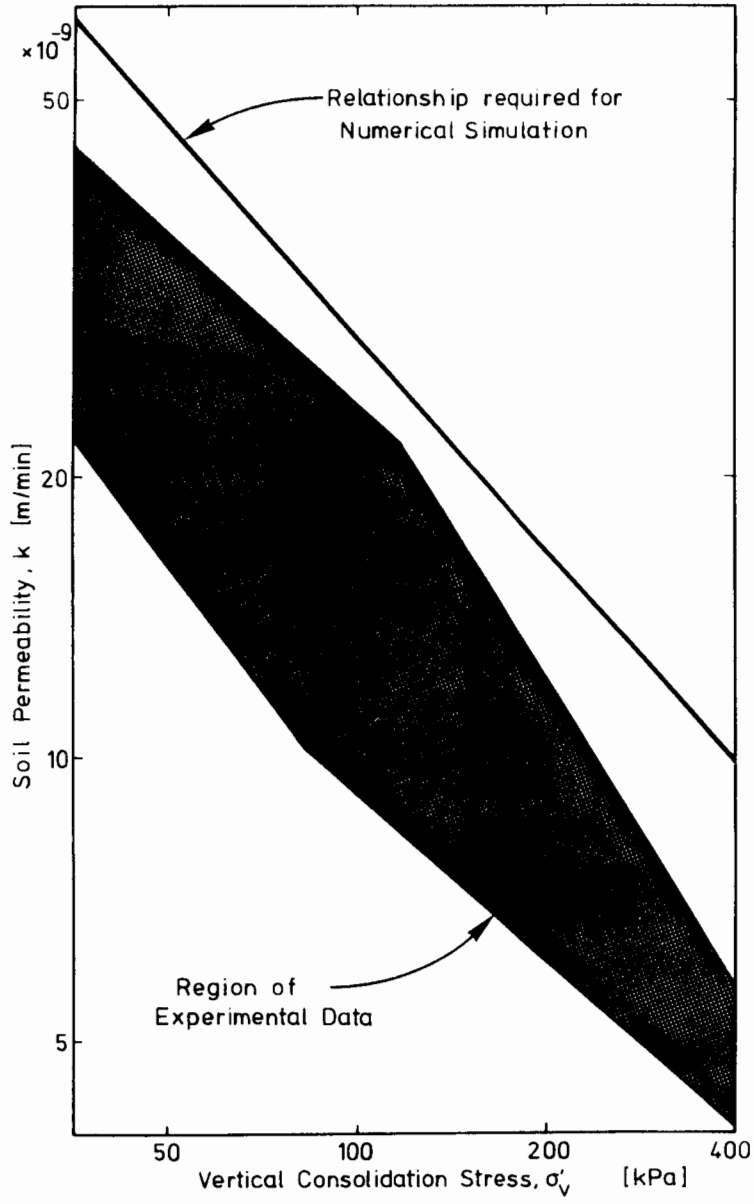

Figure 5.4 The permeability/consolidation stress relationship required for the simulation of test SDTA1

is that it could be due to the presence of air in the system causing slight compressibility of the pore fluid. This would produce a lower value of pore water pressure than that expected, and thus a higher permeability would be required to model it. The most probable cause, however, is the fact that the friction between the soil and the cell wall will prevent all the total stress being applied to the soil. Again, this will produce a lower pore water pressure response than that expected.

Nevertheless, using the soil permeability-effective stress relationship as defined in Figure 5.1 and the void ratio-effective stress relationship as defined in Figure 5.2, a good match of the pore water pressure on the undrained face was produced as illustrated in Figure 5.5. The characteristic initial test rise, peaking at a maximum followed by a slow decline in pore water pressure, is due to a reduction in the thickness of the sample (see Figure 5.3) rather than to any material non-linear behaviour. It must be noted that for all remaining simulations of the tests in series A, the same soil permeability and soil matrix void ratio relationships were used and no curves were "matched". The resulting comparison of the decrease in void ratio for SDTA1 is presented in Figure 5.6. For this particular test, the sample was fully saturated. Therefore there was no response in the change in gas volume, as can be seen by the gas void ratio change lying along the time axis.

5.2.2 Modelling of tests SDTA2 to SDTA7

In order to simulate the consolidation behaviour of a gassy soil, test SDTA6 was chosen to be modelled initially, as this was the test with the largest initial gas porosity (n_{go}=0.091). The pore water pressure response measured on the undrained face and the components of void ratio versus time were then simulated using a variety of theoretical models.

The first attempt at modelling the pore water pressure response incorporated the hybrid approach as used by Nageswaran (1983). It was assumed that the pore water and gas could be combined to produce a single homogeneous compressible fluid. At the same time, it was assumed that the water void ratio was solely a function of the vertical consolidation stress. The derivation of

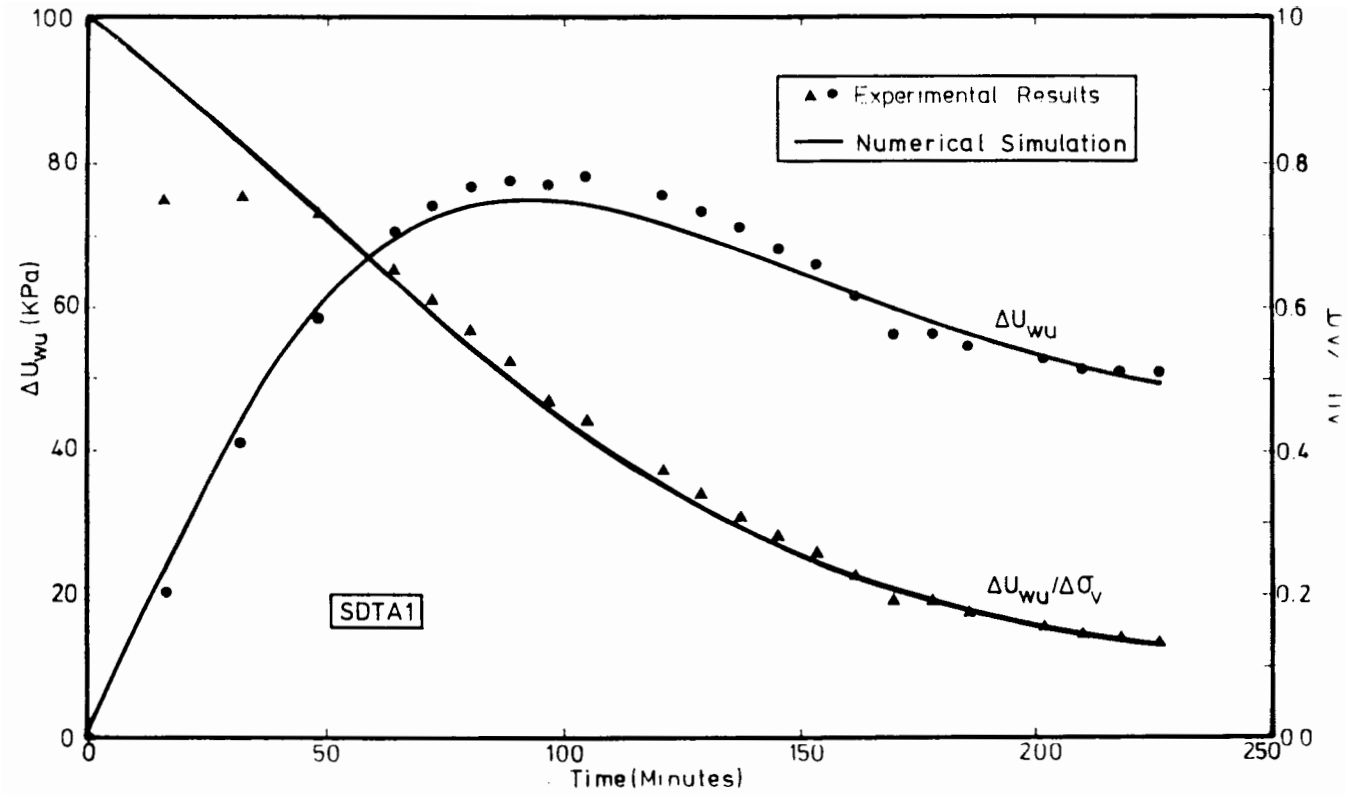

Figure 5.5 Numerical simulation of undrained face pore water pressure for test SDTA1

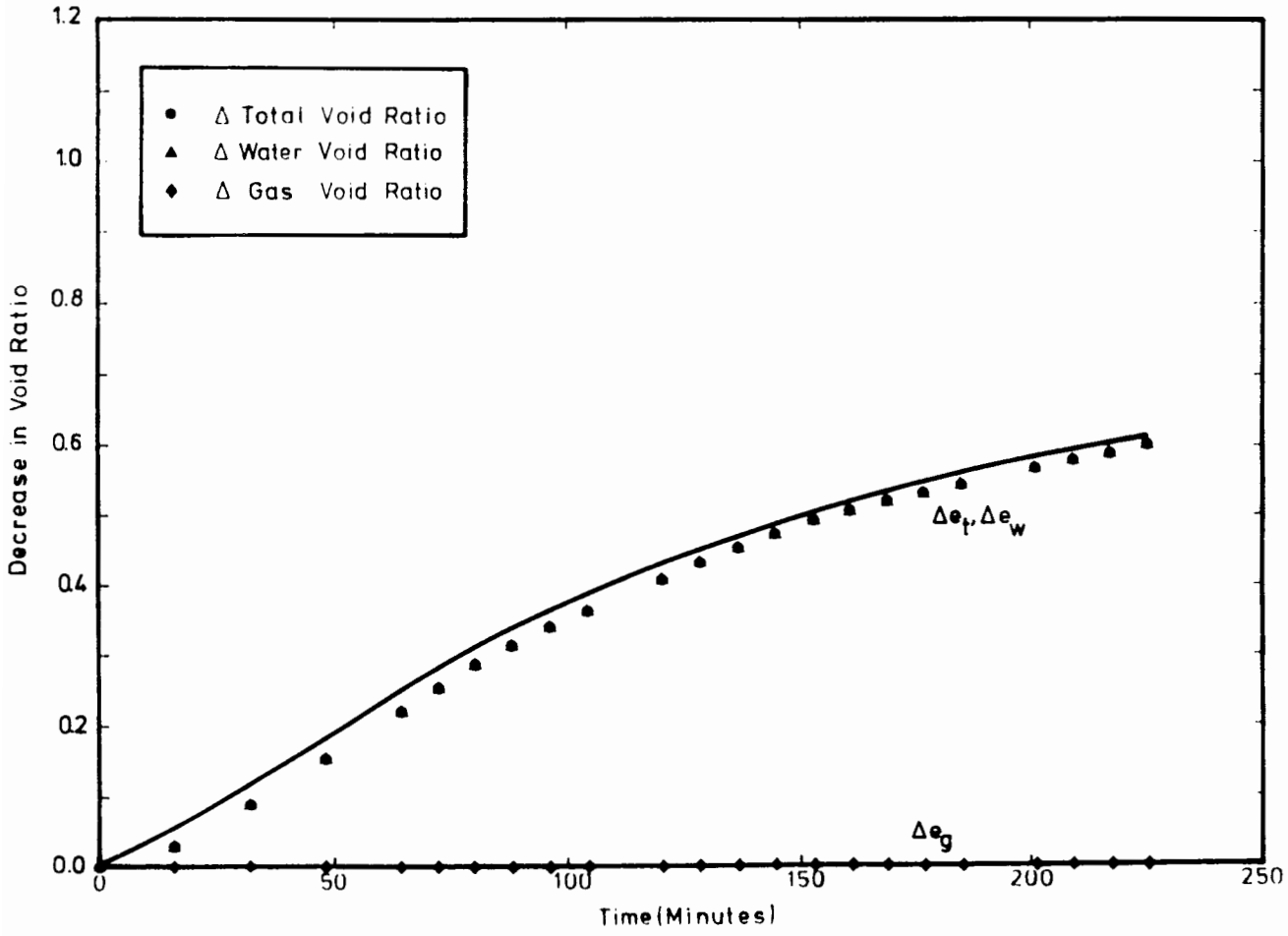

Figure 5.6 Numerical simulation of void ratio change for test SDTA1

the equation governing this process is presented in Note 5.2 at the end of the chapter. The same constitutive relationships of water void ratio and soil permeability were used as for the saturated model. Assuming that the gas pressure was equal to the pore water pressure, the resulting pore water pressure response on the undrained face and the decrease in the components of void ratio with time are presented in Figures 5.7 and 5.8 respectively. It can be seen from these figures that the compressible fluid theory, with $u_g = u_w$, is not able to simulate adequately the observed consolidation behaviour of a gassy soil under laboratory conditions.

After giving much thought to the physical process and to photographic observations of Nageswaran (1983)--[see Plate 2.1]--it was realized that on undrained compression of a gassy soil sample, the saturated soil matrix simply changes shape, without any change in volume, to accommodate the volume change of the gas voids. Therefore, it is assumed that the volume change of the saturated soil matrix only occurs under drained conditions when there is a change in consolidation stress. The governing consolidation equation, based on such compressible gas void theory, is derived for this case in Note 5.3.

The surprising result of this derivation is that the equation becomes almost identical to that of the consolidation equation of a saturated soil. The only effect of the gas content on the pore water pressure response is to increase the thickness of the sample, which causes a higher drainage path length. The total settlement is evaluated from the sum of the settlement caused by the drainage of water from the sample and that caused by the compression and dissolution of the free gas where the gas pressure is equal to the product of the stress transfer coefficient, α, and the vertical total stress σ_v.

The first simulation was made with a value of α of 0.7 (taken from the experimental results) and with the permeability-consolidation stress relationship used in the simulation of test SDTA1. The results of this simulation were immediately encouraging. The simulated pore water pressure on the undrained face compared favourably with the measured result, with no further change in any governing parameters. This comparison is presented in Figure 5.9 where the simulation of the undrained face pore water pressure response is

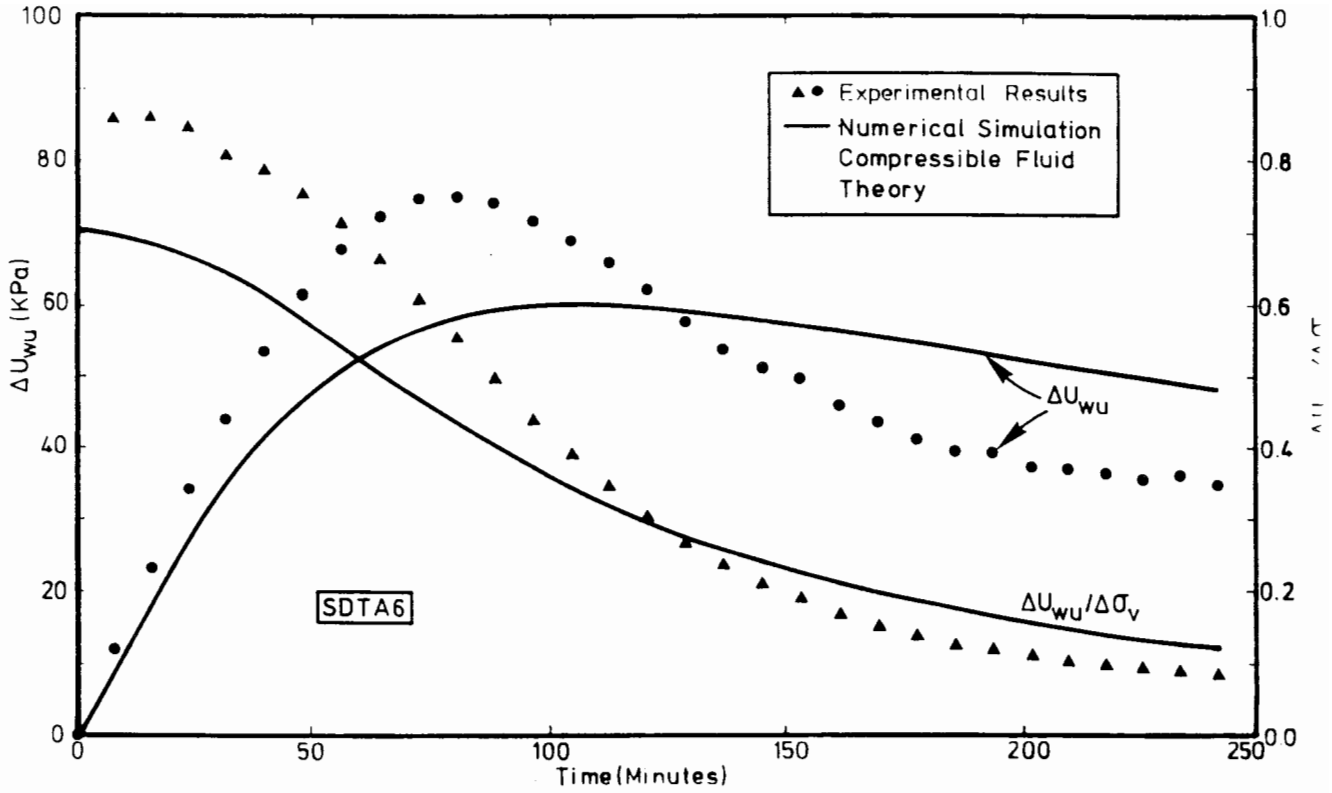

Figure 5.7 Numerical simulation of undrained face pore water pressure using compressible fluid theory for test SDTA6

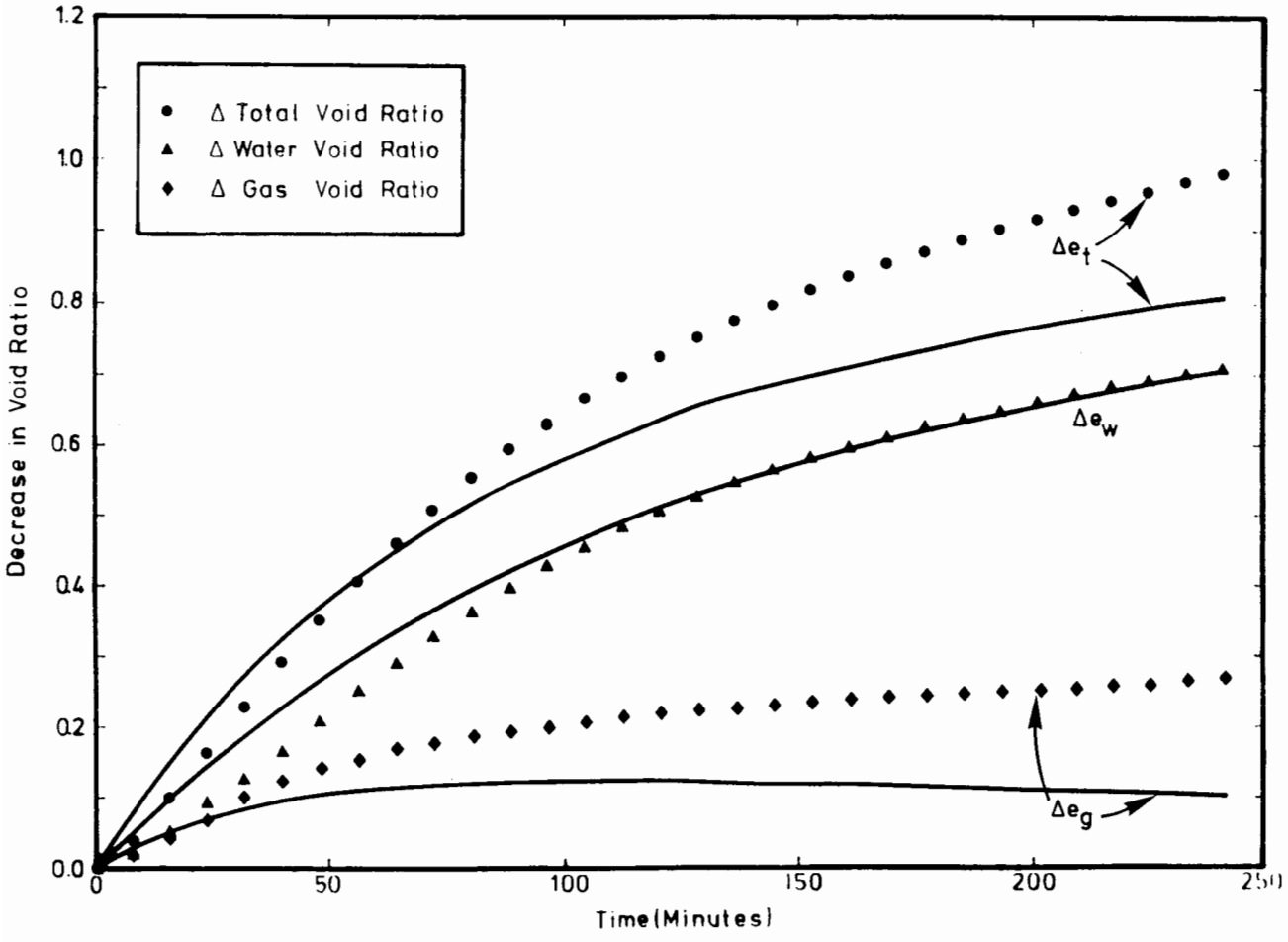

Figure 5.8 Numerical simulation of void ratio change using compressible fluid theory for test SDTA6

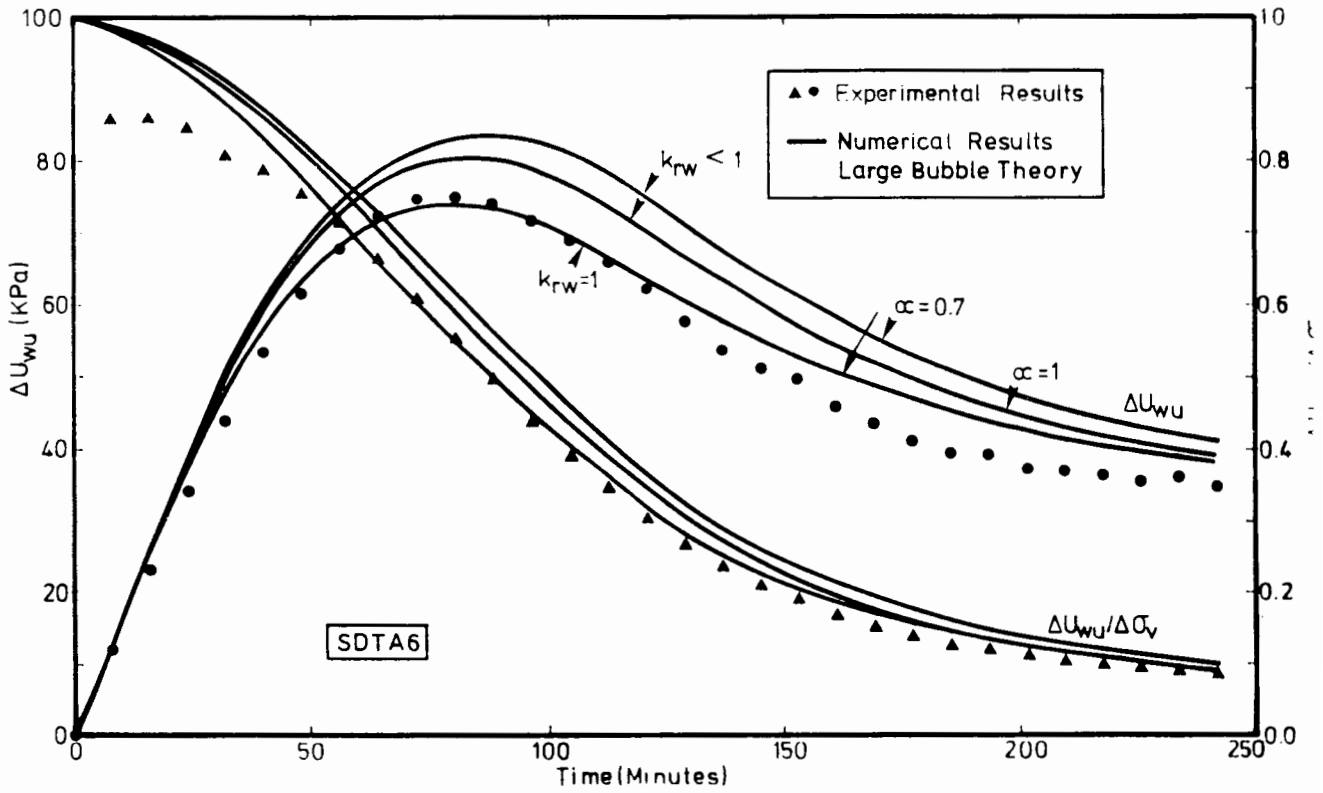

Figure 5.9 Numerical simulation of undrained face pore water pressure using compressible gas void theory for test SDTA6

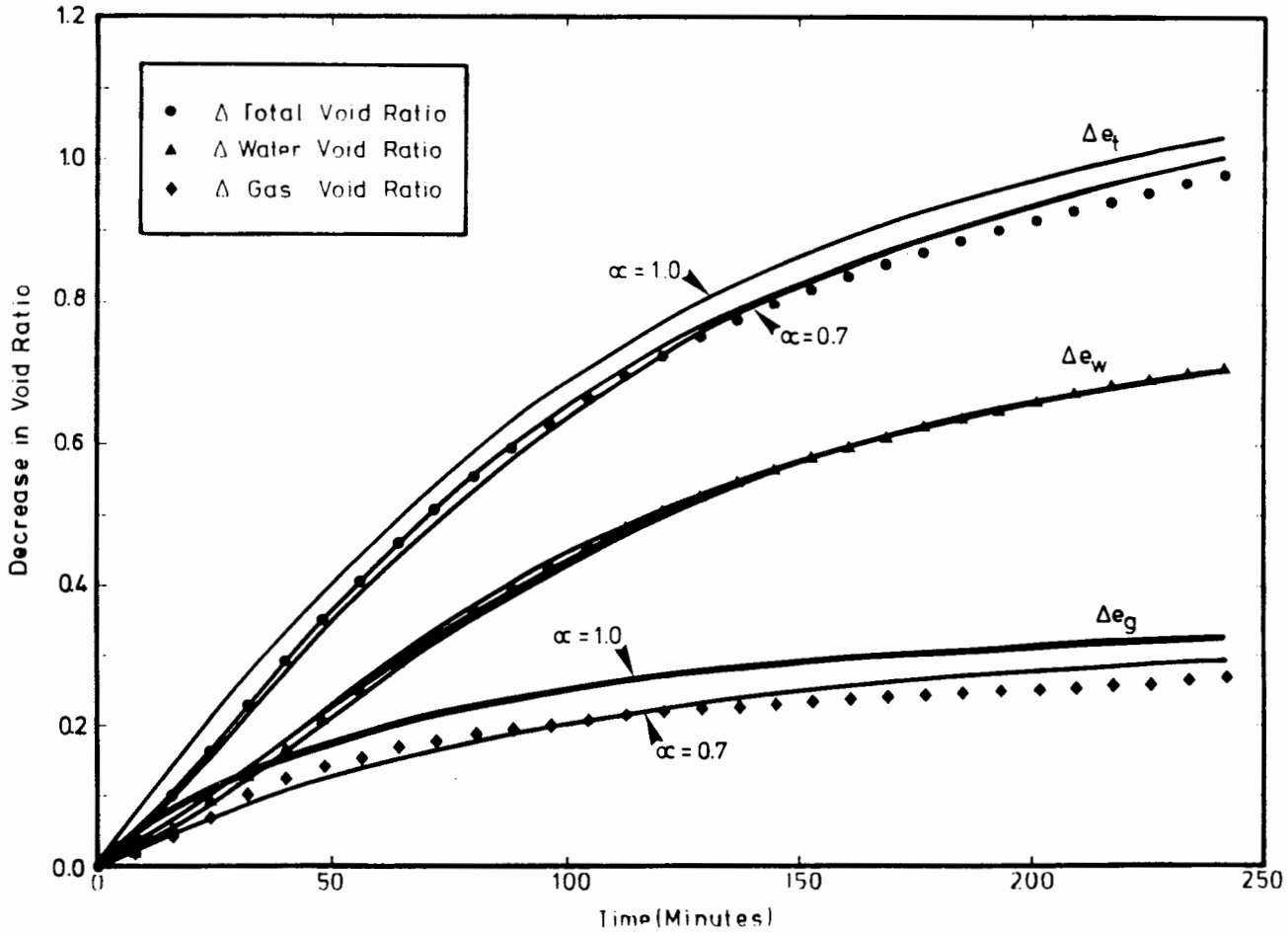

Figure 5.10 Numerical simulation of void ratio change using compressible gas void theory for test SDTA6

presented as the lowest line of the upper set of lines. Also presented in this figure is the undrained face pore water pressure normalized with respect to the value of the total vertical stress at the same time. This simulation is represented again by the lowest line of the lower set of lines in Figure 5.9.

It is well documented, however, that the presence of gas normally reduces the permeability of a soil due to the gas restricting the flow of water (Wycoff and Botset, 1936, Orlob and Radhakrishna, 1958, Brooks and Corey, 1964). For a gassy soil this would not necessarily be the case, as the water flows in the saturated matrix where no gas is present. Nevertheless, the presence of the gas would lower the overall soil permeability, as the water would have to flow around these gas voids which act as impermeable obstructions in the matrix.

Appendix A presents a detailed theoretical development of the effect of a fluid flowing through a porous medium of permeability k, containing a volume fraction n_g, of spheroidal inclusions of permeability k′ and aspect ratio, A_r. For the case of impermeable gas inclusions, there is a reduction in overall permeability which was found to be dependent on both the volume fraction of the gas inclusions and the aspect ratio of the spheroid. The solution was produced in terms of relative permeability, k_{rw}, and can be written as

$$k_{rw} = \frac{k}{k_{sat}} = 1 - n_g/[1-C_o(1-n_g)] \qquad (5.1)$$

where k is the permeability of the gassy soil, k_{sat} of an equivalent fully saturated soil and C_o is a function of the aspect ratio of the gas void. The resulting values of relative permeability for a variety of values of aspect ratio are plotted against the gas fraction in Figure A.4.

This relative permeability function was then programmed into UNIFLOW with the dubious assumption that on consolidation of the soil, all particles moved only in the vertical direction, with the width of a bubble therefore always remaining constant. On the basis of this assumption it was possible to evaluate the aspect ratio of the gas voids from the knowledge of the gas volume fraction

$$A_r = a/c = v_g^o/v_g \qquad (5.2)$$

where A_r is the aspect ratio of the spheroidal void, a is the width and c is the height of the void, and v_g^o is the initial free gas volume when it is assumed

that the void is spherical.

When this relative permeability function was used, however, the resulting pore water pressure response on the undrained face did not give such a good match of the data as when using the saturated permeability, as can be seen by the upper line of Figure 5.9. In fact, there were no simulations at all in which the relative permeability function produced a better result than when using the saturated soil permeability. Although it was disappointing that this theoretical study did not improve the modelling of the experimental results, the fact that the gassy soil appeared to have the same permeability as a saturated soil under the same conditions of consolidation stress compares well with the direct measurement of permeability as presented in Chapter 4. Therefore, for the remainder of the numerical modelling, it was assumed that all soils possessed the same permeability-consolidation stress relationship which was independent of the gas content.

In addition, it was found that increasing the value of the stress transfer coefficient, α, to 1.0 brought the simulated curve closer to the measured pore water pressure. However, when the time dependent behaviour of the components of void ratio were modelled, as illustrated in Figure 5.10, $\alpha = 0.7$ was found to produce a better simulation of the time dependent volume change behaviour.

Based on these simulations, the same parameters were used to model the remainder of the tests in series A. The results of this modelling are presented in Figures 5.11 to 5.16 for tests SDTA2 to SDTA7 respectively. All the simulations (with the exception of the pore water pressure response of test SDTA5) produced very satisfactory comparisons between the results of the numerical model and those of the experimental tests.

5.3 Numerical Modelling of Test Series B

As it was not possible to measure the pore water pressure on the undrained face for this series of tests, it was only possible to compare the settlement behaviour of the sample as a function of time. To illustrate the behaviour of a single increment of total stress applied to a gassy soil sample, UNIFLOW was used to simulate the settlement-time response of test SDTB3 (as it has the

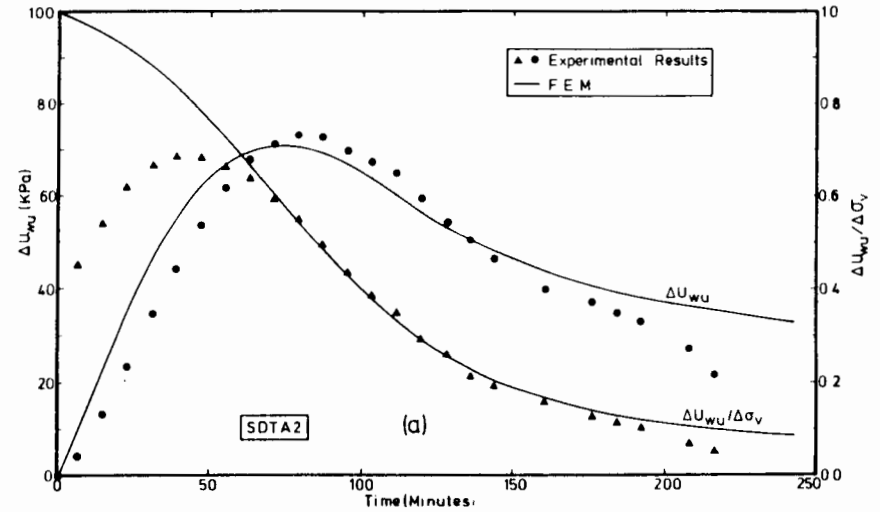

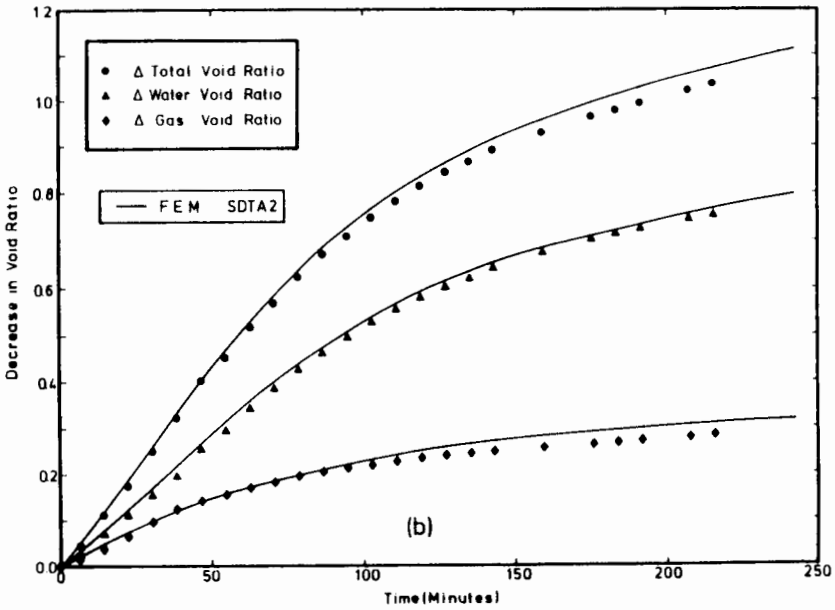

Figure 5.11 Numerical simulation of test SDTA2

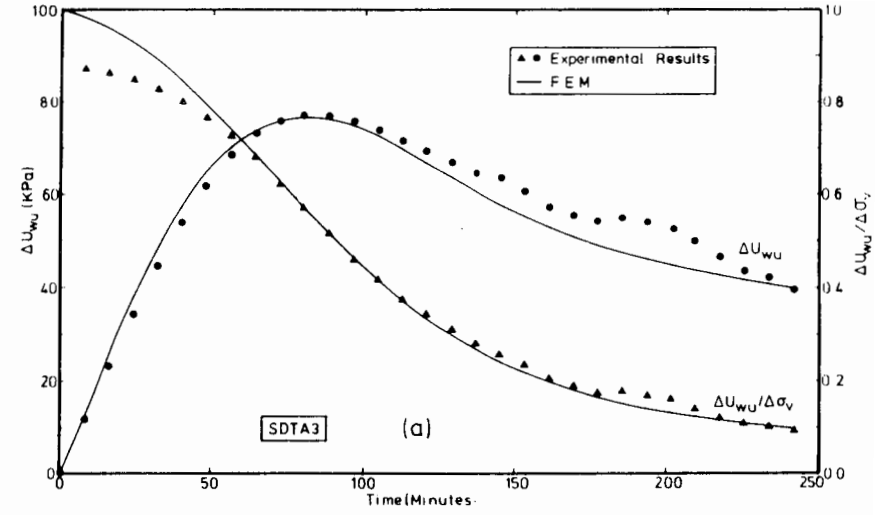

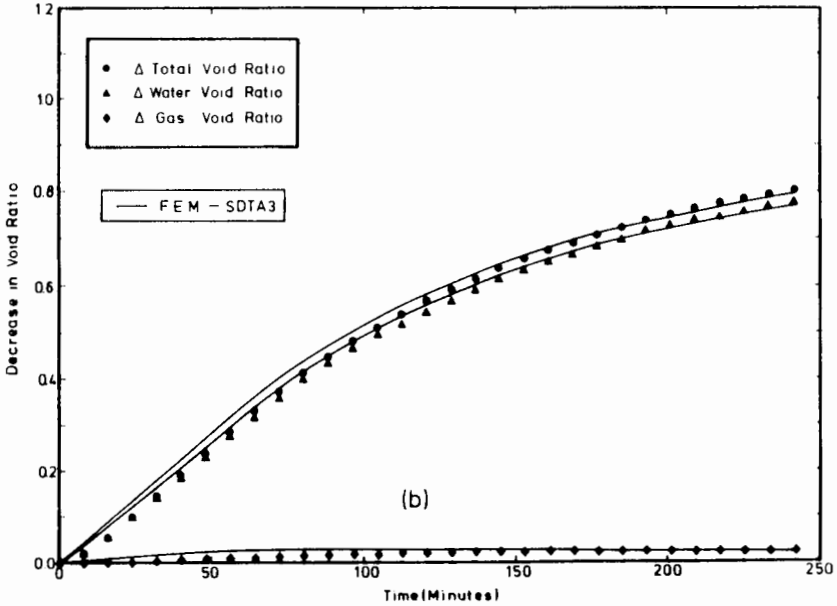

Figure 5.12 Numerical simulation of test SDTA3

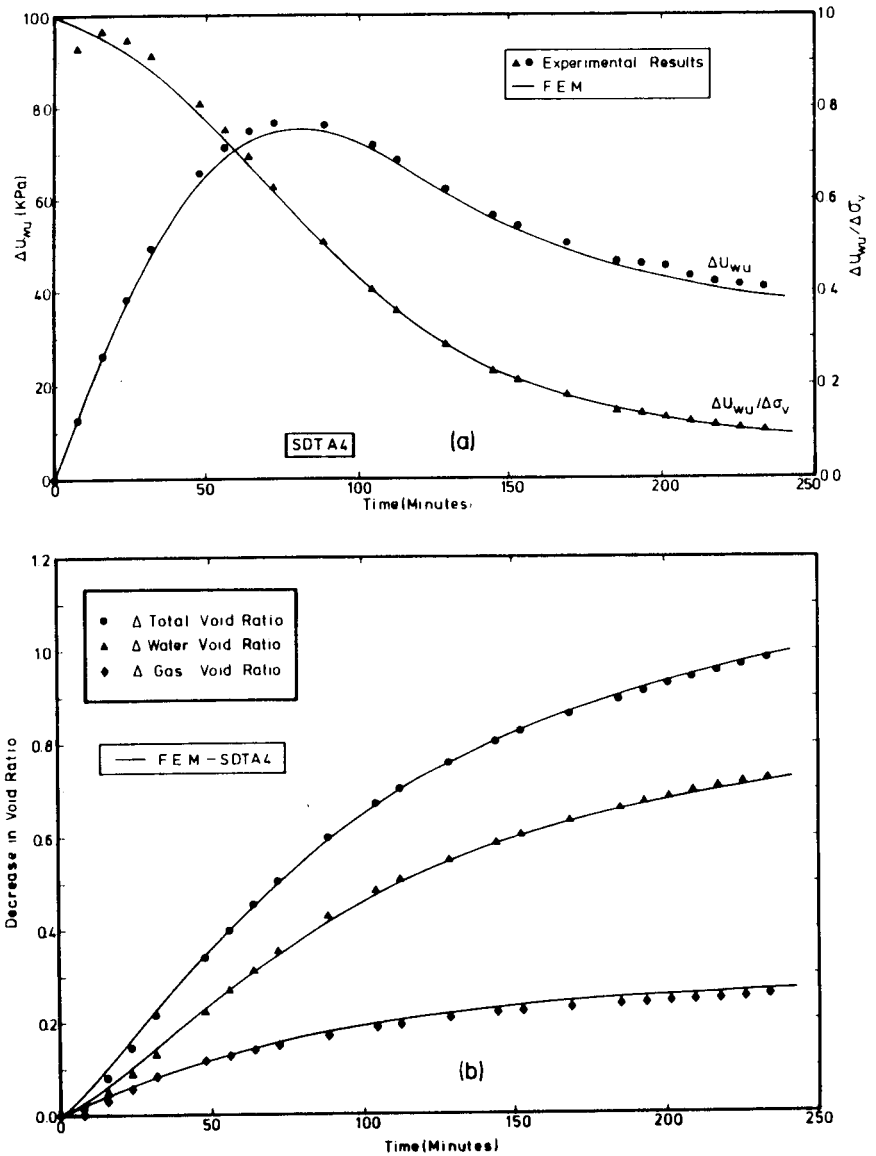

Figure 5.13 Numerical simulation of test SDTA4

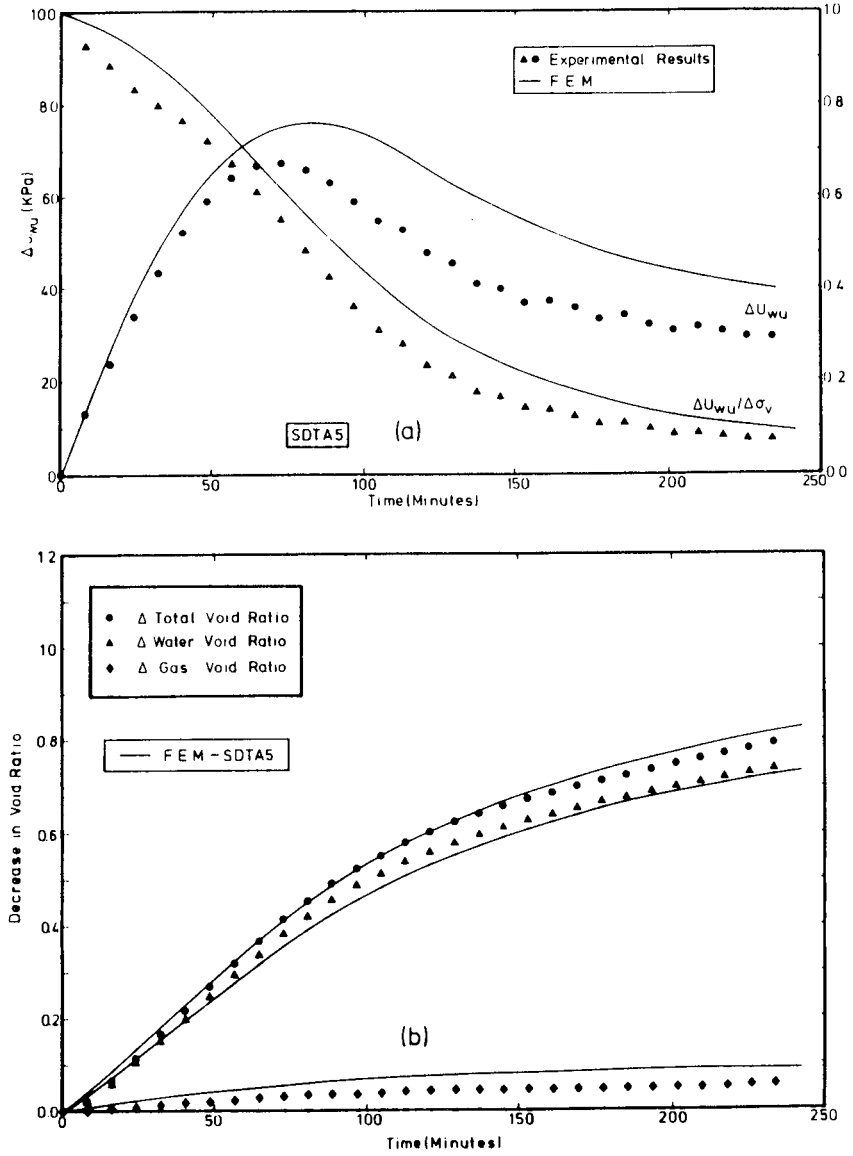

Figure 5.14 Numerical simulation of test SDTA5

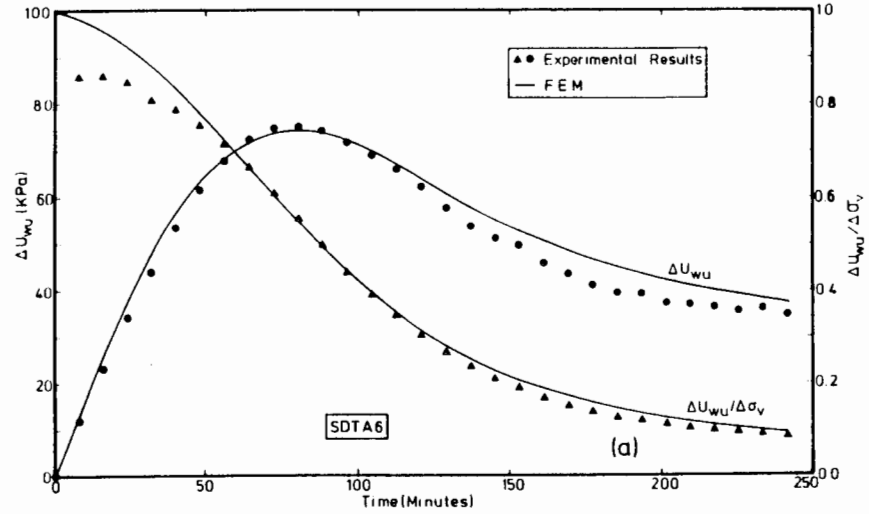

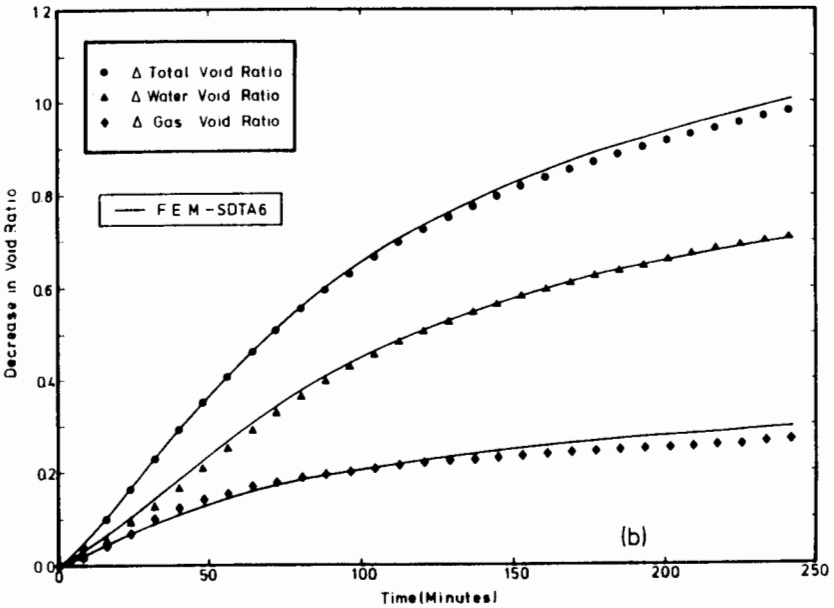

Figure 5.15 Numerical simulation of test SDTA6

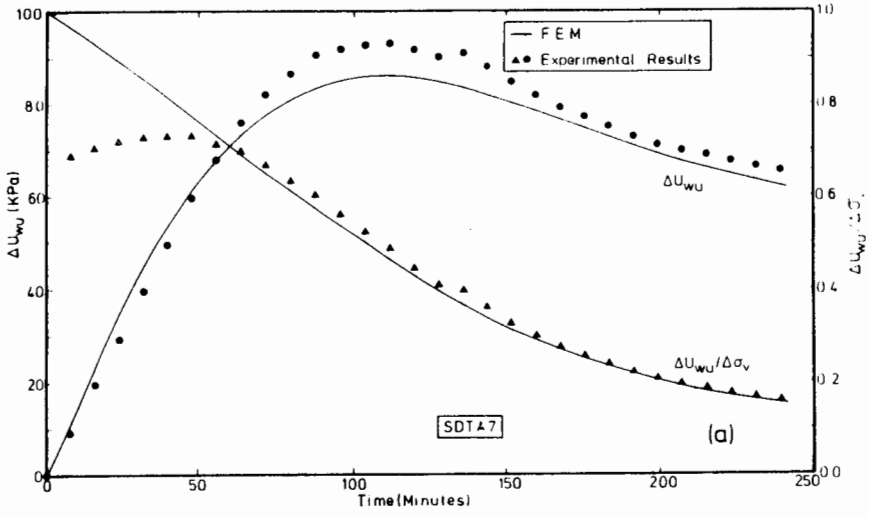

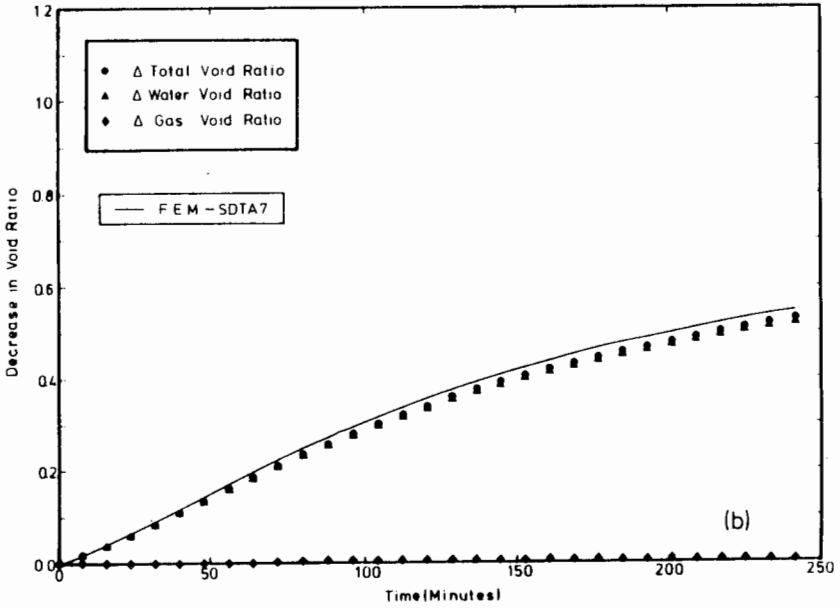

Figure 5.16 Numerical simulation of test SDTA7

highest initial gas content). The same saturated soil permeability relationship was used as for the A series simulations, although a different matrix void ratio-consolidation stress relationship was employed as shown in Figure 4.13.

The resulting comparison between the measured and simulated consolidation behaviour is presented in Figure 5.17, from which it can be seen that a satisfactory comparison of volume change behaviour is obtained for $\alpha = 1.0$.

In addition to this specific modelling exercise, the whole range of tests was modelled using the Taylor's (1948) analytical solution of the one-dimensional Terzaghi (1944) consolidation equation. This analytical model could be used in this instance as each stage produces a relatively small stress increment. Based on this modelling, it was possible to produce values of the vertical coefficient consolidation, c_v, which were presented as a function of consolidation stress in Chapter 4.

5.4 Interpretation of Numerical Modelling

The numerical modelling of test series A and B, as presented in the previous sections, has illustrated clearly that the gas present in a gassy soil cannot be assumed simply to combine with the pore water to produce a single homogeneous compressible fluid. It appears, both from physical modelling and theoretical analysis of the pore water pressure and volume change response, that the gas void takes the form of a compressible inclusion fixed in an otherwise saturated soil matrix. It also appears that the gas void remains in one particular location with respect to the position of the solid particles. During the undrained compression of the gassy soil, there is no volume change of the saturated matrix, only a change in the volume of the gas. In addition, during the consolidation process--when there is no change in the value of total vertical stress--there is no change in the volume of the gas.

5.5 Consolidation of a Saturated Soil Containing Compressible Solid Inclusions

To verify the assumption that a gassy soil appears to behave as a saturated soil containing discrete compressible inclusions remaining in the same location with respect to the soil particles, a laboratory test was conducted in which the

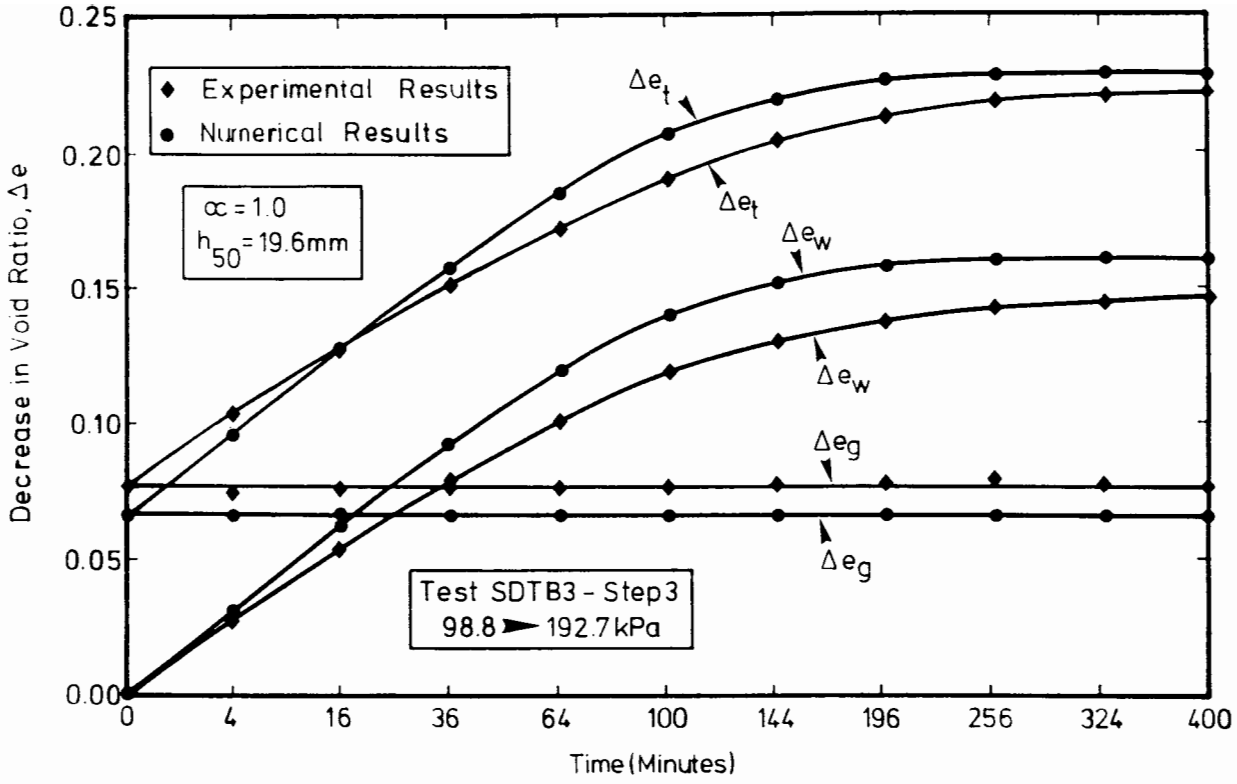

Figure 5.17 Numerical simulation of test SDTB3

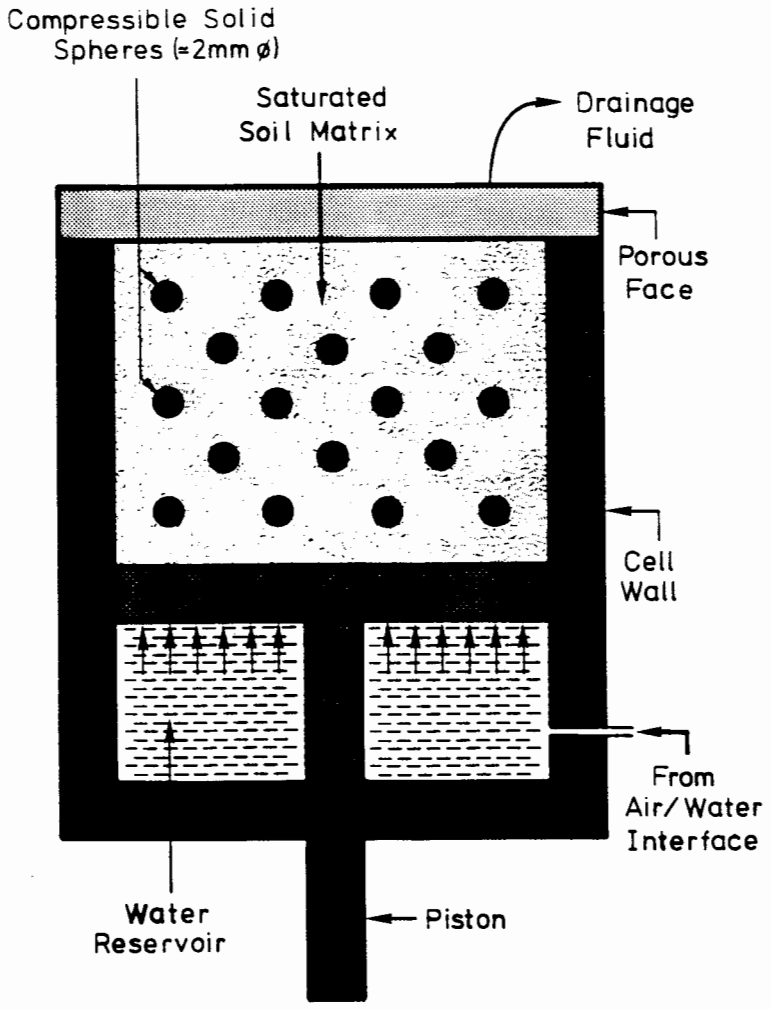

Figure 5.18 Schematic description of the consolidation of a saturated soil matrix containing compressible solid spheres

gas voids were replaced by compressible solid inclusions. In order to maintain the same soil matrix behaviour as that of a gassy soil, 15% by volume of water saturated zeolite was also included. The compressible solid inclusions used for this test were polystyrene balls with diameters ranging between 1 and 3 mm.

As test series B clearly illustrates the effect of the gas on the undrained volume change and its non-participation during the drained behaviour of a gassy soil, it was decided to perform a similar three stage undrained - drained loading test on the composite three phase material of soil particles, water and compressible solids. The results of this test would then show whether the assumption that the gas behaves as a compressible solid is valid or not.

5.5.1 Calibration of the compressible solid

One of the aims of this test was to evaluate the stress that is transferred to the compressible particles from the soil matrix. Consequently, if the compressibility of the particles is known along with the initial volume and the volume change of the solids throughout the test, the stress transferred to the compressible solids may be calculated throughout.

Therefore, before any consolidation tests were performed, the bulk compressibility of the polystyrene balls was evaluated by placing a known volume of these solids in the oedometer. The apparatus was then filled with water making sure that there was no trapped air. The mixture of water and polystyrene balls was then compressed under undrained conditions. The increase in water pressure and displacement were both recorded. Using this procedure, it was then possible to obtain a relationship between the compressive strain ($\Delta v_c / v_{co}$) of the compressible solids versus the water pressure, where Δv_c is the volume change and v_{co} is the initial volume of solids.

5.5.2 Sample preparation and consolidation - Test SDTC1

The required volume of polystyrene was mixed with a Combwich slurry of 1.41 relative bulk density. A higher relative density was used for this test, as due to the bouyancy of the polystyrene, the movement of the polystyrene balls relative to the solid particles prior to consolidation needed to be avoided.

From later observation of the sample after oven drying at the completion of the test, the balls appeared to be evenly distributed and therefore the mixing technique was adequate. The water saturated zeolite was also added to this mixture at this point. The contents were then poured into the oedometer, carefully avoiding any entrapment of air. The oedometer was then assembled, followed immediately by the application of a vertical total stress of 35 kPa to the sample. A schematic description of the oedometer containing the composite material of a saturated soil enclosing compressible solid inclusions is presented in Figure 5.18.

This sample was allowed to consolidate for three days for all pore water pressure to dissipate. The sample was then subjected to an increment of total vertical stress under undrained conditions with the drainage lines closed. Even though there was no gas present in this sample, the undrained displacement was still time dependent. After no further displacement, the drainage lines were opened and the soil was allowed to consolidate for 22 hours (2 hours were taken up with undrained compression), which was ample time for all pore water pressure to dissipate to atmospheric pressure.

This procedure was repeated until three loading increments had been applied. After dissipation of the last increment, the sample was then unloaded slowly in order to prevent large suction pressures being produced in the sample. After evaluation of the final weights and volumes of the three phases in the sample, it was then possible to evaluate the void ratios of each phase throughout the test.

5.5.3 Experimental results of test SDTC1

To illustrate the consolidation behaviour of this composite soil, the three phase void ratios e_t, e_w, and e_c are plotted versus the square root of time for each of the three loading increments. The void ratio of the compressible solid, e_c, is given by v_c/v_s where v_s is the volume of soil particles. The three components of void ratio are presented in Figure 5.19, which portrays the same type of behaviour as for a gassy soil under similar loading conditions. It can be seen that the undrained displacement is due to the compression of the

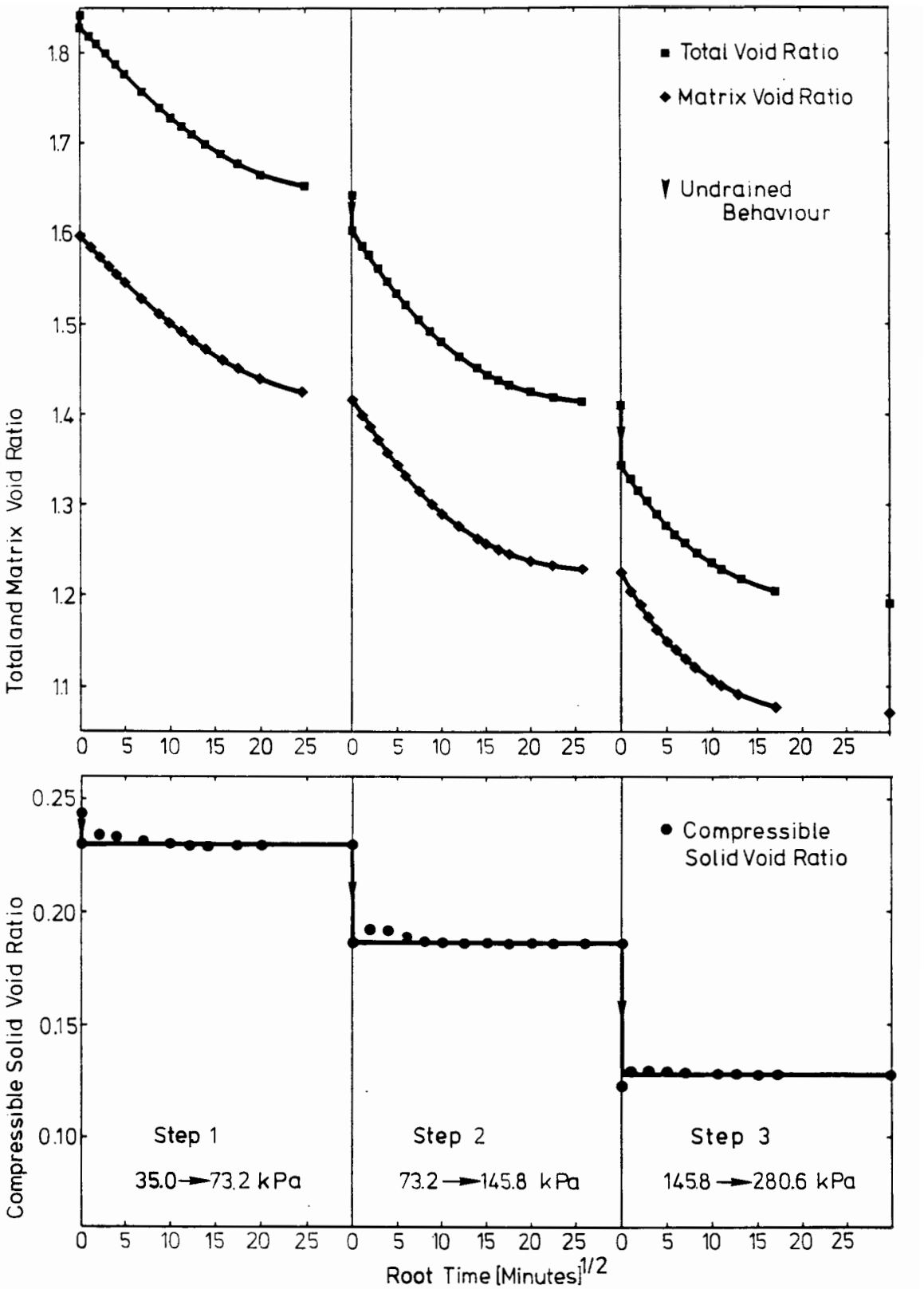

Figure 5.19 Illustration of the phase void ratio behaviour for a saturated soil containing compressible solid spheres (Test SDTC1)

polystyrene balls, yet during the drained stage, there is little volume change of the polystyrene and the volume change of the sample is due almost totally to the loss of the pore water draining from the sample.

From the measurement of the total stress at the end of each loading increment, it is possible to plot both the total and matrix void ratio against the vertical consolidation stress. This plot is presented in Figure 5.20.

To compare these results against those of a gassy soil, the matrix void ratio versus consolidation stress of test SDTC1 is superimposed on the same relationship obtained from test series B, as shown in Figure 5.21. It can be seen that the comparison is excellent. This shows that for a saturated soil containing compressible inclusions, the soil matrix void ratio, e_w, as for a gassy soil, is also related to the vertical consolidation pressure, $\sigma_v - u_w$.

Finally, as it is possible to evaluate the stress on the solid inclusions from the volumetric strain, it is also possible to evaluate the proportion of stress that is transferred from the external load to the solid inclusions. Figure 5.22 shows the third (compressible solid) phase void ratio, e_c, plotted against total vertical stress for test SDTC1. The resulting linear relationship was extrapolated to the void ratio axis to give an initial void ratio, e_c, of 0.26. In addition, from the knowledge of the initial volume of compressible solids, it is possible to evaluate the volumetric strain of these solids. These are also plotted against the total vertical stress in Figure 5.22. This volumetric strain, plotted against total vertical stress, is then superimposed on the theoretical volumetric strain for α values of 1.0, 0.9, 0.8 and 0.7. These curves are evaluated from the calibration of the compressible solids. The resulting plot is presented in Figure 2.23, where it can be seen that the stress transfer coefficient α for this composite material is about 0.8, that is, between the 0.7 and 1.0 values that were obtained for a gassy soil.

5.5.4 Interpretation of results

From this consolidation test SDTC1 it can be quite clearly seen that the consolidation behaviour of a soil containing discrete voids of a compressible solid behaves in an almost identical manner to a gassy soil. The only slight

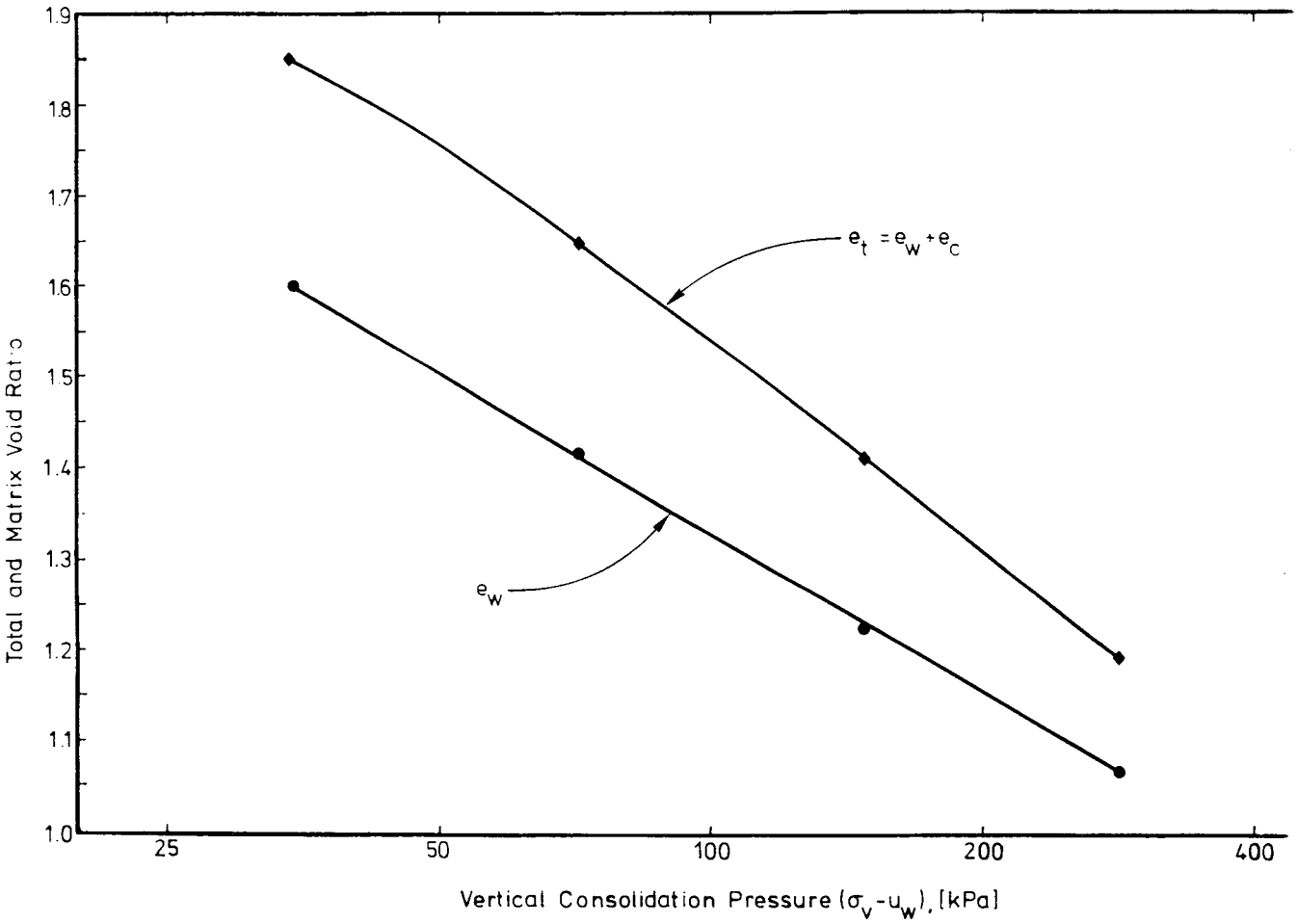

Figure 5.20 Total and matrix void ratio versus vertical consolidation stress for test SDT

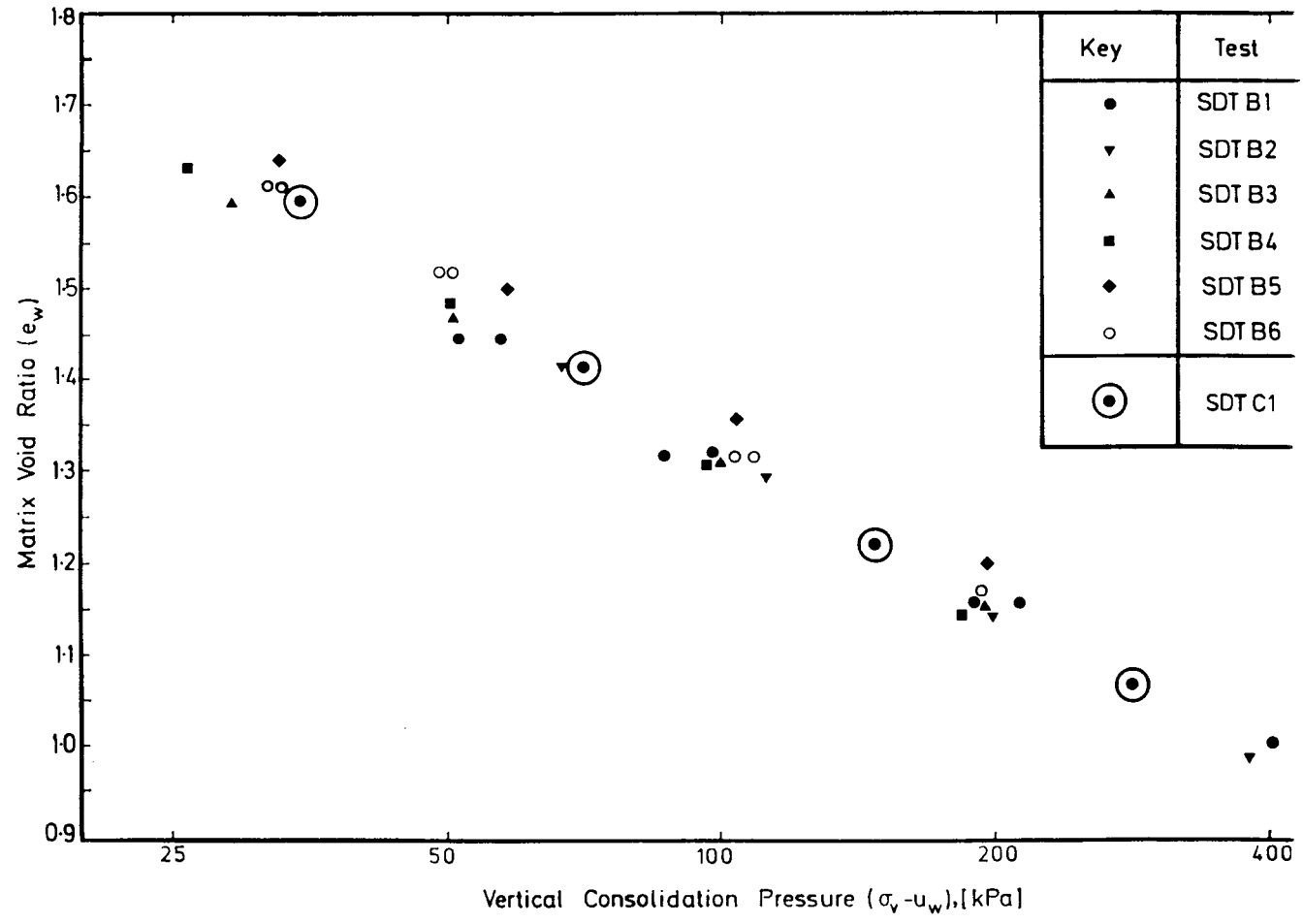

Figure 5.21 Matrix void ratio versus vertical consolidation stress for test SDTC1 and test series B

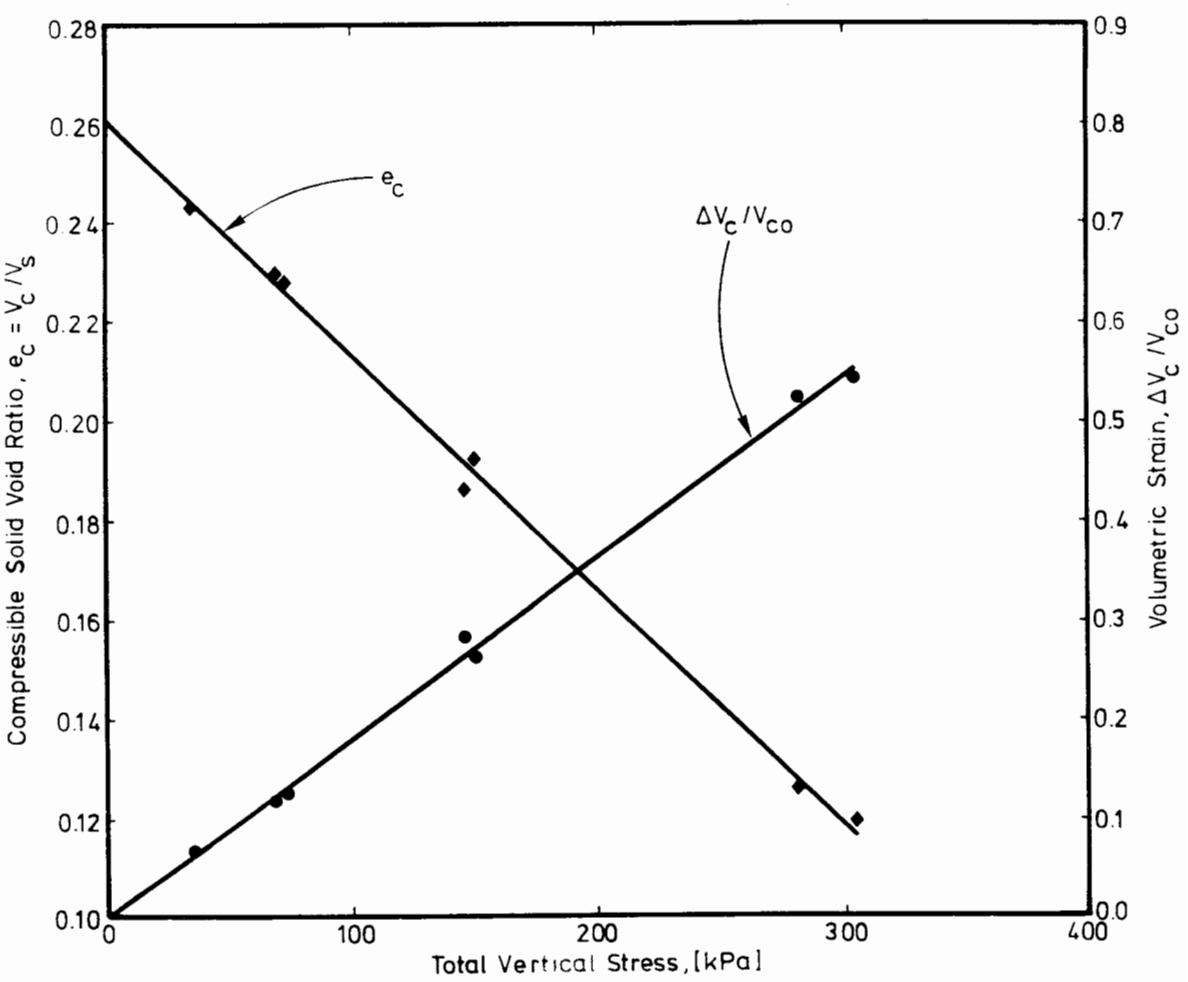

Figure 5.22 Evaluation of compressible solid void ratio and volumetric strain for test SDTC1

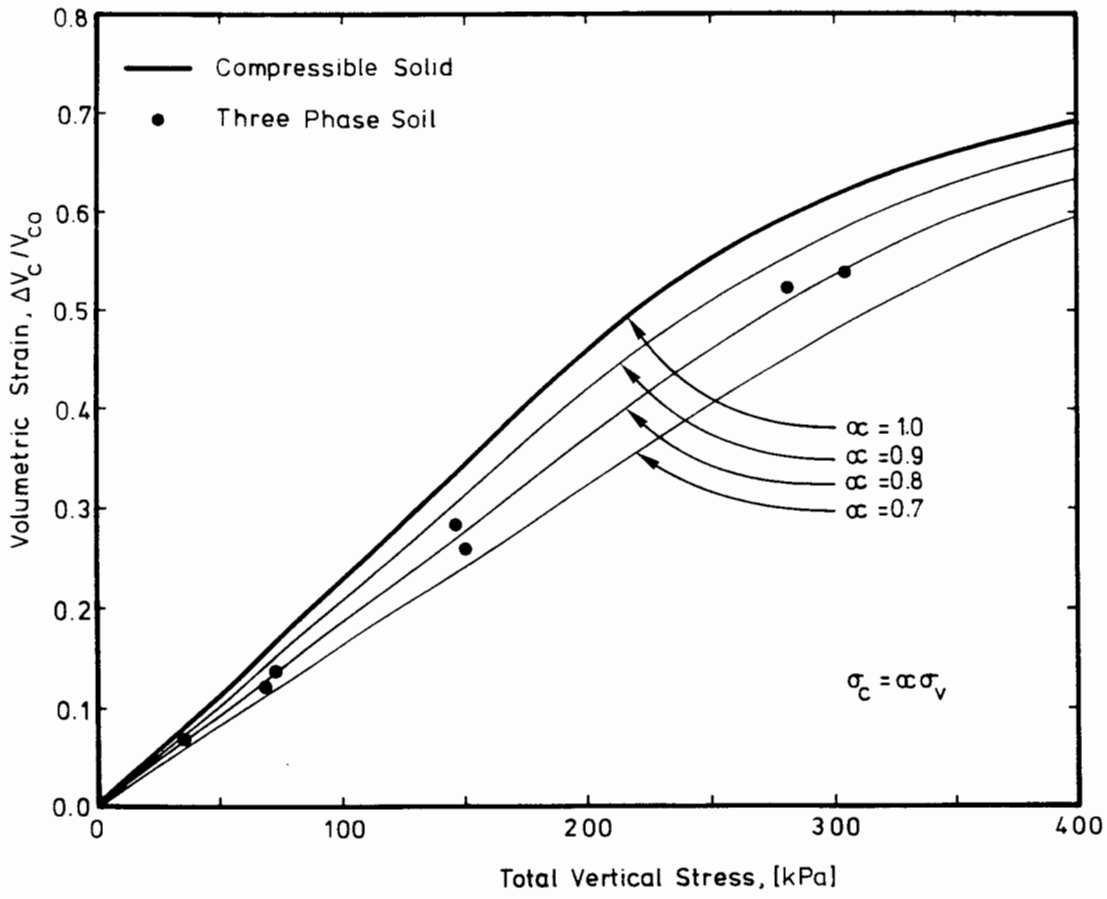

Figure 5.23 Evaluation of the stress transfer coefficient from the initial calibration curve for the compressible spheres

difference in results is that the gassy soil test using a three stage loading sequence produced a stress transfer coefficient, α, of 1.0, yet for the compressible solid case the α value was approximately 0.8. This is most probably due to the fact that for a gassy soil, the aspect ratio of the gas void may be as high as 5, thus producing high stress concentrations in the saturated soil matrix which results in most of the external load being transferred to the gas void. Due to the higher stiffness of the compressible solid, however, the highest possible value of the aspect ratio is 2. Therefore, lower stresses occur in the saturated matrix surrounding this solid resulting in less of the external stress being transferred to it.

5.6 Summary

In order to model the one-dimensional consolidation behaviour of the saturated soil test SDTA1, a finite element program was written in which the soil permeability and the void ratio were non-linear functions of the vertical effective stress. In addition, it was necessary for the finite element mesh to deform to take into account the changing thickness of the soil sample. By modifying the relationship between the soil permeability and the effective stress, satisfactory simulations of the time dependent undrained face pore water pressure and soil settlement were obtained.

The initial modelling of the consolidation behaviour of a gassy soil was based on the assumption that the pore water and gas combine to produce a single compressible fluid. The first gassy soil simulation of test SDTA6 assumed that the gas pressure was equal to the pore water pressure. The comparisons between the simulated and observed responses of pore water pressure and volume change behaviour were very weak. Finally, the gassy soil was treated as a saturated soil containing discrete compressible solids. The resulting equation that was produced based on this assumption turned out to be almost identical to that governing the consolidation of a saturated soil. Using this equation in the numerical model produced a good simulation of the observed pore water pressure and volume change response for the majority of the tests of series A. This was then followed by the simulation of the gassy soil test SDTB3 based on the same

assumption of compressible solid inclusions. Once again, good comparisons of volume change behaviour with time were observed.

As the numerical model was based on the assumption that the gas voids acted as compressible solid inclusions, it was subsequently decided to perform a consolidation test--similar to the tests in series B--on a composite soil consisting of a saturated soil matrix containing compressible polystyrene balls. The resulting behaviour of matrix void ratio, undrained compression, drained consolidation and transfer of stress to the compressible solid inclusions was similar to the behaviour observed in a gassy soil. This experiment, together with the findings of the numerical modelling, illustrates clearly that the gas, rather than combining with the water to produce a compressible fluid, can be treated as discrete compressible solid inclusions embedded in an otherwise saturated soil matrix.

Note 5.1 Consolidation of a saturated soil.

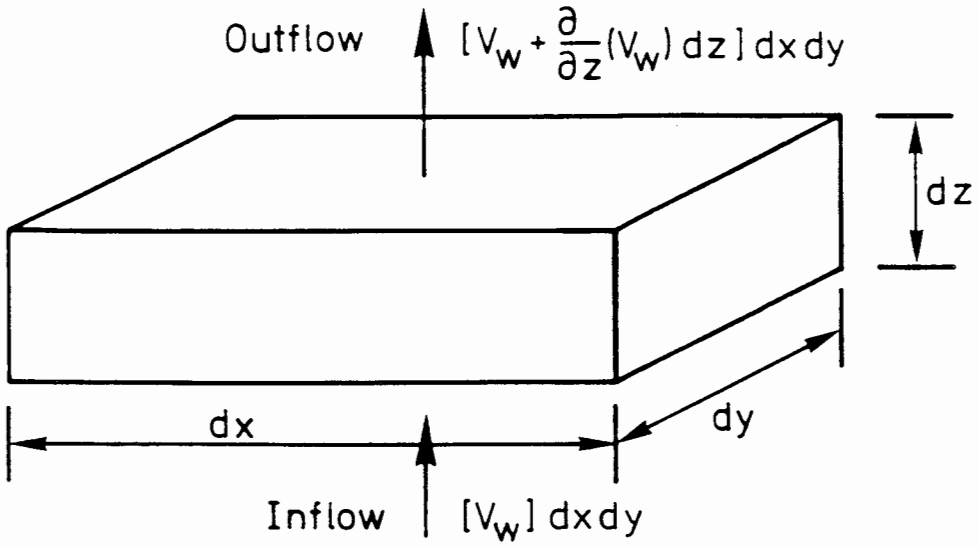

Following the method of Terzaghi (1944), the rate of flow of water entering the above element is

$$V_w\,dx\,dy = -\frac{k}{\gamma}\frac{\partial u_w}{\partial z}\,dx\,dy \qquad (5.1.1)$$

The net rate of flow from the element can then be written as

$$\frac{\partial V_w}{\partial z}\,dx\,dy\,dz = \frac{\partial}{\partial z}\left[-\frac{k}{\gamma}\frac{\partial u_w}{\partial z}\right]dx\,dy\,dz \qquad (5.1.2)$$

Writing the volume of voids as

$$\left(\frac{e}{(1+e)}\right)dx\,dy\,dz \qquad (5.1.3)$$

Then the rate of change of the void volume is

$$\frac{\partial}{\partial t}\left(\frac{e}{(1+e)}\right)dx\,dy\,dz = \frac{dx\,dy\,dz}{(1+e)}\frac{\partial e}{\partial t} \qquad (5.1.4)$$

as dx dy dz/(1+e) is the volume of soil particles which is assumed to be constant. Therefore, from the conservation of volume of the incompressible water and solid soil grains, it follows that

$$\frac{\partial}{\partial z}\left[-\frac{k}{\gamma}\frac{\partial u_w}{\partial z}\right]dx\,dy\,dz = \frac{dx\,dy\,dz}{(1+e)}\frac{\partial e}{\partial t} \qquad (5.1.5)$$

However, for a saturated soil, the void ratio is governed by the effective stress, thus

$$\frac{\partial}{\partial z}\left[\frac{k}{\gamma}\frac{\partial u_w}{\partial z}\right] = -\frac{1}{(1+e)}\frac{de}{d\sigma'}\frac{\partial \sigma'}{\partial t} \qquad (5.1.6)$$

However,

$$\sigma' = \sigma - u_w \quad \text{and} \quad m_v = -\frac{1}{(1+e)}\frac{de}{d\sigma'} \qquad (5.1.7)$$

Therefore,

$$\frac{\partial}{\partial z}\left[\frac{k}{\gamma}\frac{\partial u_w}{\partial z}\right] = m_v\frac{\partial u_w}{\partial t} - m_v\frac{\partial \sigma}{\partial t} \qquad (5.1.8)$$

Note 5.2 Consolidation of a soil containing a compressible pore fluid.

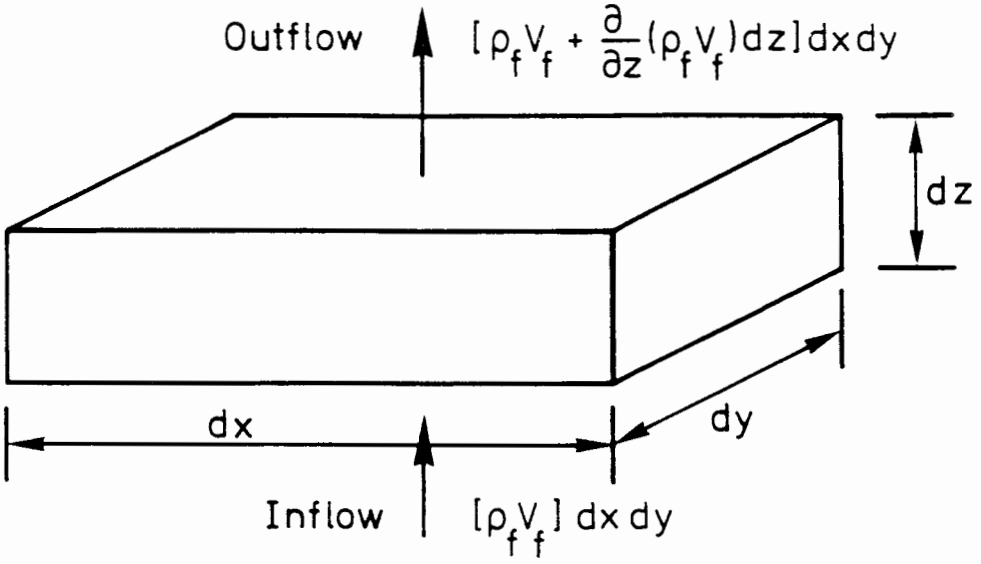

Following the method of Terzaghi (1944), the rate of fluid mass entering the above element of soil is

$$\rho_f V_f \, dx \, dy = - \rho_f \frac{k}{\gamma} \frac{\partial u_f}{\partial z} dx \, dy \qquad (5.2.1)$$

The net rate of flow from the element can then be written as

$$\rho_f \frac{\partial}{\partial z}\left(V_f \, dx \, dy \right) dz = \rho_f \frac{\partial}{\partial z}\left[- \frac{k}{\gamma} \frac{\partial u_f}{\partial z} \right] dx \, dy \, dz \qquad (5.2.2)$$

assuming that the pore fluid is only slightly compressible and that dx and dy are constant. Writing the mass of fluid in the above element as

$$\rho_f \left(\frac{e}{(1+e)} \right) dx \, dy \, dz \qquad (5.2.3)$$

Then the rate of change of the mass of pore fluid is

$$\frac{\partial}{\partial t} \left[\rho_f \left(\frac{e}{(1+e)} \right) \right] dx \, dy \, dz = \frac{dx \, dy \, dz}{(1+e)} \frac{\partial}{\partial t} \left(\rho_f \, e \right) \qquad (5.2.4)$$

as dx dy dz/(1+e) is the volume of soil particles which is assumed to be constant. Therefore, from the conservation of mass, it follows that

$$\rho_f \frac{\partial}{\partial z}\left[- \frac{k}{\gamma} \frac{\partial u_f}{\partial z} \right] dx \, dy \, dz = \frac{dx \, dy \, dz}{(1+e)} \frac{\partial}{\partial t} \left(\rho_f \, e \right) \qquad (5.2.5)$$

which may be expanded to give

$$\frac{\partial}{\partial z}\left[- \frac{k}{\gamma} \frac{\partial u_f}{\partial z} \right] = \frac{1}{(1+e)} \frac{\partial e}{\partial t} + \frac{n_f}{\rho_f} \frac{\partial \rho_f}{\partial t} \qquad (5.2.6)$$

However, as the pore fluid has been made up of a combination of water and gas of which only the gas is compressible and in which the saturation remains fairly constant, the above equation can be written in the form

$$\frac{\partial}{\partial z}\left[\frac{k}{\gamma} \frac{\partial u_f}{\partial z} \right] = - \frac{1}{(1+e)} \frac{\partial e}{\partial t} + n_g \, c_g \frac{\partial \rho_f}{\partial t} \qquad (5.2.7)$$

where c_g and u_g are the compressibility and pressure of the gas respectively. If it is assumed that the gas pressure is equal to the pore water pressure and noting that

$$\sigma' = \sigma - u_w \quad \text{and} \quad m_v = - \frac{1}{(1+e)} \frac{de}{d\sigma'} \qquad (5.2.8)$$

the final form of this equation can be written as

$$\frac{\partial}{\partial z}\left[\frac{k}{\gamma} \frac{\partial u_w}{\partial z} \right] = (m_v + c_g \, n_g) \frac{\partial u_w}{\partial t} - m_v \frac{\partial \sigma}{\partial t} \qquad (5.2.9)$$

Note 5.3 Consolidation of a soil containing discrete gas voids.

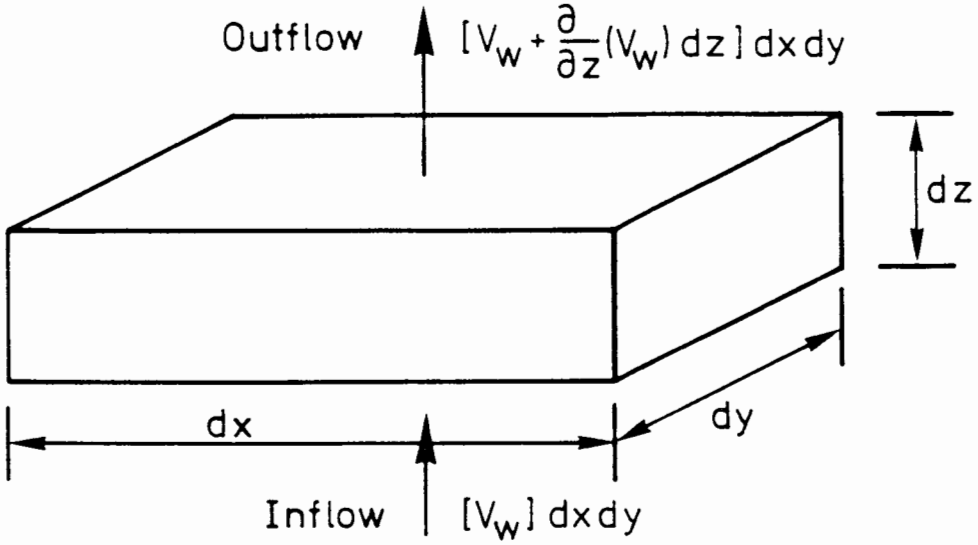

Following the method of Terzaghi (1944), the rate of flow of water entering the above element is

$$V_w \, dx \, dy = - \frac{k}{\gamma} \frac{\partial u}{\partial z}_w \, dx \, dy \qquad (5.3.1)$$

The net rate of flow from the element can then be written as

$$\frac{\partial V}{\partial z}_w \, dx \, dy \, dz = \frac{\partial}{\partial z}\left[- \frac{k}{\gamma} \frac{\partial u}{\partial z}_w \right] dx \, dy \, dz \qquad (5.3.2)$$

Writing the volume of water filled voids as

$$\left(\frac{S_w \, e_t}{(1+e_t)}\right) dx \, dy \, dz = \left(\frac{e_w}{(1+e_w+e_g)}\right) dx \, dy \, dz \qquad (5.3.3)$$

then the rate of change of the water void volume is

$$\frac{\partial}{\partial t}\left(\frac{e_w}{(1+e_t)}\right) dx \, dy \, dz = \frac{dx \, dy \, dz}{(1+e_t)} \frac{\partial e}{\partial t}_w \qquad (5.3.4)$$

as $dx\,dy\,dz/(1+e_t)$ is the volume of soil particles which is assumed to be constant. Therefore, from the conservation of volume of the incompressible water and solid soil grains, it follows that

$$\frac{\partial}{\partial z}\left[- \frac{k}{\gamma} \frac{\partial u}{\partial z}_w \right] dx \, dy \, dz = \frac{dx \, dy \, dz}{(1+e_t)} \frac{\partial e}{\partial t}_w \qquad (5.3.5)$$

or

$$\frac{\partial}{\partial z}\left[- \frac{k}{\gamma} \frac{\partial u}{\partial z}_w \right] = \frac{(1+e_w)}{(1+e_t)} \frac{1}{(1+e_w)} \frac{\partial e}{\partial t}_w \qquad (5.3.6)$$

However, from the experimental evidence, it has been shown that the matrix void ratio, e_w, is governed by the consolidation stress, $\sigma' = \sigma - u_w$. Subsequently

$$\frac{\partial}{\partial z}\left[\frac{k}{\gamma} \frac{\partial u}{\partial z}_w \right] = - \frac{(1-n_g)}{(1+e_w)} \frac{de_w}{d\sigma'} \frac{\partial \sigma'}{\partial t} \qquad (5.3.7)$$

Noting that

$$\sigma' = \sigma - u_w \quad \text{and} \quad m_v = - \frac{1}{(1+e_w)} \frac{de_w}{d\sigma'} \, , \qquad (5.3.8)$$

$$\frac{\partial}{\partial z}\left[\frac{k}{\gamma} \frac{\partial u}{\partial z}_w \right] = (1-n_g) \, m_v \frac{\partial u}{\partial t}_w - (1-n_g) \, m_v \frac{\partial \sigma}{\partial t} \qquad (5.3.9)$$

or

$$\frac{\partial}{\partial z}\left[\frac{k}{\gamma} \frac{\partial u}{\partial z}_w \right] = m_v^g \frac{\partial u}{\partial t}_w - m_v^g \frac{\partial \sigma}{\partial t} \qquad (5.3.10)$$

where m_v^g is the adjusted coefficient of volume change for a gassy soil.

CHAPTER 6

INTERPRETATION OF EXPERIMENTAL AND NUMERICAL MODELLING

CHAPTER 6

INTERPRETATION OF EXPERIMENTAL AND NUMERICAL MODELLING

6.1 Introduction

This chapter attempts to understand the compressive behaviour of a gassy soil and to explain some of the results that were observed from both the experimental and numerical modelling. At this point, the concept that the gas and water combine to form a compressible pore fluid is completely abandoned. The conceptual model that is presently used assumes that the gassy soil is made up of numerous discrete gas voids randomly distributed in a saturated soil matrix. Wheeler (1986) calls this the "large bubble model" which is conceptualized in Figure 6.1a and idealized in Figure 6.1b. Furthermore, it is assumed that the position of the gas voids is fixed with respect to the surrounding solid particles and that these do not flow with the pore water. The initial theoretical analysis presented in this chapter uses basic elastic and plastic solutions to illustrate qualitatively the behaviour of gassy soil using the above conceptual model. No attempt is made to use these solutions to simulate the experimental results directly. This is followed by the introduction of a model which is based on the concept that a gassy soil deforms independently due to both changes of total stress and consolidation stress, each deformation mode having an independent compressibility. This "double compressibility model" can not only explain the results obtained in this thesis, but is also able to model the triaxial results of Wheeler (1986). Finally, to check the validity of the double compressibility model, a power input analysis is performed to evaluate the work done on each phase of a gassy soil.

6.2 The Volume Change Behaviour of the Saturated Matrix

This section attempts to explain the fact that for a gassy soil, for consolidation under either isotropic or K_o loading conditions, the relationship between the matrix void ratio and the mean consolidation pressure appears to be the same as the relationship between the void ratio and the mean effective stress for the same soil when saturated.

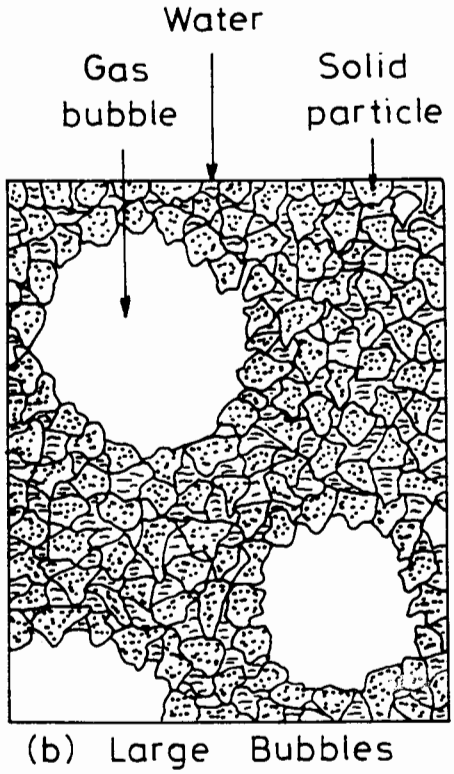

Figure 6.1a Conceptualization of gassy soil (Wheeler, 1986)

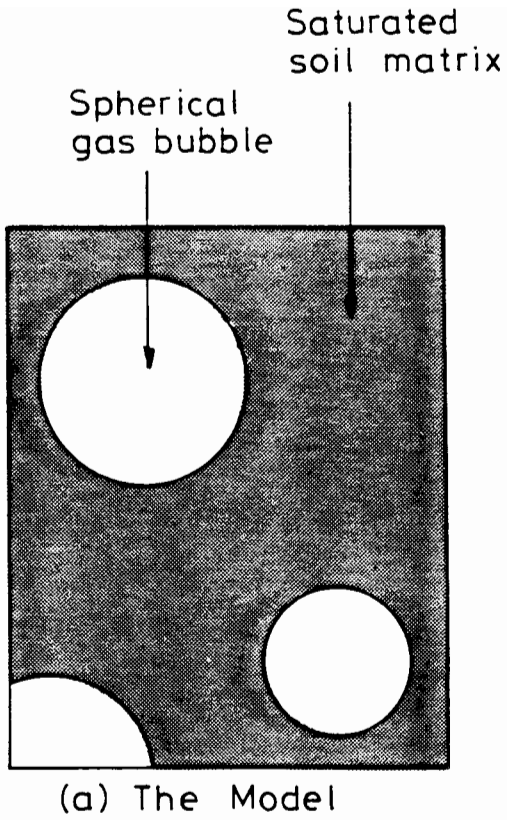

Figure 6.1b Idealization of gassy soil as "Large Bubble Model" (Wheeler, 1986)

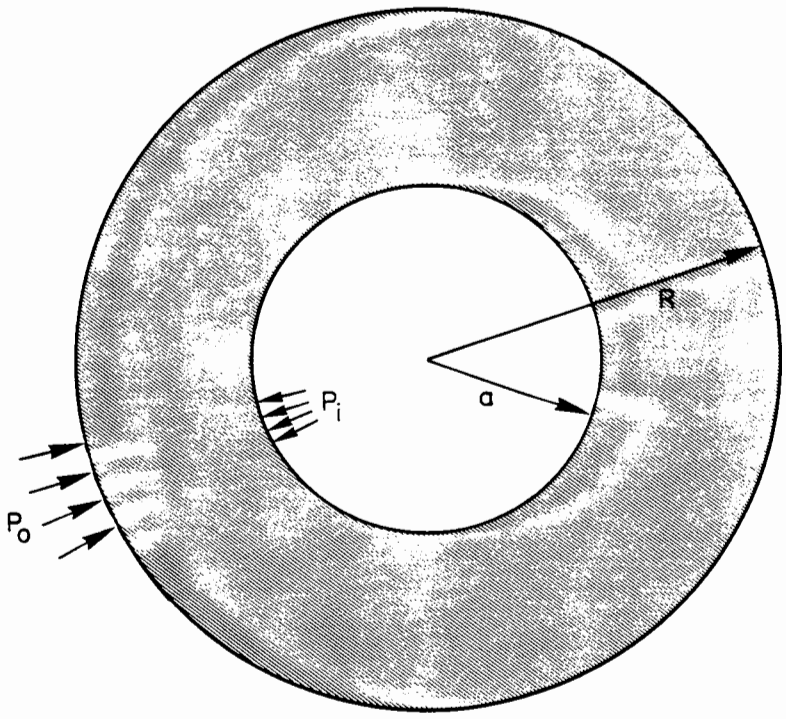

Figure 6.2 Idealization of gassy soil as a hollow sphere

6.2.1 The stress distribution around a hollow elastic sphere under isotropic loading conditions

In this analysis it is assumed that a gassy soil can be idealized as a single spherical gas void surrounded by a larger sphere of an elastic saturated soil matrix. This gassy soil, idealized as a hollow elastic sphere, is then subjected to an internal and external isotropic stress of p_i and p_o respectively, as illustrated in Figure 6.2. The resulting stress distribution in the elastic material of the hollow sphere, derived by Lamé (1852), is presented by Timoshenko and Goodier (1970, pp. 394-5). The radial stress, σ_r, and tangential stress, σ_t, may be written as

$$\sigma_r = p_o \frac{R^3}{r^3} \frac{(r^3 - a^3)}{(R^3 - a^3)} + p_i \frac{a^3}{r^3} \frac{(R^3 - r^3)}{(R^3 - a^3)} \tag{6.1}$$

and

$$\sigma_t = p_o \frac{R^3}{2r^3} \frac{(2r^3 + a^3)}{(R^3 - a^3)} - p_i \frac{a^3}{2r^3} \frac{(2r^3 + R^3)}{(R^3 - a^3)} \tag{6.2}$$

where a and R are the internal and external radii of the hollow sphere, as illustrated in Figure 6.2, and r is the radial distance to a stress point in the hollow sphere. If it is assumed that the volume change behaviour of the soil matrix is governed by the mean normal effective stress acting on the soil matrix, however, then this stress can be written as

$$\sigma'_{sm} = \sigma_{sm} - u_w = \frac{1}{3}[\sigma_{s1} + \sigma_{s2} + \sigma_{s3}] - u_w \tag{6.3}$$

where σ_{s1}, σ_{s2}, σ_{s3} are any three orthogonal stress components at a point in the soil domain, u_w is the pore water pressure, and the subcript "m" indicates stresses in the saturated matrix. The mean normal stress may be found from the radial and tangential stresses to give

$$\sigma_{sm} = \frac{1}{3}[\sigma_r - 2\sigma_t] \tag{6.4}$$

which on substitution of equations 6.1 and 6.2 may be shown to be

$$\sigma_{sm} = \left[\frac{p_o R^3 - p_i a^3}{R^3 - a^3} \right] \tag{6.5}$$

For a gassy soil of gas volume fraction n_g, internal gas pressure u_g and external applied mean total stress σ_m, the mean total stress in the soil matrix

may be written as

$$\sigma_{sm} = \left[\frac{\sigma_m - u_g n_g}{1 - n_g} \right] \tag{6.6}$$

Furthermore, the experimental work illustrated that the gas pressure may be approximated by $u_g = \alpha \sigma_m$, and thus the mean isotropic stress in the hollow sphere may be written as

$$\sigma_{sm} = \sigma_m \left[\frac{1 - \alpha n_g}{1 - n_g} \right] \tag{6.7}$$

6.2.2 Stress in the matrix of a gassy soil under anisotropic conditions

An alternative procedure in the evaluation of the matrix stress is to consider a sample of gassy soil under a uniform but anisotropic loading condition. If an arbitrary plane is cut across this sample as illustrated in Figure 6.3, there will be a normal stress σ_i exerted on this plane. If it is also assumed that this plane cuts a proportional area of n_g of the gas bubbles, then the stress acting on this plane may be written as

$$\sigma_i = \bar{\sigma}_{si}(1-n_g) + u_g n_g \tag{6.8}$$

where $\bar{\sigma}_{si}$ is the average saturated soil matrix stress acting normal to this plane. If two further cuts are made at orthogonal directions to this first cut, the same conditions will hold producing a total of three stress components

$$\sigma_i = \bar{\sigma}_{si}(1-n_g) + u_g n_g \quad , \tag{6.9}$$

$$\sigma_j = \bar{\sigma}_{sj}(1-n_g) + u_g n_g \quad , \text{ and} \tag{6.10}$$

$$\sigma_k = \bar{\sigma}_{sk}(1-n_g) + u_g n_g \tag{6.11}$$

These equations may be combined from the fact that

$$\sigma_m = \frac{1}{3}(\sigma_i + \sigma_j + \sigma_k) \quad \text{and} \quad \bar{\sigma}_{sm} = \frac{1}{3}(\bar{\sigma}_{si} + \bar{\sigma}_{sj} + \bar{\sigma}_{sk}) \tag{6.12}$$

to give

$$\bar{\sigma}_{sm} = \frac{\sigma_m - u_g n_g}{1 - n_g} \tag{6.13}$$

Using the assumption that $u_g = \alpha \sigma_m$

$$\bar{\sigma}_{sm} = \sigma_m \left[\frac{1 - \alpha n_g}{1 - n_g} \right] \tag{6.14}$$

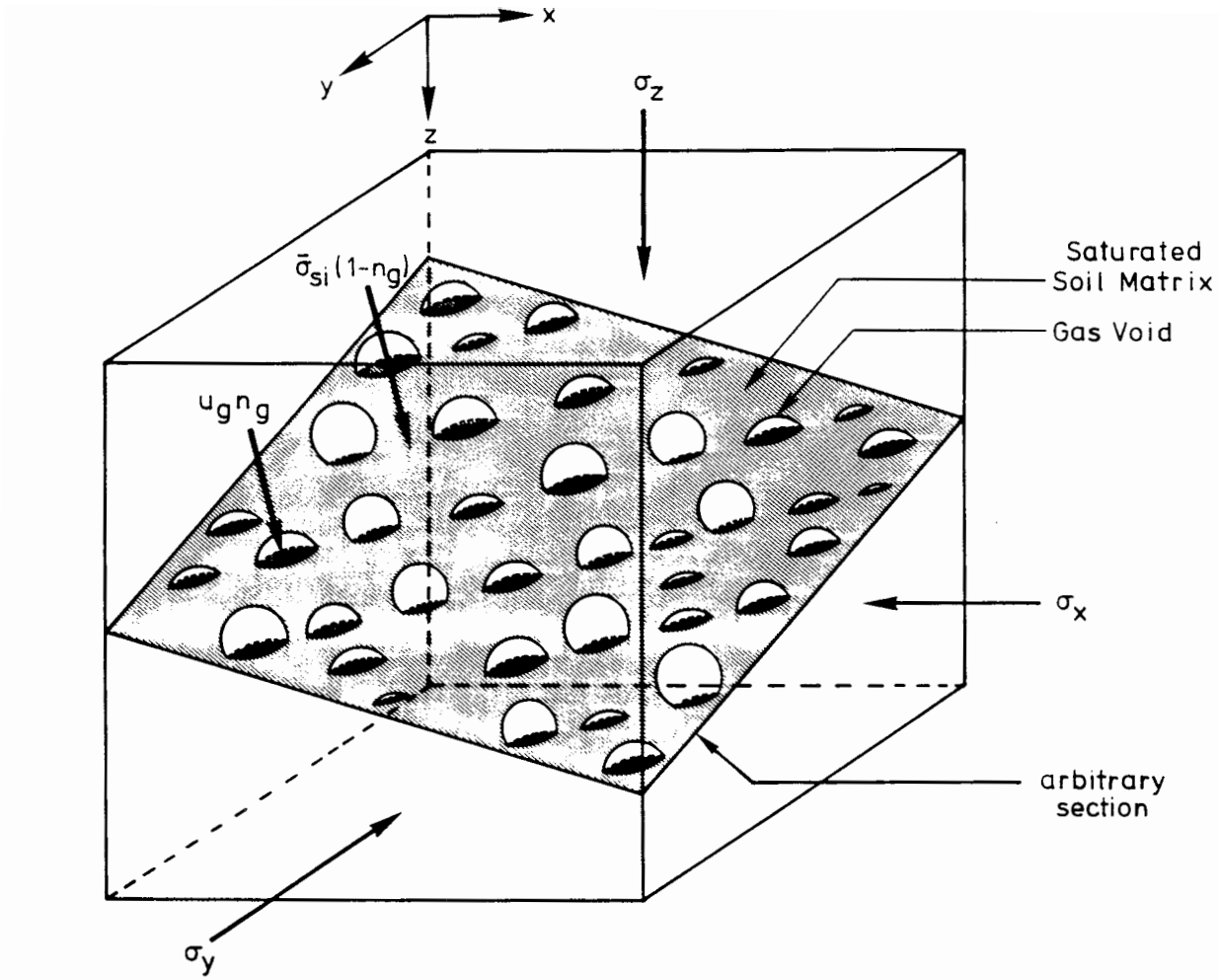

Figure 6.3 Stresses on an arbitrary plane through a gassy soil

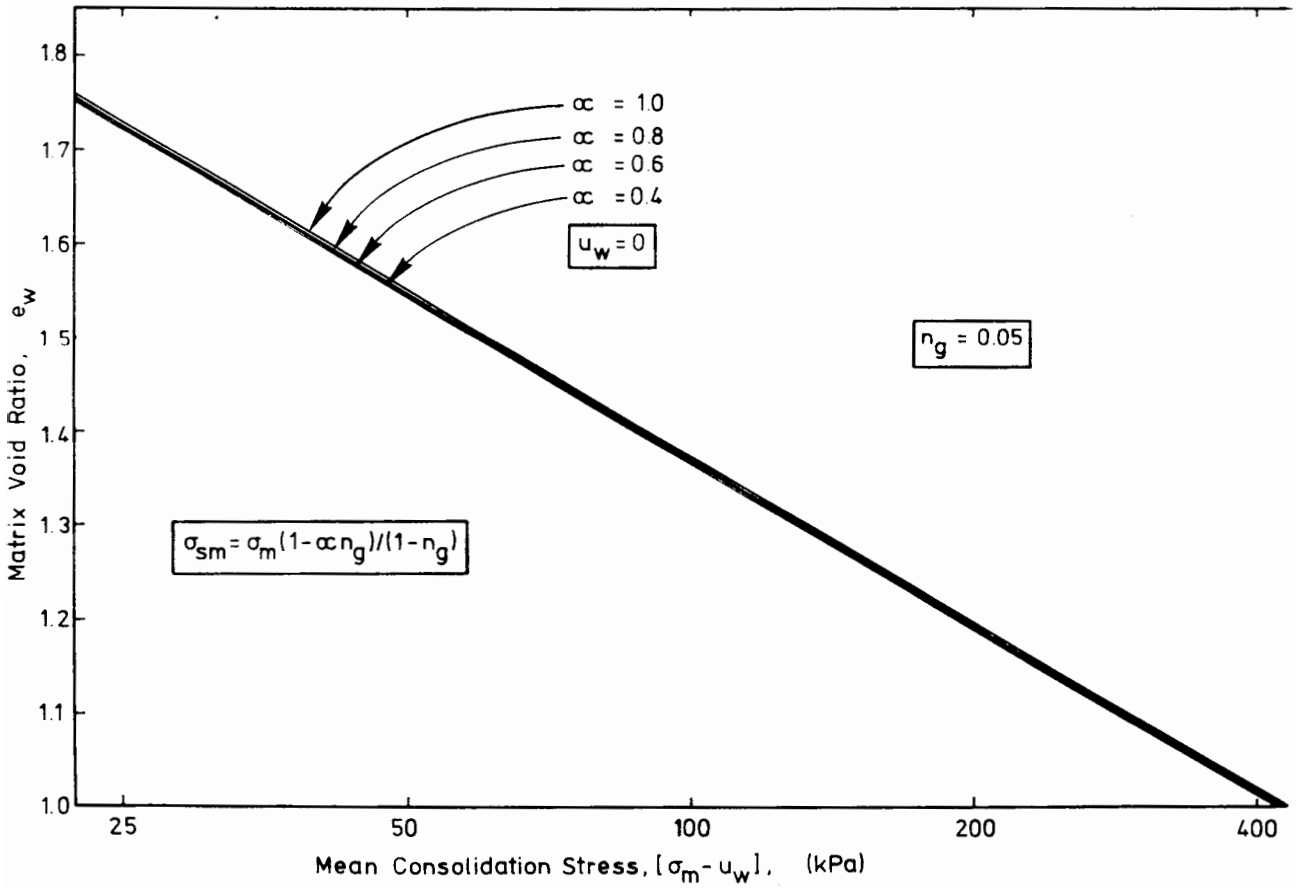

Figure 6.4 Theoretical matrix void ratio versus mean consolidation stress

where $\bar{\sigma}_{sm}$ is the average mean normal stress throughout the soil matrix.

6.2.3 The effect of the matrix stress on the matrix void ratio

To illustrate the effect on the void ratio of the saturated soil matrix in a gassy soil, the matrix void ratio versus consolidation stress is calculated for a soil of 0.05 gas fraction. This corresponds to about a 90% water saturation at 100 kPa. In this analysis, it is assumed that the relationship between the average matrix void ratio and the average mean normal effective stress in the soil matrix is the same as the relationship between the void ratio and the mean normal effective stress would be if the soil were fully saturated. Thus the average mean effective stress can be written as

$$\bar{\sigma}'_{sm} = \bar{\sigma}_{sm} - u_w = \sigma_m\left[\frac{1 - \alpha n_g}{1 - n_g}\right] - u_w = \sigma'_m\left[\frac{1 - \alpha n_g}{1 - n_g}\right] + n_g u_w\left[\frac{1 - \alpha}{1 - n_g}\right] \qquad (6.15)$$

and can be seen to be a function of both the pore water pressure u_w, and the mean consolidation stress $(\sigma_m - u_w)$. To illustrate the effect of the presence of the gas voids using the above relationship, a case is considered where the pore water pressure is assumed to be small compared with the value of the total mean stress. For this condition, the last term in the above equation becomes negligible producing

$$\bar{\sigma}'_{sm} = \bar{\sigma}_{sm} - u_w \simeq (\sigma_m - u_w)\left[\frac{1 - \alpha n_g}{1 - n_g}\right] = \sigma'_m\left[\frac{1 - \alpha n_g}{1 - n_g}\right] \qquad (6.16)$$

This approximation would be valid for a test similar in type to test series B, as the pore water pressures are at atmospheric when the consolidation stress is evaluated. However, this approximation would not hold at early time for tests such as those in test series A, where the pore water pressure is of the same order as the total stress. Nevertheless, by assuming that the matrix void ratio is dependent on the matrix mean normal effective stress, then from equation 6.16 it is possible to calculate the mean consolidation stress from a known value of the mean matrix effective stress to produce a theoretical relationship between mean consolidation stress and the matrix void ratio. Figure 6.4 presents the corresponding matrix void ratio versus the average mean consolidation stress for α values of 1.0, 0.8, 0.6 and 0.4. It can be seen that even for this large

range in α values, the effect on the matrix void ratio is minimal. Thus for the test series A and B where α values were found to be around 0.7 and 1.0 respectively, the above analysis illustrates that for all intents and purposes, the relationship between the matrix void ratio, e_w, and the mean consolidation stress, $(\sigma_m - u_w)$, may be treated as unique.

6.3 Determination of the Gas Pressure in a Gassy Soil

It has been widely accepted in the field of unsaturated soils that the pore gas pressure is related to the value of the pore water pressure, the difference between them being known as the capillary pressure, p_c (Collins, 1961), as

$$u_g - u_w = p_c\ (S_w) \tag{6.17}$$

This relationship is well understood as the water and gas co-exist in the same pore structure. It has been shown in this thesis, however, that the gas pressure is not governed by the pore water pressure and furthermore, it appears that the gas pressure is related to the mean total stress. The only restraint on this gas pressure is that there would be a minimum and maximum value of the capillary pressure as the gas must still be held in position by the menisci that exist between the soil particles on the wall of the gas void. Wheeler (1986) presented a detailed analysis of this phenomenon. He stated that the capillary pressure must lie within the bounds

$$-\frac{2T}{R_c} \leq (u_g - u_w) \leq +\frac{2T}{R_c} \tag{6.18}$$

where R_c is the radius of curvature of the gas-water meniscus and T is the surface tension between methane and water (0.07 Pa). Figure 6.5a presents a three-dimensional view of the soil arrangement and analysis used by Wheeler who obtained an upper and lower bound of the capillary pressure as $2/\sqrt{3}R_p$, where R_p is the radius of each particle. Figure 6.5b presents the arrangement of three different sized particles, where the radius of curvature of the gas-water meniscus bounded by these particles is in the order of the smallest. Therefore, as the particles in this soil can be as low as 0.0002 mm (Gardner, 1987), the capillary pressure can be as high as 700 kPa before the water enters the void. Therefore as long as the capillary pressure remains within these bounds, the gas

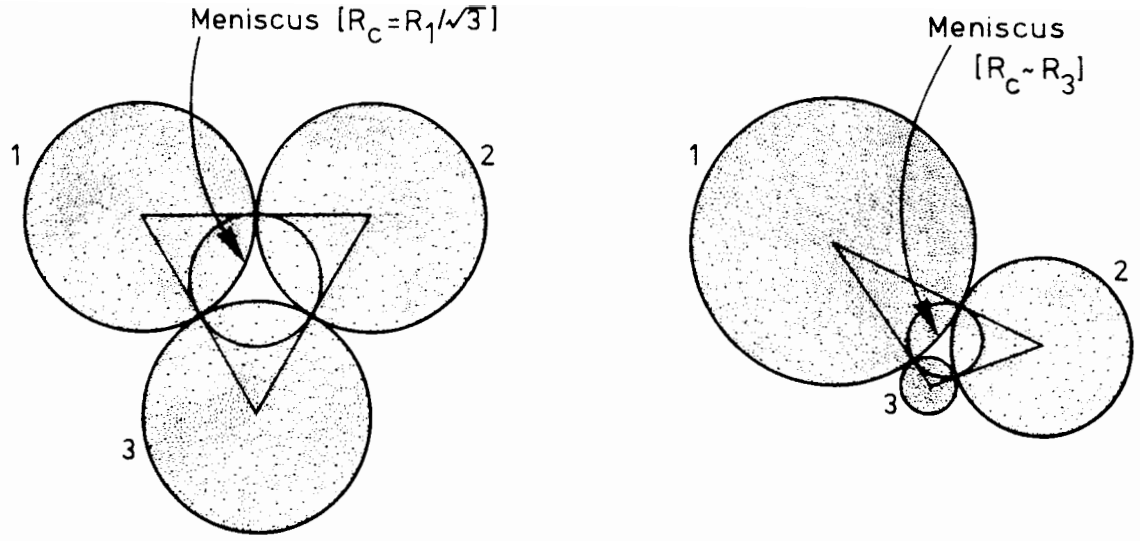

Figure 6.5 Meniscus between 3 soil particles

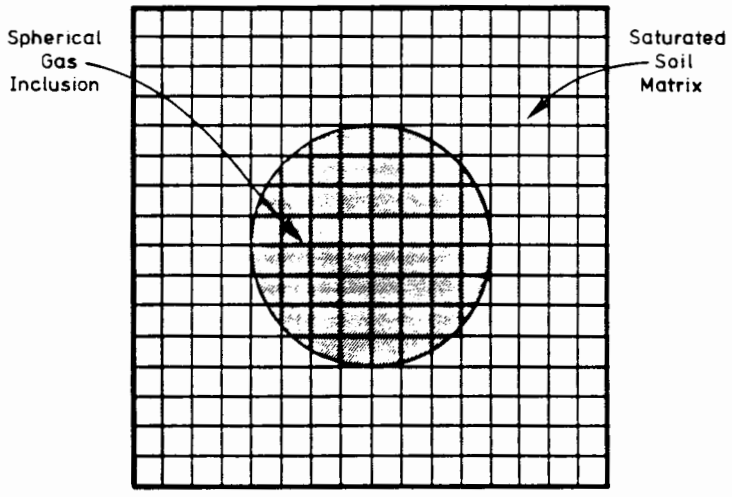

Idealization of Gassy Soil

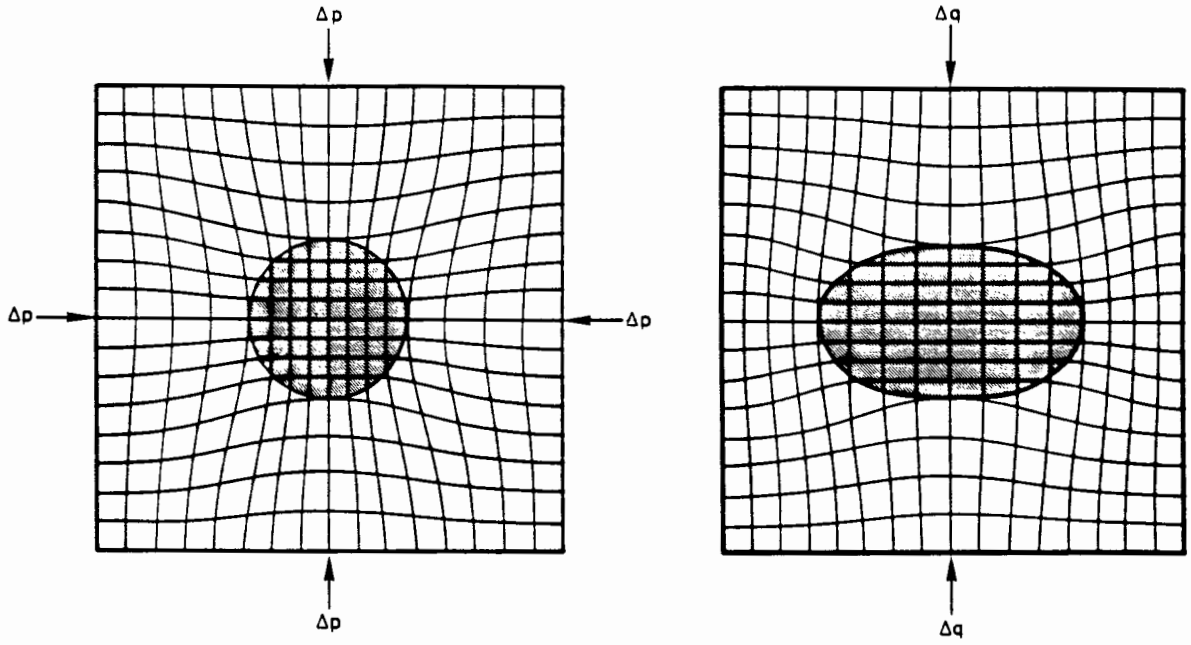

Isotropic Stress Increment

Uniaxial Stress Increment

Figure 6.6 Deformation behaviour of an idealized gassy soil

pressure is not controlled by the pore water pressure. The capillary pressure is simply an independent by-product due to the difference between the gas pressure in the voids and the pore water pressure in the soil matrix.

The relationship between the gas pressure and the total stress is based on the fact that the gas voids appear to act as discrete compressible solids embedded in a saturated soil matrix. The volume change of the gas void will therefore depend on the amount of stress that is transferred through the soil matrix to the void. As an example of this stress transfer, Figure 6.6 represents the deformation behaviour of an individual spherical gas void within a gassy soil sample which is subjected to an increment of undrained isotropic pressure and uniaxial load. It can be seen from this figure that for undrained conditions there is no volume change of the saturated matrix, but that it has to deform to accommodate the changing shape of the gas void. It is therefore clear that the amount of stress that is transferred to the gas will depend upon the ease with which the soil matrix is able to deform in shear.

6.3.1 Single spherical cavity in an infinite elastic-plastic material

The compression of a gas bubble in a saturated matrix may be viewed as the inverse problem of the expansion of a spherical cavity in the same saturated soil matrix. Vesic (1972) considered the problem of a spherical cavity expanded by a uniformly distributed internal pressure p_i. If this pressure is increased, a spherical zone around the cavity will pass into a state of plastic equilibrium. The plastic zone will expand to a radius R_p, where the pressure reaches an ultimate value p_{iu}. Beyond that radius, the rest of the mass remains in a state of elastic equilibrium.

During the compression of a gassy soil, it is the external isotropic stress, p_o, that is increased causing cavity compression. The internal pressure is increased to maintain plastic equilibrium. If it is assumed that the saturated soil is a frictionless material with shear strength s_u, then the theory of Vesic can be used to give the ultimate internal gas pressure p_{iu}, as

$$p_{iu} = p_o - \frac{4}{3}s_u[\log_e(I_r) + 1] \qquad (6.19)$$

where I_r is known as the rigidity index and is the ratio of the shear modulus to the shear strength, G_u/s_u.

6.3.2 Compression of a rigid-perfectly plastic solid sphere

If a gassy soil is idealized as a hollow sphere of a rigid-perfectly plastic material as illustrated in Figure 6.2, then unlike the elastic-plastic theory of Vesic, there will be no deformation until the entire material reaches a plastic state. Figure 6.7 illustrates the plastic stress distribution in a hollow sphere with external isotropic stress p_o and internal gas pressure u_g, as presented by Wheeler (1986). Wheeler also produced an expression for the difference between the external and internal pressures based on a constant ultimate deviator stress q_u, given as

$$|p_o - u_g| \leq F(s_u) = 2q_u \log_e(R/a) = 4s_u \log_e(R/a) \qquad (6.20)$$

where a and R are the internal and external radii of the hollow sphere.

Based on this simple expression for the bounds of the gas pressure, it is possible to produce a qualitative estimate of the behaviour of the gas pressure for the loading - unloading tests as performed in test series A. Figure 6.8 depicts the path of the internal and external isotropic pressures under the same loading conditions as test series A, with the assumption that the shear strength, s_u, remains constant throughout the test.

The test starts when the external pressure at Point A is $F(s_u)$ above the internal pressure at Point G. As the external pressure increases with time along the path A-B, the internal pressure also increases along path G-H. Along these paths the difference between these pressures is maintained at a value of $F(s_u)$. At point B there is no further increase in either internal or external pressure. The external pressure then follows the path B-C until it begins to decrease at point C. The internal pressure also remains constant, only beginning to fall when it is $F(s_u)$ above the value of the external pressure at Point I. The internal pressure then begins to decrease and continues to do so to Point J, when the total stress also becomes constant and follows the path E-F. Again the internal pressure remains $F(s_u)$ above the external pressure and follows the path J-K.

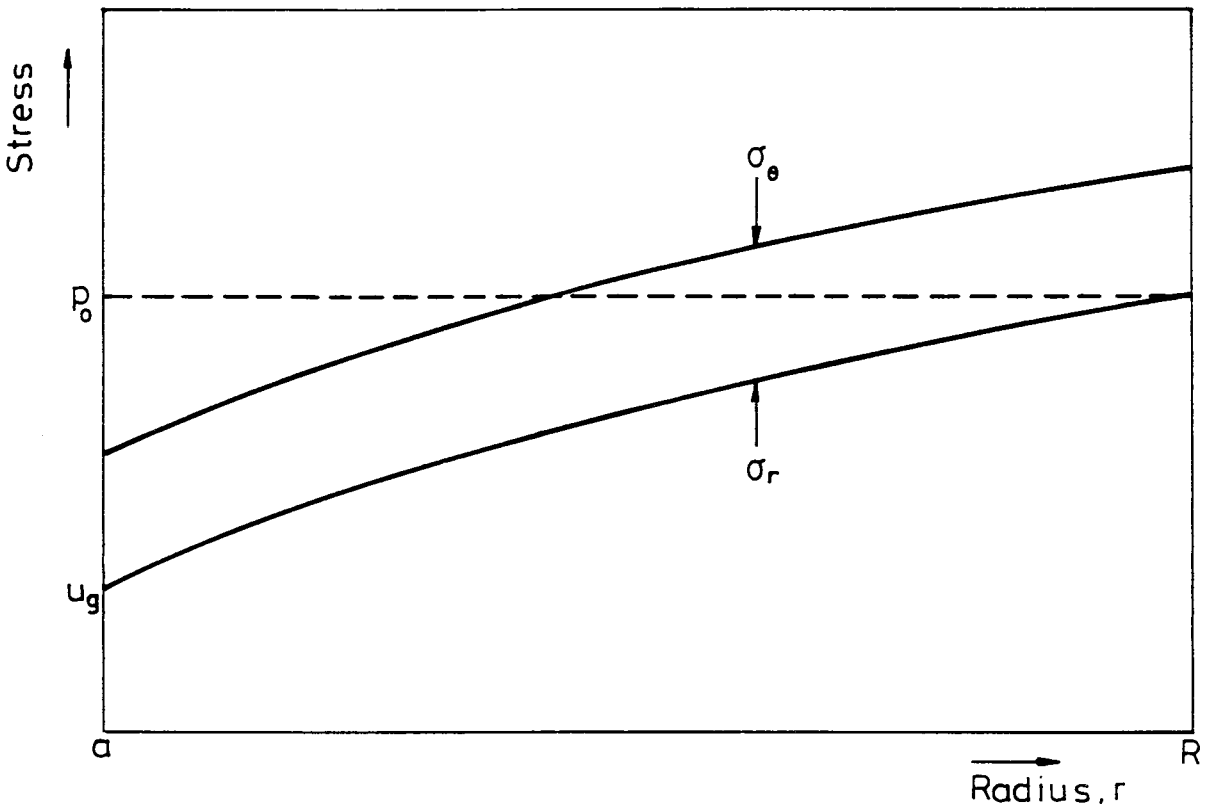

Figure 6.7 Plastic stress distribution within a hollow perfectly plastic sphere (Wheeler, 1986)

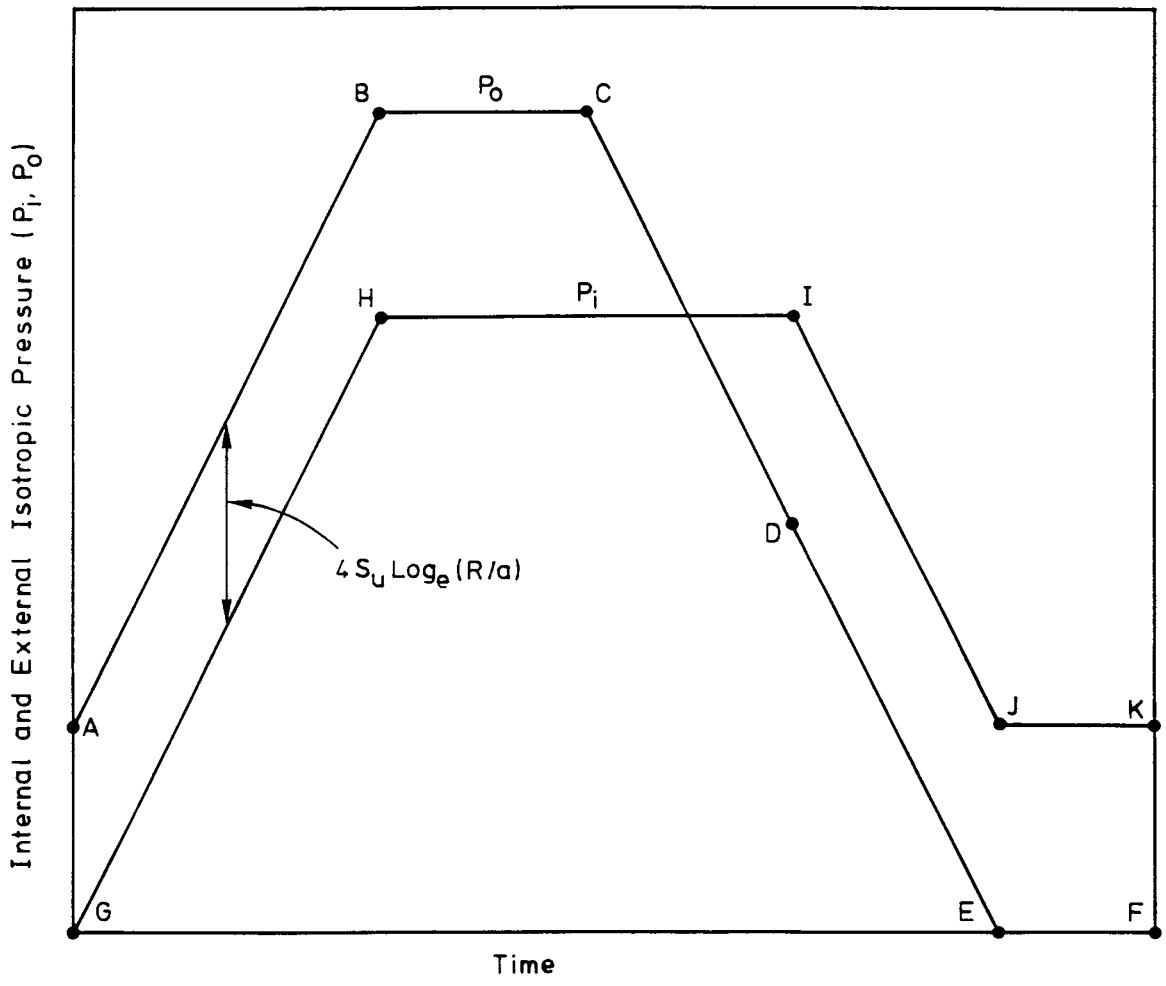

Figure 6.8 Illustration of internal and external pressures for the perfectly plastic hollow sphere model

Although this is a highly simplified model for a gassy soil, it can be seen that the resulting paths of internal and external pressure produce a fair qualitative representation of the value of the experimental gas pressure and total stress as illustrated in Figure 4.8.

In practice, however, the stress that is transferred via the saturated matrix will depend on various factors--including the shear strength and shear modulus of the soil, the shape, volume fraction and compressibility of the gas void and the direction and magnitude of the external applied load. That is

$$| P_o - P_i | \leq (s_u, G_u, A_r, n_g, c_g, \sigma_{ij}) \qquad (6.21)$$

where s_u is the undrained shear strength and G_u is the undrained shear modulus of the saturated soil matrix that surrounds the gas void, A_r is the aspect ratio of the gas void (width/height of void), n_g and c_g are the gas volume fraction (gas porosity) and the gas compressibility respectively, and σ_{ij} is the external stress tensor acting on the sample.

6.4 Stresses Around an Oblate Spheroidal Cavity in an Elastic Material

Although the assumption of a hollow sphere of a perfectly plastic material produces a good qualitative representation of a gassy soil, the difference between the internal and external pressures predicted are much higher than those that are observed. The fact that the soil has a finite shear modulus, and that the external stress is not normally isotropic around a void, means that the difference between the internal and external pressures will be reduced. One of the main causes of the high pressure difference, however, is inherent in the assumption that the gas voids remain spherical. On visual observation of a gassy soil after extrusion from an oedometer cell, it can be seen that the voids are not spherical but are significantly flattened. This shape of a flattened sphere is known as an oblate spheroid (as opposed to an elongated sphere which is known as a prolate spheroid). Although the mechanism of deformation around a gas void is mainly due to plastic flow of the soil, an elastic analysis of the material at least gives an indication of when the soil just begins to fail. Thus in this section, an analysis of the stress distribution around an oblate spheroidal cavity in an elastic material is performed.

Edwards (1951) applied the theory of elasticity to solve the problem of the stress distribution about a prolate spheroidal cavity in a stressed elastic material. Terzaghi and Richart (1952) followed this work by transforming the Edwards equation to apply to an oblate spheroidal cavity. Both methods evaluate the stress field produced by the application of five possible loading cases. However, only case 1 (uniform horizontal biaxial stress) and Case 3 (uniaxial vertical stress) are required to obtain the stress field around a single gas void in a gassy soil subjected to a triaxial stress field.

6.4.1 Analytical solution of the elastic stress field

The analytical solution, presented by Terzaghi and Richart (1952), evaluates the stress components around the ellipsoidal cavity at any point in the surrounding material from a given oblate spheroidal coordinate. Appendix B sets out the step-by-step transformation of this coordinate system to one of axisymmetric coordinates (r,z), and presents the stress calculations for a uniform uniaxial stress field in the z direction and for a uniform horizontal biaxial stress field in the r direction. These solutions may be combined using the principle of superposition to obtain the stress components at any point in the elastic medium which is subjected to any triaxial stress field.

6.4.2 Programming and verification of solution

The Edwards equations as presented in Appendix B were programmed in FORTRAN producing a working interactive computer code named OBLATE. This code produces both numerical and graphical output of the stress invariants around an oblate spheroidal cavity due to an external triaxial stress field. The input of the program is simply the aspect ratio of the cavity, the external radial and vertical stress field, and the coordinates at which the stresses are required.

The computer code was first verified successfully with the results presented by Terzaghi and Richart (1952) in which values of the stresses were computed along both the vertical and radial axes outside an oblate spheroid of aspect ratio 5.0 under a triaxial loading condition. A further comparison was then made with the solution of Goodier (1933), in which the stress distribution due

to a uniform uniaxial load was evaluated about a spherical cavity in an elastic medium. The comparisons between both solutions were identical.

6.4.3 The stress field around an oblate spheroidal cavity

After the verification of OBLATE it was then possible to use the program to view the stress distribution around an oblate spheroidal cavity in order to understand further the stress behaviour and evaluate the areas of high stress concentration. Various permutations of aspect ratio, Poisson's ratio and triaxial stress application were input to understand the stress field behaviour. As an example of the use of the program, Figure 6.9 illustrates the (a) mean normal stress, (b) octahedral shear stress, (c) radial stress and (d) tangential stress in the vicinity of one oblate spheroidal cavity of aspect ratio of four, in a soil matrix of Poisson's ratio 0.5, caused by the application of a uniform isotropic load. From these four figures it can be seen that the highest stress concentrations occur at the equator of the cavity. To reinforce this further, both the mean normal stress and the octahedral shear stress were evaluated along the radial axis for cavities of a range of values of aspect ratio under isotropic conditions--as illustrated in Figures 6.10 and 6.11 respectively. In addition, the program OBLATE was able to evaluate the relationship between the tangential stress at the equator and on the roof of a spheroidal cavity versus the aspect ratio as illustrated in Figure 6.12.

6.4.4 Consequences of stress concentrations around a spheroidal cavity

On the basis of this elastic analysis it is clear that there is a significant increase in stress concentration at the equator of the spheroidal inclusion as the aspect ratio increases. Even under isotropic loading conditions, it can be seen from Figure 6.12 that the tangential shear stress increases seven times by changing the aspect ratio from 1 to 5. Consequently, although this analysis does not evaluate the pressure transferred to the gas in the void, it does illustrate that the soil will enter into a plastic state of stress around the equator of the void at a much lower external stress than for a spherical cavity. Figure 6.13 presents a possible scenario of the undrained

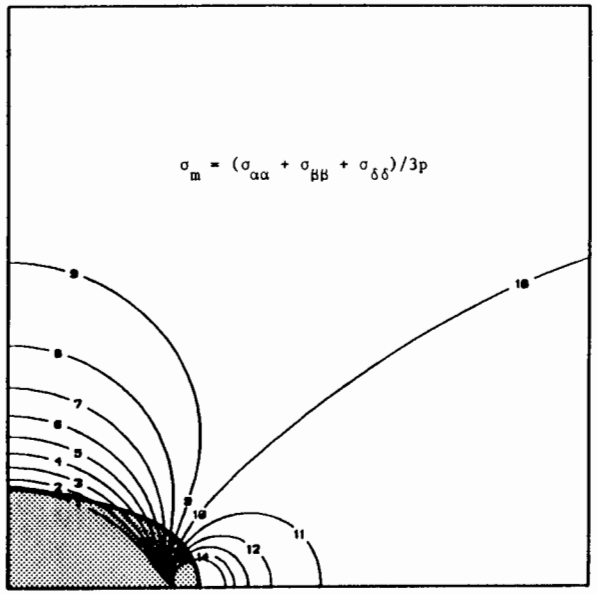

CONTOUR KEY	
1	0.585E+00
2	0.631E+00
3	0.677E+00
4	0.724E+00
5	0.770E+00
6	0.816E+00
7	0.862E+00
8	0.908E+00
9	0.955E+00
10	0.100E+01
11	0.105E+01
12	0.109E+01
13	0.114E+01
14	0.119E+01
15	0.123E+01
16	0.128E+01
17	0.132E+01
18	0.137E+01
19	0.142E+01
20	0.146E+01

(a) Normalized mean normal stress around ellipsoidal cavity, aspect ratio = 2.

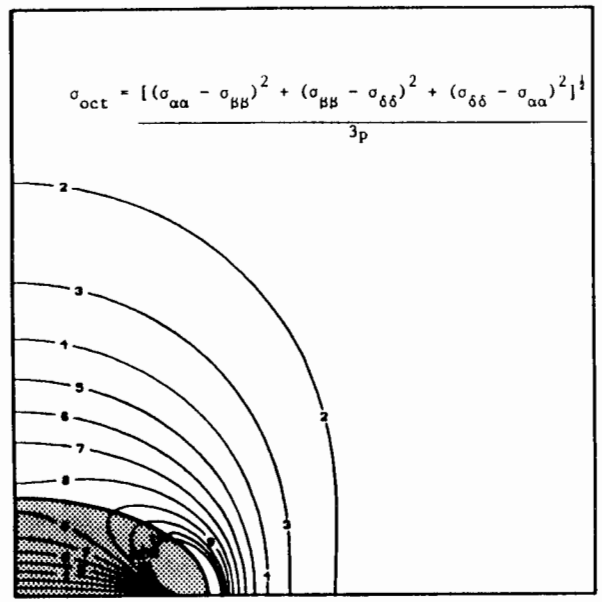

CONTOUR KEY	
1	0.671E-02
2	0.640E-01
3	0.121E+00
4	0.178E+00
5	0.236E+00
6	0.293E+00
7	0.350E+00
8	0.407E+00
9	0.465E+00
10	0.522E+00
11	0.579E+00
12	0.637E+00
13	0.694E+00
14	0.751E+00
15	0.808E+00
16	0.866E+00
17	0.923E+00
18	0.980E+00
19	0.104E+01
20	0.109E+01

(b) Normalized octahedral shear stress around ellipsoidal cavity, (a/c =2.)

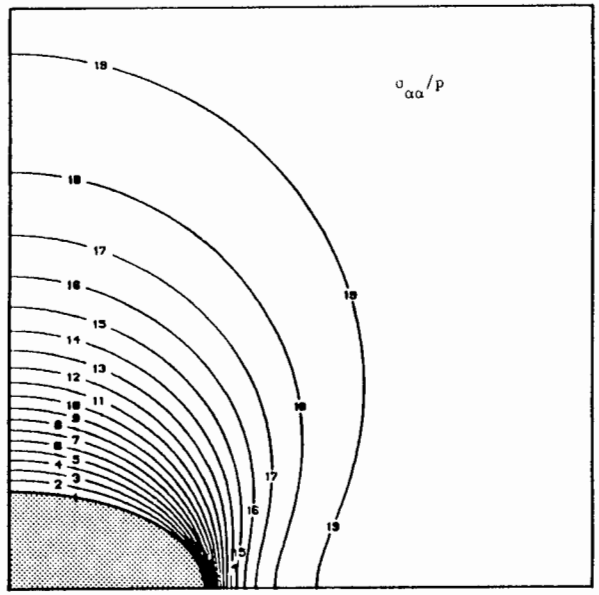

CONTOUR KEY	
1	0.220E-12
2	0.523E-01
3	0.105E+00
4	0.157E+00
5	0.209E+00
6	0.262E+00
7	0.314E+00
8	0.366E+00
9	0.419E+00
10	0.471E+00
11	0.523E+00
12	0.575E+00
13	0.628E+00
14	0.680E+00
15	0.732E+00
16	0.785E+00
17	0.837E+00
18	0.889E+00
19	0.942E+00
20	0.994E+00

(c) Normalized radial stress around ellipsoidal cavity, aspect ratio = 2.

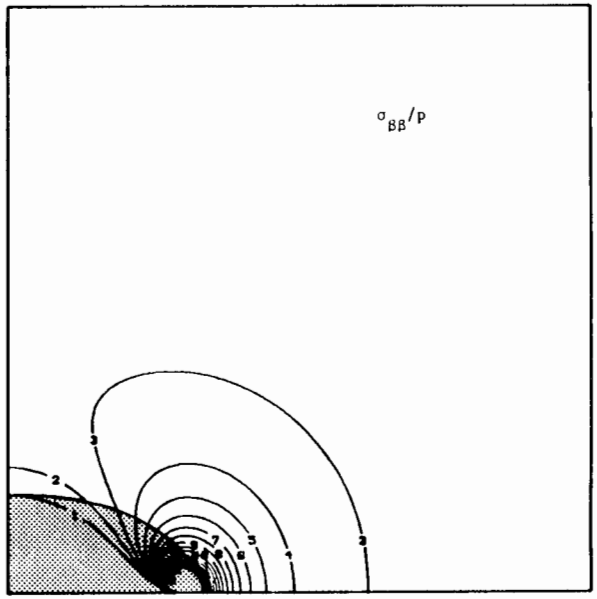

CONTOUR KEY	
1	0.878E+00
2	0.970E+00
3	0.106E+01
4	0.115E+01
5	0.125E+01
6	0.134E+01
7	0.143E+01
8	0.152E+01
9	0.162E+01
10	0.171E+01
11	0.180E+01
12	0.189E+01
13	0.199E+01
14	0.208E+01
15	0.217E+01
16	0.226E+01
17	0.236E+01
18	0.245E+01
19	0.254E+01
20	0.263E+01

(d) Normalized tangential stress around ellipsoidal cavity, aspect ratio = 2.

oblate spheroidal cavity

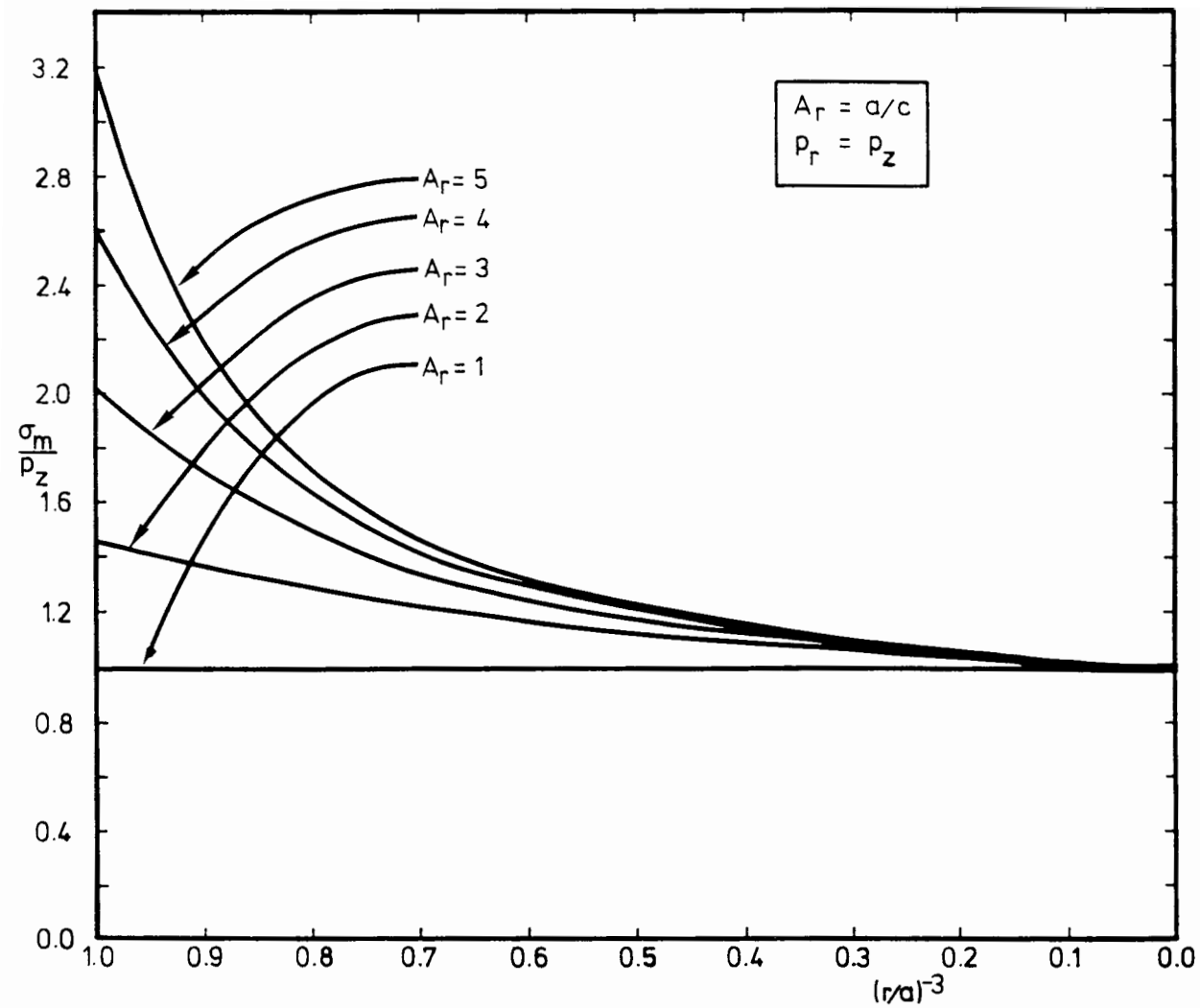

Figure 6.10 Mean normal stress along the radial axis of a spheroidal cavity

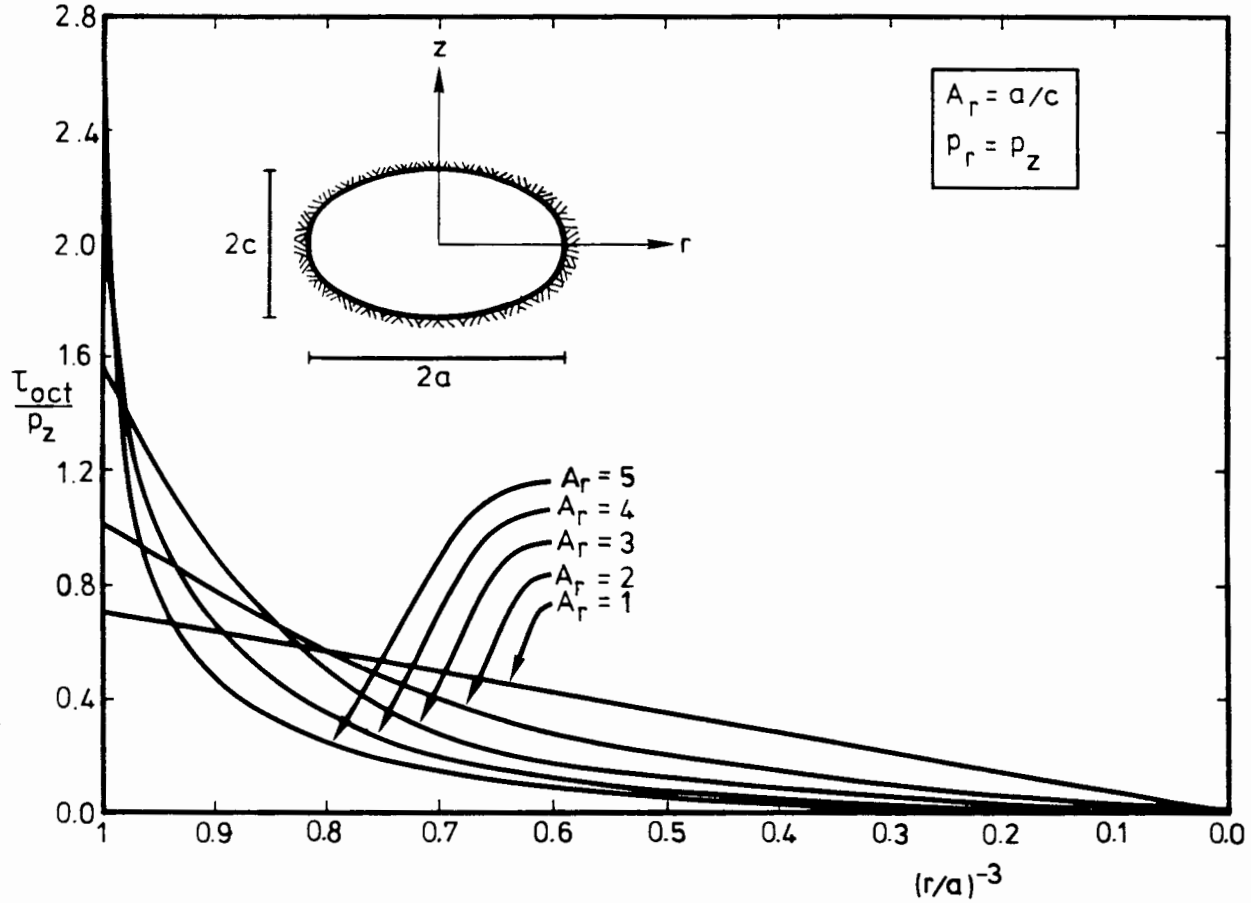

Figure 6.11 Octahedral shear stress along the radial axis of a spheroidal cavity

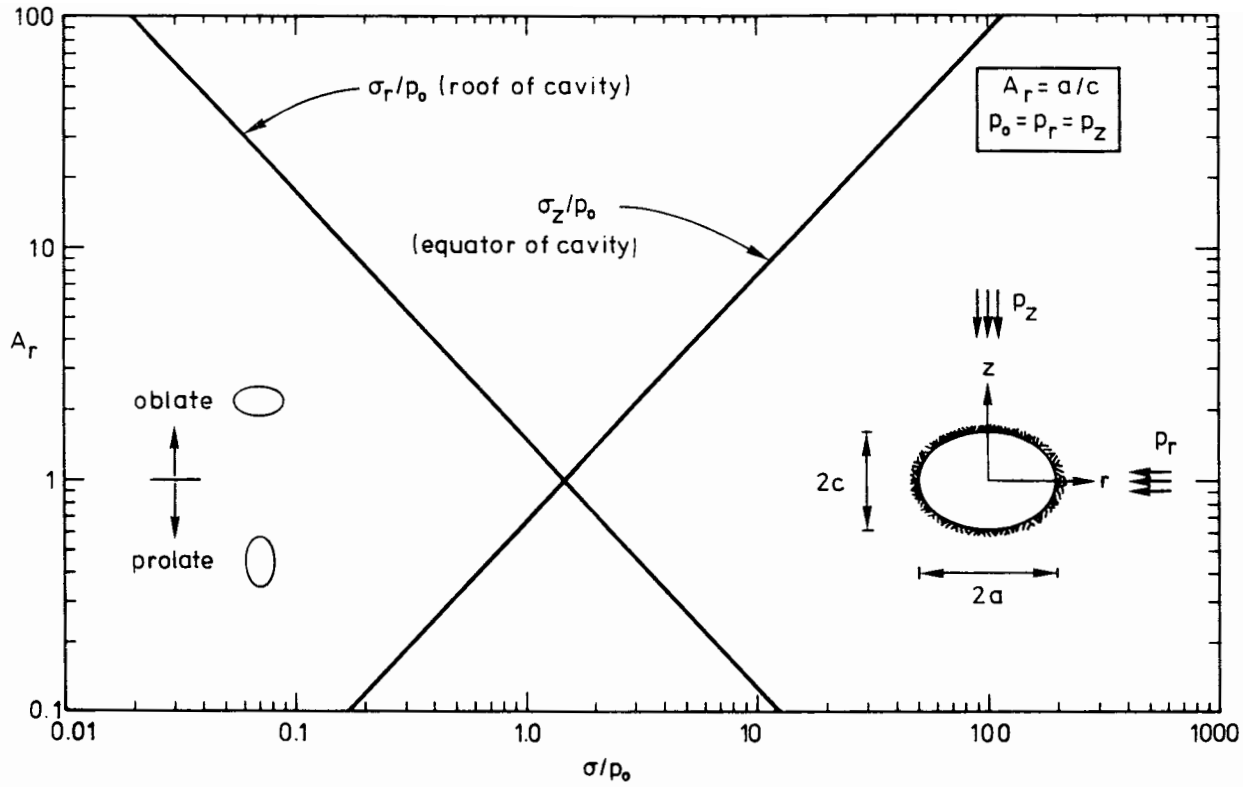

Figure 6.12 Tangential stress at the equator and roof of a spheroidal cavity versus aspect ratio

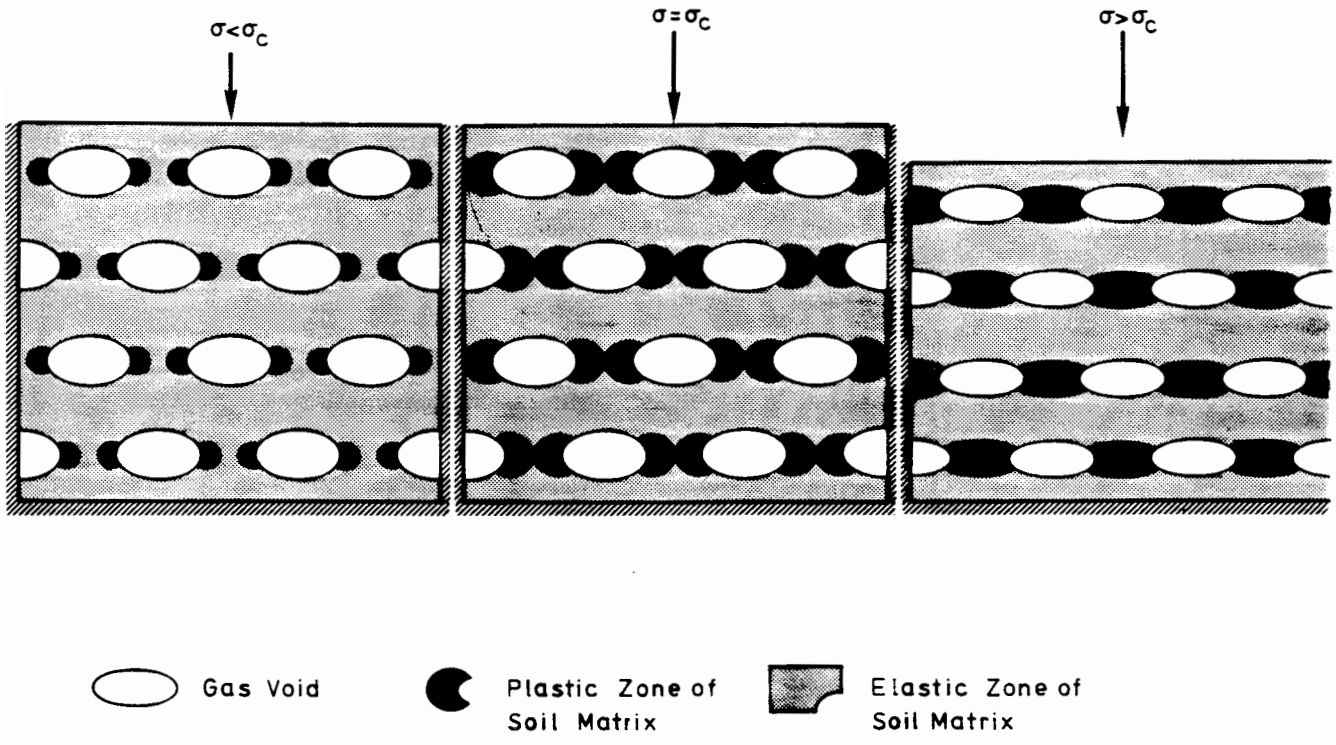

Figure 6.13 Possible failure mechanism scenario for gassy soil

compression behaviour of a soil containing a number of discrete spheroidal cavities embedded in a perfectly plastic soil matrix. Figure 6.13a presents the soil under a vertical application of load in an oedometer cell under undrained conditions. At this stage there is sufficient load to produce a small plastic zone around each void. However, no overall settlement has taken place as the remainder of the soil is assumed to be rigid outside the plastic zone. Figure 6.13b represents the critical loading stage when the plastic zones are just connecting. Nevertheless, there is still no settlement up to this point. Figure 6.13c then presents the case after the plastic zones have connected, producing a mechanism which will then deform plastically to allow load to be transferred to the gas resulting in an overall settlement of the soil.

6.5 Introduction of the Double Compressibility Model

The experimental and numerical results that have been presented in this thesis have illustrated clearly that there are two independent modes of deformation of a gassy soil. The first mode of deformation is due to the local shear behaviour and the compression and dissolution of the gas which accompany changes in total stress. The second mode of deformation is due to the overall drainage or shear behaviour of the saturated matrix and is caused by changes in consolidation stress. The gassy soil appears therefore, to have a double mode of compressibility or deformation. Accordingly, the model used to describe such behaviour has been termed the "double compressibility model".

6.5.1 Definition of phase strains

The first mode of compression, caused by the volume change of the gas phase from changes in total stress, may be written in terms of the gas void ratio as

$$\Delta e_g = \Delta v_g / v_s = F(\sigma) \qquad (6.22)$$

where e_g is the gas void ratio, v_g is the gas volume and v_s is the volume of the solid grains that are present in a given volume of gassy soil. Thus any increment of total stress will cause a deformation of the soil which may be translated into a soil strain. Figure 6.14 depicts the strain caused by changes in total stress. To illustrate the components of strain, one-dimensional

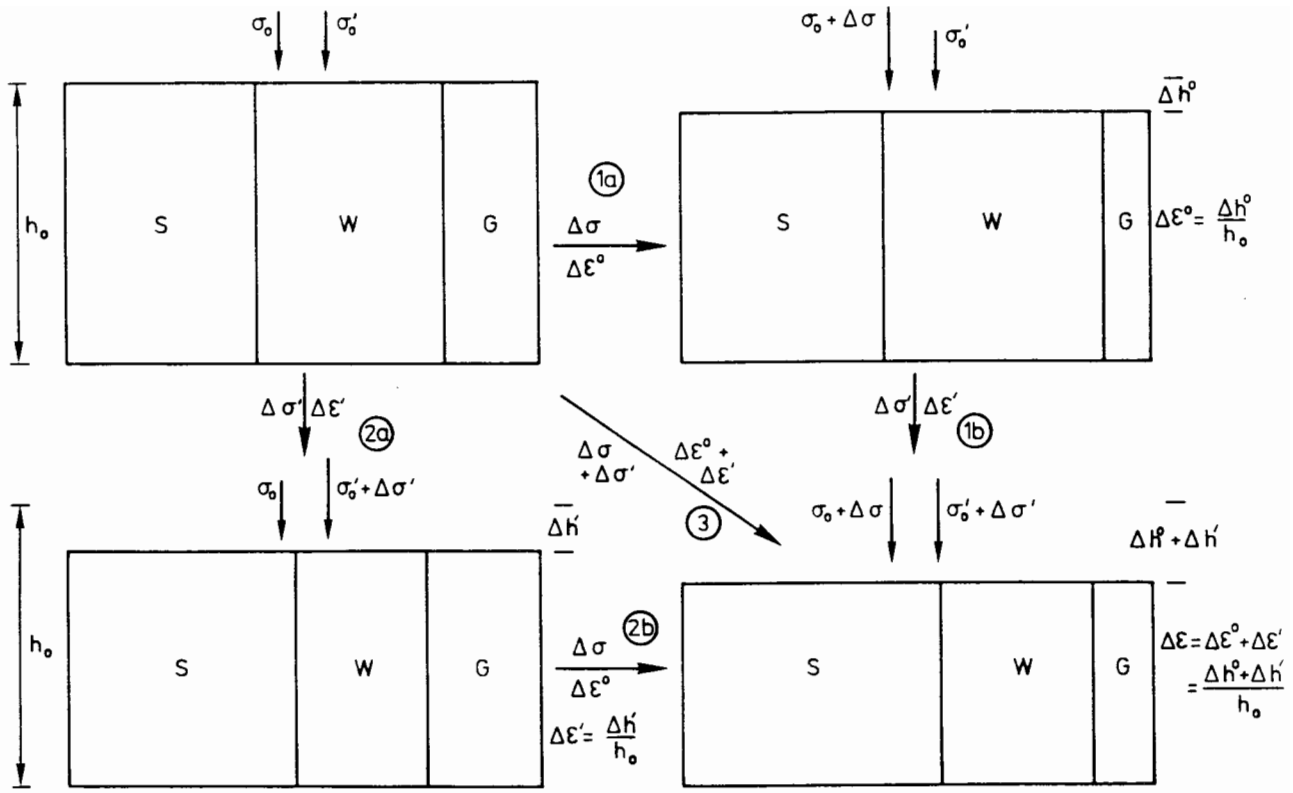

Figure 6.14 Illustration of gas and soil matrix strains

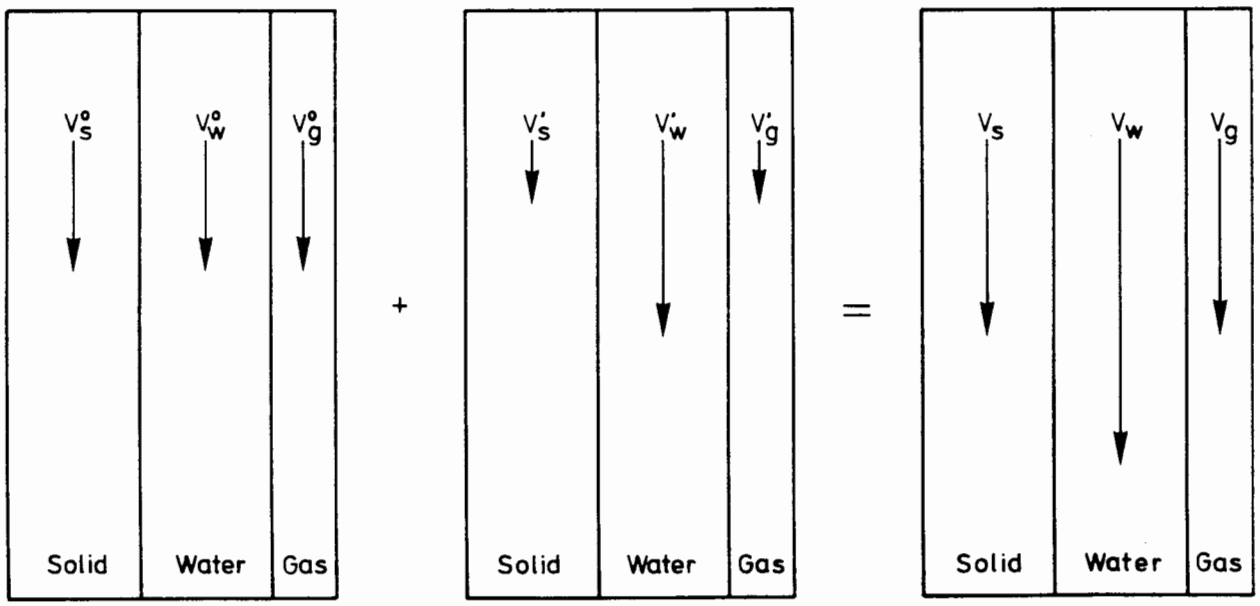

Figure 6.15 Illustration of phase velocities

deformation only has been considered. Thus the strain caused by the deformation of the gas--signified by the supercript °--can be written as

$$\varepsilon^{\circ} = \Delta h^{\circ}/h_o = \sigma^{\circ}/E^{\circ} \qquad (6.23)$$

Similarly, the deformation of the saturated matrix due to changes in consolidation stress--signified by the superscript '--has been found to obey the relationship

$$e_w = v_w/v_s = F(\sigma - u_w) = F(\sigma') \qquad (6.24)$$

where e_w is the matrix void ratio and v_w is the matrix volume in a specified total sample volume. Once again, the deformation due to changes in consolidation stress can be represented in terms of soil matrix strain as depicted in Figure 6.14 and can be written as

$$\varepsilon' = \Delta h'/h_o = \sigma'/E' \qquad (6.25)$$

Therefore if a gassy soil is subjected to changes in both total and consolidation stresses, both gas and matrix strains will occur. Figure 6.14 presents three paths in which this behaviour can be viewed--all leading to the same final result. If there is an increase first in total stress under undrained conditions, there will be a change in the gas volume causing an overall strain represented by stage 1a. If this is followed by the drainage of the pore water causing increasing consolidation stresses, stage 1b will result.

It is also theoretically possible first to apply a suction pressure to the soil--producing consolidation stresses--with no increase in total stress, thus following stage 2a. If this is succeeded by an increase in total stress, stage 2b will result, ending up at the same point as when following the previous procedure.

Alternatively, if the total stress is applied gradually with simultaneous drainage of the sample, both total and consolidation stresses are applied--thus producing stage 3 which will again end up at the same point as the other procedures.

Consequently, the total strain caused by the combined loss of pore water and gas volume can then be added to give

$$\Delta\varepsilon^{\circ} + \Delta\varepsilon' = \frac{\Delta h^{\circ}}{h_o} + \frac{\Delta h'}{h_o} = \frac{\Delta h}{h_o} = \Delta\varepsilon \qquad (6.26)$$

To illustrate the behaviour of the double compressibility model in multi-dimensions, the initial approach undertaken assumes an elastic stress-strain relationship for both the soil matrix and gas phases. Although it is fully appreciated that in practice both the soil matrix and gas voids exhibit plastic deformation behaviour, at this stage in the development of the combined governing equations it is more effective to treat each phase as elastic so that the effect of a soil having two apparent moduli can be fully realized. In addition, if a plastic approach was undertaken at this stage, many of the parameters required for such an analysis would be difficult to evaluate and some would no longer be constants so that a more sophisticated plastic model would be necessary. In this thesis therefore, the development has been restricted to an elastic model for which the general three-dimensional form of the constitutive stress-strain equations for a double compressibility material can be written as

$$\sigma_{ij} = 2G^{\circ}\,\varepsilon^{\circ}_{ij} + \lambda^{\circ}\,\varepsilon^{\circ}_{kk}\,\delta_{ij} \qquad i,j = 1,2,3 \qquad (6.27)$$

for the gas phase, and

$$\sigma'_{ij} = 2G'\,\varepsilon'_{ij} + \lambda'\,\varepsilon'_{kk}\,\delta_{ij} \qquad i,j = 1,2,3 \qquad (6.28)$$

for the matrix phase. It is important to note that ε°_{ij} are the components of strain caused by the deformation of the gas, and ε'_{ij} are the components of strain caused by the deformation of the saturated matrix.

6.5.2 Definition of phase velocities

During the later derivation of the governing flow equations in a gassy soil, it is necessary to understand the roles of the separate phase velocities. Each of these velocities has two components, one due to the change in the volume of gas (denoted by superscript °) and one due to the change in the volume of water (denoted by superscript ′). The total phase velocity is the sum of the two component velocities for each phase. Figure 6.15 illustrates the components of velocity for each phase. The first section of the figure illustrates the phase velocities resulting solely from the changes in gas volume, caused by both compression and dissolution of the gas. Under these conditions all the phases "stick together" and consequently there will be no relative flow between each phase. Thus all velocities are the same. This may be written as

$$V_s^\circ = V_w^\circ = V_g^\circ \tag{6.29}$$

The second section of Figure 6.15 illustrates the phase velocities when there is no change in gas volume, but when there is a loss in water volume (normally due to flow of water from the soil). Under this condition the gas phase will still "stick" to the solid phase to give

$$V'_s = V'_g \tag{6.30}$$

The water velocity V'_w, however, will have a different value from the above due to the water flow. The difference between the velocities in this instance is related to the Darcy velocity, which may be defined as

$$W = n_w(V'_w - V'_s) \tag{6.31}$$

The third section of Figure 6.15 illustrates the total velocity of each phase for a change in both water and gas velocity. The total phase velocity is simply the sum of the two velocity components and can be written as

$$V_s = V_g = V_s^\circ + V'_s = V_g^\circ + V'_g \tag{6.32}$$

for the solid and gas phases, and

$$V_w = V_w^\circ + V'_w \tag{6.33}$$

for the water phase. In addition to the above definitions, the Darcy velocity can now be written as

$$W = n_w(V_w - V_s) = n_w(V'_w - V'_s) \tag{6.34}$$

6.6 Theoretical Evaluation of the Elastic Moduli of a Gassy Soil Based on the Double Compressibility Model

The one-dimensional consolidation tests on gassy soil samples illustrated that the soil matrix behaviour appeared to be governed by the difference between total stress and pore water pressure. The volume change of gas, however, appeared to be related to the total applied stress. In fact, the assumption that the gas pressure equals the total stress leads to very good predictions of both the drained and undrained volume change behaviour of the gas. Although it was not clear from the experiments if the total stress in question was the

vertical or mean stress, later theoretical work illustrated that the gas is most likely to be dominated by the mean total stress.

6.6.1 Mechanism of displacement

During undrained compression of a gassy soil, the volume of the saturated soil matrix remains constant and therefore, any volume change of the gas must be accompanied by a local deformation of the saturated matrix to accommodate the gas volume change as already discussed earlier and illustrated in Figure 6.6. As this saturated matrix distortion must be caused by local plastic failure of the soil, it cannot be assumed that the local shear modulus around the gas void is equal to the shear modulus of the soil matrix evaluated from a triaxial test.

In the following analysis, the gassy soil is treated as a double compressibility material as depicted in Figure 6.14 in which the total displacements are obtained from the sum of the displacement of the saturated matrix and the displacement of the gas.

6.6.2 Undrained bulk modulus

During the undrained compression of a gassy soil--as the soil grains and pore water are virtually incompressible--the change in volume is solely due to the volume change of the gas. This volume change of gas may be caused both by compression of the gas and by the dissolution of the gas into the pore water. Therefore, if the simple assumption is made that the gas pressure is equal to the mean total stress, then from Boyle's law, the instantaneous or short term bulk compressibility of a gassy soil of gas fraction, n_g, is

$$c_{us} = 1/K_{us} = n_g/(u_g + u_a) = n_g/(\sigma_m + u_a) \qquad (6.35)$$

and the long term undrained bulk compressibility from a combination of Boyle's and Henry's laws is

$$c_{ul} = 1/K_{ul} = (n_g + Hn_w)/(u_g + u_a) = (n_g + Hn_w)/(\sigma_m + u_a) \qquad (6.36)$$

where c_{us} and c_{ul} are the short and long term undrained compressibility respectively (not to be confused with c_u which is sometimes used as the notation for undrained shear strength), K_{us} and K_{ul} are the short term and long term

undrained moduli, H is Henry's coefficient of solubility, σ_m is the mean total stress and u_a is the atmospheric pressure.

Thus from the above equations, a theoretical plot of $(\sigma_m + u_a)/K_u$ versus the gas volume fraction yields a straight line. Figure 6.16 illustrates the results of Wheeler (1986) plotted on such axes. Superimposed on these results are the short term solution (S.T.S.) for H = 0, and the long term solution (L.T.S.) for H = 0.0333 for the gassy soil compressibility. In order to compare the bulk moduli, Figure 6.17 presents the values of normalized bulk modulus plotted against the initial gas fraction. These results are superimposed on the short term and long term theoretical values of bulk moduli. It can be seen that although a very simple definition of gas pressure is used, a remarkably good representation of bulk modulus has been achieved.

6.6.3 Undrained shear modulus

In the analysis of the one-dimensional consolidation behaviour of gassy soils, the concept of a double compressibility model was introduced. This may be extended to volumetric strains as

$$\varepsilon_{vt} = \frac{\Delta v}{v_{to}}t = \frac{\Delta v}{v_{to}}g + \frac{\Delta v}{v_{to}}w = \varepsilon_{vg} + \varepsilon_{vw} \qquad (6.37)$$

where ε_{vt} is the total volumetric strain and v_{to} is the initial total volume of the sample. The strain components ε_{vg} and ε_{vw} are caused by changes in gas volume and water volume respectively. These strain components may also be extended to vertical and radial strains to give

$$\varepsilon_{zt} = \frac{\Delta L}{L_{zo}}zt = \frac{\Delta L}{L_{zo}}zg + \frac{\Delta L}{L_{zo}}zw = \varepsilon_{zg} + \varepsilon_{zw} \qquad (6.38)$$

for the vertical direction, and

$$\varepsilon_{rt} = \frac{\Delta L}{L_{ro}}rt = \frac{\Delta L}{L_{ro}}rg + \frac{\Delta L}{L_{ro}}rw = \varepsilon_{rg} + \varepsilon_{rw} \qquad (6.39)$$

for the radial direction, where L_{ro} and L_{zo} are the initial width and height of an arbitrary sample.

Values of the total vertical and radial strains can be evaluated from the values of bulk moduli and shear moduli of gassy soil as presented by Wheeler (1986). The definitions of bulk modulus and shear modulus used by Wheeler are

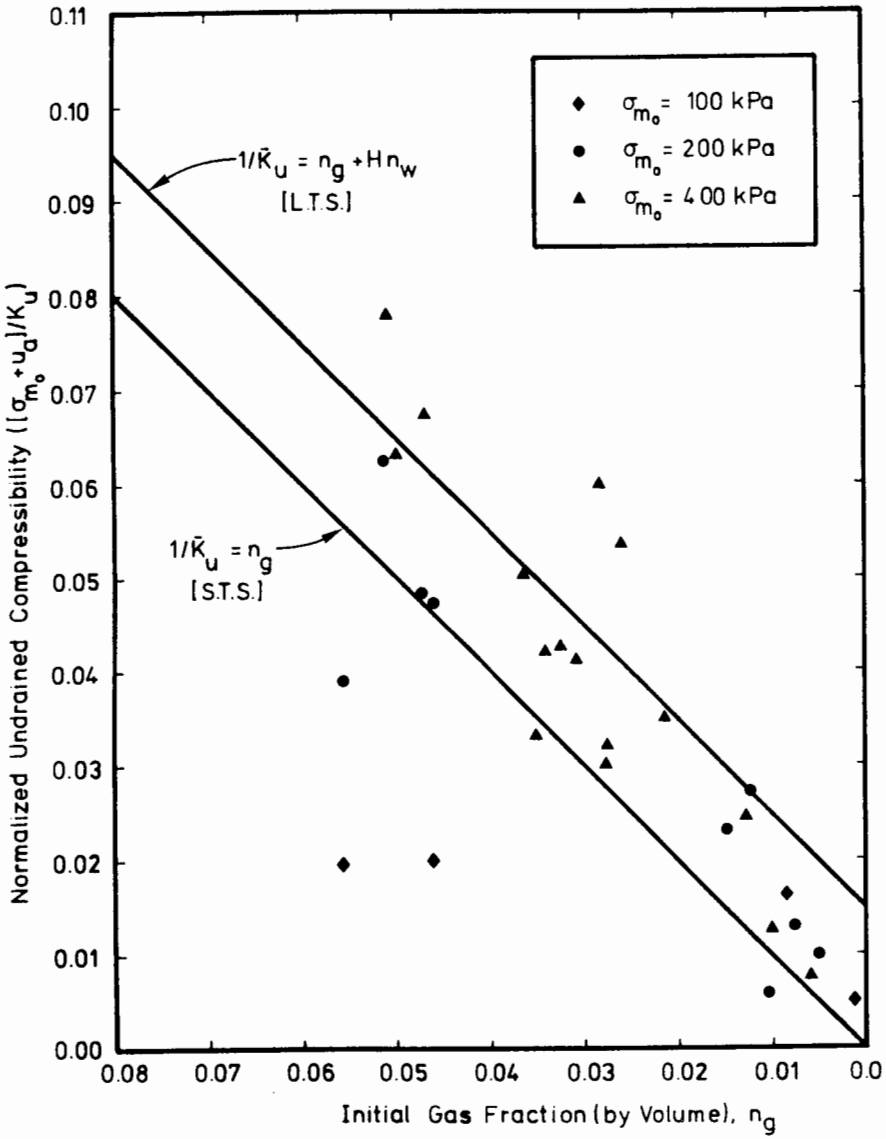

Figure 6.16 Comparison of theoretical undrained bulk compressibility with the experimental results of Wheeler (1986)

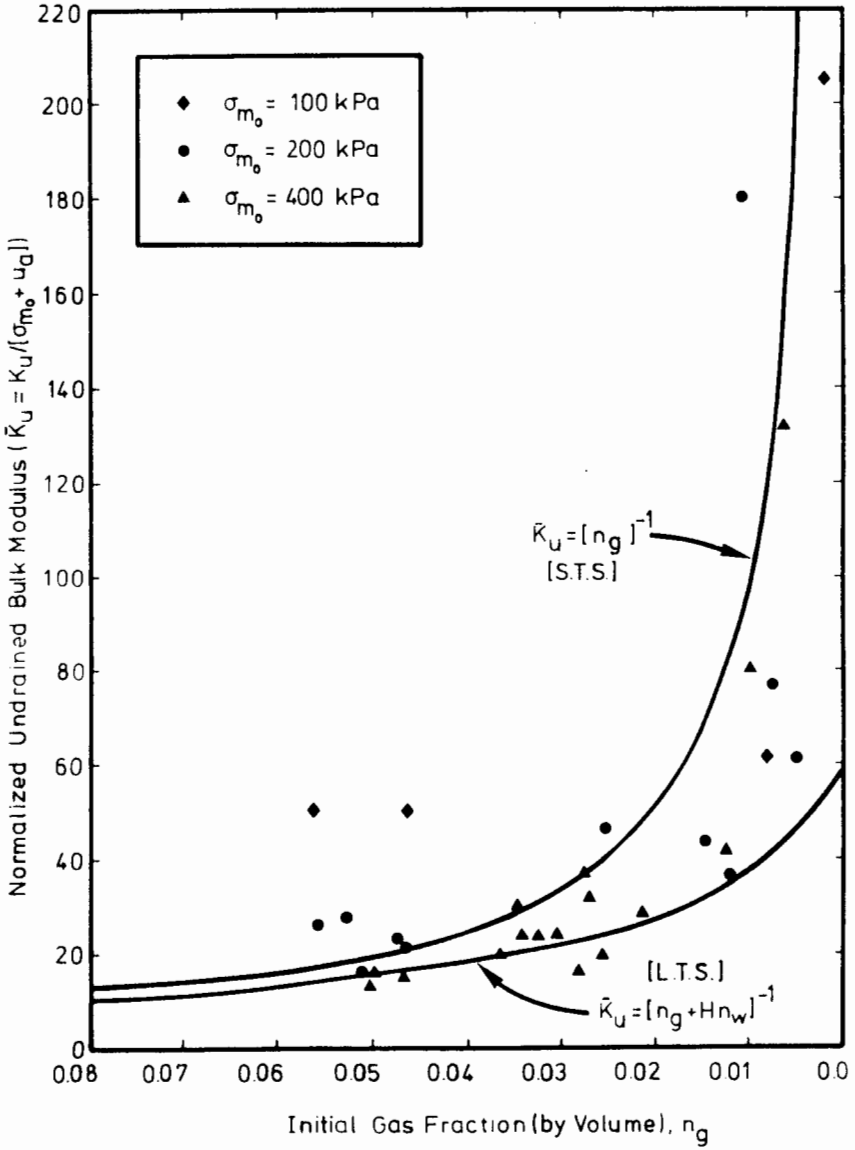

Figure 6.17 Comparison of theoretical undrained bulk modulus with the experimental results of Wheeler (1986)

$$K_u = \frac{\Delta p}{\Delta \varepsilon_v} \quad \text{and} \quad G_u = \frac{\Delta q}{2(\Delta \varepsilon_z - \Delta \varepsilon_r)} \tag{6.40}$$

where p is the mean total stress and q is the deviator stress. The above two equations may be rearranged to evaluate the axial and radial strains as

$$\frac{2\Delta \varepsilon_1}{\Delta q} = \frac{2}{9}\left[\frac{1}{K_u} + \frac{3}{G_u}\right] \tag{6.41}$$

and

$$\frac{2\Delta \varepsilon_3}{\Delta q} = \frac{1}{9}\left[\frac{2}{K_u} - \frac{3}{G_u}\right] \tag{6.42}$$

for the stress path

$$\Delta p = \Delta q/3 \tag{6.43}$$

where subscripts 1 and 3 refer to the z and r directions respectively. Therefore, by combining the above equation with the double compressibility model equations 6.37 and 6.38, the inverse of the total shear modulus can be seen to consist of two components given by

$$\frac{1}{G_u} = \frac{2}{\Delta q}[\Delta \varepsilon_1 - \Delta \varepsilon_3] = \frac{2}{\Delta q}[(\Delta \varepsilon_{g1} - \Delta \varepsilon_{g3}) + (\Delta \varepsilon_{w1} - \Delta \varepsilon_{w3})] = \frac{1}{G_{ug}} + \frac{1}{G_{uw}} \tag{6.44}$$

Figure 6.18 illustrates the inverse of Wheeler's experimental shear moduli, over the deviator stress range 0 to $q_{max}/2$, plotted against the initial gas volume fraction, together with a least square best fit through these points. It can be seen from this figure that it takes the same form as equation 6.44 in which the inverse of the shear modulus is related to the deformation behaviour of the saturated matrix, $[1/G'_u = 2(\Delta \varepsilon'_1 - \Delta \varepsilon'_3)/\Delta q]$--which is given a constant value over this saturation range--and by the deformation behaviour of the gas voids, $[1/G^\circ_u = 2(\Delta \varepsilon^\circ_1 - \Delta \varepsilon^\circ_3)/\Delta q]$--which is seen to increase with increasing gas content.

6.6.4 Evaluation of Poisson's ratio

For an elastic material, the shear modulus can be written in terms of the bulk modulus and Poisson's ratio as

$$G_u = \frac{3K_u}{2}\left(\frac{1 - 2\nu}{1 + \nu}\right) \tag{6.45}$$

Various analytical techniques to evaluate the Poisson's ratio of a gassy soil were attempted. The critical parameter required in the analysis, however, is the local shear modulus surrounding the gas void. This shear modulus, due to

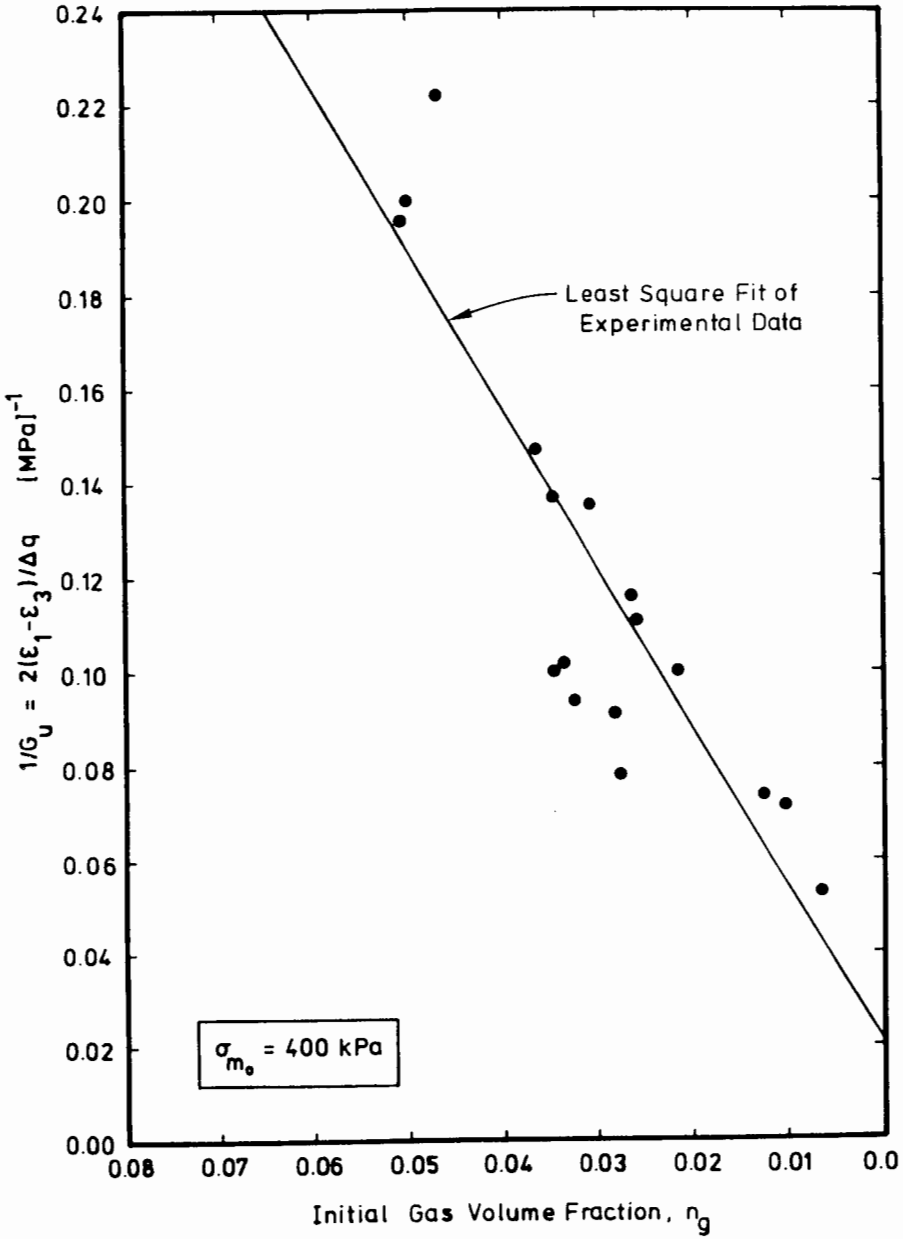

Figure 6.18 Best fit straight line through the inverse of shear modulus from the tests of Wheeler, 1986

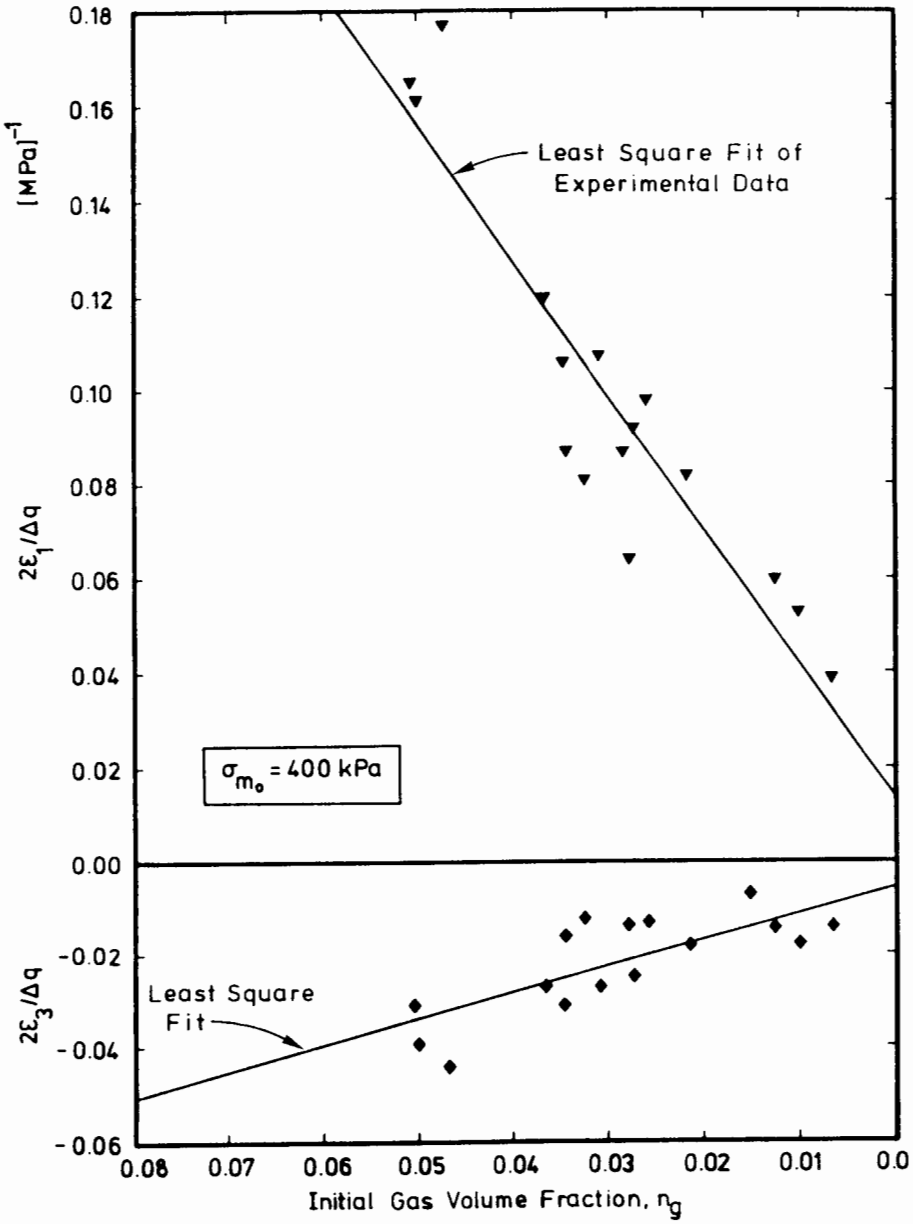

Figure 6.19 Best fit straight lines through the axial and radial strains from the tests of Wheeler, 1986

the high local shear strains, would be very much lower than the global shear modulus of a saturated sample. Consequently, all theoretical analyses produced overall moduli that were far higher than those observed. Therefore, to obtain the shear modulus from equation 6.45, it was decided to combine the theoretical value of bulk modulus--as presented in equations 6.34 and 6.35--with an empirical value of Poisson's ratio. Thus for uniaxial compression,

$$\Delta\varepsilon_1 = \Delta\sigma_1/E \quad ; \quad \Delta\varepsilon_3 = -\nu\Delta\sigma_1/E \tag{6.46}$$

and

$$\nu = -\Delta\varepsilon_3/\Delta\varepsilon_1 \tag{6.47}$$

Furthermore, by fitting a least square straight line through both the values of the radial and axial strain versus gas volume fraction--as shown in Figure 6.19--values of ε_{g1} and ε_{g3} can be evaluated at any gas volume fraction from which a value of $\nu_g = 0.21$ is obtained from equation 6.47. Substitution of this value of Poisson's ratio into equation 6.44 produces $G_u = 0.7189\ K_u$, from which

$$\frac{2\varepsilon}{\Delta q}1g = \frac{1.150}{K_u} = \frac{1.150\ n^*}{(\sigma_m+u_a)^g} \tag{6.48}$$

and

$$\frac{2\varepsilon}{\Delta q}3g = -\frac{0.241}{K_u} = -\frac{0.241\ n^*}{(\sigma_m+u_a)^g} \tag{6.49}$$

where n_g^* represents n_g for the short term solution (S.T.S.) and $n_g + Hn_w$ for the long term solution (L.T.S.), and H has a value of 0.0333.

Thus using equations 6.48 and 6.49, Figure 6.20 presents the prediction of the axial and radial strains superimposed on the strains derived from the experimental results of Wheeler (1986). It can be seen from this figure that the strain behaviour can be modelled quite well using an empirical value of Poisson's ratio and the theoretical value of bulk modulus.

Figure 6.21 depicts the prediction of the inverse of the shear modulus, found from the addition of the above equations 6.48 and 6.49, superimposed on Wheeler's experimental results. Once again the behaviour is well modelled.

Finally, Figures 6.22a, 6.22b and 6.22c present the experimental and theoretical values of axial and radial strain for the triaxial tests of Wheeler with initial isotropic consolidation stresses of 200 kPa and 100 kPa (for an atmospheric back pressure) and 200 kPa (at a back pressure of 100 kPa). In

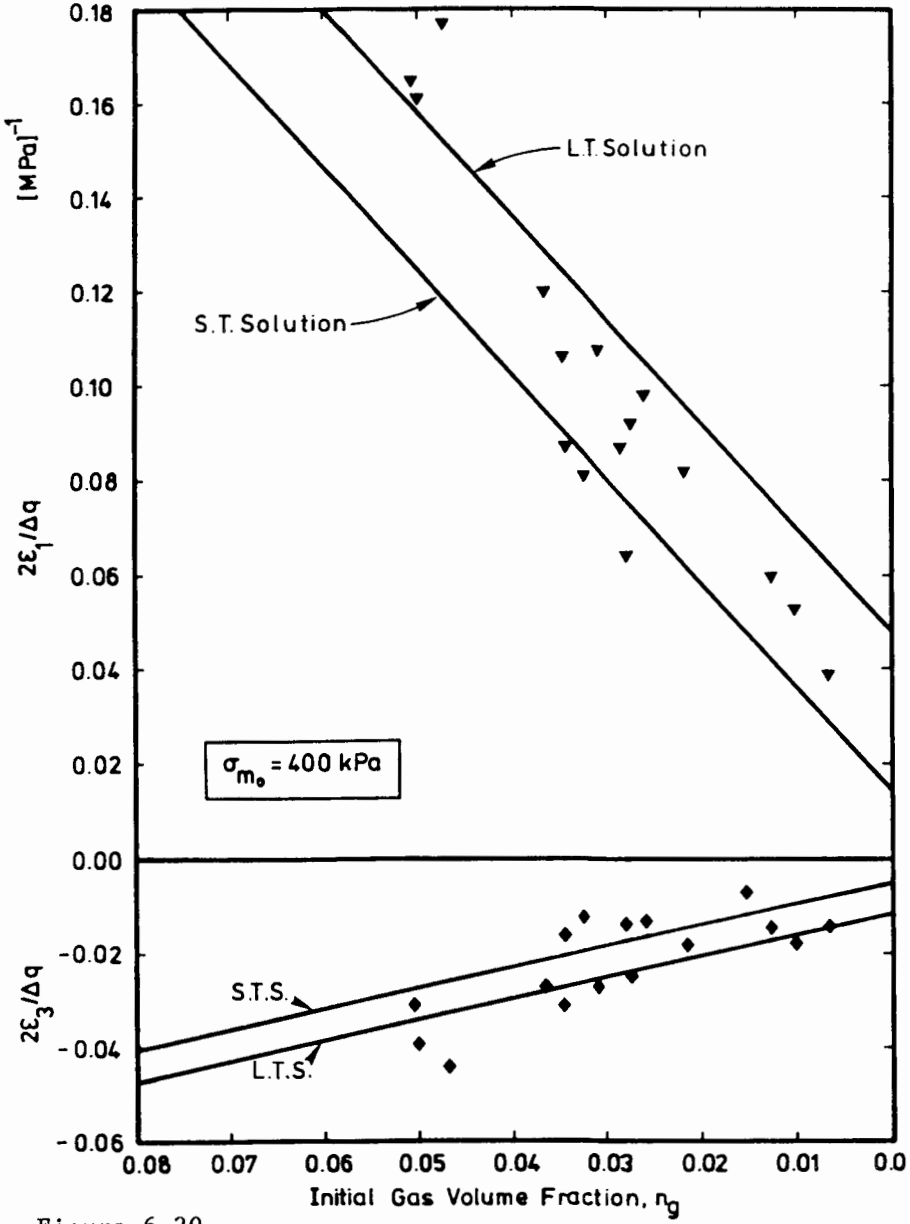

Figure 6.20
Theoretical prediction of axial and radial strains plotted against the experimental results of Wheeler (1986)

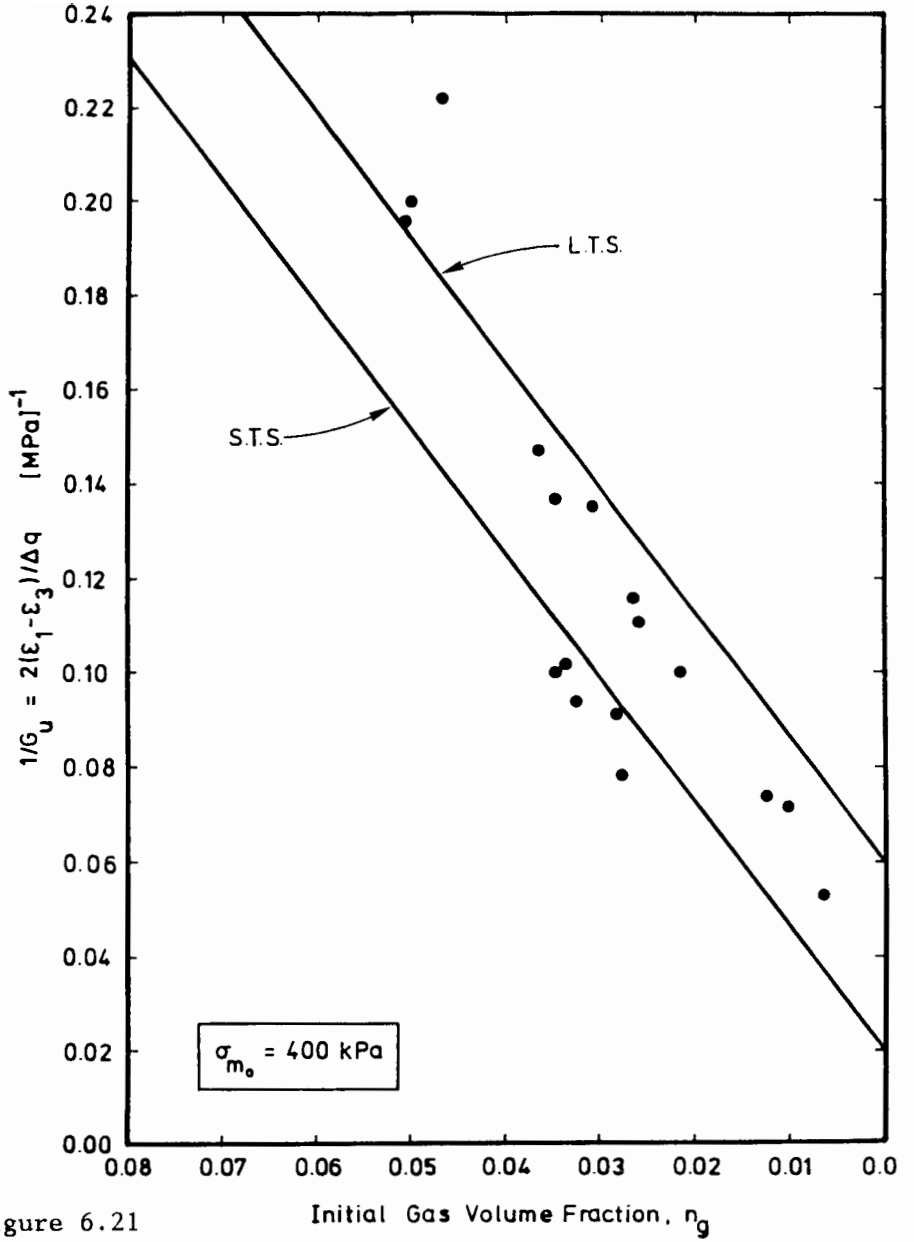

Figure 6.21
Theoretical prediction of the inverse of shear modulus plotted against the experimental results of Wheeler (1986)

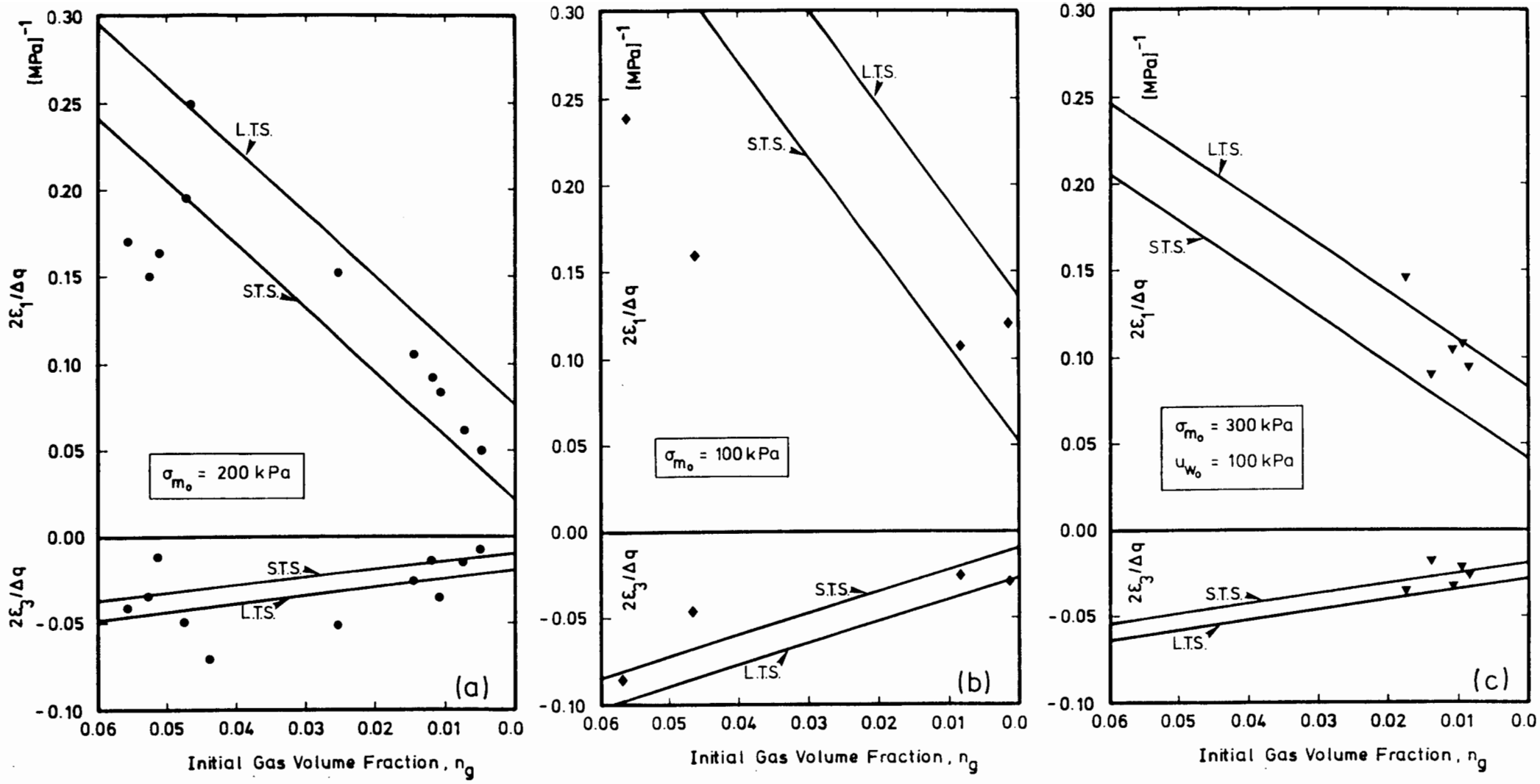

Figure 6.22 Theoretical prediction of axial and radial strains versus the triaxial results of Wheeler (1986)

general, the behaviour was modelled well for the tests in the higher stress range but not so well at lower stresses.

It can be seen that the assumption that the gas pressure is equal to the mean total stress, combined with an empirically derived Poisson's ratio of 0.21, produces a fair representation of the undrained shear moduli of a gassy soil.

6.7 The Work Input to a Gassy Soil

This analysis follows closely the work performed by Houlsby (1979) on the work input to a granular material. Houlsby states that for a single-phase material, the power input per unit volume is simply the product of the stress and the strain rates. For a multiphase material, however, the stresses on each phase and the velocities of each phase may be different. Consequently, the total power input per unit volume to a multiphase material must therefore be derived by considering the rate at which the work is done within each phase.

The analysis presented by Houlsby considers stresses and strains in three-dimensions and includes gravitational effects. The analysis presented here only considers stresses and strains in the vertical direction with the gravitational effects neglected, as the aim is to evaluate the principal effects of the work input to a gassy soil.

The first stage is to evaluate the compatibility equation for the gassy soil during consolidation. From the experimental results and subsequent numerical modelling, it appears that the volume change is due to two independent conditions. One mode of volume change is caused by the compression and dissolution of the gas, whereas the other mode results from the drainage of pore water. As these modes are completely independent, only the compatibility equation due to the flow of water is required to simulate the gassy soil consolidation behaviour, as given by

$$\frac{\partial V'_s}{\partial z} + \frac{\partial W}{\partial z} = 0 \qquad (6.50)$$

where W is the Darcy velocity and V'_s is the velocity of the solid particles solely due to the drainage of water with no change in gas volume.

Now consider an arbitrary horizontal section across a sample of gassy soil cutting gas, water and solid particles. To maintain equilibrium across this cut, neglecting surface tension forces, the sum of the stresses multiplied by their respective volume fractions must equal the total vertical stress on the sample. Consequently, the resulting equilibrium equation may be written as

$$\sigma_v = n_g u_g + n_w u_w + n_s u_s \tag{6.51}$$

where n_p is the volume fraction and u_p the vertical stress for each phase p.

The power input across any arbitrary section can then be obtained from the sum of the products of the various forces with their respective phase velocities. If the power input at any particular point z in a gassy soil sample of cross sectional area A is P, then the total power input over an arbitrary sample height h can be written as

$$\frac{A}{h}\int_h P\,dz = -\frac{A}{h}\int_h \left[n_g u_g V_g + n_w u_w V_w + n_s u_s V_s \right] dz \tag{6.52}$$

where the negative sign arises from the compression positive convention for the stress used in soil mechanics. For a gassy soil, however, the gas void always has the same velocity as the solid particles, as it is assumed that the same soil particles always "stick" to the gas void. Thus by assuming the gas velocity equals the solid velocity, the power input equation becomes

$$\int_h P\,dz = -\int_h \left[(n_g u_g + n_w u_w + n_s u_s)V_s + u_w n_w (V_w - V_s) \right] dz \tag{6.53}$$

Thus by substituting in the equilibrium equation 6.50 and introducing the definition of the Darcy velocity as

$$W = n_w (V_w - V_s) \tag{6.54}$$

the power input equation becomes

$$\int_h P\,dz = -\int_h \left[(\sigma_v V_s + u_w W \right] dz \tag{6.55}$$

As the height, h, is arbitrary, this expression may be written in local form by differentiating the above equation to give

$$P = -\left[\sigma_v \frac{\partial V_s}{\partial z} + u_w \frac{\partial W}{\partial z} + W \frac{\partial u_w}{\partial z} \right] \tag{6.56}$$

assuming that the total vertical stress is constant over the arbitrary height.

The solid velocity, V_s, in this above expression can be separated into the two independent modes of velocity, with V_s^o caused by the volume change of gas and V_s' caused by the drainage of pore water, to give

$$V_s = V_s^o + V_s' \tag{6.57}$$

which when inserted into equation 6.55 gives

$$P = - \left[\sigma_v \frac{\partial V^o}{\partial z}s + \sigma_v \frac{\partial V'}{\partial z}s + u_w \frac{\partial W}{\partial z} + W \frac{\partial u}{\partial z}w \right] \tag{6.58}$$

Substitution of the compatibility equation 6.49 then yields

$$P = - \left[\sigma_v \frac{\partial V^o}{\partial z}s + \sigma_v \frac{\partial V'}{\partial z}s - u_w \frac{\partial V'}{\partial z} + W \frac{\partial u}{\partial z}w \right] \tag{6.59}$$

or

$$P = - \left[\sigma_v \frac{\partial V^o}{\partial z}s + (\sigma_v - u_w) \frac{\partial V'}{\partial z}s + W \frac{\partial u}{\partial z}w \right] \tag{6.60}$$

At this point, the strain rate of each phase is introduced as

$$\frac{\partial \varepsilon^o}{\partial t} = - \frac{\partial V^o}{\partial z}s \quad \text{and} \quad \frac{\partial \varepsilon'}{\partial t} = - \frac{\partial V'}{\partial z}s \tag{6.61}$$

and the definition of vertical consolidation stress as

$$\sigma_v' = \sigma_v - u_w \tag{6.62}$$

from which the work input into a gassy soil can be written as

$$P = \sigma_v \frac{\partial \varepsilon^o}{\partial t} + \sigma_v' \frac{\partial \varepsilon'}{\partial t} - W \frac{\partial u}{\partial z}w \tag{6.63}$$

Following the discussion of Houlsby (1979), if the movement of the soil skeleton is controlled by the consolidation stress $(\sigma_v - u_w)$, it is observed that the total rate of work input per unit length of the soil is given by the three terms

$$\left(\sigma_v \frac{\partial \varepsilon^o}{\partial t} \right), \left(\sigma_v' \frac{\partial \varepsilon'}{\partial t} \right) \text{ and } \left(W \frac{\partial u}{\partial z}w \right) \tag{6.64}$$

Clearly these may be interpreted as the rates of work per unit volume to the gas voids, the soil skeleton and the pore fluid, and there is no coupling between these three processes as long as the behaviour of the soil skeleton is controlled by the consolidation stress $(\sigma_v - u_w)$.

In addition, if the above assumption is true, it follows that the gas pressure is controlled by the vertical total stress. It is interesting that this expression is produced in this analysis for which no assumption of the gas pressure was made.

Previous analyses in this chapter, however, indicated that although the void ratio of the saturated soil matrix of a gassy soil appeared to be dependent on the value of $(\sigma_v - u_w)$, it was shown that the gas pressure could vary significantly and have very little effect on the position of the corresponding matrix void ratio-consolidation stress plot. Conversely, a small deviation on this plot from the saturated line would theoretically produce a large change in the value of the gas pressure. If we consider the average vertical stress on the saturated soil matrix, σ_{sv}, as defined by

$$\sigma_{sv} = \sigma_v (1 - \alpha n_g)/(1 - n_g) \tag{6.65}$$

and assume that the behaviour of the saturated matrix is dependent on the average effective stress in the matrix

$$\sigma'_{sv} = (\sigma_{sv} - u_w) \tag{6.66}$$

then the work equation 6.57 can be written as

$$P = - \left[\sigma_v \frac{\partial V^o}{\partial z}s - n_g \sigma_v \frac{(1-\alpha)}{(1-n_g)} \frac{\partial V'}{\partial z}s + (\sigma_{sv} - u_w)\frac{\partial V'}{\partial z} + W \frac{\partial u}{\partial z}w \right] \tag{6.67}$$

from which

$$P = \sigma_v \frac{\partial \varepsilon^o}{\partial t} - \sigma_v n_g \frac{(1-\alpha)}{(1-n_g)} \frac{\partial \varepsilon'}{\partial t} + \sigma'_{sv} \frac{\partial \varepsilon'}{\partial t} - W \frac{\partial u}{\partial z}w \tag{6.68}$$

This equation illustrates that if the gas pressure is not equal to the vertical total stress, the total power input is not determined by the three terms as presented in equation 6.63. In general, however, gassy soils have low gas contents, and as observed from the experimental tests of gassy soil, have α values in the range 0.7 to 1.0. Under these conditions, the second term of the above equation becomes small compared with the remainder of the coefficients resulting in the approximation

$$P \simeq \sigma_v \frac{\partial \varepsilon^o}{\partial t} + \sigma'_{sv} \frac{\partial \varepsilon'}{\partial t} - W \frac{\partial u}{\partial z}w \tag{6.69}$$

6.8 Summary

In this chapter an attempt has been made to interpret the experimental and numerical observations of the behaviour of a gassy soil under both drained and undrained conditions. With the concept of a compressible fluid phase abandoned, the gassy soil is idealized as a saturated soil matrix containing discrete

compressible gas voids. The first analysis on this material illustrates that for gassy soils of the type considered in this research, the theoretical average stress on the saturated matrix is very close to that of a fully saturated soil under the same external stress conditions. Consequently, the relationship between the matrix void ratio and the mean consolidation pressure is very similar to that between the void ratio and effective stress of a saturated soil.

The problem of pore gas pressure evaluation is also treated in this chapter, with the gas first idealized as a spherical void in a saturated soil matrix. Treating the soil as a perfectly plastic material produced a good qualitative representation of one of the tests of series A. The representation of a gassy soil as non-spherical or spheroidal cavities in an elastic matrix is also considered with the help of a FORTRAN program, developed to observe the stress concentrations around an oblate spheriod. Computer runs illustrated that, with the same soil strengths, the soil around the spheroidal cavity would enter a localized state of failure far earlier than for a spherical cavity. A scenario of the settlement behaviour based on the formation of a plastic failure mechanism is also presented.

Based on these findings, the concept of the double compressibility model is introduced in which all changes in gas volume are due to changes in total stress, whereas all changes in the soil matrix volume are due to changes in the consolidation stress.

Using the double compressibility model, theoretical predictions are made of the undrained bulk and shear moduli to compare with the moduli obtained experimentally by Wheeler (1986). Even though the definitions of Poisson's ratio and bulk compressibility were based on very simple relationships, the predictions of the shear and bulk moduli were remarkably close to the experimental values.

Finally, a one-dimensional power input analysis on an idealized sample of gassy soil is performed. The resulting power input equation illustrates that the work done can be approximated by the product of the total stress and the gas strain rate, plus the product of the consolidation stress and the matrix strain rate, minus the product of the pore water pressure gradient and Darcy velocity.

CHAPTER 7

DCFEM2 - DOUBLE COMPRESSIBILITY FINITE ELEMENT MODEL IN TWO DIMENSIONS

DERIVATION OF THE GOVERNING CONSOLIDATION EQUATIONS

CHAPTER 7

DCFEM2 - DOUBLE COMPRESSIBILITY FINITE ELEMENT MODEL IN TWO DIMENSIONS

DERIVATION OF THE GOVERNING CONSOLIDATION EQUATIONS

7.1 Introduction

It has been shown from experimental modelling on gassy soil that the deformation of the soil takes place as a result of two independent processes. The first is due to the compressibility and solubility of the gas in the water. This is an undrained process, although not necessarily instantaneous. Without any change in volume, the soil matrix surrounding the gas void deforms to accommodate the reduction in volume of the gas. The second mode of displacement is due to loss of pore water from the saturated matrix under drained conditions.

This chapter describes the step-by-step development of the equations governing the consolidation behaviour of a double compressibility material. The equations fully couple the deformation behaviour of both the gas voids and the soil matrix with the flow of pore water through the porous material. The equations are finally presented in a similar form to that developed by Biot (1941) for the coupled fluid flow and soil deformation of a saturated soil. The final equations are presented in terms of total displacements and pore water pressure for both cartesian and axisymmetric conditions.

7.2 General Multi-Dimensional Stress-Strain Behaviour

In the following section, the total stress tensor acting on a gassy soil is expressed as a general function of the total strain tensor, the pore water pressure and the drained and undrained elastic moduli. In this development, the gassy soil is idealized as an elastic medium that deforms due to changes in both total and consolidation stresses. In tensorial notation, the stress-strain behaviour may be expressed as

$$\sigma_{ij} = D^{o}_{ijkl}\, \varepsilon^{o}_{kl} \tag{7.1}$$

for deformation due to changes in total stress, and

$$\sigma'_{ij} = \sigma_{ij} - \delta_{ij} u_w = D'_{ijkl}\, \varepsilon'_{kl} \tag{7.2}$$

for deformation due to changes in consolidation stress. Due to the fact that it is not possible to measure the two components of strain separately, it is necessary to evaluate the constitutive material behaviour in terms of total stresses and strains. This can be performed by first inverting the D matrices in equations 7.1 and 7.2 to give

$$\varepsilon^{o}_{kl} = \left[D^{o}_{ijkl}\right]^{-1} \sigma_{ij} \tag{7.3}$$

and

$$\varepsilon'_{kl} = \left[D'_{ijkl}\right]^{-1} \sigma'_{ij} = \left[D'_{ijkl}\right]^{-1} (\sigma_{ij} - u_w \, \delta_{ij}) \tag{7.4}$$

The total strain which can be separated into two components (see Chapter 6),

$$\varepsilon_{kl} = \varepsilon^{o}_{kl} + \varepsilon'_{kl} \tag{7.5}$$

can now be written as

$$\varepsilon_{kl} = \left\{\left[D^{o}_{ijkl}\right]^{-1} + \left[D'_{ijkl}\right]^{-1}\right\} \sigma_{ij} - \left[D'_{ikjl}\right]^{-1} \delta_{ij} \, u_w \tag{7.6}$$

Rearranging this equation, followed by a second matrix inversion, produces the total stress tensor in the form of total strains and pore water pressures.

$$\sigma_{ij} = \left\{\left[D^{o}_{ijkl}\right]^{-1} + \left[D'_{ijkl}\right]^{-1}\right\}^{-1} \left\{\varepsilon_{kl} + \left[D'_{ijkl}\right]^{-1} \delta_{ij} \, u_w\right\} \tag{7.7}$$

7.3 Double Compressibility Model in Cartesian Coordinates

For an elastic material, the stress-strain behaviour may be represented by

$$\Delta\sigma_{ij} = 2G \, \Delta\varepsilon_{ij} + \lambda \, \Delta\varepsilon_{kk} \, \delta_{ij} \qquad i,j = 1,2,3 \tag{7.8}$$

where the Lame's constants G and λ for the material can be defined as,

$$G = E/2(1+\nu) \quad \text{and} \quad \lambda = E\nu/[(1+\nu)(1 - 2\nu)] = 3K\nu/(1+\nu) \tag{7.9}$$

where E is the Young's modulus, ν is Poisson's ratio and K is the bulk modulus. Using the additional fact that

$$\lambda+2G = \lambda(1-\nu)/\nu = 2G(1-\nu)/(1-2\nu) \tag{7.10}$$

and

$$\lambda = 2G\nu/(1-2\nu) \tag{7.11}$$

equation 7.8 may be written in matrix form as

$$\begin{Bmatrix} \Delta\sigma_{11} \\ \Delta\sigma_{22} \\ \Delta\sigma_{33} \end{Bmatrix} = \frac{2G}{(1-2\nu)} \begin{bmatrix} 1-\nu & \nu & \nu \\ \nu & 1-\nu & \nu \\ \nu & \nu & 1-\nu \end{bmatrix} \begin{Bmatrix} \Delta\varepsilon_{11} \\ \Delta\varepsilon_{22} \\ \Delta\varepsilon_{33} \end{Bmatrix} \quad \text{and} \quad \Delta\sigma_{ij} = 2G\Delta\varepsilon_{ij} \quad [i\neq j] \tag{7.12}$$

from which

$$\begin{Bmatrix}\Delta\varepsilon_{11}\\ \Delta\varepsilon_{22}\\ \Delta\varepsilon_{33}\end{Bmatrix} = \frac{1}{2G(1+\nu)}\begin{bmatrix}1 & -\nu & -\nu\\ -\nu & 1 & -\nu\\ -\nu & -\nu & 1\end{bmatrix}\begin{Bmatrix}\Delta\sigma_{11}\\ \Delta\sigma_{22}\\ \Delta\sigma_{33}\end{Bmatrix} \quad \text{and} \quad \Delta\varepsilon_{ij} = \frac{1}{2G}\Delta\sigma_{ij} \qquad [i\neq j] \qquad (7.13)$$

It is assumed that this stress-strain behaviour applies both to strains caused by gas displacement and those caused by saturated soil displacement. Thus noting that the superscript " ° " represents all values associated with gas deformation, whereas the superscript " ′ " represents all values associated with the soil matrix deformation, the total strain may be written as the sum of the gas and soil matrix strains to give

$$\begin{Bmatrix}\Delta\varepsilon_{11}\\ \Delta\varepsilon_{22}\\ \Delta\varepsilon_{33}\end{Bmatrix} = \begin{Bmatrix}\Delta\varepsilon^{\circ}_{11}\\ \Delta\varepsilon^{\circ}_{22}\\ \Delta\varepsilon^{\circ}_{33}\end{Bmatrix} + \begin{Bmatrix}\Delta\varepsilon'_{11}\\ \Delta\varepsilon'_{22}\\ \Delta\varepsilon'_{33}\end{Bmatrix} = \frac{1}{2G^{\circ}(1+\nu^{\circ})}\begin{bmatrix}1 & -\nu^{\circ} & -\nu^{\circ}\\ -\nu^{\circ} & 1 & -\nu^{\circ}\\ -\nu^{\circ} & -\nu^{\circ} & 1\end{bmatrix}\begin{Bmatrix}\Delta\sigma_{11}\\ \Delta\sigma_{22}\\ \Delta\sigma_{33}\end{Bmatrix}$$

$$+ \frac{1}{2G'(1+\nu')}\begin{bmatrix}1 & -\nu' & -\nu'\\ -\nu' & 1 & -\nu'\\ -\nu' & -\nu' & 1\end{bmatrix}\begin{Bmatrix}\Delta\sigma'_{11}\\ \Delta\sigma'_{22}\\ \Delta\sigma'_{33}\end{Bmatrix} \qquad (7.14)$$

and

$$\Delta\varepsilon_{ij} = \Delta\varepsilon^{\circ}_{ij} + \Delta\varepsilon'_{ij} = \left[\frac{1}{2G^{\circ}} + \frac{1}{2G'}\right]\Delta\sigma_{ij} \qquad [i\neq j] \qquad (7.15)$$

Now substituting the consolidation stress increment

$$\Delta\sigma'_{ij} = \Delta\sigma_{ij} - \Delta u_w\,\delta_{ij} \qquad (7.16)$$

into equation 7.14 yields

$$\begin{Bmatrix}\Delta\varepsilon_{11}\\ \Delta\varepsilon_{22}\\ \Delta\varepsilon_{33}\end{Bmatrix} = \begin{bmatrix}a & -b & -b\\ -b & a & -b\\ -b & -b & a\end{bmatrix}\begin{Bmatrix}\Delta\sigma_{11}\\ \Delta\sigma_{22}\\ \Delta\sigma_{33}\end{Bmatrix} - \frac{\Delta u_w}{3K'}\begin{Bmatrix}1\\ 1\\ 1\end{Bmatrix} \qquad (7.17)$$

where K' is the drained bulk modulus for the saturated soil matrix, and the parameters a and b are defined as

$$a = \frac{1}{2G^{\circ}(1+\nu^{\circ})} + \frac{1}{2G'(1+\nu')} = \frac{1}{E^{\circ}} + \frac{1}{E'} \qquad (7.18)$$

and

$$b = \frac{\nu^{\circ}}{2G^{\circ}(1+\nu^{\circ})} + \frac{\nu'}{2G'(1+\nu')} = \frac{\nu^{\circ}}{E^{\circ}} + \frac{\nu'}{E'} \qquad (7.19)$$

from which it can be shown that

$$\begin{bmatrix}a & -b & -b\\ -b & a & -b\\ -b & -b & a\end{bmatrix}^{-1} = \frac{1}{a+b}\begin{bmatrix}1 & 0 & 0\\ 0 & 1 & 0\\ 0 & 0 & 1\end{bmatrix} + \frac{b}{(a+b)(a-2b)}\begin{bmatrix}1 & 1 & 1\\ 1 & 1 & 1\\ 1 & 1 & 1\end{bmatrix} \qquad (7.20)$$

Substituting the above matrix inversion into equation 7.17 produces

$$\Delta\sigma_{ij} = 2\bar{G}\Delta\varepsilon_{ij} + \bar{\lambda}\Delta\varepsilon_{kk}\delta_{ij} + \bar{B}\Delta u_w\,\delta_{ij} \qquad (7.21)$$

However, as it is not possible to measure initial strains in a material, strains can only be evaluated relative to its initial state. Consequently, with the initial strains assumed to be zero, the current state of strain, ε_{ij}, has the same value as the increment of strain, $\Delta\varepsilon_{ij}$. Therefore,

$$\sigma_{ij} = 2\bar{G}\varepsilon_{ij} + \bar{\lambda}\varepsilon_{kk}\delta_{ij} + \bar{B}u_w\delta_{ij} + \sigma^*_{ij} \tag{7.22}$$

where

$$\sigma^*_{ij} = \left[\sigma_{ij} - \Delta\sigma_{ij}\right] - \left[\bar{B}u_w - \bar{B}\Delta u_w\right]\delta_{ij} = \tilde{\sigma}_{ij} - \bar{B}\tilde{u}_w\delta_{ij} \tag{7.23}$$

$$\bar{G} = \left[\frac{1}{G^\circ} + \frac{1}{G'}\right]^{-1} \tag{7.24}$$

$$\bar{\lambda} = 6\bar{G}\left[\frac{\nu^\circ/E^\circ + \nu'/E'}{1/K^\circ + 1/K'}\right] \tag{7.25}$$

$$\bar{B} = \left[1 + K'/K^\circ\right]^{-1} \tag{7.26}$$

in which $\tilde{\sigma}_{ij}$ is the initial total stress tensor and $\tilde{u}_w$ is the initial pore water pressure. For a saturated soil, σ^*_{ij} becomes the initial effective stress $\tilde{\sigma}'_{ij}$.

7.4 Derivation of the Three-Dimensional Governing Displacement Equation for a Double Compressibility Material

The distribution of total stress in a homogeneous soil sample is given by

$$\frac{\partial\sigma_{ij}}{\partial x_j} = F_i \qquad i,j = 1,2,3 \tag{7.27}$$

where F_i is the body force vector per unit volume of soil. The sign convention for the above equation is such that compressive stresses are positive (which is the normal convention in soil mechanics). Substituting the stress-strain equation 7.22 into the above equilibrium equation gives

$$2\bar{G}\frac{\partial\varepsilon_{ij}}{\partial x_j} + \bar{\lambda}\frac{\partial\varepsilon_{kk}}{\partial x_i} + \bar{B}\frac{\partial u_w}{\partial x_i} + \frac{\partial\sigma^*_{ij}}{\partial x_j} = F_i \tag{7.28}$$

For the case of small deformations, the strain components are assumed to be related to displacement via the following relationship

$$\varepsilon_{ij} = -\frac{1}{2}\left[\frac{\partial w_i}{\partial x_j} + \frac{\partial w_j}{\partial x_i}\right] \tag{7.29}$$

where w_i denotes the incremental displacement vector of the sample. Thus, substitution into equation 7.28 gives

$$\bar{G}\frac{\partial}{\partial x_j}\left[\frac{\partial w_i}{\partial x_j} + \frac{\partial w_j}{\partial x_i}\right] + \bar{\lambda}\frac{\partial}{\partial x_i}\left[\frac{\partial w_j}{\partial x_j}\right] - \bar{B}\frac{\partial u_w}{\partial x_i} = \frac{\partial\sigma^*_{ij}}{\partial x_j} - F_i \tag{7.30}$$

which can be written as

$$\bar{G}\frac{\partial^2 w_i}{\partial x_j \partial x_j} + \bar{G}\frac{\partial^2 w_j}{\partial x_j \partial x_i} + \bar{\lambda}\frac{\partial^2 w_j}{\partial x_i \partial x_j} - \bar{B}\frac{\partial u}{\partial x_i}w = \frac{\partial \sigma^*_{ij}}{\partial x_j} - F_i \qquad (7.31)$$

This equation is the required result in which the governing equation is in the form of total displacements and pore water pressures.

7.5 The Flow Equation for a Double Compressibility Material

Considering a soil consisting of three phases--solid, water and gas--the continuity equation of each phase may be written as (Barden, 1965),

$$\frac{\partial}{\partial x_i}(n_s V_{si} \rho_s) + \frac{\partial}{\partial t}(n_s \rho_s) = 0 \qquad (7.32)$$

$$\frac{\partial}{\partial x_i}(n_w V_{wi} \rho_w) + \frac{\partial}{\partial t}(n_w \rho_w) = 0 \qquad (7.33)$$

$$\frac{\partial}{\partial x_i}(n_g V_{gi} \rho_g + H n_w V_{wi} \rho_g) + \frac{\partial}{\partial t}(n_g \rho_g + H n_w \rho_g) = 0 \qquad (7.34)$$

where n_k is the volume fraction, V_{ki} is the actual velocity component and ρ_k is the density of each phase k. H is Henry's coefficient of solubility, x_i is the spatial cartesian coordinate and t is time. Barden applies the above equations to unsaturated soils, ignoring the effects of solubility. For this gassy soil model, solubility effects are not to be ignored because for low gas saturations the effect of dissolved gas becomes very important.

Meiri and Karadi (1982) present the governing equations used for the simulation of air storage in aquifers. Their equations assume no deformation of the aquifer and hence only the water and gas equations are presented.

Due to the deformation of the soil matrix in gassy soils, however, it is essential for the continuity equation of the solid phase to be included. The above authors also include the effects of both solubility of the air in water and the volatility of water in air. For a gassy soil of low gas content, the effect of dissolved gas in the pore water is included, but the secondary effect of the transport of evaporated water in the gas is neglected.

At this stage it is assumed that the solid grains are incompressible. The assumption of an incompressible water phase is not made, however. Thus expanding the above three phase equations produces

$$\frac{\partial}{\partial x_i}(n_s V_{si}) + \frac{\partial n_s}{\partial t} = 0 \tag{7.35}$$

for the solid phase,

$$\frac{\partial}{\partial x_i}(n_w V_{wi}) + \frac{n_w V_{wi}}{\rho_w}\frac{\partial \rho_w}{\partial x_i} + \frac{\partial n_w}{\partial t} + \frac{n_w}{\rho_w}\frac{\partial \rho_w}{\partial t} = 0 \tag{7.36}$$

for the water phase, and

$$\frac{\partial}{\partial x_i}(n_g V_{gi}) + H\frac{\partial}{\partial x_i}(n_w V_{wi}) + \frac{n_g V_{gi}}{\rho_g}\frac{\partial \rho_g}{\partial x_i} + H\frac{n_w V_{wi}}{\rho_g}\frac{\partial \rho_g}{\partial x_i} + \frac{\partial n_g}{\partial t} + \frac{n_g}{\rho_g}\frac{\partial \rho_g}{\partial t} + H\frac{\partial n_w}{\partial t} + \frac{H n_w}{\rho_g}\frac{\partial \rho_g}{\partial t} = 0 \tag{7.37}$$

for the gas phase. Substitution of equation 7.36 into the gas equation 7.37 then gives

$$\frac{\partial}{\partial x_i}(n_g V_{gi}) + \left(\frac{n_g V_{gi}}{\rho_g} + \frac{H n_w V_{wi}}{\rho_g}\right)\frac{\partial \rho_g}{\partial x_i} - H\frac{n_w V_{wi}}{\rho_w}\frac{\partial \rho_w}{\partial x_i} + \frac{\partial n_g}{\partial t} + \left(\frac{n_g}{\rho_g} + H\frac{n_w}{\rho_g}\right)\frac{\partial \rho_g}{\partial t} - H\frac{n_w}{\rho_w}\frac{\partial \rho_w}{\partial t} = 0 \tag{7.38}$$

Adding both the solid and water continuity equation to the above equation gives

$$\frac{\partial}{\partial x_i}(n_s V_{si} + n_w V_{wi} + n_g V_{gi}) + \left(\frac{n_g V_{gi} + H n_w V_{wi}}{\rho_g}\right)\frac{\partial \rho_g}{\partial x_i} + (1-H)\frac{n_w V_{wi}}{\rho_w}\frac{\partial \rho_w}{\partial x_i} + \left\{\frac{n_g + H n_w}{\rho_g}\right\}\frac{\partial \rho_g}{\partial t} + (1-H)\frac{n_w}{\rho_w}\frac{\partial \rho_w}{\partial t} = 0 \tag{7.39}$$

which is the general flow equation for any partly saturated soil.

At this stage all assumptions pertaining to a gassy soil will be introduced. Firstly, due to the fact that in a gassy soil the gas exists in discrete occluded voids (much larger than the individual soil grains) surrounded by a saturated soil matrix, there is no relative displacement between the gas and the solid grains. Thus the gas appears to "stick" to the surrounding soil particles and will therefore have the same average velocity. Furthermore, each phase has a velocity which consists of two independent velocity components.

The first velocity component, V^{o}_{ki}, is a result of the change in the volume of free gas due to both compressibility and solubility effects. During this phase of deformation, there is no volume change of the water phase and no relative movement between the solid, water and gas phases. Thus the phase velocities are all equal and may be written as

$$V_{si} = V_{wi} = V_{gi} = V^{o}_{si} = V^{o}_{wi} = V^{o}_{gi} \tag{7.40}$$

Thus the general continuity equation 7.39 becomes

$$\frac{\partial V^{o}_{si}}{\partial x_i} + \frac{(n_g V^{o}_{si} + Hn_w V^{o}_{si})}{\rho_g} \frac{\partial \rho_g}{\partial x_i} + \frac{(1-H)n_w V^{o}_{si}}{\rho_w} \frac{\partial \rho_w}{\partial x_i} + \frac{n_g + Hn_w}{\rho_g} \frac{\partial \rho_g}{\partial t} = 0 \tag{7.41}$$

The second component of velocity, V'_{ki}, is due to the loss of volume of water. This results in a change of volume of the saturated matrix without any change in the volume of gas. The water volume change can be a result of the water compressibility, but is chiefly due to the flow of water from the sample. It is still assumed that the gas voids "stick" to the soil particles and accordingly have the same velocity. Therefore, the phase velocities for this condition may be written as

$$V_{si} = V_{gi} = V'_{si} = V'_{gi} \tag{7.42}$$

and

$$V_{wi} = V'_{wi} \tag{7.43}$$

Consequently, the general continuity equation 7.39 becomes

$$\frac{\partial V'_{si}}{\partial x_i} + \frac{\partial W_i}{\partial x_i} + \frac{(n_g V'_{si} + Hn_w V'_{wi})\partial \rho_g}{\rho_g} \frac{\partial \rho_g}{\partial x_i} + \frac{(1-H)n_w V'_{wi}}{\rho_w} \frac{\partial \rho_w}{\partial x_i} + \frac{(1-H)n_w}{\rho_w} \frac{\partial \rho_w}{\partial t} = 0 \tag{7.44}$$

where the relative velocity between the water and the solid grains is known as the Darcy Velocity, W_i, and may be written as

$$W_i = n_w(V'_{wi} - V'_{si}) \tag{7.45}$$

At this stage it is still possible to treat the gassy soil as having a compressible pore fluid instead of discrete gas voids. This is obtained by giving the water a value of compressibility corresponding to a mixture of gas and water. For the volumes of gas present in a gassy soil (n_g<0.05), the overall compressibility is small. For fluids of small or slight compressibility, Peaceman (1977) has shown that the term including the spatial derivative of fluid density is negligible compared with the remaining spatial derivatives due to changes in Darcy velocities. This assumption is used by many authors in their treatment of unsaturated soils, including Ghaboussi and Wilson (1973), Chang and Duncan (1983) and Meiri and Karadi (1982).

Furthermore, if the gas is present in the form of discrete gas voids which move with the solid grains, not only is the spatial derivative of the density term small due to the low compressibility, but also because the term is

premultiplied by the solid velocity and not the fluid velocity as is the case for the compressible fluid. In addition, as it has been shown in the previous chapters that the gas pressure is dependent on the total stress rather than the pore water pressure, the spatial variation of gas density becomes very small.

Thus, from the above explanation, the spatial derivatives of density in equations 7.41 and 7.44 will be neglected producing the governing equations

$$\frac{\partial V^{\circ}_{si}}{\partial x_i} + \frac{(n_g + Hn_w)}{\rho_g} \frac{\partial \rho_g}{\partial t} = 0 \tag{7.46}$$

for no change in water volume, and

$$\frac{\partial V'_{si}}{\partial x_i} + \frac{\partial W_i}{\partial x_i} + \frac{(1-H)n_w}{\rho_w} \frac{\partial \rho_w}{\partial t} = 0 \tag{7.47}$$

for no change in gas volume. It is interesting to note that the final term in the above equation illustrates the fact that any change in water volume, Δv_w, associated with the water compressibility, will be accompanied by a change in gas volume, $- H\Delta v_w$, that is held as dissolved gas. Thus the net change in total volume due to a change in water volume, Δv_w, will be $(1-H)\Delta v_w$.

Considering now a case in which there are simultaneous changes in both gas and water volumes, the total phase velocities are the sum of the two component velocities. This is presented for each phase as

$$V_{si} = V^{\circ}_{si} + V'_{si} \tag{7.48}$$

$$V_{wi} = V^{\circ}_{wi} + V'_{wi} \tag{7.49}$$

$$V_{gi} = V^{\circ}_{gi} + V'_{gi} \tag{7.50}$$

which states that the total velocity of each phase is the sum of the velocity due to changes in gas volume, V°, and that due to changes in water volume, V'. Thus summing equations 7.46 and 7.47 and substituting equations 7.48, 7.49 and 7.50, the governing equation for combined conditions becomes

$$\frac{\partial V_{si}}{\partial x_i} + \frac{\partial W_i}{\partial x_i} + \frac{(n_g+Hn_w)}{\rho_g} \frac{\partial \rho_g}{\partial t} + \frac{(1-H)n_w}{\rho_w} \frac{\partial \rho_w}{\partial t} = 0 \tag{7.51}$$

It can be seen, however, that the two component equations 7.46 and 7.47 are totally independent and therefore may be solved independently. The first equation equates the spatial change of velocities due to gas volume changes with

the change in density of the gas. At this stage the density of the gas is not required, thus it is not necessary to solve this equation.

The second equation equates the spatial changes of solid and Darcy velocities with the change in density of the water. This equation governs the flow of the water and will therefore be included in the solution process. To solve equation 7.47 in terms of pore pressures and displacements, the change in water density may be modified to changes in pore water pressure as

$$\frac{1}{\rho_w}\frac{\partial \rho_w}{\partial t} = \frac{1}{\rho_w}\frac{d\rho_w}{du_w}\frac{\partial u_w}{\partial t} = c_w \frac{\partial u_w}{\partial t} \tag{7.52}$$

where c_w is the water compressibility. We now introduce Darcy's Law for unsaturated soils in the form

$$W_i = -\frac{\bar{k}_{ij}}{\gamma_w}\left[\frac{\partial u_w}{\partial x_j} - \gamma_w e_j\right] = n_w(V'_w - V'_s) \tag{7.53}$$

where W_i is the Darcy Velocity, γ_w is the unit weight of water, e_j is the unit gravitational vector and $\bar{k}_{ij}$ is the permeability tensor for an unsaturated soil and can be related to the permeability of a saturated soil, k_{ij}, by

$$\bar{k}_{ij} = k_{rw}\, k_{ij} \tag{7.54}$$

where k_{rw} is the relative permeability for an unsaturated soil. Substituting equation 7.53 into equation 7.47 yields

$$\frac{\partial W_i}{\partial x_i} + \frac{\partial V'_{si}}{\partial x_i} = \frac{\partial}{\partial x_i}\left[-\frac{\bar{k}_{ij}}{\gamma_w}\left(\frac{\partial u_w}{\partial x_j} - \gamma_w e_j\right)\right] + \frac{\partial V'_{si}}{\partial x_i} = -(1-H)n_w c_w \frac{\partial u_w}{\partial t} \tag{7.55}$$

Finally, velocities and strains may be written in terms of temporal and spatial derivatives of displacement in the form of

$$V'_{si} = \frac{\partial w'_i}{\partial t} \quad \text{and} \quad \varepsilon'_{ii} = -\frac{\partial w'_i}{\partial x_i} \tag{7.56}$$

Thus

$$\frac{\partial V'_{si}}{\partial x_i} = \frac{\partial}{\partial x_i}\left(\frac{\partial w'_i}{\partial t}\right) = \frac{\partial}{\partial t}\left(\frac{\partial w'_i}{\partial x_i}\right) = -\frac{\partial \varepsilon'_{ii}}{\partial t} \tag{7.57}$$

Substitution of the above velocity derivative into equation 7.55 yields

$$\frac{\partial}{\partial x_i}\left[\frac{\bar{k}_{ij}}{\gamma_w}\left[\frac{\partial u_w}{\partial x_j} - \gamma_w e_j\right]\right] = (1-H)n_w c_w \frac{\partial u_w}{\partial t} - \frac{\partial \varepsilon'_{ii}}{\partial t} \tag{7.58}$$

7.6 Coupling of Flow and Displacement Equations

In order to couple fully the flow equation with the displacement equations, the flow equation must be written in terms of pore pressures and total

displacements. As the left-hand side of the governing flow equation 7.58 only contains pore water pressure as an unknown variable, it is only the right-hand side that needs to be adjusted. The right-hand side of this equation may be written in terms of total strains and pore water pressures by considering that the total strain is the sum of the strains due to changes in gas plus water volumes, from which

$$\varepsilon'_{ii} = \varepsilon_{ii} - \varepsilon^{o}_{ii} \tag{7.59}$$

However, from equation 7.14 it can be shown that

$$\varepsilon_{ii} = \left[\frac{1}{3K^{o}} + \frac{1}{3K'} \right] \sigma_{ii} - \frac{u_w}{K'} \tag{7.60}$$

Thus

$$\sigma_{ii} = \left[\varepsilon_{ii} + \frac{u_w}{K'} \right] \left[\frac{1}{3K^{o}} + \frac{1}{3K'} \right]^{-1} \tag{7.61}$$

And from equation 7.13

$$\varepsilon'_{ii} = \frac{1}{3K'} \sigma_{ii} - \frac{u_w}{K'} = \left[1 + K'/K^{o} \right]^{-1} \varepsilon_{ii} - \left[K^{o} + K' \right]^{-1} u_w \tag{7.62}$$

Substitution into equation 7.58 then gives

$$\frac{\partial}{\partial x_i} \left[\frac{k_{ij}}{\gamma_w} \left(\frac{\partial u_w}{\partial x_j} - \gamma_w e_j \right) \right] = \bar{C} \frac{\partial u_w}{\partial t} - \bar{B} \frac{\partial \varepsilon_{ii}}{\partial t} \tag{7.63}$$

where

$$\bar{B} = \left[1 + K'/K^{o} \right]^{-1} \tag{7.64}$$

and

$$\bar{C} = (1-H) n_w c_w + \left[K^{o} + K' \right]^{-1} \tag{7.65}$$

Substitution of the definition of strain given by equation 7.56 yields the final form of the flow equation, which may be presented as

$$\frac{\partial}{\partial x_i} \left[\frac{k_{ij}}{\gamma_w} \left(\frac{\partial u_w}{\partial x_j} - \gamma_w e_j \right) \right] = \bar{C} \frac{\partial u_w}{\partial t} + \bar{B} \frac{\partial}{\partial t} \left[\frac{\partial w_i}{\partial x_i} \right] \tag{7.66}$$

7.7 Derivation of the Governing Displacement Equations under Axisymmetric Conditions for a Double Compressibility Material

The general equations for axisymmetric stress and deformation in a solid of revolution may be written as (Timoshenko and Goodier, 1970, pp. 380),

$$\varepsilon_{rr} = - \frac{\partial w}{\partial r} r \; ; \; \varepsilon_{zz} = - \frac{\partial w}{\partial z} z \; ; \; \varepsilon_{\theta\theta} = - \frac{w}{r} r \; ; \; \varepsilon_{rz} = \varepsilon_{zr} = - \frac{1}{2} \left[\frac{\partial w}{\partial z} r + \frac{\partial w}{\partial r} z \right] \tag{7.67}$$

(Note that a negative sign has been included which is the sign convention for soil mechanics.) The equilibrium equations may be written as

$$\frac{\partial \sigma}{\partial r}rr + \frac{\partial \sigma}{\partial z}rz + \frac{\sigma}{r}rr - \frac{\sigma}{r}\theta\theta = F_r \tag{7.68}$$

and

$$\frac{\partial \sigma}{\partial r}zr + \frac{\partial \sigma}{\partial z}zz + \frac{\sigma}{r}rz = F_z \tag{7.69}$$

For axisymmetric loading and displacement conditions, the stress-strain equations may be written as

$$\sigma_{rr} = (2\bar{G} + \bar{\lambda})\,\varepsilon_{rr} + \bar{\lambda}\,\varepsilon_{zz} + \bar{\lambda}\,\varepsilon_{\theta\theta} + \bar{B}\,u_w + \sigma^*_{rr} \tag{7.70}$$

$$\sigma_{zz} = (2\bar{G} + \bar{\lambda})\,\varepsilon_{zz} + \bar{\lambda}\,\varepsilon_{\theta\theta} + \bar{\lambda}\,\varepsilon_{rr} + \bar{B}\,u_w + \sigma^*_{zz} \tag{7.71}$$

$$\sigma_{\theta\theta} = (2\bar{G} + \bar{\lambda})\,\varepsilon_{\theta\theta} + \bar{\lambda}\,\varepsilon_{rr} + \bar{\lambda}\,\varepsilon_{zz} + \bar{B}\,u_w + \sigma^*_{\theta\theta} \tag{7.72}$$

$$\sigma_{rz} = 2\bar{G}\,\varepsilon_{rz} + \sigma^*_{rz} \quad ; \quad \sigma_{zr} = 2\bar{G}\,\varepsilon_{zr} + \sigma^*_{zr} \tag{7.73}$$

Substitution of the above into the equilibrium equations 7.68 and 7.69 yields

$$\frac{\partial}{\partial r}\left[(2\bar{G} + \bar{\lambda})\varepsilon_{rr} + \bar{\lambda}\varepsilon_{zz} + \bar{\lambda}\varepsilon_{\theta\theta} + \bar{B}u_w\right] + 2\bar{G}\frac{\partial \varepsilon}{\partial z}rz + \frac{2\bar{G}}{r}(\varepsilon_{rr} - \varepsilon_{\theta\theta})$$

$$= F_r - \frac{\partial \sigma^*}{\partial r}rr - \frac{\partial \sigma^*}{\partial z}rz - \frac{\sigma^*}{r}rr + \frac{\sigma^*}{r}\theta\theta \tag{7.74}$$

for the radial direction, and

$$\frac{\partial}{\partial z}\left[(2\bar{G} + \bar{\lambda})\varepsilon_{zz} + \bar{\lambda}\varepsilon_{\theta\theta} + \bar{\lambda}\varepsilon_{rr} + \bar{B}u_w\right] + 2\bar{G}\frac{\partial \varepsilon}{\partial r}zr + \frac{2\bar{G}}{r}\varepsilon_{rz}$$

$$= F_z - \frac{\partial \sigma^*}{\partial r}zr - \frac{\partial \sigma^*}{\partial z}zz - \frac{\sigma^*}{r}rz \tag{7.75}$$

for the axial direction.

Finally, substitution of the general strain-displacement equations yields

$$(\bar{\lambda}+2\bar{G})\frac{\partial^2 w}{\partial r\,\partial r}r + (\bar{\lambda}+2\bar{G})\frac{\partial}{\partial r}\left[\frac{w}{r}r\right] + \bar{\lambda}\,\frac{\partial^2 w}{\partial r\,\partial z}z + \bar{G}\,\frac{\partial^2 w}{\partial z\,\partial r}z + \bar{G}\,\frac{\partial^2 w}{\partial z\,\partial z}r - \bar{B}\,\frac{\partial u}{\partial r}w$$

$$= \frac{\partial \sigma^*}{\partial r}rr + \frac{\partial \sigma^*}{\partial z}rz + \frac{\sigma^*}{r}rr - \frac{\sigma^*}{r}\theta\theta = F_r \tag{7.76}$$

for equilibrium in the radial direction, and

$$(\bar{\lambda}+2\bar{G})\frac{\partial^2 w}{\partial z\,\partial z}z + \bar{G}\,\frac{\partial^2 w}{\partial r\,\partial z}r + \bar{\lambda}\,\frac{\partial^2 w}{\partial z\,\partial r}r + \bar{G}\,\frac{\partial^2 w}{\partial r\,\partial r}z - \bar{B}\,\frac{\partial u}{\partial z}w + \left(\frac{\bar{\lambda}+\bar{G}}{r}\right)\frac{\partial w}{\partial z}r + \frac{\bar{G}}{r}\,\frac{\partial w}{\partial r}z$$

$$= \frac{\partial \sigma^*}{\partial r}zr + \frac{\partial \sigma^*}{\partial z}zz + \frac{\sigma^*}{r}rz - F_z \tag{7.77}$$

for equilbrium in the axial direction.

7.8 Equation of Flow in a Double Compressibility Material - Axisymmetric Conditions

The flow equation in a double compressibility material was derived earlier for a three-dimensional cartesian coordinate system and can be written as

$$\frac{\partial}{\partial x_i}\left[\frac{\bar{k}}{\gamma_w}ij\left(\frac{\partial u}{\partial x_i}w - \gamma_w e_j\right)\right] = (1-H)n_w c_w \frac{\partial u}{\partial t}w - \frac{\partial \varepsilon'}{\partial t}ii \qquad i,j = 1,2,3 \tag{7.78}$$

For axisymmetric conditions, the flow equation can be written as

$$\frac{1}{x_1}\frac{\partial}{\partial x_i}\left[x_1 \frac{\bar{k}_{ij}}{\gamma_w}\left(\frac{\partial u}{\partial x_j}w - \gamma_w e_j\right)\right] = (1-H)n_w c_w \frac{\partial u}{\partial t}w - \frac{\partial \varepsilon'}{\partial t}ii \qquad i,j = 1,2 \qquad (7.79)$$

In addition, it has been shown that

$$\varepsilon'_{ii} = \left[1 + K'/K^o\right]^{-1}\varepsilon_{ii} - \left[K^o + K'\right]^{-1}u_w \qquad (7.80)$$

from which the final form of the flow equation can be written as

$$\frac{1}{x_1}\frac{\partial}{\partial x_i}\left[x_1 \frac{\bar{k}_{ij}}{\gamma_w}\left(\frac{\partial u}{\partial x_j}w - \gamma_w e_j\right)\right] = \bar{C}\frac{\partial u}{\partial t}w + \bar{B}\frac{\partial}{\partial t}\left[\frac{\partial w}{\partial x_i}i\right] \qquad i,j = 1,2 \qquad (7.81)$$

where the subscripts 1 and 2 refer to the radial and axial directions respectively.

7.9 Summary

This chapter presents the derivation of the fully coupled displacement and pore water flow equations that govern the consolidation of a gassy soil. The soil is treated as a double compressibility material in which the saturated matrix deforms due to changes in consolidation stress, whereas the gas component of the soil deforms due to changes in total stress. The equations are first derived for a fully three-dimensional cartesian coordinate system. This is followed by the derivation of the equations under axisymmetric conditions.

CHAPTER 8

DCFEM2 - DOUBLE COMPRESSIBILITY FINITE ELEMENT MODEL IN TWO DIMENSIONS

NUMERICAL APPROXIMATION OF GOVERNING EQUATIONS

CHAPTER 8

DCFEM2 - DOUBLE COMPRESSIBILITY FINITE ELEMENT MODEL IN TWO DIMENSIONS

NUMERICAL APPROXIMATION OF GOVERNING EQUATIONS

8.1 Introduction

The governing equations for displacement and flow in a gassy soil are solved using the Galerkin finite element method. The numerical approximation and solution procedure consists of the following steps:

- Discretization of the region into a network of rectangular finite elements. The influence coefficient method is used to derive the element stiffness matrices, which proves to be a highly efficient technique.
- Formulation of the governing consolidation equations into a series of algebraic equations describing the behaviour of each finite element.
- Assembly of the element equations into a global system of algebraic equations and the incorporation of boundary conditions.
- Solution of the resulting system of algebraic equations and evaluation of stresses, strains and velocities.

The last three steps are performed for every time increment. Initial conditions are incorporated before the first time increment. If the elastic moduli are linear, no iterations are required. If the moduli are non-linear, however, the resulting system of equations is also non-linear and it is necessary for iterations to be performed within each time step until satisfactory convergence of the nodal displacement and pore pressure values to a required tolerance is achieved.

8.2 Numerical Technique

Initially, a detailed development is presented describing the Galerkin approximation of the governing equation for displacement and pore water flow in a gassy soil, followed by the derivation of a procedure for formulating element matrices using the highly efficient influence coefficient method. As derived in

the previous chapter, the governing fully coupled consolidation equations in three-dimensional Cartesian coordinates can be written in the form

$$\bar{G}\frac{\partial^2 w_i}{\partial x_j \partial x_j} + \bar{G}\frac{\partial^2 w_j}{\partial x_j \partial x_i} + \bar{\lambda}\frac{\partial^2 w_j}{\partial x_i \partial x_j} - \bar{B}\frac{\partial u}{\partial x_i}w = \frac{\partial \sigma^*_{ij}}{\partial x_j} - F_i \qquad (8.1)$$

and

$$\frac{\partial}{\partial x_i}\left[\frac{\bar{k}_{ij}}{\gamma_w}\left(\frac{\partial u}{\partial x_j}w - \gamma_w e_j\right)\right] = \bar{C}\frac{\partial u}{\partial t}w + \bar{B}\frac{\partial}{\partial t}\left[\frac{\partial w_i}{\partial x_i}\right] \qquad i,j = 1,3 \qquad (8.2)$$

where the symbols are defined in the previous chapter. To approximate these equations using the finite element Galerkin procedure, the solution domain must be subdivided into a number of finite elements in which trial solutions for any parameter ψ are expressed in the form

$$\psi(x_i, t) \simeq \hat{\psi}(x_i, t) = N_I(x_i)\,\psi_I(t), \quad I=1,2.....n \qquad (8.3)$$

The unknown parameter, ψ, which is a function of space and time, is approximated by the product of the nodal values of the parameter, $\hat{\psi}_I(t)$, which are functions of time, and a basis or shape function, $N_I(x_i)$, which is a function of space only. The number of nodal points is denoted by n. To obtain the approximated form of the governing equations 8.1 and 8.2, it is possible to apply the Galerkin procedure to these equations. It is felt here, however, that the procedure is better illustrated if the Galerkin procedure is applied to the original equilibrium and continuity equations. A more detailed description is given in texts such as Huyakorn and Pinder (1983), Hinton and Owen (1979), Zienkiewicz (1977) and Cook (1974).

8.3 Approximation of Displacement Equations - Plane Strain Conditions

If a trial solution to a governing equation is inserted into the equation, there will be a resulting error. This applies throughout the solution domain. Writing the equilibrium equation as

$$\frac{\partial \sigma_{ij}}{\partial x_j} - F_i = 0 \qquad (8.4)$$

then if an approximating solution for stress $\hat{\sigma}_{ij}$ is used, there will be a corresponding error e_R over the required domain such that

$$\frac{\partial \hat{\sigma}_{ij}}{\partial x_j} - F_i = e_R \qquad (8.5)$$

The Galerkin procedure sets the integral of this error weighted with the approximating shape function to zero for each element. Thus

$$\int_{R_e} N_I \; e_R \; dR_e = \int_{R_e} N_I \left[\frac{\partial \hat{\sigma}}{\partial x_j} ij - F_i\right] dR_e = 0 \tag{8.6}$$

where R_e denotes the element domain. Applying Green's Theorem to the above equation yields

$$\int_{B_e} N_I \; \hat{\sigma}_{ij} \; n_j \; dB_e - \int_{R_e} \frac{\partial N_I}{\partial x_j} \; \sigma_{ij} \; dR_e = \int_{R_e} N_I \; F_i \; dR \tag{8.7}$$

where B_e denotes the element boundary. From this point, the subscript e indicating the integral over an elemental domain will be dropped, as all integrals are assumed to take place over an element.

It can be noted that the first term of the above equation is the total stress acting on the boundary of the element. To denote that this is a boundary effect, the Cauchy surface traction boundary condition is used

$$S_i = - \sigma_{ij} \; n_j \quad \text{on } B_e \tag{8.8}$$

where n_j is the unit outward normal vector to the boundary B, which leads to

$$- \int_B N_I \; S_i \; dB \; - \int_R \frac{\partial N_I}{\partial x_j} \; \hat{\sigma}_{ij} \; dR \; = \int_R N_I \; F_i \; dR \tag{8.9}$$

The stress $\hat{\sigma}_{ij}$ for a double compressibility material has been expressed in terms of total strains and pore pressures in equation 7.22. Consequently,

$$\hat{\sigma}_{ij} = 2\bar{G}\hat{\varepsilon}_{ij} + \bar{\lambda}\hat{\varepsilon}_{kk}\delta_{ij} + \bar{B}\hat{u}_w\delta_{ij} + \hat{\sigma}^*_{ij} \tag{8.10}$$

where

$$\hat{\varepsilon}_{ij} = - \frac{1}{2} \left[\frac{\partial \hat{w}_i}{\partial x_j} + \frac{\partial \hat{w}_j}{\partial x_i}\right] \tag{8.11}$$

Thus the approximating equation may be written as

$$\int_R \frac{\partial N_I}{\partial x_i}\left[\bar{G}\left(\frac{\partial \hat{w}_i}{\partial x_j} + \frac{\partial \hat{w}_j}{\partial x_i}\right) + \left(\bar{\lambda}\frac{\partial \hat{w}_k}{\partial x_k} - \bar{B}\hat{u}_w\right)\delta_{ij} - \hat{\sigma}^*_{ij}\right] dR = \int_R N_I F_i \; dR + \int_B N_I S_i \; dB \tag{8.12}$$

At this point the following approximations are made

$$\hat{w}_1(x_i, \; t) = N_J(x_i) \; w_{1J} \tag{8.13}$$

$$\hat{w}_2(x_i, \; t) = N_J(x_i) \; w_{2J} \tag{8.14}$$

$$\hat{u}_w(x_i, \; t) = N_J(x_i) \; u_{wJ} \tag{8.15}$$

From which for i=1, equation 8.12 yields

$$\int_R \left[(\bar{\lambda}+2\bar{G}) \frac{\partial N_I}{\partial x_1} \frac{\partial N_J}{\partial x_1} + \bar{G} \frac{\partial N_I}{\partial x_2} \frac{\partial N_J}{\partial x_2} \right] w_{1J} \, dR + \int_R \left[\bar{\lambda} \frac{\partial N_I}{\partial x_1} \frac{\partial N_J}{\partial x_2} + \bar{G} \frac{\partial N_I}{\partial x_2} \frac{\partial N_J}{\partial x_1} \right] w_{2J} \, dR$$

$$- \int_R \left[\bar{B} \frac{\partial N_I}{\partial x_1} N_J \, u_{wJ} \, dR = \int_B N_I \, S_1 \, dB \, dR + \int_R \left[N_I \, F_1 + \frac{\partial N_I}{\partial x_j} \sigma^*_{1j} \right] dR \right. \tag{8.16}$$

and for i=2,

$$\int_R \left[\bar{\lambda} \frac{\partial N_I}{\partial x_2} \frac{\partial N_J}{\partial x_1} + \bar{G} \frac{\partial N_I}{\partial x_1} \frac{\partial N_J}{\partial x_2} \right] w_{1J} dR + \int_R \left[\bar{G} \frac{\partial N_I}{\partial x_1} \frac{\partial N_J}{\partial x_1} + (\bar{\lambda}+2\bar{G}) \frac{\partial N_I}{\partial x_2} \frac{\partial N_J}{\partial x_2} \right] w_{2J} \, dR$$

$$- \int_R \left[\bar{B} \frac{\partial N_I}{\partial x_2} N_J \, u_{wJ} \, dR = \int_B N_I \, S_2 \, dB + \int_R \left[N_I \, F_2 + \frac{\partial N_I}{\partial x_j} \sigma^*_{2j} \right] dR \right. \tag{8.17}$$

These two equations are the required results from the Galerkin approximation of the displacement equations under plane strain conditions.

8.4 Approximation of Flow Equation - Plane Strain Conditions

In a similar procedure to that above, the flow equation 7.66 can also be approximated using the Galerkin weighted residual method to give

$$\int_R \left[- \frac{\partial N_I}{\partial x_i} W_{iJ} + \bar{C} N_I N_J \frac{\partial u}{\partial t} wJ + \bar{B} N_I \frac{\partial N_J}{\partial x_i} \frac{\partial w}{\partial t} iJ \right] dR + \int_B N_I W_i n_i \, dB = 0 \tag{8.18}$$

where W_{iJ} is the nodal Darcy velocity of the pore water. Replacing the Darcy velocity by the spatial derivatives of the pore water pressure yields

$$\int_R \left[\frac{\bar{k}_{ij}}{\gamma_w} \frac{\partial N_I}{\partial x_i} \frac{\partial N_J}{\partial x_j} u_{wJ} - \bar{k}_{ij} e_j \frac{\partial N_I}{\partial x_i} + \bar{C} N_I N_J \frac{\partial u}{\partial t} wJ \right.$$

$$\left. + \bar{B} N_I \frac{\partial N_J}{\partial x_i} \frac{\partial w}{\partial t} iJ \right] dR + \int_B N_I q_B \, dB = 0 \tag{8.19}$$

where q_B is a water flux boundary condition. Application of the finite difference time stepping procedure then gives

$$\int_R \left[\bar{B} N_I \frac{\partial N_J}{\partial x_i} w_{iJ}^{t+\Delta t} + \left(\bar{C} N_I N_J + \Theta \Delta t \frac{\bar{k}_{ij}}{\gamma_w} \frac{\partial N_I}{\partial x_i} \frac{\partial N_J}{\partial x_j} \right) u_{wJ}^{t+\Delta t} \right] dR = - \int_B N_I q_B \Delta t \, dB$$

$$+ \int_R \left[\bar{B} N_I \frac{\partial N_J}{\partial x_i} w_{iJ}^{t} + \left(\bar{C} N_I N_J - (1-\Theta) \Delta t \frac{\bar{k}_{ij}}{\gamma_w} \frac{\partial N_I}{\partial x_i} \frac{\partial N_J}{\partial x_j} \right) u_{wJ}^{t} + \bar{k}_{ij} e_j \Delta t \frac{\partial N_I}{\partial x_i} \right] dR \tag{8.20}$$

where q_B is the boundary water flux, w_i^t and u_w^t denote the nodal displacement vector and pore water pressure values at the old time levels, and Θ is the time weighting factor. (The use of $\Theta = 0.5$ is recommended to obtain solutions with second order accuracy in time.) The three governing integral equations 8.16,

8.17 and 8.20 are presented in matrix form in Table 8.1. It must be noted that symmetry is obtained by reversing the signs of the components of equation 8.20

8.5 Approximation of Displacement Equations - Axisymmetric Conditions

Following the same procedure as for a plane strain case, the equilibrium equation under axisymmetric conditions may be written as

$$\frac{\partial \sigma}{\partial x_j} ij + \frac{\sigma}{x_1} i1 - \frac{\sigma}{x_1} \theta\theta \; \delta_{i1} - F_i = 0 \tag{8.21}$$

On application of the Galerkin procedure, the integrand must be multiplied by $2\pi x_1$ to account for the increase in domain size as the radius, x_1, increases. Thus equation 8.21 becomes

$$\int_{R_e} N_I \left[\frac{\partial \hat{\sigma}}{\partial x_j} ij + \frac{\hat{\sigma}}{x_1} i1 - \frac{\hat{\sigma}}{x_1} \theta\theta \; \delta_{i1} - F_i \right] 2\pi x_1 \; dR_e = 0 \tag{8.22}$$

which may be rewritten as

$$\int_{R_e} N_I \left[\frac{\partial}{\partial x_j} (x_1 \hat{\sigma}_{ij}) - \hat{\sigma}_{\theta\theta} \delta_{i1} - x_1 F_i \right] dR_e = 0 \tag{8.23}$$

Applying Green's Theorem to the first term of the above equation yields

$$\int_{B_e} N_I x_1 \hat{\sigma}_{ij} n_j \; dB_e - \int_{R_e} \left[\frac{\partial N}{\partial x_j} I (x_1 \hat{\sigma}_{ij}) - N_I \hat{\sigma}_{\theta\theta} \delta_{i1} - N_I x_1 F_i \right] dR_e = 0 \tag{8.24}$$

From this point, the subscript e indicating the integral over an elemental domain will be dropped, as all integrals are assumed to take place over an element. Again it can be noted that the first term is the total stress acting on the boundary of the element. To denote that this is a boundary effect, the Cauchy surface traction boundary condition is used

$$S_i = - \sigma_{ij} \; n_j \quad \text{on } B_e \tag{8.25}$$

from which

$$\int_B N_I S_i \; dB + \int_R \left[\frac{\partial N}{\partial x_j} I (x_1 \hat{\sigma}_{ij}) - N_I \hat{\sigma}_{\theta\theta} \delta_{i1} - N_I x_1 F_i \right] dR = 0 \tag{8.26}$$

The stress $\hat{\sigma}_{ij}$ is expressed in terms of total strains and pore pressures in equation 7.22. This leads to

$$\hat{\sigma}_{ij} = 2\bar{G} \; \hat{\varepsilon}_{ij} + \bar{\lambda} \; \hat{\varepsilon}_{kk} \delta_{ij} + \bar{B} \; \hat{u}_w \delta_{ij} + \hat{\sigma}^*_{ij} \tag{8.27}$$

where

$$\hat{\varepsilon}_{ij} = - \frac{1}{2} \left[\frac{\partial \hat{w}_i}{\partial x_j} + \frac{\partial \hat{w}_j}{\partial x_i} \right] \qquad \text{for } i,j = 1,2 \tag{8.28}$$

Table 8.1 Presentation of Approximating Equations in Matrix Form - Plane Strain

The plane strain gassy soil consolidation equations in their approximated matrix form for each element may be given as

$$\begin{bmatrix} a_{IJ} & b_{IJ} & -c_{IJ} \\ b_{IJ}^T & d_{IJ} & -e_{IJ} \\ -c_{IJ}^T & -e_{IJ}^T & -f_{IJ} \end{bmatrix} \begin{Bmatrix} w_{xJ} \\ w_{yJ} \\ u_{wJ} \end{Bmatrix} = \begin{Bmatrix} R_{1I} \\ R_{2I} \\ -R_{3I} \end{Bmatrix}$$

where

$$a_{IJ} = \langle \bar{\lambda}+2\bar{G} \rangle \iint \frac{\partial N_I}{\partial x} \frac{\partial N_J}{\partial x} \, dx \, dy + \langle \bar{G} \rangle \iint \frac{\partial N_I}{\partial y} \frac{\partial N_J}{\partial y} \, dx \, dy$$

$$b_{IJ} = \langle \bar{\lambda} \rangle \iint \frac{\partial N_I}{\partial x} \frac{\partial N_J}{\partial y} \, dx \, dy + \langle \bar{G} \rangle \iint \frac{\partial N_I}{\partial y} \frac{\partial N_J}{\partial x} \, dx \, dy$$

$$c_{IJ} = \langle \bar{B} \rangle \iint \frac{\partial N_I}{\partial x} N_J \, dx \, dy$$

$$d_{IJ} = \langle \bar{\lambda}+2\bar{G} \rangle \iint \frac{\partial N_I}{\partial y} \frac{\partial N_J}{\partial y} \, dx \, dy + \langle \bar{G} \rangle \iint \frac{\partial N_I}{\partial x} \frac{\partial N_J}{\partial x} \, dx \, dy$$

$$e_{IJ} = \langle \bar{B} \rangle \iint \frac{\partial N_I}{\partial y} N_J \, dx \, dy$$

$$f_{IJ} = \Theta \Delta t \langle \frac{\bar{k}}{\gamma_w} xx \rangle \iint \frac{\partial N_I}{\partial x} \frac{\partial N_J}{\partial x} \, dx \, dy + \Theta \Delta t \langle \frac{\bar{k}}{\gamma_w} yy \rangle \iint \frac{\partial N_I}{\partial y} \frac{\partial N_J}{\partial y} \, dx \, dy$$
$$+ \Theta \Delta t \langle \frac{\bar{k}}{\gamma_w} xy \rangle \iint \frac{\partial N_I}{\partial x} \frac{\partial N_J}{\partial y} \, dx \, dy + \Theta \Delta t \langle \frac{\bar{k}}{\gamma_w} yx \rangle \iint \frac{\partial N_I}{\partial y} \frac{\partial N_J}{\partial x} \, dx \, dy + \langle \bar{C} \rangle \iint N_I \, N_J \, dx \, dy$$

The corresponding elements of $\{R_I\}$ are

$$R_{1I} = - \int_B N_I \, S_x \, dB + \iint N_I \, F_x \, dx \, dy + \iint \left(\frac{\partial N_I}{\partial x} \sigma^*_{xx} + \frac{\partial N_I}{\partial y} \sigma^*_{xy} \right) dx \, dy$$

$$R_{2I} = - \int_B N_I \, S_y \, dB + \iint N_I \, F_y \, dx \, dy + \iint \left(\frac{\partial N_I}{\partial x} \sigma^*_{yx} + \frac{\partial N_I}{\partial y} \sigma^*_{yy} \right) dx \, dy$$

$$R_{3I} = \langle \bar{B} \rangle \iint N_I \frac{\partial N_J}{\partial x} w^t_{xJ} \, dx \, dy + \langle \bar{B} \rangle \iint N_I \frac{\partial N_J}{\partial y} w^t_{yJ} \, dx \, dy$$
$$- (1-\Theta) \Delta t \langle \frac{\bar{k}}{\gamma_w} xx \rangle \iint \frac{\partial N_I}{\partial x} \frac{\partial N_J}{\partial x} u^t_{wJ} \, dx \, dy - (1-\Theta) \Delta t \langle \frac{\bar{k}}{\gamma_w} yy \rangle \iint \frac{\partial N_I}{\partial y} \frac{\partial N_J}{\partial y} u^t_{wJ} \, dx \, dy$$
$$- (1-\Theta) \Delta t \langle \frac{\bar{k}}{\gamma_w} xy \rangle \iint \frac{\partial N_I}{\partial x} \frac{\partial N_J}{\partial y} u^t_{wJ} \, dx \, dy - (1-\Theta) \Delta t \langle \frac{\bar{k}}{\gamma_w} yx \rangle \iint \frac{\partial N_I}{\partial y} \frac{\partial N_J}{\partial x} u^t_{wJ} \, dx \, dy$$
$$+ \Delta t \langle \bar{k}_{xx} e_x + \bar{k}_{xy} e_y \rangle \iint \frac{\partial N_I}{\partial x} \, dx \, dy + \Delta t \langle \bar{k}_{yx} e_x + \bar{k}_{yy} e_y \rangle \iint \frac{\partial N_I}{\partial y} \, dx \, dy$$
$$+ \langle \bar{C} \rangle \iint N_I \, N_J \, u^t_{wJ} \, dx \, dy + \Delta t \, Q_I + \int_B N_I \, \Delta t \, q \, dB$$

and where

$$\hat{\varepsilon}_{33} = \hat{\varepsilon}_{\theta\theta} = -\frac{\hat{w}_1}{x_1} \quad ; \quad \hat{\varepsilon}_{13} = \hat{\varepsilon}_{23} = 0 \tag{8.29}$$

in which subscript 1 refers to the radial coordinate r, 2 refers to the axial coordinate z, and 3 refers to the tangential coordinate θ.

Substitution of the above definitions of stress and strain into the integral equation 8.26 then yields

$$\iint\Bigg(r\frac{\partial N_I}{\partial r}\Big[(\bar{\lambda}+2\bar{G})\frac{\partial \hat{w}}{\partial r} + \bar{\lambda}\,\frac{\partial \hat{w}}{\partial z} + \bar{\lambda}\,\frac{w}{r}\Big] + r\bar{G}\,\frac{\partial N_I}{\partial z}\Big[\frac{\partial \hat{w}}{\partial z} + \frac{\partial \hat{w}}{\partial r}\Big] - r\bar{B}\,\frac{\partial N_I}{\partial r}\,\hat{u}_w$$

$$+ N_I\Big[(\lambda+2G)\frac{\hat{w}}{r} + \bar{\lambda}\,\frac{\partial \hat{w}}{\partial r} + \bar{\lambda}\,\frac{\partial \hat{w}}{\partial z} - \bar{B}\,\hat{u}_w\Big]\Bigg)\,dr\,dz = \int_B rN_I S_r\,dB$$

$$+ \iint\Big[rN_I F_r + r\frac{\partial N_I}{\partial r}\,\sigma^*_{rr} + r\frac{\partial N_I}{\partial z}\,\sigma^*_{rz} + N_I\sigma^*_{\theta\theta}\Big]\,dr\,dz \tag{8.30}$$

in the radial direction, and

$$\iint\Bigg(r\frac{\partial N_I}{\partial z}\Big[(\bar{\lambda}+2\bar{G})\frac{\partial \hat{w}}{\partial z} + \bar{\lambda}\,\frac{\partial \hat{w}}{\partial r} + \bar{\lambda}\,\frac{w}{r} - \bar{B}\,u_w\Big]$$

$$+ r\bar{G}\,\frac{\partial N_I}{\partial r}\Big[\frac{\partial \hat{w}}{\partial z} + \frac{\partial \hat{w}}{\partial r}\Big]\Bigg)\,dr\,dz = \int_B rN_I S_z\,dB$$

$$+ \iint\Big[rN_I F_z + r\frac{\partial N_I}{\partial r}\,\sigma^*_{zr} + r\frac{\partial N_I}{\partial z}\,\sigma^*_{zz}\Big]\,dr\,dz \tag{8.31}$$

in the axial direction. The approximations are then made that

$$\hat{w}_r(x_i,\ t) = N_J(x_i)\ w_{rJ} \tag{8.32}$$

$$\hat{w}_z(x_i,\ t) = N_J(x_i)\ w_{zJ} \tag{8.33}$$

$$\hat{u}_w(x_i,\ t) = N_J(x_i)\ u_{wJ} \tag{8.34}$$

From which, in the radial direction, equation 8.30 becomes

$$\iint\Big[r(\bar{\lambda}+2\bar{G})\frac{\partial N_I}{\partial r}\,\frac{\partial N_J}{\partial r} + r\bar{G}\,\frac{\partial N_I}{\partial z}\,\frac{\partial N_J}{\partial z}$$

$$+ \bar{\lambda}\Big(N_I\,\frac{\partial N_J}{\partial r} + \frac{\partial N_I}{\partial r}\,N_J\Big) + \frac{\bar{\lambda}+2\bar{G}}{r}\,N_I N_J\Big]w_{rJ}\,dr\,dz$$

$$+ \iint\Big[r\bar{\lambda}\,\frac{\partial N_I}{\partial r}\,\frac{\partial N_J}{\partial z} + r\bar{G}\,\frac{\partial N_I}{\partial z}\,\frac{\partial N_J}{\partial r} + \bar{\lambda}\,N_I\,\frac{\partial N_J}{\partial z}\Big]w_{zJ}\,dr\,dz$$

$$- \iint\bar{B}\Big[r\frac{\partial N_I}{\partial r}\,N_J + N_I N_J\Big]u_{wJ}\,dr\,dz = \int_B r\,N_I S_r\,dB$$

$$+ \iint\Big[r\,N_I F_r + r\frac{\partial N_I}{\partial r}\,\sigma^*_{rr} + r\frac{\partial N_I}{\partial z}\,\sigma^*_{rz} + N_I\,\sigma^*_{\theta\theta}\Big]\,dr\,dz \tag{8.35}$$

and in the axial direction, equation 8.31 becomes

$$\iint\left[r\bar{\lambda}\,\frac{\partial N_I}{\partial z}\,\frac{\partial N_J}{\partial r}+r\bar{G}\,\frac{\partial N_I}{\partial r}\,\frac{\partial N_J}{\partial z}+\bar{\lambda}\,\frac{\partial N_I}{\partial z}\,N_J\right]w_{rJ}\,dr\,dz$$

$$+\iint\left[r(\bar{\lambda}+2\bar{G})\frac{\partial N_I}{\partial z}\,\frac{\partial N_J}{\partial z}+r\bar{G}\,\frac{\partial N_I}{\partial r}\,\frac{\partial N_J}{\partial r}\right]w_{zJ}\,dr\,dz-\iint\bar{B}\left[r\,\frac{\partial N_I}{\partial z}\,N_J\right]u_{wJ}\,dr\,dz$$

$$=\int_B r\,N_I\,S_z\,dB+\iint\left[r\,N_I\,F_z+r\,\frac{\partial N_I}{\partial r}\,\sigma^*_{zr}+r\,\frac{\partial N_I}{\partial z}\,\sigma^*_{zz}\right]dr\,dz \qquad (8.36)$$

These two equations are the required results from the Galerkin approximation of the displacement equations.

8.6 Approximation of Flow Equation - Axisymmetric Conditions

The governing equation for pore water flow in a gassy soil under axisymmetric conditions can be written as

$$\frac{1}{x_1}\frac{\partial}{\partial x_i}\left[x_1\,\frac{\bar{k}_{ij}}{\gamma_w}\left(\frac{\partial u_w}{\partial x_j}-\gamma_w e_j\right)\right]=\bar{C}\,\frac{\partial u_w}{\partial t}+\bar{B}\,\frac{\partial}{\partial t}\left[\frac{\partial w_i}{\partial x_i}\right] \qquad i,j=1,2 \qquad (8.37)$$

After application of the Galerkin approximation and Green's theorem, followed by a finite difference time stepping procedure, the resulting integral equation may be written as

$$\iint r\left(\bar{C}N_IN_J+\Theta\Delta t\,\frac{\bar{k}_{ij}}{\gamma_w}\,\frac{\partial N_I}{\partial x_i}\,\frac{\partial N_J}{\partial x_j}\right]u_{wJ}^{t+\Delta t}-\Delta t\,\bar{k}_{ij}e_j\,\frac{\partial N_I}{\partial x_i}\right)dr\,dz$$

$$+\iint\left(\bar{B}\left[N_IN_J+rN_I\,\frac{\partial N_J}{\partial r}\right]w_{rJ}^{t+\Delta t}+\bar{B}\left[rN_I\,\frac{\partial N_J}{\partial z}\right]w_{zJ}^{t+\Delta t}\right)dr\,dz$$

$$=\iint\left(\bar{B}\left[rN_I\,\frac{\partial N_J}{\partial r}\,w_{rJ}^{t}+rN_I\,\frac{\partial N_J}{\partial z}\,w_{zJ}^{t}+N_IN_Jw_{rJ}^{t}\right]\right)dr\,dz+r\,\Delta t\,Q_I$$

$$+\iint\left(\left[r\bar{C}N_IN_J-r(1-\Theta)\Delta t\frac{\bar{k}_{ij}}{\gamma_w}\,\frac{\partial N_I}{\partial x_i}\,\frac{\partial N_J}{\partial x_j}\right]u_{wJ}^{t}\right)dr\,dz+\int_B r\,N_I\Delta t\,q_b\,dB \qquad (8.38)$$

The three governing integral equations for gassy soil consolidation under axisymmetric conditions 8.35, 8.36 and 8.38 are presented in matrix form in Table 8.2. Again it can be observed that symmetry has been produced by the reversal of the signs in equation 8.38.

8.7 Alternative Formulation due to Non-Linear Behaviour

During the consolidation process of a gassy soil, many of the material properties do not remain constant as they are often affected by other physical

Table 8.2 Presentation of Approximating Equations in Matrix Form - Axial Symmetry

The axisymmetric gassy soil consolidation equations may be written in their approximated matrix form, for each element, as

$$\begin{bmatrix} \tilde{a}_{IJ} & \tilde{b}_{IJ} & -\tilde{c}_{IJ} \\ \tilde{b}^{T}_{IJ} & \tilde{d}_{IJ} & -\tilde{e}_{IJ} \\ -\tilde{c}^{T}_{IJ} & -\tilde{e}^{T}_{IJ} & -\tilde{f}_{IJ} \end{bmatrix} \begin{Bmatrix} w_{rJ} \\ w_{zJ} \\ u_{wJ} \end{Bmatrix} = \begin{Bmatrix} \tilde{R}_{1I} \\ \tilde{R}_{2I} \\ -\tilde{R}_{3I} \end{Bmatrix}$$

where

$$\tilde{a}_{IJ} = \langle\bar{\lambda}+2\bar{G}\rangle \iint r \frac{\partial N_I}{\partial r} \frac{\partial N_J}{\partial r} \, dr \, dz + \langle\bar{G}\rangle \iint r \frac{\partial N_I}{\partial z} \frac{\partial N_J}{\partial z} \, dr \, dz$$
$$+ \langle\bar{\lambda}+2\bar{G}\rangle \iint \frac{1}{r} N_I N_J \, dr \, dz + \langle\bar{\lambda}\rangle \iint \left(N_I \frac{\partial N_J}{\partial r} + \frac{\partial N_I}{\partial r} N_J\right) dr \, dz$$

$$\tilde{b}_{IJ} = \langle\bar{\lambda}\rangle \iint r \frac{\partial N_I}{\partial r} \frac{\partial N_J}{\partial z} \, dr \, dz + \langle\bar{G}\rangle \iint r \frac{\partial N_I}{\partial z} \frac{\partial N_J}{\partial r} \, dr \, dz + \langle\bar{\lambda}\rangle \iint N_I \frac{\partial N_J}{\partial z} \, dr \, dz$$

$$\tilde{c}_{IJ} = \langle\bar{B}\rangle \iint \left(r \frac{\partial N_I}{\partial r} N_J + N_I N_J\right) dr \, dz$$

$$\tilde{d}_{IJ} = \langle\bar{\lambda}+2\bar{G}\rangle \iint r \frac{\partial N_I}{\partial z} \frac{\partial N_J}{\partial z} \, dr \, dz + \langle\bar{G}\rangle \iint r \frac{\partial N_I}{\partial r} \frac{\partial N_J}{\partial r} \, dr \, dz$$

$$\tilde{e}_{IJ} = \langle\bar{B}\rangle \iint r \frac{\partial N_I}{\partial z} N_J \, dr \, dz$$

$$\tilde{f}_{IJ} = \Theta\Delta t\langle\frac{\bar{k}}{\gamma_w}rr\rangle \iint r \frac{\partial N_I}{\partial r} \frac{\partial N_J}{\partial r} \, dr \, dz + \Theta\Delta t\langle\frac{\bar{k}}{\gamma_w}zz\rangle \iint r \frac{\partial N_I}{\partial z} \frac{\partial N_J}{\partial z} \, dr \, dz$$
$$+ \Theta\Delta t\langle\frac{\bar{k}}{\gamma_w}rz\rangle \iint r \frac{\partial N_I}{\partial r} \frac{\partial N_J}{\partial z} \, dr \, dz + \Theta\Delta t\langle\frac{\bar{k}}{\gamma_w}zr\rangle \iint r \frac{\partial N_I}{\partial z} \frac{\partial N_J}{\partial r} \, dr \, dz + \langle\bar{C}\rangle \iint r N_I N_J \, dr \, dz$$

The corresponding elements of $\{R_I\}$ are given by

$$\tilde{R}_{1I} = \int_B r N_I S_r \, dB + \iint r N_I F_r \, dr \, dz + \iint r\left(\frac{\partial N_I}{\partial r} \sigma^*_{rr} + \frac{\partial N_I}{\partial z} \sigma^*_{rz}\right) dr \, dz + \iint N_I \sigma^*_{\theta\theta} \, dr \, dz$$

$$\tilde{R}_{2I} = \int_B r N_I S_z \, dB + \iint r N_I F_z \, dr \, dz + \iint r\left(\frac{\partial N_I}{\partial r} \sigma^*_{zr} + \frac{\partial N_I}{\partial z} \sigma^*_{zz}\right) dr \, dz$$

$$\tilde{R}_{3I} = \langle\bar{B}\rangle \iint \left(r N_I \frac{\partial N_J}{\partial r} w^t_{rJ} + r N_I \frac{\partial N_J}{\partial z} w^t_{zJ} + N_I N_J w^t_{rJ}\right) dr \, dz$$
$$- (1-\Theta)\Delta t\langle\frac{\bar{k}}{\gamma_w}rr\rangle \iint r \frac{\partial N_I}{\partial r} \frac{\partial N_J}{\partial r} u^t_{wJ} \, dr \, dz - (1-\Theta)\Delta t\langle\frac{\bar{k}}{\gamma_w}zz\rangle \iint r \frac{\partial N_I}{\partial z} \frac{\partial N_J}{\partial z} u^t_{wJ} \, dr \, dz$$
$$- (1-\Theta)\Delta t\langle\frac{\bar{k}}{\gamma_w}rz\rangle \iint r \frac{\partial N_I}{\partial r} \frac{\partial N_J}{\partial r} u^t_{wJ} \, dr \, dz - (1-\Theta)\Delta t\langle\frac{\bar{k}}{\gamma_w}zr\rangle \iint r \frac{\partial N_I}{\partial z} \frac{\partial N_J}{\partial r} u^t_{wJ} \, dr \, dz$$
$$+ \Delta t\langle\bar{k}_{rr}e_r + \bar{k}_{rz}e_z\rangle \iint r \frac{\partial N_I}{\partial r} \, dr \, dz + \Delta t\langle\bar{k}_{zr}e_r + \bar{k}_{zz}e_z\rangle \iint r \frac{\partial N_I}{\partial z} \, dr \, dz$$
$$+ \langle\bar{C}\rangle \iint r N_I N_J u^t_{wJ} \, dr \, dz + \Delta t \, r_I Q_I + \int_B r N_I \Delta t \, q \, dB$$

parameters such as pore water pressure, total stress or gas volume. Therefore in order to model such behaviour, it is necessary to modify the previous formulation so that non-linear material behaviour can be incorporated. The main modification to the formulation is that the governing equation is solved in increments--the beginning of each time step is treated as a new problem with updated material parameters and initial conditions. Thus, considering first the stress-strain equation 7.22

$$\sigma_{ij} = 2\bar{G}\varepsilon_{ij} + \bar{\lambda}\varepsilon_{kk}\delta_{ij} + \bar{B}u_w\delta_{ij} + \sigma^*_{ij} \tag{8.39}$$

then this may be rewritten in terms of increments of stress and strain as

$$\Delta\sigma_{ij} = 2\bar{G}\Delta\varepsilon_{ij} + \bar{\lambda}\Delta\varepsilon_{kk}\delta_{ij} + \bar{B}\Delta u_w\delta_{ij} \tag{8.40}$$

Substitution of this equation into the governing equilibrium equation followed by the application of the Galerkin finite element method, gives

$$\begin{bmatrix} a_{IJ} & b_{IJ} & -c_{IJ} \\ b^T_{IJ} & d_{IJ} & -e_{IJ} \end{bmatrix} \begin{Bmatrix} \Delta w_{1J} \\ \Delta w_{2J} \\ \Delta u_{wJ} \end{Bmatrix} = \begin{Bmatrix} \Delta R_{1I} \\ \Delta R_{2I} \end{Bmatrix} + \begin{Bmatrix} \Delta B_{1I} \\ \Delta B_{2I} \end{Bmatrix} \tag{8.41}$$

which applies to both plane strain and axisymmetric conditions. For this method the increment of displacement is set equal to the displacement that takes place over an increment of time, resulting in

$$\Delta w_{iJ} = w^{t+\Delta t}_{iJ} - w^t_{iJ} \tag{8.42}$$

from which equation 8.41 becomes

$$\begin{bmatrix} a_{IJ} & b_{IJ} & -c_{IJ} \\ b^T_{IJ} & d_{IJ} & -e_{IJ} \end{bmatrix} \begin{Bmatrix} w_{1J} \\ w_{2J} \\ u_{wJ} \end{Bmatrix}^{t+\Delta t} = \begin{bmatrix} a_{IJ} & b_{IJ} & -c_{IJ} \\ b^T_{IJ} & d_{IJ} & -e_{IJ} \end{bmatrix} \begin{Bmatrix} w_{1J} \\ w_{2J} \\ u_{wJ} \end{Bmatrix}^t - \begin{Bmatrix} R_{1I} \\ R_{2I} \end{Bmatrix}^t + \begin{Bmatrix} R_{1I} \\ R_{2I} \end{Bmatrix}^{t+\Delta t} - \begin{Bmatrix} B_{1I} \\ B_{2I} \end{Bmatrix}^t + \begin{Bmatrix} B_{1I} \\ B_{2I} \end{Bmatrix}^{t+\Delta t} \tag{8.43}$$

Thus in order to solve the above equation, the nodal values and the right-hand side vector from the previous time step must be stored. These values may then simply be incorporated into the right-hand side vector during the assembly process. The resulting stiffness matrix and right-hand side vector can then be solved in the same way as for the linear elastic formulation.

8.8 Non-Linear Solution Method and Convergence Criteria

At the end of each time increment in the solution procedure, it is necessary for the solution to converge to a required tolerance, otherwise the

errors at the end of each time step will accumulate and result in a large error at late time. There are numerous non-linear iterative methods--the two most commonly used being the Direct method (sometimes known as the Picard method) and the Newton-Raphson method. Both of these methods are described in detail by Owen and Hinton (1980). In general, the Newton-Raphson method requires a lesser number of iterations for convergence than the Direct method.

The Newton-Raphson method, however, produces an asymmetric stiffness matrix which in turn requires more computer storage and time for each iteration. In addition, when modelling a gassy soil, it is possible that all the gas may dissolve into the pore water producing a saturated soil and thus abruptly changing many of the material parameters. This causes severe problems for the Newton-Raphson iterative method. Consequently, for the purposes of this model the Direct iteration scheme has been chosen as the problems treated are not highly non-linear due to the fact that an incremental solution has been adopted.

During the iterative process, the solutions are updated but may be relaxed by

$$\psi_I^{i+1} = \psi_I^i + R_f\left[\psi_I^{i+1} - \psi_I^i\right] \tag{8.44}$$

where R_f is known as the relaxation factor which is introduced if it is apparent that oscillations are present in a solution. Introduction of R_f has the effect of damping the solution scheme enabling convergence to occur.

The convergence criterion used in this model is such that all variables at every node must comply to

$$\left| \frac{\psi_I^{i+1} - \psi_I^i}{\psi_I^i} \right| < TOL \tag{8.45}$$

where TOL is the tolerance criteria. TOL is normally set to about 0.01.

8.9 Summary

This chapter presents the approximation of the governing coupled consolidation equations of a double compressible material using the Galerkin finite element method. The formulation approximates the consolidation equations for both plane strain and axisymmetric conditions. This formulation is presented in general form such that any type of finite element can be used.

CHAPTER 9

DCFEM2 - DOUBLE COMPRESSIBILITY FINITE ELEMENT MODEL IN TWO DIMENSIONS

RECTANGULAR FINITE ELEMENT FORMULATION

CHAPTER 9

DCFEM2 - DOUBLE COMPRESSIBILITY FINITE ELEMENT MODEL IN TWO DIMENSIONS

RECTANGULAR FINITE ELEMENT FORMULATION

9.1 Introduction

In the previous chapter, the equations governing gassy soil consolidation have been approximated using the Galerkin finite element method. This chapter applies the general finite element approximation to one particular element so that the governing consolidation equations can be solved numerically. The resulting implementation of a particular element type produces a stiffness matrix and right-hand side load vector for the element which is presented in this chapter. A computer program can then be written to assemble the element matrices and vectors into global form over a soil domain. This program can subsequently be used to solve consolidation problems for which there is no analytical solution. However, these approximated equations may be applied to any type of two-dimensional finite element for plane strain and axisymmetric conditions. The next stage is to choose the type of finite element that is to be used for the discretization of the domain, and then to formulate the approximated equations specifically to this element type.

9.2 Choice of Finite Element

The main purpose in the development of the finite element model DCFEM2 is to simulate the consolidation behaviour of a gassy soil that has been tested under laboratory conditions. At the present time, the apparatus used for such testing has been limited to the triaxial and oedometer cells. Both of these apparatus impose an initial cylindrical domain on the soil sample. Thus if an axisymmetric formulation is adopted, both cases may be simulated using a rectangular domain. Accordingly, one of the simplest elements required to model this domain is a four noded rectangular element.

Another point to note is that at this stage of gassy soil research, the main object is to test the validity of the governing consolidation equations

that have been developed for a gassy soil. The purpose is not to test the validity of the finite element method or to evaluate the performance of one particular element. The four noded rectangular element has been used widely to model the flow of multiphase fluids in a porous medium, and has also been used successfully in the modelling of the fully coupled consolidation behaviour of a land based unsaturated soil (Huyakorn, Thomas and Thompson, 1984).

Chang and Duncan (1983) successfully used 8 noded rectangular elements for the simulation of the consolidation of a partly saturated soil. The soil was treated as having Modified Cam-Clay behaviour and the water and gas phases were combined to act as a single compressible fluid. In situations where there is a high degree of bending or shear in a material, it is necessary to use a higher order element. If the domain is dominated by compressive stresses, however, lower order elements are sufficient. This is illustrated quite clearly by the work of Ghaboussi and Wilson (1971) who used four noded isoparametric elements to model the deformation and pore flow behaviour of a soil containing a compressible pore fluid in a two-dimensional plane strain domain.

Huyakorn et al. (1984) applied a technique to four noded rectangular elements in their treatment of the equation governing unsaturated flow in a porous medium. This technique replaced the Gauss weighting integration method with one of direct analytical integration. The technique was described as "the influence coefficient technique". This technique was limited to the flow equations under two-dimensional plane strain conditions. The work at Oxford has extended this method to apply to pore water flow and soil deformation in a gassy soil under both two-dimensional plane strain and axisymmetric conditions.

9.3 Integration and Matrix Computation of Rectangular Finite Elements

Due to the non-linearities associated with changes in the material parameters during the consolidation of a gassy soil, the stiffness matrix and the right-hand side vector must be computed after each iteration for every time increment. Because the total number of repetitions of such a computation can be up to several thousand in a long term simulation of a field problem, it is desirable to minimize the computational effort required to obtain the element

stiffness matrix and the right-hand side vector. One of the methods for speeding up this process is to change the method of integration of the elements from a numerical to an analytical technique.

For a linear four noded rectangular element, 2x2 point Gauss-Legendre quadrature is required to produce an exact integration of the element under plane strain conditions, with higher order quadrature required for axisymmetric conditions. The following development, however, describes a technique where numerical integration is not required in which the stiffness matrix and right-hand side vector can be predetermined using a direct integration method. The resulting matrices are presented in algebraic form such that the material parameters and element geometry that influence the matrix can be simply inserted as coefficients. This method is known as the influence coefficient method.

In order to perform integration of a finite element, it is often easier to convert all global coordinates (x,y; r,z) into local coordinates (ξ,η). The local shape functions and shape function derivatives are then identical for each element in the domain. Once these have been found, it is a simple case of converting back to a global shape function from the knowledge of the geometry of the element. Table 9.1 presents the coodinate system, shape functions and shape function derivatives for both local and global systems.

9.4 Stiffness Matrix and Load Vector for Plane Strain Conditions.

The integral equations governing the consolidation behaviour of gassy soil under plane strain conditions have been presented in Table 8.1 along with the components of the matrix. At this stage this matrix may apply to any type of finite element. In order to produce the element matrix for a four noded rectangular element, the shape functions and the shape function derivatives--as presented in Table 9.1--must be substituted into the matrix components of Table 8.1. This substitution produces the need for integration, over the rectangular element, of various shape functions and their derivatives. Table 9.2a presents all the integrals required for plane strain conditions.

Substitution of these integral definitions into the components of Table 8.1 results in the element stiffness matrix and the right-hand side load vector

Table 9.1 Shape Functions and Derivatives for the Four-Noded Rectangular Finite Element

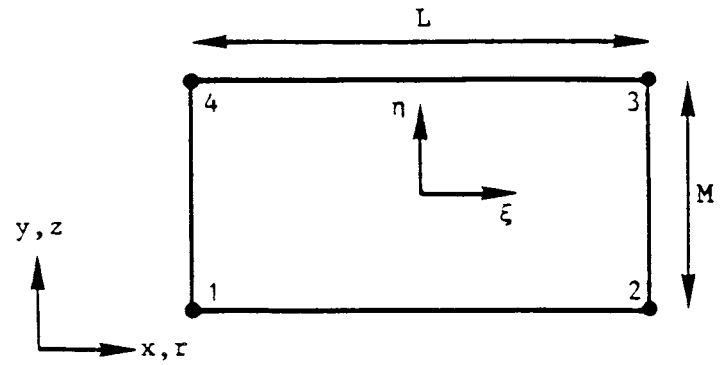

Dimensionless Coordinates

$$\xi = 2(x - x_o)/L$$

$$\eta = 2(y - y_o)/M$$

where

$$x_o = (x_1 + x_2 + x_3 + x_4)/4$$

$$y_o = (y_1 + y_2 + y_3 + y_4)/4$$

Shape Functions

LOCAL	GLOBAL
$N_1 = \frac{1}{4}(1-\xi)(1-\eta)$	$= +\frac{1}{LM}(x_3 - x)(y_3 - y)$
$N_2 = \frac{1}{4}(1+\xi)(1-\eta)$	$= -\frac{1}{LM}(x_1 - x)(y_3 - y)$
$N_3 = \frac{1}{4}(1+\xi)(1+\eta)$	$= +\frac{1}{LM}(x_1 - x)(y_1 - y)$
$N_4 = \frac{1}{4}(1-\xi)(1+\eta)$	$= -\frac{1}{LM}(x_3 - x)(y_1 - y)$

Shape Function Derivatives

LOCAL		GLOBAL	
$\frac{\partial N_1}{\partial \xi} = -\frac{1}{4}(1-\eta)$	$\frac{\partial N_1}{\partial \eta} = -\frac{1}{4}(1-\xi)$	$\frac{\partial N_1}{\partial x} = -\frac{1}{2L}(1-\eta)$	$\frac{\partial N_1}{\partial y} = -\frac{1}{2M}(1-\xi)$
$\frac{\partial N_2}{\partial \xi} = +\frac{1}{4}(1-\eta)$	$\frac{\partial N_2}{\partial \eta} = -\frac{1}{4}(1+\xi)$	$\frac{\partial N_2}{\partial \xi} = +\frac{1}{2L}(1-\eta)$	$\frac{\partial N_2}{\partial \eta} = -\frac{1}{2M}(1+\xi)$
$\frac{\partial N_3}{\partial \xi} = +\frac{1}{4}(1+\eta)$	$\frac{\partial N_3}{\partial \eta} = +\frac{1}{4}(1+\xi)$	$\frac{\partial N_3}{\partial \xi} = +\frac{1}{2L}(1+\eta)$	$\frac{\partial N_3}{\partial \eta} = +\frac{1}{2M}(1+\xi)$
$\frac{\partial N_4}{\partial \xi} = -\frac{1}{4}(1+\eta)$	$\frac{\partial N_4}{\partial \eta} = +\frac{1}{4}(1-\xi)$	$\frac{\partial N_4}{\partial \xi} = -\frac{1}{2L}(1+\eta)$	$\frac{\partial N_4}{\partial \eta} = +\frac{1}{2M}(1-\xi)$

General Relationship between Derivatives

$$\frac{\partial N_I}{\partial x} = \frac{\partial N_I}{\partial \xi}\frac{d\xi}{dx} = \frac{2}{L}\frac{\partial N_I}{\partial \xi} \quad ; \quad \frac{\partial N_I}{\partial y} = \frac{\partial N_I}{\partial \eta}\frac{d\eta}{dy} = \frac{2}{M}\frac{\partial N_I}{\partial \eta}$$

Table 9.2 Integrals Required for Rectangular Finite Element Approximation

(a) Plane Strain Conditions

$$\iint \frac{\partial N_I}{\partial x} \frac{\partial N_J}{\partial x}\, dx\, dy = \frac{M}{6L} \begin{bmatrix} +2 & -2 & -1 & +1 \\ -2 & +2 & +1 & -1 \\ -1 & +1 & +2 & -2 \\ +1 & -1 & -2 & +2 \end{bmatrix}$$

$$\iint \frac{\partial N_I}{\partial y} \frac{\partial N_J}{\partial y}\, dx\, dy = \frac{L}{6M} \begin{bmatrix} +2 & +1 & -1 & -2 \\ +1 & +2 & -2 & -1 \\ -1 & -2 & +2 & +1 \\ -2 & -1 & +1 & +2 \end{bmatrix}$$

$$\iint \frac{\partial N_I}{\partial x} \frac{\partial N_J}{\partial y}\, dx\, dy = \frac{1}{4} \begin{bmatrix} +1 & +1 & -1 & -1 \\ -1 & -1 & +1 & +1 \\ -1 & -1 & +1 & +1 \\ +1 & +1 & -1 & -1 \end{bmatrix}$$

$$\iint \frac{\partial N_I}{\partial y} \frac{\partial N_J}{\partial x}\, dx\, dy = \frac{1}{4} \begin{bmatrix} +1 & -1 & -1 & +1 \\ +1 & -1 & -1 & +1 \\ -1 & +1 & +1 & -1 \\ -1 & +1 & +1 & -1 \end{bmatrix}$$

$$\iint \frac{\partial N_I}{\partial x} N_J\, dx\, dy = \frac{M}{12} \begin{bmatrix} -2 & -2 & -1 & -1 \\ +2 & +2 & +1 & +1 \\ +1 & +1 & +2 & +2 \\ -1 & -1 & -2 & -2 \end{bmatrix}$$

$$\iint \frac{\partial N_I}{\partial y} N_J\, dx\, dy = \frac{L}{12} \begin{bmatrix} -2 & -1 & -1 & -2 \\ -1 & -2 & -2 & -1 \\ +1 & +2 & +2 & +1 \\ +2 & +1 & +1 & +2 \end{bmatrix}$$

$$\iint N_I \frac{\partial N_J}{\partial x}\, dx\, dy = \frac{M}{12} \begin{bmatrix} -2 & +2 & +1 & -1 \\ -2 & +2 & +1 & -1 \\ -1 & +1 & +2 & -2 \\ -1 & +1 & +2 & -2 \end{bmatrix}$$

$$\iint N_I \frac{\partial N_J}{\partial y}\, dx\, dy = \frac{L}{12} \begin{bmatrix} -2 & -1 & +1 & +2 \\ -1 & -2 & +2 & +1 \\ -1 & -2 & +2 & +1 \\ -2 & -1 & +1 & +2 \end{bmatrix}$$

$$\iint N_I N_J\, dx\, dy = \frac{LM}{36} \begin{bmatrix} +4 & +2 & +1 & +2 \\ +2 & +4 & +2 & +1 \\ +1 & +2 & +4 & +2 \\ +2 & +1 & +2 & +4 \end{bmatrix}$$

$$\iint \frac{\partial N_I}{\partial x} \sigma_{ix}\, dx\, dy = \frac{M\sigma_{ix}}{2} \begin{bmatrix} -1 \\ +1 \\ +1 \\ -1 \end{bmatrix}$$

$$\iint \frac{\partial N_I}{\partial y} \sigma_{iy}\, dx\, dy = \frac{L\sigma_{iy}}{2} \begin{bmatrix} -1 \\ -1 \\ +1 \\ +1 \end{bmatrix}$$

$$\iint N_I\, dx\, dy = \frac{LM}{4} \begin{bmatrix} +1 \\ +1 \\ +1 \\ +1 \end{bmatrix}$$

$$\int_B N_I S_i\, dx = \frac{LS_i}{2} \begin{bmatrix} +1 \\ +1 \end{bmatrix}$$

$$\int_B N_I S_i\, dy = \frac{MS_i}{2} \begin{bmatrix} +1 \\ +1 \end{bmatrix}$$

(b) Axisymmetric Conditions

$$\iint \xi \frac{\partial N_I}{\partial r} \frac{\partial N_J}{\partial r}\, dr\, dz = \begin{bmatrix} 0 & 0 & 0 & 0 \\ 0 & 0 & 0 & 0 \\ 0 & 0 & 0 & 0 \\ 0 & 0 & 0 & 0 \end{bmatrix}$$

$$\iint \xi \frac{\partial N_I}{\partial z} \frac{\partial N_J}{\partial z}\, dr\, dz = \frac{L}{6M} \begin{bmatrix} -1 & 0 & 0 & +1 \\ 0 & +1 & -1 & 0 \\ 0 & -1 & +1 & 0 \\ +1 & 0 & 0 & -1 \end{bmatrix}$$

$$\iint \xi \frac{\partial N_I}{\partial r} \frac{\partial N_J}{\partial z}\, dr\, dz = \frac{1}{12} \begin{bmatrix} -1 & +1 & -1 & +1 \\ +1 & -1 & +1 & -1 \\ +1 & -1 & +1 & -1 \\ -1 & +1 & -1 & +1 \end{bmatrix}$$

$$\iint \xi \frac{\partial N_I}{\partial z} \frac{\partial N_J}{\partial r}\, dr\, dz = \frac{1}{12} \begin{bmatrix} -1 & +1 & +1 & -1 \\ +1 & -1 & -1 & +1 \\ -1 & +1 & +1 & -1 \\ +1 & -1 & -1 & +1 \end{bmatrix}$$

$$\iint \xi \frac{\partial N_I}{\partial r} N_J\, dr\, dz = \frac{M}{36} \begin{bmatrix} +2 & -2 & -1 & +1 \\ -2 & +2 & +1 & -1 \\ -1 & +1 & +2 & -2 \\ +1 & -1 & -2 & +2 \end{bmatrix}$$

$$\iint \xi \frac{\partial N_I}{\partial z} N_J\, dr\, dz = \frac{L}{12} \begin{bmatrix} +1 & 0 & 0 & +1 \\ 0 & -1 & -1 & 0 \\ 0 & +1 & +1 & 0 \\ -1 & 0 & 0 & -1 \end{bmatrix}$$

$$\iint \xi N_I \frac{\partial N_J}{\partial r}\, dr\, dz = \frac{M}{36} \begin{bmatrix} +2 & -2 & -1 & +1 \\ -2 & +2 & +1 & -1 \\ -1 & +1 & +2 & -2 \\ +1 & -1 & -2 & +2 \end{bmatrix}$$

$$\iint \xi N_I \frac{\partial N_J}{\partial z}\, dr\, dz = \frac{L}{12} \begin{bmatrix} +1 & 0 & 0 & -1 \\ 0 & -1 & +1 & 0 \\ 0 & -1 & +1 & 0 \\ +1 & 0 & 0 & -1 \end{bmatrix}$$

$$\iint \xi N_I N_J\, dx\, dy = \frac{LM}{36} \begin{bmatrix} -2 & 0 & 0 & -1 \\ 0 & +2 & +1 & 0 \\ 0 & +1 & +2 & 0 \\ -1 & 0 & 0 & -2 \end{bmatrix}$$

$$\iint \xi \frac{\partial N_I}{\partial r} \sigma_{ir}\, dr\, dz = \frac{M\sigma_{ir}}{6} \begin{bmatrix} 0 \\ 0 \\ 0 \\ 0 \end{bmatrix}$$

$$\iint \xi \frac{\partial N_I}{\partial z} \sigma_{iz}\, dr\, dz = \frac{L\sigma_{iz}}{6} \begin{bmatrix} +1 \\ -1 \\ +1 \\ -1 \end{bmatrix}$$

$$\iint \xi N_I\, dr\, dz = \frac{LM}{12} \begin{bmatrix} -1 \\ +1 \\ +1 \\ -1 \end{bmatrix}$$

$$\int_B r N_I S_i\, dr = \frac{LS_i}{6} \begin{bmatrix} 3r_0 - L \\ 3r_0 + L \end{bmatrix}$$

$$\int_B r N_I S_i\, dz = \frac{MS_i}{2} \begin{bmatrix} r \\ r \end{bmatrix}$$

for plane strain conditions. These are presented in Table 9.3 and Table 9.4 respectively. It can be seen that in both these matrices only material properties, previous nodal values and element geometries need be known. There are no further calculations involved. Thus for plane strain conditions, the matrix equation may be written as,

$$\begin{bmatrix} & \psi & \end{bmatrix}^{ps} \begin{Bmatrix} w_{xJ} \\ w_{yJ} \\ u_{wJ} \end{Bmatrix}^{ps} = \begin{Bmatrix} R_{1I} \\ R_{2I} \\ R_{3I} \end{Bmatrix}^{ps} + \begin{Bmatrix} B_{1I} \\ B_{2I} \\ B_{3I} \end{Bmatrix}^{ps} \tag{9.1}$$

where $[\psi]^{ps}$ is the 12x12 stiffness matrix for plane strain conditions (Table 9.3), and w_{xJ}, w_{yJ} and u_{wJ} are the x-displacements, y-displacements and pore water pressures respectively at each of the four nodes of the rectangular element. R_I is the right-hand side loading vector (Table 9.4), and B_I is the additional vector due to boundary forces and reactions.

For convenience, Tables 9.3 and 9.4 contain terms that have lumped various parameters together to give

$$K_x = \Delta t\ \Theta\ \frac{\bar{k}_{xx}}{\gamma_w} \quad ; \quad K_y = \Delta t\ \Theta\ \frac{\bar{k}_{yy}}{\gamma_w} \quad ; \quad K_{xy} = \Delta t\ \Theta\ \frac{\bar{k}_{xy}}{\gamma_w}$$

$$K_{ex} = \Delta t(k_{xx}e_x + k_{xy}e_y) \quad ; \quad K_{ey} = \Delta t(k_{yx}e_x + k_{yy}e_y) \tag{9.2}$$

9.5 Stiffness Matrix and Load Vector for Axisymmetric Conditions

The stiffness matrix and load vector for gassy soil consolidation under axisymmetric conditions are presented in Table 8.2 along with the components of the matrix. The 12x12 element stiffness matrix can be obtained by again substituting in the definition of shape functions and the shape function derivatives in the same way as for plane strain conditions. It can be seen from Table 8.2 that many of the terms in the axisymmetric derivation have a radius term premultiplying the integrand. It therefore becomes very useful to employ the following equation which simplifies the integral

$$\iint r\,\tilde{\chi}\,dr\,dz = \iint \left[r_o\tilde{\chi} + (r - r_o)\tilde{\chi}\right] dr\,dz = r_o \iint \tilde{\chi}\,dr\,dz + \frac{L}{2} \iint \xi\,\tilde{\chi}\,dr\,dz \tag{9.3}$$

where $\tilde{\chi}$ is any arbitrary function, r_o is the radial distance to the centre of area of the rectangular element and L is the radial length of the element.

$+(\lambda+2G)M/3L$ $+GL/3M$	$+(\lambda+G)/4$	$+BM/6$	$-(\lambda+2G)M/3L$ $+GL/6M$	$+(\lambda-G)/4$	$+BM/6$	$-(\lambda+2G)M/6L$ $-GL/6M$	$-(\lambda+G)/4$	$+BM/12$	$+(\lambda+2G)M/6L$ $-GL/3M$	$-(\lambda-G)/4$	$+BM/12$
$+(\lambda+G)/4$	$+(\lambda+2G)L/3M$ $+GM/3L$	$+BL/6$	$-(\lambda-G)/4$	$+(\lambda+2G)L/6M$ $-GM/3L$	$+BL/12$	$-(\lambda+G)/4$	$-(\lambda+2G)L/6M$ $-GM/6L$	$+BL/12$	$+(\lambda-G)/4$	$-(\lambda+2G)L/3M$ $+GM/6L$	$+BL/6$
$+BM/6$	$+BL/6$	$-K_xM/3L-K_yL/3M$ $-K_{xy}/2-CLM/9$	$-BM/6$	$+BL/12$	$+K_xM/3L-K_yL/6M$ $-CLM/18$	$-BM/12$	$-BL/12$	$+K_xM/6L+K_yL/6M$ $+K_{xy}/2-CLM/36$	$+BM/12$	$-BL/6$	$-K_xM/6L+K_yL/3M$ $-CLM/18$
$-(\lambda+2G)M/3L$ $+GL/6M$	$-(\lambda-G)/4$	$-BM/6$	$+(\lambda+2G)M/3L$ $+GL/3M$	$-(\lambda+G)/4$	$-BM/6$	$+(\lambda+2G)M/6L$ $-GL/3M$	$+(\lambda-G)/4$	$-BM/12$	$-(\lambda+2G)M/6L$ $-GL/6M$	$+(\lambda+G)/4$	$-BM/12$
$+(\lambda-G)/4$	$+(\lambda+2G)L/6M$ $-GM/3L$	$+BL/12$	$-(\lambda+G)/4$	$+(\lambda+2G)L/3M$ $+GM/3L$	$+BL/6$	$-(\lambda-G)/4$	$-(\lambda+2G)L/3M$ $+GM/6L$	$+BL/6$	$+(\lambda+G)/4$	$-(\lambda+2G)L/6M$ $-GM/6L$	$+BL/12$
$+BM/6$	$+BL/12$	$+K_xM/3L-K_yL/6M$ $-CLM/18$	$-BM/6$	$+BL/6$	$-K_xM/3L-K_yL/3M$ $+K_{xy}/2-CLM/9$	$-BM/12$	$-BL/6$	$-K_xM/6L+K_yL/3M$ $-CLM/18$	$+BM/12$	$-BL/12$	$+K_xM/6L+K_yL/6M$ $-K_{xy}/2-CLM/36$
$-(\lambda+2G)M/6L$ $-GL/6M$	$-(\lambda+G)/4$	$-BM/12$	$+(\lambda+2G)M/6L$ $-GL/3M$	$-(\lambda-G)/4$	$-BM/12$	$+(\lambda+2G)M/3L$ $+GL/3M$	$+(\lambda+G)/4$	$-BM/6$	$-(\lambda+2G)M/3L$ $+GL/6M$	$+(\lambda-G)/4$	$-BM/6$
$-(\lambda+G)/4$	$-(\lambda+2G)L/6M$ $-GM/6L$	$-BL/12$	$+(\lambda-G)/4$	$-(\lambda+2G)L/3M$ $+GM/6L$	$-BL/6$	$+(\lambda+G)/4$	$+(\lambda+2G)L/3M$ $+GM/3L$	$-BL/6$	$-(\lambda-G)/4$	$+(\lambda+2G)L/6M$ $-GM/3L$	$-BL/12$
$+BM/12$	$+BL/12$	$+K_xM/6L+K_yL/6M$ $+K_{xy}/2-CLM/36$	$-BM/12$	$+BL/6$	$-K_xM/6L+K_yL/3M$ $-CLM/18$	$-BM/6$	$-BL/6$	$-K_xM/3L-K_yL/3M$ $-K_{xy}/2-CLM/9$	$+BM/6$	$-BL/12$	$+K_xM/3L-K_yL/6M$ $-CLM/18$
$+(\lambda+2G)M/6L$ $-GL/3M$	$+(\lambda-G)/4$	$+BM/12$	$-(\lambda+2G)M/6L$ $-GL/6M$	$+(\lambda+G)/4$	$+BM/12$	$-(\lambda+2G)M/3L$ $+GL/6M$	$-(\lambda-G)/4$	$+BM/6$	$+(\lambda+2G)M/3L$ $+GL/3M$	$-(\lambda+G)/4$	$+BM/6$
$-(\lambda-G)/4$	$-(\lambda+2G)L/3M$ $+GM/6L$	$-BL/6$	$+(\lambda+G)/4$	$-(\lambda+2G)L/6M$ $-GM/6L$	$-BL/12$	$+(\lambda-G)/4$	$+(\lambda+2G)L/6M$ $-GM/3L$	$-BL/12$	$-(\lambda+G)/4$	$+(\lambda+2G)L/3M$ $+GM/3L$	$-BL/6$
$+BM/12$	$+BL/6$	$-K_xM/6L+K_yL/3M$ $-CLM/18$	$-BM/12$	$+BL/12$	$+K_xM/6L+K_yL/6M$ $-K_{xy}/2-CLM/36$	$-BM/6$	$-BL/12$	$+K_xM/3L-K_yL/6M$ $-CLM/18$	$+BM/6$	$-BL/6$	$-K_xM/3L-K_yL/3M$ $+K_{xy}/2-CLM/9$

Table 9.4 Right-Hand Side Vector used for Plane Strain Conditions

$LMF_x/4 - M\sigma^*_{xx}/2 - L\sigma^*_{xy}/2$
$LMF_y/4 - M\sigma^*_{yx}/2 - L\sigma^*_{yy}/2$
$\frac{(1-\Theta)}{\Theta}\left[\frac{MK}{6L}x(2u^t_{w1}-2u^t_{w2}+u^t_{w4}-u^t_{w3}) + \frac{LK}{6M}y(2u^t_{w1}-2u^t_{w4}+u^t_{w2}-u^t_{w3}) + \frac{K}{2}xy(u^t_{w1}-u^t_{w3})\right] + \frac{MK}{2}ex + \frac{LK}{2}ey$ $- \bar{B}\left[\frac{M}{12}(2w^t_{x2}-2w^t_{x1}+w^t_{x3}-w^t_{x4}) + \frac{L}{12}(2w^t_{y4}-2w^t_{y1}+w^t_{y3}-w^t_{y2})\right] - \bar{C}\frac{LM}{36}\left[4u^t_{w1}+2u^t_{w2}+u^t_{w3}+2u^t_{w4}\right]$
$LMF_x/4 + M\sigma^*_{xx}/2 - L\sigma^*_{xy}/2$
$LMF_y/4 + M\sigma^*_{yx}/2 - L\sigma^*_{yy}/2$
$\frac{(1-\Theta)}{\Theta}\left[\frac{MK}{6L}x(2u^t_{w2}-2u^t_{w1}+u^t_{w3}-u^t_{w4}) + \frac{LK}{6M}y(2u^t_{w2}-2u^t_{w3}+u^t_{w1}-u^t_{w4}) + \frac{K}{2}xy(u^t_{w4}-u^t_{w2})\right] - \frac{MK}{2}ex + \frac{LK}{2}ey$ $- \bar{B}\left[\frac{M}{12}(2w^t_{x2}-2w^t_{x1}+w^t_{x3}-w^t_{x4}) + \frac{L}{12}(2w^t_{y3}-2w^t_{y2}+w^t_{y4}-w^t_{y1})\right] - \bar{C}\frac{LM}{36}\left[2u^t_{w1}+4u^t_{w2}+2u^t_{w3}+u^t_{w4}\right]$
$LMF_x/4 + M\sigma^*_{xx}/2 + L\sigma^*_{xy}/2$
$LMF_y/4 + M\sigma^*_{yx}/2 + L\sigma^*_{yy}/2$
$\frac{(1-\Theta)}{\Theta}\left[\frac{MK}{6L}x(2u^t_{w3}-2u^t_{w4}+u^t_{w2}-u^t_{w1}) + \frac{LK}{6M}y(2u^t_{w3}-2u^t_{w2}+u^t_{w4}-u^t_{w1}) + \frac{K}{2}xy(u^t_{w3}-u^t_{w1})\right] - \frac{MK}{2}ex - \frac{LK}{2}ey$ $- \bar{B}\left[\frac{M}{12}(2w^t_{x3}-2w^t_{x4}+w^t_{x2}-w^t_{x1}) + \frac{L}{12}(2w^t_{y3}-2w^t_{y2}+w^t_{y4}-w^t_{y1})\right] - \bar{C}\frac{LM}{36}\left[u^t_{w1}+2u^t_{w2}+4u^t_{w3}+2u^t_{w4}\right]$
$LMF_x/4 - M\sigma^*_{xx}/2 + L\sigma^*_{xy}/2$
$LMF_y/4 - M\sigma^*_{yx}/2 + L\sigma^*_{yy}/2$
$\frac{(1-\Theta)}{\Theta}\left[\frac{MK}{6L}x(2u^t_{w4}-2u^t_{w3}+u^t_{w1}-u^t_{w2}) + \frac{LK}{6M}y(2u^t_{w4}-2u^t_{w1}+u^t_{w3}-u^t_{w2}) + \frac{K}{2}xy(u^t_{w2}-u^t_{w4})\right] + \frac{MK}{2}ex - \frac{LK}{2}ey$ $- \bar{B}\left[\frac{M}{12}(2w^t_{x3}-2w^t_{x4}+w^t_{x2}-w^t_{x1}) + \frac{L}{12}(2w^t_{y4}-2w^t_{y1}+w^t_{y3}-w^t_{y2})\right] - \bar{C}\frac{LM}{36}\left[2u^t_{w1}+u^t_{w2}+2u^t_{w3}+4u^t_{w4}\right]$

Using the above equation, the matrix equation governing the consolidation behaviour under axisymmetric conditions can be written as

$$\left(\frac{L}{2} \left[\quad \psi \quad \right]^{ax} + r_o \left[\quad \psi \quad \right]^{ps} \right) \begin{Bmatrix} w_{rJ} \\ w_{zJ} \\ u_{wJ} \end{Bmatrix} = \frac{L}{2} \begin{Bmatrix} R_{1I} \\ R_{2I} \\ R_{3I} \end{Bmatrix}^{ax} + r_o \begin{Bmatrix} R_{1I} \\ R_{2I} \\ R_{3I} \end{Bmatrix}^{ps} + \begin{Bmatrix} B_{1I} \\ B_{2I} \\ B_{3I} \end{Bmatrix}^{ax} \qquad (9.4)$$

where $[\psi]^{ps}$ is the 12x12 stiffness matrix for plane strain conditions, $[\psi]^{ax}$ is the additional 12x12 stiffness matrix for axisymmetric conditions, w_{rJ}, w_{zJ}, and u_{wJ} are the nodal r-displacements, z-displacements and pore water pressures respectively. Using the above information, it is possible to evaluate most of the terms required for integration of the rectangular element under axisymmetric conditions. These terms have been compiled and are presented in matrix form in Table 9.2b. The only term that has not been included and requires further definition is presented below.

$$\iint \frac{1}{r} N_I N_J \, dr \, dz = \frac{M}{6L} \begin{bmatrix} 2a & 2c & c & a \\ 2c & 2b & b & c \\ c & b & 2b & 2c \\ a & c & 2c & 2a \end{bmatrix} \qquad (9.5)$$

where

$$a = (r_1 - 3r_2)/2L + (r_2/L)(r_2/L) \log_e \left[\frac{r_2}{r_1} \right] \qquad (9.6)$$

$$b = (r_2 - 3r_1)/2L + (r_1/L)(r_1/L) \log_e \left[\frac{r_2}{r_1} \right] \qquad (9.7)$$

$$c = (r_2 + r_1)/2L + (r_2/L)(r_1/L) \log_e \left[\frac{r_2}{r_1} \right] \qquad (9.8)$$

Substitution of the above integral definition and the integral definitions of Tables 9.2a and 9.2b into the components of Table 8.2 results in the element matrix and vector as presented in Tables 9.5 and 9.6 respectively. As for the plane strain case, Tables 9.5 and 9.6 contain the following definitions

$$K_r = \Delta t \, \Theta \frac{\bar{k}_{rr}}{\gamma_w} \quad ; \quad K_z = \Delta t \, \Theta \frac{\bar{k}_{zz}}{\gamma_w} \quad ; \quad K_{rz} = \Delta t \, \Theta \frac{\bar{k}_{rz}}{\gamma_w}$$

$$K_{er} = \Delta t(k_{rr} e_r + k_{rz} e_z) \quad ; \quad K_{ez} = \Delta t(k_{zr} e_r + k_{zz} e_z) \qquad (9.9)$$

The total element stiffness matrix and right-hand side load vector for axisymmetric conditions can then be found from substitution of the matrices

$+2(\lambda+2G)Ma/3L$ $-GL/6M-2\lambda M/3L$	$-(\lambda+G)/12$ $-\lambda/3$	$-BM/18$ $-2BM/9$	$+2(\lambda+2G)Mc/3L$	$+(\lambda+G)/12$ $-\lambda/6$	$+BM/18$ $-BM/9$	$+(\lambda+2G)Mc/3L$	$-(\lambda-G)/12$ $+\lambda/6$	$+BM/36$ $-BM/18$	$+(\lambda+2G)Ma/3L$ $+GL/6M-\lambda M/3L$	$+(\lambda-G)/12$ $+\lambda/3$	$-BM/36$ $-BM/9$
$-(\lambda+G)/12$ $-\lambda/3$	$-(\lambda+2G)L/6M$	$-BL/12$	$+(\lambda+G)/12$ $-\lambda/6$	--	--	$-(\lambda-G)/12$ $-\lambda/6$	--	--	$+(\lambda-G)/12$ $-\lambda/3$	$+(\lambda+2G)L/6M$	$-BL/12$
$-BM/18$ $-2BM/9$	$-BL/12$	$K_zL/6M+K_{rz}/6$ $+CLM/18$	$+BM/18$ $-BM/9$	--	$-K_{rz}/6$	$+BM/36$ $-BM/18$	--	--	$-BM/36$ $-BM/9$	$+BL/12$	$-K_zL/6M$ $+CLM/36$
$+2(\lambda+2G)Mc/3L$	$+(\lambda+G)/12$ $-\lambda/6$	$+BM/18$ $-BM/9$	$+2(\lambda+2G)Mb/3L$ $+GL/6M+2\lambda M/3L$	$-(\lambda+G)/12$ $-\lambda/3$	$-BM/18$ $-2BM/9$	$+(\lambda+2G)Mb/3L$ $-GL/6M+\lambda M/3L$	$+(\lambda-G)/12$ $+\lambda/3$	$-BM/36$ $-BM/9$	$+(\lambda+2G)Mc/3L$	$-(\lambda-G)/12$ $+\lambda/6$	$+BM/36$ $-BM/18$
$+(\lambda+G)/12$ $-\lambda/6$	--	--	$-(\lambda+G)/12$ $-\lambda/3$	$(\lambda+2G)L/6M$	$+BL/12$	$+(\lambda-G)/12$ $-\lambda/3$	$-(\lambda+2G)L/6M$	$+BL/12$	$-(\lambda-G)/12$ $-\lambda/6$	--	--
$+BM/18$ $-BM/9$	--	$-K_{rz}/6$	$-BM/18$ $-2BM/9$	$+BL/12$	$K_{rz}/6-K_zL/6M$ $-CLM/18$	$-BM/36$ $-BM/9$	$-BL/12$	$+K_zL/6M$ $-CLM/36$	$+BM/36$ $-BM/18$	--	--
$+(\lambda+2G)Mc/3L$	$+(\lambda-G)/12$ $-\lambda/6$	$+BM/36$ $-BM/18$	$+(\lambda+2G)Mb/3L$ $-GL/6M+\lambda M/3L$	$+(\lambda-G)/12$ $-\lambda/3$	$-BM/36$ $-BM/9$	$2(\lambda+2G)Mb/3L$ $+GL/6M+2\lambda M/3L$	$+(\lambda+G)/12$ $+\lambda/3$	$-BM/18$ $-2BM/9$	$+2(\lambda+2G)Mc/3L$	$-(\lambda+G)/12$ $+\lambda/6$	$+BM/18$ $-BM/9$
$-(\lambda-G)/12$ $+\lambda/6$	--	--	$+(\lambda-G)/12$ $+\lambda/3$	$-(\lambda+2G)L/6M$	$-BL/12$	$+(\lambda+G)/12$ $+\lambda/3$	$+(\lambda+2G)L/6M$	$-BL/12$	$-(\lambda+G)/12$ $+\lambda/6$	--	--
$+BM/36$ $-BM/18$	--	--	$-BM/36$ $-BM/9$	$+BL/12$	$+K_zL/6M$ $-CLM/36$	$-BM/18$ $-2BM/9$	$-BL/12$	$-K_zL/6M-K_{rz}/6$ $-CLM/18$	$+BM/18$ $-BM/9$	--	$+K_{rz}/6$
$+(\lambda+2G)Ma/3L$ $+GL/6M-\lambda M/3L$	$-(\lambda-G)/12$ $-\lambda/3$	$-BM/36$ $-BM/9$	$+(\lambda+2G)Mc/3L$	$+(\lambda-G)/12$ $-\lambda/6$	$+BM/36$ $-BM/18$	$+2(\lambda+2G)Mc/3L$	$-(\lambda+G)/12$ $+\lambda/6$	$+BM/18$ $-BM/9$	$+2(\lambda+2G)Ma/3L$ $-GL/6M-2\lambda M/3L$	$+(\lambda+G)/12$ $+\lambda/3$	$-BM/18$ $-2BM/9$
$+(\lambda-G)/12$ $+\lambda/3$	$(\lambda+2G)L/6M$	$+BL/12$	$-(\lambda-G)/12$ $+\lambda/6$	--	--	$+(\lambda+G)/12$ $+\lambda/6$	--	--	$+(\lambda+G)/12$ $+\lambda/3$	$(\lambda+2G)L/6M$	$+BL/12$
$-BM/36$ $-BM/9$	$-BL/12$	$-K_zL/6M$ $+CLM/36$	$+BM/36$ $-BM/18$	--	--	$+BM/18$ $-BM/9$	--	$+K_{rz}/6$	$-BM/18$ $-2BM/9$	$+BL/12$	$K_{rz}/6-K_zL/6M$ $-CLM/18$

Table 9.6 Right-Hand Side Vector used for Axisymmetric Conditions

$- LMF_r/12 + L\sigma^*_{rz}/6 + M\sigma^*_{\theta\theta}/2$
$- LMF_z/12 + L\sigma^*_{zz}/6$
$\frac{(1-\theta)}{\theta}\left[\frac{K}{6}rz\ (u^t_{w2} - u^t_{w1}) + \frac{LK}{6M}z\ (u^t_{w4} - u^t_{w1})\right] + \bar{C}\ \frac{LM}{36}\left[2u^t_{w1} + u^t_{w4}\right] - \left[\frac{LK}{6}ez\right]$ $- \bar{B}\left[\frac{M}{36}(2w^t_{r1} - 2w^t_{r2} + w^t_{r4} - w^t_{r3}) + \frac{L}{12}(w^t_{z1} - w^t_{z4})\right] - \bar{B}\ \frac{LM}{36}\left[4w^t_{r1} + 2w^t_{r2} + w^t_{r3} + 2w^t_{r4}\right]$
$+ LMF_r/12 - L\sigma^*_{rz}/6 + M\sigma^*_{\theta\theta}/2$
$+ LMF_z/12 - L\sigma^*_{zz}/6$
$\frac{(1-\theta)}{\theta}\left[\frac{K}{6}rz\ (u^t_{w1} - u^t_{w2}) + \frac{LK}{6M}z\ (u^t_{w2} - u^t_{w3})\right] - \bar{C}\ \frac{LM}{36}\left[2u^t_{w2} + u^t_{w3}\right] + \left[\frac{LK}{6}ez\right]$ $- \bar{B}\left[\frac{M}{36}(2w^t_{r2} - 2w^t_{r1} + w^t_{r3} - w^t_{r4}) + \frac{L}{12}(w^t_{z3} - w^t_{z2})\right] - \bar{B}\ \frac{LM}{36}\left[2w^t_{r1} + 4w^t_{r2} + 2w^t_{r3} + w^t_{r4}\right]$
$+ LMF_r/12 + L\sigma^*_{rz}/6 + M\sigma^*_{\theta\theta}/2$
$+ LMF_z/12 + L\sigma^*_{zz}/6$
$\frac{(1-\theta)}{\theta}\left[\frac{K}{6}rz\ (u^t_{w3} - u^t_{w4}) + \frac{LK}{6M}z\ (u^t_{w3} - u^t_{w2})\right] - \bar{C}\ \frac{LM}{36}\left[2u^t_{w3} + u^t_{w2}\right] - \left[\frac{LK}{6}ez\right]$ $- \bar{B}\left[\frac{M}{36}(2w^t_{r3} - 2w^t_{r4} + w^t_{r2} - w^t_{r1}) + \frac{L}{12}(w^t_{z3} - w^t_{z2})\right] - \bar{B}\ \frac{LM}{36}\left[w^t_{r1} + 2w^t_{r2} + 4w^t_{r3} + 2w^t_{r4}\right]$
$- LMF_r/12 - L\sigma^*_{rz}/6 + M\sigma^*_{\theta\theta}/2$
$- LMF_z/12 - L\sigma^*_{zz}/6$
$\frac{(1-\theta)}{\theta}\left[\frac{K}{6}rz\ (u^t_{w4} - u^t_{w3}) + \frac{LK}{6M}z\ (u^t_{w1} - u^t_{w4})\right] + \bar{C}\ \frac{LM}{36}\left[2u^t_{w4} + u^t_{w1}\right] + \left[\frac{LK}{6}ez\right]$ $- \bar{B}\left[\frac{M}{36}(2w^t_{r4} - 2w^t_{r3} + w^t_{r1} - w^t_{r2}) + \frac{L}{12}(w^t_{z1} - w^t_{z4})\right] - \bar{B}\ \frac{LM}{36}\left[2w^t_{r1} + w^t_{r2} + 2w^t_{r3} + 4w^t_{r4}\right]$

given in Tables 9.3 to 9.6 into equation 9.3.

9.6 Stress and Strain Evaluation in Rectangular Elements

During the solution procedure, the resulting values are in the form of nodal displacements and pore water pressures. Due to the non-linear behaviour of gassy soil, it is necessary to evaluate the changes in stresses at the end of each iteration. The changes in total stress may be found from equation 8.39 which reads

$$\Delta\sigma_{ij} = 2\bar{G}\Delta\varepsilon_{ij} + \bar{\lambda}\Delta\varepsilon_{kk}\delta_{ij} + \bar{B}\Delta u_w\delta_{ij} \qquad (9.10)$$

If four point Gauss quadrature is used to evaluate the stiffness matrix, then it is standard practice to evaluate stresses at those points. However, as Gauss quadrature is not used in the influence coefficient method, the stresses are evaluated at the centroid of the rectangular finite element. For such a rectangular element used for plane strain analysis, this will be the centre of area of the rectangle. For axisymmetric conditions, however, the centroid of the element will be dependent on the distance of the element from the axis of rotation. The position of the element centroids and the corresponding stresses and strains are presented for both plane strain and axisymmetric conditions in Tables 9.7 and 9.8 respectively.

These stresses and strains, evaluated for each time step and element, can be written to a file which can then in turn be used as input to a plotting routine. This will enable the stress and strain fields to be produced in the form of graphical output.

9.7 Summary

This chapter sees the finite element approximation of the gassy soil consolidation equations formulated for rectangular elements under plane strain and axisymmetric conditions. An extremely efficient closed form solution technique, termed "the influence coefficient method", is presented for the production of the governing stiffness matrices and right-hand side load vector.

Table 9.7 Stress and Strain Evaluation - Plane Strain Conditions

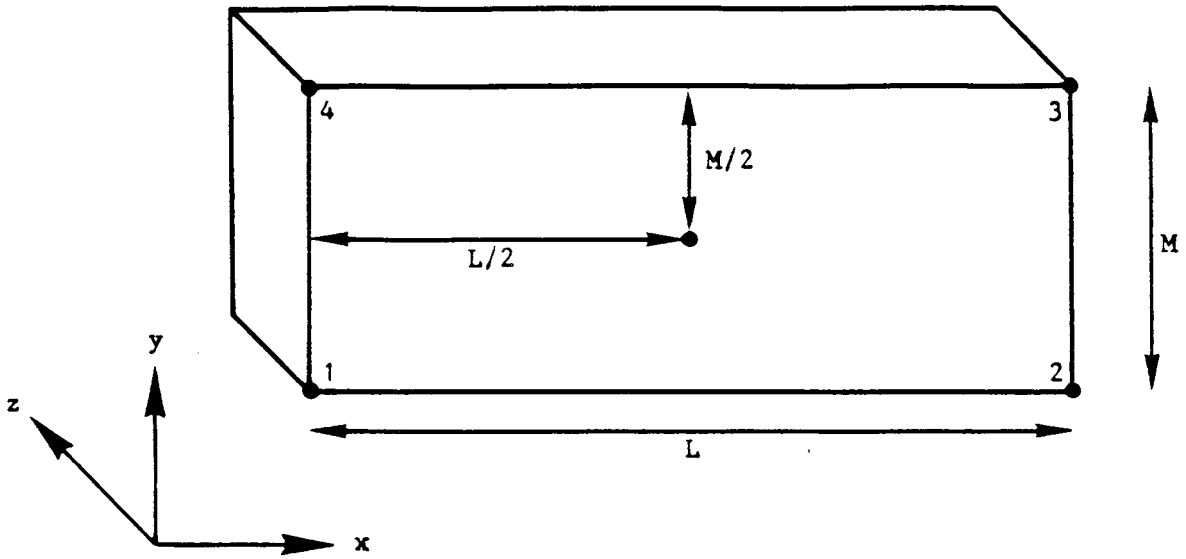

The strains may be expressed as

$$\Delta\varepsilon_{xx} = (\Delta w_{x1} - \Delta w_{x2} - \Delta w_{x3} + \Delta w_{x4})/2L$$

$$\Delta\varepsilon_{yy} = (\Delta w_{y1} + \Delta w_{y2} - \Delta w_{y3} - \Delta w_{y4})/2M$$

$$\Delta\varepsilon_{xy} = (\Delta w_{x1} + \Delta w_{x2} - \Delta w_{x3} + \Delta w_{x4})/2L$$

$$+ (\Delta w_{y1} - \Delta w_{y2} - \Delta w_{y3} + \Delta w_{y4})/2M$$

$$\Delta u_w = (\Delta u_{w1} + \Delta u_{w2} + \Delta u_{w3} + \Delta u_{w4})/4$$

$$\Delta\varepsilon_{zz} = \Delta\varepsilon_{xz} = \Delta\varepsilon_{yz} = 0$$

$$\Delta\varepsilon_{kk} = \Delta\varepsilon_{xx} + \Delta\varepsilon_{yy}$$

From which the stresses may be written as,

$$\Delta\sigma_{xx} = 2\bar{G}\Delta\varepsilon_{xx} + \lambda\Delta\bar{\varepsilon}_{kk} + \bar{B}\Delta u_w$$

$$\Delta\sigma_{yy} = 2\bar{G}\Delta\varepsilon_{yy} + \lambda\Delta\bar{\varepsilon}_{kk} + \bar{B}\Delta u_w$$

$$\Delta\sigma_{zz} = \lambda\Delta\bar{\varepsilon}_{kk} + \bar{B}\Delta u_w$$

$$\Delta\sigma_m = (\Delta\sigma_{xx} + \Delta\sigma_{yy} + \Delta\sigma_{zz})/3$$

$$\Delta\tau_{oct} = \frac{1}{3}\left[(\Delta\sigma_{xx} - \Delta\sigma_{yy})^2 + (\Delta\sigma_{yy} - \Delta\sigma_{zz})^2 + (\Delta\sigma_{zz} - \Delta\sigma_{xx})^2\right]^{1/2}$$

Table 9.8 Stress and Strain Evaluation - Axisymmetric Conditions

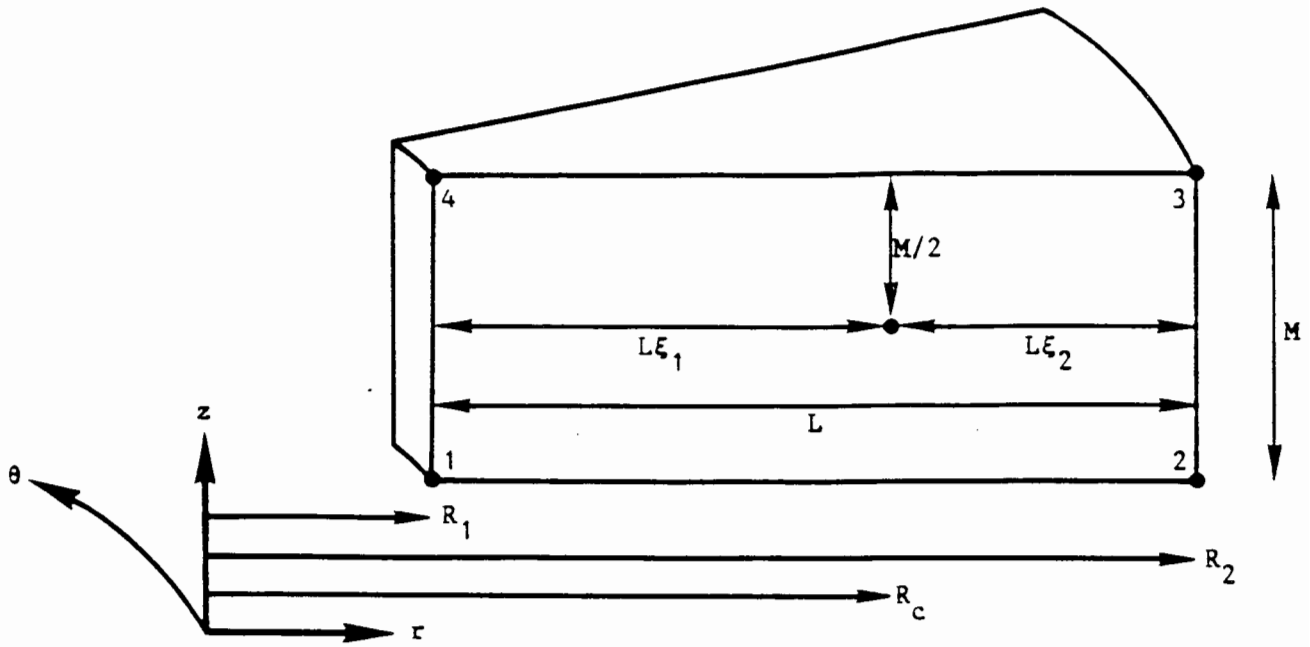

$$R_c = 2(R_2^3 - R_1^3)/3(R_2^2 - R_1^2)$$

$$\xi_1 = (R_c - R_1)/L \quad ; \quad \xi_2 = (R_2 - R_c)/L$$

The strains can be expressed as

$$\Delta\varepsilon_{rr} = (\Delta w_{r1} - \Delta w_{r2} - \Delta w_{r3} + \Delta w_{r4})/2L$$

$$\Delta\varepsilon_{\theta\theta} = -(\Delta w_{r1} + \Delta w_{r2} + \Delta w_{r3} + \Delta w_{r4})/2(R_1 + R_2)$$

$$\Delta\varepsilon_{rz} = (\Delta w_{z1} - \Delta w_{z2} - \Delta w_{z3} + \Delta w_{z4})/4L + [(\Delta w_{r1} - \Delta w_{r4})\xi_2 + (\Delta w_{r2} - \Delta w_{y4})\xi_1]/2M$$

$$\Delta\varepsilon_{zz} = [(\Delta w_{z1} - \Delta w_{z4})\xi_2 + (\Delta w_{z2} - \Delta w_{z3})\xi_1]/M$$

$$\Delta u_w = [(\Delta u_{w1} + \Delta u_{w2})\xi_2 + (\Delta u_{w3} + \Delta u_{w4})\xi_1]/2$$

$$\Delta\varepsilon_{kk} = \Delta\varepsilon_{rr} + \Delta\varepsilon_{zz} + \Delta\varepsilon_{\theta\theta}$$

From which the stresses can be written as,

$$\Delta\sigma_{rr} = 2\bar{G}\Delta\varepsilon_{rr} + \lambda\Delta\bar{\varepsilon}_{kk} + \bar{B}\Delta u_w$$

$$\Delta\sigma_{zz} = 2\bar{G}\Delta\varepsilon_{zz} + \lambda\Delta\bar{\varepsilon}_{kk} + \bar{B}\Delta u_w$$

$$\Delta\sigma_{\theta\theta} = 2\bar{G}\Delta\varepsilon_{\theta\theta} + \lambda\Delta\bar{\varepsilon}_{kk} + \bar{B}\Delta u_w$$

$$\Delta\sigma_m = (\Delta\sigma_{rr} + \Delta\sigma_{zz} + \Delta\sigma_{\theta\theta})/3$$

$$\Delta\tau_{oct} = \frac{1}{3}\left[(\Delta\sigma_{rr} - \Delta\sigma_{zz})^2 + (\Delta\sigma_{zz} - \Delta\sigma_{\theta\theta})^2 + (\Delta\sigma_{\theta\theta} - \Delta\sigma_{rr})^2\right]^{1/2}$$

CHAPTER 10

DCFEM2 - DOUBLE COMPRESSIBILITY FINITE ELEMENT MODEL IN TWO DIMENSIONS

CONSTITUTIVE RELATIONSHIPS AND STRUCTURE OF DCFEM2

CHAPTER 10

DCFEM2 - DOUBLE COMPRESSIBILITY FINITE ELEMENT MODEL IN TWO DIMENSIONS

CONSTITUTIVE RELATIONSHIPS AND STRUCTURE OF DCFEM2

10.1 Introduction

The following chapter consists of two main sections. The first section describes the constitutive material relationships incorporated into DCFEM2 that are available to the user of the model. The second section describes the structure of the finite element program DCFEM2, including a brief description of the main program and the various subroutines, followed by an illustration of the arrangement of the nodal and elemental numbering.

10.2 Constitutive Relationships

The previous three chapters have described the development and consequent finite element approximation of the governing equations of gassy soil consolidation as idealized by a double compressibility material. These equations contain material properties which affect the consolidation and deformation behaviour of the soil. In most cases, however, these material properties are not constant but often vary due to changes in other parameters--such as total stress, pore water pressure, gas pressure or gas volume fraction. The relationships between these material properties and their governing physical parameters are known as constitutive relationships. This section describes the constitutive relationships that have been incorporated in this gassy soil model.

10.2.1 Double compressibility model - Constant properties

This option of DCFEM2 considers a double compressibility model with constant material properties. Both the soil and gas phases are given linear elastic bulk and shear moduli, K',G' and K°,G° respectively, as defined in Chapter 6. The permeability tensor and the water compressibility are also given constant values. This option forms the basic skeleton of DCFEM2 and is used for verification of the model with existing analytical solutions.

10.2.2 Gassy soil model - Bulk modulus evaluation

During the compression and subsequent consolidation of a gassy soil, the gas volume and hence the gas compressibility can change dramatically. The volume of pore water will also change. This does not have such a marked effect on the soil behaviour during consolidation, however, and for this reason DCFEM2 treats the saturated soil matrix bulk modulus as a constant material property.

This is not the case for changes in gas volume, as it can be shown that a small change in gas volume can result in a large change in gas bulk modulus. To evaluate the change in modulus due to changes in gas content, first consider the volume of gas that is available for compression, v_c, in a given volume of gassy soil, v_t. This is given by

$$v_c = v_g + Hv_w \tag{10.1}$$

where v_g is the volume of free gas, v_w is the volume of pore water and H is Henry's coefficient of solubility. It must be noted that the above equation only holds when there is a volume of free gas present.

Considering next a volume of gassy soil subjected to an increase in total stress--which in turn produces an increase in gas pressure--then assuming no change in temperature, Boyle's Law and Henry's Law can be combined to give

$$(u_{g1} + u_a)(v_{g1} + Hv_w) = (u_{g2} + u_a)(v_{g2} + Hv_w) \tag{10.2}$$

from which it can be shown that

$$v_{g2} = (v_{g1} + Hv_w)(u_{g1} + u_a)/(u_{g2} + u_a) - Hv_w \tag{10.3}$$

where u_{g1} and v_{g1} are the initial gas pressure and volume, u_{g2} and v_{g2} are the final gas pressure and volume, and u_a is the atmospheric pressure. It can be seen from the above equation, however, that in some circumstances, v_{g2} can become negative. This condition is reached when all the gas goes into solution, after which the negative sign indicates that the volume available for further compression (or expansion) is less than Hv_w.

To illustrate this point, consider a 250cc volume of gassy soil containing 5cc of gas, 150cc of pore water and 95cc of solid grains, at an initial mean stress of 100 kPa. Recalling equation 1.8 which relates the gas pressure and mean total stress as

$$u_g = \alpha \sigma_m \tag{10.4}$$

then for the case of unit α, the initial gas pressure will also be 100 kPa. It is also assumed that H has a value of 0.03333 and atmospheric pressure is 100 kPa. Figure 10.1 shows the path of the gas volume as the total stress is increased slowly to 400 kPa. Point A is the initial condition where the total volume available for compression is given by

$$v_c = v_g + Hv_w = 10cc \tag{10.5}$$

As the gas pressure increases, so the gas volume decreases until reaching Point B at which the gas pressure is 300 kPa and all the gas goes into solution. Increasing the gas pressure from this Point causes no further changes in volume, and the gas volume path proceeds to Point D. However, equation 10.3 produces a path to Point C. Therefore, although the free gas volume is zero, the free gas volume available for compression at 400 kPa is -1cc. This can be confirmed by treating Point C as the starting Point for unloading from 400 kPa to 100 kPa. This unloading path reverses the loading path CBA, ending at our original starting Point A. However, if D is chosen as the starting Point--that is working in terms of the free gas volume instead of the volume available for compression or expansion--the resulting unloading path is DEF. This path is incorrect as it does not follow the original loading path and results in an increase in the mass of gas at 100 kPa at Point F from the starting Point A.

As DCFEM2 evaluates all parameters over a discrete increment of time or stress, the bulk modulus will be averaged over such an increment. The bulk modulus can be written as

$$K^o = \Delta\sigma_m/\Delta\varepsilon_v = -\Delta u_g/\alpha\Delta\varepsilon_v \tag{10.6}$$

where ε_v is the volumetric strain. Thus if the previous example is plotted in terms of volumetric strain, Figure 10.2 results. To illustrate the method of evaluating the bulk modulus, consider an increase of stress of 100 kPa from 150 kPa (Point X) to 250 kPa (Point Y). The change in gas porosity can be evaluated from equation 10.3, and hence the bulk modulus from equation 10.6.

Considering the next 100 kPa stress increment from 250 kPa (Point Y) to 350 kPa (Point Z), it can be seen that during this increment, all the gas goes into

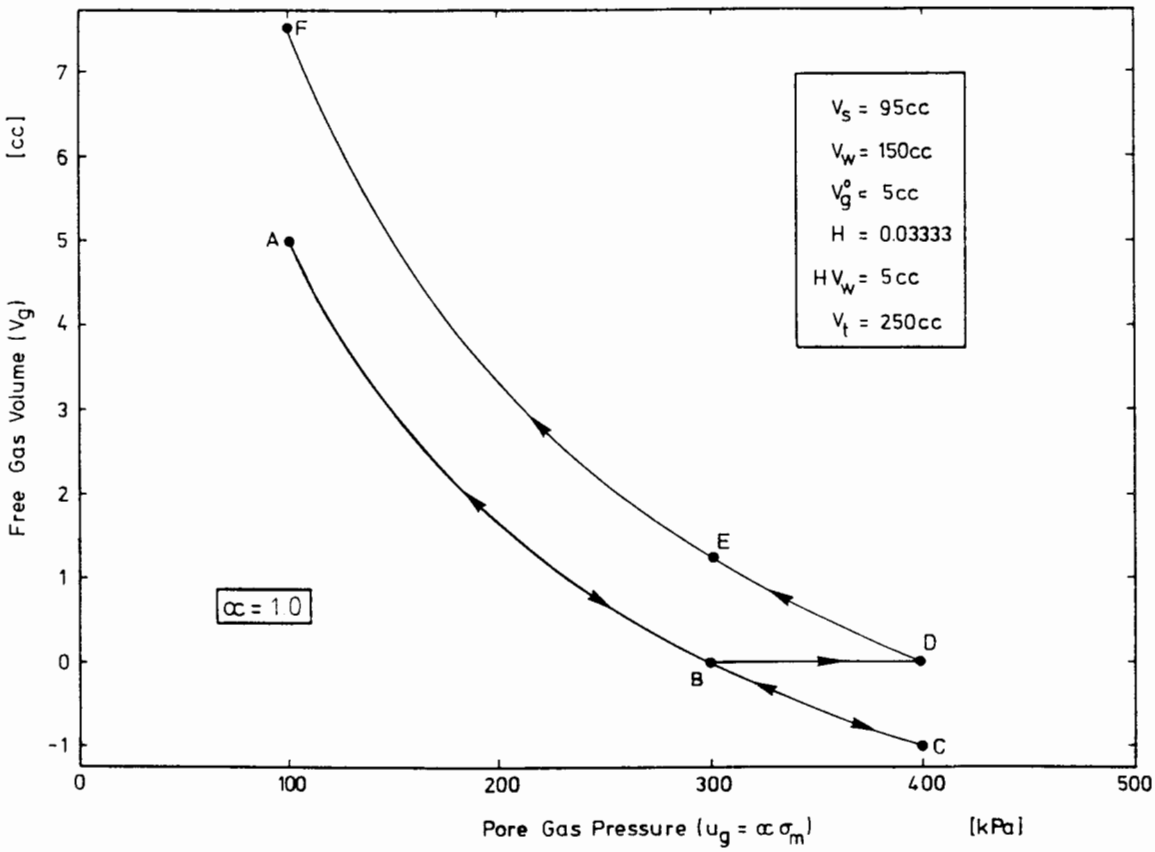

Figure 10.1 Free gas volume versus gas pressure for example problem

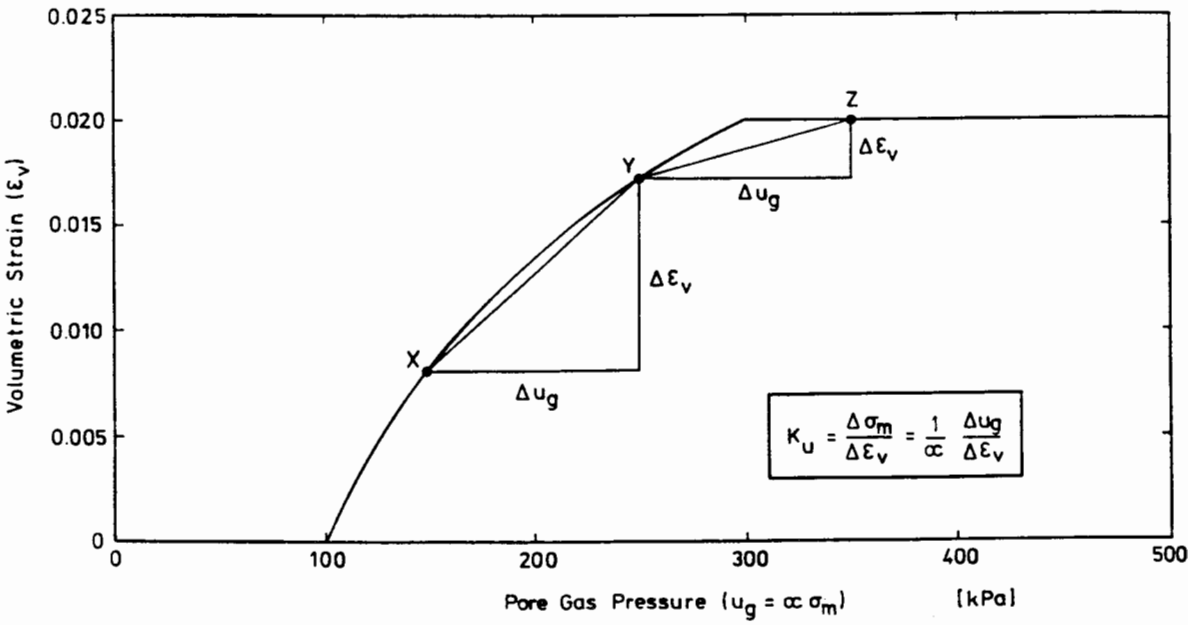

Figure 10.2 Volumetric strain versus gas pressure and evaluation of bulk modulus for example problem

solution and there is an abrupt change in the slope of the stress-strain curve. The same procedure of using equation 10.3 to evaluate the updated value of gas porosity can be used, however, with the condition that if the value of calculated gas volume is negative, the gas volume used in this bulk modulus calculation must be set to zero. Figure 10.2 illustrates this bulk modulus calculation.

10.2.3 Gassy soil model - Shear modulus evaluation

A typical deviator stress-strain curve obtained from a uniaxial loading, unloading and reloading test on a soil sample under triaxial conditions is presented in Figure 10.3a. This soil behaviour may be approximated using an elastic-plastic relationship, as illustrated in Figure 10.3b, in conjunction with a suitable yield criteria and flow rule. Alternatively, the stress-strain behaviour may be approximated using a non-linear elastic relationship as shown in Figure 10.3c. Although this does not model unloading or failure conditions, this relationship gives a good approximation of the deformation behaviour of a saturated soil for monotonic uniaxial loading under triaxial conditions. Consequently, as the emphasis in this thesis is on the effect of the gas on the behaviour of the gassy soil, at this stage the simpler non-linear elastic model has been incorporated into DCFEM2. The stress-strain curves obtained from triaxial tests by Wheeler (1986) can be approximated for monotonic loading using the non-linear elastic relationship

$$\frac{\varepsilon}{\varepsilon_{50}} = \left(\frac{q}{q_{max} - q} \right)^n \qquad (10.7)$$

where q is the deviator stress, $\sigma_1 - \sigma_3$, ε is the deviator strain, $2(\varepsilon_1 - \varepsilon_3)/3$, q_{max} is the maximum value of the deviator stress and ε_{50} is the deviator strain at half the maximum deviator stress. This analytical function is programmed into DCFEM2. From numerical experiments using this approximation, however, convergence was made far more stable by evaluating the stress from the strain component. This may be obtained by rearranging equation 10.7 to give

$$q = \left(\frac{X \, q_{max}}{1 + X} \right) \qquad (10.8)$$

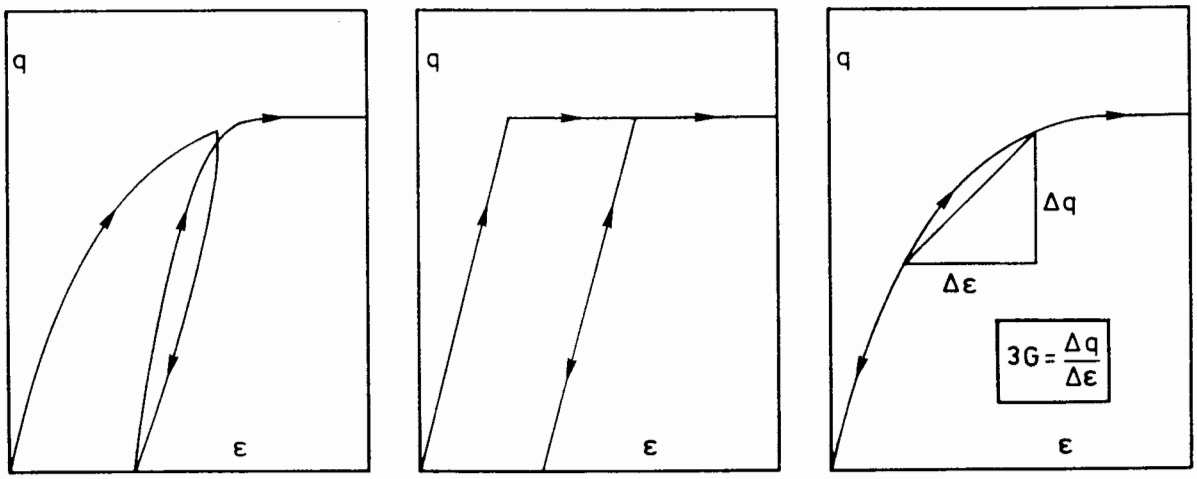

(a) Deviator Stress - Strain Soil Behaviour

(b) Elastic-Perfectly Plastic Soil Model

(c) Non-Linear Elastic Soil Model

Figure 10.3 Various approximations of deviator stress-strain soil behaviour

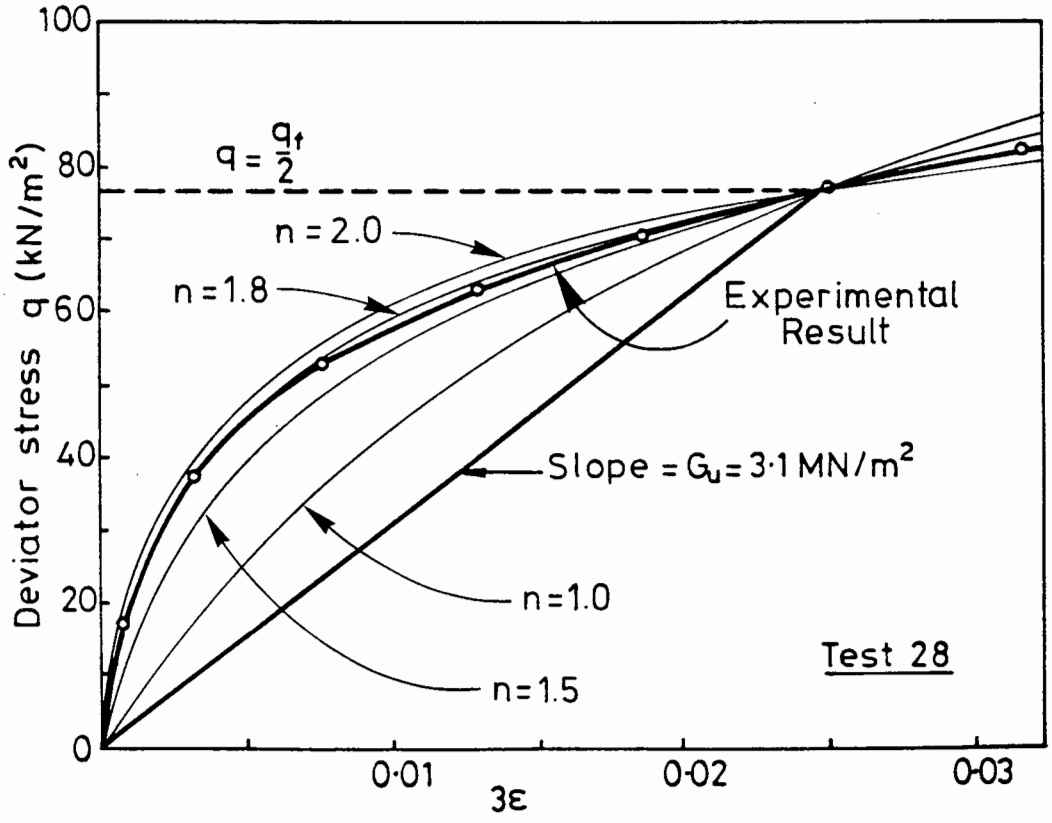

Figure 10.4 Comparison of non-linear elastic approximation with triaxial result of Wheeler, 1986

where

$$X = \left[\varepsilon/\varepsilon_{50} \right]^{1/n} \tag{10.9}$$

Figure 10.4 illustrates the approximation to one of Wheeler's experimental results for various values of n. The code DCFEM2 requires the undrained shear strength, s_u, and matrix shear modulus, G'_u, as shown in Figure 10.4. From these parameters, it is possible to evaluate the required parameters from

$$q_{max} = 2\, s_u \tag{10.10}$$

and

$$\varepsilon_{50} = \frac{1}{3} \frac{G'_u}{s_u} \tag{10.11}$$

Once the stress-strain curve has been defined in some way, the shear modulus of the saturated matrix can then be evaluated by the same method as the bulk modulus for the gassy soil. The value of the stresses and strains is evaluated at the beginning and end of each time increment, from which the shear modulus can be derived from

$$3G' = \frac{q_2 - q_1}{\varepsilon_2 - \varepsilon_1} = \frac{\Delta q}{\Delta \varepsilon} \tag{10.12}$$

where q and ε denote the deviator stress and deviator strain respectively. This procedure for evaluating the shear modulus is presented in Figure 10.3c.

In the evaluation of the bulk and shear moduli of a gassy soil in the triaxial apparatus as described in Chapter 6, it was found that the shear modulus due to the presence of gas was directly related to the gas volume fraction n_g. It was also found that the shear modulus due to the gas, G°, could be approximated by a constant Poisson's ratio, ν°, and the non-linear bulk modulus, K°, as given by

$$2G^\circ = 3K^\circ \left[\frac{1 - 2\nu^\circ}{1 + \nu^\circ} \right] \tag{10.13}$$

Thus within the code DCFEM2, the combined shear modulus--as derived in Chapter 7--can be evaluated from

$$\bar{G} = \left[\frac{1}{\bar{G}^\circ} + \frac{1}{\bar{G}'} \right]^{-1} \tag{10.14}$$

10.2.4 Future extension to model

In the numerical model DCFEM2, the gas is treated as a compressible solid where the bulk modulus is a non-linear function of the total stress with the saturated soil matrix modelled using a simple non-linear elastic stress-strain relationship. Therefore, to increase the applicability of this model, it is recommended that the saturated soil matrix be treated as an elasto-plastic material using the same approach as Carter et al. (1979). It must be noted that if this approach is undertaken, the order of the finite element used must be increased as the four noded element is not of sufficient order to simulate adequately plastic deformation behaviour.

10.3 The Structure and Specifications of the Code DCFEM2

The following section describes the structure of the FORTRAN computer code DCFEM2, which includes the compilation of the complete model from the ten subprograms, the specification of the nodal and element numbering and the choice of boundary conditions open to the user.

10.3.1 Description of subprograms

The code DCFEM2 is written in FORTRAN for use on a VAX/VMS computer system. Only the input and output file specification would have to be modified, however, for the code to be fully compatible with any other machine. DCFEM2 consists of a main program and nine subroutines. A simplified flow chart is presented in Figure 10.5 which illustrates the roles of the main program and the various subroutines. The functions of the main program and the subroutines are presented below in the order that they are first called.

MAIN — Performs the reading and writing of input data, generates the mesh and numbers the nodes and elements. Initial conditions are allocated to the domain. A loop is set up to perform the finite element analysis for each time step.

EBFIND — Computes the matrix bandwidths for the generated mesh and determines the maximum bandwidth.

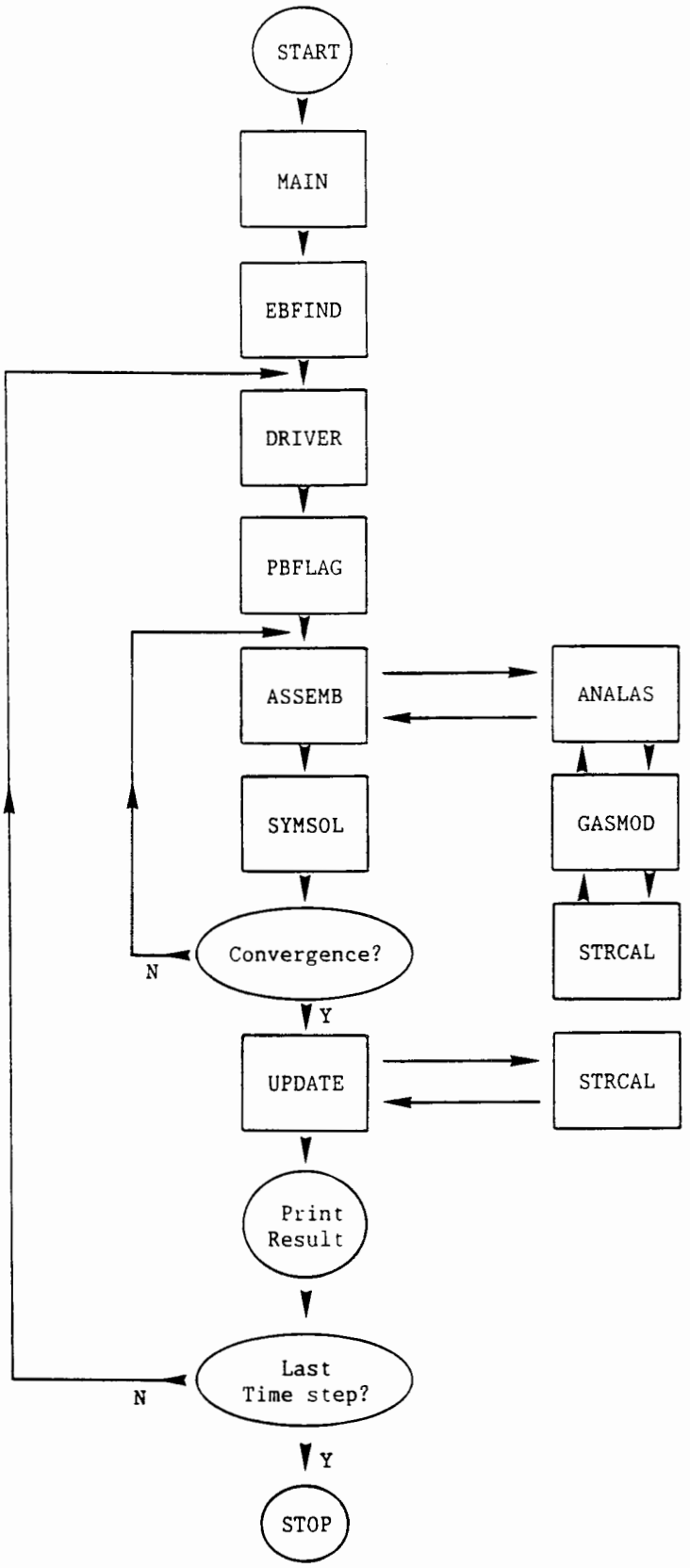

Figure 10.5 Flow chart of DCFEM2

DRIVER This is the main driving routine that is called during each time step. This subroutine calls all other routines to perform the finite element analysis. If the solution does not converge to the required tolerance the process is repeated until convergence is reached. The resulting nodal and elemental values are then written to an output file.

PBFLAG Identifies the position of the Dirichlet boundary nodes within the future global stiffness matrix in order to modify the matrix to take these prescribed nodes into account at a later stage of the model.

ASSEMB Assembles the global stiffness matrix and right-hand side vector from the element stiffness matrices and load vectors. The right-hand side vector is then updated to take into account the prescribed flux boundary conditions. Both the global stiffness matrix and the right-hand side vector are then further modified to take into account the prescribed Dirichlet boundary conditions.

ANALAS Performs the assembly of the stiffness matrix and right-hand side vector for each rectangular element using the influence coefficient method. The element matrices and vectors are generated for both plane strain and axisymmetric conditions.

GASMOD Evaluates the elastic bulk and shear moduli and other non-linear parameters that are required for the gassy soil model.

STRCAL Computes the values of strain, pore water pressure, total stress and consolidation stress at the element centroids.

SYMSOL Performs the solution of the banded symmetric system of algebraic equations using the Gauss elimination scheme.

UPDATE Updates the nodal values of displacement and pore pressure. It also updates the element values of gas porosity, stress and strain.

10.3.2 Element and node numbering

DCFEM2 has been written principally to solve problems associated with gassy soil consolidation. This includes consolidation under both laboratory and field conditions. At the present time, all initial soil domains for the experimental tests that have taken place have a rectangular vertical cross-section. Correspondingly, at this stage of development DCFEM2 is limited to a finite element mesh to give a rectangular domain. It must be noted that an extension to an arbitrary shaped domain is only a matter of modifying the mechanics of the finite element program and not redeveloping the governing theory. A combination of four noded elements is used to produce a rectangular grid, with element and node numbering as illustrated in Figure 10.6. It is also possible to specify an arbitrary value of the gravitational vector as a function of the unit weight of water and the components of the unit vector in the X/R and Y/Z directions respectively, as also shown in this figure.

10.3.3 Description of boundary conditions

The soil boundary conditions that were encountered under laboratory conditions can be subdivided into two types. The first type boundary condition is a prescribed value or Dirichlet boundary condition. For DCFEM2 this may correspond to a prescribed horizontal displacement, vertical displacement or pore water pressure boundary.

The second type boundary condition is a prescribed force or flux known as a Cauchy boundary condition. Again for DCFEM2 this would correspond to a prescribed value of vertical or horizontal stress, or the prescribed rate of removal or injection of pore water. A special case of a Cauchy boundary condition is when there is no boundary condition prescribed--which is also known as a "natural" boundary condition. This takes the form of a no-stress boundary when solving the equilibrium equation, and a no-flow boundary when solving the flow equation.

In addition, as in both the consolidation and triaxial tests described in this report, the boundary conditions on some occasions are time dependent. Therefore, DCFEM2 also permits the boundary conditions to be time dependent.

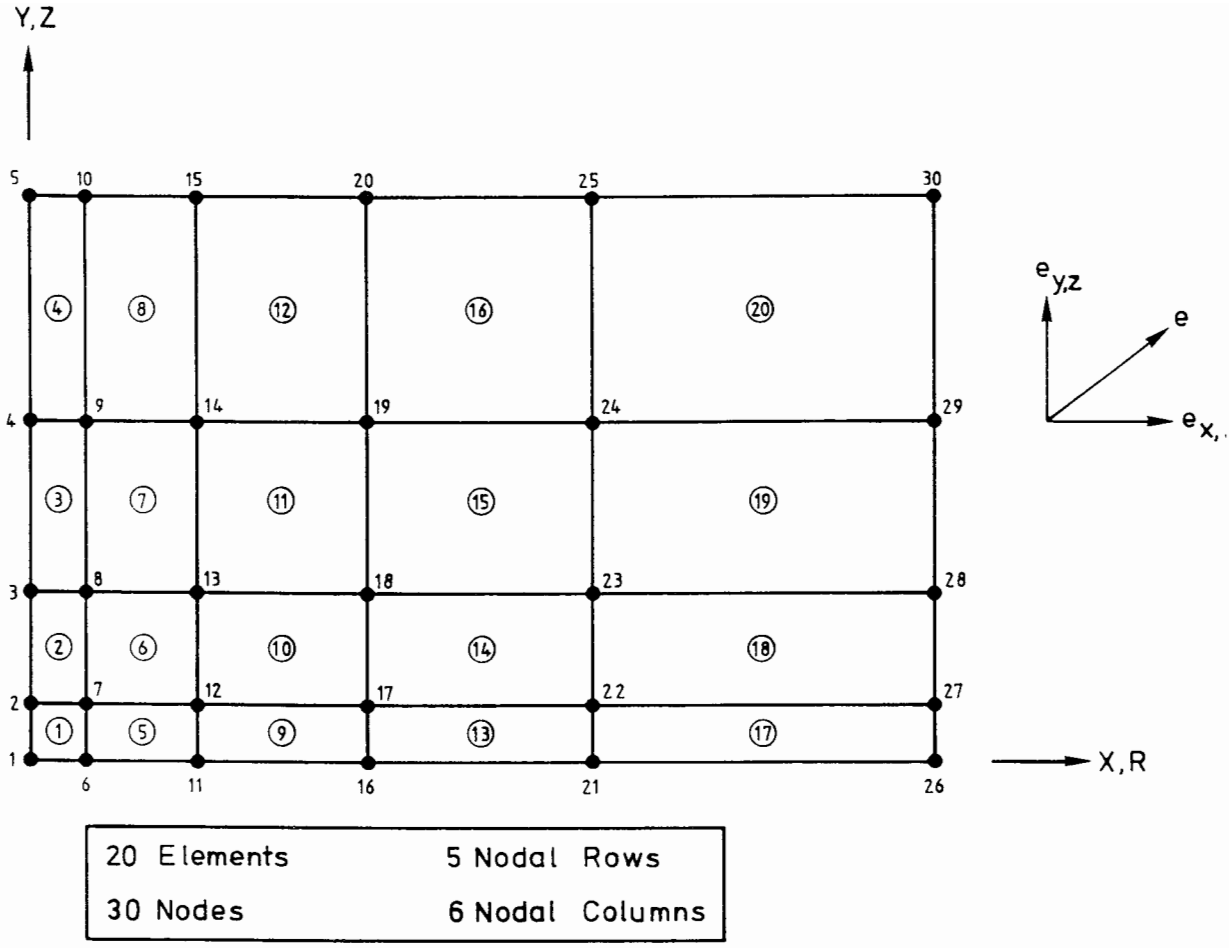

Figure 10.6 Illustration of node and element numbering used in DCFEM2

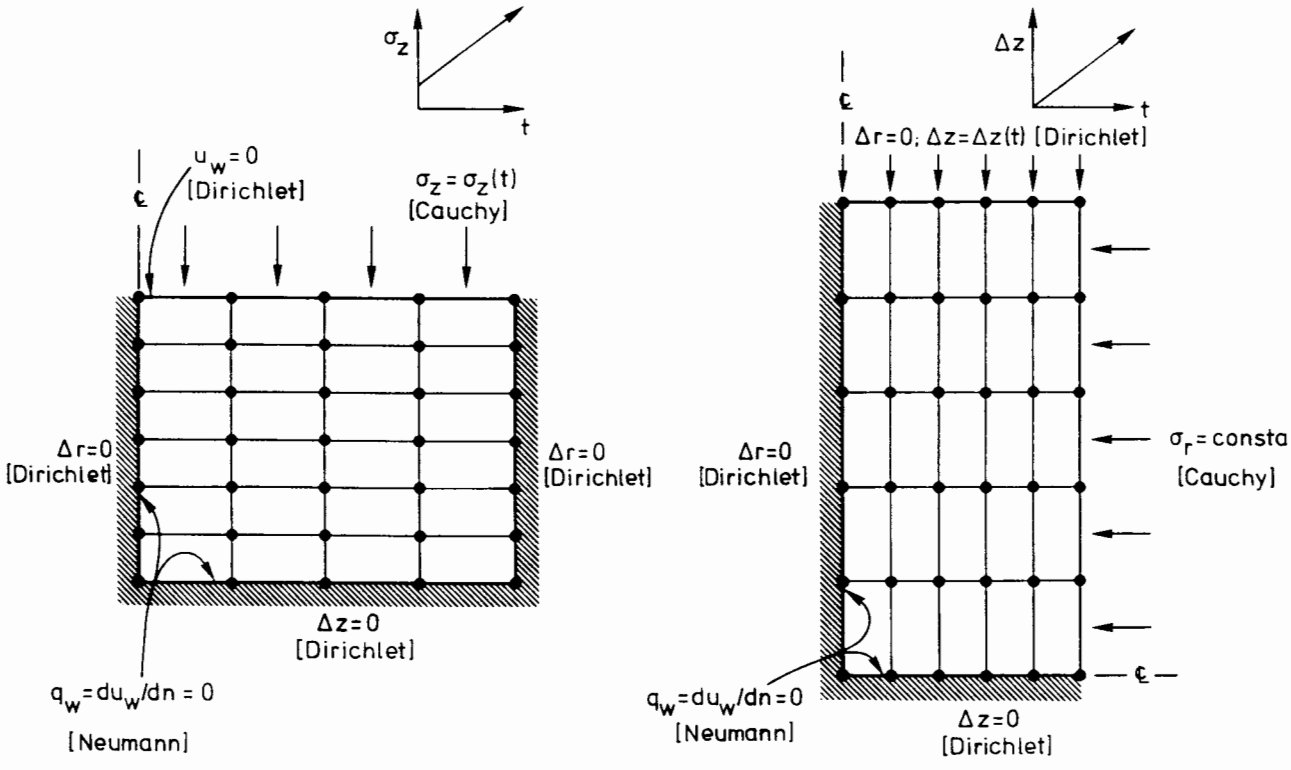

Figure 10.7 Illustration of boundary conditions available in DCFEM2

Figure 10.7 illustrates the boundary conditions that are available in DCFEM2 for the simulation of the experimental tests performed on gassy soil samples where both the stress and displacement can increase linearly with time. For marine soils under field conditions, however, it is often the case that the soil is subjected to a sinusoidal variation in total stress. This condition can also be simulated by DCFEM2 and is illustrated in the next chapter.

10.4 Summary

This chapter presents the constitutive relationships incorporated in the finite element model DCFEM2. Two basic options are open to the user of the model. The first option is to assume that the elastic moduli are constant for the two materials in the model, whereas the second option assumes non-linearity of the bulk modulus of the gas phase as a function of the total stress and non-linearity of the matrix shear modulus as a function of the shear stress.

Also described in this chapter is the structure of the computer model DCFEM2. A brief description of the main program and the nine subroutines is provided, along with a flow chart of the model and an illustration of the element and node numbering of the finite element mesh. Finally, the boundary condition choices are presented which include constant value, linear increases with time and sinusoidally varying Dirichlet and Neumann conditions.

Recommendations for future work in the theoretical and numerical modelling of the drained and undrained behaviour of gassy soils include the incorporation of an elastic-plastic constitutive relationship governing the deformation behaviour of the soil matrix. In addition, this model must include the increase in pore water pressure due to shear and the reduction of the shear strength due to the presence of gas voids.

CHAPTER 11

DCFEM2 - DOUBLE COMPRESSIBILITY FINITE ELEMENT MODEL IN TWO DIMENSIONS

VERIFICATION AND APPLICATION OF MODEL

CHAPTER 11

DCFEM2 - DOUBLE COMPRESSIBILITY FINITE ELEMENT MODEL IN TWO DIMENSIONS

VERIFICATION AND APPLICATION OF MODEL

11.1 Introduction

After the approximated finite element equations and the governing constitutive relationships have been programmed into computer code, it is essential to verify this model with existing analytical solutions. Although it is not possible to verify every problem that the code DCFEM2 could simulate, it is possible to test the most critical areas of the model. Verification problems are presented in this chapter which test the consolidation equations in both coupled and decoupled form. In addition to the verification problems, three case problems are presented at the end of the chapter which illustrate the capability of the model to simulate field and laboratory conditions.

11.2 One-Dimensional Consolidation

In order to test the time dependent nature of DCFEM2, the model was used to solve the one-dimensional Terzaghi (1944) consolidation equation as first solved analytically by Taylor (1948). This problem may be treated in two ways by DCFEM2. The first method treats the soil as a rigid porous medium, allowing the fluid compressibility to take the same value as the coefficient of volume change, m_v, which is present in the Terzaghi equation. The pore water pressure is assumed to be initially constant throughout the domain, with dissipation of pore water permitted from one end. The grid used is presented in Figure 11.1. The resulting pore water pressure response on the undrained face, plotted against dimensionless time, is illustrated by ringed solid circles in Figure 11.2. Also plotted on the same axes, shown by the continuous line, is Taylor's analytical solution to this problem, for which the comparison is excellent.

Alternatively, DCFEM2 can solve the Terzaghi equation by using the fully coupled flow and deformation equations. The pore fluid compressibility must be set to zero and the shear modulus of the soil set to a low value ($G' < K'/1000$). Under these conditions, the drained bulk modulus becomes equal to the

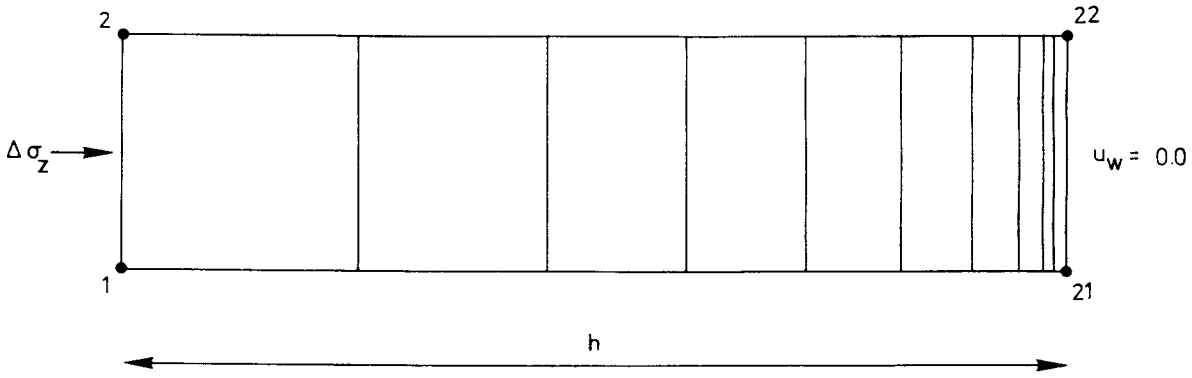

Figure 11.1 Finite element grid used for one-dimensional consolidation

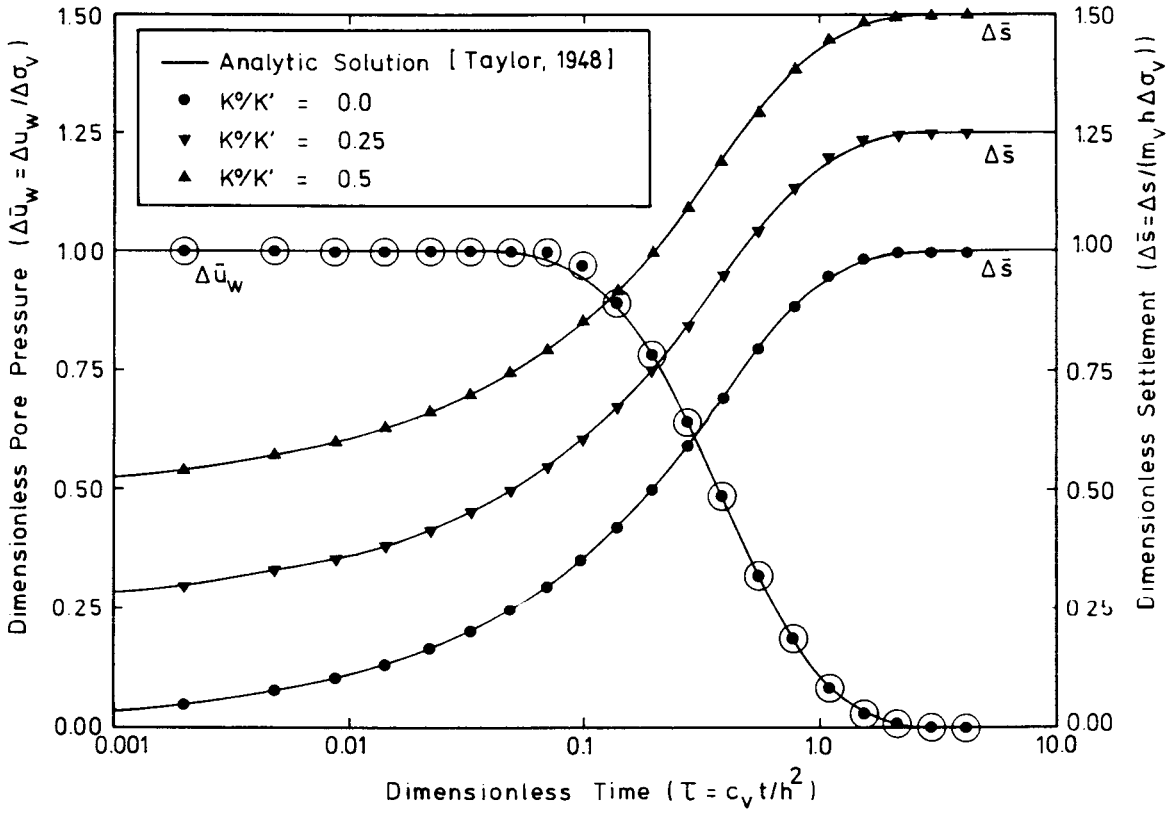

Figure 11.2 Simulated settlement and pore water pressure response using DCFEM2

coefficient of volume change. Running this problem produces identical results to those obtained using a compressible pore fluid. Additionally, when the fully coupled flow and displacement equations are used, the total settlement is output and can be plotted against time, as shown by the points marked $K^o/K'=0$ in Figure 11.2. This also gives excellent comparisons with the analytical solution.

The code DCFEM2 can also be used to test the flow and deformation of a double compressible material. The previous test was rerun with the addition of a gas bulk modulus (i) one-half ($K^o/K'=0.5$), and (ii) one-quarter ($K^o/K'=0.25$) of the drained bulk modulus of the saturated matrix. For all the simulations using a compressible soil matrix, the resulting pore water pressures on the undrained face--illustrated by ringed solid circles in Figure 11.2--were almost identical for each test. Again these agreed very well with the analytical solution of Taylor. It must be noted here, however, that the analytical expression given for the time dependent settlement behaviour of a double compressibility material is simply the settlement evaluated for a saturated soil, plus the increment of settlement that is produced by the compression of the gas under undrained conditions. This is not the case, however, for the procedure used by DCFEM2, as here the elastic moduli are supplied for each phase and therefore a different set of equations is solved for each case.

11.3 Two-Dimensional Radial Consolidation caused by Pumping of Pore Water

To verify the fully coupled flow and displacement capabilities of DCFEM2 under two-dimensional plane strain and axisymmetric conditions, the problem of the consolidation of a soil surrounding a well--pumping water at a constant rate--was simulated. For the same soil conditions as above ($G' < K'/1000$), this problem becomes mathematically equivalent to a pump test in a confined aquifer as depicted in Figure 11.3. The solution of this problem, which was developed by Theis (1935) in terms of the pore water pressure u_w, can be adapted to incorporate soil material properties to give

$$\Delta u_w = \frac{Q}{4\pi k/\gamma} \int_{\tau}^{\infty} \frac{e^{-y}}{y}\, dy = \frac{Q}{4\pi k/\gamma}\, W(\tau) \qquad (11.1)$$

where the exponential integral is identified by the well function $W(\tau)$, and

$$\tau = 4Ktk/\gamma_w r^2 = 4ct/r^2 \qquad (11.2)$$

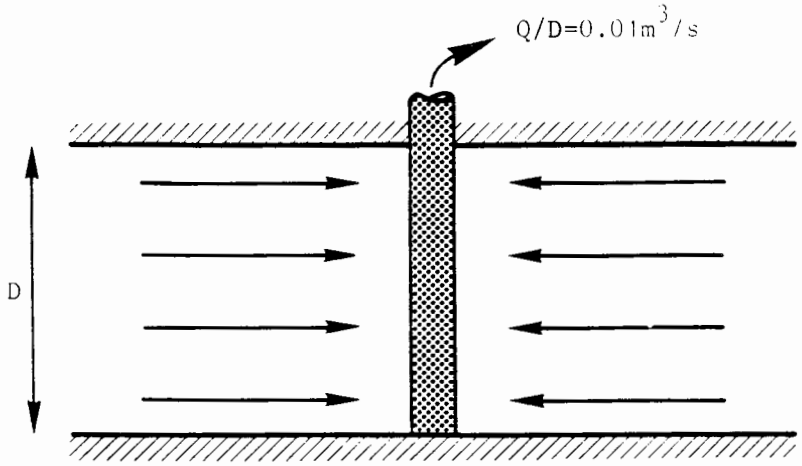

Figure 11.3 Schematic description of the well pumping problem

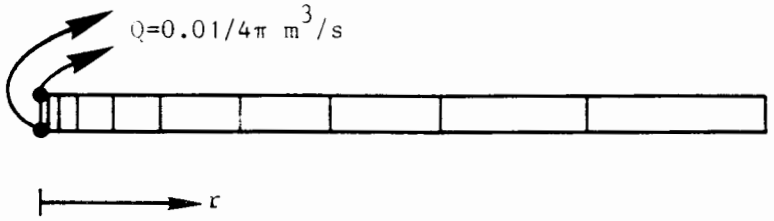

Figure 11.4a Axisymmetric element mesh for well pumping problem.

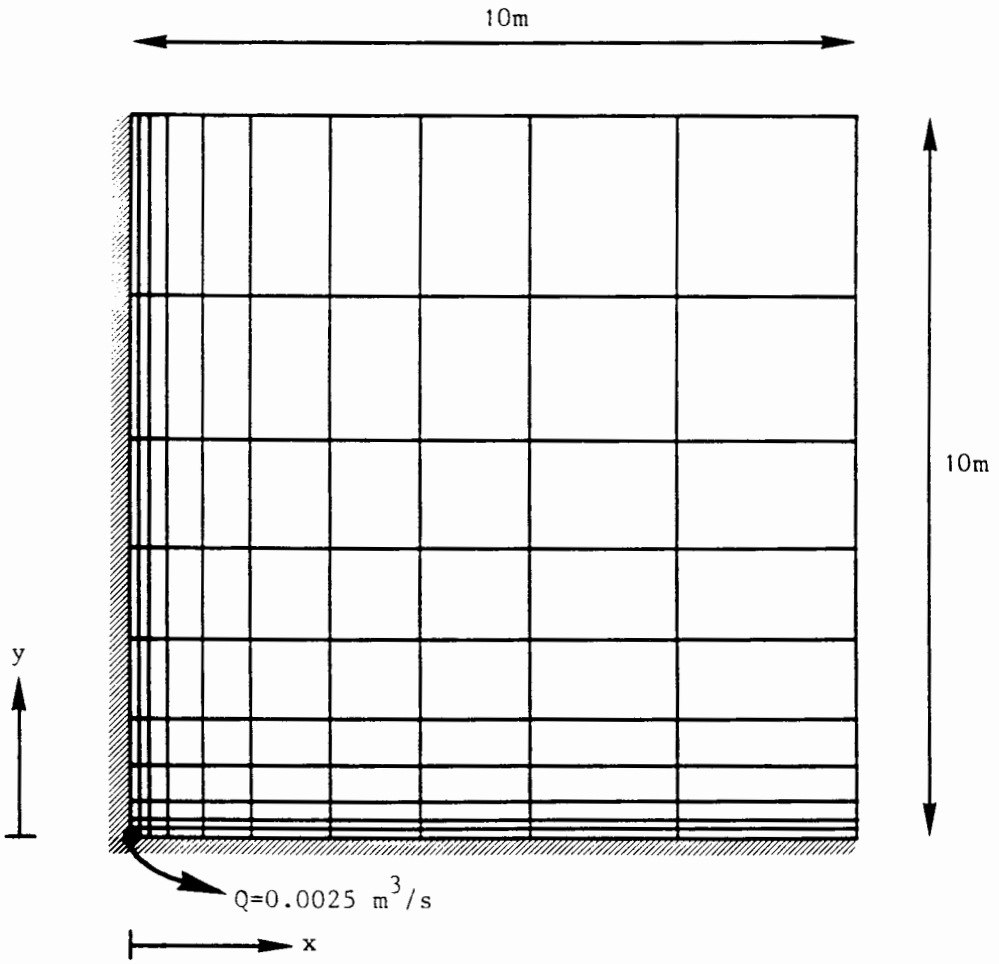

Figure 11.4b Plane strain element mesh for well pumping problem

where the coefficient of consolidation is defined as

$$c = Kk/\gamma_w \tag{11.3}$$

and where Q is the volume of water pumped from the well per unit time per unit thickness of the soil layer, r is the radial distance from the centre of the well, K is the drained bulk modulus of the soil, t is time and k/γ_w is the soil mobility. The analytical solution of the function $W(\tau)$ and tabulated values of the well function versus time are presented in Walton (1962).

DCFEM2 can simulate this problem in two ways. The first involves reducing the problem to one-dimensional axisymmetric conditions. The total well discharge must then be divided by 2π as the model only simulates one radian of the axisymmetric problem. The grid used for this simulation is presented in Figure 11.4a. The problem may also be simulated by using a two-dimensional grid under plane strain conditions. Again, as only a quadrant of the domain is required--as illustrated in Figure 11.4b--the total well discharge must be divided by 4.

Figure 11.5 presents the change in the value of pore pressure with dimensionless time at 1m from the centre of the well. Also presented is the analytical solution from Walton (1962). The sudden divergence of the numerical solution from that of the analytical at late time is due to a reflection at the boundary of the finite size domain that the finite element method has to adopt.

Also evaluated in this simulation is the variation in pore water pressure in the radial direction at a constant value of time. The comparison between the numerical and analytical results is presented in Figure 11.6.

11.4 The Mandel-Cryer Effect

The previous two consolidation problems can be solved by considering solely the flow of a pore fluid in a porous medium. This dissipation approach is sometimes known as Rendulic theory (Rendulic, 1936). When the fully three-dimensional coupled fluid flow and soil displacement theory is applied to some simple problems, however, it is observed that in certain regions of the soil domain the pore water pressure rises before it decays. This phenomenon is called the "Mandel-Cryer effect" after Mandel (1957)--who demonstrated it for the consolidation of a brick-shaped body loaded uniaxially under conditions of plane strain--and Cryer (1963)--who demonstrated it for the consolidation of a

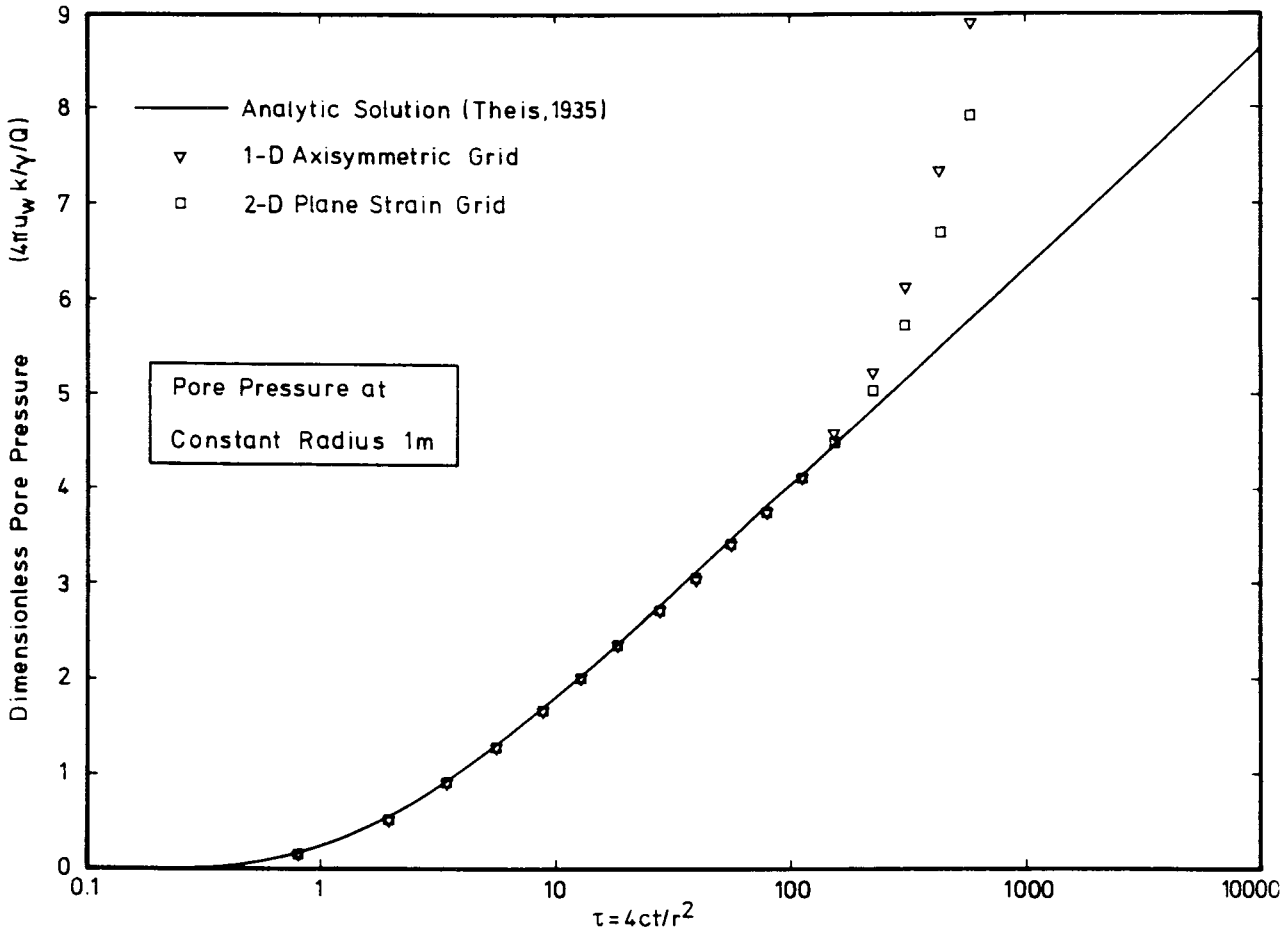

Figure 11.5 Pore water pressure variation with time at 1 metre from centre of pumping well

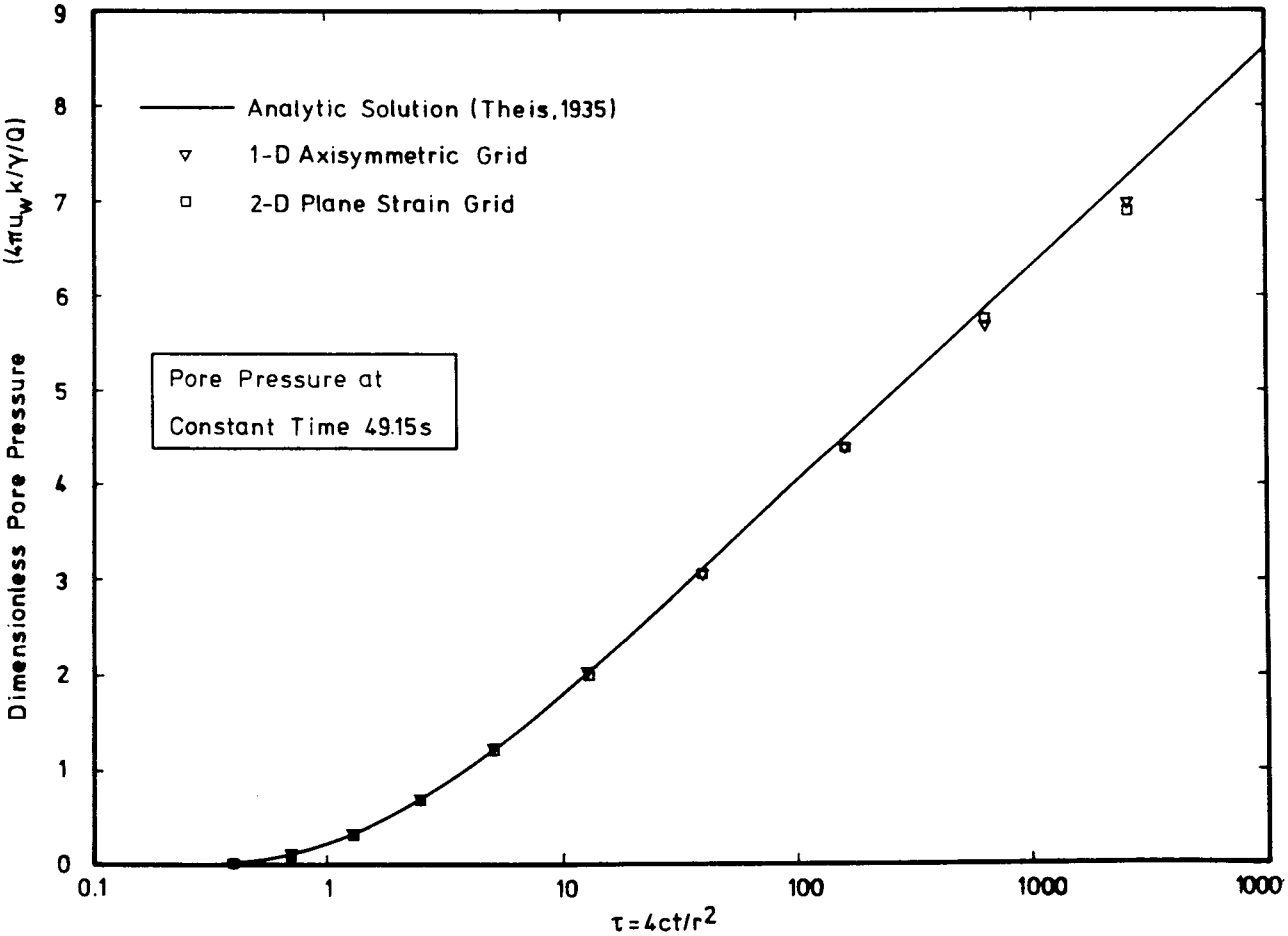

Figure 11.6 Pore water pressure variation with radial distance from centre of pumping well at constant time

uniformly squeezed sphere drained at its surface. Rendulic theory does not predict the Mandel-Cryer effect because it treats the flow equation by pure diffusion theory, producing a monotonic decrease in pore water pressure.

To illustrate this effect, the problem of a cylindrical saturated soil sample initially loaded under isotropic conditions, followed by drainage from all surfaces, is simulated by DCFEM2 using the grid for a symmetric quarter of the problem as illustrated in Figure 11.7. Three test problems are run with a drained Poisson's ratio of 0.5, 0.333 and 0.0. The results of these are shown in Figure 11.8. The Mandel-Cryer effect is clearly illustrated in this figure, with pore water pressures rising first before falling for Poisson's ratio less than 0.5. The problem is also run using dissipation theory by giving the water a finite compressibility and initial pore pressure. The results are identical to those produced using fully coupled theory with a 0.5 Poisson's ratio.

11.5 Surface Footing on a Semi-Infinite Elastic Porous Medium

In order to verify the behaviour of the finite element model DCFEM2 under two-dimensional conditions, the problem of a surface footing on an elastic porous medium having a semi-infinite domain was treated. Due to the nature of the finite element formulation, both strip and circular footings could be modelled. Simulations of surface settlement with horizontal distance from the footing centre were made, as were pore pressures with depth below the footing.

The finite element mesh used in all these simulations is illustrated in Figure 11.9. A 10x10 rectangular grid is used consisting of 100 four noded rectangular elements and 121 nodes, each with three degrees of freedom (horizontal displacement, vertical displacement and pore water pressure). On the left-hand line or axis of symmetry and the lower boundaries, a no-flow and no-displacement condition is imposed. The right-hand distant boundary also has a no-flow condition, but it has a constant stress boundary imposed. The top boundary has both pore water pressures and vertical stresses specified.

The solution for surface settlement due to the application of a strip or circular footing on a semi-infinite elastic material is presented by Poulos and Davis (1974). The solution gives the difference between the surface settlement

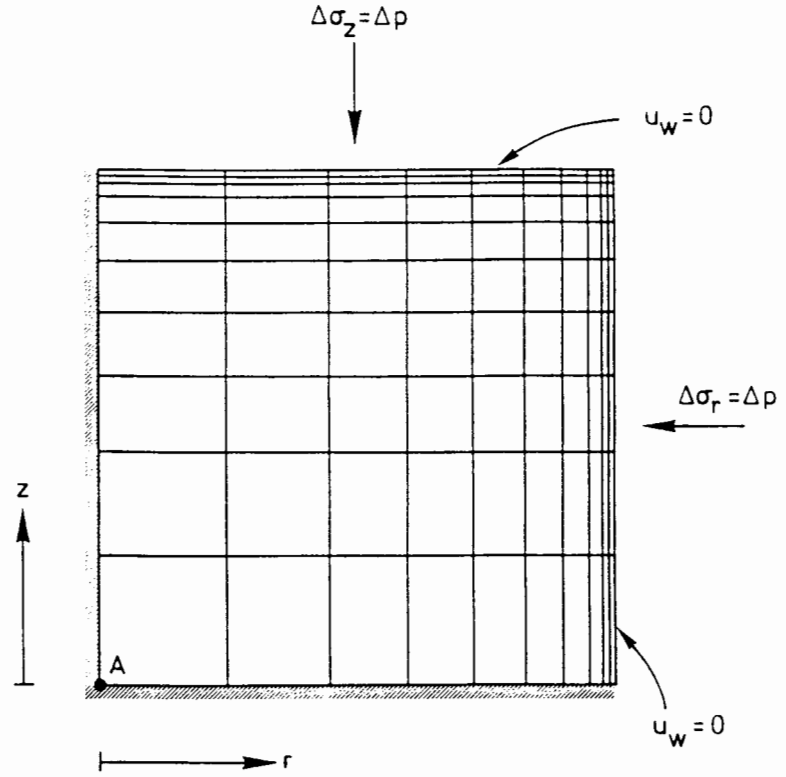

Figure 11.7 Axisymmetric finite element mesh used for the simulation of the Mandel-Cryer effect

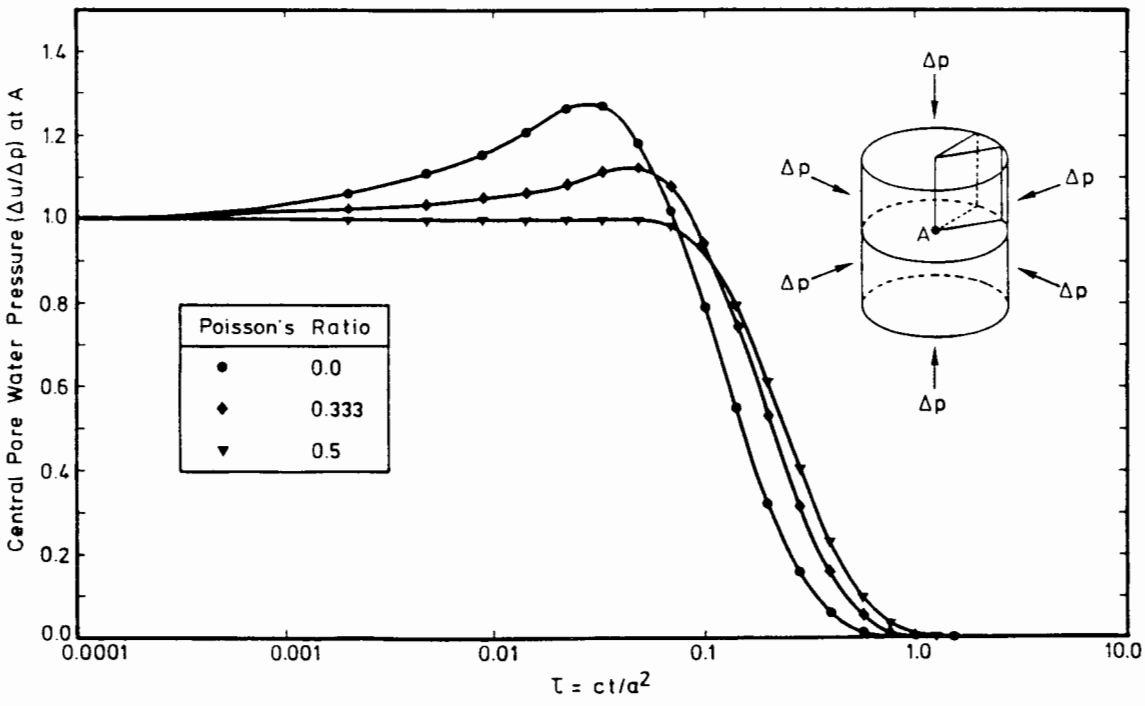

Figure 11.8 Pore pressure at the centre of a cylindrical soil sample subjected to an increase of isotropic pressure

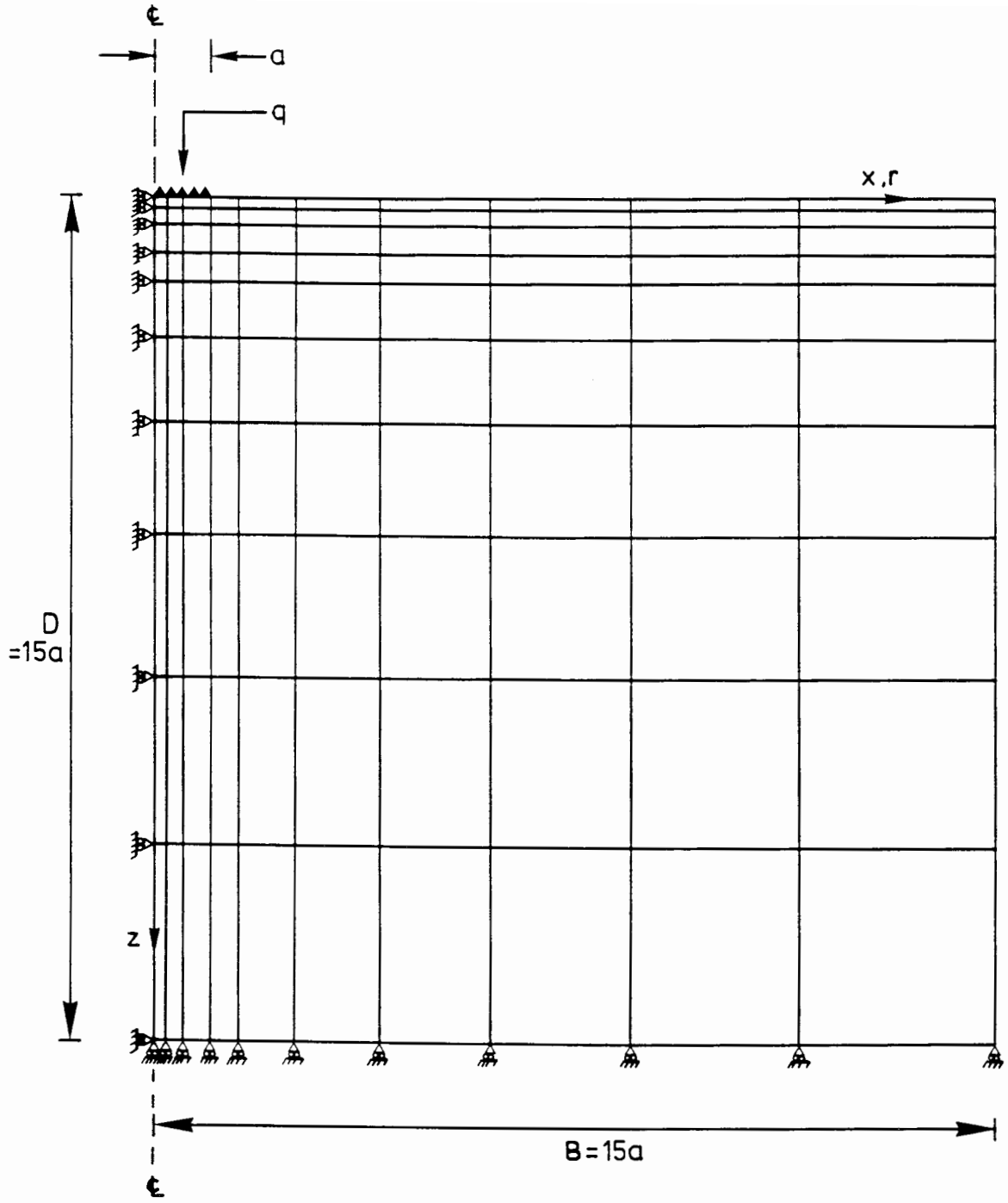

Figure 11.9 Finite element mesh used for the surface footing problem

at the centre of the footing and the surface settlement at some distance away. The Young's modulus and Poisson's ratio of the material are required, along with the diameter of the footing and the applied distributed load. Simulations of surface settlement were made at various distances from the centre of both strip and circular footings for drained (ν=0.0) and undrained (ν=0.5) conditions, and are compared with the analytical solutions in Figures 11.10 and 11.11.

The solution for the time dependent soil displacement and pore water pressure in a semi-infinite soil caused by a circular or strip surface load was treated analytically by McNamee and Gibson (1960). In the present simulation, the pore water pressure versus time at a depth of one quarter of the width of the footing was calculated using the finite element method for both central and backward finite difference in time. These pore water pressures are plotted against time for both strip and circular footings in Figures 11.12 and 11.13 respectively. It can be seen that for most of the curve, the comparison is very good. The variation at early time is due to the initial oscilliatory behaviour of the numerical method which could be reduced using a finer element mesh.

11.6 Case Problem 1 - Plate Test on a Saturated Soil

This example simulates a plate test in which a semi-infinite domain of saturated soil is subjected to an increasing distributed circular surface load. This loading condition assumes that the plate has a flexible surface in contact with the soil. The soil is assumed to have a non-linear deviator stress-strain behaviour. A schematic description of the problem and the relationship between the deviator stress and strain are presented in Figure 11.14. The uniformly distributed circular load is assumed to increase linearly with time. It is also assumed that this load takes place over a short time period so that undrained conditions prevail. To model this loading test, an axisymmetric finite element grid is used as presented in Figure 11.15. To represent a semi-infinite domain, the boundaries of the finite element grid are placed at a distance of fifteen times the radius of the loaded area from the load centre so as not to cause any significant boundary effects. DCFEM2 was run for eight time steps with the load

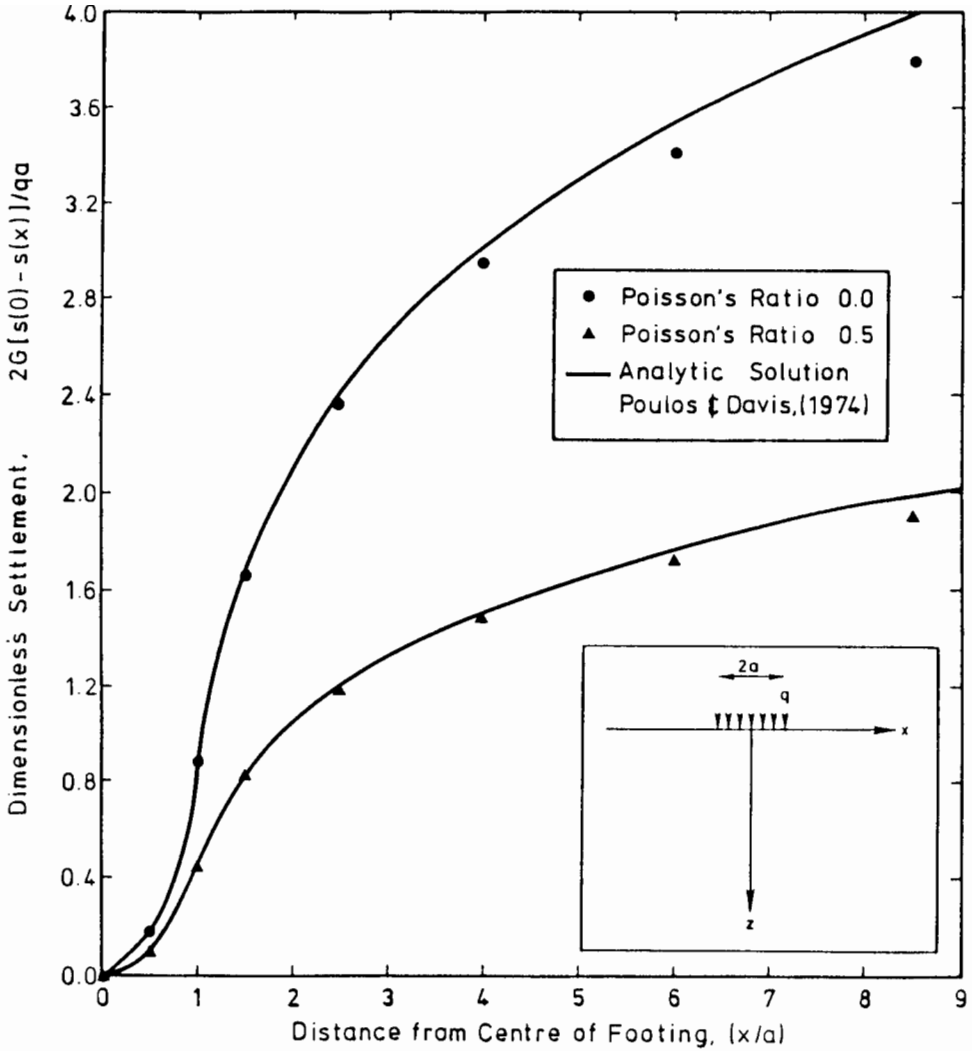

Figure 11.10 Surface settlement relative to the centre of a strip footing

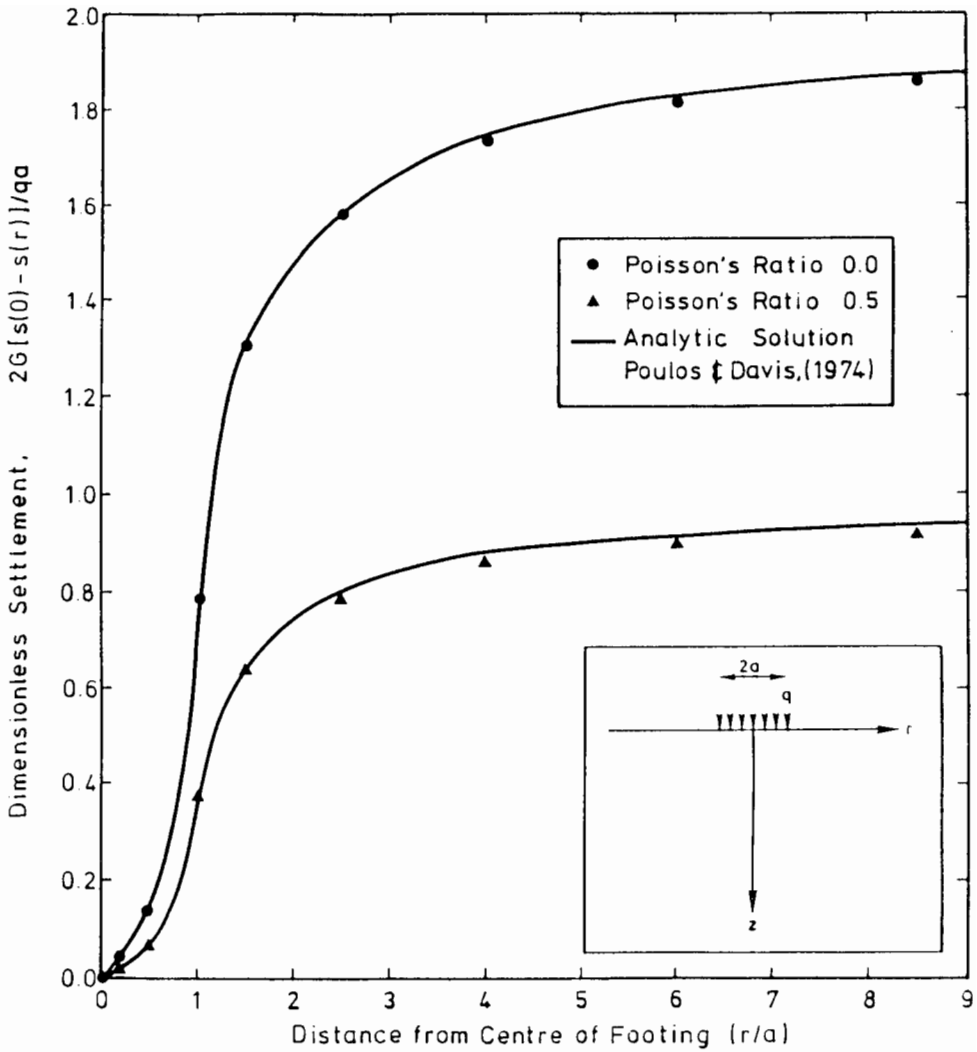

Figure 11.11 Surface settlement relative to the centre of a circular footing

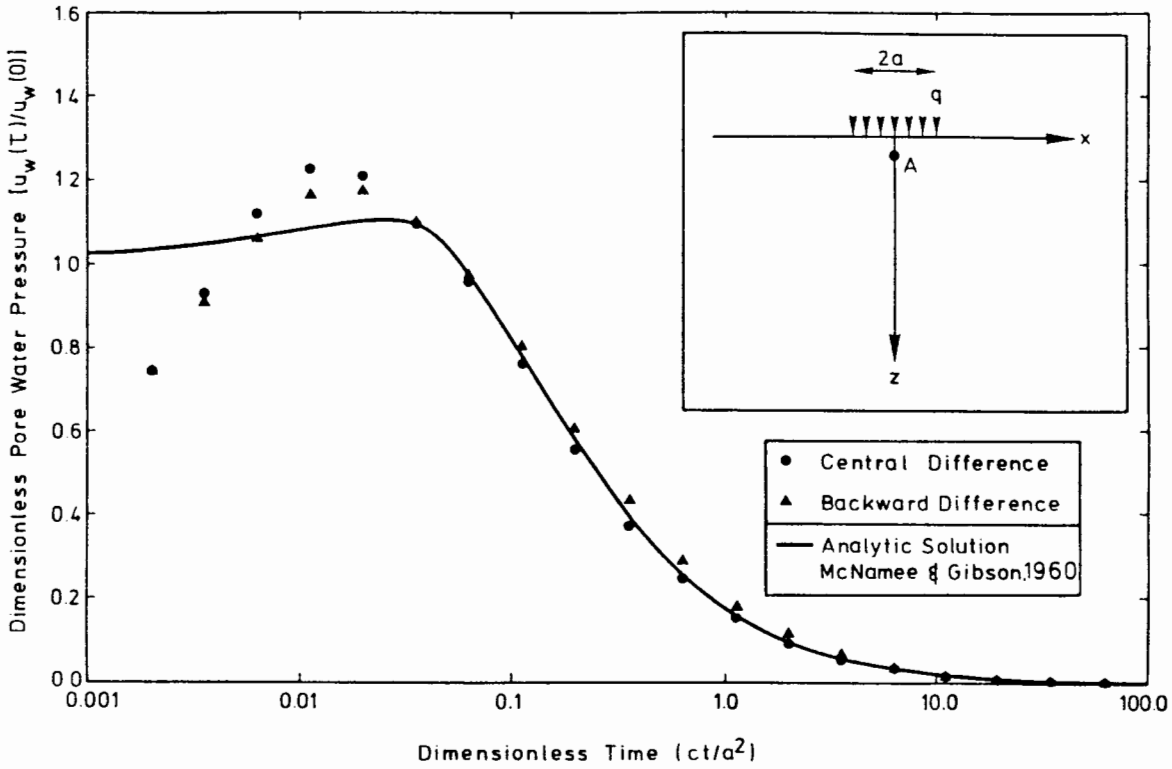

Figure 11.12 Pore water pressure response beneath a surface strip footing

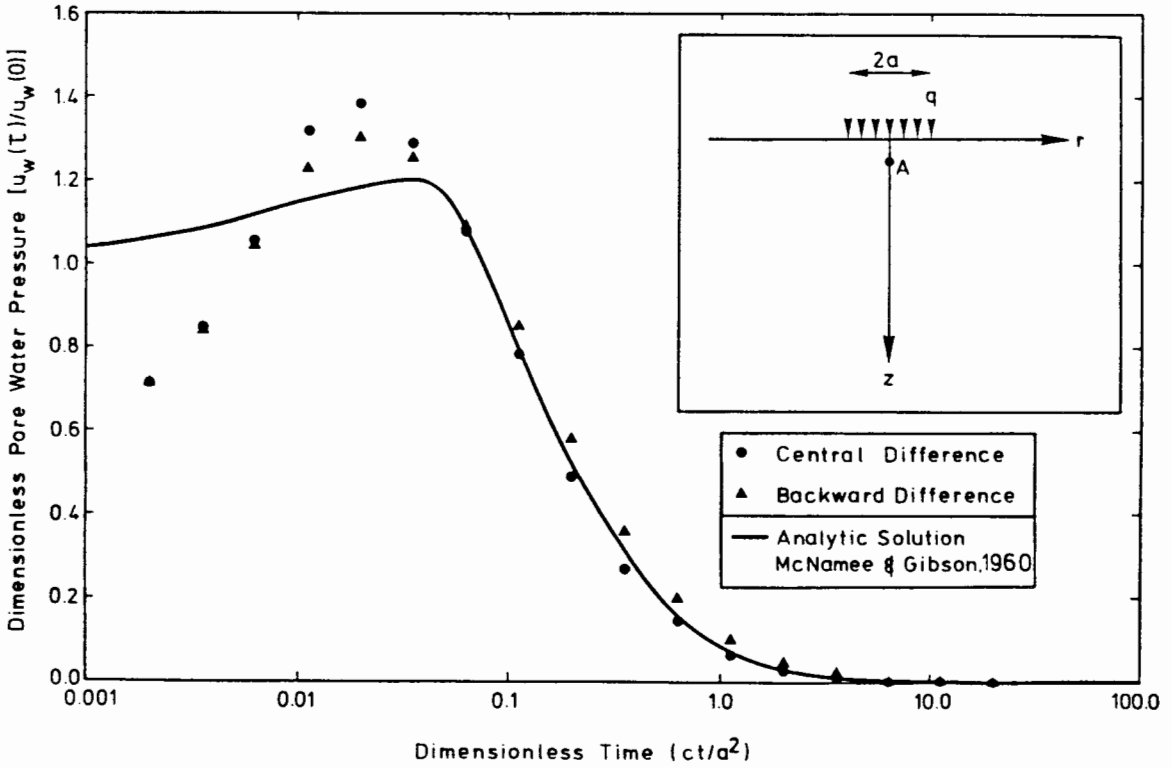

Figure 11.13 Pore water pressure response beneath a surface circular footing

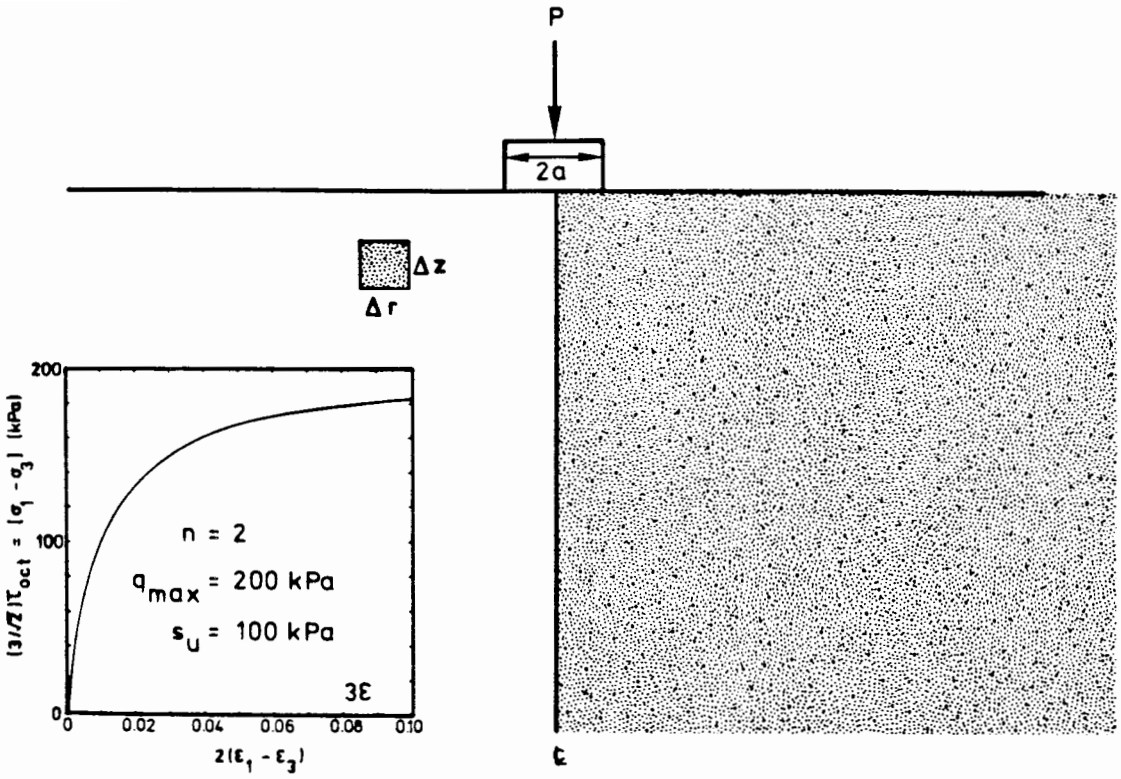

Figure 11.14 Schematic description of circular load on a semi-infinite soil domain

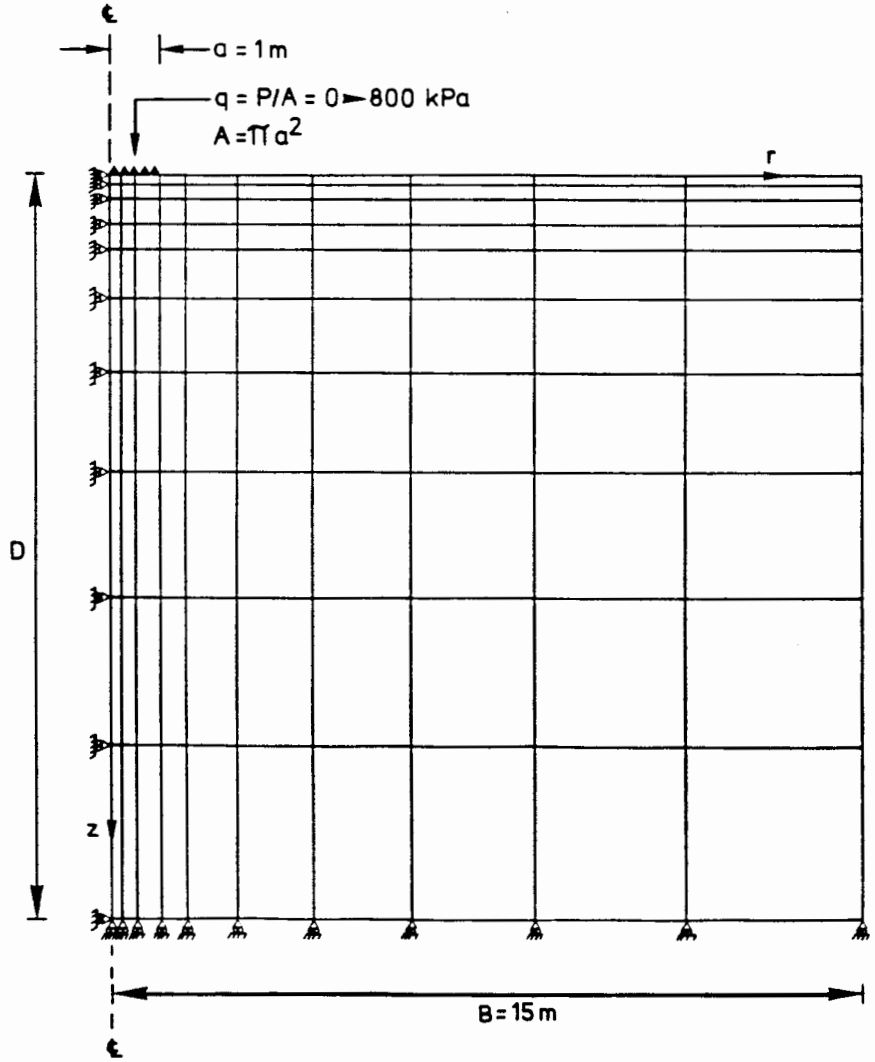

Figure 11.15 Axisymmetric finite element grid used for the circular footing problem

increasing steadily from 0 kPa to to 800 kPa. Within each time step, about ten non-linear iterations were required to converge to a tolerance of 0.001.

Figure 11.16 presents the results of stress and surface displacement calculated by DCFEM2 at the loading stages of 400 and 800 kPa. Also presented is the octahedral stress distribution below the loaded area. This shows that the highest stress concentration occurs at a distance of approximately one diameter of the loaded area below the soil surface. It can also be seen that the stress reduces quickly with radial distance and that by four plate diameters away from the central axis, little stress remains. To illustrate the stress distribution with depth, the shear stress is presented along the centre line below the load. Finally, for each loading stage, the surface settlement at the centre of the plate is plotted against the distributed load.

Although this method of analysis proved successful in the simulation of the stress and deformation behaviour of a porous elastic material, inaccuracies can occur in problems that exhibit a high degree of shear strain. This particular problem illustrates this fact as the maximum allowable distributed surface load, as given by Cox, Eason and Hopkins (1961), is 5.69 s_u--which is 569 kPa for this problem--whereas it can be seen from Figure 11.16 that the soil has not failed at a distributed load of 800 kPa. A finer finite element mesh would possibly reduce the inaccuracy at this high strain. However, the most likely cause is the overstiff response in shear of the four noded elements illustrating that higher order elements should be used in future for such problems.

11.7 Case Problem 2 - Triaxial Test on a Gassy Soil Sample

This example illustrates the simulation of a gassy soil under undrained triaxial conditions for three samples of different initial gas porosities. It is assumed for all three soil samples that the volume of water and solids is equal and that all have been consolidated to the same consolidation pressure of 200 kPa. The three gas porosities are 0.00, 0.01 and 0.05. In addition, due to the solubility of the gas in the pore water, it is assumed that for all three samples the effective porosity of the dissolved gas, Hn_g, is equal to 0.02. The

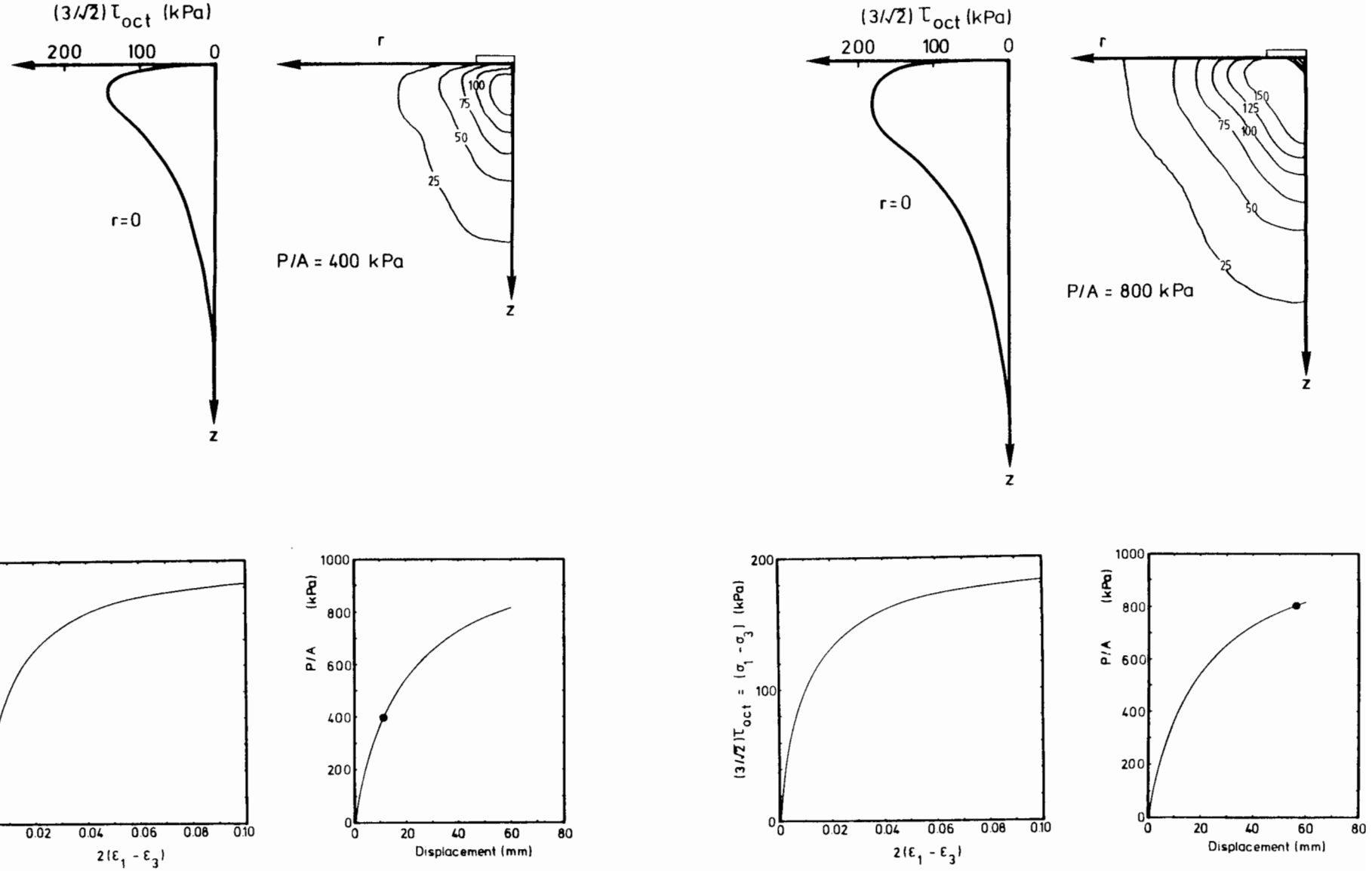

Figure 11.16 Surface displacements, deviator stresses and strains at surface loads of 400 and 800 kPa

sample is assumed to be at an initial isotropic pressure of 200 kPa, with the pore water pressure at an atmospheric back pressure. The sample is loaded from the top surface by the application of a constant rate of vertical displacement of 0.02 mm/min. Due to the vertical axis of symmetry and the horizontal plane of symmetry, only a segment of this domain in the upper half of the sample need be modelled. The finite element grid used to discretize this domain is illustrated in Figure 11.17. As only half of the z domain is modelled, the rate of displacement must then be reduced by half to 0.01 mm/min.

In order to compare the internal stresses produced in all three samples due to the same rate of axial strain, the first simulation that was performed used only one element and assumed that the surface of the loaded area was perfectly smooth so that any radial displacement along this boundary was not restricted. The three samples were all strained until they reached a deviator stress of 120kPa (75% of the ultimate deviator stress). The deviator stress versus deviator strain is presented for each sample in Figure 11.18. It can be seen from this figure that although the strain rate is identical for all three tests, the saturated sample reaches failure far sooner than the gassy samples.

The second simulation modelled the laboratory condition that the top boundary of the soil sample is fixed along the radial direction and is not free to move horizontally. This corresponds to the prescribed zero radial displacement boundary along the top face of the finite element grid as illustrated in Figure 11.17. To evaluate the variation in the deviator stresses under laboratory boundary conditions, the 25 element grid was then used to simulate the triaxial test on the sample with a 0.01 initial porosity. Figure 11.19 illustrates the stress behaviour at element 1 and element 5 (illustrated in Figure 11.17), along with the stresses obtained in the single element test. It can be seen that the stress near the centre of the sample is very close to the one element result, whereas the stress near the surface of the top boundary --due to the restriction of radial displacement along that boundary--has a significantly lower value.

An encouraging result was produced by this simulation when it was decided to evaluate the average deviator stress by integrating the non-uniform vertical

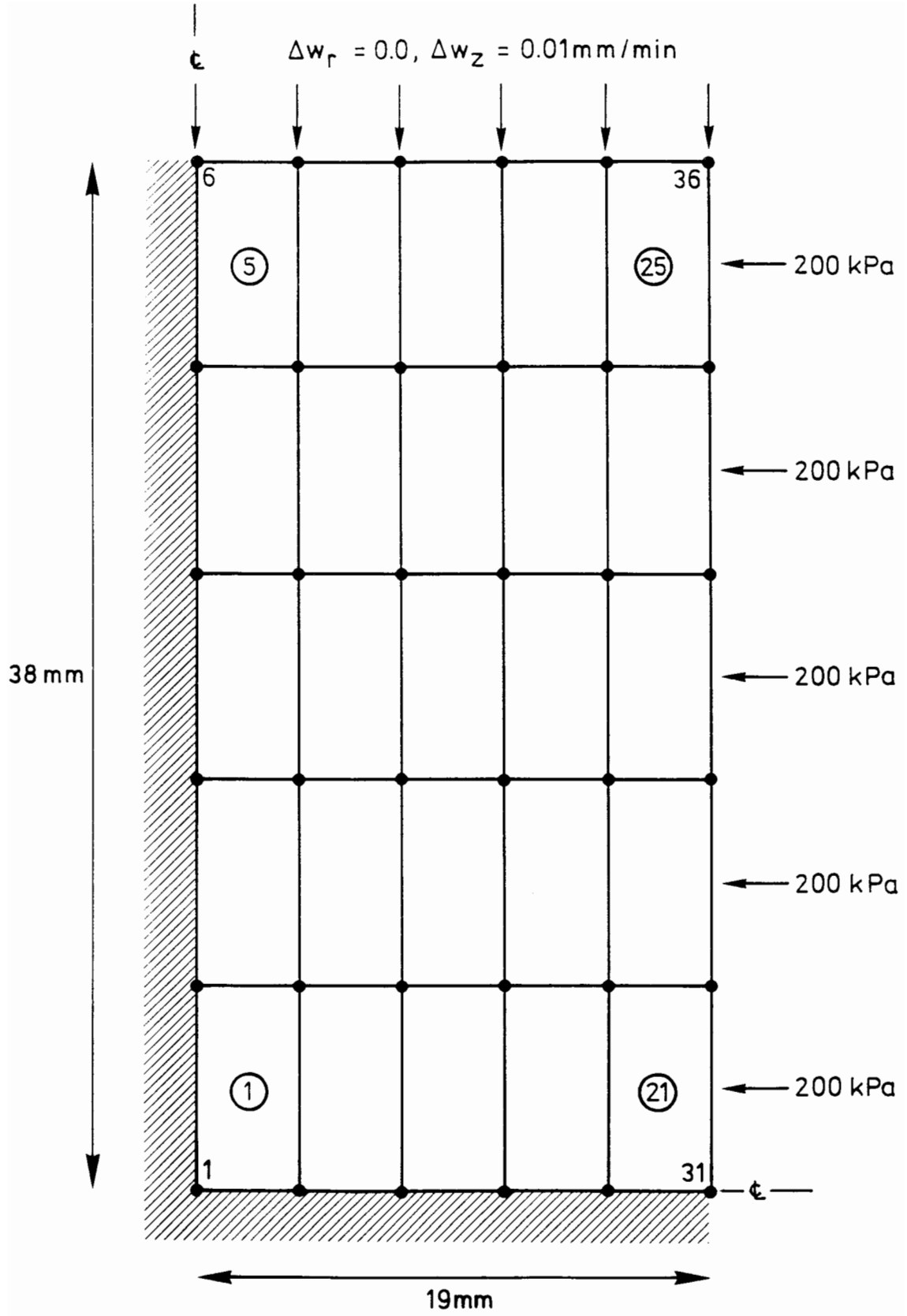

Figure 11.17 Axisymmetric finite element grid used for the triaxial simulation

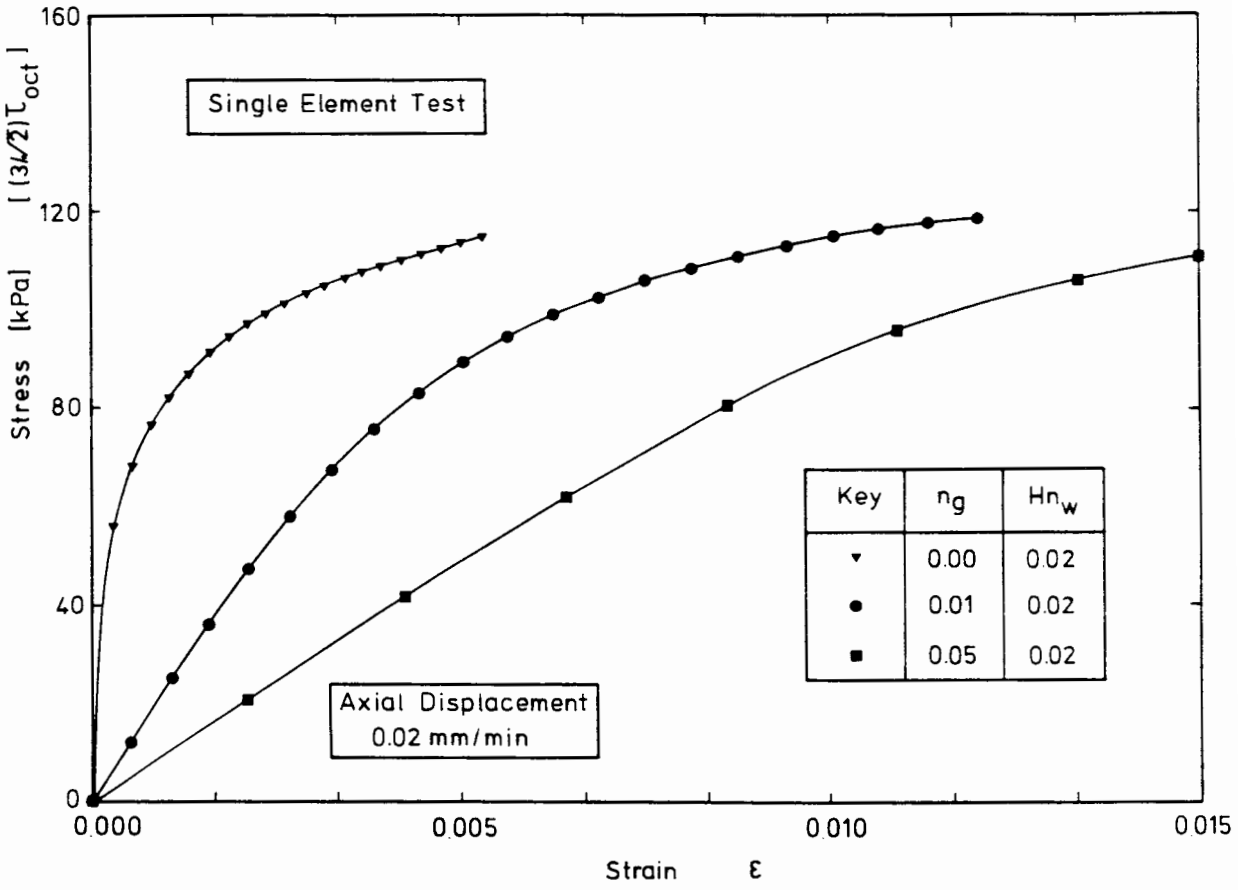

Figure 11.18 Deviator stresses and strains for gassy soils of various gas contents

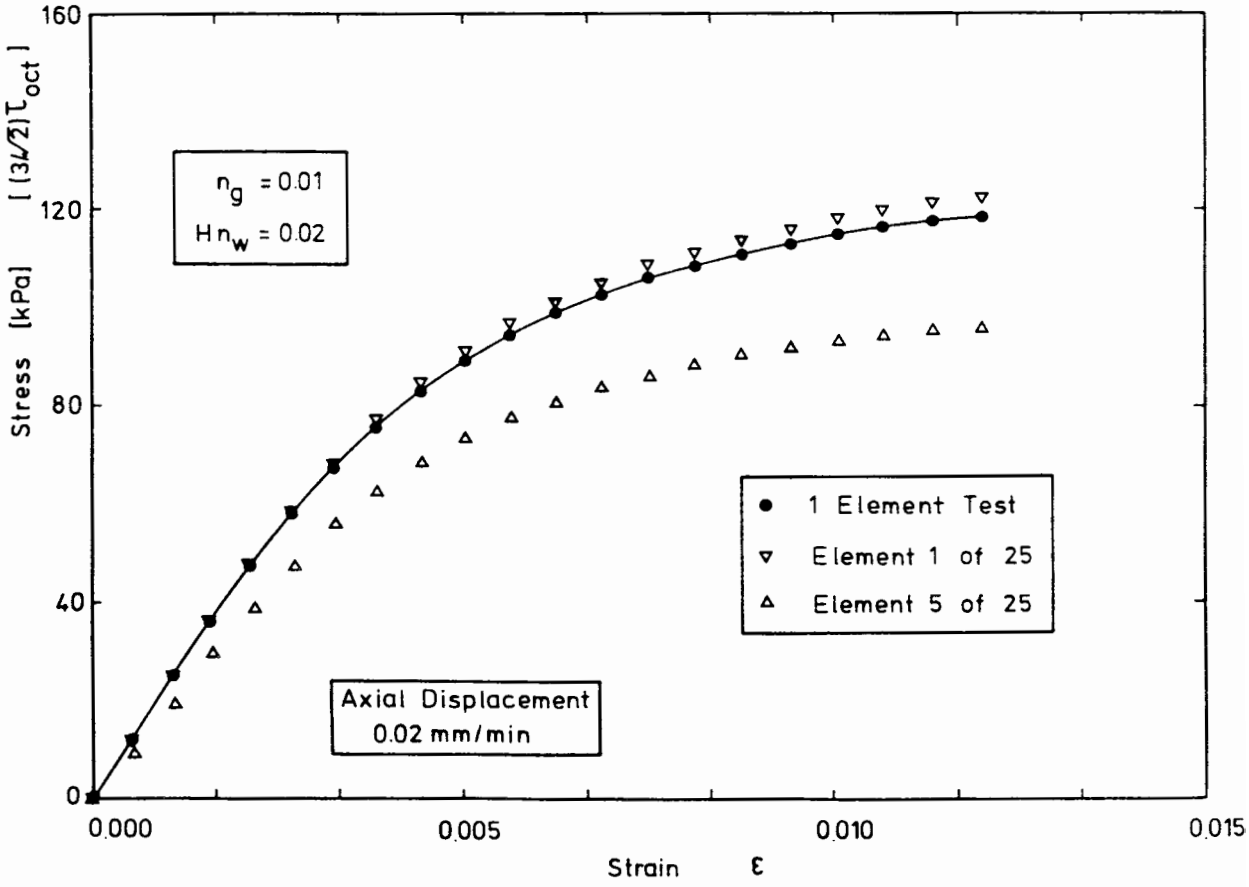

Figure 11.19 Deviator stresses and strains at discrete points in a triaxial sample of a gassy soil

stress reaction on the top face of the sample and dividing by the cross-sectional area. This average deviator stress could then be plotted against the deviator strain calculated from the prescribed displacement of the top face. In all the above runs, the resulting average deviator stress-strain curves were almost identical to those obtained using the one element test. This indicates that the procedure of calculating the stress-strain behaviour in the triaxial cell has no inherent inaccuracies when testing gassy soil.

Also evaluated were the pore water pressures produced during loading. The pore water pressures for the single element test for all three samples are presented in Figure 11.20, from which it can be seen that the pore water pressure is generated more rapidly for a saturated soil than for a gassy soil. (Note that $\Delta u_w = \Delta q/3$ as an elastic model is used.) Figure 11.21 presents the generation of pore water pressure using the 25 element grid for the sample of 0.01 gas porosity. Pore water pressures are plotted for the single element test, node 1 and node 36. Node 1 corresponds to the bottom left node, which is the centre of the sample, whereas node 36 corresponds to the top right node. It must be made quite clear at this point that the generation of these pore water pressures is solely due to elastic responses. The additional pore water pressure generation due to changes in shear is not included in this model.

11.8 Case Problem 3 - Pore Water Pressure Response in a Gassy Seabed

Recent work at Oxford has led to the development of a differential piezometer which has the ability to measure the difference between the pore water pressure at a depth in the seabed and the sea water pressure just above the mudline. For a fully saturated soil, any increase in water pressure above the mudline will cause an equal increase in pore water pressure in the seabed, and no excess pore water pressures are generated. This response is observed by the differential piezometer where the difference between the sea water pressure and the pore water pressure remains constant throughout the tidal cycle.

When the same piezometer tests were performed in regions of gassy soil, however, it was observed that the increment of pore water was not equal to the increment in water pressure above the seabed. This behaviour had previously

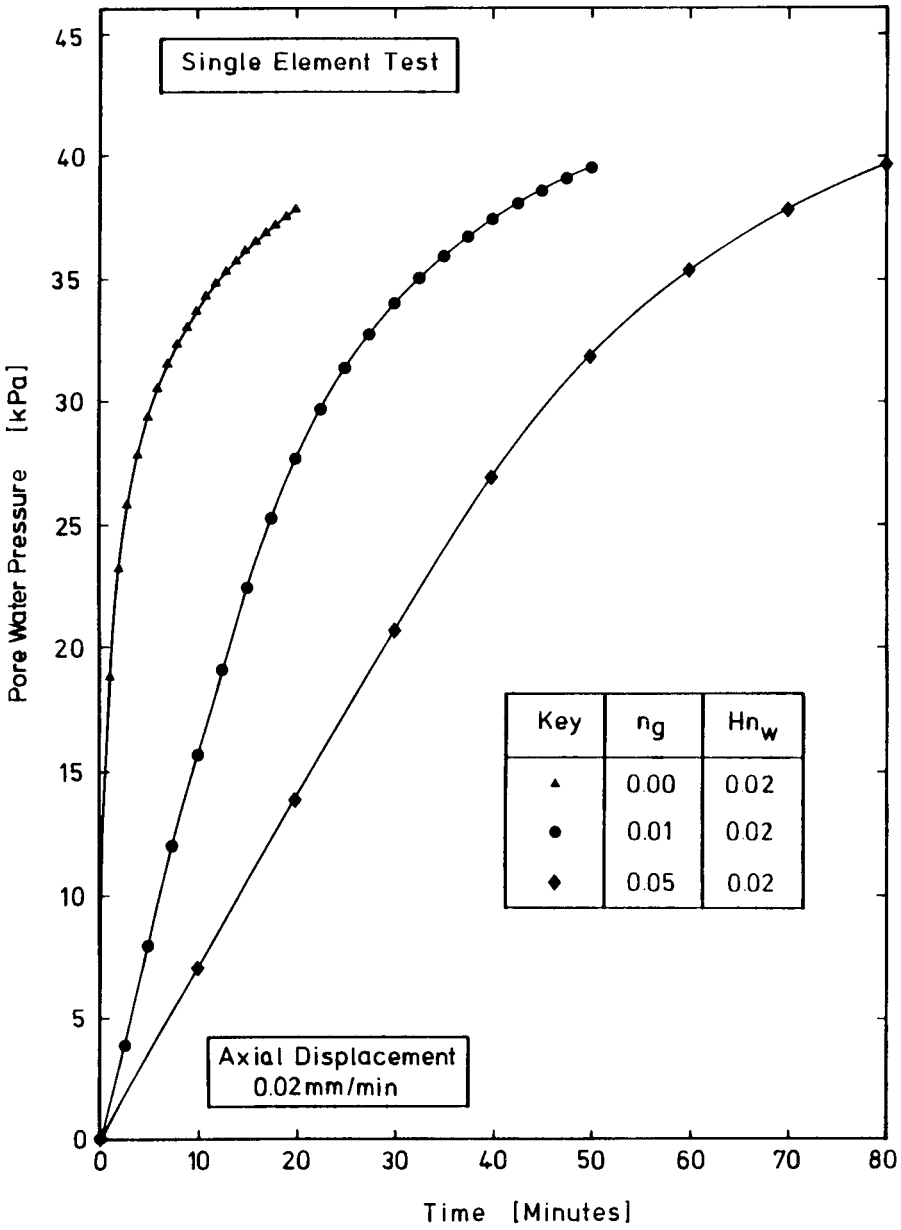

Figure 11.20 Pore water pressure versus time for gassy soils of various gas contents

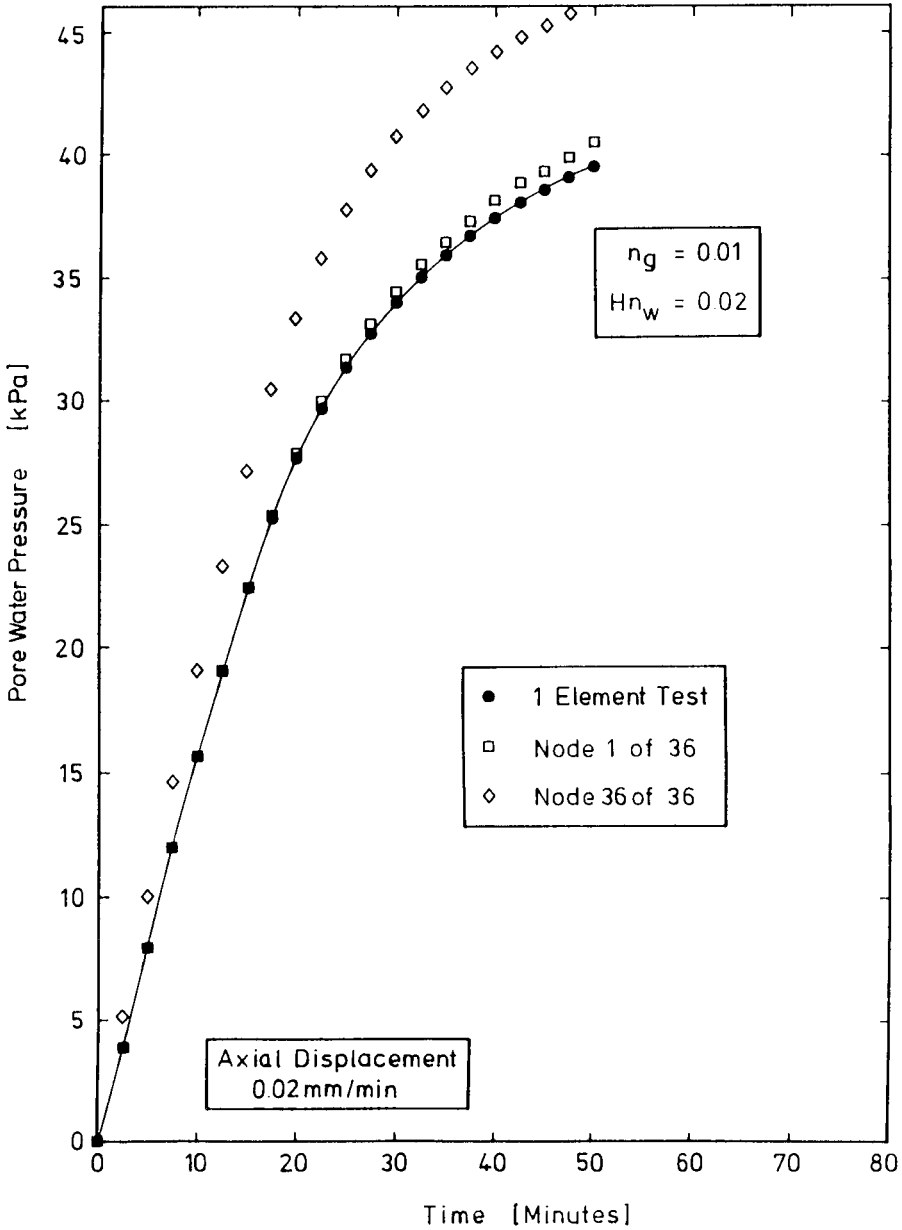

Figure 11.21 Pore water pressure versus time at discrete points in a triaxial sample

been explained by the fact that any gas present in the seabed exists within the pores of the soil skeleton. These gas bubbles can then combine with the pore water to produce a compressible pore fluid. Therefore, if an increase in vertical stress--caused by an increase in water depth--is applied to the surface of the seabed, any increase in stress will be shared by increases in both the pore fluid pressure and the effective stress due to the compressibility of the fluid. This combination of pore fluid compression and effective stress increase will then result in settlement of the seabed.

The experimental results presented in this thesis, however, illustrate that although settlement of a gassy soil sample does take place under undrained conditions due to an increase in total vertical stress, it is not necessarily caused by an effective stress increase, as the measured pore water pressures are seen to rise at least to the increment of total stress.

As a result of these findings, the double compressibility model was developed from which it is possible to treat the gas voids and the saturated soil matrix as two separate phases. Each of the two phases has two elastic constants, these being the shear modulus G and the bulk modulus K. In addition, for undrained or fully drained conditions it is possible to produce combined elastic moduli for a gassy soil from

$$\bar{K} = (1/K^{\circ} + 1/K')^{-1} \tag{11.4}$$

and

$$\bar{G} = (1/G^{\circ} + 1/G')^{-1} \tag{11.5}$$

where the superscript $^{\circ}$ corresponds to the gas voids and superscript $'$ to the saturated soil matrix. For undrained conditions--due to the low value of the compressibility of the pore water and the soil grains--the value of the bulk modulus is dominated by the effect of the gas compression.

$$\bar{K} = K^{\circ} \tag{11.6}$$

Furthermore, it is possible to obtain the combined Poisson's ratio for a gassy soil from a combination of equations 11.4 to 11.6 to give

$$\bar{\nu} = \frac{\nu^{\circ}/G^{\circ}(1+\nu^{\circ}) + \nu'/G'(1+\nu')}{1/G^{\circ}(1+\nu^{\circ}) + 1/G'(1+\nu')} \tag{11.7}$$

from which the change in mean total stress can be found from

$$\frac{\Delta\sigma_m}{\Delta\sigma_v} = \frac{1}{3}\,\frac{(1+\bar{\nu})}{(1-\bar{\nu})} \tag{11.8}$$

to give

$$\frac{\Delta\sigma_m}{\Delta\sigma_v} = \frac{1}{3}\left[\frac{1/G^o + 1/G'}{(1-\nu^o)/G^o(1+\nu^o) + (1-\nu')/G'(1+\nu')}\right] \tag{11.9}$$

If it is further assumed that for this elastic material, any increase in pore water pressure is equal to the increase in mean total stress, then for undrained conditions ($\nu' = 0.5$)

$$\frac{\Delta u_w}{\Delta\sigma_v} = \left[\frac{1 + G^o/G'}{3(1-\nu^o)/(1+\nu^o) + G^o/G'}\right] \tag{11.10}$$

From the above equation it can be seen that the increase in pore water pressure, normalized with respect to the total stress, is a function of the gas phase Poisson's ratio, ν^o, and the shear modulus ratio, G^o/G'. The effect of these parameters on the pore water pressure increment is presented in Figure 11.22. It can be seen from this figure that for a shear modulus ratio less than 100, and for ν^o less than 0.5, quite a significant reduction in the change in excess pore water pressure is predicted. Consequently, the double compressibility model can offer an alternative explanation of the production of excess pore water pressures in a gassy seabed to the concept of a compressible pore fluid.

Yet another approach would be to consider the possible localized stress concentration around a piezometer, even when the shear modulus ratio was sufficiently high that no changes in excess pore water pressure would be expected. The possibility of stress concentrations came about when observing that when the piezometer is pulled out of the seabed, there is a layer of soil attached to it over the entire length. Therefore, if the soil were stuck in position next to the piezometer, then for a gassy soil, this would restrict the movement of the soil from moving up and down during the tidal cycle. Consequently, this could reduce or increase the soil stress around the piezometer due to sinusoidal loading.

To analyze this problem, a finite element mesh was set up as illustrated in Figure 11.23. It can be seen that the nodes adjacent to the piezometer are

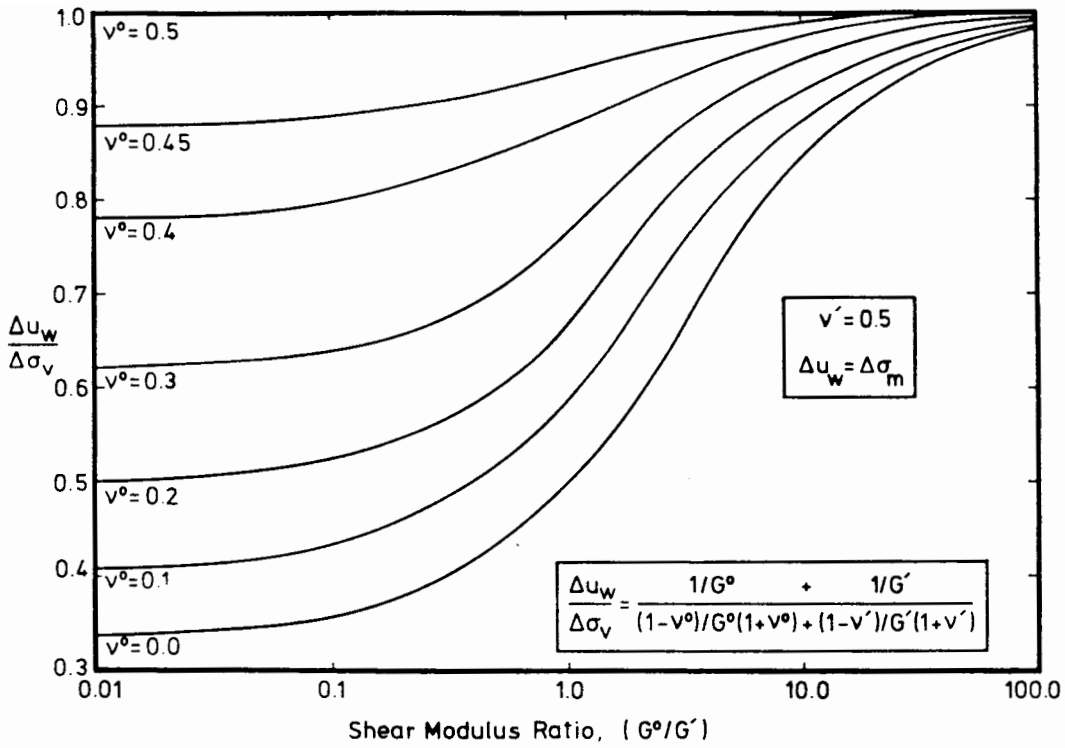

Figure 11.22 Dimensionless pore water pressure increment versus shear modulus ratio for various values of gas phase Poisson's ratio using the double compressibility model

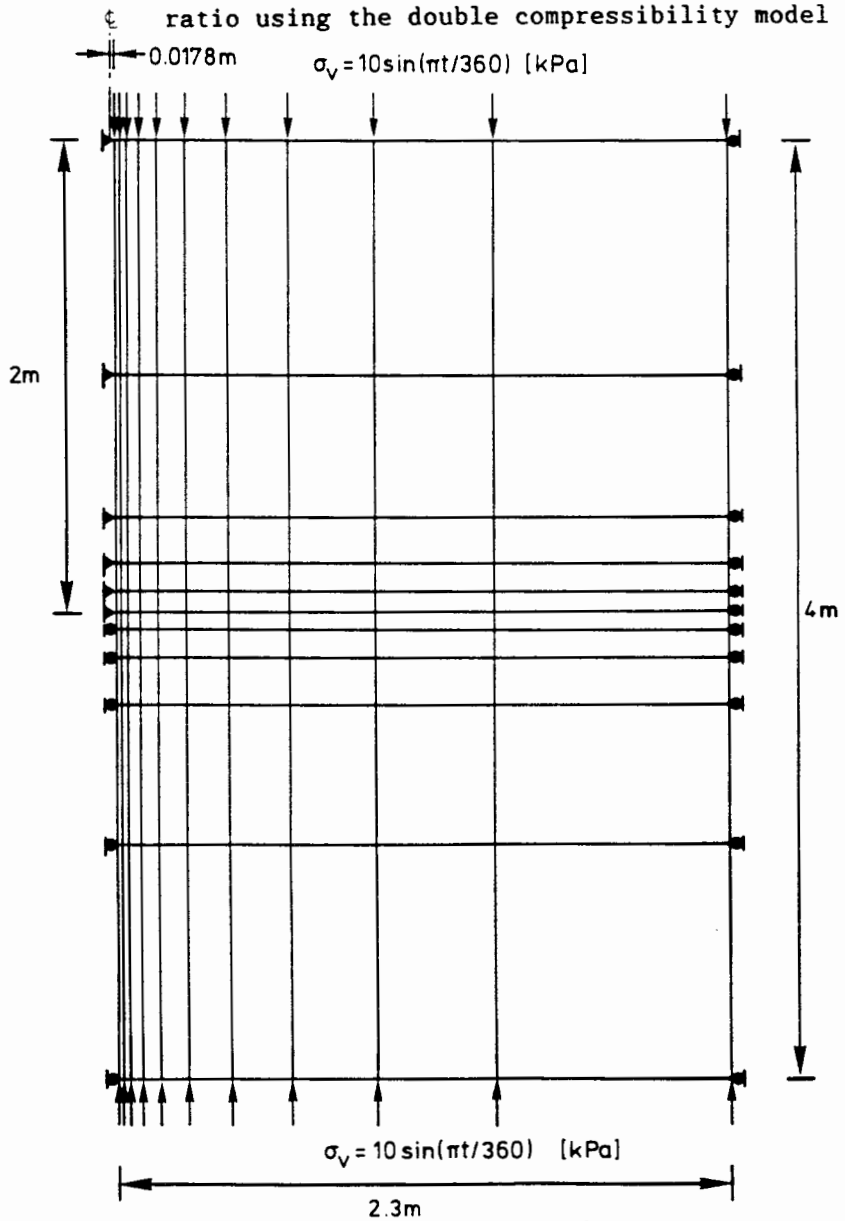

Figure 11.23 Axisymmetric finite element grid used to simulate the stress behaviour around a differential piezometer

fixed in position in both the vertical and radial direction. The nodes below the piezometer, however, are free to move in the vertical direction.

The sample was then subjected to a sinusoidal load of two tidal cycles every 24 hours. The finite element model DCFEM2 was run such that the pore water pressures and soil settlements were output after each time step of 36 minutes. Figure 11.24a presents the variation of the excess pore water pressure along the side of the piezometer, and continuing into the soil below. It can be seen from this figure that at this point of highest total stress, i.e. at high tide, there is a reduction in the excess pore water pressure along the piezometer. However, due to the abrupt changes in the boundary condition at the end of the piezometer, severe spatial oscillations are produced. Nevertheless, the general decrease in excess pore water pressure along the piezometer can still be seen clearly. In addition, Figure 11.24b presents the distribution of the excess pore water pressure in the soil in the vicinity of the piezometer.

To illustrate the cyclic response of the excess pore water pressure with time, Figure 11.25 presents the total increment of total stress and the increment of excess pore water pressure plotted against time. It can be seen that during the stage of increased total stress (high tide), there is a reduction of excess pore water pressure, whereas the opposite is true at low tide. Figure 11.25 illustrates the same type of response as observed by Sills and Austin (1982), during their measurements of excess pore water pressure in gassy sediments. This gives an alternative approach to the compressible fluid model as used by Nageswaran (1983).

11.9 Summary

This chapter presents the verification of the finite element model DCFEM2 with a number of analytical solutions for the consolidation of a saturated soil for plane strain and axisymmetric coditions. DCFEM2 is then used to predict the behaviour of saturated and gassy soils under laboratory and field conditions.

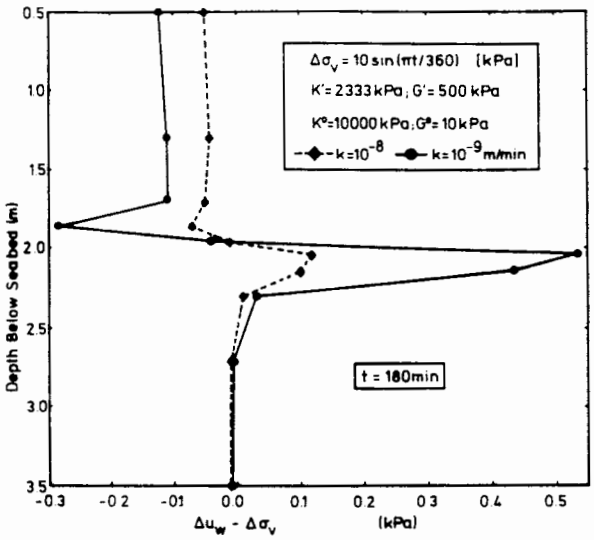

Figure 11.24a Excess pore water pressure along the length of a piezometer at high tide

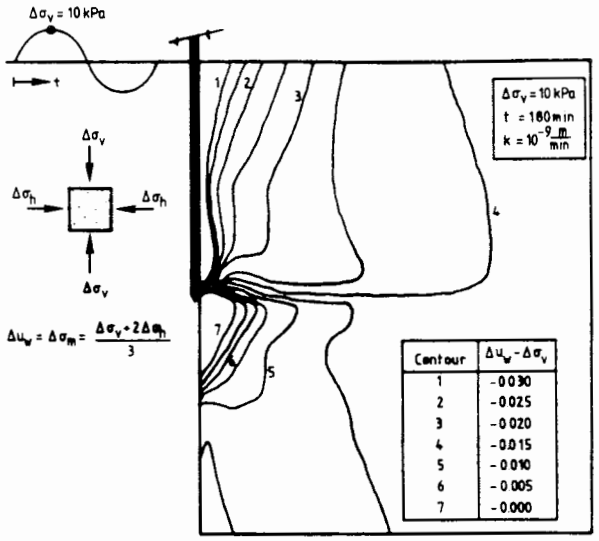

Figure 11.24b Excess pore water pressure distribution in the soil surrounding a piezometer at high tide

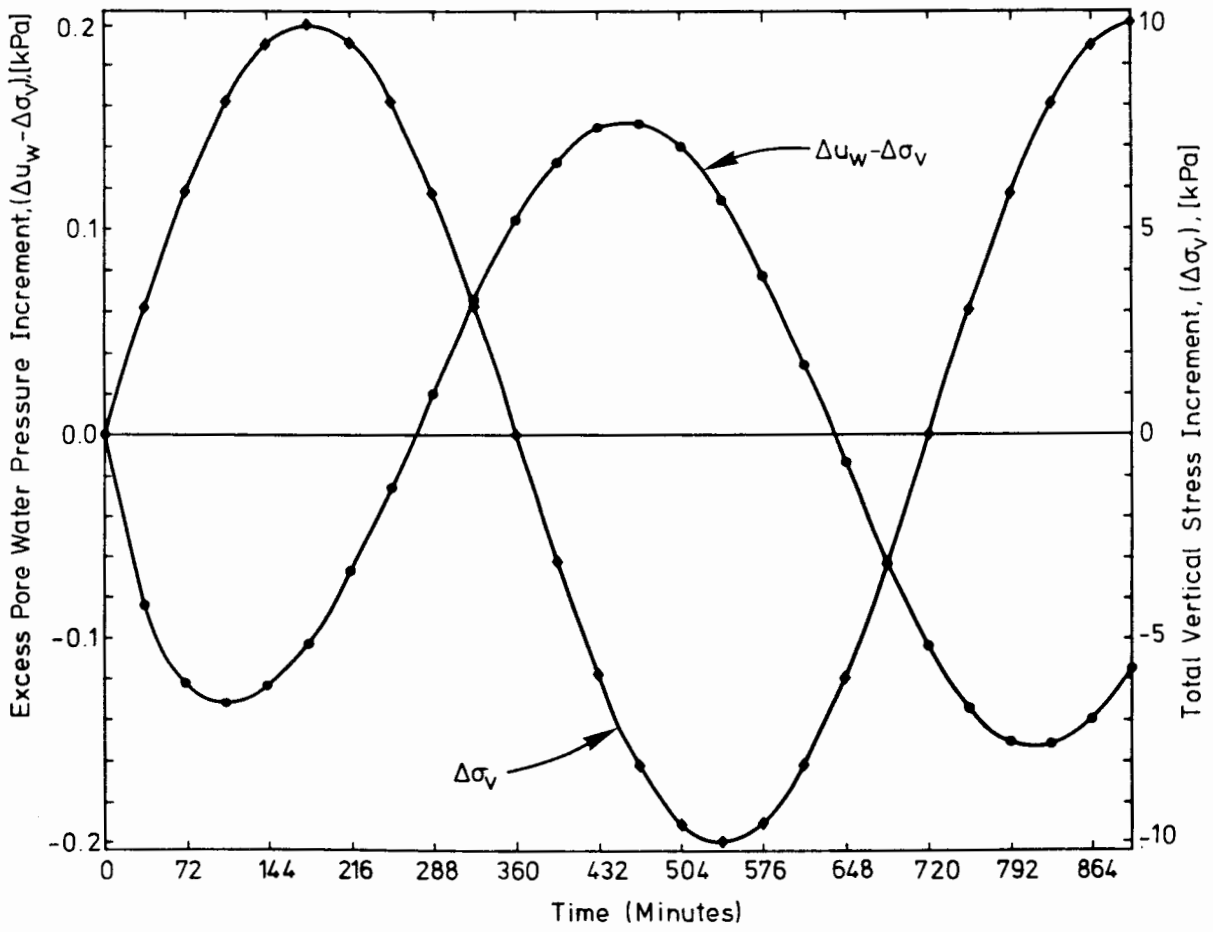

Figure 11.25 Time-dependent excess pore water pressure reponse on a piezometer at 1.6 metres below the seabed.

CHAPTER 12

CONCLUDING REMARKS

CHAPTER 12

CONCLUDING REMARKS

12.1 Brief Summary of Findings

This thesis describes both the experimental and theoretical work that has been performed at Oxford University to further the understanding of gassy soil behaviour. As a result of this research, it was discovered that a gassy soil behaves as a saturated soil containing discrete compressible solid inclusions. It was subsequently found that the gas inclusions deformed due to changes in the total stress on the sample, whereas the deformation of the soil matrix was caused by changes in the consolidation stress. This discovery led to the development of the double compressibility model for gassy soils.

A more detailed description of the work performed and the conclusions which were subsequently drawn is presented in the summary at the end of each chapter.

12.2 Recommendations for Future Work

12.2.1 Theoretical development

Under the experimental conditions described in this thesis, the equation

$$u_g = \alpha \sigma_v \qquad (12.1)$$

was used to approximate successfully the gas pressure u_g above atmospheric. This equation would be unlikely to hold, however, for cases where a high back pressure is applied to a gassy soil. That this is so can be seen by considering a gas void one metre into the seabed under a total stress of 200 kPa and an effective stress of 10 kPa. For $\alpha = 0.7$, equation 12.1 then predicts a gas pressure of 140 kPa--thus producing a pressure difference between the inside and outside of the void of 60 kPa. Results presented in this thesis have illustrated that the soil would have been consolidated to a pressure of 100 kPa in order for the soil matrix to maintain such a pressure difference. This is extremely unlikely at this distance below the seabed. From this example, it would seem more appropriate therefore to relate the pressure difference between the gas pressure and the total stress with the shear strength of the saturated

soil matrix, as it is this parameter that is most likely to govern the amount of stress that is transferred through the soil to the gas inclusion.

Furthermore, for a normally consolidated soil, the shear strength--for both saturated and gassy soils--is a function of the consolidation stress. Consequently, it would be reasonable to assume that the pressure difference between the gas pressure and the total stress depends upon the consolidation stress of the gassy soil, from which the following is suggested

$$\left| \sigma_m - u_g \right| \leq \beta \sigma'_m \qquad (12.2)$$

This equation takes into account that the experiments in this thesis illustrated that the final gas pressure was also dependent on the method of consolidation.

For gassy soils described here, β was found to be in the order of 0.6 (for H = 0.0333) for both sets of tests. This was in contrast to the α value which was found to be in the order of 0.7 for continuous loading and 1.0 for step loading. Based on equation 12.2, the gas pressure in the above problem would have a value of 194 kPa which would be far more appropriate for this situation. The above equation could then be extended to account for the behaviour of overconsolidated gassy soils by relating the difference in gas pressure and total stress to the shear strength of a saturated soil at the same value of consolidation stress and stress history, to give

$$\left| \sigma_m - u_g \right| \leq f(s_u) = f(\sigma', \sigma'_{max}) \qquad (12.3)$$

where σ'_{max} is the maximum consolidation stress previously applied to the soil.

12.2.2 Experimental testing

This thesis introduces the double compressibility model, in which a shear and bulk modulus are required for both the gas and soil matrix. As this model produced a successful interpretation of the undrained triaxial results of Wheeler (1986), it would be of great interest to design an experimental test specifically to obtain these double compressibility soil parameters.

One of the methods by which this could be accomplished would be to use the triaxial apparatus to apply an isotropic pressure increasing linearly with time under undrained conditions. In this way, the sample will be under a uniform isotropic stress at all times from which a relationship between volumetric

strain and isotropic stress can be obtained. In addition, if the test is performed slowly, then it may be possible to confirm whether there is an initial stiff response due to the elastic behaviour of the soil matrix, followed by a failure type response caused by the connection of the plastic envelopes in the soil matrix around the gas voids as illustrated earlier in Figure 6.13.

This isotropic test could also be applied to a soil under drained conditions so that the volumetric strain can be evaluated from changes in soil matrix and gas volumes. A comparison of the bulk modulus due to gas compression under drained conditions can then be made with that under undrained conditions.

The bulk moduli calculated from the application of an isotropic pressure can then be compared to those evaluated using uniaxial compression tests. During isotropic compression, the gas voids will remain approximately spherical, but under uniaxial compression they will become flattened. From the analysis of the stress distribution around a flattened sphere--or oblate spheroid--the indication is that the soil matrix around an oblate spheroidal cavity would enter a state of plastic failure before that of a spherical cavity. Consequently, there would be a higher amount of total stress transferred to the gas void than for the uniaxial loading case. This would lead to a higher amount of gas volume change for the same increment of mean total stress, and hence a lower bulk modulus than for isotropic compression.

It must also be noted that during triaxial testing, the uniaxial load is produced by the application of a constant strain rate. A constant strain rate applied to a gassy soil, however, produces lower stresses than for a saturated sample for the same strain rate. This was observed in the triaxial experiments of Wheeler and was modelled successfully in section 11.8. Therefore, to perform a comparable test between soils of different saturations either the strain must be applied such that the stress behaviour is the same between two different tests or the tests must be performed slowly enough so that the strain rate effects are not significant.

Recent enquiries from the offshore industry have shown that there is a real interest in the problems associated with gassy soils. This research should help to provide solutions to some of the problems encountered in this area.

REFERENCES

Abbot, M.B. (1960). One-Dimensional Consolidation of Multi-Layered Soils. Geotechnique, Vol. 10, pp. 151-165.

Anderson, A.L. and Hampton, L.D. (1980). Acoustics of Gas-Bearing Sediments. J. Acoust. Soc. Am., Vol. 67, No. 6, pp. 1865-1903.

Atkinson, J.H. and Bransby, P.L. (1978). The Mechanics of Soils: An Introduction to Critical State Soil Mechanics. McGraw-Hill.

Barden, L. (1965). Consolidation of Compacted and Unsaturated Clays. Geotechnique, Vol. 15, No. 3, pp. 267-286.

Biot, M.A. (1941). General Theory of Three-Dimensional Consolidation. J. Appl. Phys., Vol. 12, pp. 155-164.

Bishop, A.W. (1959). The Principle of Effective Stress. Tek. Ukeblad, Vol. 39, pp. 859-863.

Bishop, A.W. and Blight, G.E. (1963). Some Aspects of Effective Stress in Saturated and Partly Saturated Soils. Geotechnique, Vol. 13, No. 3, pp. 177-197.

Bishop, A.W. and Donald, I.B. (1961). The Experimental Study of Partly Saturated Soils in the Triaxial Apparatus. Proc. 5th Int. Conf. Soil Mech. Found. Eng., Paris, pp. 13-21.

Brooks, R.H. and Corey, A.T. (1964). Hydraulic Properties of Porous Media. Hydrology Papers, No. 3, Colorado State University, Fort Collins, p. 27.

Booker, J.R. (1973). A Numerical Method of Solution of Biot's Consolidation Theory. Q. J. Mech. Appl. Math., Vol. 26, Pt. 4, pp. 445-470.

Britto, A.M. and Gunn, M.J. (1987). Critical State Soil Mechanics Via Finite Elements. Ellis Horwood Ltd.

Buckley, S.E. and Leverett, M.C. (1942). Mechanism of Fluid Displacement in Sands. Trans. AM, Inst. Min. Metall. Pet. Eng., 237, pp. 377-388.

Carslaw, H.S. and Jaeger, J.C. (1959). Conduction of Heat in Solids. Clarendon Press, Oxford, 2nd Ed.

Carter, J.P., Booker, J.R. and Davis, E.H. (1977). Finite Deformation of an Elasto-Plastic Soil. Int. J. Num. Anal. Meth. Geomech., Vol. 1, No. 1, pp. 25-43.

Carter, J.P., Booker, J.R. and Small, J.C. (1979). The Analysis of Finite Elasto-Plastic Consolidation. Int. J. Num. Anal. Meth. Geomech., Vol. 3, No. 2, pp. 107-129.

Carter, J.P., Small, J.C. and Booker, J.R. (1977). A Theory of Finite Elastic Consolidation. Int. J. Solids Struct., Vol 13, pp. 467-478.

Chang, C.S. and Duncan, J.M. (1983). Consolidation Analysis for Partly Saturated Clay by Using an Elastic-Plastic Effective Stress-Strain Model. Int. J. Num. Anal. Methods Geomech., Vol. 7, No. 1, pp. 39-55.

Claypool, G.E and Kaplan, I.R. (1974). The Origin and Distribution of Methane in Marine Sediments. Natural Gases in Marine Sediments. Ed. I.R. Kaplan, Plenum Press, pp. 99-139.

Collins, R.E. (1961). Flow of Fluids Through Porous Materials. Reinhold, New York.

Cook, R.D. (1974). Concepts and Applications of Finite Element Analysis. John Wiley and Sons.

Cox, A.D., Eason, G. and Hopkins, H.G. (1961). Axially Symmetric Plastic Deformation in Soils. Phil. Trans. Roy. Soc., Series A, Vol. 254, August, pp. 1-45.

Cryer, C.W. (1963). A Comparison of the Three-Dimensional Consolidation Theories of Biot and Terzaghi. Quart. J. Mech. and Appl. Math., Vol. 16, pp. 401-412.

Edwards, R.H. (1951). Stress Concentrations around Spheroidal Inclusions and Cavities. J. Appl. Mech. Vol. 18, No. 1.

Elzeftawe, A. and Cartwright, K. (1983). Undisturbed Core Method for Determining and Evaluating the Hydraulic Conductivity of Unsaturated Sediments. Illinois State Geological Survey Report UILU-WRC-83-0177.

Esrig, M.I and Kirby, R.C. (1977). Implications of Gas Content for Predicting the Stability of Submarine Slopes. Marine Geotechnology, Vol. 2, pp. 81-100.

Fannin, N.G.T. (1979). IGS Pockmark Investigations 1974-1978. IGS Report No. 98.

Fredlund, D.G. (1976). Density and Compressibility Characteristics of Air-Water Mixtures. Can. Geotech. J. Vol. 13, pp. 386-396.

Fredlund, D.G. and Morgenstern, N.R. (1976). Constitutive Relations for Volume Change in Unsaturated Soils. Can. Geotech. J., Vol. 13, pp. 261-267.

Fredlund, D.G. and Morgenstern, N.R. (1977). Stress State Variables for Unsaturated Soils. Proc. ASCE, Vol. 103, No. GT5, pp. 447-466.

Gardner, T.N. (1987). The Acoustic Properties of Gassy Soil. D. Phil. Thesis, Oxford University. (In preparation).

Ghaboussi, J. and Wilson, E.L. (1973). Flow of Compressible Fluid in Porous Elastic Media. Int. J. Num. Meth. Eng., Vol. 5, pp. 419-442.

Gibson, R.E., England, G.L. and Hussey, M.J.L. (1967). The Theory of One-Dimensional Consolidation of Saturated Clays. Geotechnique, Vol. 17, pp. 261-273.

Green, R.J. (1972). A Plasticity Theory for Porous Solids. Int. J. Mech. Sci., Vol. 14, pp. 215-224.

Hill, R. (1965). A Self-Consistent Mechanics of Composite Materials. J. Mech. Phys. Solids, Vol. 13, pp. 213-222.

Hinton, E. and Owen, D.R.J. (1979). An Introduction to Finite Element Computations. Pineridge Press, Swansea, United Kingdom.

Hinton, E. and Owen, D.R.J. (1977). Finite Element Programming. Academic Press.

Houlsby, G.T. (1979). The Work Input to a Granular Material. Geotechnique, Vol. 29, No. 3, pp. 354-358.

Huyakorn, P.S. and Pinder, G.F. (1983). Computational Methods in Subsurface Flow. Academic Press.

Huyakorn, P.S., Thomas, S.D. and Thompson, B.M. (1984). Techniques for Making Finite Elements Competitive in Modelling Flow in Variably Saturated Porous Media. Water Resources Research, Vol. 20, No. 8, pp. 1099-1115.

Jennings, J.E.B. and Burland, J.B. (1962). Limitations to the Use of Effective Stresses in Partly Saturated Soil. Geotechnique, Vol. 12, No. 2, pp. 125-144.

Kanwisher, J. (1962). Gas Exchange of Shallow Marine Sediments, from Proc. Symp. U. Rhode Island. The Environmental Chemistry of Marine Sediments. Narragansett Marine Laboratories.

Kanwisher, J. (1962). Sulphur Chemistry in Marine Muds, Biochemistry of Sulphur Isotopes. Ed. M.L. Jensen, NSF Symposium Volume, Yale University, New Haven, CT, pp. 94-103.

Lamé. (1852) Lecons sur la Théorie . . . de l'Elasticité. Gauthier-Villars, Paris.

Lewis, R.W., Verner, E.A. and Zienkiewicz, O.C. (1975). A Finite Element Approach to Two-Phase Flow in Porous Media. Finite Elements in Fluids, Ed. R.H. Gallagher et al., Vol. 1, pp. 183-199, John Wiley and Sons.

Lloret, A. and Alonso, E.E. (1980). Consolidation of Unsaturated Soils Including Swelling and Collapse Behaviour. Geotechnique, 30 (4), pp. 449-477.

Mandel, J. (1957). Consolidation des Sols. Geotechnique, Vol. 3, pp. 287-299.

Matyas, E.L and Radhakrishna, H.S. (1968). Volume Change Characteristics of Partially Saturated Soils. Geotechnique, Vol. 18, No. 4, pp. 432-448.

McNamee, J. and Gibson, R.E. (1960). Plane Strain and Axially Symmetric Problems of Consolidation of Semi-Infinite Clay Stratum. Quart. J. Mech. Appl. Math. Vol. 13, pp. 210-227.

Mieri, D. and Karadi, G.M. (1982). Simulation of Air Storage Aquifer by Finite Element Model. Int. J. Num. Anal. Meth. Geomech. Vol. 6, pp. 339-351.

Nageswaran, S. (1983). Effect of Gas Bubbles on the Seabed Behaviour. D. Phil. Thesis, Oxford University.

Narasimhan, T.N. and Witherspoon, P.A. (1978). Numerical Model for Saturated-Unsaturated Flow in Deformable Porous Media, 2: The Alogorithm. Water Resources Research, 14 (2), pp. 255-261.

Orlob, G.T. and Radhakrishna, G.N. (1958). The Effect of Entrapped Gases on the Hydraulic Characteristics of Porous Media. Trans. Amer. Geo Phys. Union. Vol. 39, No. 4, pp. 648-659.

Owen, D.R.J. and Hinton, E. (1980). Finite Elements in Plasticity - Theory and Practice. Pineridge Press, Swansea, United Kingdom.

Peaceman, D.W. (1977). Fundamentals of Numerical Reservoir Simulation. Development in Petroleum Science, 6, Elsevier.

Poulos, H.G. and Davis, E.H. (1974). Elastic Solutions for Soil and Rock Mechanics. John Wiley and Sons.

Rendulic, L. (1936). Porenziffer und Poren Wasserdruck in Tonen. Bauingenieur, Vol. 17, pp. 559-564.

Schiffman, R.L. and Gibson, R.E. (1964). Consolidation of Nonhomogeneous Clay Layers. J. Soil. Mech. Found. Div., pp. 1-30.

Scott, C.R. (1974). An Introduction to Soil Mechanics and Foundations. Applied Science Publishers Ltd., 2nd Ed.

Settari, A. and Aziz, K. (1975). Treatment of Nonlinear Terms in the Numerical Solution of Partial Differential Equations for Multiphase Flow in Porous Media. Int. J. Multiphase Flow, Vol. 1, pp. 817-844.

Settari, A., Price, H.S. and Dupont, T. (1977). Development and Application of Variational Methods for Simulation of Miscible Displacement in Porous Media. Soc. Pet. Eng. J., Vol. 17, pp. 228-246.

Sills, G.C. and Austin, G. (1982). Pore Pressure Measurement in a Seabed Containing Gas Bubbles. Oxford Univ. Dept. Eng. Sci. Report No. SMO 28/82.

Sills, G.C. and Nageswaran, S. (1984). Compressibility of Gassy Soil. Oceanology Int. Exhib. Conf., Brighton, Soc. Underwater Tech., 0.1.2.6.

Taylor, D.W. (1984). Fundamentals of Soil Mechanics. John Wiley and Sons.

Terzaghi, K. (1923). Die Berechnung der Durchlaessigkeitsziffer des Tones aus dem Verlauf der Hydrodynamischen Spannungserscheinungen. (Calculation of the Porosity Index of Clay from Hydrodynamic Pressure Conditions.) Sitzbericht (Abt. 3a), Akademie der Wissenschaften, Vienna, p. 132.

Terzaghi, K. (1944). Theoretical Soil Mechanics. John Wiley and Sons.

Terzaghi, K. and Richart, F.E. Jr. (1952). Stresses in Rock about Cavities. Geotechnique, Vol. 3, pp. 57-90.

Theis, C.V. (1935). The Relation Between the Lowering of the Piezometric Surface and the Rate and Duration of Discharge of a Well Using Groundwater Storage. AM. Geophys. Union Trans., Vol. 16, pp. 519-524.

Timoshenko, S.P. and Goodier, J.N. (1970). Theory of Elasticity. McGraw-Hill, 3rd Ed.

Vesic, A.S. (1972). Expansion of Cavities in Infinite Soil Mass. Proc. ASCE, Vol. 98, No. SM3, pp. 265-290.

Walton, W.C. (1962). Selected Analytical Methods for Well and Aquifer Evaluation. Illinois State Water Survey Bull., No. 49.

Wheeler, S.J. (1986). Soils Containing Gas Bubbles: A Review. Oxford Univ. Dept. Eng. Sci. Report No. OUEL 1629/86.

Wheeler, S.J. (1986). The Stress-Strain Behaviour of Soils Containing Gas Bubbles. D. Phil Thesis, Oxford University.

Whelan, T. III, Coleman, J.M., Roberts, H.H. and Suhayda, J.N. (1976). The Occurrence of Methane in Recent Deltaic Sediments and its Effect on Soil Stabililty. Bull. Int. Assoc. Eng. Geol., No. 14, pp. 55-64.

Wyckoff, R.D. and Botset, H.G. (1936). The Flow of Gas-Liquid Mixtures Through Unconsolidated Sands. Physics, Vol. 7.

Yamamoto, S., Alcauskas, J.B. and Crozier, T.E. (1976). Solubility of Methane in Distilled Water and Seawater. J. Chem. Eng. Data, Vol. 21, No. 1.

Zienkiewicz, O.C. (1977). The Finite Element Method. McGraw-Hill, 3rd Ed.

APPENDIX A

THE PERMEABILITY OF A GASSY SOIL

APPENDIX A

THE PERMEABILITY OF A GASSY SOIL

A.1 Introduction

Various research workers including Wyckoff and Botset (1936), Orlob and Radhakrishna (1958), Brooks and Corey (1964) and Elzeftawe and Cartwright (1983) have shown experimentally that any gas present in a porous material significantly reduces the permeability of the material.

The reason for this reduction of permeability is due to the gas restricting the water flow by blocking various drainage paths in the porous medium. The effects of entrapped gas on flow through porous media is described in detail by Orlob and Radhakrishna (1958).

All the above workers have produced empirical relationships between the saturation and the relative permeability of the material (relative permeability being defined as the measured permeability divided by the saturated permeability of the same material). This is reasonable because in all the materials used by the above researchers, the basic particle structure remains unchanged so that although the degree of saturation changes with increased gas content, the void volume changes very little.

A.2 The Effect of Gas Voids on the Flow of Water in a Soil

Work at Oxford on the structure of gassy soils has shown that the gas exists in the form of discrete gas voids, these being on average two orders of magnitude larger in diameter than the soil particles. Thus unlike a conventional unsaturated soil in which the gas blocks the drainage paths, in a gassy soil the water must flow in the soil matrix around the larger gas voids.

If the one-dimensional flow of pore water in a soil is considered--despite the fact that on a microscopic scale the water follows a tortuous path around the solid particles--the average flow paths will be approximately linear. For a soil containing spherical inclusions that are much larger than the individual grain size, however, the overall permeability will be reduced due to the increased path length of the streamlines as illustrated in Figure A.1a. Furthermore, in addition to the fact that a certain volume of inclusions will

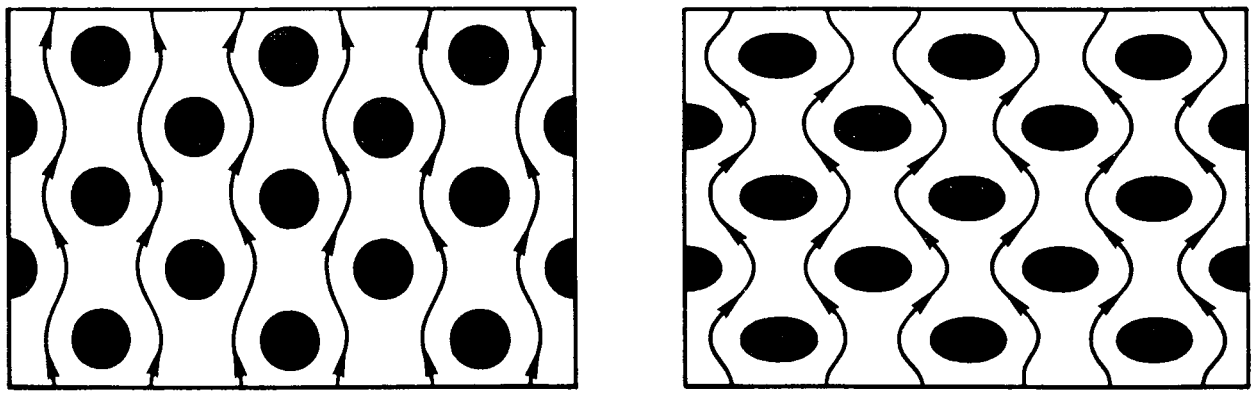

Figure A.1 Idealization of fluid flow through a soil medium containing impermeable inclusions

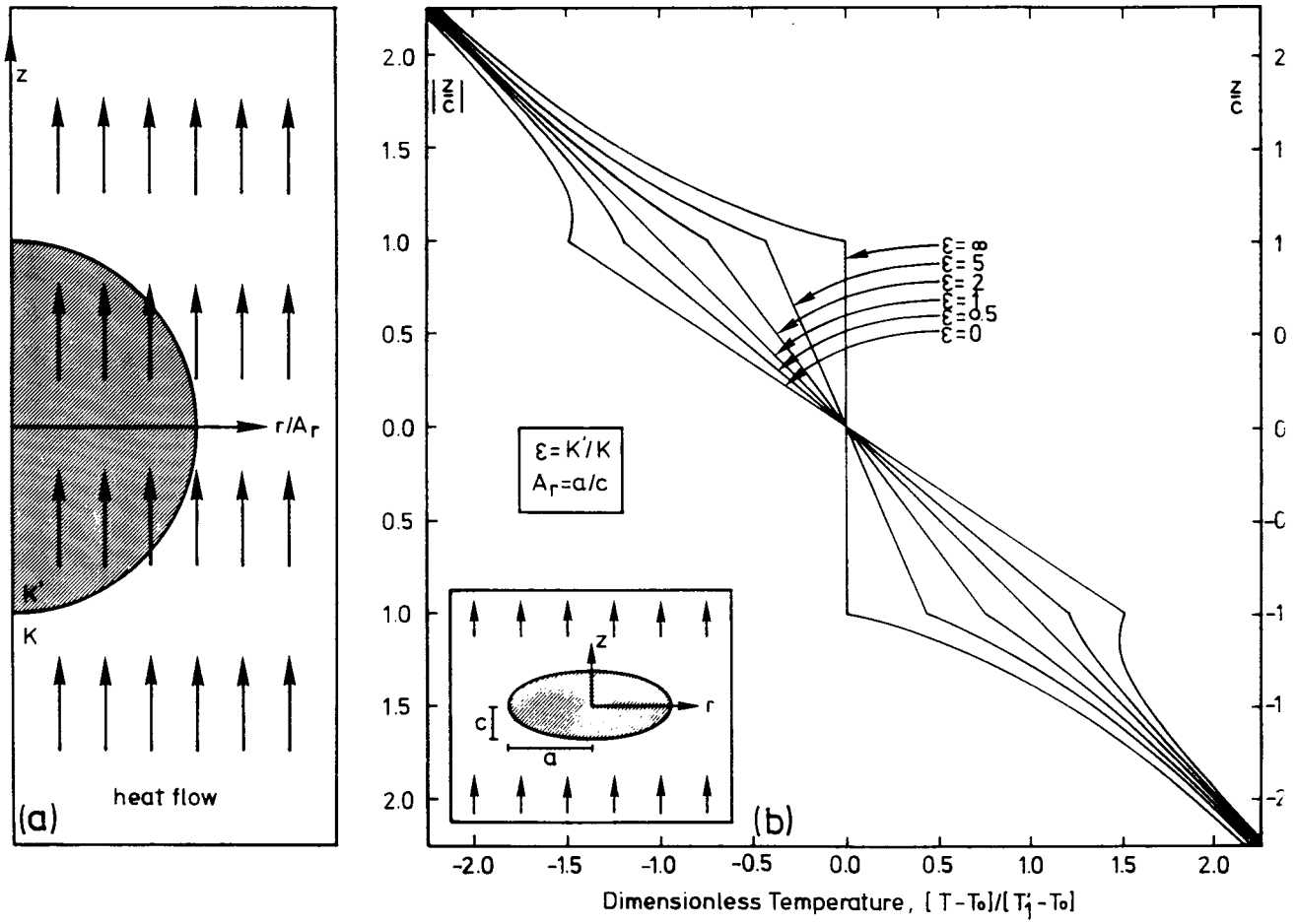

Figure A.2 Temperature profile along the z-axis inside and outside a spheroidal inclusion of conductivity K' embedded in a material of conductivity K

reduce the overall permeability of the medium, the permeability may also be affected by the shape and orientation of the inclusions. Figure A.1b illustrates the flow paths through a soil containing a number of oblate spheroidal inclusions. It can be noted that although the volume fraction of these inclusions is the same as for the spheres of Figure A.1a, the overall flow path length is increased due to the increased width of the inclusions.

A.3 Flow Through a Composite Material

The equations governing flow of pore water through a porous medium are similar to those equations governing heat flow through a conductive solid. For example, the one-dimensional steady state heat flow velocity can be written as

$$V_h = -K_t \frac{dT}{dz} \tag{A.1}$$

where V_h denotes the velocity of the flow of heat, K_t is the thermal conductivity and T is temperature. For fluid flow in a porous medium, Darcy's Law gives

$$V_w = -\frac{k_w}{\gamma_w} \frac{du_w}{dz} \tag{A.2}$$

where V_w is the average velocity of the pore water, k_w is the permeability (as defined in soil mechanics) of the porous medium, γ_w is the specific weight of water and u_w is the excess pore water pressure.

In addition to the above velocity equation, the continuity equations are also similar. Therefore assuming homogeneity of the porous medium and linearity of the various parameters, solutions to problems that have been solved for heat flow in a solid may be used as solutions to the same problems of fluid flow in a porous medium.

Carslaw and Jaeger (1959, pp. 425-429) have presented solutions to various problems of steady heat flow in composite media. They considered the flow of heat around a single spherical or spheroidal inclusion of conductivity K′ embedded in a second material of conductivity K. This was extended to a simple granular material consisting of a volume fraction, f, of spherical inclusions of conductivity K′ embedded in a matrix of conductivity K. The following analysis is performed in terms of heat flow as it is an extension of the theory presented

by Carslaw and Jaeger. However, the final solution may be transformed into porous media flow parameters.

A.4 Flow In and Around a Single Oblate Spheroidal Inclusion

For the steady state temperature distribution in the z-direction in a uniform medium of thermal conductivity K, the resulting temperature distribution can be given by

$$T = T_o - zT' \tag{A.3}$$

where T′ is the temperature gradient and T° is the temperature at z=0 before any inclusion is present. The initial temperature at z/c=1 is noted by T_1'.

Considering the steady state heat flow in and around a single oblate spheroidal inclusion of thermal conductivity K′ embedded in the original material of conductivity K, as shown in Figure A.2a, the temperature distribution along the z-axis both inside and outside the inclusion can be derived from Carslaw and Jaeger (p.427) to give

$$T^i = T_o - zT' \left[\frac{1}{1 + C_o(\varepsilon-1)}\right] \tag{A.4}$$

for inside the inclusion and

$$T^o = T_o - zT' \left[1 - \frac{(\varepsilon-1)C_\lambda}{1+C_o(\varepsilon-1)}\right] \tag{A.5}$$

for outside the inclusion where $\varepsilon = K'/K$. The temperature distribution along the z-axis for various values of ε is illustrated in Figure A.2b.

C_λ is a spatial integral which for an oblate spheroid is given by

$$C_\lambda = \frac{(1 - e^2)^{1/2}}{e^3} \left\{x_\lambda - \tan^{-1}x_\lambda\right\} \tag{A.6}$$

where

$$e^2 = (a^2 - c^2)/a^2 \tag{A.7}$$

$$x_\lambda^2 = (a^2 - c^2)/(c^2 + \lambda^2) \tag{A.8}$$

$$\lambda^2 = z^2 - c^2 \tag{A.9}$$

where C_λ is equal to C_o for $\lambda = 0$. Thus,

$$x_\lambda^2 = \frac{a^2 - c^2}{z^2} \quad \text{and} \quad x_o^2 = \frac{a^2 - c^2}{c^2} \tag{A.10}$$

which when inserted into equation A.6 yields

$$C_\lambda = \left[\frac{c^2}{a^2 - c^2}\right]^{\frac{1}{2}} \left[\frac{a^2}{a^2 - c^2}\right] \left[\frac{a^2 - c^2}{z^2}\right]^{\frac{3}{2}} \left\{\frac{1}{x_\lambda^2}(1 - \frac{1}{x_\lambda} \tan^{-1}x)\right\}$$

$$= \frac{ca^2}{z^3}\left\{\frac{1}{x_\lambda^2}\ (1 - \frac{1}{x_\lambda} \tan^{-1}x_\lambda)\right\} \qquad (A.11)$$

which also leads to

$$C_o = \left[\frac{c^2}{a^2 - c^2}\right]^{\frac{1}{2}} \left[\frac{a^2}{a^2 - c^2}\right] \left[\frac{a^2 - c^2}{c^2}\right]^{\frac{1}{2}} \left\{1 - \frac{1}{x_o}\ \tan^{-1}\ x_o\right\} \qquad (A.12)$$

It can be seen from the above equation that C_o is purely a function of the aspect ratio and can be rewritten for convenience as

$$C_o = \left[\frac{x_o^2 + 1}{x_o^2}\right] \left\{1 - \frac{1}{x_o}\ \tan^{-1}\ x_o\right\} \quad \text{where} \quad C_o \to \frac{1}{3} \quad \text{when} \quad a \to c \qquad (A.13)$$

where $x_o^2 = A_r^{\ 2} - 1$, in which A_r is the aspect ratio = a/c.

A.5 The Conductivity of a Medium Containing Oblate Spheroidal Inclusions

Consider a material consisting of a volume fraction, f, of oblate spheroids of conductivity K′ embedded in a matrix of conductivity K. The inclusions have width 2a and height 2c. Then consider a larger spheroid of width $2\bar{a}$ and height $2\bar{c}$ containing n of the smaller inclusions such that $na^2c = f\bar{a}^2\bar{c}$, as shown in Figure A.3a. Following the method of Carslaw and Jaeger (p.423), if it is assumed that the spheroids are so far apart as to have no influence on one another, then from equation A.5 the temperature at great distances due to the n spheroids in the linear temperature gradient is

$$T_z = T^o - zT' \left[1 - \frac{(K'-K)\ nca^2}{3z^3[K+C_o(K'-K)]}\right] \qquad (A.14)$$

and for great distances from the spheroid (z>2a)

$$C_\lambda = \frac{ca^2}{z^3}\left(\frac{1}{x_\lambda^2}\ (1 - 1 + \frac{x_\lambda^2}{3}\right) = \frac{ca^2}{3z^3} \qquad (A.15)$$

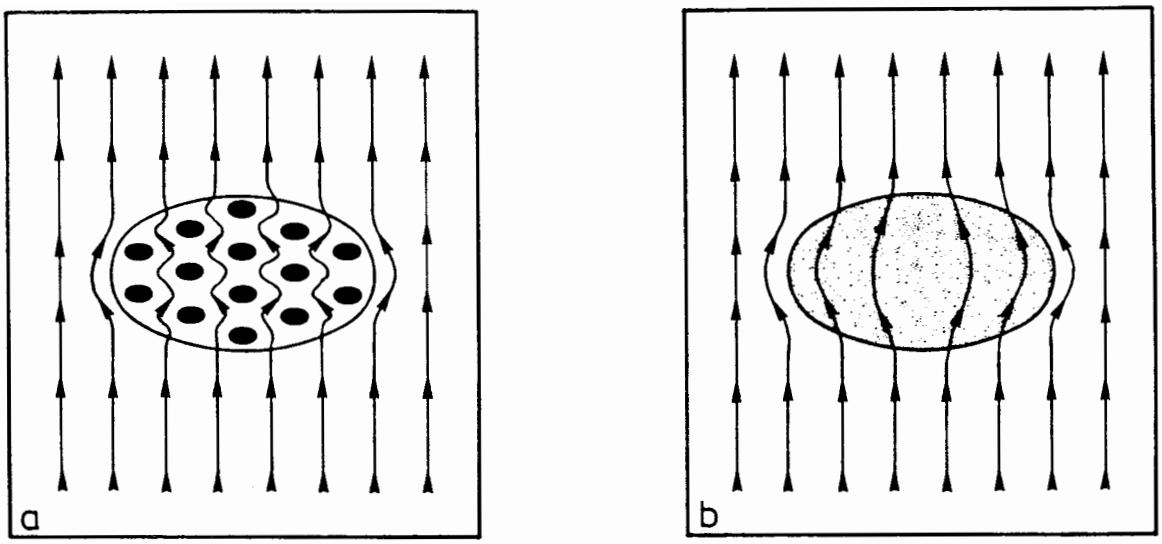

Figure A.3 Idealization of a number of spheroidal inclusions of conductivity K' replaced by a single spheroidal inclusion of conductivity K"

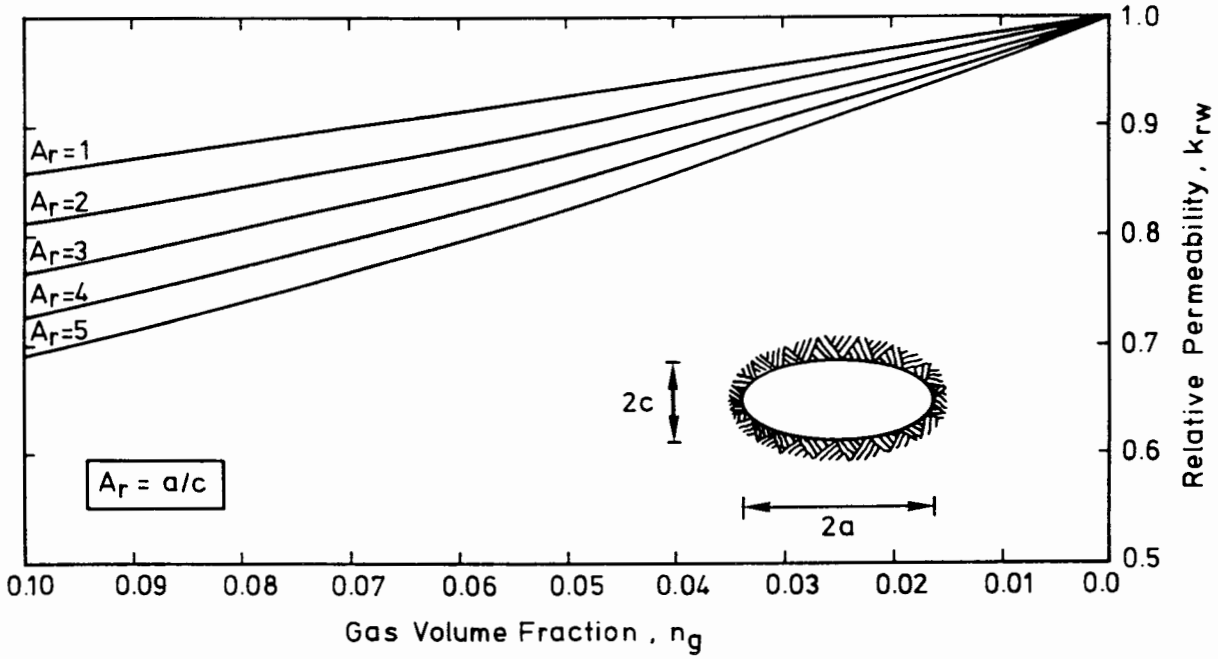

Figure A.4 Theoretical relative permeability versus gas volume fraction

Table A.1. Relative Permeability as a Function of Aspect Ratio and of Gas Volume Fraction.

A_r	C_o	n_g = 0	0.01	0.02	0.03	0.04	0.05	0.06	0.07	0.08	0.09	0.10
1	0.333	1.00	.985	.970	.956	.941	.927	.913	.899	.885	.871	.857
2	0.527	1.00	.979	.959	.939	.919	.900	.881	.863	.845	.827	.810
3	0.635	1.00	.973	.947	.922	.897	.894	.851	.829	.807	.787	.766
4	0.704	1.00	.967	.936	.906	.877	.849	.823	.797	.773	.750	.727
5	0.751	1.00	.961	.924	.890	.857	.826	.796	.768	.742	.716	.692

The relative permeability is given by

$$k_r = 1 - n_g/[1-C_o(1-n_g)]$$

where

$$C_o = \left(\frac{x_o^2 + 1}{x_o^2}\right)\left[1 - \frac{1}{x_o}\tan^{-1}x_o\right] \quad \text{and} \quad x_o^2 = A_r^2 - 1$$

while, if K" is the average conductivity of the granular material, the composite material may be treated as a single spheroid as shown in Figure A.3b in which the temperature is also equal to

$$T_z = T^\circ - T'\left[1 - \frac{(K'' - K)\,\bar{c}a^2}{3z^3(K+C_o(K''-K)}\right] \tag{A.16}$$

Equating these two expressions gives

$$\frac{(K' - K)\,f}{K+C_o(K'-K)} = \frac{(K'' - K)}{K+C_o(K''-K)} \tag{A.17}$$

which may be expanded to

$$\frac{K''}{K} = \frac{f(K'-K)(C_o-1) - (K+C_o(K'-K))}{C_o(K'-K)(f-1) - K} = \frac{f(\varepsilon-1)(C_o-1) - (1+C_o(\varepsilon-1))}{C_o(\varepsilon-1)(f-1) - 1} \tag{A.18}$$

For a spherical inclusion, $C_o = 1/3$ resulting in

$$\frac{K''}{K} = \frac{3K'f + (2K+K')(1-f)}{3Kf + (2K+K')(1-f)} = \frac{3\varepsilon f + (2+\varepsilon)(1-f)}{3f + (2+\varepsilon)(1-f)} \tag{A.19}$$

This agrees with the result given by Carslaw and Jaeger (1959, p.428) for the case of a granular material consisting of spherical inclusions.

For the case of gassy soil, it is assumed that the inclusions are gas and that there is no flow of water through the gas voids. Therefore K′ may be set to zero. Thus for a soil containing n_g volume fraction of gas inclusions

$$\frac{K''}{K} = k_r = \frac{n_g(C_o-1) + (1-C_o)}{1 - C_o(1-n_g)} = \frac{(1-C_o)(1-n_g)}{1 - C_o(1-n_g)} = 1 - n_g/[1-C_o(1-n_g)] \tag{A.20}$$

where k_r is defined as relative permeability of the composite material. It can be seen from the above equation that the relative permeability, k_r, is a function of both the shape and volume of the gas bubbles. This may be illustrated by evaluating the relative permeabilities for gas fractions between 0.0 and 0.1 and for aspect ratios 1, 2, 3, 4 and 5. The results are plotted and tabulated in Figure A.4 and Table A.1 respectively.

APPENDIX B

THE ELASTIC STRESS DISTRIBUTION AROUND AN OBLATE SPHEROIDAL CAVITY

B.1 Spheroidal Coordinate System

B.2 The Uniform Vertical Uniaxial Stress Field

B.3 The Uniform Horizontal Biaxial Stress Field

B.4 Evaluation of Stress Components Under Triaxial Loading Conditions

APPENDIX B

THE ELASTIC STRESS DISTRIBUTION AROUND AN OBLATE SPHEROIDAL CAVITY

B.1 Spheroidal Coordinate System

The axisymmetric oblate spheroidal coordinate system, as presented by Terzaghi and Richart (1952), may be defined by the equations of transformation

$$R = \cosh \alpha \sin \beta \quad \text{and} \quad Z = \sinh \alpha \cos \beta \tag{B.1}$$

where

$$R^2 = r^2/[a^2-c^2] \quad \text{and} \quad Z^2 = z^2/[a^2-c^2] \tag{B.2}$$

in which 2a and 2c are the width and height respectively of the oblate spheroid, r is the radial distance from the axis of symmetry and z is the height above the equator of the spheroid.

In addition, by considering any arbitrary point outside the spheroid, it can also be shown that

$$2\cos^2\beta = [(R^2+Z^2+1)^2 + 4Z^2]^{1/2} - [R^2+Z^2-1] \tag{B.3}$$

and that

$$2\sinh^2\alpha = [(R^2+Z^2-1)^2+4Z^2]^{1/2} - [R^2+Z^2-1] \tag{B.4}$$

Thus by combining equations B2 to B4, values of α and β can be evaluated from the cylindrical coordinates r and z.

The following notation was used in the expression for the stress components where α and β are the spheroidal coordinates and ν is the Poisson's ratio of the elastic body.

$$\left.\begin{array}{l} q = \cosh \alpha \; ; \; p = \cos \beta \\ \bar{q} = \sinh \alpha \; ; \; \bar{p} = \sin \beta \\ h^2 = -1/(\bar{q}^2+p^2) \end{array}\right\} \text{auxiliary position parameters for spheroidal coordinate system} \tag{B.5}$$

$$Q = 1 - \bar{q} \cot^{-1}(\bar{q}) \quad \text{auxiliary harmonic function for an oblate spheroid.}$$

The following sections describe the stress distribution around the spheroidal cavity caused by two types of uniform stress fields.

B.2 The Uniform Vertical Uniaxial Stress Field

The boundary conditions are: as $q \to \infty$; $\sigma_z \to 1.0$; σ_x, σ_y, τ_{xy}, τ_{yz}, $\tau_{xz} \to 0$ from which

$$a_{13} = \frac{\bar{q}_o^3}{D}\left[-\frac{1}{q_o^2} - Q_o\right] + \frac{2}{3}\frac{\bar{q}_o}{D}\left[2(1-\nu Q_o) - \frac{1}{q_o^2}\right] \tag{B.6}$$

$$a_{23} = \frac{\bar{q}_o}{D}\left[-\frac{1}{q_o^2} - Q_o\right] \; ; \; a_{33} = -\frac{2}{3}\frac{\bar{q}_o}{D}\left[2(1-\nu Q_o) - \frac{1}{q_o^2}\right] \tag{B.7}$$

$$D = -2(1+\nu)Q_o^2 + \frac{Q_o}{q_o^2}\left[-4(1-\nu) + 6q_o^2\right] - \frac{2}{q_o^2} + \frac{2(1-\nu)}{q_o^2\, q_o^2} \tag{B.8}$$

and

$$\left.\begin{aligned} \sigma_{\alpha_{o3}} &= q^2 + h^2q^2\bar{q}^2 \quad ; \quad \sigma_{\delta_{o3}} = 0 \\ \sigma_{\beta_{o3}} &= -\bar{q}^2 - h^2q^2\bar{q}^2 \; ; \quad \tau_{\alpha\beta_{o3}} = h^2q\bar{q}p\bar{p} \end{aligned}\right\} \tag{B.9}$$

$$\left.\begin{aligned} \sigma_{\alpha_{13}} &= -h^2\bar{q}\left[h^2 - \frac{1}{q^2}\right] \; ; \quad \sigma_{\beta_{13}} = -h^2h^2\bar{q} \\ \sigma_{\delta_{13}} &= -h^2\bar{q}\left[\frac{1}{q^2}\right] \quad ; \quad \tau_{\alpha\beta_{13}} = h^2h^2\,\frac{p\,\bar{p}}{q} \end{aligned}\right\} \tag{B.10}$$

$$\left.\begin{aligned} \sigma_{\alpha_{23}} &= -\frac{1}{\bar{q}}\left\{3 - 2\nu) + 2Q[(\nu - 1) - \bar{q}^2(1-2\nu) - \frac{1}{q^2}\right\} \\ &\quad - \bar{q}h^2\left\{2(1-\nu) - 2(1-2\nu)q^2Q - h^2\bar{q}^2 - \frac{1}{q^2}\right\} \\ \sigma_{\beta_{23}} &= -\frac{1}{\bar{q}}\left\{2\nu - 2Q\left[\nu - (1-2\nu)\bar{q}^2\right]\right\} + \bar{q}h^2\left\{-2(1-2\nu)q^2Q - h^2\bar{q}^2 - (1+2\nu)\right\} \\ \sigma_{\delta_{23}} &= \frac{1}{\bar{q}}\left\{2\nu Q - \left(\frac{2\nu-(1-2\nu)\bar{q}^2}{q^2}\right)\right\} + \bar{q}h^2\left\{1 - 2\nu - \frac{1}{q^2}\right\} \\ \tau_{\alpha\beta_{23}} &= h^2p\bar{p}\left\{-\frac{1}{q}\left[1 - 2\nu + h^2\bar{q}^2\right] + 2(1-2\nu)\,qQ\right\} \end{aligned}\right\} \tag{B.11}$$

$$\left.\begin{aligned} \sigma_{\alpha_{33}} &= -\frac{3}{2\bar{q}}\left\{-\frac{2+\bar{q}^2}{q^2} + (2+3\bar{q}^2)Q\right\} + \frac{3\bar{q}h^2}{2}\left\{\frac{3\bar{q}^2+5}{3q^2} - 3q^2Q - \frac{2}{3}h^2\right\} \\ \sigma_{\beta_{33}} &= -\frac{3}{2\bar{q}}\left\{1 - (1+3\bar{q}^2)Q\right\} - \frac{3\bar{q}h^2}{2}\left\{1 - 3q^2Q - \frac{2}{3}h^2\right\} \\ \sigma_{\delta_{33}} &= -\frac{3}{2\bar{q}}\left\{\frac{1}{q^2} - Q\right\} - \bar{q}\,\frac{h^2}{q^2} \\ \tau_{\alpha\beta_{33}} &= +\frac{3}{2}\,\frac{h^2p\bar{p}}{q}\left\{1 - 3q^2Q + \frac{2}{3}h^2\right\} \end{aligned}\right\} \tag{B.12}$$

Then σ_{α_3} for example, under the uniaxial vertical stress field is found at any point by:

$$\sigma_{\alpha_3} = \sigma_{\alpha_{o3}} - a_{13}\sigma_{\alpha_{13}} - a_{23}\,\sigma_{\alpha_{23}} - a_{33}\,\sigma_{\alpha_{33}} \tag{B.13}$$

B.3 The Uniform Horizontal Biaxial Stress Field

The boundary conditions are given by:

as $q \to \infty$; $\sigma_x = \sigma_y \to 1.0$ and $\sigma_z, \tau_{zx}, \tau_{zy}, \tau_{xy} \to 0$

$$a_{11} = -\frac{2}{3}\frac{\bar{q}_o}{Dq_o^2}\left\{3 - 2\nu - q_o^2 - q_o^2 Q_o[5 - 2\nu - 3q_o^2]\right\} \tag{B.14}$$

$$a_{21} = -\frac{2\bar{q}_o}{D}\left\{Q_o - \frac{1}{q_o^2}\right\} \tag{B.15}$$

$$a_{31} = \frac{2}{3}\frac{\bar{q}_o}{D}\left\{-\frac{2\nu}{q_o^2} - 2(1 - \nu)Q_o + 2\right\} \tag{B.16}$$

$$\left.\begin{aligned} &\sigma_{\alpha_{o1}} = -\bar{q}^2 - h^2 q^2 \bar{q}^2 \;;\quad \sigma_{\delta_{o1}} = 1.0 \\ &\sigma_{\beta_{o1}} = q^2 + h^2 q^2 \bar{q}^2 \;;\quad \tau_{\alpha\beta_{o1}} = -h^2 p\bar{p}q\bar{q} \\ &\tau_{\alpha\delta_{o1}} = \tau_{\beta\delta_{o1}} = 0 \end{aligned}\right\} \tag{B.17}$$

$$\sigma_{\alpha_{i1}} = \sigma_{\alpha_{i3}} \qquad i = 1,2,3 \tag{B.18}$$

$$\sigma_{\beta_{i1}} = \sigma_{\beta_{i3}} \qquad i = 1,2,3 \tag{B.19}$$

$$\sigma_{\delta_{i1}} = \sigma_{\beta_{i3}} \qquad i = 1,2,3 \tag{B.20}$$

$$\tau_{\alpha\delta_{i1}} = \tau_{\alpha\delta_{i3}} \qquad i = 1,2,3 \tag{B.21}$$

The component stress σ_α at any point produced by the uniform horizontal biaxial stress field is determined by

$$\sigma_{\alpha_1} = \sigma_{\alpha_{o1}} - a_{11}\,\sigma_{\alpha_{11}} - a_{21}\,\sigma_{\alpha_{21}} - a_{31}\,\sigma_{\alpha_{31}} \tag{B.22}$$

B.4 Evaluation of Stress Components under Triaxial Loading Conditions

From the above solutions, the stress σ_α at any point produced by the triaxial field is found by superposition of the stresses produced by each of the two stress fields. Therefore,

$$\sigma_\alpha = p_z \sigma_{\alpha_3} + p_r \sigma_{\alpha_1} \tag{B.23}$$

where p_z is the uniform vertical stress field and p_r is the uniform biaxial stress field. The determination of the other stress components is similar.

In addition to the four stress components σ_α, σ_β, σ_δ and $\tau_{\alpha\beta}$, it is possible to evaluate the first two stress invariants, the mean normal stress and the octahedral shear stress, from

$$\sigma_{oct} = \frac{1}{3}(\sigma_\alpha + \sigma_\beta + \sigma_\delta) \tag{B.24}$$

and

$$\tau_{oct} = \frac{1}{3}\left[(\sigma_\alpha - \sigma_\beta)^2 + (\sigma_\beta - \sigma_\delta)^2 + (\sigma_\delta - \sigma_\alpha)^2\right]^{1/2} \tag{B.25}$$